JPL Publication 91-28

Proceedings of the Third Airborne Visible/Infrared Imaging Spectrometer (AVIRIS) Workshop

May 20 and 21, 1991

Robert O. Green
Editor

August 1, 1991

NASA
National Aeronautics and
Space Administration

Jet Propulsion Laboratory
California Institute of Technology
Pasadena, California

This publication was prepared by the Jet Propulsion Laboratory, California Institute of Technology, under a contract with the National Aeronautics and Space Administration.

FOREWORD

Reference is made to color slides in the text and figure captions of some of the papers; these 35-mm slides are located in a pocket at the end of the Proceedings. They are color versions of some of the referenced black-and-white figures within the Proceedings.

ABSTRACT

The Third AVIRIS Workshop was held on May 20 and 21, 1991 at the Jet Propulsion Laboratory, California Institute of Technology, Pasadena, California. This workshop followed the successful operation of AVIRIS for acquisition of more than 1000 calibrated data scenes during 1989 and 1990. Attendance at the 2-day workshop exceeded 250 persons with 43 presentations and posters given. Results were presented for the scientific disciplines of ecology, geology, limnology, snow hydrology, atmospheric water vapor studies, oceanography, cloud studies, calibration, and quantitative data analysis. As in previous years, the presentations demonstrated the continuing trend towards quantitative utilization of imaging spectroscopy data to address research questions over a wide range of Earth science disciplines.

AVIRIS has flown successfully in 1991 throughout the western United States. In June and July 1991, AVIRIS operated for 6 weeks in Europe acquiring data for scientists pursuing a diverse set of investigations. Results from these 1991 North American and European data and further analyses of the data collected in 1989 and 1990 will be presented at the Fourth AVIRIS Science Workshop, which is planned for summer 1992.

CONTENTS

AVIRIS OVERVIEW ABSTRACT

Robert O. Green
Jet Propulsion Laboratory
California Institute of Technology
Pasadena, California

The Airborne Visible/Infrared Imaging Spectrometer (AVIRIS) is a National Aeronautics and Space Administration (NASA)-sponsored Earth-observing imaging spectrometer designed, built, and operated by the Jet Propulsion Laboratory (JPL). AVIRIS acquires flight data from the Q-bay of a NASA ER-2, operated at the NASA Ames Research Center. This imaging spectrometer measures the total upwelling radiance from 400 to 2450 nm in the electromagnetic spectrum through 224 channels at 10-nm spectral intervals. Data are acquired as 11- by ≤100-km images with 20- by 20-m spatial resolution. These data are rigorously calibrated for their spectral, radiometric, and geometric characteristics.

An example of AVIRIS data sets acquired over Mount Shasta in northern California is given in Slide 1. The front panel of this image presents the spatial content of three AVIRIS radiance channels. The upper and right panels of the image display the 224 spectral channels from the upper and right margins of the data set. Slide 2 shows the 224 individual spectral images of Mount Shasta measured from 400 to 2450 nm at 10-nm intervals. In this sequence of images, the transition in the spectral reflectance of snow from high to low in the region from 1000 to 1200 nm is measured. Aspects of the spectral signatures of clouds and several volcanic rock units are also apparent in this image.

Mapping with Imaging Spectrometer Data Using the Complete Band Shape Least-Squares Algorithm Simultaneously Fit to Multiple Spectral Features from Multiple Materials

By

Roger N. Clark[1], Gregg A. Swayze[1], Andrea Gallagher[1],

Noel Gorelick[1], and Fred Kruse[2]

[1] U. S. Geological Survey
Box 25046 Federal Center
Denver, CO 80225

[2] Center for the Study of Earth from Space (CSES), CIRES
and Dept. of Geological Sciences
Univ. of Colorado, Boulder, CO 80309

The algorithm for least squares fitting spectroscopic absorption bands with features from library reference spectra, first reported by Clark, Gallagher and Swayze (1990, Proceedings of the Second Airborne AVIRIS Workshop, JPL Publication 90-54, pp. 176-186), has been substantially extended. The same basic algorithm is still used, but multiple absorption features are fit at one time, and the fits from multiple minerals are compared to determine what mineral absorption features are present in the spectrum. While the method works equally well on any material having diagnostic absorption features, this abstract considers discrimination and mapping of minerals.

This new method substantially increases the ability to discriminate between two minerals. The algorithm has been thoroughly tested using mineral spectra where controlled amounts of noise have been added. For example, the minerals calcite and dolomite have very similar, mostly overlapping absorption bands near 2.3 μm. Noise was systematically added to spectra of calcite and dolomite and the spectra fit with reference spectra of calcite and dolomite, as well as a suite of other minerals. It was found that calcite can be separated from dolomite at a signal-to-noise of about 7 at AVIRIS spectral resolution. Other minerals are separated at much lower signal-to-noise levels. Other mineral combinations have been separated at similarly low signal-to-noise levels. Use of multiple diagnostic absorption features should allow discrimination at even lower signal to noise levels.

When mapping multiple minerals and multiple features, spectral regions are grouped. For example, the 2.3-μm region may be analyzed for chlorites, carbonates, Mg-bearing clays, and other minerals having diagnostic features in the 2.3-μm region. Then the 2.2-μm region is analyzed for minerals such as montmorillonites, muscovites, illites, kaolinites, and other minerals having 2.2-μm features. The 1.0-μm region is analyzed for minerals having diagnostic electronic transitions, like hematite, goethite, ferrihydrite, nontronite, jarosite and others. Thus, the analysis of the whole spectrum may find multiple minerals, one in each spectral region. Mineral mixtures may also be analyzed by using reference library spectra of mixtures.

The multiple feature, multiple material algorithm has been applied to mapping minerals at Canon City, Colorado, as well as at Cuprite, Nevada.

At Canon City, 10 minerals have been mapped using AVIRIS data from September, 1989 where the signal-to-noise is typically 25 at a reference albedo of 50%. The minerals hematite, goethite, Na-montmorillonite, Ca-montmorillonite, well-crystallized kaolinite, poorly crystallized kaolinite or halloysite, calcite and dolomite are the primary minerals mapped. Also mapped is a medium crystalline kaolinite and a ferrihydrite or amorphous iron. The mineral maps differentiate shales, sandstones, conglomerates, dolomites and limestones, and subtle variations within the units. Field work has confirmed most minerals mapped, although verification of ferrihydrite or amorphous iron is proving difficult.

At Cuprite, Nevada, 19 minerals have been mapped and 14 additional minerals were searched for but not detected using 1990 AVIRIS data. Minerals found are: hematite, goethite, jarosite, potassium alunite, two natroalunites containing 65 and 80 mole percent Na, highly-crystalline and medium-crystalline kaolinite, poorly crystalline kaolinite or halloysite, dickite, Na-montmorillonite, Ca-montmorillonite, calcite, dolomite, buddingtonite, ammonium illite smectite, opal, Fe-chlorite, and paragonite.

The alteration mapped at Cuprite spectrally corresponds closely to previously published studies. The differentiation of members of the alunite solid solution series and the gradational trend from well-crystallized kaolinite to poorly crystallized kaolinite with increasing distance from the alunite zones shows the alteration in more detail than has previously been mapped. Although complete field verification of these minerals will take considerable work, some minerals have already been confirmed using a field portable spectrometer (Huntington, personal communication): dickite, potassium alunite, natroalunites, and variation in kaolinite crystallinity. Field samples have been analyzed and jarosite, kaolinites, alunites, buddingtonite, ammonium illite smectite, calcite, hematite, and goethite are verified in at least some localities in the image.

This new mapping algorithm can be used to map spectral features in imaging spectrometer data in both emission and absorption, and should be applicable to all disciplines using spectroscopy: geology, botany, oceanography, ice and snow research, and atmospheric research.

Sedimentary Facies Analysis Using AVIRIS Data : A Geophysical Inverse Problem

Joe W. Boardman and Alexander F. H. Goetz
Center for the Study of Earth from Space
Cooperative Institute for Research in Environmental Sciences
University of Colorado
Boulder, Colorado

Abstract. AVIRIS data can be used to quantitatively analyze and map sedimentary lithofacies. The observed radiance spectra can be reduced to "apparent reflectance" spectra by topographic and reflectance characterization of several field sites within the image. These apparent reflectance spectra correspond to the true reflectance at each pixel, multiplied by an unknown illumination factor (ranging in value from zero to one). The spatial abundance patterns of spectrally defined lithofacies and the unknown illumination factors can be simultaneously derived using constrained linear spectral unmixing methods. Estimates of the minimum uncertainty in the final results (due to noise, instrument resolutions, degree of illumination and mixing systematics) can be made by forward and inverse modeling. Specific facies studies in the Rattlesnake Hills region of Wyoming illustrate the successful application of these methods.

I. Introduction

This study illustrates how AVIRIS data can be used to study sedimentary facies. The problem is cast in the form of a geophysical inversion process. A forward model, describing the relationship between the observed radiance and the surficial composition, is developed and then inverted. The inversion process, employing a modified linear spectral unmixing technique, permits quantitative mapping and analyses of sedimentary lithofacies. However, a lower bound exists on the uncertainty associated with such spectral unmixing results. Noise in the data, the local degree of illumination, finite spectral and radiometric resolutions and the spectral mixing systematics of the particular lithofacies being studied all combine to create some uncertainty in the unmixing results. A method of modeling and deriving this limiting uncertainty is illustrated here. This minimum uncertainty is in general different for each spectrally-defined lithofacies being studied and different for each pixel within the AVIRIS scene. Using geophysical inversion methods to analyze AVIRIS data permits derivation of quantitative geological results, and equally important, estimation of the uncertainty in these results.

The process outlined here demonstrates how AVIRIS data can be used, subsequent to initial field work, to extend the results of that field work over large areas. The process has several steps. First, the observed AVIRIS radiance data are reduced to "apparent reflectance" (modeling true reflectance multiplied by some unknown illumination factor between zero and one at each pixel). Then, the spectral distribution of noise in the data is derived using a new method. Limited field work is conducted to observe and to spectrally characterize the materials present on the surface, including the lithofacies outcrops of interest and all other abundant surface materials. Then, a constrained linear unmixing method is used to derive images of the spatial patterns of abundance of the various surface materials. Next, iterations of simulated forward and inverse modeling of the spectral mixing are performed to derive the minimum systematic uncertainty for each endmember at each individual pixel. This last process creates "uncertainty images" corresponding to the "endmember abundance images" derived by the foregoing spectral unmixing. Finally, sedimentary facies mapping and analyses are performed using the abundance and uncertainty images.

II. Reduction of Radiance to Apparent Reflectance

The observed spectral radiance at the AVIRIS instrument can be modeled as the sum of two terms, path radiance and reflected radiance. If a Lambertian model of the surface is used, diffuse

irradiance is ignored and the atmosphere is assumed to be uniform, then the observed radiance can be modeled as follows.

$$L_o(s,l,\lambda) = L_p(\lambda) + (1/\pi)*E_{sun}(\lambda)*T_{tw}(\lambda)*IF(s,l)*R(s,l,\lambda)$$

Sample, line and spectral channels are denoted by s, l and λ respectively. L_o and L_p are the observed and path radiance values, E_{sun} is the solar irradiance spectrum, T_{tw} is the two-way atmospheric transmission spectrum, IF is the local illumination factor (cosine of the local solar incidence angle) and R is the reflectance spectrum for the surface. Apparent reflectance is defined as IF*R. A pixel oriented normal to the solar incidence direction will have an IF of 1.0, so the apparent reflectance and true reflectance will be equal. A pixel receiving little irradiance, shaded by topography or turned away from the sun, will have an IF of near zero and a very low apparent reflectance spectrum.

Five ground sites were spectrally characterized with a field spectrometer and the local slopes and aspects were recorded to permit calculation of offset (L_p) and gain ($(1/\pi)*E_{sun}*T_{tw}$) spectra for reduction to apparent reflectance . Local IF values for these sites were calculated using the field measurements in conjunction with the calculated azimuth and elevation of the sun at the time of AVIRIS overflight (AZ=187.5, EL=37.0, time=10/18/89 19:20 GMT). The observed reflectance, calculated IF values and the 70 extracted AVIRIS radiance spectra (corresponding to the ground sites) were used to solve, on a band-by-band basis, a system of 70 linear equation in two unknowns. The resulting path radiance (offset) and maximum reflected radiance (gain) spectra are shown in Figure 1. The Lp offset spectrum shows the expected low level and the fall-off at longer wavelengths, associated with atmospheric scattering. The $(1/\pi)*E_{sun}*T_{tw}$ gain spectrum shows the combined effects of solar irradiance and atmospheric absorption. The observed radiance spectra can now be reduced to apparent reflectance by subtracting the L_p spectrum and dividing by the $(1/\pi)*E_{sun}*T_{tw}$ spectrum. Three typical reduced spectra are shown in Figure 2.

III. Derivation of Noise Levels

The spectra shown in Figure 2 obviously are contaminated with considerable noise. A measure of this noise is essential in any attempt to use these data quantitatively. An improved method for noise derivation, more widely applicable than past methods, is outlined here. Past methods have required a large and spectrally uniform target, such as a playa or runway, for noise derivation. Such targets are not found in most AVIRIS scenes. The method presented here allows for some natural variance in the area chosen for noise derivation. The observed variance is modeled as the sum of the natural and noise variances.

The most nearly uniform large area of the scene is selected and the associated spectra are extracted from the AVIRIS radiance data. The standard deviation of these pixels, band-by-band, is calculated to form a "standard deviation spectrum". Then the spectra are averaged together in groups of two and another standard deviation spectrum is calculated. This process is repeated, averaging the pixels in groups of 4, 5, 8, 10, 16, 20 and 25. For each band, nine standard deviations are calculated, each corresponding to a different degree of spatial averaging. The noise level in a band can be estimated by fitting a line to these calculated points after they are plotted versus the reciprocal of the square root of the number of pixels averaged. The noise portion of the variance should drop predictably. The natural variance should remain nearly constant until the spatial averaging crosses a natural "texture scale" of the area being used. By examining the linearity of these plots, the validity of the underlying assumptions can be assessed. Application to a typical AVIRIS band is shown in Figure 3.

The derived noise level represents an estimate of the standard deviation of the noise at each spectral band, in terms of apparent reflectance. This spectrum is shown in Figure 4. Since the apparent reflectance signal varies both spatially and spectrally, so does the signal-to-noise-ratio. Poorly illuminated and/or low reflectance pixels have lower signal-to-noise ratios than fully illuminated

and/or high reflectance pixels. Figure 5 shows the mean signal-to-noise spectrum for the three AVIRIS segments studied. The low signal-to-noise levels are a result of the low signal levels, in turn caused by the low sun angle at the time of the mid-October acquisition. The derived noise level spectrum (Figure 4) plays a key role in modeling the uncertainty in the results of the spectral unmixing procedure.

IV. Modified Linear Spectral Unmixing and Uncertainty Modeling

A modified linear spectral unmixing method is used to map the spatial distributions of, and thus the stratigraphic relationships among, the lithofacies being studied. Field spectral measurements and laboratory measurements of field samples are used to form a mixing library for the specific region being studied. The AVIRIS apparent reflectance spectra are modeled as linear combinations of these endmember spectra. A system of simultaneous equations can be developed at each pixel and solved in a least-squares sense to estimate the abundance of each endmember material within each pixel.

Several modifications are made to this least-squares procedure, compared to similar applications previously reported by other workers (Adams and others, 1986; Gillespie and others, 1990). The apparent reflectance spectra, reduced from the observed AVIRIS radiance spectra, are unmixed using absolute reflectance spectral endmembers. The derived abundances are constrained to be non-negative and to sum to one or less, using the numerical methods described by Lawson and Hanson (1974). The effect of these two modifications is to allow a simultaneous derivation of estimates for the unknown endmember abundances and the unknown local illumination factor, IF, at each individual pixel. This method treats illumination and shadowing effects as an unknown gain factor, IF, rather than including shade as a mixing endmember as done by others (Gillespie and others, 1990). The gain factor method is numerically more stable since the shade endmember, by definition a very dark spectrum, makes the mixing library more ill-conditioned (Menke,1984; Press and others, 1986) since it is nearly linearly dependent with all spectra in the library and their linear combinations.

Noise, finite resolutions, variable illumination and the mixing systematics of the particular library combine to limit the certainty in unmixing results. Forward modeling, simulations of observed data, can be used to derive this lower limit on uncertainty. The mixing library is modified to match the spectral and radiometric resolutions of the AVIRIS instrument. Then the spectra are mixed, in known proportions, and degraded by the addition of a proper noise spectrum. Unmixing of many of these simulated spectra provides estimates of the minimum uncertainty for each endmember as a function of abundance of every endmember and the degree of illumination.

V. Facies Study Example

An example study is illustrated here of the Cretaceous Frontier and Mowry Formations, which crop out in the Rattlesnake Hills region of central Wyoming. The Rattlesnake Hills area has been previously mapped and studied, using conventional field methods (Bogrett,1951; Pekarek, 1974). The Mowry Formation is a siliceous ridge-forming shale and the Frontier is a thick sequence of interbedded and discontinuous sandstone and black shale facies. A bentonite bed also occurs near the contact between the two formations. This example illustrates how spectral unmixing of AVIRIS data, applied after initial field work, can successfully create detailed lithofacies maps for these clastic formations.

The first step in the process is the spectral characterization of the common materials found on the surface in the study area. The surface materials were divided into seven mixing endmembers, four lithofacies (Mowry shale, Frontier sandstone, Frontier black shale and the bentonite unit) and three unrelated but abundant surface materials (green vegetation, dry vegetation and soil A horizon). The reflectance properties of these "pure" endmember materials were measured using a field spectrometer in a laboratory setting. Composite average spectra, convolved with the AVIRIS spectral bandpasses, are shown in Figure 6. These seven spectra form the mixing library.

The spatial patterns of abundance of each of the seven endmembers were determined using modified linear spectral unmixing. The AVIRIS data, reduced to apparent reflectance spectra, were unmixed using the seven-member library of absolute reflectance spectra. The sum of the seven derived abundances, each constrained to be positive, is an estimate of the local illumination factor, IF. At each pixel the derived abundances were normalized by this sum to form abundance images relatively uninfluenced by illumination variation. These normalized abundance images and the corresponding IF image are shown in Figure 7. Also shown is the root-mean-square error image illustrating the goodness of fit between the modeled and observed spectra. These nine images illustrate how the geologic information in AVIRIS data can be extracted and quantified using spectral unmixing methods. The stratigraphic relationships among the various lithofacies can be mapped and analyzed using these results and an image processing workstation. Figure 8 shows the unmixing results for a single pixel found to be rich in bentonite. This figure illustrates the advantage of using the full spectral range for curve-fitting, as opposed to analysis of discrete spectral absorption features such as the clay band at 2.2 μm. The noise in the data prevents a direct visual identification of the spectral feature but the unmixing method, using all but the 60 noisiest channels, was able to correctly identify the surface composition.

Minimum unmixing uncertainties in the unmixing results were modeled using the methods outlined above. Figure 9 shows images of the uncertainties for the abundance images of Figure 7. Each endmember has a unique sensitivity to noise and instrument resolutions in the context of the particular mixing library. The black shale endmember, devoid of spectral features and low in albedo, has the least distinct spectrum and accordingly the highest uncertainty. Conversely, the vegetation endmembers, being more linearly independent, have the lowest uncertainties. For a single endmember, the uncertainty varies spatially due to illumination variation and changes in abundance of the other mixing endmembers.

VI. Conclusions

Geophysical inversion methods can be applied to AVIRIS data to quantitatively map and analyze sedimentary lithofacies. The modified linear spectral unmixing approach, outlined here, provides a numerically stable method for the simultaneous derivation of endmember abundance and illumination patterns. Using forward modeling methods and an accurate noise level spectrum, the minimum uncertainty for each endmember at each pixel can be determined. This application of geophysical methods to AVIRIS data analysis illustrates the usefulness of the data. Even in the presence of significant noise, lithofacies information and associated uncertainties can be derived.

References

Adams, J.B. and Smith, M.O., 1986, Spectral mixture modeling : a new approach to analysis of rock and soil types at the Viking lander 1 site, J. Geoph. Res., v. 91, p. 8098-8112.

Bogrett, J.W., 1951, Geology of the northwestern end of the Rattlesnake Hills, Natrona County, Wyoming, M.S. thesis , University of Wyoming.

Gillespie, A.R., Smith, M.O., Adams, J. B., Willis, S.C. , Fischer III, A.F. and Sabol, D.E., 1990, Interpretation of residual images : Spectral mixture analysis of AVIRIS images, Owens valley, California, in: Proceedings of the Second Airborne Visible/Infrared Imaging Spectrometer (AVIRIS) Workshop, JPL Pub. 90-54, 243-270.

Lawson, C.L. and Hanson, R.J., 1974, Solving least square problems, Prentice-Hall, Englewood Cliffs, N.J.

Menke, W., 1984, Geophysical data analysis: discrete inverse theory, Academic Press, Orlando.

Pekarek, A.H., 1974, Structural geology and volcanic petrology of the Rattlesnake Hills, Wyoming, Ph.D. dissertation, University of Wyoming.

Press, W.H., Flannery, B.P., Teukolsky, S.A. and Vetterling, W.T., 1986, Numerical Recipes, Cambridge University Press, New York.

Acknowledgments

This work was conducted at the Center for the Study of Earth from Space at the University of Colorado. The first author was funded through a NASA Graduate Student Researcher Fellowship, through JPL, NGT-50490. Other funding came from a NASA grant to the second author, NGT-958039. We also wish to thank Dr. Harold Lang for his insights into the local geology and the local landowners for providing access to the study area.

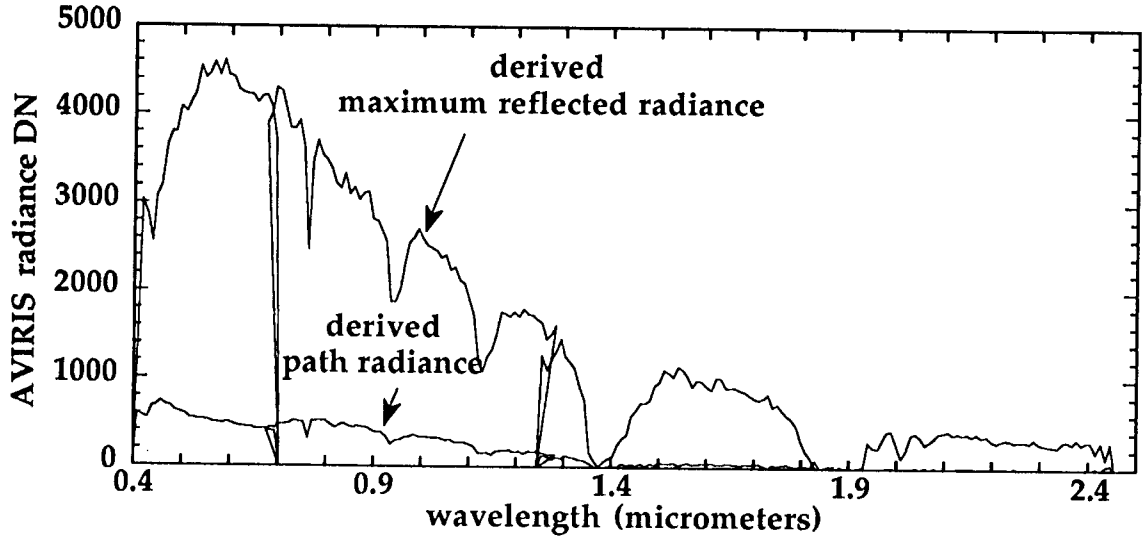

Figure 1. Derived gain and offset spectra.

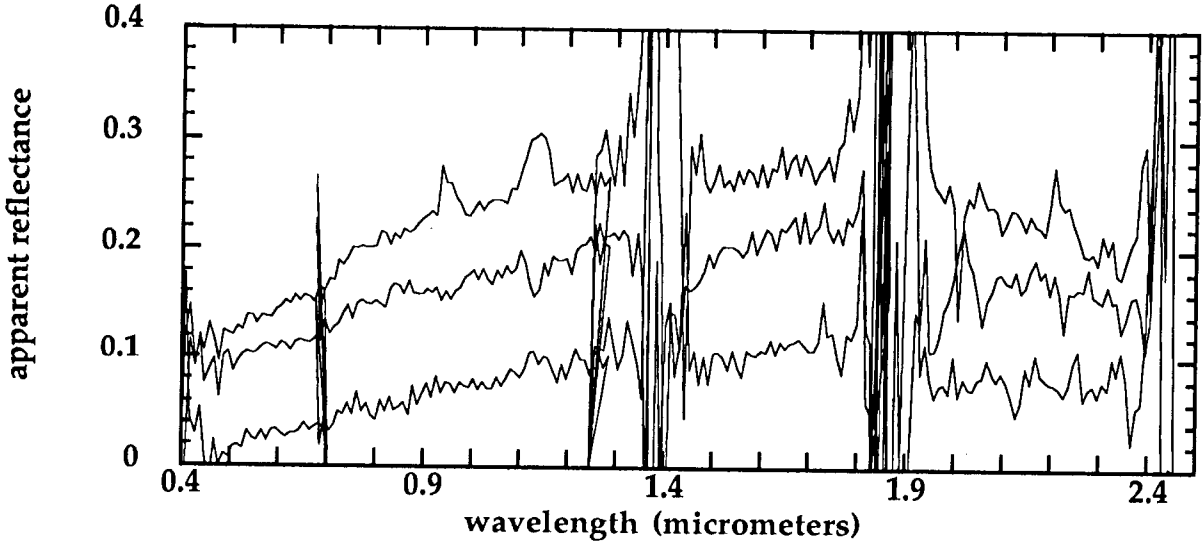

Figure 2. Three typical apparent reflectance spectra.

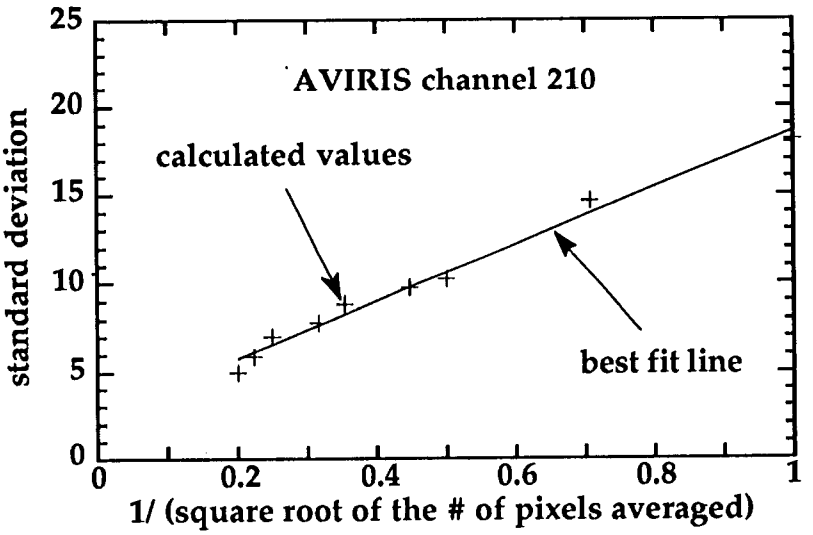

Figure 3. Application of the new noise derivation to AVIRIS band 210.

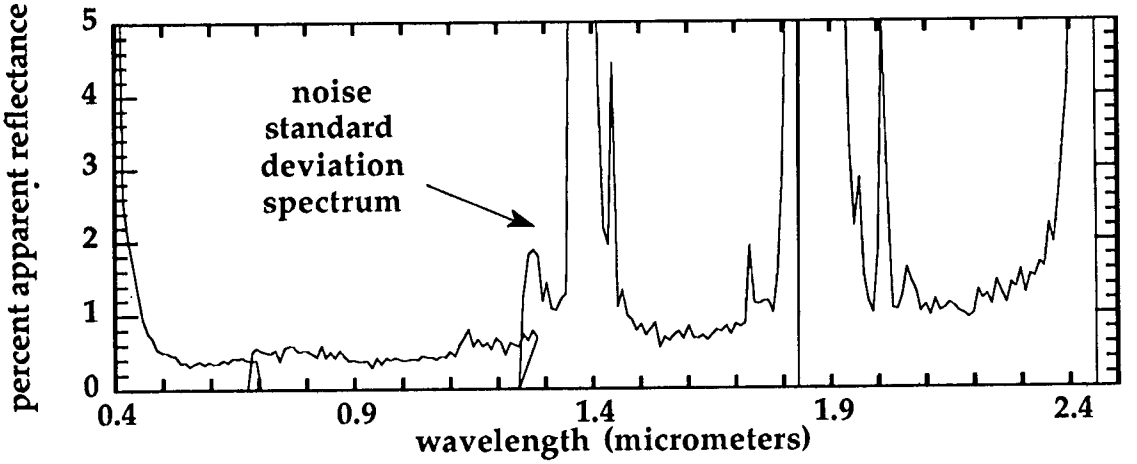

Figure 4. Noise standard deviation spectrum.

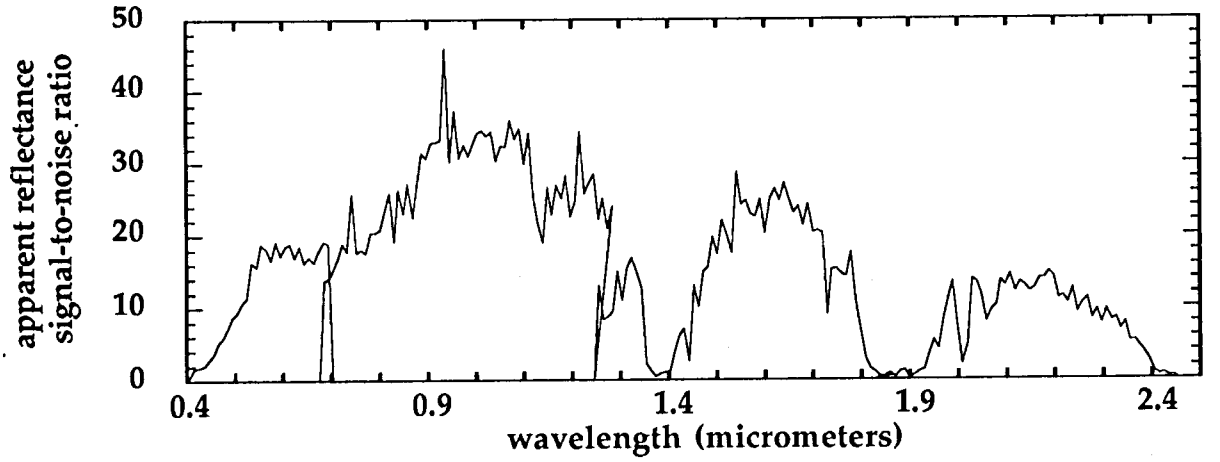

Figure 5. Mean signal-to-noise ratio spectrum.

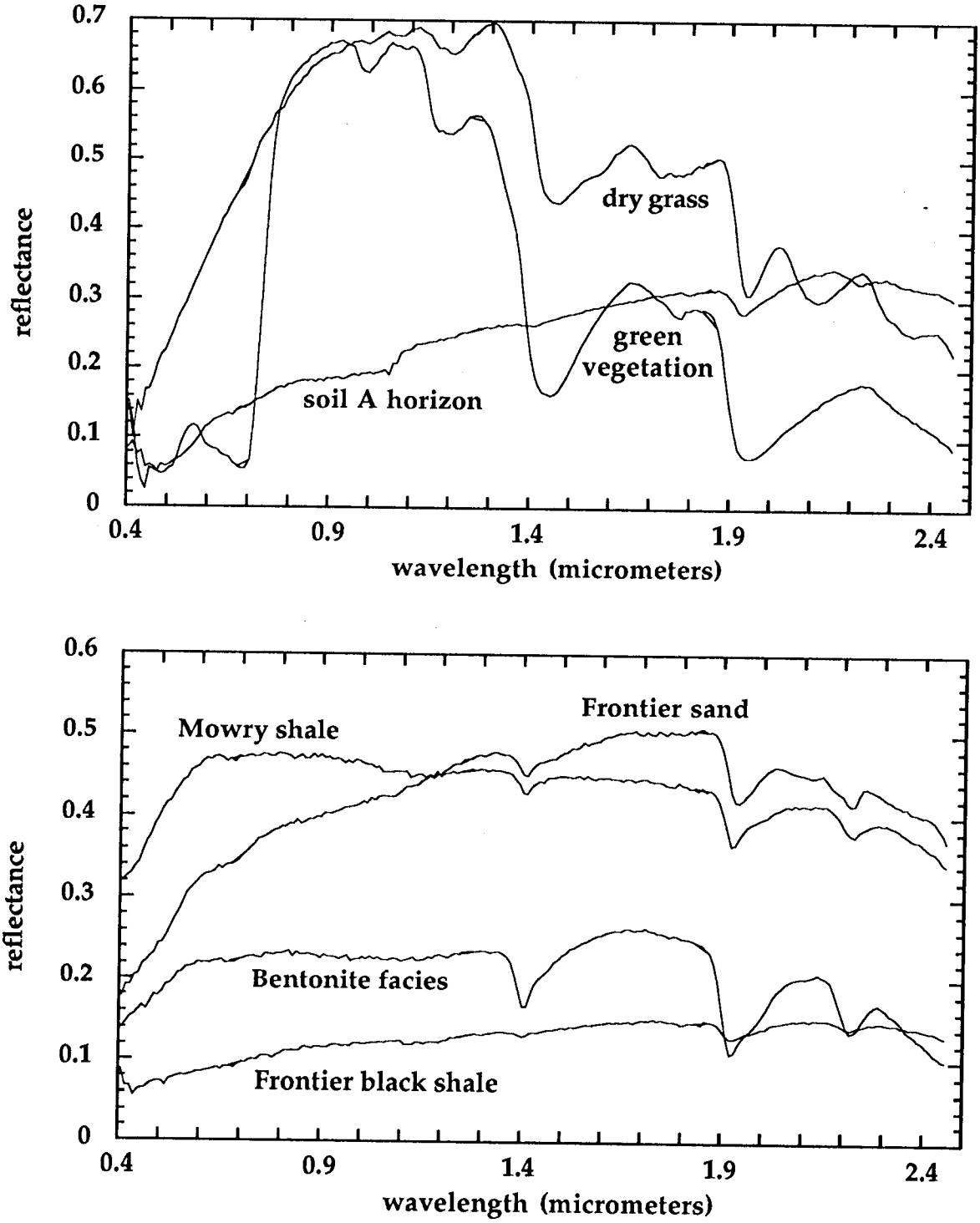

Figure 6. Frontier/Mowry mixing library endmembers.

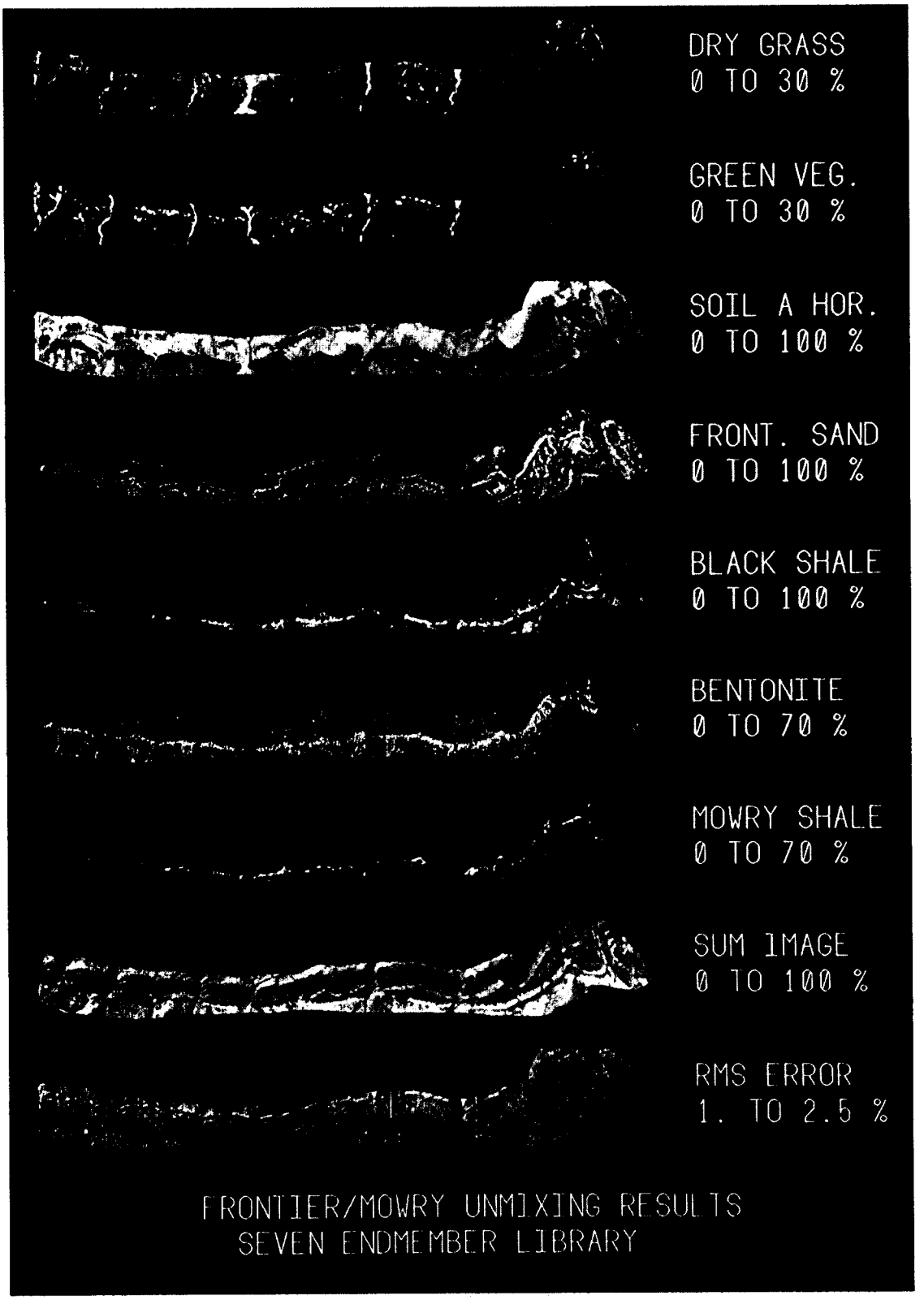

Figure 7. Endmember abundance images.

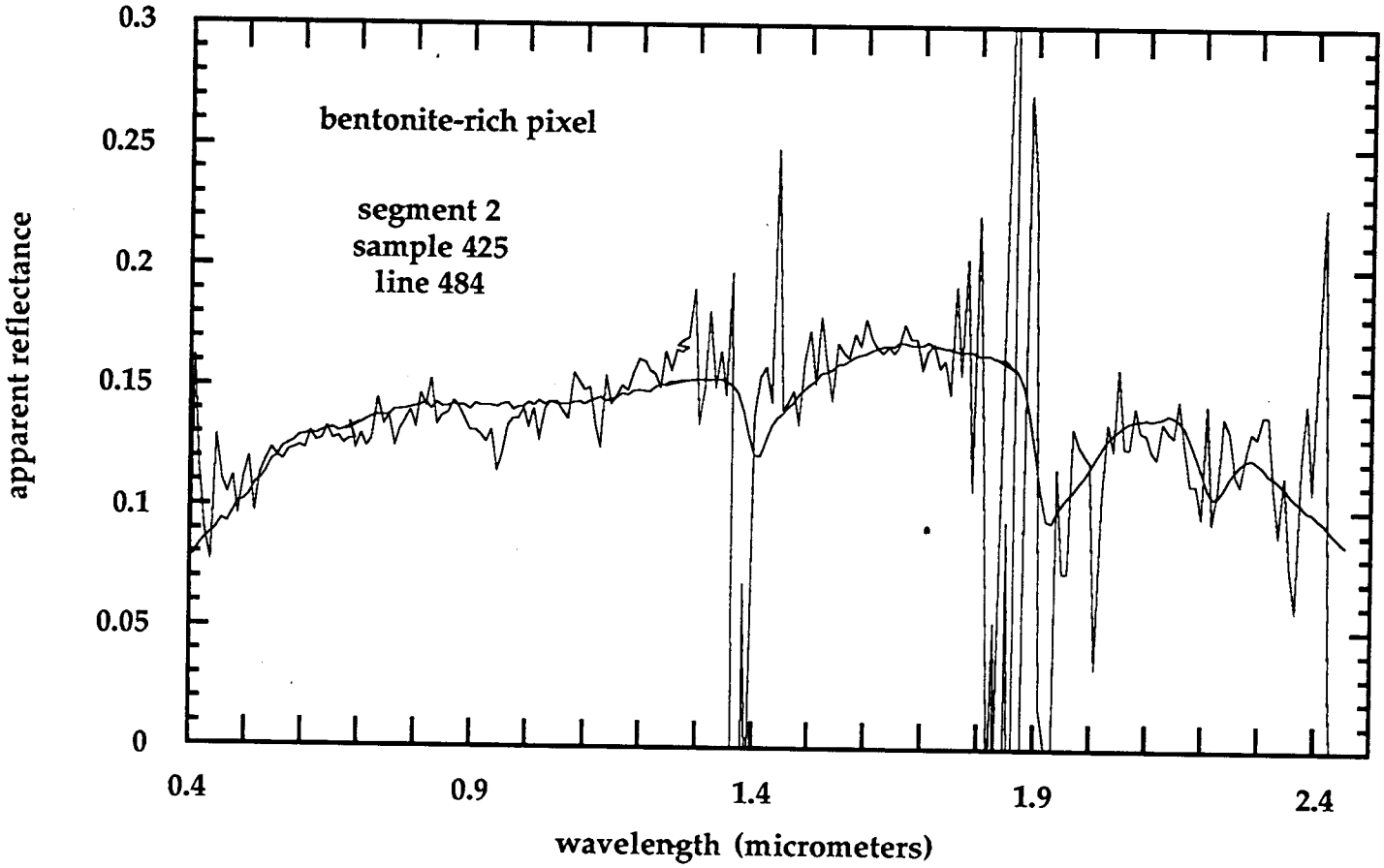

Figure 8. Single pixel observed spectrum and best fit model.

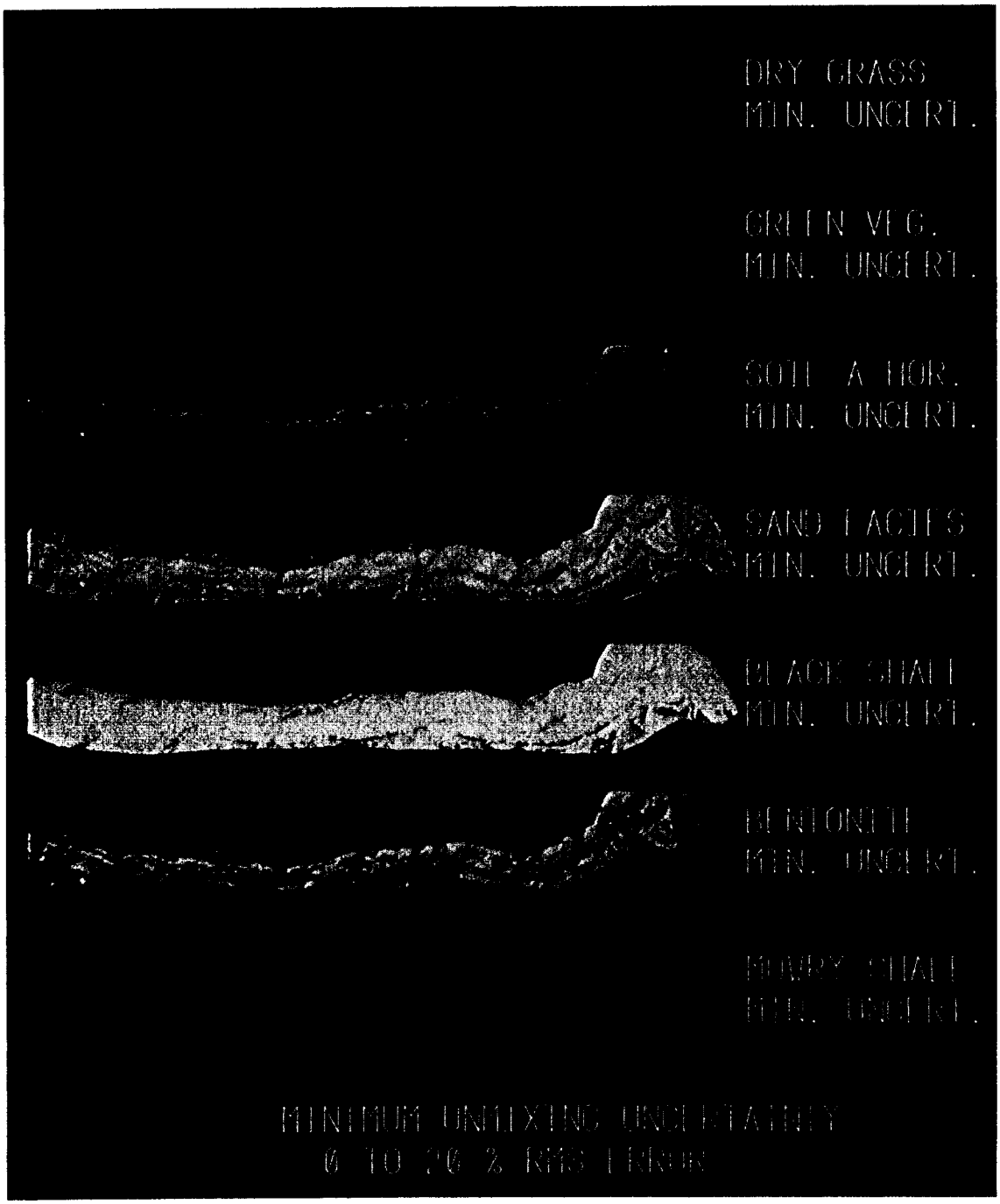

Figure 9. Minimum uncertainty images corresponding to Figure 7.

Distributions of Soil, Rock, and Grass in the Western Foothills of the Sierra Nevada

John F. Mustard
Department of Geological Sciences
Brown University, Providence RI

Abstract

A linear mixing model is used to model the spectral variability of an AVIRIS scene from the western foothills of the Sierra Nevada. This approach permitted a preliminary estimate of the ground reflectance to be derived. Residual calibration issues that remain are well understood and will be corrected in the future. Five spectral endmembers from the AVIRIS data plus a model shade were used to model the continuum reflectance of each pixel of the AVIRIS image. Three of these endmembers exhibit spatial associations and spectral properties that are best interpreted as different soil types. Composition is clearly a controlling factor on the observed distributions of the different soil types.

I Introduction

Understanding the role of soils as an element in the global climatic web is an important new direction identified as part of NASA's Land Processes investigations. Soils represent the interface between the atmosphere and solid earth and mark a dynamic region for the formation, evolution, and exchange of gases, organic compounds, and mineral constituents. An important step towards determining the global implications of soil processes is developing an inventory of soil types and their spatial distributions. This information also plays a fundamental role in unravelling time dependent evolution of landscapes and climatic influences. It is desirable to identify and map soil types from remote sensing platforms to take advantage of the synoptic perspectives vital to understanding regional to global scale issues. Initial results of an investigation to map the spatial distribution and abundance of surface materials with an emphasis on soil distributions are presented here. In this investigation, AVIRIS data are used, in coordination with laboratory spectral data and analyses, to conduct the majority of the tasks because of the significant advantages of high spectral and spatial resolution data for discriminating subtle differences in soil properties.

II Field Site

The location of this study lies primarily within the Kaweah serpentinite melange in the western foothills of the Sierra Nevada near Fresno CA (Figure 1). The topography is hilly, but smoothly varying with few extensive rock faces or cliffs and a maximum topographic variation of ≈200 meters. The substrate lithology of the region is dominated by the components of a tectonically deformed ophiolite melange in the western half of the site and volcanoclastic sediments and plutonic rocks of the Sierra Nevada in the eastern half. The distribution of primary rock types and general mineral constituents of the melange is well known from extensive field studies conducted by J. Saleeby (Saleeby, 1977; 1978; 1984). Substantial blocks of the coherent ophiolite components generally occupy the higher topographic regions while the intervening regions are composed of the compositionally complex melange. The overall composition of the substrate is mafic to ultramafic and therefore contains abundant magnesium and iron and little potassium, sodium, etc. The extent of the melange can readily be recognized by the distinct lack of trees and uniform cover of soils and grasses. In regions with little or no rock exposure the surface is composed of a mixture of grasses and soil. Although the abundance of grass is quite variable, 100%, or even 50% cover by grass is rare the soils are generally well exposed.

Surface Materials

There are four primary surface materials exposed in the field site: green vegetation, senescent grasses, rock, and soil. Green vegetation will not be treated in any detail since it is restricted primarily to irrigated fields, active water courses, and hills in the northeastern corner of the site.

The lithologic components underlying this region are extraordinarily complex and diverse. Because of the primarily mafic and ultramafic mineralogy, these components are well distinguished by visible to near-infrared reflectance spectra. A selection of reflectance spectra representative of the diversity of the block and matrix lithologies is shown in Figure 2a. These materials are both characterized and distinguished by the strength, position, and shape of the broad ferric and ferrous absorptions between 0.5 and 1.4 μm and the narrow hydroxyl overtone and combination overtones near 1.4 μm and longwards of 1.8 μm. Based on the characteristics of these spectral features it is possible to identify the mineral species (i.e. Burns, 1970; Farmer, 1974; Hunt and Salisbury, 1970), the abundance of minerals (Clark 1987; Mustard and Pieters, 1987a; 1989), and estimate the chemical composition of the minerals (Sunshine, et al, 1990; Mustard, 1990).

Laboratory reflectance spectra of representative vegetation components are shown in Figure 2b. The spectra of the grasses are the most important for this analysis and will be discussed briefly. The spectrum of senescent grass is characterized by a very steep and smooth rise in reflectance between 0.4 and 0.7 μm with cellulose, lignin, and molecular water absorptions longwards of 1.2 μm (Elvidge, 1988). The spectrum of partially decayed grasses differs from senescent grasses primarily in the shape of the spectrum between 0.3 and 1.3 μm where the decay grasses exhibit a distinct slope. The differences in albedo are not considered important since this depends on the albedo of the starting material (i.e. stalks, leaves, seed pods). All components of senescent grasses exhibit broadly similar spectral features but the overall albedo varies with the plant part. Fires are not uncommon in this region and a spectrum of burnt grass is included for comparison to the green and senescent vegetation.

Laboratory reflectance spectra of bulk soil specimens collected from the field site are shown in Figure 2c. Common to all these spectra are the bound water and hydroxyl absorptions near 1.4 and 1.9 μm. Longwards of 2.0 μm are narrow absorptions near 2.2 and 2.3 μm probably due to Al-OH and Mg-OH combination overtones. In the visible to near-infrared wavelength region (0.3 to 1.7 μm) the spectra of these soils are distinguished by iron absorptions. The reddish soil (D) exhibits a strong absorption near 0.5 μm and a weak absorption near 0.9 μm indicating the presence of ferric iron. The two strongly sloped spectra of soils B and C also exhibit weak ferric absorptions. The strong positive slope towards longer wavelengths indicates the probable presence of ferrous iron as well.

III Analysis

Data Reduction and Calibration Estimates

AVIRIS data were acquired over this region on October 2, 1989 under generally clear conditions. Although it was not possible to coordinate field activities for this overflight, field observations, collection of surface samples, and measurement of field reflectance using the PIDAS spectrometer had been accomplished in June and September 1987. There are few time invariant, large spatially and compositionally homogeneous regions of the surface in the AVIRIS window that could be used as calibration targets. However an extensive library of spectra representative of the surface materials in the field site has been developed and therefore the mixing method approach to calibration discussed in detail by Smith et al (1990) and Gillespie et al (1990) was employed as a guide for calibration. The raw AVIRIS data were first corrected to radiance using engineering and calibration files provided by JPL. These corrected data were inspected channel by channel for data quality and image channels with poor quality were discarded. For this analysis only data from the A, B, and C spectrometers were used. A total of 104 channels out of 160 was selected. A subsection of the total image that included agricultural lands was then extracted. An interactive linear mixture analysis was performed on this subset to identify the image endmembers. A small number of image endmembers were selected that best describe the overall spectral properties of the scene. For the initial subset of the total scene 4 image endmembers plus shade were required to accurately model the scene radiance.

The 4 image endmembers were then compared to the spectral library developed for this site using the linear gain, offset, and fractional abundance relationships given by Smith et al (1990) and Gillespie et al (1990). The purpose of this analysis was to derive a set of calibration coefficients to

correct for the additive and multiplicative effects of instrument and atmosphere and thereby convert the AVIRIS radiance to an estimate of surface reflectance. Convergence to an acceptable solution was hindered by the low spectral contrast between the image endmembers and the lack of relevant vegetation spectra in the spectral library used. Nevertheless inspection of the gain and offset factors indicated little variation among the solutions for the offset term. Since the additive terms are more critical than the multiplicative terms for mathematical analyses of spectra, an average of the offset terms from several solutions was subtracted from the AVIRIS radiance. To convert to reflectance a region of apparent homogeneous grass cover was used as a relative reflectance calibration standard (Mustard and Pieters, 1987b). A plot of the multiplicative and additive terms used to convert the AVIRIS radiance to approximate reflectance is shown in Figure 3. Note that the additive term shows an exponential decrease with increasing wavelength typically of atmospheric scattering. There are still lingering calibration difficulties at this stage and refinements of the calibration are continuing.

Spatial Distributions

In the initial linear mixing analysis of the raw data, a subset of the total AVIRIS scene was used to expedite the analysis and interpretation of results. Using the data corrected for estimates of the additive and multiplicative calibration factors (calibrated data) this analysis was expanded to encompass the entire image. In addition to the four image endmembers identified during data reduction, a fifth image endmember was required to achieve an acceptable solution. This is the minimum number of endmembers that could be selected to model the image. The spatial distribution and abundance of the 5 image endmembers plus a model shade of 0.01% reflectance to account for illumination effects (Adams et al, 1986; Smith et al, 1990) are shown in Figure 4 along with an image of the total rms error of the fit of the image endmembers to each spectrum in the image. All calculations were carried out at the full dynamic range of the AVIRIS data. The average rms error for the entire image is less than 3% reflectance. Inspection of the rms error image shows a high quality fit with only a few regions of high error. However inspection of error as a function of wavelength or band residual images shows a few wavelength regions (0.7-0.8 μm, 1.5-1.65 μm) where the error is correlated with illumination indicating errors in the removal of additive terms in the calibration.

Nevertheless, the fraction images reveal many interesting relationships amongst the surface components. Note that the fraction images are largely uncorrelated with illumination (compare to the complimented shade image). This indicates that the only the fractional contributions from the actual spectral endmembers are being identified and not effects of illumination. The elements of green vegetation are extremely well modelled and partitioned into the vegetation fraction image which illustrates that vegetation is localized in irrigated fields and along water courses. The grass endmember is highly correlated with albedo (though not illumination) but the spatial patterns agree with general field observations. The other three images are thought to represent the distributions of different soil units. Soil1 exhibits a broad diffuse pattern and is concentrated in the western and south western portion of the image. In this region the substrate is dominated by lithologies of the ophiolitic melange and suggests that the spectral properties of this soil unit are strongly influenced by this substrate material. High values in the Soil2 fraction image exhibit a strong association with valley floors in the western portion of the image and also in a spatially coherent arcuate zone extending towards the southeast of the image. This arcuate zone correlates with a fault block of ophiolitic material which also suggests an physical association between this soil unit and substrate composition. However the association of this same soil unit with restricted valley bottoms implies alternative explanations. Finally distributions of Soil3 are strongly concentrated in the eastern portion of the image over substrates dominated by plutonic and volcanoclastic rocks. This again implies a strong association between substrate and soil compositions.

As discussed in detail by Gillespie et al (1990) and Roberts et al (1990), linear mixture analysis primarily models overall spectral continuum. Surface materials that exhibit small amplitude and narrow absorptions not contained in the spectra of the model endmembers may be identified through analysis of band residual images. Also materials that demonstrate nonlinear mixing systematics may be identified on the basis of band residual images. By using the wavelength

dependent character of band residual errors it is possible to identify unmodelled compositional elements of the surface and their spatial distributions. Analysis of band residual images for the Kaweah field site to identify spectral elements of the surface not accounted for with the linear mixture model is continuing. The foci of this analysis are the Fe^{3+} and Fe^{2+} absorptions between 0.5 and 1.4 μm specifically to identify any exposed rock outcrops which are expected to have significantly stronger iron absorptions and to detect subtleties in the iron mineralogy of the soils. Although there are several intriguing possible relationships evident the analyses to date, a thorough band residual analysis must wait for the resolution of the lingering calibration issues.

Endmember Spectral Properties

AVIRIS approximate reflectance spectra of the 5 image endmembers used to compute the distribution and abundance of surface components are shown in Figure 5. These spectra are averages of about 20 spectra each. The grass spectrum exhibits the characteristic steep rise in reflectance and smoothly varying spectrum discussed above. The green vegetation spectrum exhibits classic features of green vegetation such as the 0.55 μm reflectance peak and the sharp edge of the chlorophyll absorption near 0.7 μm. The soil spectra are distinguished primarily by the shape of the spectrum between 0.5 and 1.3 μm and the character of the spectra between 1.5 and 1.7 μm. Clearly some of these "soil" endmembers contain senescent vegetation which is indicated by a reflectance maximum near 1.65 μm. This is likely partially decayed grasses with spectral properties discussed above. The other soil components which do not exhibit the 1.65 μm reflectance peak nor a drop in reflectance between 1.35 and 1.5 μm are likely to be primarily composed of soil. Note that the soil spectra between 0.7 and 1.0 μm are clearly lower in reflectance that the continuum on either side of this section. This is an artifact of the calibration and is seen to be correlated with a similar feature in the the plot of the offset terms in Figure 3. The correlation of this spectral segment with the red edge and near infrared plateau of the green vegetation spectrum implies that the green vegetation spectra in our library are inappropriate to model the vegetation components in this scene.

IV Conclusion

General distributions and abundances of the major surface components in the foothills of the Sierra Nevada were determined using a linear mixing model. Three of the endmembers are apparently related to different soil types and the distributions of these soils have strong associations with substrate lithology. This implies a strong link between the soil spectral properties and substrate lithology. Only the broad, continuum spectral properties have been modelled in this analysis and only with image endmembers. A refined calibration will be obtained and a spectral library used to derive more accurate analysis of surface components. Also the band residual images will be investigated in detail following the final calibration to provide additional constraints on spectral variability and soil compositions. Nevertheless, this preliminary analysis has clearly demonstrated that subtle soil spectral properties are distinguished using quantitative modelling approaches of imaging spectrometer data and that these soil properties can be mapped.

References

Adams, J. B., M. O. Smith, and P. E. Johnson, Spectral mixture modeling: A new analysis of rock and soil types at Viking Lander 1, J. Geophys. Res., 91, 8113-8125, 1986.

Burns, R. G., Mineralogical Application to Crystal Field Theory. Cambridge University Press, London. 224 pp. 1970.

Clark, R. N., Deconvolution of reflectance spectra of mineral mixtures into component abundance and grain size (abstract), Trans. of Am. Geophys. Union, 68, 464, 1987.

Elvidge, C. D., Vegetation reflectance features in AVIRIS data, Int'l Symposium Rem. Sens. Envir. Sixth Thematic Conference on Remote Sensing for Exploration Geology, 169-182, 1988.

Farmer, V. C. ed., The Infrared Spectra of Minerals, The Mineralogical Society, London, pp. 539, 1974.

Gillespie. A. R., M. O. Smith, J. B. Adams, S. C. Willis, A. F. Fischer III, and D. E. Sabol, Interpretation of residual images: Spectral mixture analysis of AVIRIS images, Owens Valley, California, in Proc. of the Second Airborne Visible/Infrared Imaging Spectrometer (AVIRIS) Workshop (R. O. Green, ed.) JPL publication 90-54, 243-270, 1990.

Hunt, G. R., and J. W. Salisbury, Visible and near-infrared spectra of minerals and rocks: I Silicate minerals. Mod. Geol., 1, 283-300, 1970.

Mustard, J. F., and Pieters C. M., Quantitative abundance estimates from bidirectional reflectance measurements. Proc. Lunar Planet. Sci. Conf. 17th, Part 2, in J. Geophys. Res., 92, E617-E626, 1987a.

Mustard, J. F., and Pieters C. M., Abundance and distribution of ultramafic microbreccia in Moses Rock Dike: Quantitative application of mapping spectrometer data. J. Geophys. Res., 92, 10376-10390, 1987b.

Mustard, J. F., and C. M. Pieters, Photometric phase functions of common geologic minerals and applications to quantitative analysis of mineral mixture reflectance spectra, J. Geophys. Res., 94, 13619-13634, 1989.

Mustard, J. F., Methods of quantitative analysis of reflectance spectra and application to imaging spectrometer data, Ph.D. Thesis, Brown University, Providence RI, USA, pp. 231 1990.

Roberts, D. A., M. O. Smith, J. B. Adams, D. E. Sabol, A. R. Gillespie, and S. C. Willis, Isolating woody plant material and senescent vegetation from green vegetation in AVIRIS data, in Proc. Second Airborne Visible/ Infrared Imaging Spectrometer (AVIRIS) Workshop (R. O. Green, ed.) JPL publication 90-54, 42-57, 1990

Saleeby, J. B., Fracture zone tectonics, continental margin fragmentation, and emplacement of the Kings-Kaweah ophiolite belt, southwestern Sierra Nevada, California, in R. G. Coleman and W. P. Irwin (eds.) North American Ophiolites, Oregon Dept. Geol. Min. Ind. Bull., v 91, p 141-160, 1977

Saleeby, J. B., Kaweah serpentinite melange, southwest Sierra Nevada foothills, California, Geol. Soc. Am. Bull., v 90, p 24-46, 1978.

Saleeby, J. B., Tectonic significance of serpentinite mobility and ophiolite melange, in L. A. Raymond (ed) Melanges; Their nature, origin, and significance, Geol. Soc. Am. Special Paper 198, 153-168, 1984.

Smith, M. O, Ustin, S. L., Adams, J. B., and A. R. Gillespie, Vegetation in deserts: I A regional measure of abundance from multispectral images, Remote Sensing of Environment, 31, 1-26, 1990.

Sunshine, J. M., C. M. Pieters, and S. F. Pratt, Deconvolution of mineral absorption bands: An improved approach, J. Geophys. Res, 95, 6955-6966, 1990.

Acknowledgements: Support from NASA grant NAGW-1118 is gratefully acknowledged. Many thanks to Rob Green for assistance in collecting field spectra with the PIDAS instrument, C. Pieters for thoughtful discussions, and to J. Adams, M. Smith, and S. Willis at the University of Washington for an introduction to the linear mixing approach to data reduction.

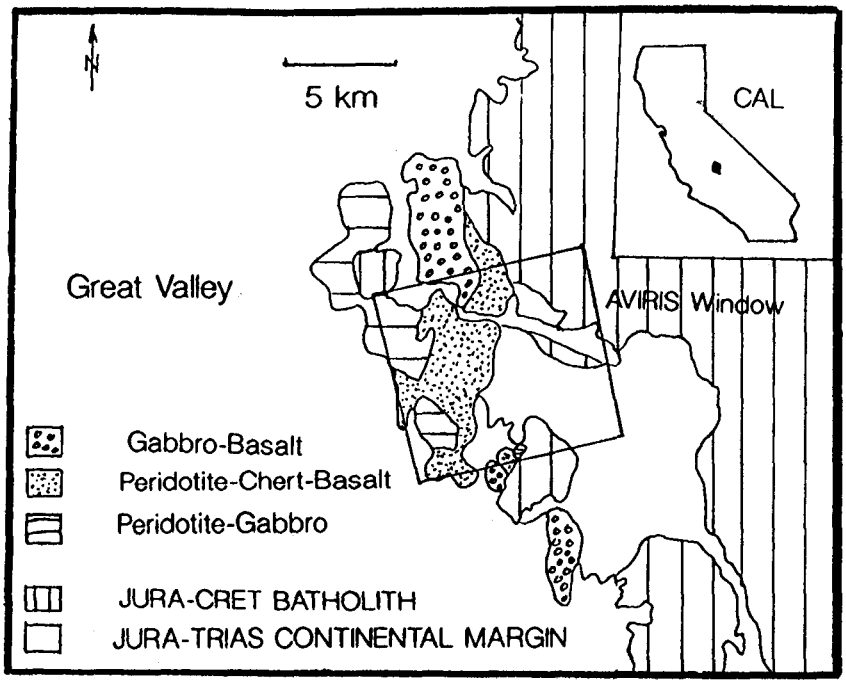

Figure 1. Generalized bedrock geology map of the region of the western foothills of the Sierra Nevada investigated (after Saleeby, 1979). The AVIRIS window used in this investigation is outlined.

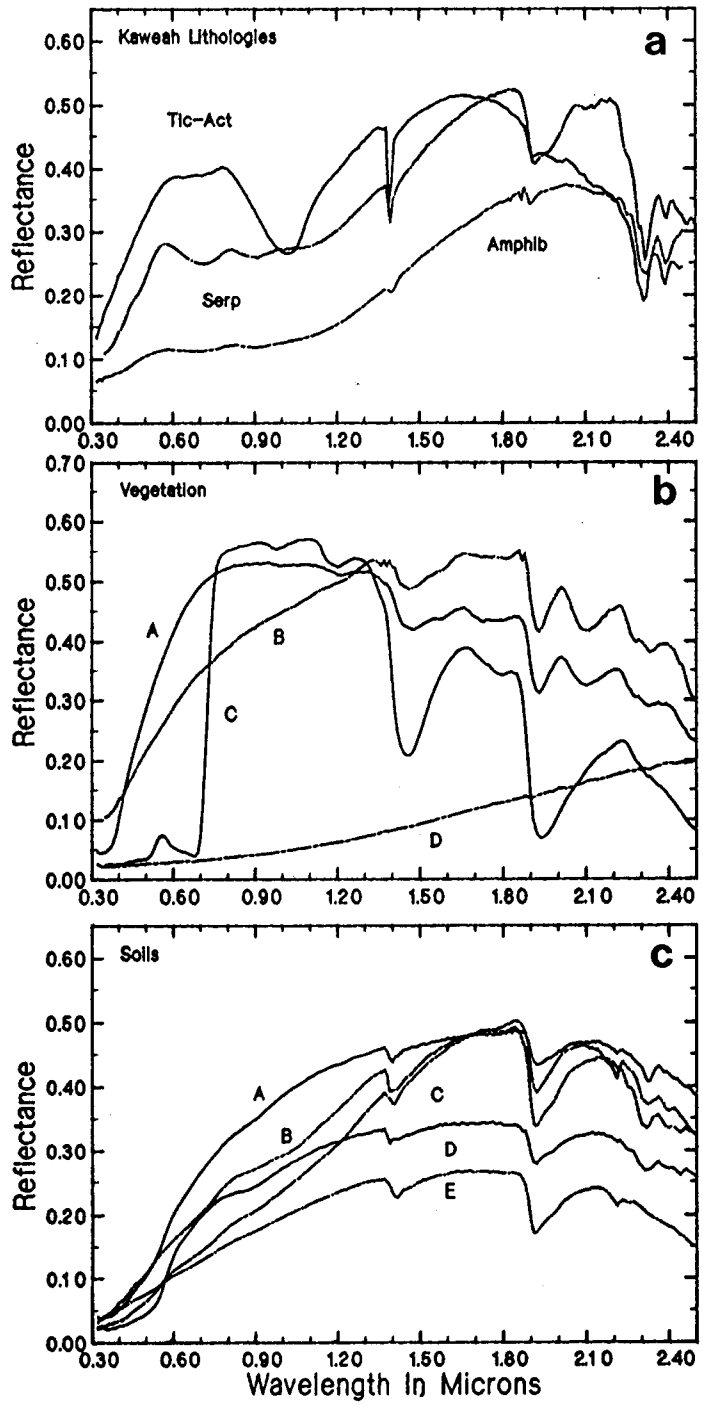

Figure 2. Representative laboratory reflectance spectra of the major lithologic, vegetative, and soil types from the field sites. All spectra were measure in RELAB at Brown University. For the vegetation spectra, A is senescent grass, B is partially decayed senescent grass, C is green vegetation (maple leaf) and D is burnt grass. For the soil spectra note the presence of a distinct 2.3 μm hydroxyl absorption in most of the soils and 2.2. μm absorption in some. Also note the ferric and ferrous absorptions in the strongly oxidized soil (D) and the steep spectral slopes in the spectra B and C relative to the more concave continua of spectra A, D, and E.

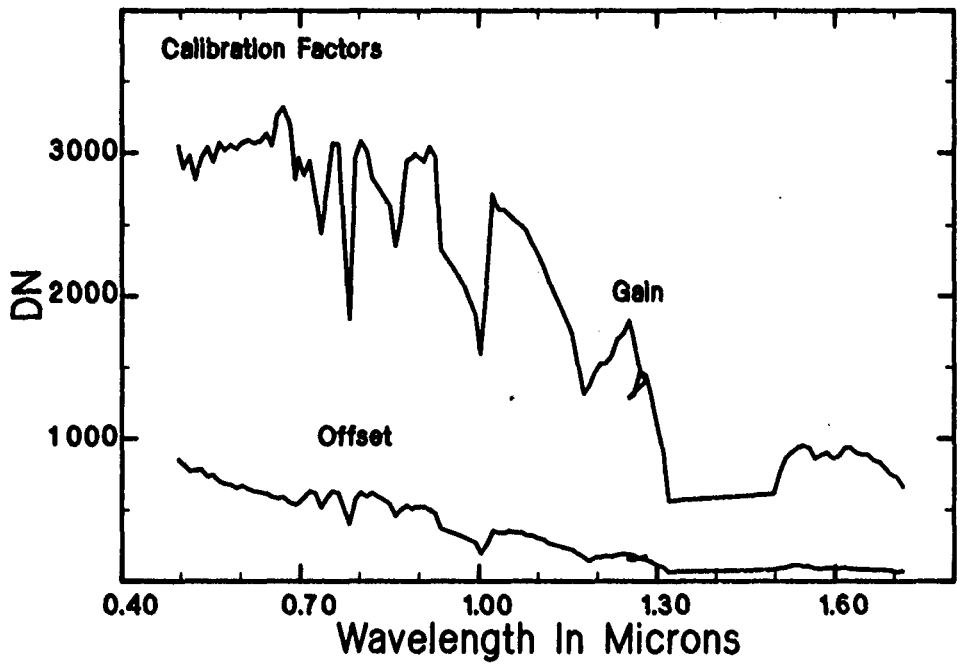

Figure 3. Gain and offset terms used to calibrate the AVIRIS radiance data to reflectance. Offset terms were determined using a linear mixing approach (i.e. Gillespie et al, 1990) and gain values were determined by a relative reflectance method (Mustard and Pieters, 1987b).

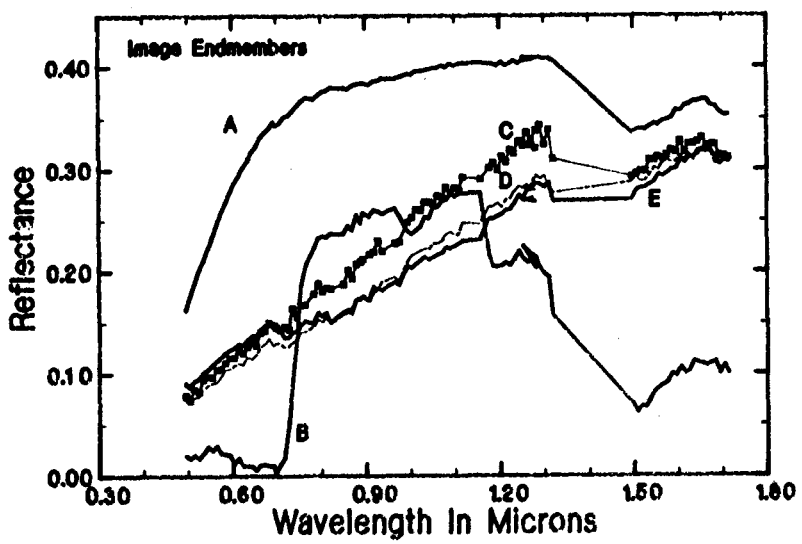

Figure 5. AVIRIS reflectance spectra of the image endmembers used to calculate the surface abundances shown in Figure 4. A is the GRASS endmember, B is the VEGETATION endmember, C is SOIL2, D is SOIL1 and E is SOIL3. There are small calibration errors evident between 0.7 and 1.0 μm that are currently being corrected. The soil endmembers are distinguished primarily by differences in slope and the strength of the senescent vegetation absorptions between 1.5 and 1.7 μm.

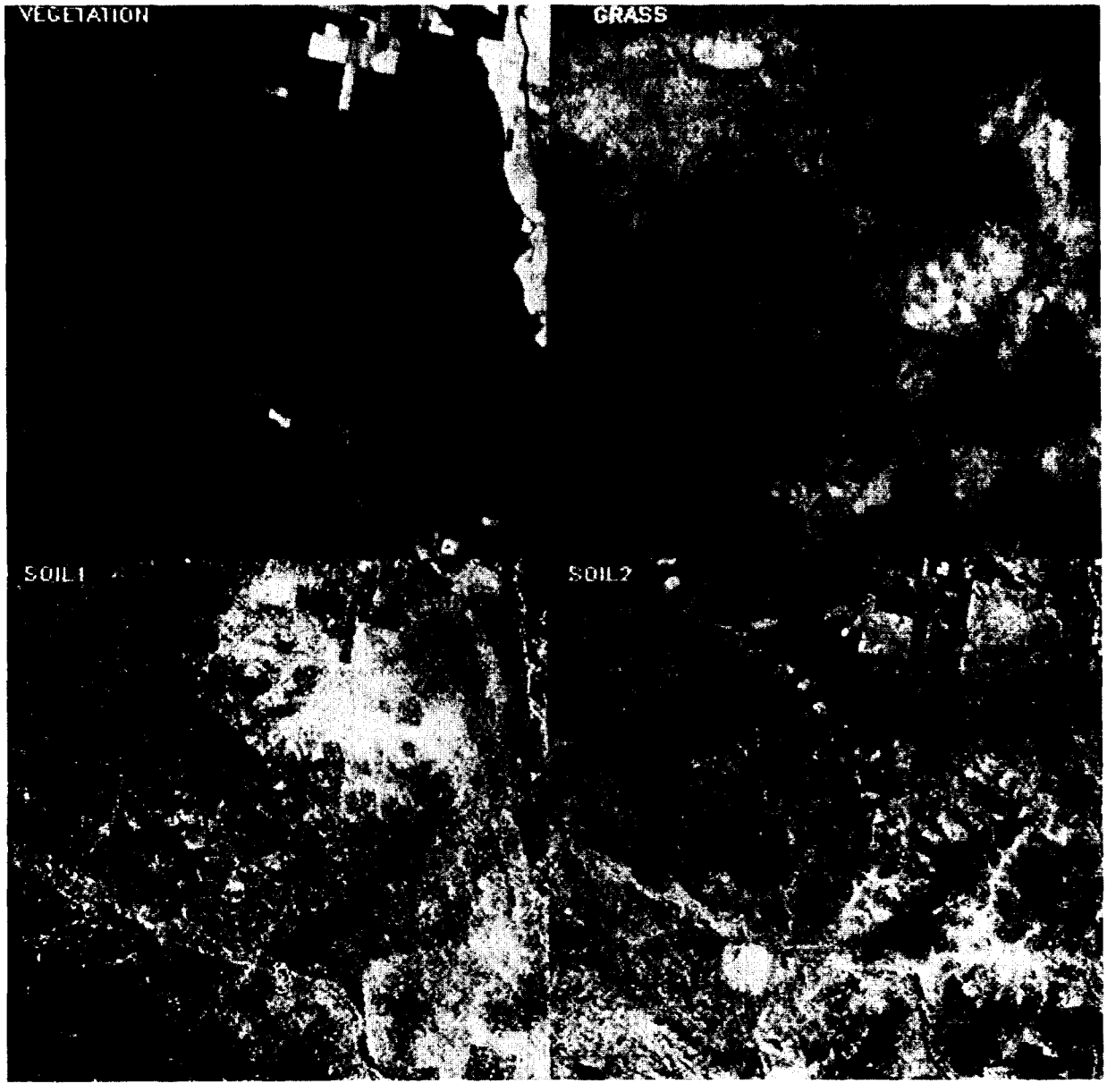

Figure 4. These images present the solution to the linear mixing equation applied to the AVIRIS data using image endmembers. Each image shows the spatial distribution and abundance of an image endmember where bright values represent higher abundance. The label for each abundance image in the upper left corner gives an interpretation to the most abundance surface component in the endmember. Discussion of the distributions is given in the text. The "SHADE" abundance image has been complimented. The "VARIANCE" image shows the total RMS error of the fit of the image endmembers to each pixel and for this solution the average RMS error is 75 DN or about 2-3% reflectance. Spectra of the image endmembers used in the calculations are shown in Figure 5. North is towards the bottom in all these images and the ground coverage of the AVIRIS data is shown in Figure 1.

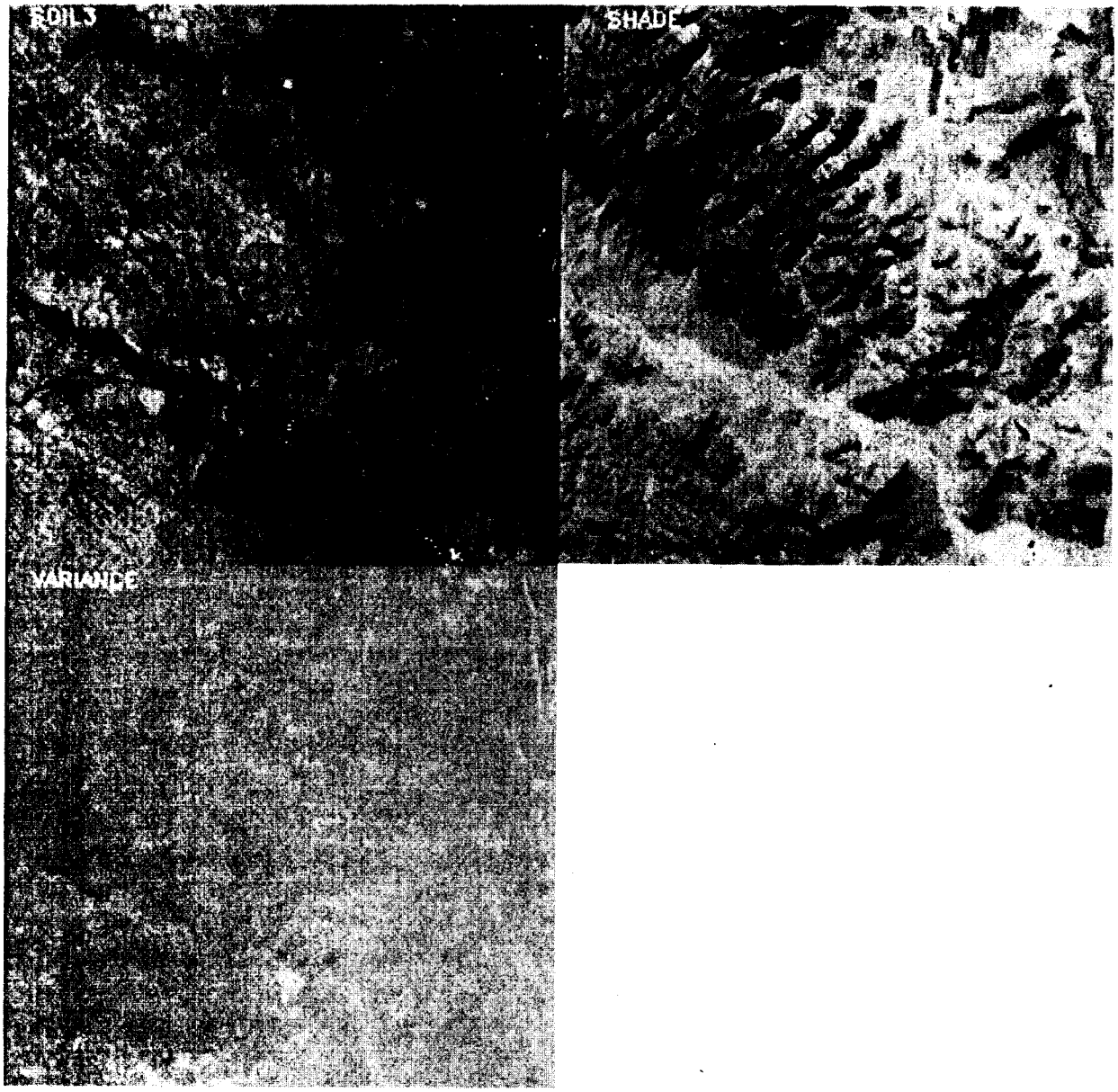

Figure 4 (cont'd)

MAPPING AND CORRELATING DESERT SOILS AND SURFACES WITH IMAGING SPECTROSCOPY

Arthur F. Fischer III
Departments of Natural Resources and Geology
Humboldt State University
Arcata, California

Abstract. The soils and geomorphic surfaces of large regions of semi-arid and arid land in North America (Basin and Range, Mojave and Sonoran Deserts) are unmapped and uncorrelated. AVIRIS provides a vehicle to test the special capabilities and potential limitations of imaging spectrometers to monitor and detect continuous broad spectral changes, characteristic of soil spectral evolution, as well as narrow absorption features associated with variations in clay concentration and mineralogy in developing soils. It has been demonstrated that the relative ages of stable geomorphic surfaces and certain developmental properties of the "soil chronosequences" associated with these surfaces, are "spectrally" correlated and can be assessed by remote sensing. Regional mapping of contemporaneous geomorphic surfaces, by fully exploiting soil spectral evolution with imaging spectroscopy, would provide valuable new interpretive base maps linking soils and geomorphology, their temporal relationships, and potentially paleoclimates. Studies based on these maps would guide researchers to concentrate their efforts on either focused or regional spatial scales and would facilitate investigations into geomorphic thresholds, paleoclimatic boundaries and impacts, and soil developmental relationships (genesis and morphology).

Introduction

Soils developed on granitic alluvial fans of the broad Sierran piedmont of Owens Valley, California, over the past 0.5 Million years have been differentiated by their reflectance spectra, as measured by the six-channel Landsat Thematic Mapper (TM) [Gillespie et. al., 1986, Smith et. al., 1990a,b], the seven-channel airborne Thematic Mapper Simulator (TMS) [Gillespie et. al., 1986, Fischer, 1991], and most recently by the the 224-channel Airborne Visible / Infrared Imaging Spectrometer (AVIRIS) [Gillespie et. al., 1990b, Fox et. al.,1990, Fischer, 1990]. The soils range from undeveloped or very weakly developed Torriorthents on recent (Holocene age) inset and distal fans, to well developed Haplargids on older (late Pleistocene age) proximal and medial fans. These soils have developed without significant eolian carbonate enrichment or organic carbon accumulation in 'A' horizons but, display distinct morphologic development in: Horizonation, structure, consistence, clay formation, and oxidation with a consistent increase in color rubification; reddening (hue) and brightening (chroma), with increasing age.

Reflectance spectra of the fans differ in proportion to the concentrations of iron oxides and hydrous clay minerals coating sand grains exposed or deposited at the surface through "bioturbation"(accelerated soil mixing caused by burrowing fauna).

Soil-geomorphic field studies at Oak Creek and Birch Creek, on the Sierran piedmont, have demonstrated that surface spectral differences (spectral signatures) are associated with real differences in soil development through time [Burke et. al., 1986, Gillespie et. al., 1986]. Thus it appears that remote sensing can be used to differentiate relative soil ages and correlate contemporaneous geomorphic surfaces in arid and semi-arid deserts, possibly over vast regions. The spectral resolution of imaging systems like TM are too coarse (low-dimensional) to resolve the sharp hydroxyl absorption bands of clays near 2.2 μm. Thus multispectral systems like TM are insensitive to variations in clay mineralogy, which are important in characterizing soils and are diagnostic of climatic and paleoclimatic regimes. Furthermore, the band positions and the limited number of TM channels are such that dry grass and certain mixtures of soil and shrubs appear spectrally similar. This ambiguity increases the uncertainty of soil spectra estimated from TM data.

Pine Creek offers a geological setting where alluvial fans are correlated to an established "sequence" of glacial moraines with regional expression. The age limits placed on these moraines also constrain the ages of adjacent, geomorphically related alluvial fans. Pulses of fan deposition were roughly synchronous with Pleistocene glacial-interglacial cycles driven by paleoclimatic change. Lateral breaches of specific moraine crests resulted in a sequence of discrete lateral debris flow fans. The breaches were apparently induced by supraglacial streams during periods of maximum glacial advance. Distal fans associated with the same glacial stages, however, were deposited dominantly during deglaciations. This temporal control provides an advantageous environment in which to test the capabilities and limitations of AVIRIS to differentiate broad spectral signatures associated with the subtle spectral evolution of surfaces only slightly different in age. In addition, AVIRIS sensitivity to narrow clay absorbtion features, potentially diagnostic of soil genesis and ancient climatic regimes, was also evaluated.

Methods

Field soil investigations were conducted on the geomorphic surfaces of the Pleistocene and Holocene distal fan sequence (Figure 4a, letters 'D' & 'H') and the Pleistocene lateral fan sequence (Figure 4b, letter 'L') to obtain surface and soil-specific data. Soil profiles were described, samples were collected and analyzed for particle size distribution (sand, silt, clay), and clay characterization (X-Ray Diffraction). Profile Development Index (PDI) [Harden, 1982, Harden and Taylor, 1983] was used to quantify selected properties of each soil, providing an independent semi-quantitative age estimate for each fan surface. About 1 centimeter thick surface soil samples were collected and sieved to retain the 250 μm - 2 mm sand fraction. Beckman laboratory spectral analysis (0.4 - 2.45 μm region) was performed on these sands to determined the "spectral signature" of each surface and to provide the ' reference' spectrum of both soil endmember components used in modelling. These field and laboratory data, evaluated with respect to the age constraints established for each surface, became the independent variables or standards against which AVIRIS capabilities, limitations, and sensitivity were measured.

High-dimensional (224 channel; 0.4 - 2.45 μm) AVIRIS images of the Pine Creek area were acquired by NASA on July 29, 1989. 171 channels of meaningful data were obtained. Spectral Mixture Analysis (SMA) was used to process the data. In essence, SMA provides a strategy for analyzing images to extract compositional information based on the principles of field mapping. Signals from each pixel, as expressed by radiance or reflectance values in each channel, are separated into components (endmembers) representing spectrally distinct surface materials and instrumental or atmospheric effects. Endmember components are selectively edited and recombined to form image units interpretable within the framework of field map units [Adams et. al., 1989, Adams et. al., 1990]. This approach calibrates the image data and models them as linear mixtures of laboratory reference spectra (Beckman spectra of field surface samples used for soil endmembers). Four reference endmembers, present in various proportions, at the pixel 20 meter scale, were selected: RED SOIL (moderately developed, well oxidized and argillic), WHITE SOIL (undeveloped and sandy), vegetation (alfalfa field), and shade/shadow. The final result of SMA is a "fraction" image of proportions of each spectral endmember. The remaining unmodelled data, are concentrated in residual images for each band [Gillespie et. al., 1990]. The spectral effects of vegetation (~15% cover on distal fans, mainly *Coleogyne* ; and ~15 -20% cover on medial fans, largely *Ephedra*, *Artemisia*, and *Purshia*) and topography (shade and shadow) present in various additive proportions of each pixel and modelled as scaled fractions in DN s of brightness may be suppressed or removed from the data at this point, leaving information on soil alone. In such a display, soil development proceeds along a spectral evolutionary path or trajectory (soil spectral evolution) between the undeveloped WHITE SOIL and the moderately developed RED SOIL reference endmembers. Any given soil unit in the image will plot along this trajectory, at a position that corresponds to its degree of development (Figure 2). In this manner, statistical testing of differences and similarities, and thus quantitative relative dating, is possible.

The "soil-surface-spectral" relationships that support the strategy for regional chronocorrelation and mapping of geomorphic surfaces are summarized in Figure 1. This flow chart depicts the general processes and procedures required to effect results. Initially a climatic change, either gradual or abrupt, must trigger local or regional geomorphic thresholds to be exceeded. In the case of regions with similar geologic settings, lithologies, and climatic influence, the triggered geomorphic response may in fact be regional, producing depositional or erosional surfaces that are contemporaneous across large or even vast areas. Localized chronosequences in such cases could be chronocorrelated to others within the region. Where settings, lithologies, and climatic influences are highly variable or complex within or across regional or threshold boundaries, synchroneity of events on broad spatial scales is unlikely and local chronosequences may be out of phase with others within the region (Figure 5) [Fischer and Booker, 1989]. When a new surface is abandoned following an event it becomes geomorphically stable and time zero for soil development begins. Soil horizonation begins to concentrate soil properties within shallow layers that thicken and deepen with time. Bioturbation by burrowing insects and rodents then excavates sand grains from these horizons (primarily the 'B' horizons where clay minerals accumulate and iron oxides form) and deposits representative samples at the surface. The concentration of iron oxides and hydrous clays coating these exposed sand grains become the surface expression of soil development at depth.

This enables soil spectral evolution to function as a remote measure of soil development and surface age. Detection, modelling, correlation, and mapping of surfaces can then follow. Ground-truthing and age control must be maintained to ensure accurate mapping, keep the model calibrated to surface soil, vegetation, geomorphic, and geologic units or parameters, and to signal the need to reevaluate the model endmembers as thresholds or boundaries are crossed.

Results and Implications

Color slide 3 shows a fully modelled scene at Pine Creek and is provided at the back of this publication. Discussion of results and interpretations, however, will be referred primarily to the scaled fraction images of the WHITE SOIL and RED SOIL reference endmembers (Figure 4a & 4b) respectively. It is quite evident that effective spectral differentiation of the surfaces has been achieved. The differences, while subtle on individual surfaces, are quite diagnostic when comparing the pleistocene lateral and distal fans. PDI age difference between the two is only about 5 - 8 ka (laterals fans are ~28 ka and the distal fans ~20 ka). The lateral debris flow fans show subtle gray scale differences among themselves in Figure 4b, and when viewing the modelled color slide, differences are apparent. It also became evident that areas of dry grass are still being spectrally confused. In this case with the moderately developed RED SOIL endmember (Figure 3). This problem is also prominent in the RED SOIL reference endmember fraction image (Figure 4b) where it can be located by the letter 'G' on Holocene age surfaces in distal fan and ephemeral stream delta positions. While the slide shows RED assigned to the developed RED SOIL component, BLUE to the undeveloped WHITE SOIL component, and GREEN to VEGETATION, the dry grass sites appear quite red. The problem of dry grasses and senescent vegetation (Figure 3) can be reduced or eliminated by a number of strategies and techniques now being studied or tested [see Roberts et. al., 1990, Smith et. al., 1990a,b, Gillespie et. al., 1990a,b]. Spalling granitic clasts mantling a surface and exposed granitic boulders that form debris flow levees have also be confused with undeveloped sandy soil in some areas where they are unrelated to surface age or reflect original surface condition [Gillespie et. al., 1986; Fischer, 1991]. Figures 4a & 4b are essentially reciprocals or compliments of one another which can be conceptually represented by the spectral relationship shown in Figure 2. The advantage provided by high-dimensional imaging spectrometers to monitor continuous broad spectral signatures and detect broad often subtle transitions or changes (soil spectral evolution), that may go unnoticed or undetected in low-dimensional systems like TM, make it possible to resolve these problems through modelling techniques, spatial interpretation, or evaluation of residual images of unmodelled scene constituents or narrow diagnostic absorbtion features. Secondary clay minerals developed in soils and brought to the surface, if detectable, would provide valuable information about soil genesis and paleoclimatic regimes. Particle size determination of the surface soils showed a range of only about 1 - 4% clay. Inspection of the band residual images near 2.2 μm after modelling revealed no residual clays [Gillespie et. al., 1990]. This means that either all the clays present, in low concentration, were effectively modelled by the RED SOIL endmember, or that the instrument was insensitive to small differences in clay concentration or mineralogy. XRD of several surface soil samples indicated that smectites dominate the clay fraction with Montmorillonite most abundant. Traces of Kaolinite were also present.

Spectral detection and discrimination of 1 - 4% clay concentrations in surface soils may be close to the limit of AVIRIS sensitivity in spectrometer D. With improved SNR this capability will be a powerful diagnostic tool. Spectral sensitivity to subtle differences in surface/soil ages appears to be at least as accurate as would be determined from conventional mapping techniques. However, mapping and chronocorrelation of geomorphic surfaces and their soils on regional scales, in semi-arid and arid environments, using remote sensing, is much more practicable than conventional mapping techniques. The soil-surface-spectral relationships and SMA provide a strategy to effectively study geomorphic patterns, transitions or thresholds on broad regional scales. Regional maps would serve as a guide for more focused research into clues to regional geomorphic and soil developmental response to paleoclimatic change.

References

Adams, J.B., Smith, M.O., and Gillespie, A. R. 1989. Simple models for complex natural surfaces: A strategy for the hyperspectral era of remote sensing. Proceedings IEEE International Geoscience and Remote Sensing Symposium '89 1:16-21.

Adams, J.B., Smith, M.O., and Gillespie, A.R. 1990. Imaging spectroscopy: Data analysis and interpretation based on spectral mixture analysis. *In* Pieters, C.M., and Englert, P.J., *eds.*, Remote Geochemical Analysis: Elemental and Mineralogical Composition, Lunar and Planetary Institute, Houston, TX, *in press.*

Burke, R.M., Lunstrum, S., Harden, J., Gillespie, A.R., and Berry, M. 1986. Soil chronosequence on eastern Sierra Nevada fans, CA, supports remote sensing studies. Geological Society of America Abstracts with Program 18(6):553.

Fischer, A.F. III 1990. Testing the sensitivity of hyperspectral AVIRIS imagery to detect clay minerals and to differentiate a soil chronosequence, Pine Creek, California. NASA - Graduate Student Researchers Program Annual Symposium Abstract Booklet. Washington D. C., 14-17 May.

Fischer, A.F. III 1991. Sensitivity of spectral differentiation of desert soils: Implications for regional chronocorrelation and mapping of geomorphic surfaces. NASA - Graduate Student Researchers Program Annual Symposium Abstract Booklet. Washington D. C., 14-17 May.

Fischer, A.F. III, and Booker, F. A . 1989. Paleoclimatic depositional pulses, pedologic development rates, and a need for further testing of remote sensing in various settings. A case study from the Inyo Mountains, California. NASA - Graduate Student Researchers Program Annual Symposium Abstract Booklet. Washington D. C., 16-19 May.

Fox, L. III, Fischer, A.F. III, Gillespie, A.R., and Smith, M.O. 1990. Using spectral mixture analysis of AVIRIS high dimensional data for distinguishing soil chronosequences. Proceedings of the Second Airborne (AVIRIS) Workshop. Jet Propulsion Laboratory, Pasadena, California, JPL Pub. 90-54.

Gillespie, A.R., Abbott, E.A., and Hoover, G.L. 1986. Spectral basis for relative dating of granitic alluvial fans, Owens Valley, California. Geological Society of America Abstracts with Program 18(6):614.

Gillespie, A.R., Burke, R.M., Fischer, A.F. III, Smith, M.O., and Fox, L. III 1990a. Distinguishing soils and surfaces in a carbonate-enriched desert chronosequence with TIMS. Proceedings of the Second Airborne (TIMS) Workshop. Jet Propulsion Laboratory, Pasadena, California, JPL Pub. 90-55.

Gillespie, A.R., Smith, M.O., Adams, J.B., Willis, S.C., Fischer, A.F. III, and Sabol, D.E. 1990b. Interpretation of residual images: Spectral mixture analysis of AVIRIS images, Owens Valley, California. Proceedings of the Second Airborne (AVIRIS) Workshop. Jet Propulsion Laboratory, Pasadena, California, JPL Pub. 90-54.

Harden, J.W. 1982. A quantitative index of soil development from field descriptions: Examples from a chronosequence in central California. Geoderma 28:1-28.

Harden, J.W., and Taylor, E.M. 1983. A quantitative comparison of soil development in four climatic regimes. Quaternary Research 20:342-359.

Roberts, D.A., Smith, M.O., Adams, J.B., Sabol, D. E., Gillespie, A.R., and Willis, S.C. 1990. Isolating woody plant material and senescent vegetation in AVIRIS data. Proceedings of the Second Airborne (AVIRIS) Workshop. Jet Propulsion Laboratory, Pasadena, California, JPL Pub. 90-54.

Smith, M.O., Ustin, S.L., Adams, J.B., and Gillespie, A.R. 1990a. Vegetation in deserts: I. A regional measure of abundance from multispectral images. Remote Sensing of Environment. Vol. 3, pp. 1-26.

Smith, M.O., Ustin, S.L., Adams, J.B., and Gillespie, A.R. 1990b. Vegetation in deserts: II. Environmental influences on regional abundance. Remote Sensing of Environment. Vol.3, pp. 27-52.

Acknowledgments

This research was funded by a fellowship awarded by the NASA- Graduate Student Researchers Program, NASA Headquarters, Washington D. C., 1989-91. Many thanks to Dr, Alan R. Gillespie, Dr. Milton O. Smith, Steve Willis, and Dr. John Adams of the Geological Remote Sensing Laboratory, University of Washington, Seattle, WA. for continuing support and encouragement and for many hours of image processing and analysis. Grateful appreciation to Elsa Abbott, Dr. Anne Kahle, Ron Alley, Cindy Grove, Joy Crisp and many others at JPL for for a multitude of technical and moral support.

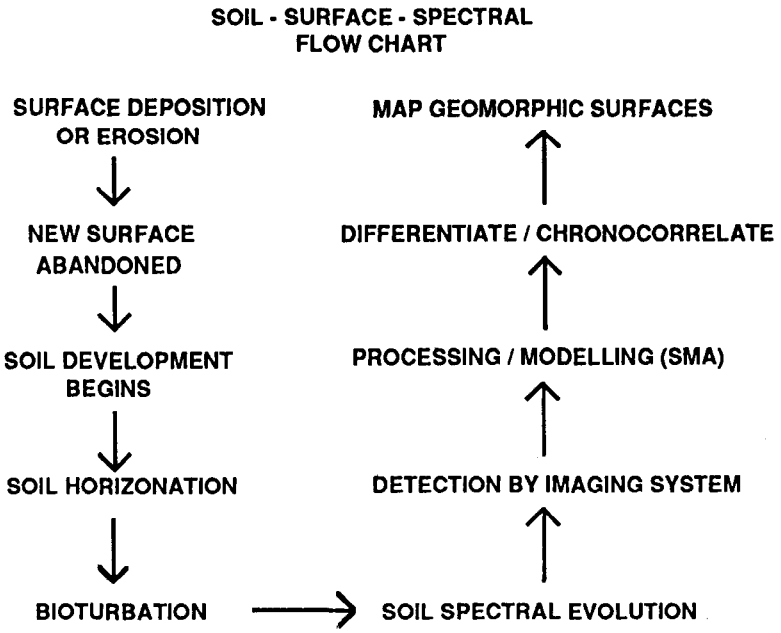

Figure 1. Flow chart depicting the processes, relationships, and gross strategy required for regional mapping of contemporaneous geomorphic surfaces by remote sensing in semi-arid and arid envirnments to be efficient and practicable.

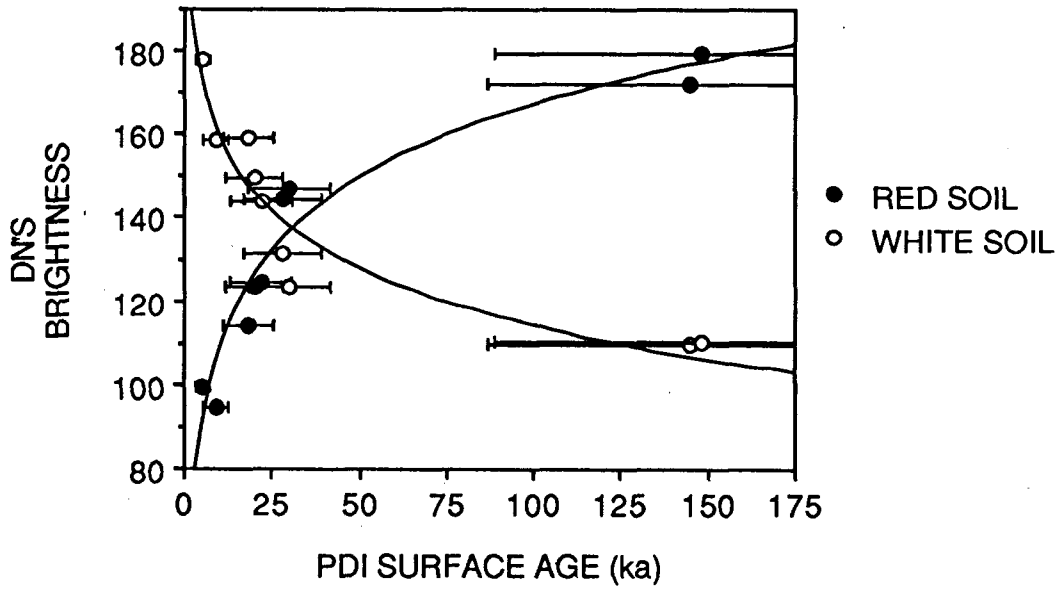

Figure 2. A plot depicting the spectral relationship between RED SOIL and WHITE SOIL reference endmember scaled fractions from surfaces with age control. The moderately developed (well oxidized and argillic) RED SOIL fractional DN's increase, while the undeveloped sandy WHITE SOIL fractional DN's decrease, with increasing surface age. (Error bars show ~40% of PDI derived surface ages as error for Quaternary surfaces in Basin and Range Province).

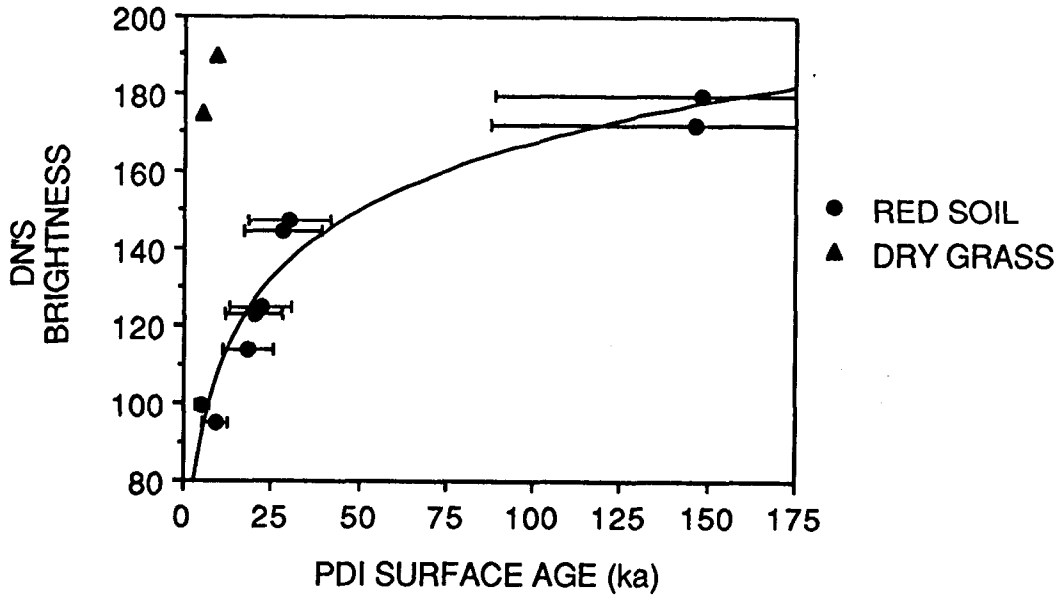

Figure 3. A plot depicting the increasing scaled fractional component of RED SOIL with increasing surface age, complicated by dry grasses on holocene age surfaces. (young Holocene surfaces appear to be pleistocene age).

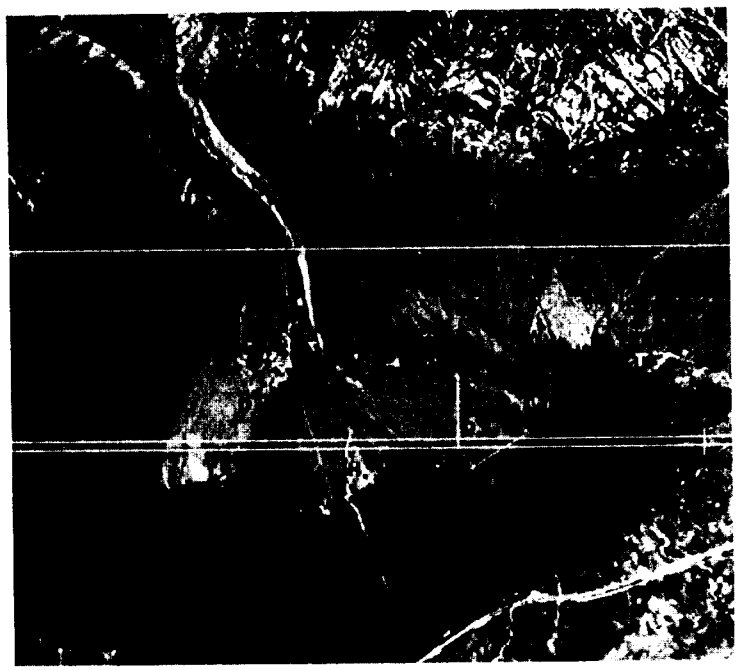

A.

B.

Figure 4. Two reference endmember fraction images, Pine Creek. (light = high fraction; dark = low fraction) **A.** (top) undeveloped sandy WHITE SOIL (H = holocene distal fan; D = pleistocene distal fan; W = white soil reference endmember sample site (Beckman lab spectra). **B.** (bottom) moderately developed, well oxidized, argillic RED SOIL (L = pleistocene lateral fans; G = dry grass areas; R = red soil reference endmember sample site. H, D, & L letter placement on images denotes soil pit locations. North is right.

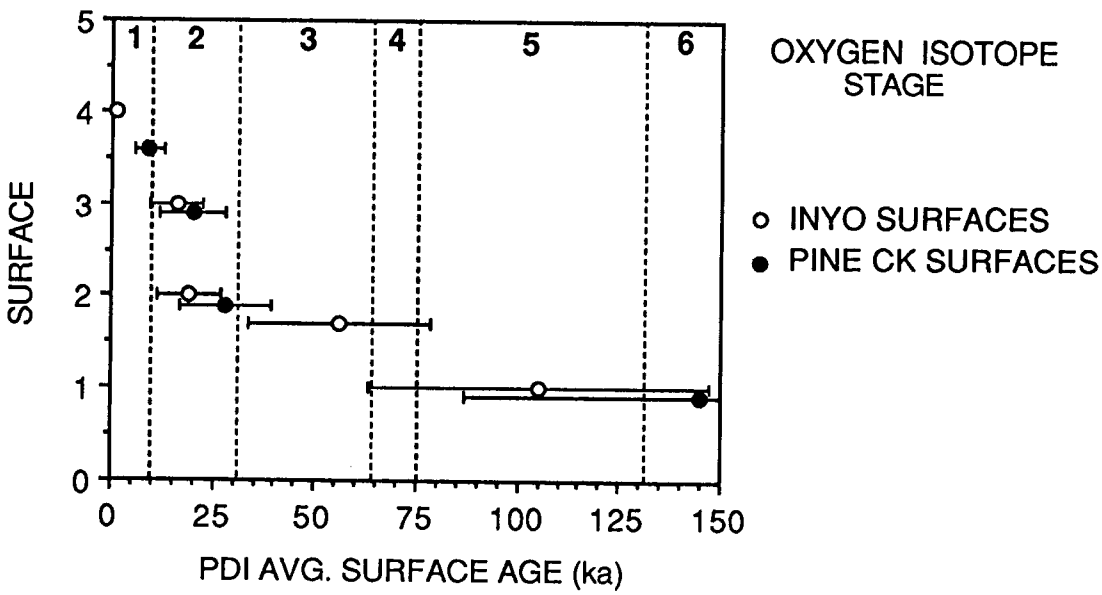

Figure 5. Geomorphic threshold affect on surface deposition and formation. PDI derived average surface ages for Pine Creek, Sierra Neveda and Inyo Mountain fans. Roughly synchronous glaciations of Eastern Sierra produced contemporaneous soils and surfaces. The fans of the unglaciated Inyo Mountains, however, are out of phase with the Sierran Fans, but display their own chronsequences. Rain shadow of Sierra Nevada during glacials and interglacials (Pleistocene).

Comparative Analysis of Radiance Data from AVIRIS, ASAS, and a Helicopter-borne Spectroradiometer

William T. Lawrence, Darrel L. Williams, and K. Jon Ranson
NASA/Goddard Space Flight Center
Biospheric Sciences Branch, Code 923
Greenbelt, Maryland

Abstract. Multispectral radiance data were acquired by several airborne sensor systems on September 8th, 1990 over the Northern Experimental Forest near Bangor, Maine as part of the Forest Ecosystem Dynamics (FED) Multi-sensor Aircraft Campaign (MAC). High resolution spectral data (5nm to 15nm bandwidths) were acquired nearly simultaneously by the AVIRIS and ASAS imaging spectrometers, and with a non-imaging, helicopter-borne spectroradiometer under extremely clear atmospheric aerosol conditions. Intercomparisons of radiance data acquired with these sensors in the nadir view-angle position are presented for several important ecosystem classes.

I. Introduction

A. Forest Ecosystems Dynamics Project

1. Rationale - The Forest Ecosystems Dynamics (FED) project (Williams et al. 1991) is fundamentally concerned with ecosystem pattern and process within northern forests across a hierarchy of both temporal and spatial scales. The underlying thesis of the FED project is that through careful observation, experiments, and modeling, the interactions of the vegetation, soil, and energy components of the forest ecosystem can be understood. An important aspect of the FED project is to incorporate remote sensing into these modeling efforts in a significant way. The repetitive, multi-scale, multi-spectral observation capabilities afforded by remote sensing platforms make this type of data one of the premier tools for ecosystem modeling, environmental assessment and the detection/monitoring of global change phenomenon.

In this paper we will compare initial results from observations made with three remote sensing sensors flown as part of the FED Multi-sensor Aircraft Campaign (MAC) in September 1990. These instruments are the Airborne Visible/Infrared Imaging Spectrometer (AVIRIS, Green, 1990), the Advanced Solid-State Array Spectroradiometer (ASAS, Irons et al., 1990), and a helicopter-borne Spectron Engineering SE-590 spectrometer. The AVIRIS, ASAS and SE-590 cover a range of both spatial and spectral resolution and coverage at operational altitudes of 20 km, 5 km, and 250 m respectively. A wide range of information may eventually be derived from these data sets with inversion techniques (Boardman, 1990), including information on atmospheric conditions (Gao and Goetz, 1990), vegetation stress (Rock et al., 1990), canopy biochemistry (Martin and Aber, 1990), and a suite of data useful in ecological modeling (Wessman and Curtiss, 1990; Williams et al., 1991).

2. Research Area - The primary research site for this project is a 10 X 10 km area of mixed deciduous and coniferous forests located approximately 40 km north of Bangor, Maine. The research site lies primarily within International Papers' Northern Experimental Forest, just west of the Howland interchange on Interstate 95. Based on an analysis of stand maps, approximately 60% of the site is covered by softwood dominated stands (spruce, hemlock, fir, and white pine); the remaining areas consist mostly of successional hardwoods (birch, poplar, aspen), with some scrub-type vegetation in the poorly drained bog areas. The elevational gradient across the site is approximately 50 m, so topographic effects are slight. This site is ideal for ecological research with an emphasis on input from remote sensing platforms for several reasons, including: its location near a major airport; the nearby research support of a major university; the mix of vegetation types across short distances; the low topographic relief; and the large body of information that is already available for the forest.

B. Data Collection

FED-related field research has been under way on the site since 1988 and its scope is cataloged in Smith et al. (1990). For the purposes of this paper, we are focusing on remotely-sensed optical data gathered during the late summer field campaign of 1990 (September 3-14). More specifically, we are addressing the near-simultaneous acquisition of data from AVIRIS, ASAS, and helicopter overflights on September 8th, 1991, all within an hour of solar noon with solar zenith angles near 40°. Other data sets collected at the site, but not discussed here, include both winter and summer radar imagery (JPL AIRSAR; see Ranson & Sun, 1991), passive microwave data (PBMR & ESTAR), SPOT and Landsat image data, and extensive ground observations of important soil, vegetation, canopy and physical parameters.

The data acquired with AVIRIS provides complete coverage of the Northern Experimental Forest, while ASAS and the helicopter-mounted SE-590 bidirectional reflectance data sets were acquired for specific target areas and landscape features within the study area. For this paper, we have extracted and analyzed data for three major cover types within this northern forest ecosystem; hardwood forest, a conifer forest dominated by hemlock, and a bog containing annual grasses, scrub-type bushes (mostly blueberry) and scattered, dwarfed spruce. While we have chosen to look at only these three sites and cover types for this paper, it represents only an initial review of the large quantity of high quality data available from the FED database.

II. Methods

A. Common Sample Sites

The data used in this analysis were purposely chosen for sites where we had coverage from all three of the airborne instruments. The sites were selected after viewing the digital imagery of the AVIRIS and ASAS, and the video tape of the helicopter flights, to make sure that the instruments actually shared the same site coverage. For the AVIRIS and ASAS data sets we extracted polygons of many contigu-

ous pixels from each band to build the spectral radiance curves for each site. The polygons varied considerably in size, depending on the area of relatively uniform cover type that could be delimited. The bog radiance sample was drawn from an area of 6.8 ha, 4.4 ha for hardwoods, and 3.0 ha for conifer site dominated by hemlock. While hovering at 250 m, the helicopter-borne spectroradiometer "sees" a ground area approximately 5 to 6 m in diameter, a much smaller areal sample than either of the aircraft instruments. However, 40 to 60 scans of data are usually acquired over a given target area, so irradiance data is sampled over a much larger portion of the target area than that sampled during an individual scan.

B. Data Processing

1. AVIRIS (224 10 nm bands, 400 to 2450 nm, 20 X 20 m pixel) - We chose a single 256 X 256 pixel area from the radiometrically corrected AVIRIS image data acquired during Run 3 of the September 8th, 1990 overflights of the FED site. This subset of the entire AVIRIS data set was created to facilitate data handling. This area, roughly 5 X 5 km, is large enough to contain all of the major sites of field observations. The data had to be extracted from two adjacent image/tape segments and mosaicked. To do so we first extracted a three band subset from tape segments 1 and 2 from Run 3 to create a near-IR, red, green image to use in subset identification. The three bands were exported to the FED GIS, running on ERDAS, for display and line and element selection from each of the segments for subsetting purposes. The extraction and mosaicking of the 256 X 256 by 224 band image was done with IDL, as was later analysis and graphic production.

Once the *ca* 29 Mbyte file was extracted, we used a locally written interactive IDL screen digitizing routine to identify the vertices of each of the polygons containing the cover type of interest. With the vertices known, it was a simple matter to extract, band by band, all the pixels contained in each polygon, calculate their mean and standard deviation, and save the data in a new array. The final step in processing entailed the removal of data points within areas of band overlap.

2. ASAS (29 15 nm bands, 465 to 871 nm, 4.25 by 2 m pixel) - ASAS is a unique instrument (Irons et al., 1990) that acquires seven view angles (+45°,+30°,+15°, nadir, -15°,-30°,-45°) over a single target through the use of a tilting optical system. Due to its fine spatial resolution and narrow swath, we had to extract data from each of the flightlines which provided coverage of the three sites of interest. We only used nadir data sets in this analysis in order to match AVIRIS data acquisition conditions (i.e., look angle).

The data sets from ASAS are much smaller than those of AVIRIS, so nadir scenes could be directly imported to IDL without subsetting. The polygon selection and data reduction were carried out exactly as for the AVIRIS data, with means and standard deviations calculated and saved, band by band, for each of the polygons. We used radiometrically calibrated ASAS images provided the Goddard ASAS facility.

3. Helicopter (121 5 nm bands, 400 to 1000 nm, non-imaging) - High resolution spectral data were acquired from a NASA UH-1B helicopter, operating out of the Wallops Flight Facility, using a Spectron Engineering SE-590 spectroradiometer equipped with 1° field-of-view (FOV) optics. Given the 1° FOV and a nominal hover altitude of 250 - 300 m, irradiance from an area 5 to 6 m in diameter is recorded with this non-imaging system. A bore-sighted video camera provides a visual record of the flights, and an audible tone is generated with the acquisition of each scan so that the location of data acquisition can be easily determined. By viewing the video record simultaneously while plotting the 40 to 60 scans of spectral data acquired routinely for a single site, we are able to edit the data set for a given site to eliminate extraneous scans which missed the intended target. All of the remaining spectral scans for a given site are analyzed as a single data set, with the radiometrically calibrated means and standard deviations calculated for comparison to the AVIRIS and ASAS data.

C. Data Analysis

1. Atmospheric Conditions - The atmosphere during the acquisition of these FED data sets was extraordinarily clear. The aerosol optical thickness was measured with an 8-band sun-tracking photometer. Data acquired in 4 of the bands (at 440, 557, 612 and 872 nm) are shown in Figure 1, and compared with similar data acquired during the "best" (i.e., clearest) day encountered during any of the FIFE '87 or '89 intensive field campaigns. This comparison graphically illustrates how exceptional the atmospheric aerosol conditions were during the September 8th, 1991 overflights in Maine. During the AVIRIS overflight window, which extended from approximately 11:30 to 11:45 EDST, aerosol optical thickness was found to be less than 0.04 across all bands, and remained at that level until well into the afternoon when it slightly exceeded 0.04.

2. Conversion to Spectral Reflectance - We have not yet converted either the AVIRIS or ASAS radiance to spectral reflectance, since this will require atmospheric modeling of surface irradiance, path length radiance correction and/or reference to measured ground calibration sites. We simply did not have enough time to carry out this work, but it will be done in the near future in collaboration with FED/NASA researchers. We plan to use the atmospheric models of Tanre (personal communication, 1991) or the approaches of Gao et al. or Boardman (this volume), as well as *in situ* calibration measurements made by Dr. Barry Rock and associates from the University of New Hampshire. The helicopter SE-590 data has been converted to spectral reflectance using measured radiances from field calibration targets at the FED site, so these data can be used to test the atmospheric corrections.

3. Comparisons between Sensors - All three data sets are calibrated radiances in μwatts cm^{-2} sr^{-1} nm^{-1}, and as such can be directly compared across wavelengths in common. The calibrated AVIRIS radiance data, as distributed on tape, only had to be converted from its digital number format by dividing by a scaling factor of 200. The comparative radiances from the three instruments are grouped by vegetation cover type in Figures 2 - 4.

III. Results & Discussion

A. Spectral Radiance Comparisons

We have comparative radiance data from three different vegetated sites (i.e., conifer and hardwood forest and a bog) where radiances measured by all three instruments are available. The radiances from all of these sites are plotted by vegetation type in Figures 2 - 4. In general, the radiance curves from the three sensors are very similar within vegetation type, which is remarkable for such a diversity of instrument types and operational parameters. One very clear aspect of the data sets is the strong difference in additive radiance at shorter wavelengths due to multiple scattering and path length. This is not at all surprising given the altitude range of the sensors, ranging from 250 m to over 20 km. Even though the atmosphere was extremely clear during the overflights (Fig. 1), scattering is significant and the radiance in the visible region cannot be directly compared, as Rayleigh scattering in the blue wavelength region significantly attenuates radiance, particularly in the AVIRIS data set which was acquired through the greatest path length. Some evidence of atmospheric absorption may be present in near- to mid-IR regions of the ASAS and AVIRIS data, but the extent of its effects are not known at this point in time. These observations point out the critical need for atmospheric correction in these multiple sensor data sets even when sky conditions are extremely clear.

The conifer forest site (Fig. 2), dominated by hemlocks and other mixed conifers, has a curve shape in the visible nearly identical to that of the hardwood stand (Figs. 3). However, in the infrared portions of the spectrum radiances are much lower, which is an often described feature of conifer canopies. AVIRIS and ASAS radiance in the near-IR is higher than that of the SE-590, perhaps due to their larger sample/pixel size and the inclusion of varied amounts of hardwood crown elements (mostly beech) in their larger sample areas. The SE-590 samples at the individual crown-level, rather than the canopy-level of the AVIRIS and ASAS, so such differences are expected.

The hardwood stand has very similarly shaped spectral curves (Figs. 3), but it is much brighter in the IR. The superimposition of the data for all 3 sensors is nearly identical except in the visible where scattering has a marked additive path length effect. Sample size differences of the 3 sensors seems to have very little effect on radiance, probably an indicator of uniformity of the canopies within this site.

The bog site (Fig. 4) is a bit unusual in that the IR radiance values recorded by the SE-590 are as bright as those recorded over the hardwood site (Fig. 3), but the bog has the lowest IR radiance values of all the sites from the standpoint of AVIRIS and ASAS. As in the case of the hemlock site (Fig. 2) these differences may be due to the size of the sampling area, as the bog supports a two-storied canopy with sparse black spruce trees over a shrub and sphagnum moss understory. Inspection of the video tape revealed that the SE-590 radiance data were acquired over a more sphagnum moss dominated area within the bog. In the visible wavelength region, detail is masked by Rayleigh scattering in the AVIRIS and ASAS data sets, but the SE-590 shows an unusual plateau

in the green to red region. We believe that this increased radiance is due to the moss component with its reduced pigment absorption and strong red coloration.

B. Future Work

Our immediate plans for this AVIRIS radiance data set are to use both measured calibration surface radiances and modeled surface radiance and path length radiance corrections to calculate spectral reflectance for the surface types within the FED research site. Using the FED GIS (geographic information system) we will be able to coregister all of the AVIRIS and other image data sets to a common map projection and use these data sets to sample across the landscape and correlate image-derived data with other corollary data. Rather than hand digitizing of sample polygons, we can use stratified sampling methods to derive the landscape units of interest and extract summary data. Once appropriate algorithms are developed, the radiance or spectral reflectance values can be used alone or with other data from the GIS database to derive ecologically significant data that can be used as input to landscape and global change-related modeling.

IV. Conclusions

The initial comparison of the three high spectral resolution sensors has shown their data to be very similar and remarkably well matched, even prior to atmospheric correction. The spectral matching is excellent, with the red edge of the near-IR plateau very close among all the sensors, and the shape, if not the magnitude of the radiance plots being very close. There is a very pronounced effect of path length radiance in the blue and green portions of the radiance spectra, with the altitude of the platforms playing a clear role. This should be corrected in the near future when the sensor radiances are converted to spectral reflectance.

The results of this initial work with AVIRIS and its comparison with other high resolution spectral data sets from the FED MAC have convinced us of its promise in ecosystem research. Through future work with our collaborators in FED, we will begin to extract critical ecological parameters from the landscape-level AVIRIS data sets. Currently within the FED project, AVIRIS and HIRIS-related research efforts are underway at the leaf, branch and canopy level to elucidate the relationships between spectral reflectance and the water, pigment, nutrient, and biochemical contents of vegetation and litter, and the radiative transfer characteristics of leaves at high spectral resolution. Toward this end, a great deal of field data has already been acquired and is in the process of being analyzed. An additional field campaign with the AVIRIS will take place in early June 1991, at which time many of the questions raised in this initial research will receive further investigation.

References

Boardman, W.W. 1990. Inversion of high-spectral resolution data. p. 222-233 in Gregg Vane (ed) Imaging Spectroscopy of the Terrestrial Environment, SPIE Proceedings, vol. 1298, SPIE, Bellingham, WA.

Gao, B. and A.F. Goetz. 1990. Determination of total column water vapor in the atmosphere at high spatial resolution from AVIRIS data using spectral curve fitting and band ratioing techniques. p. 138-149 in Gregg Vane (ed) Imaging Spectroscopy of the Terrestrial Environment, SPIE Proceedings, vol. 1298, SPIE, Bellingham, WA.

Green, R.O. 1990. Proceedings of the second airborne visible/infrared imaging spectrometer (AVIRIS) workshop. JPL Publication 90-54. NASA, JPL, Pasadena, CA. 280 p.

Irons, J.R., P.W. Dabney, J. Paddon, R.R. Irish and C.A. Russell. 1990. Advanced Solid-State Array Spectrometer (ASAS) support of 1989 field experiments. p. 2-10 in Gregg Vane (ed) Imaging Spectroscopy of the Terrestrial Environment, SPIE Proceedings, vol. 1298, SPIE, Bellingham, WA.

Martin, M.E. and J.D. Aber. 1990. Effects of moisture content and chemical composition on the near-infrared spectra of forest foliage. p. 171-178 in Gregg Vane (ed) Imaging Spectroscopy of the Terrestrial Environment, SPIE Proceedings, vol. 1298, SPIE, Bellingham, WA.

Ranson, K.J. and Q.C. Sun. 1991 (in press). Progress toward SAR based ecosystem analysis. in J. Van Zyl (ed), Proc. of 3rd Airborne Synthetic Aperture Radar (AIRSAR) Workshop. JPL Publication 91-30. NASA, JPL, Pasadena, CA.

Rock, B.N., D.M. Moss, J.R. Miller, J.R. Freemantle and M.G. Boyer. 1990. Spectral characterization of forest damage occurring on Whiteface Mountain, NY: studies with the Fluorescence Line Imager and ground-based spectrometers. p. 190-201 in Gregg Vane (ed) Imaging Spectroscopy of the Terrestrial Environment, SPIE Proceedings, vol. 1298, SPIE, Bellingham, WA.

Smith, J.A., K.J. Ranson, D.L. Williams, E.R. Levine, M.S. Goltz, and R. Katz. 1990. A sensor fusion field experiment in forest ecosystem dynamics. SPIE Int. Symp. Optical Engineering & Photonics in Aerospace Sensing, Orlando, FL., Vol. 1300, pp.117-132.

Tanre, Didier. 1991. (personal communication). Irradiance will be corrected to match our aerosol optical thickness data and operational altitude of the sensor platforms. The 5S code will be used in the calculations; Simulation of the Satellite Signal in the Solar Spectrum, FIRS, Tanre et al. 1990.

Wessman, C.A. and B. Curtiss. 1990. Large-scale ecosystem modeling using parameters derived from imaging spectrometer data. p. 164-170 in Gregg Vane (ed) Imaging Spectroscopy of the Terrestrial Environment, SPIE Proceedings, vol. 1298, SPIE, Bellingham, WA.

Williams, Darrel L., H.H. Shugart, K.J. Ranson, E.R. Levine, D.L. Urban, R.G. Knox and W.T. Lawrence. 1991. Forest Ecosystems Dynamics - Phase II Proposal. NASA/Goddard Space Flight Center, Biospheric Sciences Branch, Code 923, Greenbelt, MD. 66 p.

Acknowledgements

We would like to acknowledge the help given to us by the extensive group of collaborators that have participated with us in the FED MAC's and the FED project in general. This group includes not only colleagues from NASA/Goddard, but others at a number of Universities and other NASA centers. In particular, we would like to thank Dr. Stewart (Mike) Goltz and Forrest Scott at the University of Maine for their help and hospitality while we are on-site, and International Paper for allowing us access to their land, their research staff and inventory data for the Northern Experimental Forest site. The data illustrated herein could not have been presented without the very able assistance of Karl Anderson, Ned Horning, and Moon Kim of STX Corporation, Carol Russell of NYMA, Annie Chui of Ressler Asso., and Ed Masuoka of NASA/GSFC, all of whom helped with various aspects of system administration, tape I/O, and data extraction and analysis. This research was made possible by funding from the NASA Earth Sciences and Applications Division, Ecosystem Dynamics and Biogeochemical Cycles Branch, and the Remote Sensing Science Program.

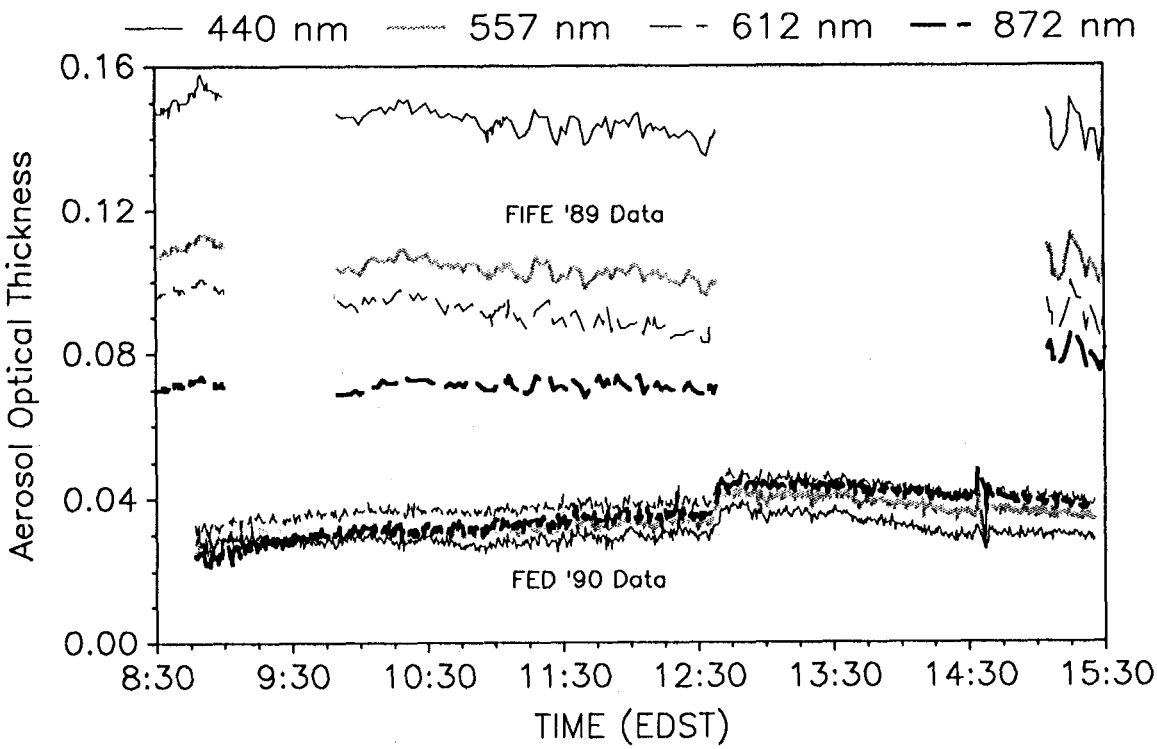

Figure 1. Comparisons of the time course of aerosol optical depth at the FED site near Howland, ME and the FIFE site in Kansas. Separate lines show the optical depth as a function of wavelength.

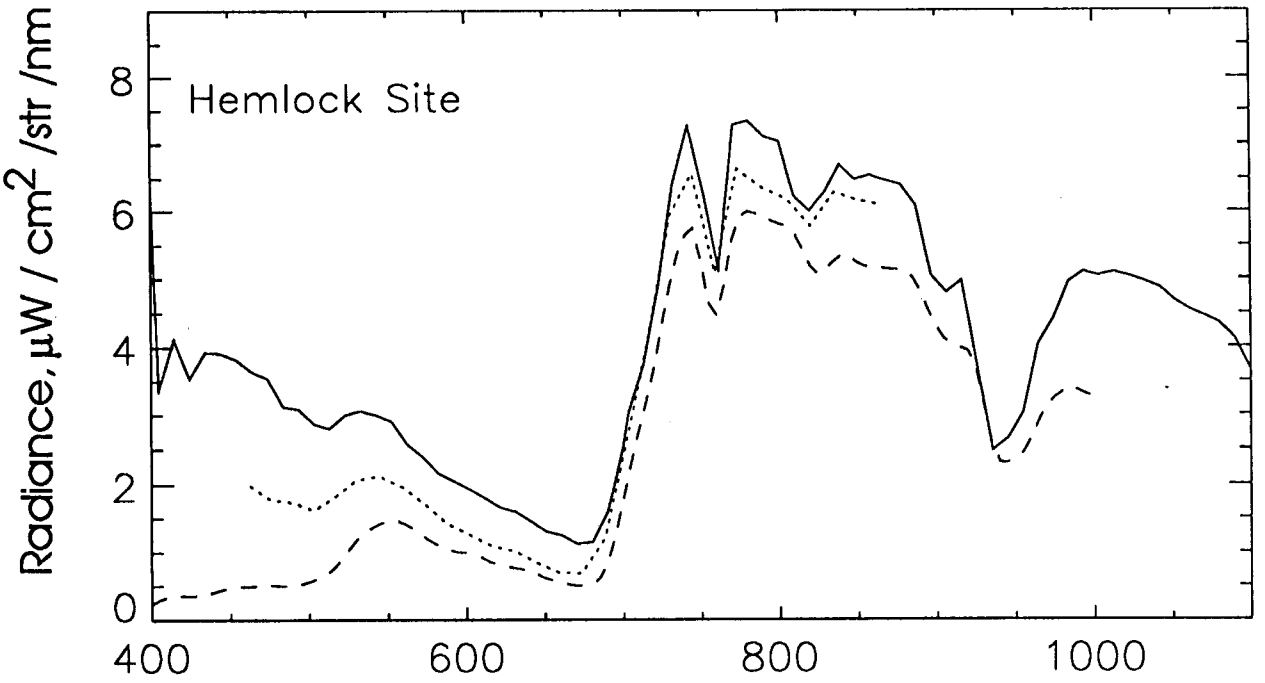

Figure 2. At-sensor radiances for the hemlock site from AVIRIS (solid line), ASAS (dotted line) and SE-590 (dashed line) instruments.

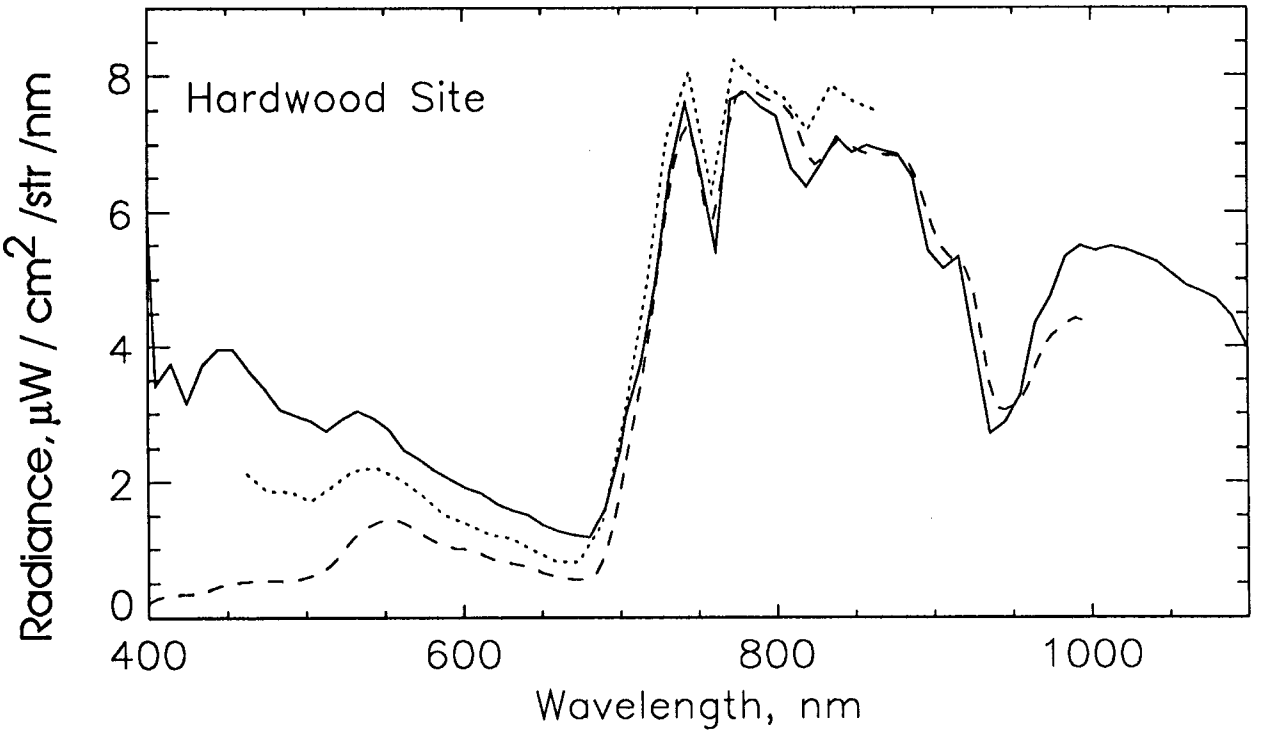

Figure 3. At-sensor radiances for the hardwood site from AVIRIS (solid line), ASAS (dotted line) and SE-590 (dashed line) instruments.

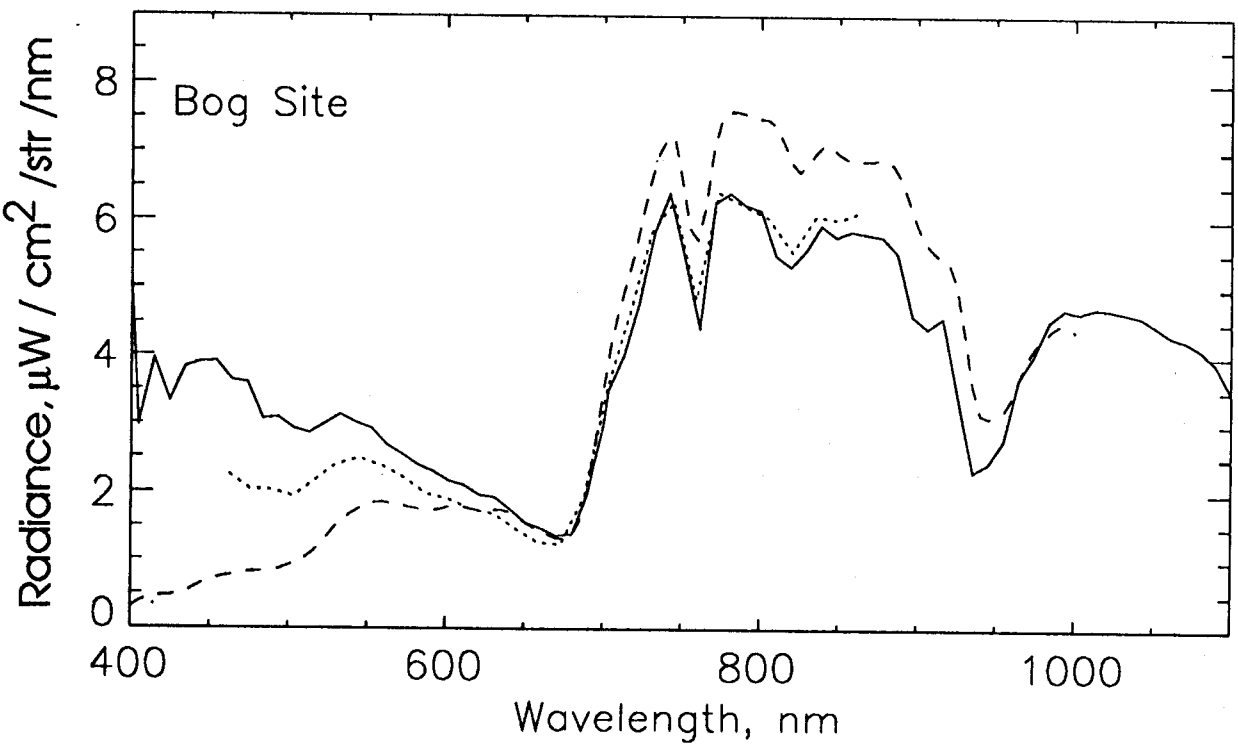

Figure 4. At-sensor radiances for the bog site from AVIRIS (solid line), ASAS (dotted line) and SE-590 (dashed line) instruments.

LEAF SPECTRAL TYPES, RESIDUALS, AND CANOPY SHADE IN AN AVIRIS IMAGE

Roberts, D.A., Smith, M.O., Adams, J.B. and Gillespie, A.R.
Department of Geological Sciences
University of Washington
Seattle, Washington

INTRODUCTION

Spectral mixture analysis was applied to AVIRIS data collected over Jasper Ridge, CA on September 20, 1989. The analysis focused on non-linear spectral mixing between green vegetation and soils and the separation of non-green vegetation, vegetation types and soils using linear spectral mixture analysis and residual analysis (Smith et al., 1987; Gillespie et al., 1990; Roberts et al., 1990; Sabol et al., 1991).

METHODS

The basic linear-spectral mixing model is shown in equation 1.

$$DN_i = g_i \sum_{j=1}^{n} f_j * \rho_{ij} + o_i + \varepsilon_i \quad [1]$$

Using this equation encoded radiance at band i, DN_i, is modeled as the sum of n laboratory reflectance endmembers, ρ_{ij}, each weighted by the fraction of the material in the field of view, f_j. Multiplicative and additive factors used to calibrate encoded radiance to reflectance are shown as g_i, and o_i, respectively. ε_i is a residual term that accounts for all spectral variability that is not accounted for by mixtures of the endmembers and the calibration terms.

Our objective when employing linear spectral mixture analysis was to locate the minimum number of endmembers that described the greatest amount of spectral variability within the scene. To locate other materials, which were not explicitly modeled using endmember spectra we analyzed residual spectra (Equation 2):

$$\varepsilon_i = DN_i - g_i \sum_{j=1}^{n} f_j * \rho_{ij} + o_i \quad [2]$$

Residual spectra can be used to identify materials based on wavelength-dependent positive or negative residuals.

Non-linear spectral mixing occurs when one or more spectra that comprise a mixture contribute more or less to the mixture than should occur based on the proportion of materials in the field of view. Non-linear spectral mixing has been shown to occur between intimate mineral mixtures (e.g. Nash and Conel, 1974; Johnson et al., 1983). Recently it has been shown to also occur between green vegetation and soils (Roberts et al., 1990b, Roberts 1991). Non-linear spectral mixing between green vegetation and soils is primarily a product of the transmission/scattering of NIR light by green vegetation. Roberts (1990a), using

numerical simulations found that a linear mixing model, when applied to mixtures of green vegetation, soils and shade overestimated the green-leaf fraction and underestimated the shade fraction. To determine whether non-linear spectral mixing was significant in AVIRIS data, linear spectral mixing analysis was applied separately to three wavelength regions, the visible, near-infrared (NIR) and short-wave-infrared (SWIR). This approach was used as a test of non-linearity, which should be expressed as different fractional estimates of green-vegetation and shade in the visible, NIR and SWIR subsets. Based on the numerical models, we predicted that the green-leaf fraction estimated from the NIR spectral subset would be higher than the estimates using the visible spectral subset.

A new method was developed to derive improved estimates of green-leaf and shade fractions from non-linear spectral mixtures. This approach was based on the derivation of a canopy shade spectrum (Equation 3).

$$S\lambda = (P\lambda - f_l * \rho_{l\lambda})/f_s \quad [3]$$

Canopy shade, $S\lambda$, was calculated by subtracting a green-leaf spectrum, $\rho_{l\lambda}$, weighted by the fraction of green-leaf, f_l, from the measured/calibrated encoded radiance spectrum, $P\lambda$, and dividing the difference by the fraction of shade, f_s. Using this approach canopy shade spectra was generated for each combination of green-leaf and shade fractions. By constraining the spectrum of shade to be near zero in red light and positive in the NIR a new set of estimates for green-leaf and shade was derived.

When a scene contains more endmembers than green-leaf and shade, equation 3 can be generalized to:

$$S\lambda = (P\lambda - \sum_{i=1}^{n-1}(f_i * \rho_{i\lambda})/f_s \quad [4]$$

RESULTS

The data were calibrated to reflectance using two techniques, an empirical line calibration (Roberts et al., 1986; Elvidge and Portigal, 1990; Conel, 1990) and the linear mixing approach (Smith et al., 1987). We found that non-linear spectral mixing between green vegetation, soils and shade adversely affected the mixing-model calibration when green vegetation was included as an endmember. In canopies, this non-linearity was expressed as a canopy shade spectrum that differed from the photometric (spectrally flat) shade used for calibration. Resulting calibration factors ($g\lambda$ and $o\lambda$) derived from the linear-mixing model produced reflectance spectra that had unreasonably high visible reflectance relative to NIR reflectance (Figure 1). The empirical line calibration was not affected by non-linearities only because vegetation was not employed as a calibration target. Under similar conditions the mixing model calibration will be comparable.

Most of the spectral variability in the image was described by three reference spectra (endmembers): green vegetation, soil and shade. Additional endmembers produced an unstable solution of the mixing equation, degrading the fractional estimates. Other materials known to occur in the image were located by analysis of residual spectra (Figure 2). Using this approach we found that senescent grass could be distinguished from soils based on negative residuals centered at 2100 and 2300 nm.

Negative residuals at 2100 and 2300 nm resulted from absorption by cellulose and lignin in the plant material. Residual analysis was also employed to map soils. Four soils were mapped based on residuals. These included a soil that produced a negative residual centered at 2207 nm, attributed to clay, one that produced a negative residual centered at 1042 nm and one that produced negative residuals at wavelengths shorter than 850 nm (e.g. J9009176 on Figure 2), probably due to ferric iron. The fourth soil corresponded to the soil endmember in the analysis.

Residual spectra were also found to be highly sensitive to spatial/elevational variability in atmospheric attenuation and backscattering. Reduced atmospheric attenuation at higher elevations than the calibration sites was expressed as positive residuals within the atmospheric water bands (Positive spikes in Figure 2). Increased atmospheric backscattering was observed on the eastern half of the image. Atmospheric backscattering did not detract greatly from analysis of the residuals but did have a severe affect on the linear models of the visible spectral subset.

Linear mixing models of the visible, NIR and SWIR spectral subsets demonstrated good correspondence with the numerical predictions for non-linearity. As predicted, green-leaf fractions estimated from the NIR spectral subset were significantly higher than those estimated from the visible spectral subset. Linear models of the visible, NIR and SWIR spectral subsets proved to be useful for distinguishing different types of vegetation, as well as for demonstrating non-linear spectral mixing. Spectrally distinct vegetation types, which could neither be treated as separate endmembers nor distinguished using residual spectra, produced different green-leaf fractions in the three spectral subsets (Figure 3). Two areas were examined in detail. One of the areas, a golf course, produced high green-leaf fractions in all three spectral subsets, suggesting that the dominant vegetation in the area has high visible, high NIR and high SWIR reflectance. This result matches the known spectral properties of leaves in the area. The other area, a forested wetland, produced low green-leaf fractions in the visible and SWIR subsets and high fractions in the NIR suggesting that the dominant vegetation has low visible and SWIR reflectance and high NIR reflectance. Once again, the results matched the known spectral properties of leaves in the area.

Improved estimates of the fraction of green leaf and shade were derived by solving for canopy shade (Figures 4 and 5). Using this approach new shade estimates were derived for the the forested wetland (Swamp) and the golf course vegetation (Lawn). The new estimates for shade were significantly higher than estimates derived from the linear-mixing model. Furthermore, it was found that the canopy shade spectrum derived using this approach was related to vegetation types, varying depending on the transmittance of leaves in the canopy and the architecture of the canopy.

REFERENCES

Conel, J.E., 1990, Determination of Surface Reflectance and Estimates of Atmospheric Optical Depth and Single Scattering Albedo from Landsat Thematic Mapper Data, *Int. J. Remote Sensing*, 11(5): 783-828.

Elvidge, C.D., and Portigal, F.P., 1990, Change Detection in Vegetation using 1989 AVIRIS data, Proc. SPIE Imaging Spectroscopy of the Terrestrial Environment, (G. Vane ed.), Orlando, FL, April 16 - 17, 1990, p. 178-189.

Gillespie, A.R., Smith, M.O., Adams, J.B., Willis, S.C., Fischer, A.F., and Sabol, D.E., 1990, Interpretation of Residual Images: Spectral Mixture Analysis of AVIRIS Images, Owens Valley, California, Proc. 2nd Airborne Visible/Infrared Imaging Spectrometer (AVIRIS) Workshop, Pasadena, Ca, June 4-5, 1990, (R.O. Green, ed.), JPL Publication 90-54, pp.243-270.

Johnson, P.E., Smith, M.O., Taylor-George, S., and Adams, J.B., 1983, A Semiempirical Method of Analysis of the Reflectance Spectra of Binary Mineral Mixtures, *J. Geophys. Res.*, 88: 3557-3561.

Nash, D.B., and Conel, J.E., 1974, Spectral Reflectance Systematics for Mixtures of Powdered Hypersthene, Labradorite, and Ilmenite, *J. Geophys. Res.*, 79(11): 1615-1621.

Roberts, D.A., 1991, Separating Spectral Mixtures of Vegetation and Soils, Unpublished Ph.D. Dissertation, University of Washington.

Roberts, D.A., Adams, J.B., and Smith, M.O., 1990a, Transmission and Scattering of Light by Leaves: Effects on Spectral Mixtures, Proc. IGARRS, College Park, Md, May 20-24, 1990, pp. 1381`-1385.

Roberts, D.A., Smith, M.O., Adams, J.B., Sabol, D.E., Gillespie, A.R., and Willis, S.C., 1990b, Isolating Woody Plant Material and Senescent Vegetation From Green Vegetation in AVIRIS Data, Proc. 2nd Airborne Visible/Infrared Imaging Spectrometer (AVIRIS) Workshop, Pasadena, Ca, June 4-5, 1990, (R.O. Green, ed.), JPL Publication 90-54, pp. 243-270.

Roberts, D.A., Yamaguchi, Y., and Lyon, R.J.P., 1986, Comparison of Various Techniques for Celebration of AIS Data, Proc. 2nd Airborne Imaging Spectrometer Data Analysis Workshop, May 6-8, 1986, JPL Publication 86-35, pp. 243-270.

Sabol, D.E., Adams, J.B., Smith, M.O., and Gillespie, A.R., 1991, Target Detection Thresholds Using Imaging Spectrometer Data, Proc. 3rd Airborne Visible/Infrared Imaging Spectrometer (AVIRIS) Workshop, Pasadena, Ca, May 20-21, 1991, (R.O. Green, ed.), JPL Publication 91-28 (this publication).

Smith, M.O., Roberts, D.A., Shipman, H.M., Adams, J.B., Willis, S.C., and Gillespie, A.R., 1987, Calibrating AIS Images Using the Surface as a Reference, Proc. 3rd Airborne Imaging Spectrometer Data Analysis Workshop, June 2-4, 1987, JPL Publication 87-30, 10 pp.

ACKNOWLEDGEMENTS

We thank Steve Willis for his programming assistance. This research was supported by NASA grant NAGW 1319 and a grant from the W.M. Keck Foundation for computer equipment and support.

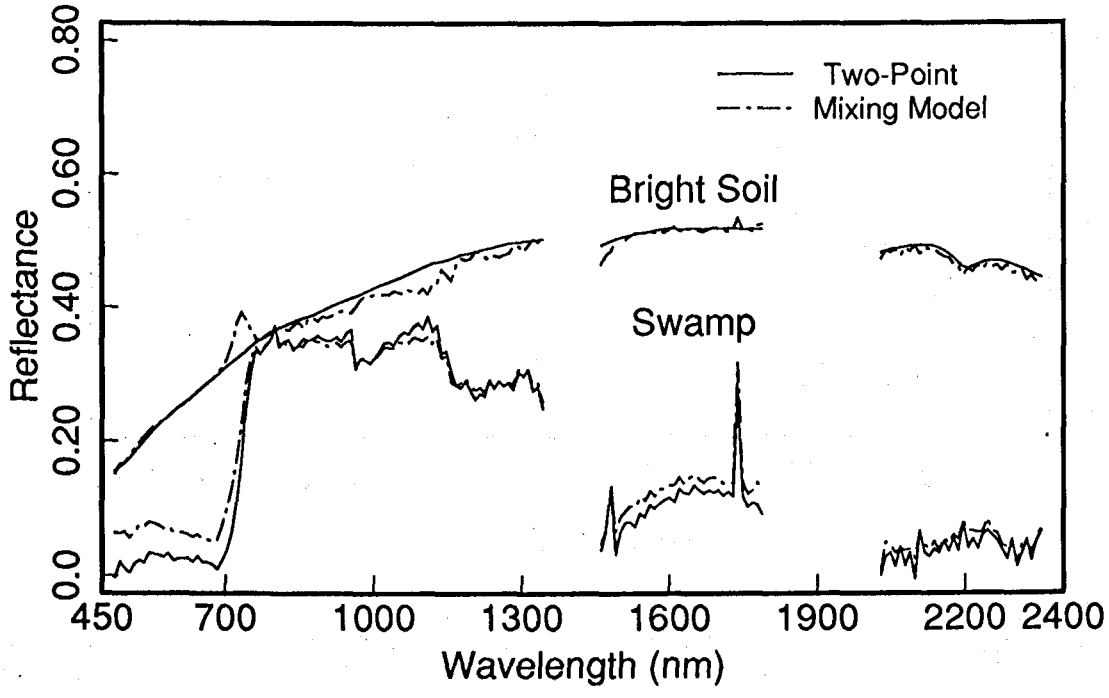

Figure 1. Comparison of the empirical line calibration using non-vegetated targets (two-point - solid) and the mixing model calibration using green vegetation as an endmember(dashed). Two of the calibration sites, Bright Soil and Swamp are shown. Note the similarity between the two results at wavelengths beyond 800 nm. At shorter wavelengths the mixing model calibration produced higher reflectance values than the empirical line calibration.

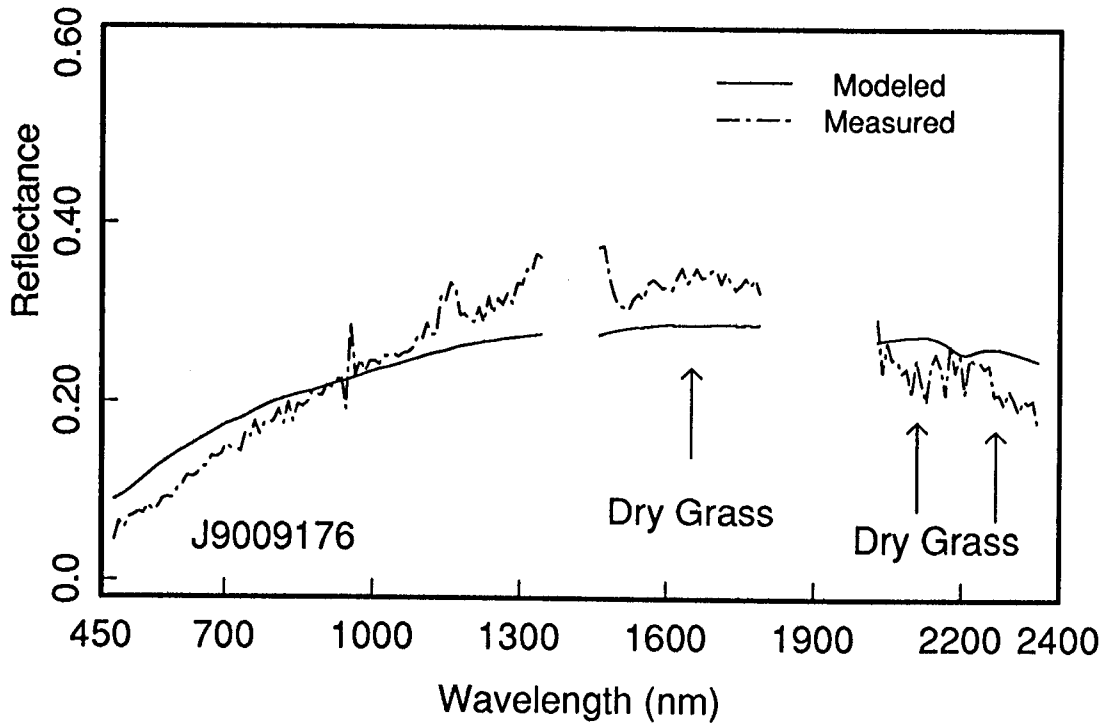

Figure 2. Modeled reflectance spectrum (solid) compared to a measured/ calibrated spectrum for an area dominated by senescent grass located on the central portion of Jasper Ridge. The modeled spectrum was calculated as the linear sum of fractions of green-leaf, shade and soil determined for the area using a linear mixing model. Cellulose and lignin in dry grass produce absorptions in the measured/calibrated spectrum at 2100 and 2300 nm. When a residual spectrum was calculated, the presence of these absorptions produced negative residuals. Negative residuals between 450 and 900 nm are a product of the background soil, which was spectrally distinct from the soil endmember used in the model. Positive features at 940, 1130 and 1400 nm are a product of reduced atmospheric attenuation with increased elevation (Green et al., 1990).

Figure 3. False color composite showing visible, NIR and SWIR green-leaf fractions estimated from the spectral subsets as red, green and blue, respectively. The most obvious feature is a pronounced west (right) to east (left) gradient from blue-green to red in the image. This gradient is a product of increased atmospheric backscattering towards the east, which is modeled as increased green-leaf fractions in the visible model (red). Different vegetation types produced different green-leaf fractions in the three wavelength regions. Grass in the golf courses appears white in the middle of the image, towards the top, due to high green-leaf fractions estimated in all three wavelength regions. Forested wetland (swamp - mid-right) appears green due to low green-leaf fractions in the visible and SWIR and a high green-leaf fraction in the NIR. In all cases, green-leaf fractions estimated using the NIR were higher than they were using visible light [see slide 4].

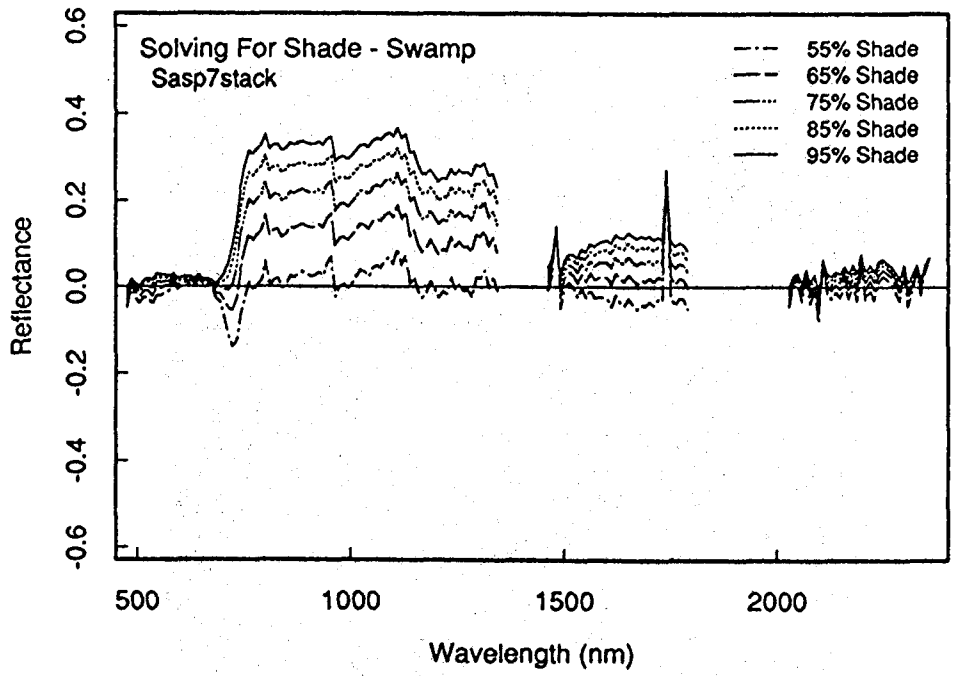

Figure 4. Canopy shade spectra for the forested wetland (Labeled swamp in the Figure). A reasonable shade spectrum was derived at a shade fraction of 85%. Linear estimates for this same area were 56% shade.

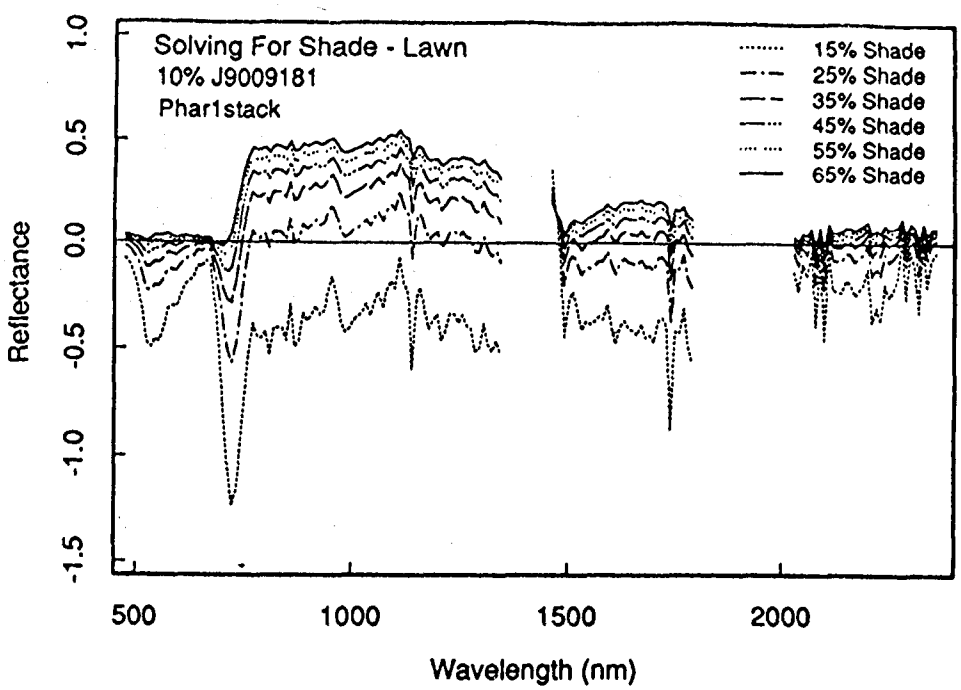

Figure 5. Canopy shade spectra for the golf course grass (Labeled lawn in figure). Shade fractions from this analysis were 65% compared to an estimate of 18% using the linear model. Compare the shade spectrum derived for the grass to the shade spectrum derived for the forested wetland (Figure 4). Note, shade fractions at the golf course were lower, yet the NIR "reflectance" of the shade was much higher.

An Inversion Algorithm for Retrieval of Atmospheric and Leaf Water Absorption From AVIRIS Radiance With Compensation for Atmospheric Scattering

Robert O. Green, James E. Conel, Jack S. Margolis,
Carol J. Bruegge, and Gordon L. Hoover

Jet Propulsion Laboratory
California Institute of Technology
Pasadena, California

Abstract. A radiative-transfer-based algorithm using a nonlinear least-squares fit for the retrieval of total atmospheric and leaf water abundance is described. This algorithm has been developed in pursuit of several objectives: (1) to study the distribution of atmospheric water vapor, which is an essential component of the hydrologic cycle; (2) to determine water vapor column abundance, which is required for the retrieval of surface reflectance from AVIRIS-measured radiance; and (3) to recover leaf water absorptions, which are important components of plant spectral signatures and can be confused with atmospheric water absorptions. The inversion algorithm operates on a nonlinear least-squares fit between the spectral radiance measured by AVIRIS and the spectral radiance calculated by a radiative transfer code. The algorithm generates parameters describing the surface reflectance, surface leaf water absorption, and atmospheric water vapor absorption. The residual error of the band fit and the number of iterations required to reach the solution are also reported. Factors of solar illumination geometry, surface pressure elevation, and atmospheric scattering are constrained and compensated for in the algorithm. Because combined atmospheric scattering and absorption are accounted for in the radiative transfer code, this algorithm allows an effective water vapor retrieval over surface water and dark targets where the upwelling radiance is derived dominantly from atmospheric scattering. Results from this algorithm are presented for an AVIRIS scene containing a healthy alfalfa field and a partially water-covered desert lake bed with in situ measurements of water vapor. For the water-saturated sediments of the lake bed, a liquid water absorption is identified and assessed. The accuracy and precision of this atmospheric and leaf water inversion algorithm are evaluated for these two examples.

1. Introduction

Atmospheric water vapor is a strong absorber across the AVIRIS spectral range, as shown in Figure 1, where spectra are presented with water vapor varying from 0 to 23.56 mm of precipitable water in the atmosphere. In addition to being a strong absorber, the amounts and distribution of the water vapor in the terrestrial atmosphere are highly variable. An example of spatial and temporal variation is given in Figure 2 [see slide 5], where water vapor was retrieved using a continuum interpolated band ratio of the 940-nm water band (Green et al., 1989) over four scenes of Rogers Dry Lake, California. Spatial variation is shown by gradients of 3 mm of precipitable water across this topographically featureless region. Temporal variation is demonstrated by the change in water vapor distribution through four images acquired at 12-min intervals.

Large variations in water vapor can also result from a change in the length of the atmospheric column due to change in surface elevation. For AVIRIS data acquired over the Ivanpah Valley at 800-m elevation and the Clark Mountains at 2000-m elevation, in southeastern California, a corresponding range of 22 to 8 mm of precipitable water vapor was retrieved (Green, 1991). Given the strength of the spectral absorption and the variability, water vapor must be accurately determined to allow the retrieval of surface reflectance from measured radiance over the AVIRIS spectral range. For vegetated areas, leaf water absorptions must be accounted for because of the overlap between the atmospheric and leaf water absorptions. Figure 3 shows these overlapping absorptions with a leaf spectrum superimposed upon a transmission spectrum for atmospheric water vapor. The overlap between the atmospheric and leaf water absorptions presents a challenge to the development of a robust retrieval algorithm. In addition, leaf water absorptions are of direct interest because they are important components of the spectral signature of vegetation.

2. Previous Work

Work on the recovery of water vapor from AVIRIS imaging spectroscopy data was originally pursued with ratios of radiance in and out of the 940-nm water band (Conel et al., 1988). These ratios were converted to precipitable water vapor using the LOWTRAN 7 (Kneizys et al., 1989) radiative transfer code. A continuum interpolated band-ratio algorithm calibrated against LOWTRAN 7 was developed to minimize the influence of change in surface reflectance with wavelength on the retrieval (Green et al., 1989). Calibration with LOWTRAN 7, which included compensation for atmospheric scattering, provided improved retrievals with typical atmospheric visibilities. An atmospheric and surface water band-fitting technique, based on an atmospheric water vapor and liquid water transmission model without compensation for atmospheric scattering, has also been developed and applied to AVIRIS data (Gao and Goetz, 1990). In addition, retrieval of terrestrial water vapor through the ratio of a wide and narrow filter centered at the 940-nm atmospheric water absorption without compensation for the asymmetric leaf water absorption has been described (Frouin and Middleton, 1990).

3. Atmospheric and Leaf Water Absorption Retrieval Algorithm

The present inversion algorithm for retrieval of atmospheric and leaf water uses a nonlinear least-squares fitting approach coupled with the MODTRAN (Berk et al., 1989) radiative transfer code. The radiative transfer code allows treatment of the atmosphere with compensation for (1) solar illumination and aircraft viewing geometries, (2) a seasonal and latitudinal atmospheric model, (3) atmospheric gaseous absorptions, and (4) molecular and aerosol scattering. In addition, the incorporation of a surface-reflectance model with the liquid water absorption of green vegetation addresses the asymmetrically overlapping absorptions of the atmospheric and leaf water.

AVIRIS measures the total upwelling radiance in nominally 10-nm spectral channels across the 940-nm atmospheric and 980-nm leaf water absorption bands. The inversion algorithm proceeds by establishing a nonlinear least-squares fit between AVIRIS-measured spectral radiance and radiative-transfer-code-modeled spectral

radiance, where the parameterized surface-spectral-reflectance function (including leaf water absorption) and the scaled atmospheric water vapor amount are allowed to vary. A computational routine applying the downhill simplex method for nonlinear least-squares fitting is applied (Nelder and Mead, 1965; and Press et al., 1986). The MODTRAN spectral radiance is calculated for each AVIRIS channel for a specific amount of atmospheric water vapor. The radiance is modeled as the total upwelling radiance, $L_t(H_2O_v)$, which results from a surface-reflected radiance, $L_r(H_2O_v)$, and an atmospheric-path-scattered radiance, $L_p(H_2O_v)$, as given in Equation 1:

$$L_t(H_2O_v) = L_r(H_2O_v) + L_p(H_2O_v) \quad (1)$$

The surface-reflected component of the radiance is described as the exoatmospheric solar irradiance multiplied by the cosine of the solar zenith angle over pi steradians, $E_s\cos\theta/\pi$, multiplied by the downward diffuse plus direct transmittance, T_d, surface lambertian reflectance, ρ, and upward diffuse plus direct transmittance, T_u, as in Equation 2:

$$L_r(H_2O_v) = [E_s\cos\theta/\pi]T_d\rho T_u \quad (2)$$

The surface reflectance is modeled as shown in Equation 3 as the sum of a reflectance offset, α, a reflectance slope, β, with respect to wavelength, λ, and a proportion, γ, of spectral leaf water absorption, H_2O_l.

$$\rho = \alpha + \beta\lambda + \gamma(H_2O_l) \quad (3)$$

The spectral region to which this algorithm applies is 850 to 1100 nm, which includes both the 940-nm atmospheric water band and the 980-nm leaf water absorption. The fit is performed with the 26 AVIRIS channels contained within this spectral region. The leaf water absorption spectrum $\alpha(\lambda)$ used for this algorithm is given in Figure 4. This spectrum was derived by normalization of a laboratory-measured alfalfa-leaf spectrum across the 980-nm water absorption region and is scaled by a factor γ.

MODTRAN is initialized with the solar illumination geometry appropriate for the AVIRIS data set. An atmospheric model is selected based on the location and season of the AVIRIS acquisition. Atmospheric-scattering properties are constrained by scaling the atmospheric model to in situ measurements of the optical depth or estimates of the visibility. In the presence of significant topographic relief, the optical depths are extrapolated across the AVIRIS scene through modulation with estimates of the surface pressure elevation derived from the absorption of carbon dioxide or oxygen measured within the AVIRIS spectrum.

The inversion algorithm operates on the spectrum of each AVIRIS spatial element and generates images of the fit parameters of reflectance offset, reflectance slope, leaf water absorption, and abundance of atmospheric water vapor. In addition, images of the root-sum-squared (RSS) residual radiance in the fit and the number of iterations required to achieve the fit are generated.

4. AVIRIS Radiance Inversion for Atmospheric and Leaf Water

This inversion algorithm has been evaluated with an AVIRIS radiance image over a portion of Mesquite Valley, California. This scene contains desert surface cover, as well as heavily vegetated fields of alfalfa grown under pivot irrigation. These data were acquired on July 23, 1990. Figure 5 shows a radiance image of the Mesquite Valley scene. The algorithm was constrained with the solar illumination geometry, in situ measurements of atmospheric optical depth, a rural midlatitude summer atmospheric model, and an estimate of the mean elevation of the scene. The optical depths were measured at a site 40 km to the south, at approximately the same elevation. At 400 nm, the total optical depth was 0.4, indicating minimal aerosol scattering. In Figure 6 [slide 6], the results of the inversion algorithm are presented. From upper left to lower right, the images correspond to the parameters of reflectance offset, reflectance slope, leaf water absorption, atmospheric water amount, RSS residual radiance, and a number of iterations required for the fit. In parameter images 3 and 4, the surface leaf water and atmospheric water vapor are successfully separated with no confusion between the leaf and atmospheric water over the alfalfa fields. Figure 7 gives a comparison of the AVIRIS-measured radiance spectrum and the inversion algorithm fit for a spectrum from the alfalfa field. The residual between these two spectra is given in Figure 8. The reflectance spectrum determined by the algorithm to achieve this fit is given in Figure 9. The presence of leaf water absorption in this spectrum is consistent with the presence of healthy alfalfa at the surface.

To further evaluate this atmospheric and leaf water inversion algorithm, an AVIRIS data set acquired over the Ivanpah Playa, on March 7, 1991, has been examined. A radiance image of the Ivanpah site is given in Figure 10. At the time of acquisition, a portion of the playa surface was inundated by water and represented a dark target at 940 nm. The algorithm was constrained with solar geometry, in situ optical-depth measurements, an appropriate atmospheric model, and mean surface elevation. The optical-depth measurements were acquired concurrently with the AVIRIS data at a site just above the oval feature on the playa. At 400 nm, the total optical depth was less than 0.4 throughout the day (visibility = 300 km). Figure 11 presents the results from the inversion algorithm. From the water vapor parameter image, a value of 3.5 mm of precipitable water vapor was retrieved for the site on the playa. An independent determination of water vapor was generated from sun photometer measurements at this site using a spectrally based retrieval algorithm (Bruegge et al., 1990). This determination produced a value of 3.7 ± 0.2 mm of water vapor at about 19:30 UCT when the AVIRIS data were acquired.

The algorithm was further evaluated for retrieval of water vapor over surface water by examining the results obtained over the inundated portion of the playa. This water vapor parameter image displays no observable boundary effects caused by the transition from the bright playa to the dark water surface implying that the method successfully compensates for spectral surface reflectance changes. Consistent retrieval of water vapor over this dark water surface results from the inclusion of a combined treatment of gaseous absorption and atmospheric scattering in the algorithm. For such targets, atmospheric-scattered-path radiance dominates the upwelling radiance measured by AVIRIS. Also associated with the inundated portion of the playa is a region of water-saturated playa sediment. These saturated sediments

exhibit a liquid water absorption analogous to the leaf water, which is partitioned into the leaf water parameter image by the inversion algorithm. Figure 12 presents the laboratory reflectance spectrum for dry and water-saturated sediment from the Ivanpah Playa. This inversion algorithm generates consistent water vapor and leaf water results over vegetated and unvegetated surfaces, as well as dark surfaces and water-saturated sediments.

5. Error Discussion

Validity of the reflectance model and radiative transfer code is a factor that directly influences the accuracy of the atmospheric and leaf water retrievals. Constraints of the input parameters of the radiative transfer code, particularly on atmospheric scattering and the spatial variation of scattering, affect the retrieval. The accuracy of atmospheric and leaf water retrieval will also be influenced by the absolute radiometric calibration of the AVIRIS sensor. The radiometric accuracy of AVIRIS is traced to the laboratory calibration (Chrien et al., 1990) and validated through periodic in-flight calibration experiments (Green et al., 1990).

To evaluate the character and accuracy of the fit between the AVIRIS-measured radiance and the MODTRAN-calculated radiance, the residual RSS error and the number of iterations to achieve the fit are reported. These parameters provide a rapid evaluation of the quality of the fit, and analysis of these images allows further refinement of this inversion algorithm.

Absolute accuracy of this algorithm is currently validated solely at the Ivanpah Playa site where in situ water vapor measurements were acquired. Additional AVIRIS scenes with in situ measurements have been identified for continued validation analysis.

Within each AVIRIS scene, the precision of water vapor retrieval will be a function of the sensor performance, solar illumination, surface reflectance, and amount of water vapor. To estimate the precision of the retrievals, a statistical method is adopted. This method proceeds by calculating the root-mean-squared deviation (RMSD) of all possible 5 by 5 spatial-element regions within the water vapor image. The lowest calculated RMSD is reported as an estimate of the water vapor retrieval precision. This lowest RMSD corresponds to the most homogeneous portion of the water vapor image, where instrument noise should represent the dominant contributor to variability. This is a worst-case estimate of the precision because any residual variability in water vapor within the 5 by 5 area is included in this precision estimate. For the Mesquite Valley scene, a precision of ±0.3 for 15.4 mm of water vapor was estimated. The Ivanpah Playa scene acquired under the winter-illumination condition yielded a precision estimate of ±0.2 for 3.4 mm of water vapor. These precision estimates are determined at the full AVIRIS spatial resolution and may be improved by spatial averaging of the data.

6. Conclusion

An inversion algorithm for retrieval of atmospheric water vapor and surface leaf water absorption from AVIRIS-measured radiance has been developed. This algorithm is

based on a nonlinear least-squares fit between an AVIRIS radiance spectrum and a radiative-transfer-code-modeled spectrum. For each spatial resolution element of the AVIRIS image, the parameters generated by the algorithm are reflectance offset, reflectance slope with respect to wavelength, surface leaf water absorption, and atmospheric water vapor absorption. Inclusion of atmospheric-scattered radiance in the MODTRAN radiative transfer code and the combined treatment of gas absorption and scattering allow retrievals over dark targets such as surface water. This algorithm has been applied to two AVIRIS scenes. The first scene of the Mesquite Valley region contains extreme contrasts in surface vegetation cover. Both atmospheric water and leaf water absorptions are retrieved by the algorithm in a manner consistent with the distribution of surface cover. A second AVIRIS scene of the Ivanpah Playa, California region was examined with the algorithm. For this image, a good agreement was obtained with in situ column water vapor measurements. In addition, water vapor was retrieved successfully over an inundated portion of the playa. This inversion algorithm has applications towards the objectives of direct study of water vapor, compensation for water vapor in the retrieval of reflectance, and study of plant spectral signatures. Future work will be directed towards further validation of absolute accuracies of the retrieval, as well as refinement of estimation of the retrieval precisions. Issues associated with the accuracy of the radiative transfer code itself with emphasis on the treatment of atmospheric scattering will also be investigated.

Acknowledgment

This research was carried out at the Jet Propulsion Laboratory, California Institute of Technology, under contract with the National Aeronautics and Space Administration.

References

Berk, A., L. S. Bernstein, and D. C. Roberson, "MODTRAN: A Moderate Resolution Model for LOWTRAN 7," U.S. Air Force Geophysical Laboratory, Hanscom Air Force Base, Massachusetts, 1989.

Bruegge, C. J., J. E. Conel, J. S. Margolis, R. O. Green, G. Toon, V. Carrere, R. G. Holm, and G. Hoover, "In-Situ Atmospheric Water Vapor Retrieval in Support of AVIRIS Validation," *Imaging Spectroscopy of the Terrestrial Environment*, SPIE Vol. 1298, 1990.

Chrien, T. G., R. O. Green, and M. Eastwood, "Laboratory Spectral and Radiometric Calibration of the Airborne Visible/Infrared Imaging Spectrometer (AVIRIS)," *Imaging Spectroscopy of the Terrestrial Environment*, SPIE Vol. 1298, 1990.

Conel, J. E., R. O. Green, V. Carrere, J. S. Margolis, R. E. Alley, G. Vane, C. J. Bruegge, and B. L. Gary, "Atmospheric Water Mapping With the Airborne Visible/Infrared Imaging Spectrometer (AVIRIS), Mountain Pass, CA," *Proceedings of the AVIRIS Performance Evaluation Workshop* (G. Vane, ed.), JPL Publication 88-38, Jet Propulsion Laboratory, Pasadena, California, pp. 21–26, 1988.

Frouin, R., and E. Middleton, *Proceedings of AMS Symposium on FIFE*, 70th AMS Annual Meeting, Anaheim, California, pp. 135–139, 1990.

Gao, B.-C., and A. F. H. Goetz, "Column Atmospheric Water Vapor and Vegetation Liquid Water Retrievals From Airborne Imaging Spectrometer Data," *J. Geophys. Res.*, Vol. 95, pp. 3549–3564, 1990.

Green, R. O., V. Carrere, and J. E. Conel, "Measurement of Atmospheric Water Vapor Using the Airborne Visible/Infrared Imaging Spectrometer," *Image Processing '89*, American Society for Programmetry and Remote Sensing (ASPRS), 1989.

Green, R. O., J. E. Conel, J. S. Margolis, V. Carrere, C. J. Bruegge, M. Rast, and G. Hoover, "In-Flight Validation and Calibration of the Spectral and Radiometric Characteristics of the Airborne Visible/Infrared Imaging Spectrometer (AVIRIS)," *Imaging Spectroscopy of the Terrestrial Environment*, SPIE Vol. 1298, 1990.

Green, R. O., "Retrieval of Reflectance From AVIRIS-Measured Radiance Using a Radiative Transfer Code," *Proceedings of the Third Airborne Visible/infrared Imaging Spectrometer (AVIRIS) Workshop*, JPL Publication 91-28, Jet Propulsion Laboratory, Pasadena, California, 1991 (this publication).

Kneizys, F. X., E. P. Shettle, G. P. Anderson, L. W. Abrew, J. H. Chetwynd, J. E. A. Shelby, and W. O. Gallery, "Atmospheric Transmittance/Radiance: Computer Code LOWTRAN 7," U.S. Air Force Geophysical Laboratory, Hanscom Air Force Base, Massachusetts, 1989.

Nelder, J. A., and R. Mead, *Computer Journal*, Vol. 7, p. 308, 1965.

Press, W. H., B. P. Flannery, S. A. Teukolsky, and W. T. Vetterling, *Numerical Recipes*, Cambridge University Press, 1986.

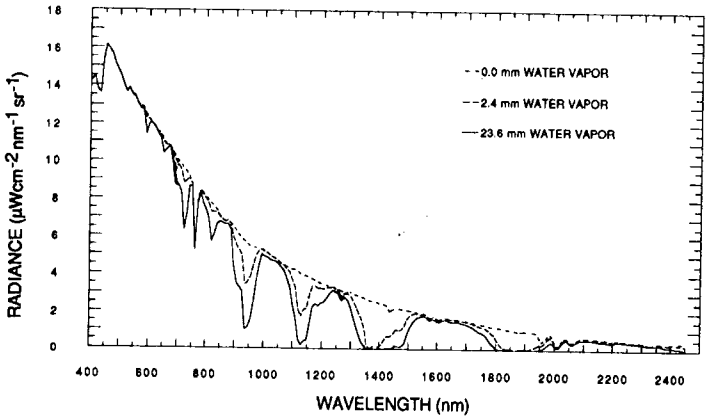

Figure 1. Water vapor absorption over the AVIRIS spectral range, modeled by MODTRAN as the total-column precipitable water varies from 0 to 23 mm.

Figure 2. Water vapor retrieved for four consecutive overflights of the Rogers Dry Lake, California calibration site. Both patchiness in water vapor and change in water vapor through time are shown.

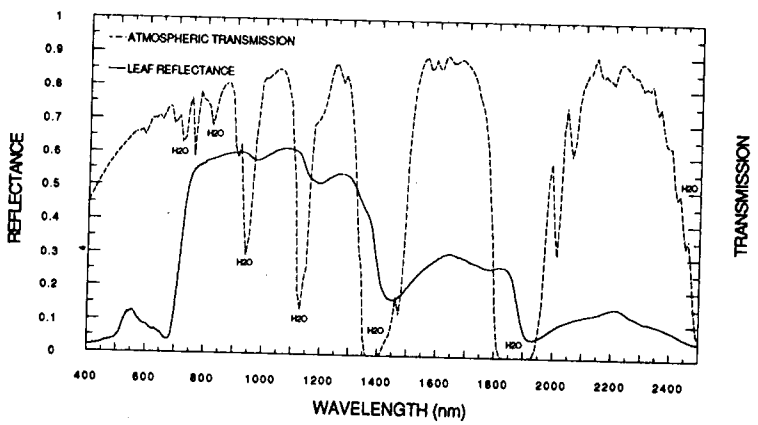

Figure 3. Laboratory reflectance spectrum of alfalfa leaves with the atmospheric transmission for water vapor superimposed. These spectra show the overlap between the atmospheric water vapor and leaf water absorptions.

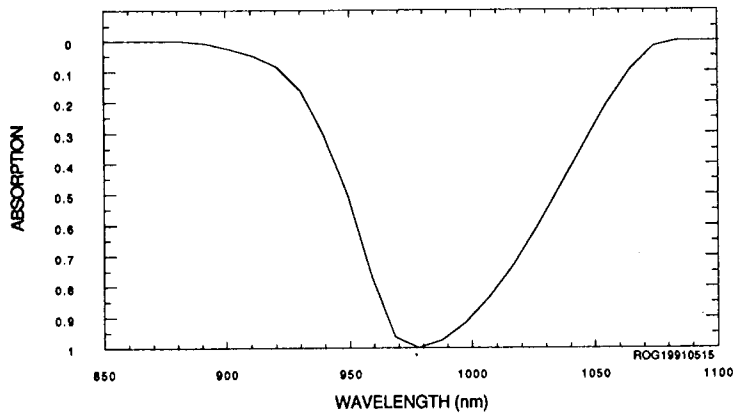

Figure 4. Normalized leaf water absorption spectrum used in the inversion algorithm.

Figure 5. An AVIRIS image of pivot irrigation field of alfalfa in Mesquite Valley, California. These data were acquired on July 23, 1990. The scene center is at 35 deg, 48.3 min north latitude, and 115 deg, 41.7 min west longitude.

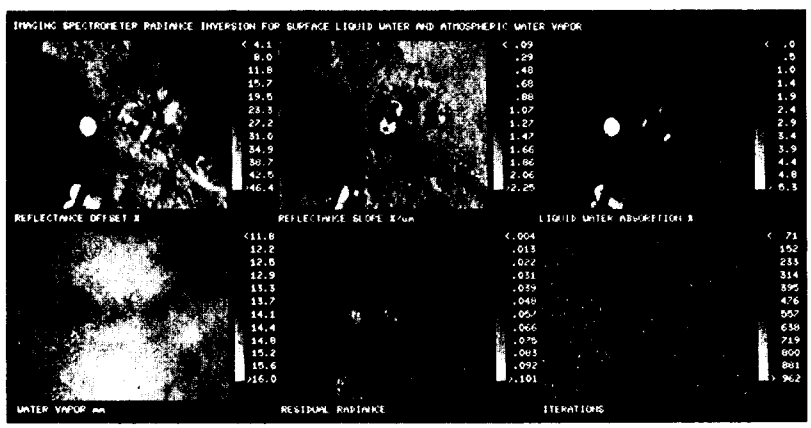

Figure 6. Retrieval of leaf and atmospheric water vapor for pivot alfalfa fields from AVIRIS-measured radiance. Top row: retrieved reflectance offset, reflectance slope, and leaf water. Bottom row: retrieved atmospheric water, residual error, and number of iterations for solution.

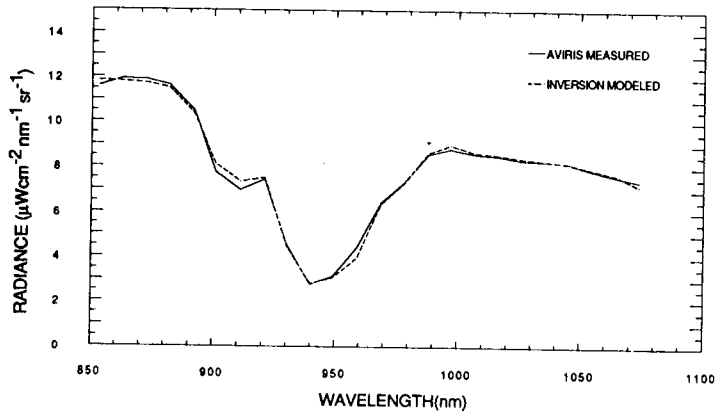

Figure 7. Result for the alfalfa field presenting the AVIRIS-measured radiance spectrum and the inversion-algorithm-calculated radiance spectrum.

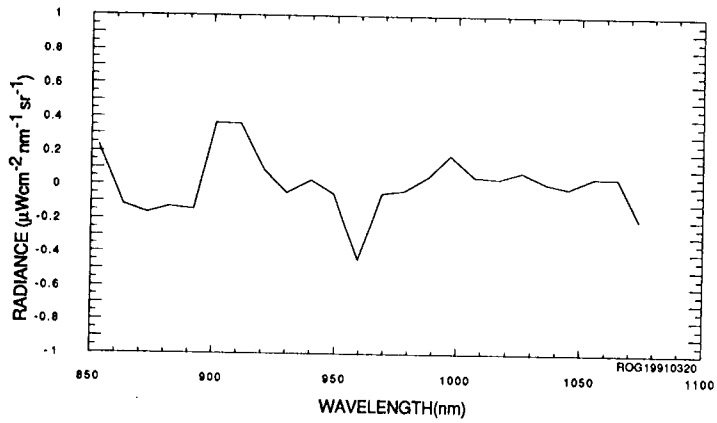

Figure 8. Radiance residual for the central alfalfa field following application of the inversion algorithm.

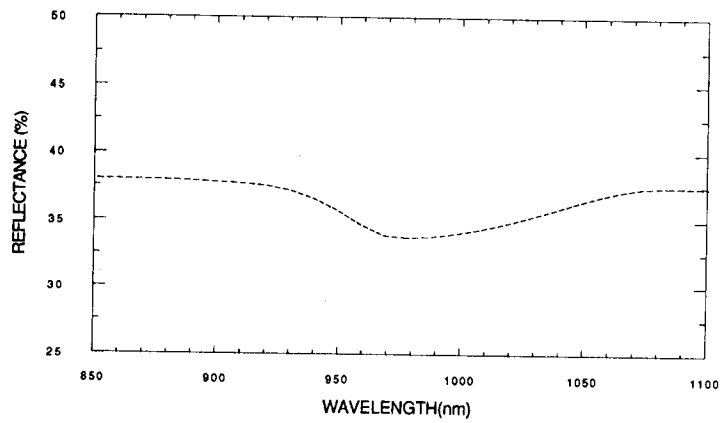

Figure 9. Reflectance spectrum determined by the nonlinear least-squares fitting algorithm for the central alfalfa field. As expected the surface leaf water absorption is recovered.

Figure 10. AVIRIS image of the Ivanpah Playa, California. A portion of the playa is inundated with water. Regions of water-saturated playa soil are found adjacent to the standing water.

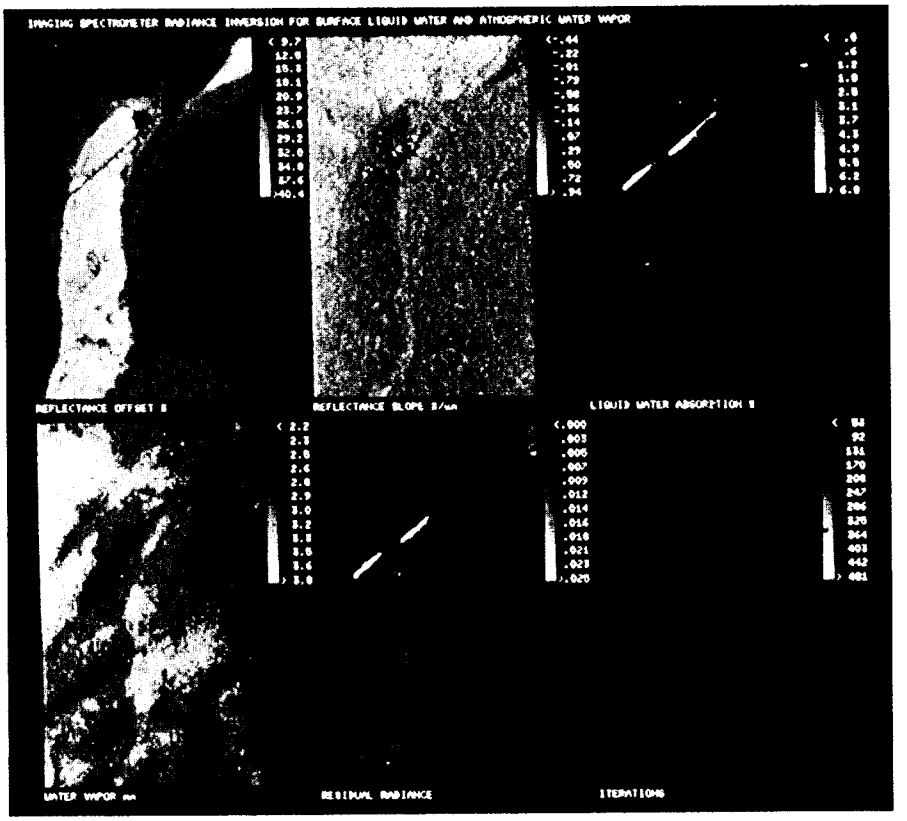

Figure 11. Atmospheric water vapor retrieval for the Ivanpah Playa AVIRIS radiance imagery. Water vapor is successfully retrieved over the standing water and regions of water-saturated playa soil. The saturation soil is isolated based on the presence of liquid water absorption features.

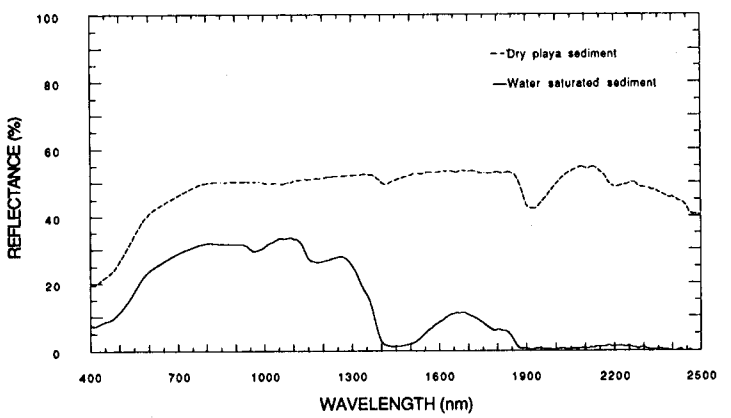

Figure 12. Reflectance spectrum of dry sediment from the Ivanpah Playa and a spectrum of water-saturated sediment. These data were acquired by a laboratory spectrometer and convolved the AVIRIS spectral characteristics.

IMAGING SPECTROSCOPY DATA USED FOR GEOLOGICAL AND ENVIRONMENTAL ANALYSIS IN EUROPE

F. Lehmann, H. Rothfuss, K. Werner
DLR - German Aerospace Research Establishment
Institute for Optoelectronics
D - 8031 Oberpfaffenhofen, Germany

Abstract. During the EISAC Campaign carried out in May/June 1989 six european countries were flown with the GER Scanner and the Metric Camera on water and land test sites for oceanographic, hydrologic, vegetation and soil spectral studies. Atmospherically corrected GER-II Imaging Spectrometry data acquired during the EISAC Campaign are employed for the spectral analysis of vegetation growing over a former waste deposit in Southern Bavaria. Spectral anomalies were observed in the vegetation cover which are likely to be attributed to the buried material. The result of a scene classification based on the spectral signatures shows a correlation with infill structures on the formerly open site. Geochemical sampling over the site revealed high heavy metal concentrations as a probable source for the spectral differences. This environmental application of imaging spectrometry data with new quantitative evaluation methods could reduce extensive ground surveys and be of economical interest if developed to an operational state.

The Almaden testsite (Spain) was selected for the spectral analysis of soil and vegetation in a mediterranean environment, taking account of the soil spectral characteristics dependent on the geological situation. A parallel field survey comprised field spectroscopy measurements, soil sampling and vegetation inventory. Results of spectral classification analyses of GER airborne data for the differentiation of soil surfaces with variable mineral content are demonstrated.

Keywords: Imaging Spectrometry, atmospheric correction, vegetation anomalies, waste deposits, geology

I. APPLICATION FOR ENVIRONMENTAL RESEARCH

A. Introduction

Regarding the number of old, unprotected waste deposits (e.g. in Germany about 50,000), and the environmental threats related to many of these sites, new methods have to be found to reduce the costly and time consuming ground surveys. Reflectance data derived from high spectral and spatial resolution Imaging Spectrometers provide a new physical parameter in the analysis of these sites. The spectral response of the vegetation cover on and near to the deposit is examined for signatures which could be related to the influence of stress caused by the buried material. Possible applications are the long term monitoring of sites, detection of leakages or the planning of ground surveys based on the delineation of spectrally anomalous areas.

B. GER-II Spectrometer Data Evaluation

1. The GER-II Imaging Spectrometer

The GER 63 channel spectrometer (also known as the GER Airborne Scanner) from Geophysical Environmental Research Corp., New York, consists of three spectrometers which view the ground through the same aperture via an optoelectronic scanning device. A

rotating Kennedy cube scanner scans a line of 512 pixels perpendicular to the flight track with a scan angle of 45° to either side of the flight direction. The incoming radiation of a ground pixel is split and sent to three spectrometers, each with a separate line detector array, giving a total of 63 spectral bands through the visible (VIS), near- and shortwave infrared (NIR, SWIR) between 0.47 μm and 2.45 μm. The specifications of the spectrometers are listed in Table 1. The digital resolution of the data is 12 bit with a dynamic range of 16 bit which makes gain changes over varying terrain conditions unnecessary. An instantaneous field of view (IFOV) of 3.3 mrad was selected for all test sites which leads to a pixel size of 10 m at 3000 m flight altitude. The swath width for this aperture size and the same altitude is 6 km. Dark currents are automatically subtracted from the signal by incorporation of dark object calibration plates in the scanner.

Spectro-meter	spectral coverage [μm]	spectral bands	sampling interval [nm]
1	0.47 - 0.84	31	12.3
2	1.40 - 1.90	4	120
3	2.00 - 2.45	28	16.2

Table 1: Spectrometer specifications of the GER Scanner.

2. Atmospheric correction

Prior to the atmospheric correction some pre-processing steps including a roll correction and electronic time constant correction were carried out. These steps and the calibration procedure are described in more detail elsewhere (Ref.1,2).
An atmospheric correction was applied to convert the digital numbers (DN) in all channels to reflectance values. The atmospheric modelling is based on the LOWTRAN-7 model which calculates atmospheric transmittance and background radiance over a very broad wavelength region, based on the geometrical configuration between sun, target and observer (Ref.3). The model incorporates multiple scattering which is important in the VIS/NIR region and provides a series of standard atmospheres, including aerosol types and ozone profiles.

For the investigated GER-Scanner scene, the atmospheric data was derived from the 12°° UT radiosonde of the nearest meteorological station. The measured atmospheric parameters included pressure, air temperature and humidity up to an altitude of 15 km. This data was fed into the LOWTRAN-7 model and supplemented with default values of a midlatitude standard atmosphere up to an altitude of 100 km. The aerosol type and visibility were determined iteratively by constraining the reflectance values of dark targets to positive values.

The results of the LOWTRAN run are the input for the DLR developed model SENSAT-3 (SENSor-Atmosphere-Target) which relates planetary albedo to ground albedo on a per-pixel basis (Ref.4). The model SENSAT takes account of the sensor characteristics and the viewing geometry. As the viewing geometry changes over 90° during a scan, the LOWTRAN/SENSAT calculations are performed in small angular steps. In the VIS/NIR wavelength region the atmospheric modelling included a correction of the adjacency effect. This correction takes account of the reflected and scattered radiation entering the sensor from pixels in the neighbourhood of the actual target.

After atmospheric correction multitemporal datasets or data of different sensors are comparable. Even for single scenes of a sensor it is useful to eliminate the atmospheric influence. The corrected airborne data only depends on the surface properties and can

therefore be directly compared with ground spectroscopic measurements.

C. Investigation of a Waste Deposit Test Site

The atmospherically corrected data of a GER-Scanner scene, recorded in the course of the European Imaging Spectrometry Airborne Campaign 1989 (EISAC 1989, Ref.1) under excellent weather conditions, was used for a spectral analysis of an old vegetation covered waste deposit.

1. Site Description

The examined waste tip in Southern Bavaria was opened in 1899 and served as a disposal site for communal and industrial waste. After the site was closed in 1949, the main part was used for agricultural purposes. At that time no protective measures were taken to prevent leakage of waste material into the surrounding environment. The site covers an area of about 1km². A field survey during the EISAC-campaign showed that the site only has little topography and that the main part was equally dense covered with corn (rye) of the same height and maturity. This corn stand was further investigated (test site).

2. Spectral Analysis and Scene Classification

Though the test site looked apparently homogeneous, spectral differences were observed in the atmospherically corrected GER-Scanner data. Averaged spectra of all 63 channels were extracted at different positions in the corn stand on the waste deposit. The corn spectra exhibit differences in reflectance which are in the range of 3% for the VIS and SWIR and up to 5% in the NIR wavelength region (Fig.1). It was found that reflectance increases across the test site. The spectral differences in the corn stand will be referred to as 'vegetation anomalies in the following, whereby the unmarked spectrum in figure 1 is "normal" (no vegetation anomaly) on a relative scale. The increasing reflectance values in the VIS and SWIR wavelength range in relation to the normal spectrum were associated with vegetation anomalies of increasing strength. Such a spectral behaviour was found in another study due to the influence of heavy metals (Ref.5).

Based on the four corn spectra in figure 1, a classification of the whole scene using the least noisy 55 channels was made on a per pixel basis. Four different class values, representing the four vegetation anomalies of different strength, could be assigned to a pixel. A pixel of the low-pass filtered image was marked as belonging to a certain vegetation anomaly class if all its spectral points fell into the range of one standard deviation below and above the corresponding classification spectrum. Otherwise the pixel was rejected. In the case of multiple assignments, a matchscore based on the average deviation of the pixel from the matched anomaly spectra was used as a criterion in the class assignment. The result of the classification, i.e. the spatial distribution of the anomaly classes is shown in figure 2.

This figure includes 2 aerial photographs, acquired in October 1941 and 1943. The photographs reveal the infill structures at a time when the site was still in use. It is noticeable that the distribution of the pixels belonging to the "strong" vegetation anomaly class correlates with infill structures of the open site, as the comparison with the old aerial photograph shows, whereas the "no" anomaly class is found in areas where no infill marks are noticeable. This correlation, the results of the field survey and the fact that the site is not sealed strongly suggests that the buried material causes the spectral differences.

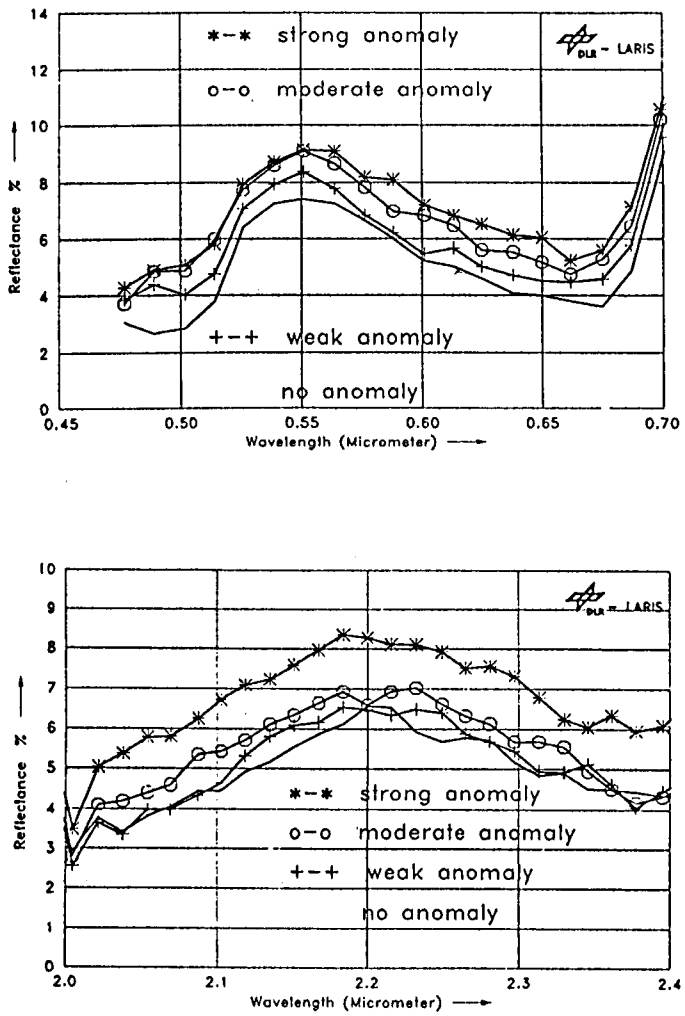

Figure 1. Average reflectance spectra from four different locations on the testsite displaying spectral anomalies in the corn stand
above: VIS wavelength range
below: SWIR wavelength range

Figure 2. Scene classification of the vegetation anomalies on the recultivated waste deposit area **blue:** no anomaly class, **light blue**: weak anomaly, **[see slide 7]**
dark green: moderate anomaly, **red**: strong anomaly class.
2 Aerial photograph of the open site in October 1941 and 1943. The infill structures show a correlation with the distribution of the "strong" anomaly class (British Crown Copyright, RAF photograph).

D. Geochemical Sampling

This year samples of soil and vegetation were taken on the test site and analysed for heavy metal concentrations. It was found that heavy metal concentrations on the waste deposit are substantially higher compared to a reference field near the site, as well for soil as for vegetation samples. Figure 3 shows the concentrations of metals Lead, Copper and Zinc in soil samples taken along a profile in the "high" anomaly area (P1 to P12), on various other locations on the site and two samples taken from a reference field (P16 and P17) outside the infill area. This data supports the suggestion, that the material present is responsible for the differences in the observed spectral signatures. Physiological plant material analyses are planned for the next growing season, which should yield more information regarding the presence and influence of stress effects.

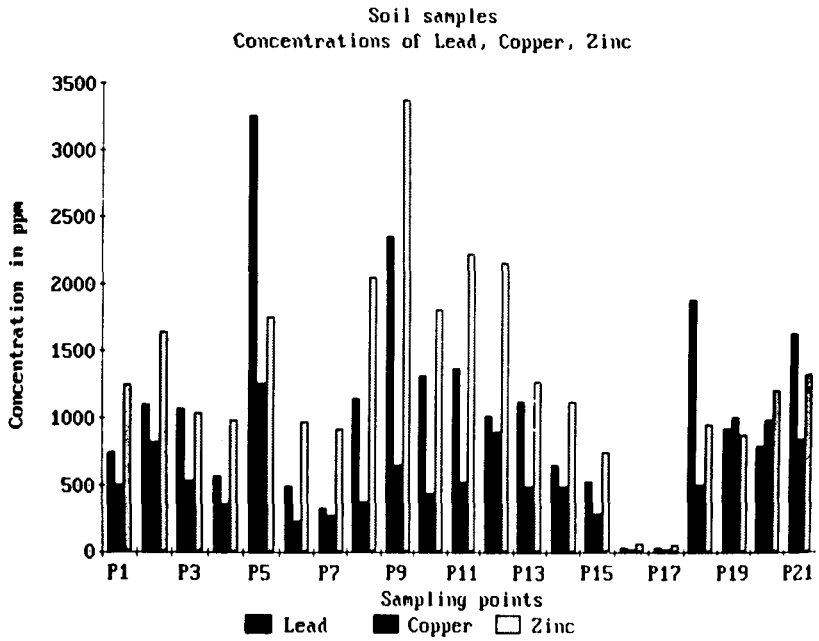

Figure 3. Concentrations of heavy metals in soil samples
Samples P16 and P17 are taken from a reference field near the waste deposit and show considerably smaller heavy metal concentrations. Allowed maximum concentrations in soils are as follows: Zinc: 300 ppm, Lead and Copper: 100 ppm.

E. Conclusions

The high spectral resolution GER-Imaging Spectrometer is a useful tool for environmental studies. In this application the vegetation cover over an old waste deposit was analysed for spectral anomalies. This remote sensing method could be employed as a fast, non-destructive way of delineating spectrally anomalous areas as an input for specific ground surveys. Atmospheric modelling is the step that leads from a qualitative to a quantitative analysis of the data and will be important in the intended analysis of multitemporal spectral data.

II. APPLICATION FOR EXPLORATION AND SOIL/VEGETATION STUDIES

A. The Almaden Test Site

The test site is located in the Central Iberian Zone of Spain. It has an extension of approx. 10 x 15 km² covering the central part of a NW-SE trending anticline consisting of precambrian sedimentary rocks and partly outcropping granitic intrusives. Contactmetamorphic influence of the granitic cupolas is displayed in the contact zone of the surrounding sedimentary boundary (see figure 4).

The topography in the investigation area is moderate with a smoothly undulated morphology and maximum altitude differences of 160 m. The region is characterised by typical mediterranean vegetation forming an irregular pattern of cultivated (oat, olive tree plantations) and uncultivated areas. Due to cultivation cycles of several years large areas are fallow land, grassland and pasture, while areas of more expressed morphology with

partly outcropping rocks and thin soil layers are not cultivated; those areas are mostly covered by garigue, macchie, and/or oak trees.

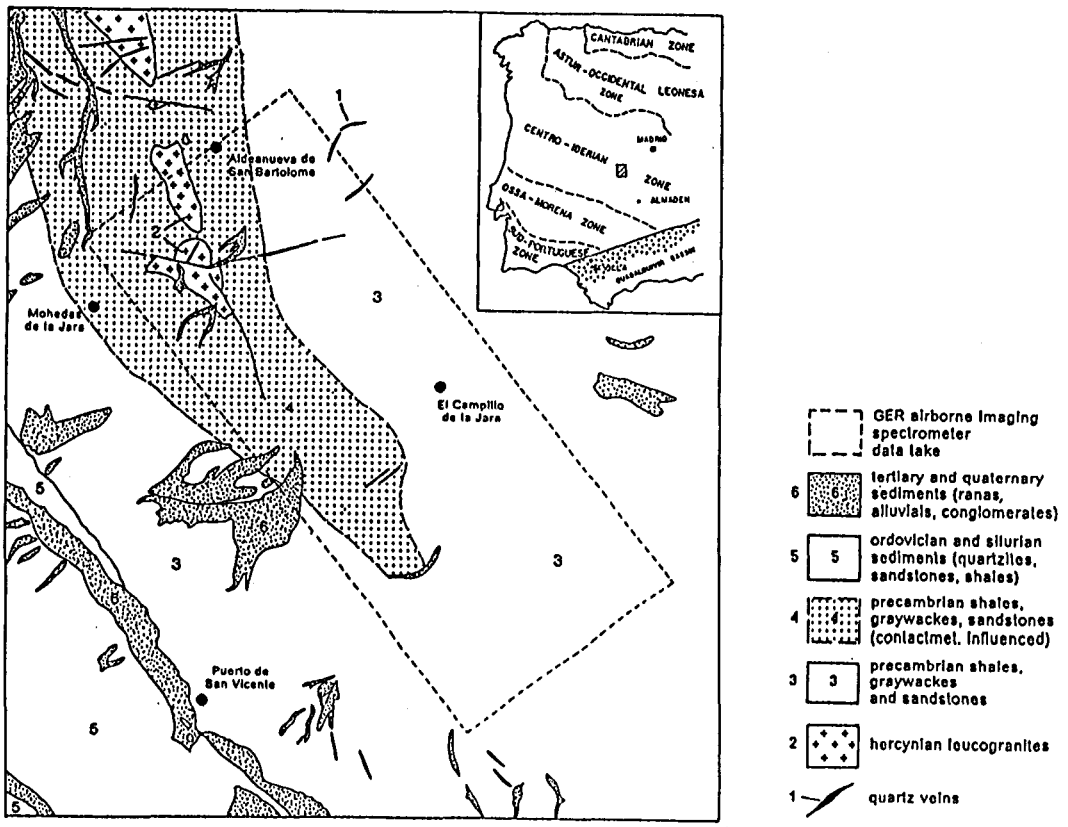

Figure 4. Geological sketch map of the Almaden testsite
(based on the geological map sheet No. 15-27 (682), 1:50 000)
Scale approx. 1 : 128 000

Soil spectral analyses have already been carried out in the framework of the Raw Materials Programme funded by the European Communities for mineral exploration purposes (Ref. 6). The aim was to delineate suboutcropping granitic cupolas (with possible mineralisations in their roof zones) coming near the topographic surface according to their contactmetamorphic influence on the sedimentary formations.

The observed variations in mineral composition in those altered areas are spectrally displayed by increasing relative reflectance intensity in the shortwave infrared wavelength range and strong 2.2 μm and 2.35 μm absorption depths.

B. Field Survey

During a three day ground survey spectral field measurements have been carried out at 22 locations in the test site. Three GER IRIS spectroradiometers covering the 0.4 - 2.5 μm spectral range were used for field spectroscopy measurements of bare soil and vegetation covered targets over outcropping granites, contactmetamorphic influenced and non influenced precambrian series. The vegetation analysis included an estimation of the

percentual vegetation coverage discriminating between green and dry vegetation, indication of the average plant height and determination of vegetation types and land use (Ref. 6).

C. GER Airborne Data Evaluation

GER airborne scanner data have been obtained from the central part of the investigation area with outcropping granites, precambrian sediments and the contactmetamorphic influenced contact zone (see figure 4). The area is mostly covered by various transition stages of grassland/pasture and macchie/garigue vegetation.

The GER preprocessed airborne data were first corrected for atmospheric and adjacency effects. These calculations allowed a conversion into relative reflectance values which are comparable to ground measurement data. Due to atmospheric inhomogenities during the flight in the Almaden test site, however, an additional correction had to be applied: relative reflectance spectra obtained on ground truth targets during the field campaign were selected and compared to reflectance spectra retrieved from GER image data of the corresponding locations. Based on the resulting spectral differences between ground and image data, correction factors have been calculated for each GER image band. They were used for the calculation of a calibrated GER image.

D. Results

First analyses of GER airborne scanner data were concentrated on the spectral charcteristics of bare soil targets / ploughed arable land. Based on GER airborne spectra a classification analysis has been carried out, taking account of the spectral response of 55 GER scanner bands (see I.C.2), (Ref. 2).

Figure 5b shows an RGB natural colour composite of the GER image using band 15 at 650 nm (red), band 7 at 551 nm (green) and band 2 at 489 nm (blue) center wavelengths. Bare soil targets are characterised by high intensities. GER band 15 (650 nm) was used in figure 5a with the classified bare soil targets marked by red, green and blue colours. Soil targets with high intensities in the SWIR and strong 2.2 μm absorption bands are displayed by red colours. Those areas are mainly occurring over outcropping granites. Soil targets with medium intensity in the SWIR and less pronounced 2.2 μm absorption features are displayed by green colours and are located close to the outcropping granites and in contactmetamorphic influenced areas, while the spectra of blue coloured targets are characterised by low SWIR intensities and very weak absorption bands.

Soil spectra calculated from GER airborne scanner data and ground spectra measured with the IRIS Mark IV spectroradiometer during the field survey at the corresponding targets are presented in figure 5c. The colours in the diagram correspond to the classified soil targets in figure 5a. In contrast to an unsignificant spectral variation in the VIS/NIR (see figure 5b) the soil spectra are well differentiated in the SWIR wavelength region.

GER airborne scanner spectra from various Almaden vegetation cover types are shown in figure 6. Due to an inhomogeneous vegetation distribution within the test site, however, spectral variations of equivalent vegetation types dependent on different soil types could not be noticed yet.

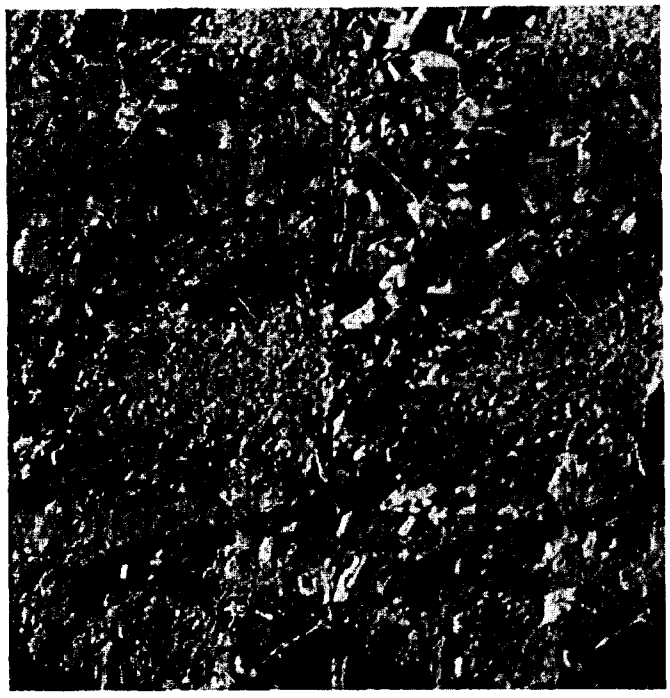

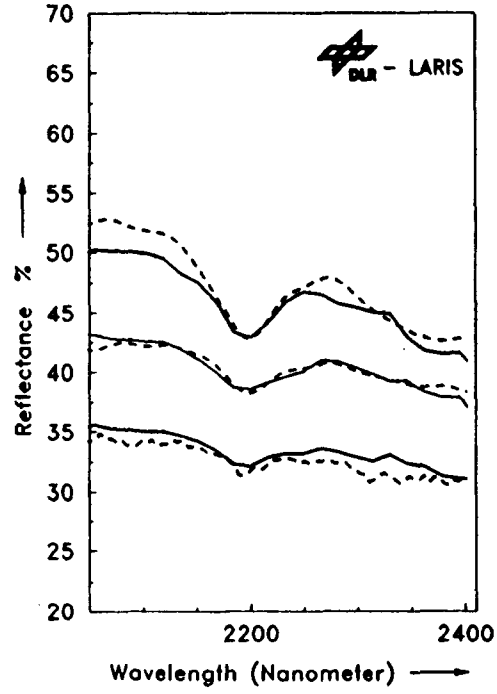

a b c

Figure 5. Classification of GER Airborne Scanner Data (Reventon) [see slide 8]
a) black & white = GER band 7 (551 nm); red, green, blue = bare soil targets with different spectral signatures (see c)

b) RGB natural colour display, GER band combination: 18=687 nm (red), band 7=551 nm (green), band 2=489 nm (blue); all bare soil targets are characterised by high intensities in channel 2, 7 and 18.

c) SWIR wavelength range of soil spectra, selected as a basis for the classification (see a). Spectral differences (albedo, absorption depth) are caused by variable mineral content. Solid lines: reflectance spectra retrieved from GER airborne scanner data; dotted lines: field spectra of the corresponding target, acquired with the IRIS Mark IV spectroradiometer during the simultaneous ground truth.

E. Conclusions

GER airborne scanner data is regarded to be very useful for soil / vegetation studies. Soil surfaces with even small mineralogical variations could be differentiated according to their spectral characteristics in the SWIR wavelength range. GER airborne scanner spectra of different vegetation types display noticeable variations in the VNIR and/or SWIR. Statistical spectral analyses are limited due to the small size of fields, the irregular pattern of cultivated and uncultivated areas and missing bare soil targets in some regions of the Almaden testsite. The relationship between geology and vegetation cover has to be examined in detail by further spectral anlysis.

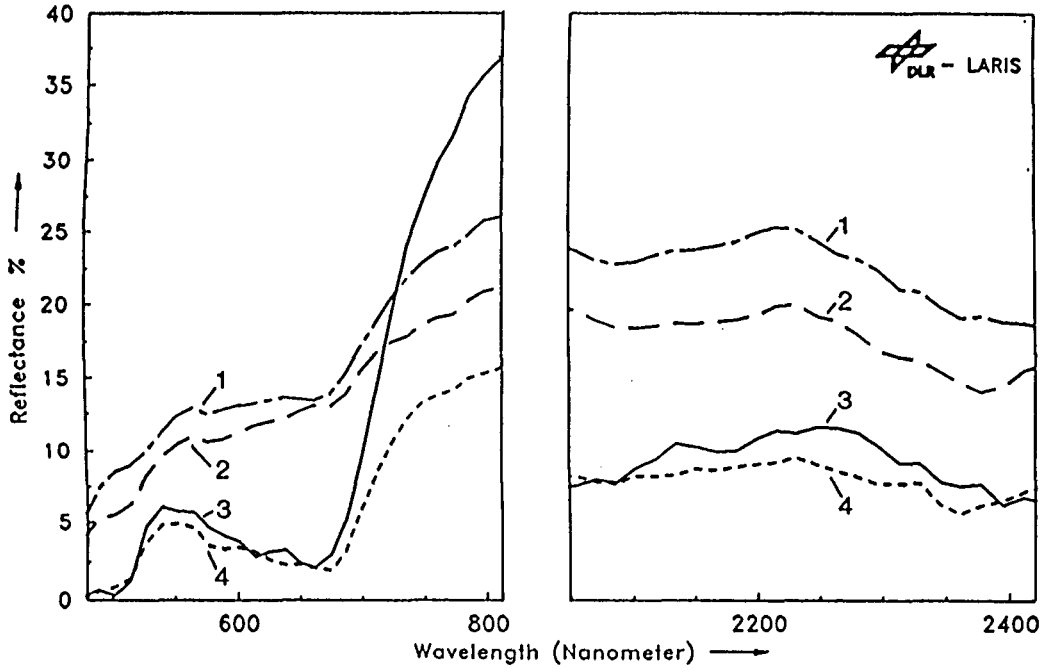

Figure 6. Reflectance spectra calculated from GER airborne data representing various vegetation cover types
1 = grassland, 2 = ripe oat,
3 = damp vegetation, 4 = cistus ladanifer macchie

References

Ref.1 Lehmann F., Mackin S., Richter R., Rothfuß H., Walbrodt A., 1989, The European Imaging Spectrometry Campaign 1989 (EISAC)- Preprocessing, Processing and Data Evaluation of the GER Airborne Imaging Spectrometer Data, Progress Report to the European Community, JRC, ISPRA. DLR, Oberpfaffenhofen.

Ref.2 Lehmann F., Rothfuß H., Richter R., 1990, Evaluation of Imaging Spectrometry data (GER) for the spectral analysis of an old vegetation covered waste deposit, **Proc. of the IGARSS'90, (20-24 Mai 1990)**, Maryland, Washington D.C., USA.

Ref.3 Kneizys F.X., Shettle E.P., Abreu L.W., Chetwynd J.H., Anderson G.P., et al., 1988, **Users Guide to LOWTRAN 7**, AFGL-TR-88-01777, Bedford MA.

Ref.4 Richter R., 1990, A fast atmospheric correction algorithm applied to Landsat TM images, **Int. J. Remote Sensing**, 11, 159-166.

Ref.5 Schwaller M.R., Schnetzler C.C., 1983, The changes in leaf reflectance of sugar maple (Acer saccharum marsh) seedlings in response to heavy metal stress, **Int. J. Remote Sensing**, 4, 93-100.

Ref.6 Werner K. & Lehmann F., 1990, Development and Testing of New Techniques for Mineral Exploration Based on Remote Sensing, Image Processing Methods and Multivariate Analysis. Report to the European Community, Raw Materials Programme, Brussels, No. MA1M1/0009-D(B), DLR Oberpfaffenhofen, F.R.G.

Sierra Nevada Forest Stress Determination From AVIRIS Data

Vincent G. Ambrosia
Jeffrey S. Myers
ATAC, Inc.
Aircraft Data Facility
NASA-Ames Research Center
Moffett Field, California

Thomas Bobbe
Paul Ishikawa
Nationwide Forestry
Applications Program
U.S. Forest Service
Salt Lake City, Utah

ABSTRACT

AVIRIS hyper-spectral remotely sensed data collected in the fall of 1989 over control and stressed Ponderosa pine (*Pinus Ponderosa*) stands in the lower elevation, western-most reaches of the Tahoe National Forest, California were examined. The forests of the Sierra Nevada had been subjected to three years of drought and an associated Western Pine Beetle (*Dendroctonus brevicomis*) presence. Two drought/beetle stress sites and two healthy/control sites were selected for canopy spectral analysis. AVIRIS data sets were reduced to non-coincident, low-noise bands and three spectral analysis procedures were implemented to determine healthy and stressed vegetation components. Full wavelength spectral analysis of the sites, first derivative approximations for red-edge shifts, and a Moisture Stress Index (MSI) calculation were performed.

Our initial findings indicate that spectral separation is possible when comparing full spectra plots, with spectral discrimination highest at 820-860nm and 1003-1023nm; no significant red-edge shifts could be determined; and, the MSI indicated a slight difference in the stress and control sites. Other conditions related to the analysis of the sites will be discussed, including the difficulties associated with selection of homogeneous control and stress plots.

I. INTRODUCTION

As of 1989, three consecutive drought years had stressed the forest stands in the Sierra Nevada of California; a drought unprecedented in the last 500 years. The drought has increased the forests susceptibility to insect and disease attack. The combination of moisture deprivation and an invasion of the Western Pine Beetle and Fir Engraver Beetle (*Scolytus ventralis*) have left the forest stands in serious danger of propagating extensive wildfires. Because these stresses affect the forest biophysical parameters, primarily leaf moisture content and chlorophyll alterations, NASA and the U.S. Forest Service are experimenting with utilizing the narrow-band, hyper-spectral AVIRIS scanner for determination of stressed canopy conditions. We have initially employed three methods to determine spectral separability of stressed and healthy canopies: full spectrum comparative analysis, first derivative analysis for red edge spectral position changes, and the calculation of a Moisture Stress Index (Miller, et al., 1990; Miller, et al., 1990; Rock, et al., 1986).

This paper will address preliminary results of our analysis of data collected with the NASA-JPL Airborne Visible-Infrared Imaging Spectrometer (AVIRIS) over a mixed forest canopy site near Nevada City, California within the Tahoe National Forest of the Sierra Nevada range. The AVIRIS data was collected on-board the NASA-Ames ER-2 high altitude aircraft on 4 October 1989 (Flight 90-004) from an altitude of 65,000 feet (19.8 km). Data collection occurred at 12:28 PM local time. An RC-10 camera with 9x9 inch format CIR film collected simultaneous data from the same platform.

A. Study Site Description

Four study sites were located in the AVIRIS data for analysis. All four sites are east of Nevada City, California at the western-most edge of the Tahoe National Forest. Elevation in the vicinity of the sites ranges from 3000-5000 feet. In this elevation range, a transitional forest exists. Lower elevations are dominated by open Manzanita (*Arctostaphylos*) brush fields with scattered Digger Pine (*Pinus Sabiniana*), Oaks, and some Ponderosa pine. Black oak (*Quercus kelloggii*) and Canyon Live Oak (*Q. chrysolepis*) occur in the mid-lower elevation ranges, usually in the river canyons and on moist slopes. As elevation increases, a change from broadleaf to conifer occurs. The mid-elevation ranges of the AVIRIS scene area include scattered Sugar pine (*P. lambertiana*) and Incense Cedar (*Libocedrus decurrens*). Ponderosa pine is found in small discontinuous stands in the remainder of the area, with Red Fir (*Abies magnifica*) and White Fir (*A. concolor)* rarely occurring in any definitive stands at this elevation.

Because of the discontinuous nature of the Ponderosa pine stands in the AVIRIS scene area, it was difficult to select control and stressed sites with similar size and age classes, crown closures and elevation characteristics. In order to facilitate spectral comparisons, we attempted to select sites with full crown closure. This reduced the likelihood of spectral contamination from understory components or bare soils/rocks. Four total sites, two control and two stressed, were selected upon examination of the available aerial photography. Control site 1, at 3800' elevation, contained 100% crown closure of Ponderosa pine with a dominance of mature timber (even age stand). Control site 2, at 4400-4600' elevation, was located on a North aspect with 80% crown closure and a mix of Ponderosa pine classes from small saw to mature saw timber. Stress site 1, located at 3800' elevation, contained 100% crown closure and evident crown needle damage on approximately 20% of the stand. Stress site 2, located at 4700-4800' elevation had an 80% crown closure of mixed size class Ponderosa pine. Damaged or stresses crowns were estimated at 35-40% of the stand. Both combinations of sites are in close proximity to each other and were selected from both the north and south sides of the South Yuba River, which runs east to west through the area.

II. DATA PREPARATION AND ANALYSIS

Two adjacent AVIRIS scenes, collected minutes apart were analyzed. Site 1 control and stress were located on the western-most scene of the two, and site 2 on the eastern. The eastern scene represented an area of slightly higher elevation. Prior to analysis, the AVIRIS data was examined and band overlap regions were eliminated, as were bands with low signal/noise ratios. From the original 224 bands, 4 overlap bands at the A/B spectrometer cross-over were eliminated; 5 at the B/C spectrometer cross-over; and 5 at the C/D spectrometer cross-over. This resulted in 210 contiguous bands (396.9-2455 nm). Because of low signal/noise ratios and general low contrast, the first 10 bands (396.9-485.7 nm) of the A spectrometer and the last 12 bands of the D spectrometer (2346-2455 nm) were not utilized in the analysis. The first 10 bands of A, in the blue EMS region had high atmospheric attenuation and low signal/noise ratios. The last 12 bands of the D spectrometers contained low signal/noise ratios as well as bands with no evident spectral data. The final data set therefore consisted of 188 bands with a spectral range of 495.6-2336 nanometers. These 188 bands were utilized for the full spectrum comparisons and to derive spectral statistics for analysis. Some of the bands in this spectral range had reduced radiance values due to H_2O, CO_2, and O_2 absorption frequencies. These bands were retained in the data set for spectral continuity. Those specific absorption features can be seen as local minimum radiance values in the plotted spectra; the strongest absorptions occurring at 940 and 1140 nm (H_2O).

Sub-windows surrounding each of the four sites were delineated. In comparing the two sets of control/stress sites, areas of similar pixel dimensions were selected to derive the

statistics. This procedure avoided any spectral differences due to a lack of statistically valid sample sizes. Control site 1 was composed of 375 pixels; Stress site 1, 275 pixels; Control site 2, 156 pixels; and Stress site 2, 154 pixels. Statistics for the sites were not merged due to their different characteristics (elevation, aspect position, and size classes). The mean radiance for each site (and each band) was calculated and used to derive the spectral plots. The mean radiance of the sub-window was determined by moving an average filter window of the same dimensions as the site, by an x-y distance equal to the dimension also. This creates a single pixel mean window value data set composed of 188 bands. Since the original AVIRIS radiometric data set was scaled by a factor of 200 to retain precision as a 16-bit integer, the mean spectral values were divided by 200 to derive the actual radiance value per band for the mean window.

Three methods were employed on the mean site spectral data to determine the separability of control and stressed Ponderosa pine sites. Initially, full spectral plots of the mean radiance counts per wave-band were derived. An attempt was also made to identify changes in the position of the red edge reflectance curve by deriving a first derivative calculation of the spectral data between 604 nm and 800 nm. Finally, we calculated the Moisture Stress Index (MSI) from two wave-bands to determine variations in moisture stress on the canopy reflectance.

A. Full Spectral Comparative Analysis

For each pair of sites (Site 1 control/stress; Site 2 control/stress), mean radiance ($\mu W\ cm^{-2} nm^{-1} sr^{-1}$) values were plotted for the wavelength region 496 nm to 2336 nm (Figure 1).

1. Site 1

As can be seen in Figure 1 (Site 1), the spectra for the stressed site is higher than the control from the blue-green region through the red trough (local minimum). In the transition from the red to the near-IR, the stressed and the control spectra track similarly with little noted shift in the red edge or the inflection point for either. As can be expected, the stressed radiance tracks lower than the control throughout the IR plateau and the remainder of the IR to the H_2O and CO_2 absorption frequency in the vicinity of 1370 nm. Beyond this absorption area, the stressed and control Ponderosa pine spectra display unique peaks at 1440 nm.

2. Site 2

The radiance plots for site 2 are shown in Figure 2. The stress site spectra tracks similar to the control site from the blue-green through the red trough. Similar to site 1, both spectra are virtually inseparable along the red/IR transition. At the IR plateau, the stressed spectra remains higher than the control site. Unlike site 1, there is no unique spectral spike at 1440 nm in either the control or stressed site 2.

B. "Red-Edge" Detection

The red-edge spectral position is a vegetation parameter related primarily to the rise and fall of leaf (needle) chlorophyll content (Miller, et al., 1990). Vegetation spectra exhibit a consistent shape in the red-edge region characterized by a broad, flat minimum at ~670 nm (see Figures 1 and 2), with an increase starting at ~685 nm, reaching to an asymptotic IR plateau beyond 780 nm (Miller, et al., 1990). It has been noted that changes in the plant chlorophyll content due to stress alter the red-edge spectral position. Given less apparent chlorophyll in the stressed needle, the slope of the spectral curve changes in the 680-720 nm region. As chlorophyll decreases, the radiance increases in the red trough (chlorophyll well), and the spectral position of the red-edge inflection point shifts towards shorter wavelengths. In the near-IR plateau region, the spectral position of stressed Ponderosa pine should be lower than a chlorophyll-rich, healthy Ponderosa pine stand. Conversely,

the more chlorophyll concentration, the stronger the shift of the inflection point to longer wavelengths, with an accompanying increased IR plateau (Ustin, et al., 1990).

We employed a first derivative approximation of the spectral profile to determine the presence of the red-edge shift. The approximation of the first derivative was calculated for the 604nm-800nm spectral region, and is represented by the equation:

$$R_N - R_{N-1} / W_N - W_{N-1}$$

where R is the radiance for wave-band W.

Changes in the red edge spectral position and the inflection point can be determined from this approximation. Spectral flat profiles (either plateaus or troughs) have a derivative value of "0" while negative derivative values represent a decreasing slope value with increased wavenumber. Positive values are indicative of an increasing spectral slope with concurrent wavelength increases. Changes in the inflection point and slope steepness can be determined from a plot of the first derivative approximation (Figures 3 and 4). First derivative "red-edge" plot were derived for the control (healthy) and stressed sites.

1. Site 1
Figure 3, the approximation of the first derivative for site 1, was plotted for the 604-800 nm spectral region. The chlorophyll well can be seen at ~675 nm while the IR plateau is at ~730 nm. Both the stressed and the healthy derivative values coincide for much of the red-IR region, with no obvious wavelength shift noted between the plotted values.

2. Site 2
Figure 4 represents a plot of the 604-800 nm first derivative approximation for site 2. No red edge-shift is visible between the healthy and the stress site.

C. Moisture Stress Index (MSI)
A moisture stress index (MSI) was calculated for the two combination of sites. The MSI has been shown to be a relative measure of canopy moisture content (Miller, et al., 1990; Rock, et al., 1986). The MSI is computed as the ratio:

$$R_{1650} / R_{850}$$

where R is the radiance value for the spectral wavelengths centered at 1650 nm and 850 nm respectively. The sensitivity of the MSI is related to total canopy water content. Sites 1 and 2 MSI ratios were different. Site 1 control MSI was 0.0743 while the stress MSI value is 0.0766. Moisture stressed vegetation canopies would have a higher ratio value than a non-stressed canopy site. Although the site 1 stressed MSI value is expectedly higher, the MSI for the site 2 stress is lower than the MSI site 2 control (0.0734 control vs. 0.0677 stress).

III. RESULTS

Our initial assessment of AVIRIS data collected over control (healthy) and stressed Ponderosa pine stands in the Sierra Nevada of California indicates that some spectral differentiation is possible. For site 1 there is a consistent, expected spectral differentiation between the control and stressed sites evident from the spectral plots (Figure 1). This differentiation includes a stressed spectra that exhibits an increased blue-green to red trough (chlorophyll well) response and a decreased IR shoulder and IR response. There is a unique, strong peak and spectral differentiation of the stress and control site occurring at ~1440nm. This is probably due to a malfunctioning detector. Further investigations are

planned. The strongest spectral separability of the stress and control sites composing site 1 occurs at 820-860nm and 1003-1023nm.

For site 1, there is no evident shift in the "red-edge" inflection point between the stressed and the control site. Although a spectral shift would be expected, it is probable that it is undetectable given the AVIRIS spectrometer A bandwidths if 9.6nm. It has been noted that the "red-edge" spectral shift, representative of variations in leaf (needle) chlorophyll concentrations may occur at levels of only 5-9nm (Baret, et al., 1990). It is likely therefore that the small levels of noted stress would not be evident with AVIRIS band sensitivities.

The MSI calculated for site 1 indicated a stress index value of 0.0766 and a control index value of 0.0743. The relative difference is small, and may not be statistically significant for these site condition determinations.

For site 2, the spectral profile for the stressed and control Ponderosa pine sites is not consistent with expected results. The stressed canopy spectra track similar to the control spectra from the blue-green thru the red trough (chlorophyll well). In the near-IR, the stressed spectra have a higher radiance profile than the control site spectra. This continues thru 2336nm.

No "red-edge" spectral shift is visible in the approximated first derivative plots, for reasons similar to those discussed above for site 1. And, similar to the spectral profile for site 2, the MSI ratios are not consistent with the expected results. The stressed MSI ratio was slightly lower than the control MSI ratio values.

We postulate that the unexpected spectral characteristics for site 2 control/stress are the result of variations in the aspect and slope terrain characteristics, coupled with stand characteristic differences. Given the N/NW aspect of the site 2 control, a lower IR response would be expected due to an increased shadow presence. The control site is also located on a steeper slope profile than the stressed site. The mix of size classes, with an inclusion of larger trees casting shadows on smaller tree crowns, also affect the spectral homogeneity of the site. Even though the control site has an 80% crown closure (20% crown openings with understory complexes), the crown openings are effectively masked by a combination of the larger tree shadow zones and less direct solar illumination, given the N/NW aspect and steeper slopes. These factors combine to lower the overall spectral characteristics of the site. Another factor contributing to the higher IR response of the stress site (site 2) is the mixing of size classes evident on aerial photography. Upon closer examination of the stand, some small size class pines composed large sections of the area. These smaller size class timber stands were more homogeneous and had less apparent crown openings. Due to this even-age stand characteristic, there was little or no dominant larger trees casting shadows on neighboring crowns. This condition would lead to a higher IR response than the older, more open crown, N/NW facing, steeper control site. Although the stress site had 35-40% evident crown canopy damage, unlike site 1, the damaged (stressed) canopies were scattered throughout the site. Without any large, contiguous regions of stress, spectral differentiation would be difficult given the spatial resolution (20 meters) of the AVIRIS data. For site 1, damaged crowns were more tightly clustered, and were spectrally significant for the averaged site spectra. These conditions would preclude the accurate spectral separation of our site 2 control/stress stands.

IV. CONCLUSIONS

The use of AVIRIS hyper-spectral scanner data for discriminating moisture/beetle stress in Ponderosa pine communities appears promising. Shortcomings in our selection of our site 2 control/stress stands led to inconsistent spectral characterizations of stress/non-stress. Given the narrow spectral shift of the "red-edge" (on the order of 5-9nm), for

discriminating needle chlorophyll content, AVIRIS data, with 9.6nm band-widths, does not appear to be an effective tool. The use of the MSI may prove beneficial, but a larger sample size for statistical purposes would be necessary to substantiate our findings. Initially, a differentiation between the control and stress sites is evident from the spectral profiles for site 1. The strongest differentiation occurs in two spectral regions: a 5-band area composed of 820-860nm, and a 3-band area from 1003-1023nm.

We encountered problems in the selection of a truly homogeneous control and stress site. Those problems were further compounded by the fact that our sites were located at the lower elevation limits of the Ponderosa pine communities in this area, and, Ponderosa pine, a drought -resistant species, may not show a significant biophysical change (stress) until moisture deprivation is much greater. Given our new knowledge of these constraints, our focus will be on developing a better understanding of the complicated biophysical and environmental factors that govern vegetation spectral characteristics. This hopefully will enable us to quantify change in forest health. In those regards, AVIRIS, and future planned hyper-spectral systems, will have great utility in the science community.

Acknowledgements
The authors would like to acknowledge the invaluable assistance and comments of: Dr. Vern Vanderbilt (NASA), Lee Johnson and Jennifer Dungin (TGS Technology), and Bob Ekstrand (ATAC, Inc.).

REFERENCES

Baret, F., S. Jacquemond, C. Leprieur, and G. Guyot, 1990. Are the Spectral Shifts an Operational Concept? Critical Analysis of Theoretical and Experimental Results. Proceedings of the Second Airborne Visible/Infrared Imaging Spectrometer (AVIRIS) Workshop, JPL Pub. 90-54, pp. 58-71.

Miller, J.R., C.D. Elvidge, B.N. Rock, J.R. Freemantle, 1990. An Airborne Perspective on Vegetation Phenology From the Analysis of AVIRIS Data Sets Over the Jasper Ridge Biological Preserve. Proceedings of the IEEE Geosciences And Remote Sensing Society/URSI 1990 Conference.

Miller, J.R., E.W. Hare, J. Wu, 1990. Quantitative Characterization of the Vegetation Red Edge Reflectance: 1. An Inverted Gaussian Model. International Journal of Remote Sensing, 0143-1161/90, paper 695726.

Rock, B.N., J.E. Vogelmann, D.L. Williams, A.F. Vogelmann, and T. Hoshizaki, 1986. Remote Detection of Forest Damage. Bioscience, Vol. 36, pp. 439-445.

Ustin, S.L., B. Curtiss, S.N. Martens, and V. Vanderbilt, 1990. Early Detection of Air Pollution Injury to Coniferous Forests Using Remote Sensing. Forest Conditions and Trends, pp. 351-377.

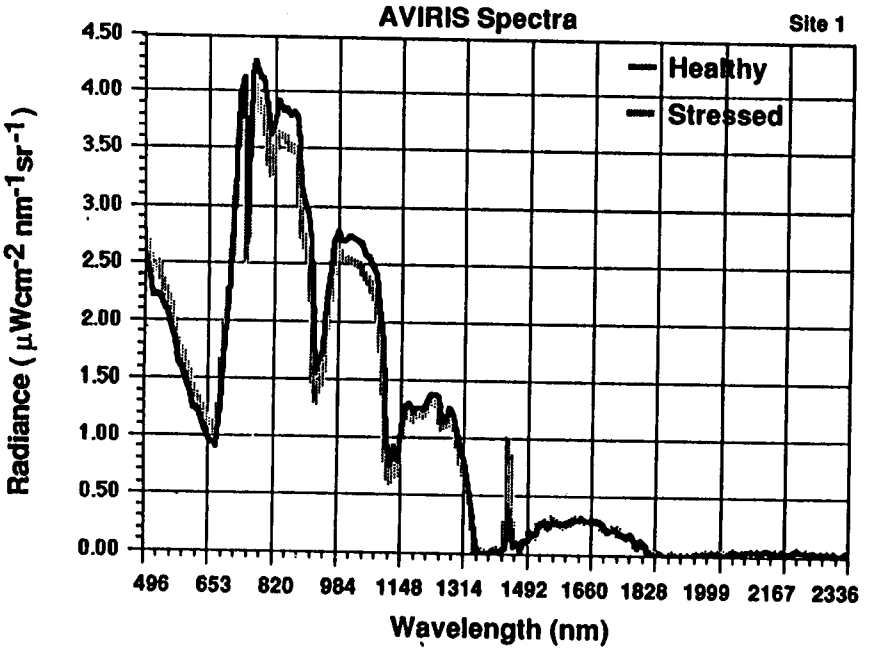

Figure 1. AVIRIS spectra for healthy (control) and stressed site 1; Ponderosa Pine stand. Reduced spectral range of 496 - 2336 nm.

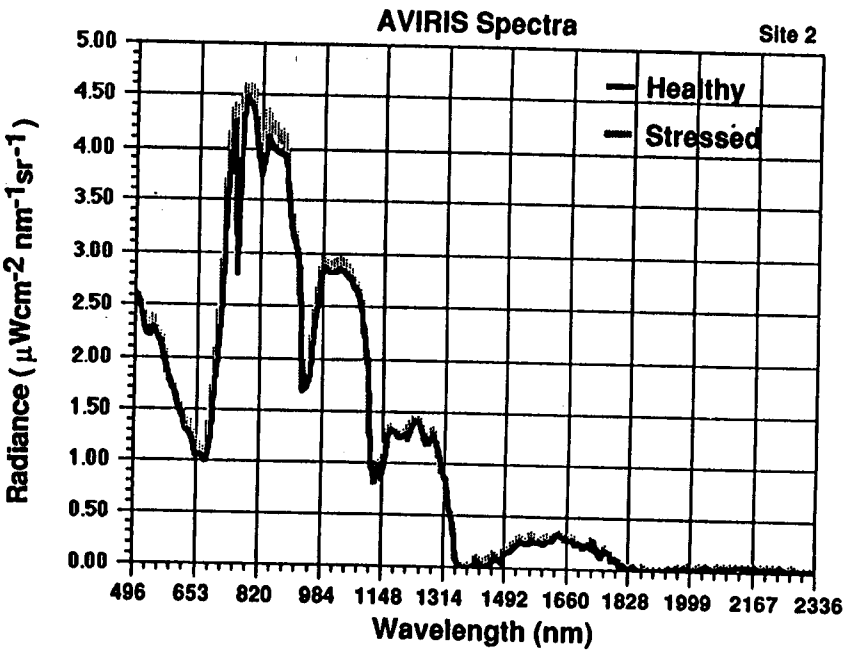

Figure 2. AVIRIS spectra for healthy (control) and stressed site 2; Ponderosa Pine stand. Reduced spectral range of 496-2336 nm.

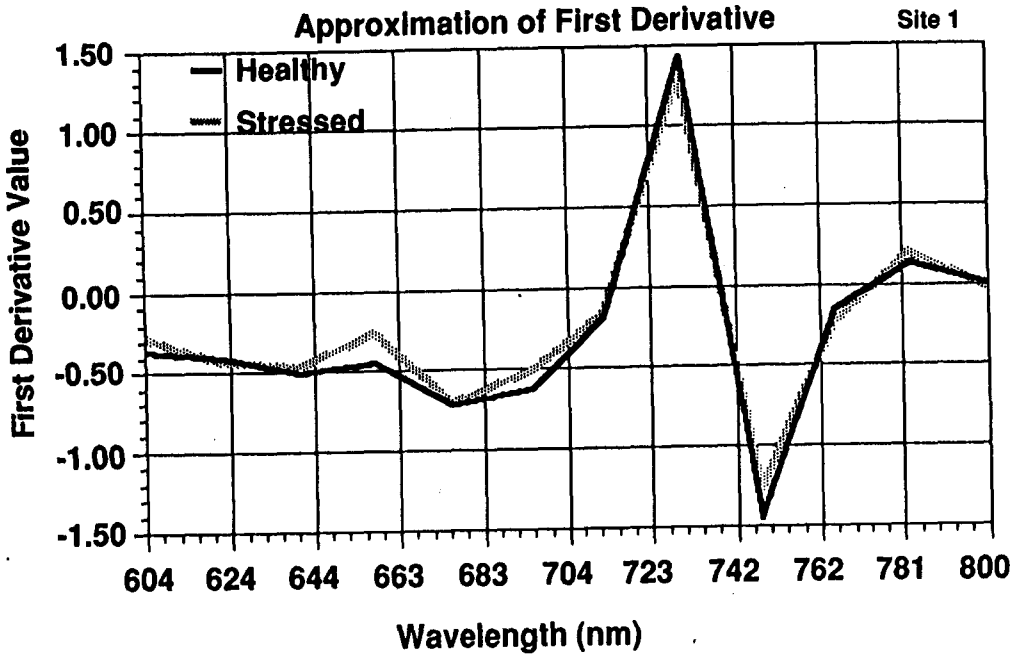

Figure 3. First Derivative Approximation plot for site 1; healthy/stressed Ponderosa Pine stand. Spectral range of 604-800 nm.

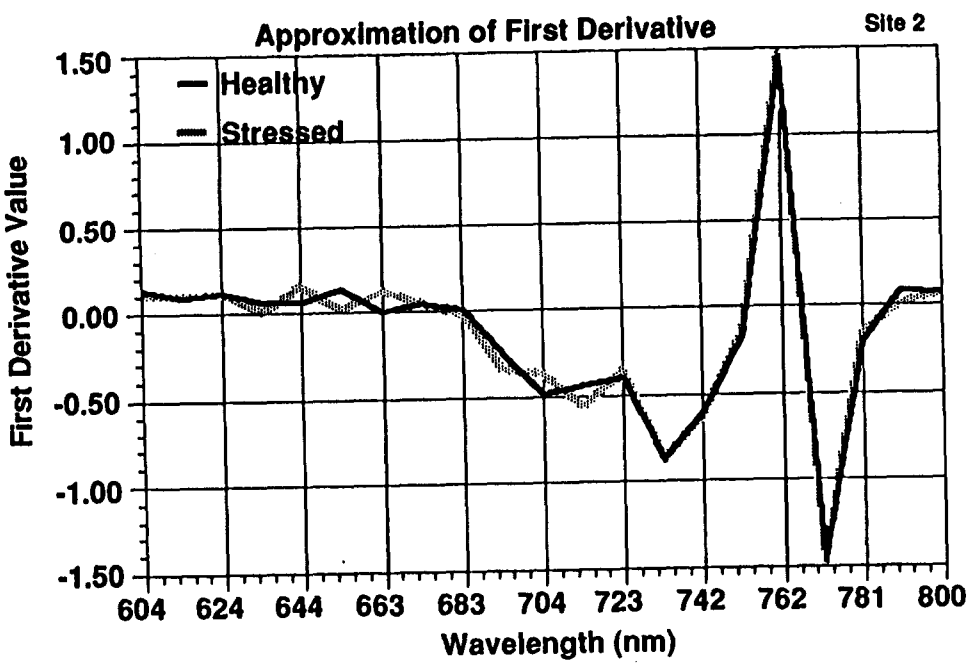

Figure 4. First Derivative Approximation plot for site 2; healthy/stressed Ponderosa Pine stand. Spectral range of 604-800 nm.

REMOVING ATMOSPHERIC EFFECTS FROM AVIRIS DATA FOR SURFACE REFLECTANCE RETRIEVALS

Bo-Cai Gao[1], Alexander F. H. Goetz[1,2], and J. A. Zamudio[1,2]

[1]Center for the Study of Earth from Space/CIRES, Campus Box 449,
[2]Department of Geological Sciences
University of Colorado, Boulder, CO

Abstract. Analysis of high resolution imaging spectrometer data requires a thorough compensation for atmospheric absorption and scattering. A method for retrieving surface reflectances from spectral data collected by the Airborne Visible/Infrared Imaging Spectrometer (AVIRIS) is being developed. In this method, the integrated water vapor amount on a pixel by pixel basis is derived from the 0.94- and 1.14-μm water vapor features. The water vapor, carbon dioxide (CO_2), oxygen (O_2) and methane (CH_4) transmission spectrum in the 0.4-2.5 μm region is calculated. The derived water vapor value and the solar and observational geometry are used in the spectral calculation. The AVIRIS spectrum is ratioed against the transmission spectrum to obtain the surface reflectance spectrum. Major mineral absorption features near 2.2 μm in retrieved reflectance spectra can be identified. Different vegetation absorption characteristics are observed. At present, the method is most useful for deriving surface reflectances from AVIRIS data measured on clear days with high visibilities. Atmospheric scattering effects will be included in our spectral calculations in the near future.

I. Introduction

Imaging spectrometers acquire images in hundreds of contiguous spectral bands such that for each picture element (pixel) a complete reflectance or emittance spectrum can be derived from the wavelength region covered (Goetz et al., 1985). In the coming decade, NASA expects to carry the High Resolution Imaging Spectrometer (HIRIS) (Goetz and Herring, 1989) aboard a platform of the Earth Observing System (Eos). The precursor to HIRIS is the Airborne Visible/Infrared Imaging Spectrometer (AVIRIS) (Vane, 1987), which is now operational. AVIRIS covers a spectral region from 0.4-2.5 μm in 10-nm bands and has a ground instantaneous field of view of 20x20 m from an altitude of 20 km. Because solar radiation is subject to atmospheric absorption and scattering in the combined Sun-surface-aircraft ray path, the radiance obtained by AVIRIS is modified by the atmosphere as well as by the Earth's surface materials. In order to properly infer the surface reflectances from AVIRIS data, accurate modeling of atmospheric absorption and scattering is necessary.

Figure 1 shows an AVIRIS spectrum measured over Rogers Dry Lake, California in February, 1990. The atmospheric water vapor absorption bands centered at approximately 0.94, 1.14, 1.38 and 1.88 μm, the oxygen bands at 0.96 and 1.27 μm, and the carbon dioxide band near 1.60 and 2.08 μm are clearly seen. Approximately half of the 0.4-2.5 μm region is affected by atmospheric gas absorptions. These atmospheric features, mainly those of water vapor, must be removed in order to obtain the surface reflectances.

II. Background

The radiance at a downward looking aircraft sensor can be written in a simplified form as

$$L_{Sensor}(\lambda) = L_{Sun}(\lambda)T(\lambda)R(\lambda) + L_{Path}(\lambda) \qquad (1)$$

where λ is the wavelength, $L_{Sensor}(\lambda)$ is the radiance at the sensor, $L_{Sun}(\lambda)$ is the solar radiance above the atmosphere, $T(\lambda)$ is the total atmospheric transmittance in the Sun-surface-sensor path, $R(\lambda)$ is the surface reflectance at the observational geometry, and $L_{Path}(\lambda)$ is the scattered path radiance, including effects of single scattering and multiple scattering. Near 0.5 μm, $L_{Path}(\lambda)$ resulting from Rayleigh and aerosol scattering is typically 50% or greater of the observed radiance. At wavelengths longer than 0.8 μm, the Rayleigh scattering effect is small, and $L_{Path}(\lambda)$ resulting mainly from aerosol scattering is on the order of 10% of the observed radiance. If the atmospheric transmittance is modeled and the path radiance is not modeled in the derivation of surface reflectances, errors of approximately 10% will be introduced in the derived surface reflectances beyond 0.8 μm.

A practical method, called the "empirical line method", for retrieving surface reflectances from AVIRIS data, has been developed by Conel et al. (1987). In this method, field measurements of surface reflectances of two targets having contrasting albedos are required. From Eq. (1), it is seen that $T(\lambda)$ and $L_{Path}(\lambda)$ can be derived from the AVIRIS radiance measurements over the two surface targets with known reflectances. The derived $T(\lambda)$ and $L_{Path}(\lambda)$ can then be used to obtain surface reflectances from AVIRIS data over other pixels, provided that $T(\lambda)$ and $L_{Path}(\lambda)$ remain constant within the image scene. The empirical line method also works well in retrieving surface reflectances from the raw AVIRIS data without radiometric calibration.

However, the empirical line method cannot effectively remove atmospheric gas absorption features from AVIRIS data over scenes with elevation variations. This is because atmospheric water vapor concentration usually decreases rapidly with height and transmittances within the scene vary with elevation. Figure 2 shows examples of derived surface reflectance curves from AVIRIS data measured over the Dolly Varden Mountains, Nevada in June, 1989 using the empirical line method. The strong water vapor absorption regions near 1.38 and 1.88 μm are not shown because these regions are opaque and contain no information from the surface. The top curve is an AVIRIS spectrum from an area lower in elevation than the two target areas used in the empirical line method, and the converse is true for the bottom curve. The top curve shows remaining water vapor features in the 0.94 and 1.14 μm regions, due to an under-correction of water vapor features with the empirical line method, while the bottom curve shows reversed water vapor features, due to an over-correction of water vapor features with the method. Figure 2 indicates that in order to remove water vapor features in AVIRIS data properly, water vapor values on a pixel-by-pixel basis are required. At present, the only practical way of obtaining the water vapor values on a pixel-by-pixel basis is to retrieve the values from the AVIRIS data themselves.

In this paper, a new method using atmospheric spectral simulations for deriving surface reflectances from AVIRIS data is described.

III. Method

The method for the derivation of surface reflectances from AVIRIS data consists of following steps:

1. The solar zenith angle is derived based on the AVIRIS' flight time and on the geographic location (latitude and longitude) of the scene.
2. Band positions and spectral resolution of AVIRIS data are verified by curve fitting absorption features of atmospheric water vapor, carbon dioxide, and oxygen. The spectral

calculation is made using a Malkmus narrow band model. The fitting is made using a nonlinear least squares program. Figure 3 shows an example of mismatching in band positions between an observed spectrum and a calculated spectrum. When this situation occurs, the band position of the observed spectrum is adjusted to obtain a better fit.

3. The AVIRIS radiance spectrum is divided by the solar radiance curve above the atmosphere (Iqbal, 1983). The resulting spectrum is referred to as the "apparent reflectance spectrum."

4. The integrated water vapor amount in the combined Sun-surface-sensor path on a pixel by pixel basis is derived from the 0.94- and the 1.14-μm water vapor features in the measured data using a band ratioing technique described in the Appendix.

5. The water vapor transmission spectrum in the 0.8-2.5 μm region is calculated using the Malkmus narrow band model and using the derived water vapor amount. The transmission spectra for well mixed gases, including carbon dioxide (CO_2), oxygen (O_2), and methane (CH_4), are calculated based on the solar and the observational geometry.

6. The apparent reflectance spectrum is then divided by the total atmospheric transmission spectrum in order to obtain the surface reflectance spectrum.

IV. Results

Our method for surface reflectance retrievals has been applied to several sets of AVIRIS data over different geographic locations. Figure 4 shows examples of derived reflectances of clouds, cloud shadow, and two types of vegetation, i.e., a golf course and pine trees, from AVIRIS data measured in June, 1989 over the Oregon Transact. It is interesting to note that the shapes of the two vegetation reflectance curves are different. The pine trees have lower reflectance near 1.7 μm region due to stronger lignin and cellulose absorptions. The golf course has lower reflectance in the 1.45-1.60 μm region due to stronger liquid water absorption.

Figure 5 shows examples of our derived surface reflectances from AVIRIS data gathered over the Dolly Varden Mountains, which contain different types of rocks. These spectra have been smoothed to 15 nm spectral resolution in order to allow better identification of broad mineral absorption features. For comparison, the reflectances obtained with the empirical line method from AVIRIS data over the same pixels, and the laboratory measured reflectances of rock samples collected from the field are also shown. A major carbonate feature near 2.34 μm is clearly seen in the upper three spectra. The lower three spectra are obtained from a quartz latite volcanic unit. The laboratory measured spectrum has nearly constant reflectances in the 2.0-2.4 μm region. The spectrum derived with our method has nearly constant reflectances in a smaller spectral region between 2.05 and 2.37 μm. The rapid drop off of our derived reflectance near 2.40 μm may be due to the fact that water vapor continuum absorption is not included in our spectral model. The above comparisons indicate that our method does a reasonably good job in recovering surface reflectance properties.

V. Discussion

The methane absorption near 2.35 μm is often considered unimportant in atmospheric modeling. For example, methane bands are not included in the 5S atmospheric transfer code (Tanre et al., 1990). However, we find that the peak absorption of the 2.35-μm methane band in a Sun-surface-sensor path is approximately 20%. It is necessary to include this methane band in the modeling. Otherwise, an error of the same magnitude will be introduced in the derived surface reflectances in the 2.35 μm region.

Our method for surface reflectance retrievals can only apply to AVIRIS data obtained on clear days with very low aerosol concentrations and for spectral regions above approximately 0.8 μm. Below 0.8 μm, atmospheric scattering must be modeled. Our method cannot be applied to AVIRIS spectra measured on hazy days, because under these situations significant portions of

measured radiation result from the aerosol scattering of solar radiation. Therefore, accurate modeling of atmospheric scattering effects is necessary.

When using our method for surface reflectance derivation, the band positions between observed and calculated spectra must be matched to 0.5 nm or better. Otherwise, peculiar features will appear in the derived surface reflectance curve, especially at the edges of atmospheric gaseous absorption features.

VI. Summary

A new method, using atmospheric spectral simulations for deriving surface reflectances from AVIRIS data, is described. The method is useful for surface reflectance retrievals in the 0.8-2.5 μm region from AVIRIS data measured on clear days with visibilities of 20 km or greater. The method has two advantages. One is that field measurements of surface reflectances are not required. The other is that atmospheric water vapor absorption features are removed on a pixel-by-pixel basis, based on the derived water vapor values from AVIRIS data themselves. Preliminary application of the technique to AVIRIS data indicates that retrieval results are reasonable. Different vegetation absorption characteristics are observed. Major mineral features are identified. In the near future, we plan to combine our program with the 5S code (Tanre et al., 1990) so that spectra corresponding to the AVIRIS' resolution and observational geometry can be calculated easily and that atmospheric scattering effects can be modeled approximately.

Acknowledgments

The authors are grateful to R. O. Green of the Jet Propulsion Laboratory for providing the AVIRIS spectral data. This work was partially supported by the Jet Propulsion Laboratory, California Institute of Technology under contract 958039 and the NASA Goddard Space Flight Center under a contract.

References

Conel, J. E., R. O. Green, G. Vane, C. J. Bruegge, and R. E. Alley, AIS-2 radiometry and a comparison of methods for recovery of ground reflectance, in *Proceedings of the Third Airborne Imaging Spectrometer Data Analysis Workshop, G. Vane, Ed., JPL Publ. 87-30,* 18-47, 1987.

Goetz, A. F. H., and M. Herring, The high resolution imaging spectrometer (HIRIS) for Eos, *IEEE Trans. Geosci. Remote Sens., 27,* 136–144, 1989.

Goetz, A. F. H., G. Vane, J. Solomon, and B. N. Rock, Imaging spectrometry for Earth remote sensing, *Science, 228,* 1147–1153, 1985.

Iqbal, M., *An Introduction to Solar Radiation,* pp. 43–95, Academic, San Diego, Calif., 1983.

Tanre, D., C. Deroo, P. Duhaut, M Herman, and J. J. Morcrette, Description of a computer code to simulate the satellite signal in the solar spectrum:the 5S code, *Int. J. Remote Sensing, 11,* 659-668, 1990.

Vane, G. (Ed.), Airborne visible/infrared imaging spectrometer (AVIRIS), *JPL Publ. 87–38,* Jet Propulsion Laboratory, Pasadena, Calif., 1987.

APPENDIX: BAND RATIOING METHOD

Figure A1 shows an apparent reflectance spectrum, in which the relevant positions and widths of spectral regions used in the band ratioing are illustrated. Specifically, apparent reflectances of 5 AVIRIS channels near 0.945 μm are averaged to give a mean apparent reflectance of the 0.94-μm water vapor band. Apparent reflectances of 3 channels near 0.86 μm are averaged to give a mean apparent reflectance at the 0.86 μm "atmospheric window" region. Apparent reflectances of 3 channels near 1.03 μm are averaged to obtain a mean apparent

reflectance at the 1.03 μm "atmospheric window" region. A mean observed transmittance for the 0.94-μm water vapor band is obtained by dividing the mean apparent reflectance at the water vapor center by one half of the sum of the mean apparent reflectances at the two window regions. A mean calculated transmittance for the 0.94-μm water vapor band is similarly obtained from a simulated spectrum with an assumed atmospheric temperature, pressure, and density model. A set of calculated mean transmittances for the 0.94-μm water vapor band is obtained from a set of simulated spectra with the same atmospheric model but with the amount of water vapor in the model being scaled by different factors. A table of water vapor amount as a function of calculated mean transmittance of the 0.94-μm water vapor band is obtained. The mean observed transmittance for the 0.94-μm water vapor band and a look-up table procedure are used to derive the amount of water vapor corresponding to the observed spectrum.

Similar band ratioing and look-up table procedures are used to derive water vapor amount from the 1.14-μm water vapor band. The average of water vapor values from the 0.94- and 1.14-μm bands is considered as the best estimate of the water vapor value corresponding to the spectrum.

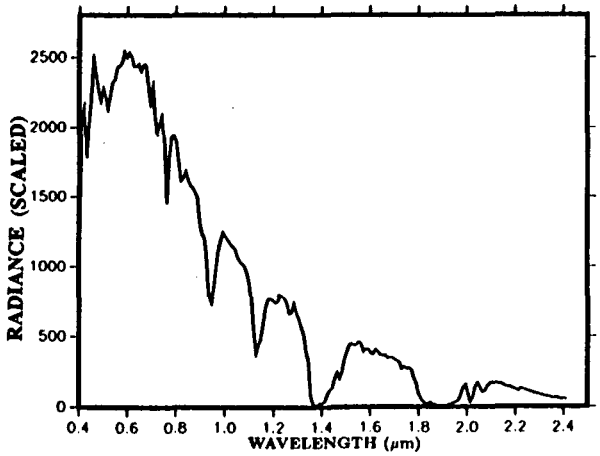

Fig. 1. An AVIRIS spectrum measured over Rogers Dry Lake, California in February, 1990. More than one third of the spectral region is affected by atmospheric water vapor absorption.

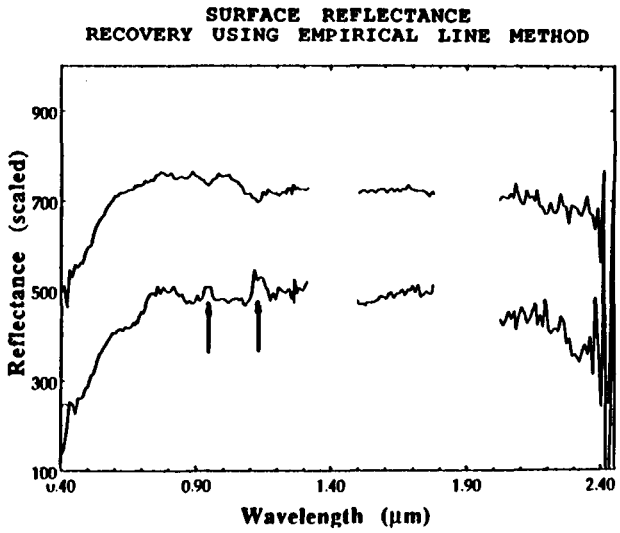

Fig. 2. Examples of derived surface reflectance spectra using the "empirical line method". Notice the under and over corrections of water vapor features near the 0.94 and 1.14 μm spectral regions.

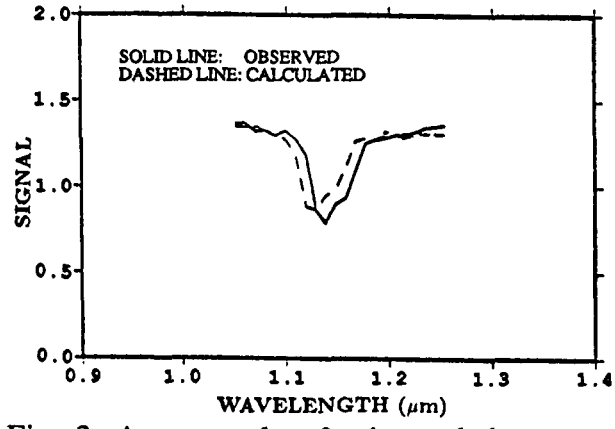

Fig. 3. An example of mismatch between calculated and observed spectra.

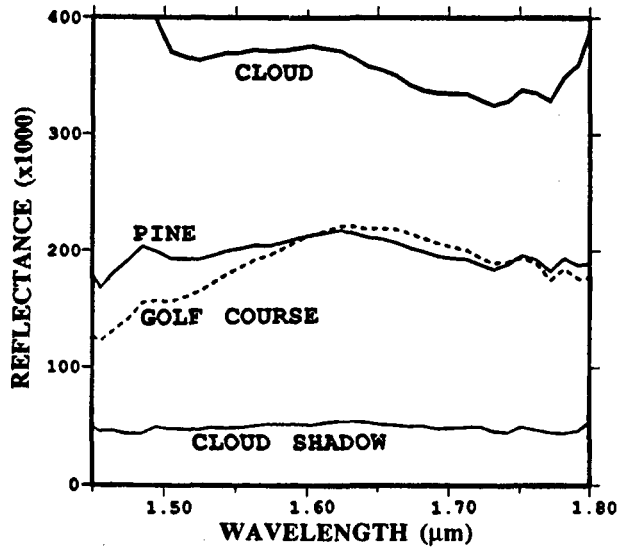

Fig. 4. Examples of derived reflectances of clouds, cloud shadows, and two types of vegetation from AVIRIS data measured in June, 1989 over the Oregon Transect.

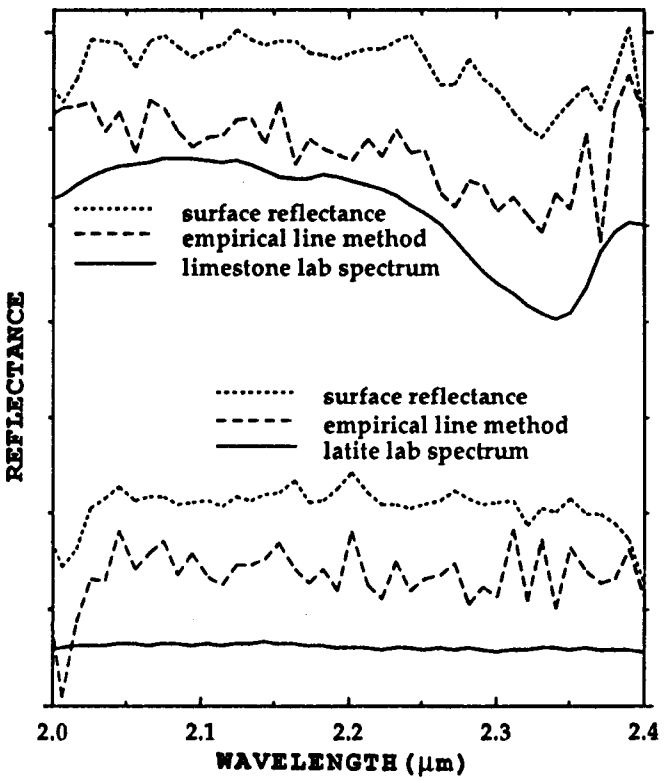

Fig. 5. Surface reflectance spectra obtained with three methods. See text for more descriptions.

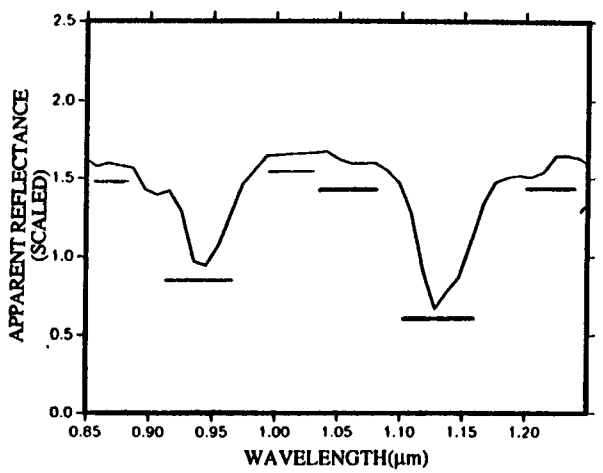

Fig. A1. An apparent reflectance spectrum with relevant positions and widths of spectral regions used in the band ratioing being illustrated.

QUANTITATIVE ANALYSIS OF THREE ATMOSPHERIC CORRECTION MODELS FOR AIRBORNE VISIBLE/INFRARED IMAGING SPECTROMETER (AVIRIS) DATA

J.M. van den Bosch
Geography Department
University of California
Santa Barbara, CA

R.E. Alley
Jet Propulsion Laboratory
California Institute of Technology
Pasadena, CA

Abstract. Current atmospheric correction models applied to imaging spectroscopy data include such methods as residual or scene average, flat field correction, regression or empirical line algorithm, the continuum interpolated band ratio (CIBR) and LOWTRAN 7. Due to the limitations of using residual and flat field corrections on vegetated scenes, three methods will be compared: regression, CIBR and LOWTRAN 7. Field-measured bright and dark targets taken at the time of the 13 April 1989 AVIRIS scene of Jasper Ridge, California were used to formulate the regression method atmospheric correction. Using this corrected scene as "ground truth," the CIBR and the LOWTRAN 7 methods are compared on the vegetated scene.

Three spectra were chosen for comparison: representative samplings of two vegetation types (chaparral and an irrigated crop) and water in the Upper Crystal Springs Reservoir. Correlation and root median squared (RMS) differences were calculated for the atmospherically corrected spectra.

Overall, CIBR and LOWTRAN 7 with radiosonde data were highly correlated and had low RMS differences. LOWTRAN 7 with radiosonde input showed closer agreement with the regression method (assumed "ground truth") than CIBR. It appears that CIBR and LOWTRAN 7 can approach fairly realistic atmospheric corrections for a vegetated AVIRIS scene. Accuracy of both CIBR and LOWTRAN 7 corrections is affected by the estimation of water vapor in the air. When assuming regression represents "ground truth," several possible sources of error can be introduced.

I. Introduction

Imaging spectrometers such as AVIRIS have been used to detect, identify and quantify ecosystems subject to changes from a local and regional scale to a global scale. The high spectral resolution of AVIRIS data with its contiguous 10 nm wide bandwidths from 0.4–2.5 μm coupled with 20 m spatial resolution allows analyses of general ecosystem characteristics such as net photosynthesis (biomass), indicators of plant productivity and stress (chlorophyll, nitrogen, leaf water absorption), nutrient availability (starch, sugar), and rate of litter decomposition (lignin, cellulose), which may serve as temporal and spatial precursors of change. Investigations of the subtle shifts in the slope of the red edge and the position and depth of absorption features in vegetation spectra require careful application of atmospheric corrections in order to extract such detailed information and also to allow comparisons of multidate imagery for phenological studies.

II. Methodology

Based on the limitations posed by the residual/log residual (or scene average) and flat field atmospheric corrections on a vegetated AVIRIS scene as discussed by van den Bosch and Alley

(1990), the regression, LOWTRAN 7 and CIBR methods were compared. A horizontally homogeneous atmosphere and a small elevation variation (El_{Δ}=101m) within the scene were assumed in all of the atmospheric correction models.

The 13 April 1989 AVIRIS image was radiometrically corrected by Jet Propulsion Laboratory (JPL). Three calibration targets (including one bright and one dark target) were used to develop linear relationships between the digital radiance data and the surface reflectance. This regression method has been described in detail (Elvidge, 1988; Elvidge and Portigal, 1990).

LOWTRAN is a model and computer code that can be used to predict spectral radiance for various viewing geometries and atmospheric conditions. The model was developed by the Air Force Geophysics Laboratory in 1972. The latest version, LOWTRAN 7, was released in 1989 and includes multiple scattering, desert aerosol haze type, and a more detailed model of trace gases (Kneizys et al., 1990).

The LOWTRAN 7 method was applied to radiometrically corrected data with input profiles of atmospheric pressure, temperature, and moisture content (dewpoint) as a function of altitude provided by radiosonde data. The viewing geometry was determined by the sensor altitude, target elevation, and solar zenith angle computed by LOWTRAN as a derivation of Julian day, time, latitude and longitude. A variable visibility override was given to the user-designated (radiosonde) geographical model atmosphere with the rural, 23 km visibility aerosol haze model. The observer visibility, V_{obs}, was converted (Kneizys et al., 1990) to meteorological range, V, as follows

$$V = 1.3 * V_{obs} \quad (1)$$

where V_{obs} = 20 km, as reported by ground observation

The second input mode for the LOWTRAN 7 method utilized ground meteorological data collected at the time of the overflight. These parameters included air temperature and visibility combined with the default conditions of the rural, mid-latitude summer model. Both the ground and radiosonde input modes assumed a spectrally constant reflectance (0.15, in this case) and LOWTRAN was used to model the expected radiance when viewing such a surface. By applying a gain and an offset derived from the LOWTRAN results, spectral reflectance was computed (van den Bosch and Alley, 1990).

The CIBR is a ratio between an estimated continuum radiance at the 940 nm water absorption band center derived by linear interpolation between out-of-band continuum radiances to either side and the actual absorption band radiance at the 940 nm wavelength of maximum absorption. The CIBRs are calibrated using LOWTRAN 7 to yield

$$CIBR = \exp(-\alpha w^{\beta}) \quad (2)$$

where w = path precipitable water in g/cm^2

α and β = constants specific to 940 nm band

After calculating the CIBR for the whole scene to recover the total column abundance of water from the atmosphere, the values obtained can then be related to the amount of water present in the scene by running LOWTRAN for varying amounts of water (between zero and twice the normal amount for the atmospheric condition of the overflight). Assuming a constant background reflectance (0.15), the CIBRs can be related to the water predicted by LOWTRAN for each pixel and then corrected to reflectance (Carrere, 1991; Carrere et al., 1991; Conel and Carrere, 1991; and Green et al., 1989).

Three target spectra were chosen: two vegetation types (chaparral and an irrigated crop) and water from the Upper Crystal Springs Reservoir. Statistics generated on the atmospherically corrected spectra include correlation and root **median** squared difference, RMS. The median squared difference was utilized rather than the mean squared difference due to the fact that the median variance was smaller than the mean variance; therefore, the median was a more efficient way of characterizing the data. This also was a protection against outliers.

III. Discussion

The corrected spectra along with the corresponding uncorrected spectra are plotted on the same graph with a 20% offset. The discontinuities in the spectra occur at the major water absorption bands. All of the corrected spectra exhibit a pronounced spike in the 0.400–0.440 μm range that is an artifact of the applied radiometric calibration. This spike can also be seen in the uncorrected spectra.

Figure 1 is an 18 pixel average of an irrigated crop. The chaparral in Figure 2 is dominated by *Adenostema fasciculatum*, a drier, south facing component of the chaparral community. The shape of all three corrected spectra (Figures 1 and 2) in the A spectrometer (0.400–0.700 μm) is very similar with a peak at 0.55 μm. The slope of the red edge at 0.700–1.1 μm in the B spectrometer (0.700–1.200 μm) shows agreement among the spectra with the height of the shoulder varying. The vegetation spectra in the C and D spectrometers (1.200–1.800 and 1.800–2.450 μmi, respectively) are markedly similar in shape. Since the crop and chaparral spectra resemble each other, the statistics were averaged (Figure 5a and 5b).

Overall, Figure 5a shows LOWTRAN 7 with radiosonde data has a higher correlation with the regression method than CIBR in all four spectrometers. However, both CIBR and LOWTRAN 7 have fairly high RMS when compared with the regression spectrum. Figure 5b compares CIBR v. LOWTRAN 7 radiosonde and CIBR v. LOWTRAN 7 ground data. Both LOWTRAN input models show high correlation with CIBR in the A and D spectrometers accompanied by low RMS. However in the B and C spectrometers, the ground input mode has a negative correlation with CIBR and a higher RMS.

Figure 3 represents a single pixel of water in the deepest part of Upper Crystal Springs Reservoir within the image boundary. All three atmospheric correction models are similar. Figure 4 compares the two input modes for the LOWTRAN 7 correction. Using the defaults of the LOWTRAN radiative transfer models in general overcompensates for the 0.94 and 1.15 μm water absorption features. Aside from the aforementioned deviation, the ground meteorological input spectrum resembles the radiosonde spectrum. The statistical analysis for regression v. CIBR and LOWTRAN 7 with radiosonde shows higher correlation in the A and D spectrometers and relatively large RMS in all four spectrometers (Figure 5c). The results of CIBR compared to both input modes of LOWTRAN 7 demonstrate the same trends (Figure 5d) as the vegetation spectra in Figure 5b.

IV. Sources of Error

As noted, there is a spike centered at approximately 0.420 μm that is associated with the 1989 calibration file. The regression method reduced this spike, while the LOWTRAN 7 and CIBR methods did not.

There are problems associated with the assumption that the regression method represents "ground truth." The vegetation spectra (Figures 1 and 2) should exhibit pronounced leaf water

absorption features located at 0.95 and 1.15μm because the imagery was acquired in the spring. However, the regression spectra are almost featureless in the B (0.670–1.290 μm) and C (1.250–1.870 μm) spectrometers. The question remains as to how deep the leaf water absorption feature should be in "reality."

A source of concern in applying the regression method is how well the laboratory or field measured reflectances represent the standard targets (Conel et al., 1988). Another source of concern is the choice of bright and dark targets. When the polo fields were used as the bright target, "anti-vegetation" peaks were introduced at the leaf water absorption features (Figure 6). The regression method was reformulated using a parking lot as the bright target. The minimal criterion for separation of the dark and bright targets should be at least 20%.

The LOWTRAN spectra exhibit more sensitivity to errors in the moisture content than to any other parameter, which may be related to the inaccuracies of radiosonde data (Bruegge et al., 1990). Sources of error for CIBR are also linked to retrieval of atmospheric water vapor and are discussed at length by Carrere (1991) and Conel and Carrere (1991).

V. Conclusions

The specific feature of interest may influence the choice of atmospheric correction. In the A spectrometer, the main absorption features are the chlorophyll a and b wells (a - 0.440 and 0.663 μm; b - 0.460 and 0.640 μm). There is close agreement among the regression method, CIBR and both input modes of LOWTRAN 7. However, the calibration spike affects the chlorophyll as well at 0.440 μm.

The red edge and the near infrared (NIR) plateau are the main features of interest in the B spectrometer. There is close agreement based on the statistics performed between CIBR and LOWTRAN 7 with radiosonde input for both features. The shoulder height of the red edge is noticeably different in the regression method and the NIR plateau is almost featureless. CIBR and LOWTRAN 7 spectra show differences in the depth of the leaf water absorption features in the B spectrometer and the "real" depth cannot be resolved without ground measurements.

In the C spectrometer, CIBR and LOWTRAN 7 with radiosonde data are consistent when looking at the 1.45 μm cellulose and protein feature and the 1.7 μm cellulose and sugar absorption feature compared with the regression method and the LOWTRAN 7 ground input.

The 2.09 and 2.27 μm ligno-cellulose and 2.18 μm nitrogen absorption features in the D spectrometer are characterized well by CIBR, regression and both input modes of LOWTRAN 7. However, there is typically low signal to noise and this could affect results based on these absorption features.

For researchers who do not have access to ground based measurements of bright and dark targets at the time of the overflight, the LOWTRAN 7 and CIBR methods seem to provide reasonable alternatives.

Acknowledgements

This research was carried out at Jet Propulsion Laboratory, California Institute of Technology, Pasadena, California. The authors would like to thank Chris Elvidge of Desert Research Institute, Reno, Nevada for applying the regression data; Veronique Carrere, Steve Carpenter and Marit Jentoft-Nilsen, all of JPL, for their invaluable assistance; Dennis Joseph of National Center for Atmospheric Research (NCAR) for the radiosonde data; and Howard Veregin, UCSB, for instructions on how to be a "digi-slave" to produce the graphics.

References

Bruegge, C.J., J.E. Conel, J.S. Margolis, R.O. Green, G. Toon, V.E. Carrere, R.G. Holm, G. Hoover. 1990. In-Situ Atmospheric Water-Vapor Retrieval in Support of AVIRIS Validation, *Imaging Spectroscopy of the Terrestrial Environment,* Gregg Vane, Editor, Proc. SPIE 1298, Orlando, Florida, pp. 150-163.

Carrere, V.E. 1991. Use of High Spectral Resolution Airborne Visible/Infrared Imaging Spectrometer Data for Geologic Mapping: An Overview, *Physical Measurements and Signatures in Remote Sensing,* Fifth International Colloquium, Courcheval, France, International Society of Photogrammetry and Remote Sensing (in press).

Carrere, V.E., J.E. Conel, R.O. Green, C.J. Bruegge, J.S. Margolis, R.E. Alley. 1991. Analysis of Atmospheric Water Vapor Maps from AVIRIS at Salton Sea, California: Part I, Experiments, Methods, Results, and Error Budgets (unpublished).

Conel, J.E. and V.E. Carrere. 1991. Analysis of Atmospheric Water Vapor Maps from AVIRIS at Salton Sea, California: Part II, Surface Moisture Flux, Boundary Conditions and Plume Measurements (unpublished).

Conel, J.E., S. Adams, R.E. Alley, G. Hoover, S. Schultz. 1988. AIS Radiometry and the Problem of Contamination from Mixed Spectral Orders, *Remote Sensing of the Environment,* 24(1), pp. 179–200.

Curran, P.J. 1989. Remote Sensing of Foliar Chemistry, *Image Processing '89,* American Society for Photogrammetry and Remote Sensing, Sparks, Nevada, 23 May 1989, pp. 166-174.

Elvidge, C.D. 1988. Vegetation Reflectance Features in AVIRIS Data, *Proceedings of International Symposium on Remote Sensing of Environment, Sixth Thematic Conference, Remote Sensing for Exploration Geology,* ERIM, Houston, Texas, pp. 169-182.

Elvidge, C.D. and F.P. Portigal. 1990. Change Detection in Vegetation Using 1989 AVIRIS Data, *Imaging Spectroscopy of the Terrestrial Environment,* Gregg Vane, Editor, Proc. SPIE 1298, Orlando, Florida, pp. 178-189.

Green, R.O., V.E. Carrere, J.E. Conel. 1989. Measurement of Atmospheric Water Vapor Using the Airborne Visible/Infrared Imaging Spectrometer, *Image Processing '89,* American Society for Photogrammetry and Remote Sensing, Sparks, Nevada, 23 May 1989, pp. 31-44.

Kneizys, F.X., E.P. Shettle, G.P. Anderson, L.W. Abrew, J.H. Chetwynd, J.E.A. Shelby, W.O. Gallery. 1990. Atmospheric Transmittance/Radiance; Computer Code LOWTRAN 7, AFGL Hanscom AFB, MA.

van den Bosch, J.M. and R.E. Alley. 1990. Application of LOWTRAN 7 as an Atmospheric Correction to Airborne Visible/Infrared Imaging Spectrometer (AVIRIS) Data, *Remote Sensing Science for the Nineties,* 10th Annual International Geoscience and Remote Sensing Symposium, Washington, D.C., v. 1, pp. 175-178.

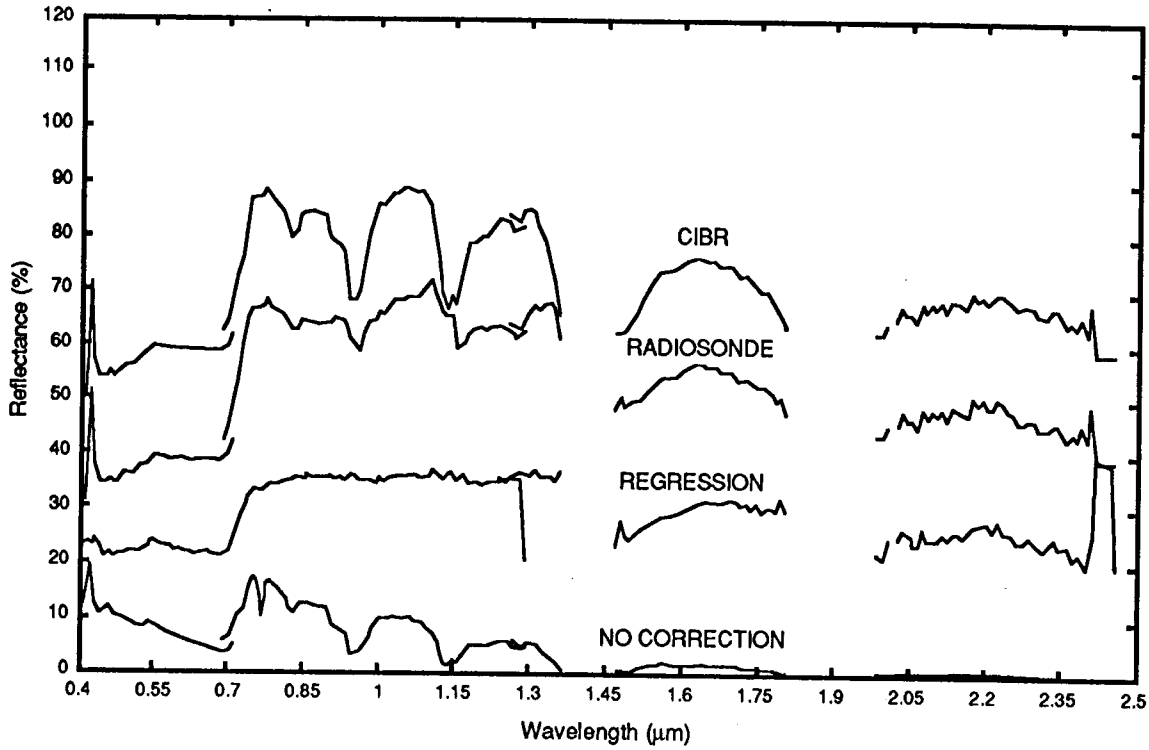

Figure 1. Irrigated Crop

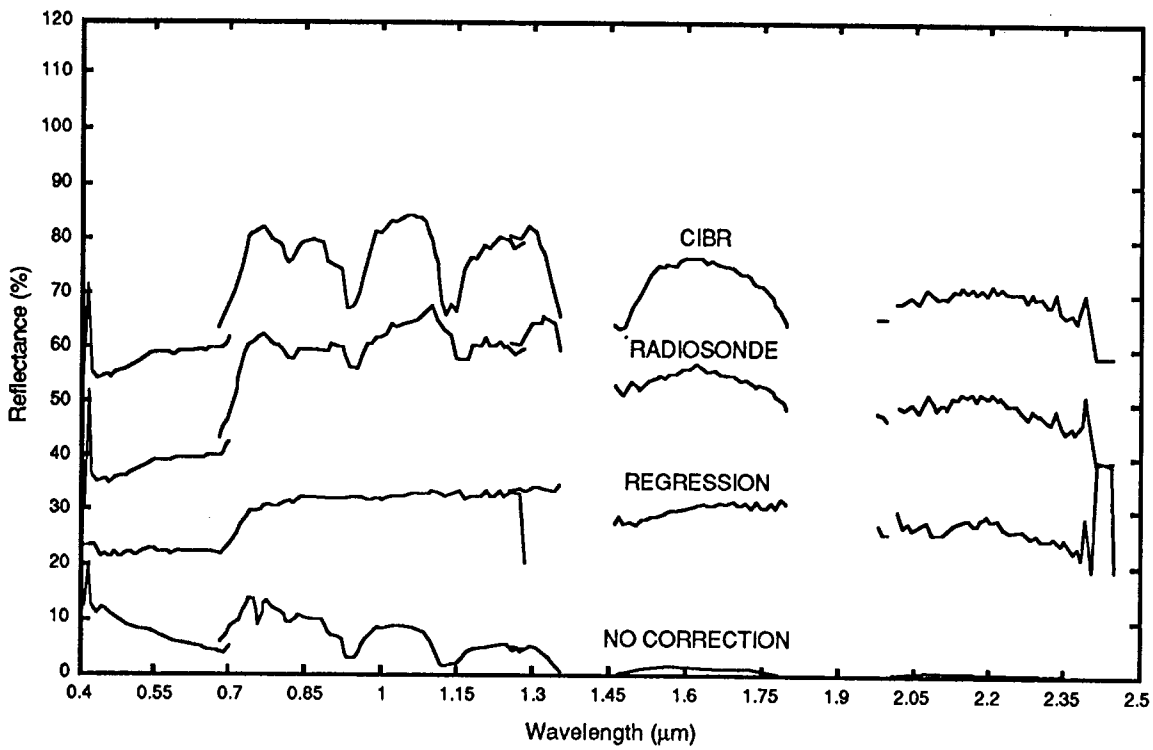

Figure 2. Chaparral

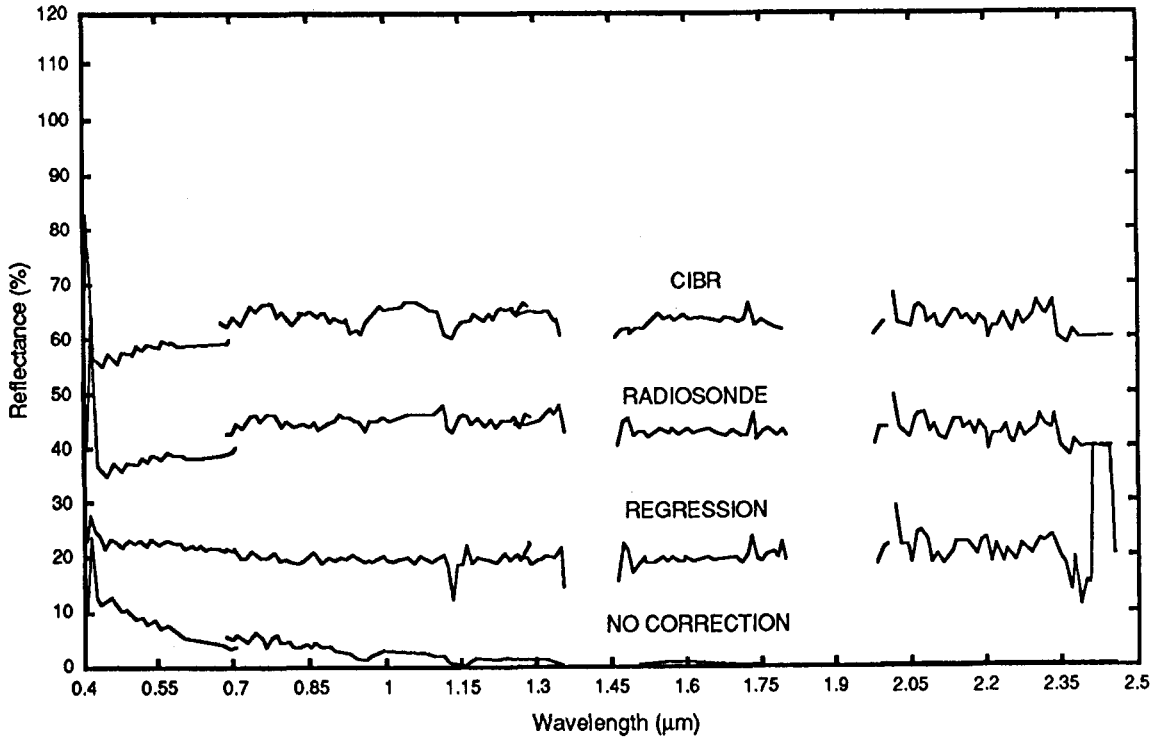

Figure 3. Water I

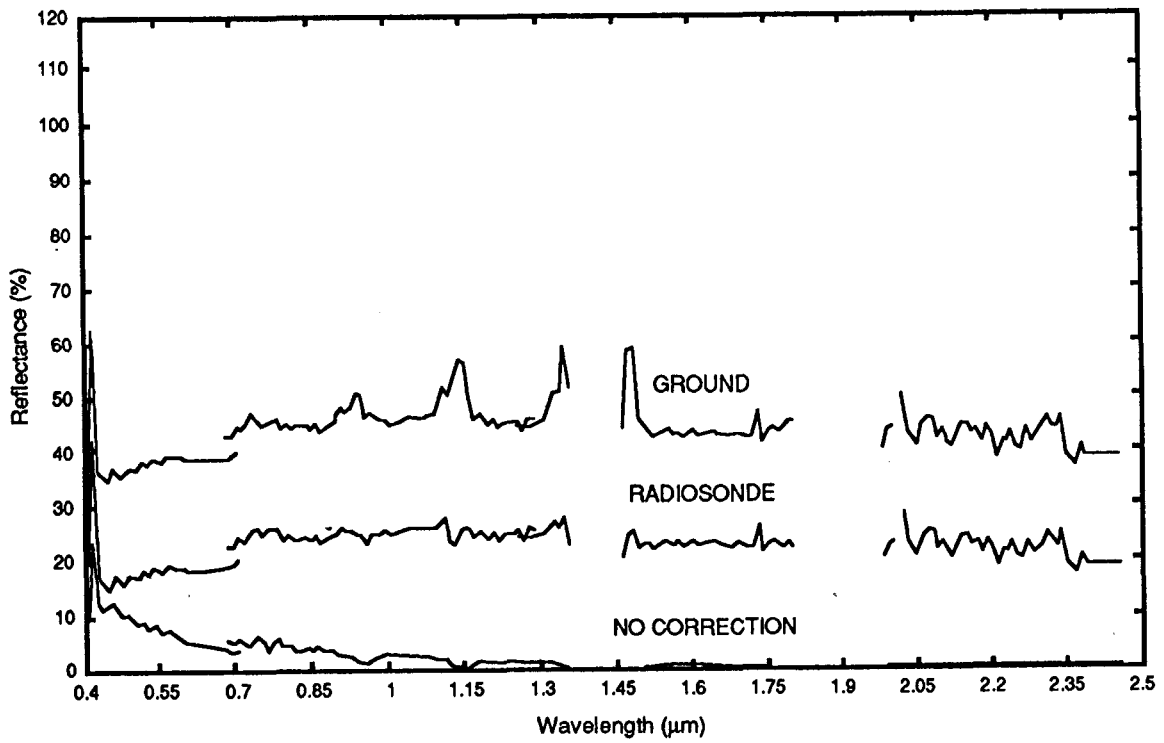

Figure 4. Water II

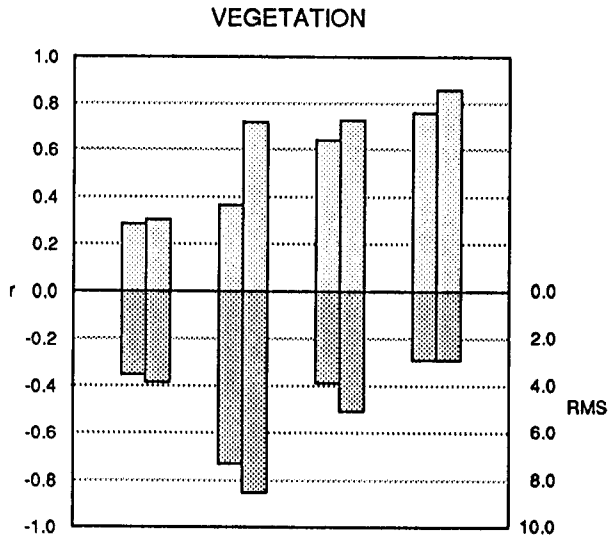

Figure 5a. Regression v. CIBR and LOWTRAN 7 with radiosonde

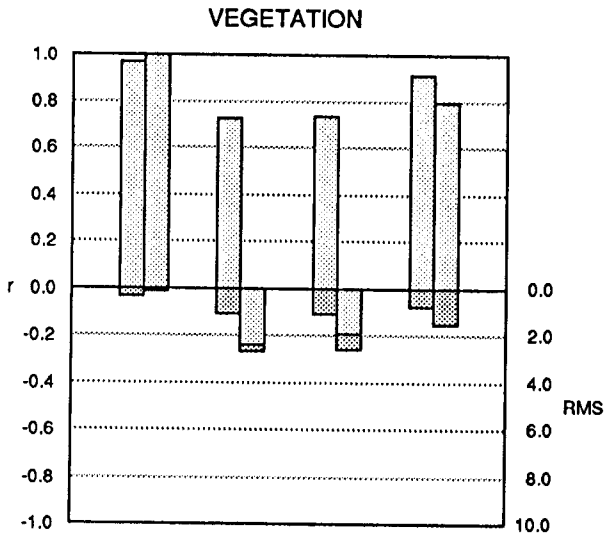

Figure 5b. CIBR v. LOWTRAN 7 with radiosonde and LOWTRAN 7 with ground inputs

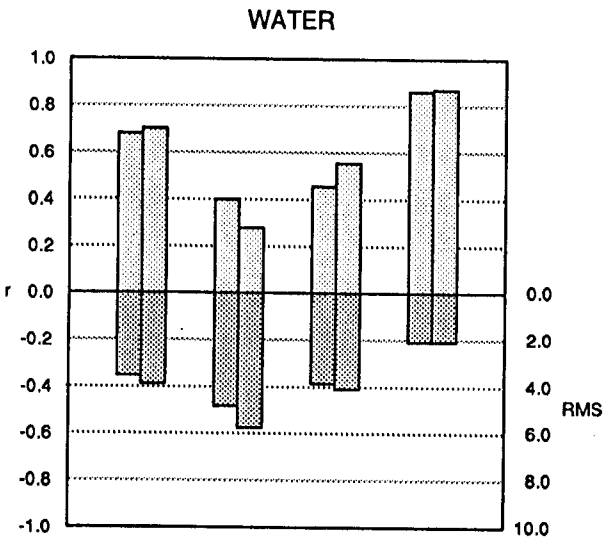

Figure 5c. Regression v. CIBR and LOWTRAN 7 with radiosonde

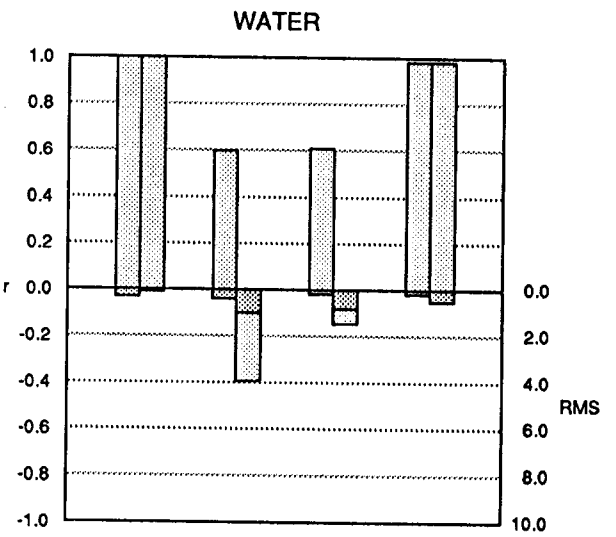

Figure 5d. CIBR v. LOWTRAN 7 with radiosonde and LOWTRAN 7 with ground inputs

Note: The four sets of bars in each graph represent spectrometers A, B, C, D. In Figures 5a and 5c, the first bar in each spectrometer is CIBR; the second bar is LOWTRAN 7 with radiosonde. In Figures 5b and 5d, the first bar in each spectrometer is LOWTRAN 7 with radiosonde input; the second bar is LOWTRAN 7 with ground data.

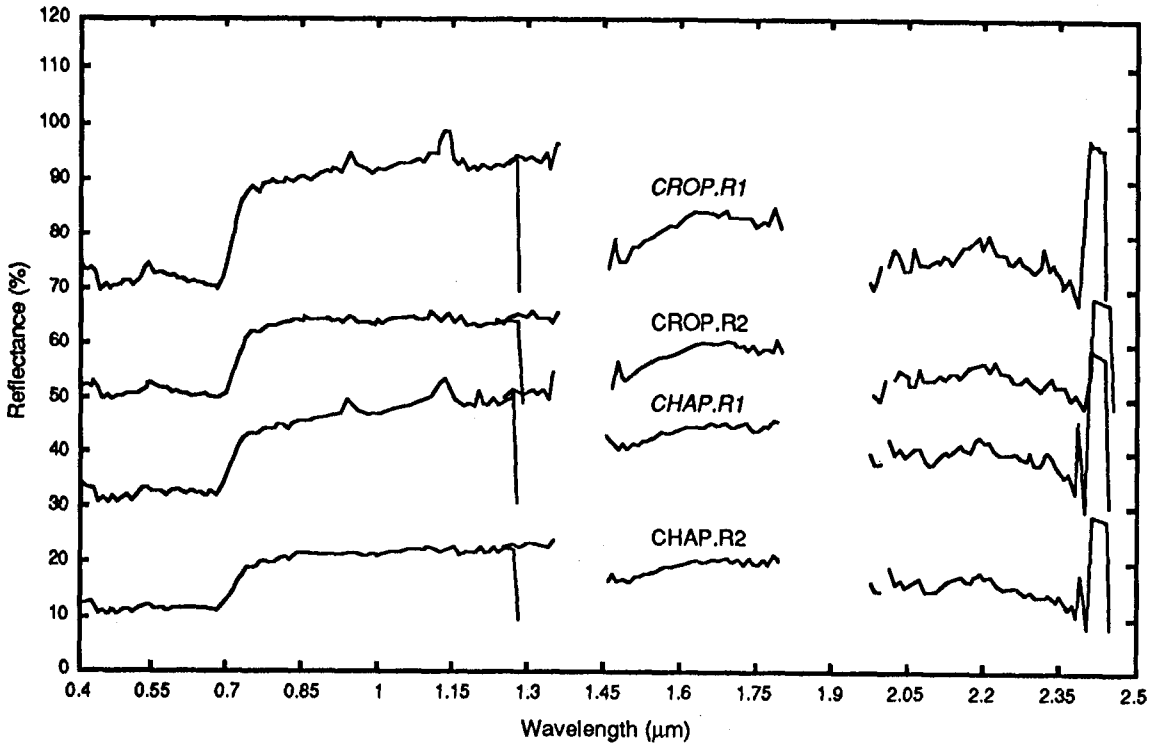

Figure 6. Comparison of two regression methods

Comparison of two simple techniques to extract path precipitable water from AVIRIS radiance data: CIBR and "Narrow/Wide band ratio" - Sensitivity analysis and application to AVIRIS data

Veronique Carrere
Jet Propulsion Laboratory
California Institute of Technology
Pasadena, California

James E. Conel
Jet Propulsion Laboratory
California Institute of Technology
Pasadena, California

Atmospheric water vapor is a key driver to global circulation. As such, it is of interest in studies involving weather, climate modeling, and hydrologic cycles. In addition, water vapor band and continuum absorptions provide substantial obstacles to remote sensing of the Earth's surface in the 400-2500 nm region. Accurate determination of the abundance and spatial variability of water vapor is therefore important for the understanding of fundamental hydrologic questions and when compensating for atmospheric effects in the determination of surface reflectance.

Two simple techniques to retrieve path precipitable water from AVIRIS high spectral resolution radiance data, using the 940 nm water absorption band, are compared. The first technique, named CIBR (Continuum Interpolated Band Ratio, Green et al., 1990), retrieves total column abundance using a ratio between the radiance at the wavelength of maximum absorption and the interpolated continuum from both sides of that absorption. The second one ("N/W", Frouin and Middleton, 1990) is based on the ratio of a "narrow band" located at the maximum absorption, consisting here of an average of three AVIRIS channels between 935 and 955 nm, to a "wide band" average of bands located in the symmetrical portion of the water absorption band and centered on the narrow band, here seven AVIRIS channels between 920 and 970 nm. In both cases, the ratio is then related to the amount of precipitable water through a calibration curve obtained by running LOWTRAN 7 for flight conditions, an assumed background reflectance of 0.25 and increasing amounts of water ranging from 0 to 200% of the standard moisture density profile resident in the code. Total radiances predicted by LOWTRAN 7 are then convolved to AVIRIS spectral resolution, CIBR or N/W is performed for each amount of water, and a file that relates the CIBR or N/W values to the amount of water is created. Previous sensitivity analysis (Carrere et al., 1990, Conel and Carrere, 1990) showed that CIBR was sensitive to background reflectance, visibility, and aerosol model. On the other hand, the N/W ratio has been shown by Frouin and Middleton (1990) to be rather insensitive to background reflectance and visibility changes when applied to field radiometer data. It is also less sensitive to changes in the amount of water due to the fact that it does not measure the full depth of the absorption band. The 940 nm water band was selected because it is not very saturated, and is thus more sensitive to any change in the amount of water. Since the shape and depth of the atmospheric water bands are influenced not only by the water present but also by surface (background) reflectance, atmospheric scattering and instrument calibration, and we are assuming a constant background reflectance and have sometimes little knowledge about the atmospheric parameters such as visibility and type of aerosols when building the calibration curve, a sensitivity analysis was performed using the radiative transfer code LOWTRAN 7 to determine which one of these two approaches will provide a better estimate. This analysis was based on a normalized difference between the reference calibration curve (constant background reflectance, 25 km visibility, rural aerosols, zero meter target elevation, April 18, 11:05 a.m.) and the new calibration curve built by varying one of

the parameters. Sensitivity to background reflectance (vegetation, gypsum, iron oxides versus an assumed constant background reflectance of 25%), visibility variations, types of aerosols, shift in AVIRIS in-flight band positions and bandwidth from the laboratory calibration as well as the effect of off-nadir viewing (15^{o}) at the edge of the flight line were analyzed. In every case, the N/W approach was less sensitive to these effects than the CIBR (average accuracy of 1%). It was, however, more sensitive to scattering due to off-nadir looking at the edge of the flight line. Both techniques were almost equally sensitive (2 to 3%) to shift in band position and change in bandwidth greater than 0.1 nm. This sensitivity analysis also pointed out problems in the way LOWTRAN 7 models visibility, scattering, and aerosols.

Both techniques were then applied to AVIRIS radiance data. When simultaneous atmospheric measurements were available, an independent estimate of water vapor from Reagan sunphotometer measurements (see Bruegge et al., 1990, for method and validation) was provided and compared to the AVIRIS estimate.
Two cases are presented:

(1) Salton Sea, California, where simultaneous atmospheric measurements were available, the environment very humid, and a variable background is present.

(2) Gypsum Plain (Texas), where nothing was known about atmospheric parameters and the background reflectance is composed of gypsum, iron oxides and carbonates.

Results show that:

(1) at Salton Sea, as predicted by the sensitivity analysis, the N/W approach retrieves an amount of water close to the amount retrieved in situ by the Reagan sunphotometer. The amount retrieved using CIBR is underestimated by up to 4 mm (14%). An analysis of the instrument noise needs to be added to take into account random errors in the recovery. This analysis is under way. Both techniques recovered more water over the green fields than over bare soils. If we calculate the difference between the amount of water retrieved by the two techniques and compare it to an NDVI, we confirm that the maximum difference between the two techniques occurs over green fields, as expected from the sensitivity analysis. The only problem is that this difference is in the wrong direction. The sensitivity analysis predicts that we should recover more water with the CIBR than with the N/W approach over the green fields whereas the reverse is actually what we observe on the images. A possible explanation is that the excess water retrieved over the fields comes from evapotranspiration and not water introduced by liquid water absorption in the plants. This has to be confirmed by acquiring sunphotometer measurements in a green field simultaneously with an AVIRIS measurement or by some measurement independent of the surface water.

(2) at Gypsum Plain, results show a very narrow range and a very low amount of water for that day. One can notice similar patterns in both maps but with a slightly wider range of water for the CIBR. This is consistent with the sensitivity analysis which predicted a similar behaviour for both techniques. The difference in amount retrieved by the two techniques shows that here, the CIBR retrieves more water than the N/W. No clear relationship could be established with outcrops of bare gypsum based on a map established using the 1750 nm diagnostic absorption feature. Higher water amounts on the South East side of the flight line can be related to backscattering, which might be an indication that the visibility of 30 km used to build the calibration file was too high.

In conclusion, comparison between sensitivity analysis and image data show that we are on the right track to accurately retrieve total column abundance of water vapor but some problems still remain. N/W proved to be a more accurate approach, although less

sensitive to changes in water amount. The approach will be validated by acquiring simultaneous measurements of water in a green field and in bare soil area.

Future plans include:

(1) Running the same sensitivity analysis for the 1130 nm water band, which is more saturated than the 940 nm one but less affected by aerosols by comparing the results; it would be interesting to do the same for the 825nm water band which is the less saturated one but it is very weak at AVIRIS resolution and might require spatial averaging to increase the signal-to-noise;

(2) Running the same sensitivity analysis using MODTRAN instead of LOWTRAN 7, the modelling of the water absorptions in MODTRAN being supposedly more accurate;

(3) Including the instrument noise as random source of error;

(4) Comparing the results from these two fast and simple techniques to more sophisticated but time-consuming approaches such as least-square-fitting.

References

C. J. Bruegge, J. E. Conel, J. S. Margolis, R. O. Green, G. Toon, V. Carrere, R. G. Holm, and G. Hoover, 1990 - In-situ atmospheric water-vapor retrieval in support of AVIRIS validation. *SPIE, vol.1298, Imaging Spectroscopy of the Terrestrial Environment, pp. 150-163.*

V. Carrere, J. E. Conel, R. O. Green, C. J. Bruegge, J. S. Margolis, and R. E. Alley, 1990 - Analysis of atmospheric water vapor maps from AVIRIS at Salton Sea, California: Part I, Experiments, Methods, Results, and Error Budgets. *Proceedings of the Second Airborne Visible/Infrared Spectrometer (AVIRIS) Workshop, June 4 and 5, 1990, JPL Publication 90-54,* Jet Propulsion Laboratory, Pasadena, California, *pp. 107-128.*

J. E. Conel and V. Carrere, 1990 - Analysis of atmospheric water vapor maps from AVIRIS at Salton Sea, California: Part II, Surface moisture flux, boundary conditions, and plume measurements. *Proceedings of the Second Airborne Visible/Infrared Spectrometer (AVIRIS) Workshop, June 4 and 5, 1990, JPL Publication 90-54,* Jet Propulsion Laboratory, Pasadena, California, *pp. 129-148.*

R. Frouin and E. Middleton, 1990 - A differential Absorption Technique to estimate atmospheric total water vapor amounts. *Proceedings of American Meteorological Society Symposium on the First ISLSCP Field Experiment (FIFE), Feb. 7-9, 1990, Anaheim, California, pp. 135-139.*

R. O. Green, V. Carrere, and J. E. Conel, 1990 - Measurement of atmospheric water vapor using the Airborne Visible/Infrared Imaging Spectrometer. *Image Processing '89, American Society for Photogrammetry and Remote Sensing, Sparks, Nevada, pp. 31-44.*

Acknowledgements

The authors would like to thank Jack Margolis for his advice and comments and Carol Bruegge for reducing the Reagan data. This work has been carried out at the Jet Propulsion Laboratory, California Institute of Technology in relation with the HIRIS Project, under a contract with the National Aeronautics and Space Administration.

Target Detection Thresholds Using Imaging Spectrometer Data

Donald E. Sabol Jr., John B. Adams,
Milton O. Smith, and Alan R. Gillespie

Department of Geological Sciences
University of Washington, Seattle, Washington

I. Introduction

Detection of target materials in image data has long been of major interest in analysis of image data. Targets (any objects or materials that are being sought in an image) can be detected in multispectral images based on their spatial or spectral properties, or a combination of both. To be detected based on spatial properties alone (e.g.: shape, size, texture), the target must be large relative to image sampling size. In this case, the target must be expressed by a group of pixels. If the multi-pixel target is also spectrally distinct from the background, it can be detected spectrally as well as spatially, which may facilitate identification.

Even though sub-pixel targets cannot be detected spatially, they can be detected spectrally under certain conditions of spectral contrast, spectral sampling, and instrumental noise. The spectrum of a sub-pixel target mixed with the spectrum (or multiple spectra) of the background results in a combined spectral signal. In the context of a multispectral image, where there is spectral variance from pixel to pixel, the target spectrum commonly can be estimated using spectral mixture analysis (e.g.: Adams et al., 1986, 1989; Smith et al., 1990; Gillespie et al., 1990). Thus, spectral mixture analysis can be used to detect and, in some instances, identify targets at the sub-pixel scale.

Many of the conditions that limit the spectral detection of sub-pixel targets have been identified in earlier studies. Siegal and Goetz (1977), for example, observed that the masking effect of vegetation on detection of rocks/soils in a composite spectrum of vegetation and substrate depends upon both the fractions and the spectra of the surface components. In one of the first studies to analyze detectability thresholds, Shipman and Adams (1987) applied two-component spectral mixture models to laboratory spectra to detect small amounts of alunite and kaolinite in desert alluvium. Johnson et al. (in review) used the standard deviation of the difference between the background spectrum and spectral mixtures of the background and target to estimate the threshold for target detection. Because both Shipman and Adams (1987) and Johnson et al. (in review) used laboratory spectra, noise (±1% reflectance), although identified as a limiting factor, was not a major source of error. However, noise can be significant (in excess of ±5% reflectance) in image data, particularity in the narrow bands of hyperspectral systems such as NASA's Airborne Imaging Spectrometer (AIS) and the Airborne Visible-Infrared Imaging Spectrometer (AVIRIS). The effect of different instrumental noise and spectral sampling intervals on spectral abundance was investigated by Goetz and Boardman (1989), who emphasized the importance of spectral contrast between endmember spectra in obtaining accurate fractions, particularly with noisy data.

Equation 1, the general equation for spectral mixture analysis, shows the relationship between the continuum and residuals in detection threshold analysis.

The linear mixing model, used in this paper, comprises linear combinations of component (endmember) spectra:

$$R_{mix,b} = \Sigma (F_{em} \quad R_{em,b}) + E_b \qquad \text{and} \qquad \Sigma F_{em} = 1 \tag{1}$$

where $R_{mix,b}$ is the reflectance of the mixed spectrum at each band (b), $R_{em,b}$ is the reflectance of each endmember (em) at each band, F_{em} is the fraction of each endmember in the scene, and E_b is the residual at each band. If a target is abundant at the sub-pixel scale and distinguishable from the other spectral components throughout the spectrum, it generally can be treated as a spectral endmember. For this case, the detection threshold is the smallest fractional abundance (F_{em}) of the endmember that can be measured above system noise. A procedure for determining this threshold was developed by Sabol et al. (1990) and is referred to as "continuum threshold analysis". However, the target is not normally modeled as an endmember when its sub-pixel abundance is low or when its spectrum deviates from mixtures of the other components at only a few wavelengths (Smith et al. 1985; Gillespie et al., 1990; Adams et al., in press). In this case, the target detection thresholds are best determined by analyzing the deviations of the modeled endmember mixtures from the image data in the band residuals (E_b) using residual threshold analysis (Gillespie et al.; 1990, Roberts et al.; 1990).

In this paper, we present an approach to predict the minimal spectral contribution necessary for detection of a target in the band residuals using residual threshold analysis. This approach was demonstrated for the case of detecting soil in the senescent grassland of the Jasper Ridge, September 1989, AVIRIS data.

II. Residual Threshold Analysis

A target spectrum that can be mimicked by mixtures of the (background) endmembers at all but a few bands may be undetectable using continuum threshold analysis. In this case, the target is detectable in precisely the bands where the endmembers are not well modeled. Using these "diagnostic" bands, threshold detection limits can be determined by residual threshold analysis. Unlike continuum analysis, the target spectrum is not included as an endmember in residual threshold analysis. Consequently, the spectral contribution of the target is partitioned among the endmembers, thereby shifting the computed fractions from the preassigned fractions in the spectral mixture. The partitioning is given by:

$$C_b = \Sigma [F_{em} + (F_t \quad Ft_{em})] R_{em,b} \tag{2}$$

$$\text{and both } \Sigma F_{em} = 1 \text{ and } \Sigma Ft_{em} = 1$$

where C_b is the reflectance of the modeled spectrum (continuum) at each band, F_t is the fraction of the target in the observed mixed spectrum, F_{em} is the fraction of each endmember in the observed spectrum, Ft_{em} is the fraction of the target attributed to each endmember, and $R_{em,b}$ is the reflectance of each endmember at each band. Ft_{em} is determined by spectrally unmixing the target spectrum relative to the endmembers.

To illustrate target detection using continuum threshold analysis, consider a surface composed of three materials that mix spectrally, a target material (covering

50% of the surface) and materials A and B (each covering 25% of the surface). In this example, the spectrum of the target is not included as an endmember. When the mixed spectrum is unmixed relative to the spectra of materials A and B (hereafter referred to as endmembers 1 [EM1] and 2 [EM2]), the fraction of the target spectrum will be partitioned among the endmembers. This partitioning ($\mathbf{Ft}_{em}$) can be determined by spectrally unmixing the target spectrum relative to the endmembers. If, for example, the target is partitioned as .77 endmember 1 and .23 endmember 2, 77% of the target's contribution to the mixed spectrum (50%) will be attributed to endmember 1 thereby shifting the fraction of EM1 to 63% while the fraction of EM2 is shifted to 27%.

In the absence of noise, the target is detected as the residual when the spectrum modeled by the endmembers (Equation 1) is subtracted from the measured spectrum that contains a contribution from the target (Equation 2). In the presence of noise, the fractions of the endmembers may vary in value. The amount of variation in the predicted continuum spectrum can be determined for a given confidence interval by repeatedly combining the predicted continuum spectrum with noise, and unmixing the noisy spectrum. The noise, modeled as having a gaussian distribution about the predicted reflectance at each band, causes the resulting distribution of the apparent fractions to be normally distributed about the initial proportions of the predicted continuum. An example of this distribution is shown in Figure 1 A where a signal-to-noise (SNR) of 50/1 (relative to a 100% reflective target) was used. In this example, the range of uncertainty in the fractions of the predicted continuum due to noise at the 90% confidence interval ranged from 58.9% EM1 and 41.1% EM2 to 67.1% EM1 to 32.9 EM2. The uncertainty in the spectrum of the predicted continuum at the 90% confidence is shown in Figure 1B. Noise also causes a range of uncertainty which also affects the observed spectral mixture ($\mathbf{R}_{mix,b}$ in Equation 1). The target is detectable in the band residuals where the uncertainty due to noise associated with the observed spectrum and predicted continuum do not overlap (Figure 2). In this example, the target is detectable in three wavelength regions: 0.5 to 0.7 μm, 2.02 to 2.2 μm, and 2.25 to 2.4 μm. For any given band, the detection threshold is reached when these uncertainty ranges begin to separate. Therefore, by varying the fractions in the spectral mixture, the detection threshold for each band can be determined.

III. Application to Jasper Ridge Data

The problem of detecting soil in the regions of senescent vegetation on Jasper Ridge, California was used to test residual threshold analysis. This problem was chosen because: 1) the minimal spectral contrast between soil and dry grass makes spectral separation of the two materials difficult (Roberts et al., 1991), and 2) the exposures of soil in the dry grasslands are small and scattered, resulting in spectral mixtures in most image pixels of the grasslands.

To be able to compare predicted detection thresholds that were determined using laboratory spectra (measured in reflectance) to image data (in encoded radiance), the image data were calibrated to reflectance. Two methods were used, the empirical-line calibration and the linear mixing calibration (Roberts et al., 1991). Because the level of noise in an image is an important factor in detecting spectral targets, the noise in the image had to be characterized before any detection analysis could be performed.

A. Evaluation of Noise in Images

We developed a new technique that employs spectral mixture analysis to evaluate image noise. Because noise is measured directly from the image, the instrumental noise is measured at the time of the over-flight. The initial step in determining image noise was to model the image as spectral mixtures of a set of endmembers that account for most of the spectral variation in the scene (low band residuals). For the senescent grasslands in the Jasper Ridge scene, three endmembers were used: "soil 176", "dry grass", and "shade" (Figure 3). The standard deviation was calculated for areas in the image where the band residuals were low (down to the noise level) (STD_b), the assumption being that these residuals contain only noise. Although a portion of the noise is found in the band residuals, the remainder affects the endmember fractions. Therefore, it is necessary to determine how the noise is partitioned between the fractions and residuals. This was determined by constructing a synthetic image composed of a range of spectral mixtures using the laboratory-measured endmember spectra. A known level of noise was added to the image. Then, by inverting the spectral mixing equation, the noisy image was unmixed relative to the endmembers to determine the predicted fractions. Band residuals were determined by subtracting the predicted reflectance from the reflectance observed in the noisy synthetic image. The standard deviation was calculated for each band residual (which contained only noise) as well as for the noise that was added to the image. The fraction of the noise in each band residuals (hereafter referred to as the partitioning coefficient [pc_b]) was determined by dividing the standard deviation of the noise in each band residual by the standard deviation of the noise input into the synthetic image. A plot of the partitioning coefficient for the endmembers used in modeling the AVIRIS scene showed that, on average, 90% of the noise was partitioned into the band residuals while only 10% of the noise caused uncertainty in the fractions (Figure 4).

The total noise in the image ($Noise_{b,Tot}$) was determined by adjusting the standard deviation of the band residuals (STD_b) in the AVIRIS scene for the noise that was partitioned into the fractions by using:

$$Noise_{(b,Tot)} = (1+pc_b)\, STD_b \qquad (3)$$

To cast the apparent image noise into an SNR (relative to a 100% reflectant material), the offsets and gains that were used to calibrate the image to reflectance were used to determine the maximum signal for each band ($R_{b,max}$). The signal-to-noise for each band in the Jasper Ridge AVIRIS image (SNR_b) was determined using:

$$SNR_b = \frac{R_{(b,max)}}{Noise_{(b,Tot)}} \qquad (4)$$

The resulting SNR_b for the Jasper Ridge AVIRIS data (September 1989) is shown in Figure 5.

B. Prediction of Residual Detection Thresholds

Using the procedures discussed above, the residual detection threshold for each band was predicted for the target ("soil 176") in backgrounds composed of "dry grass" and "shade". The results are shown in Figure 6. "Soil 176", which has no distinctive absorption features, was most detectable between 0.5 and 0.6 μm (lowest

detection threshold). Target detectability, which drastically decreased between 1.5 and 1.6 μm (where the threshold was high [> 55%]), improved at longer wavelengths (2.05 to 2.4 μm) where the detection threshold decreased to approximately 20%.

This predicted trend of high detectability at shorter wavelengths, poor detectability between 1.5 and 1.6 μm, and intermediate detectability at longer wavelengths was observed in the band residuals of areas of senescent vegetation on Jasper Ridge when the target ("soil 176") was not included as an endmember.

The bands and thresholds from residual analysis depended upon which endmember was the target. For example, when the grassland was modeled as mixtures of "dry grass" and "shade", "soil 176" (the target) was detected at lower thresholds between 0.5 and 0.75 μm (Figure 7A). However, if the target was "dry vegetation" instead of "soil 176", the grassland (modeled as mixtures of "soil 176" and "shade") would have lower thresholds for target detection at 2.09 μm and 2.27 μm (absorption features caused by cellulose and lignin in "dry grass") (Figure 7B).

IV. Summary and Conclusions

Residual analysis was applied to an AVIRIS image and used to predict spectral detection thresholds of a target in a spectral mixture. The analysis determined which bands were most useful for target detection, even when the target spectrum did not have distinctive absorption features ("soil 176" in the example shown in this paper). Because laboratory measured reflectance values were used, the results from this analysis represent a best possible case for material detection.

The detection problem presented in this paper was selected to demonstrate a method based on spectral mixture analysis to predict target detection thresholds. This method is generally applicable to imaging spectrometer data.

Detection of targets in the band residuals is only one part of spectral mixture analysis. The target may be detected as an endmember (continuum threshold analysis, Sabol et al., 1990) as well as in the band residuals. To determine the lowest detection threshold (highest detectability) of a target in a spectral mixture, both continuum and residual threshold analyses should be performed and compared.

V. References

Adams, J.B., Smith, M.O., and Gillespie, A.R., Simple models for complex natural surfaces: A strategy for the hyperspectral era of remote sensing, Proc. IEEE Intl. Geosci. Remote Sens. Symp. '89, I, 16-21, 1989.

Adams, J.B., Smith, M.O., and Johnson, P.E., Spectral mixture modeling: A new analysis of rock and soil types at the Viking Lander 1 site, J. Geophys. Res., 91, 8098-8122, 1986.

Adams, J.B., Smith, M.O., and Gillespie, A.R., Imaging Spectroscopy: Data analysis and interpretation based on spectral mixture analysis, in Pieters C.M. and Englert P. eds., Remote Geochemical Analysis: Elemental and Mineralogical Composition; LPI and Cambridge Univ. Press, in press.

Gillespie, A.R., Smith, M.O., Adams, J.B., Willis, S.C., Fischer, A.F. III, and Sabol, D.E., Interpretation of residual images: Spectral mixture analysis of AVIRIS images, Owens Valley, California, Proc. 2nd AVIRIS Workshop, Jet Propulsion Laboratory, Pasadena, CA. 4-5 June, JPL Publ. 90-54, 28 pp., 1990.

Goetz, A.F.H. and Boardman, J.W., Quantitative determination of imaging spectrometer specifications based on spectral mixing models, in Proceedings of IGARSS 1989, 1036-1039, 1989.

Johnson, P.E., Singer, R.B., Smith, M.O., and Adams, J.B., Simple algorithms for remote determination of mineral abundances and particle sizes from reflectance spectra, J. Geophys. Res., in revision.

Roberts, D.A., Smith, M.O., Adams, J.B., and Gillespie, A.R., Leaf spectral types, residuals, and canopy shade in an AVIRIS image: AVIRIS, Jet Propulsion Laboratory, Pasadena, CA. 20-24 June, (this volume), 1991.

Roberts, D.A., Smith, M.O., Adams, J.B., Sabol, D.E., Gillespie, A.R., and Willis, S.C., Isolating woody plant material and senescent vegetation from green vegetation in AVIRIS data, Proc. 2nd AVIRIS Workshop, Jet Propulsion Laboratory, Pasadena, CA. 4-5 June, JPL Publ. 90-54, 15 pp., 1990.

Sabol, D.E. Jr., Adams, J.B., and Smith, M.O., Predicting the spectral detectability of surface materials using spectral mixture analysis: Proc.of IGARSS '90 Symposium, 2, 967-970, 1990.

Shipman, H. and Adams, J.B., Detectability of minerals on desert alluvial fans using reflectance spectra, J. Geophys. Res., 92, B10, 10391-10402, 1987.

Siegal, B.S. and Goetz, A.F.H., Effect of vegetation on rock and soil type discrimination, Photogramm. Eng. Remote Sens., 43,191-106, 1977.

Smith ,M.O. and Adams, J.B., Strategy for analyzing mixed pixels in remotely sensed imagery, Proc. NASA/JPL Aircraft SAR Workshop, JPL Publ. 85-39, 47-48, 1985.

Smith ,M.O., Adams, J.B., and Gillespie, A.R., Reference endmembers for spectral mixture analysis, Proc. 5th Australian Remote Sensing Conf., Perth 1990, 331-340, 1990.

VI. ACKNOWLEDGMENTS

We thank Steve Willis for programming assistance. This research was supported by NASA grant NAGW 1319 and a grant from the W.M. Keck Foundation for computer equipment and support.

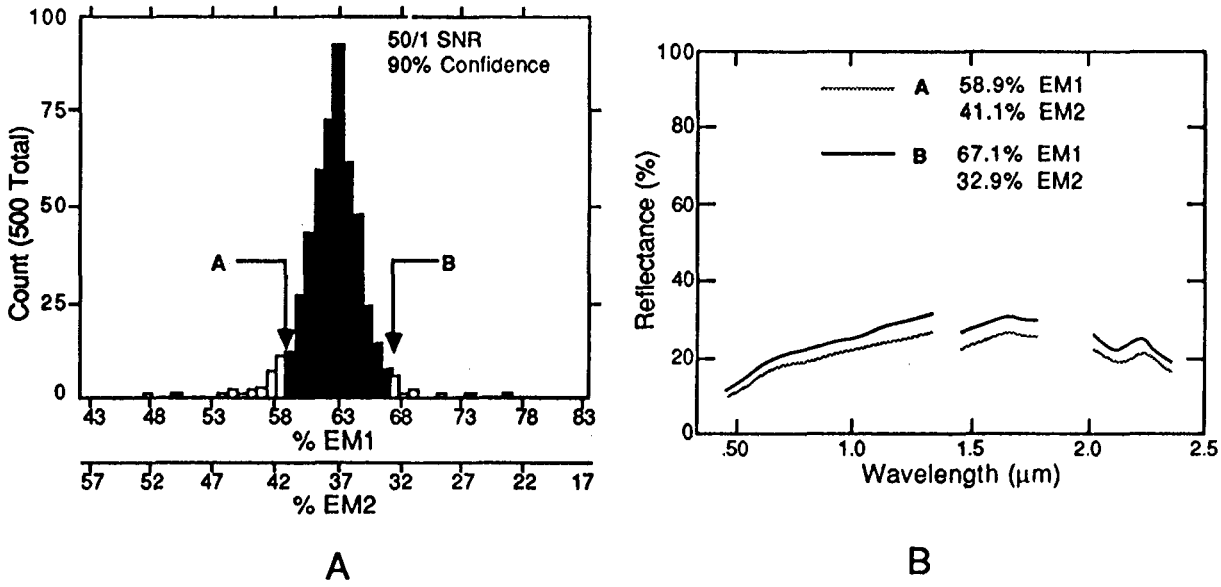

Figure 1. Determination of the uncertainty in the spectrum of the predicted continuum due to noise. For this example, the uncertainty in the fractions of the continuum (mixtures of endmembers 1 and 2) due to a 50/1 SNR at a 90% confidence) range between fractions labeled A and B in Figure 1A. The spectral continuum of these ranges are shown in Figure 1B.

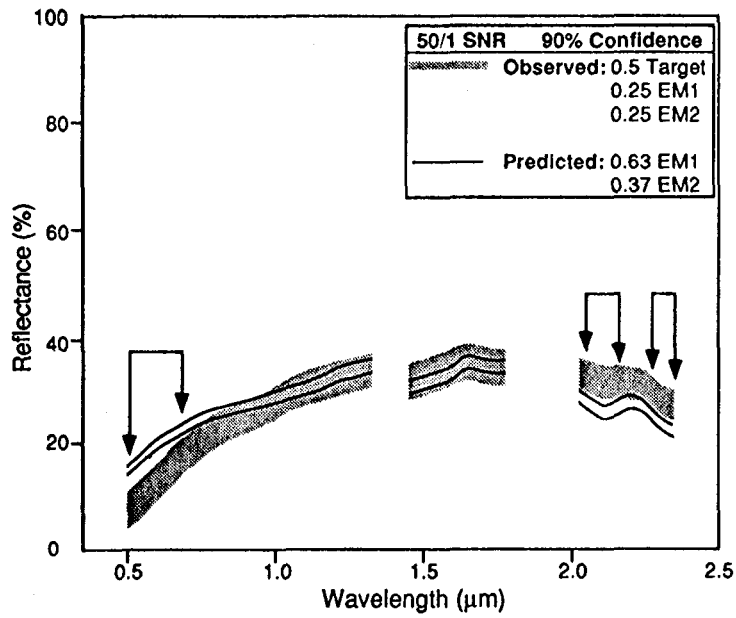

Figure 2. For any band, the target is detectable where the uncertainty due to noise in the predicted continuum (black lines) and the observed mixed spectrum (gray region) do not overlap. In this case, the target is detectable in three wavelength regions: 0.5 to 0.7 μm, 2.02 to 2.2 μm, and 2.25 to 2.4 μm.

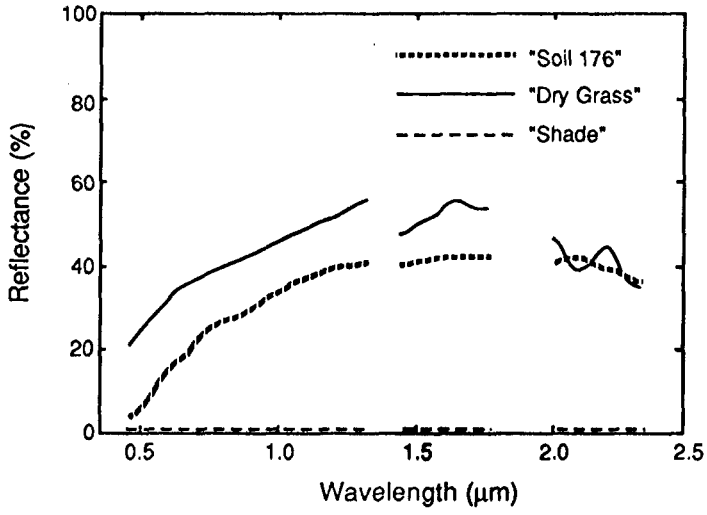

Figure 3. Spectral components observed in the senescent grasslands of Jasper Ridge. "Soil 176" and "dry grass" are laboratory measured spectra that were convolved to the AVIRIS bands used in the spectral analysis. "Shade" was modeled as having 0.1% reflectance at all wavelengths.

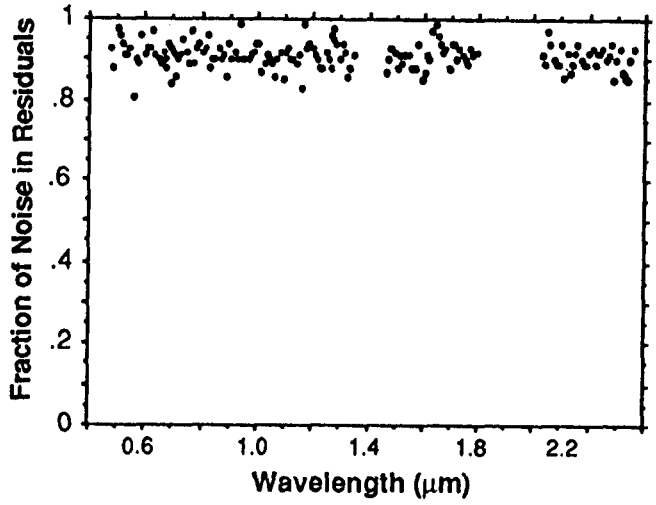

Figure 4. The fraction of the total image noise observed in the band residuals (noise partitioning coefficient) using the spectra shown in Figure 3. On average, 90% of the noise was observed in the band residuals while the remaining 10% affected the fractions.

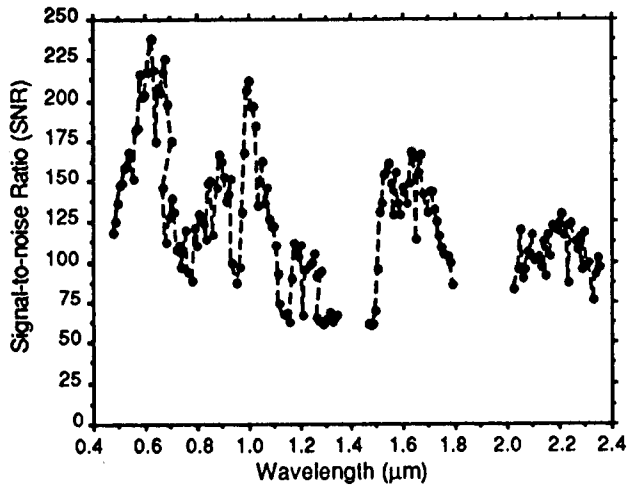

Figure 5. The signal-to-noise ratio (relative to a 100% reflective material) determined from the Jasper Ridge, September 1989, AVIRIS scene.

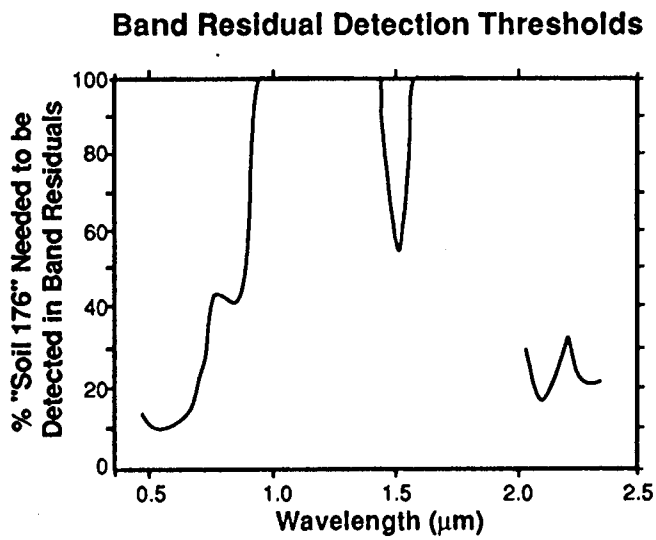

Figure 6. Predicted band residual detectability thresholds for "soil 176" in the areas of senescent vegetation on Jasper Ridge.

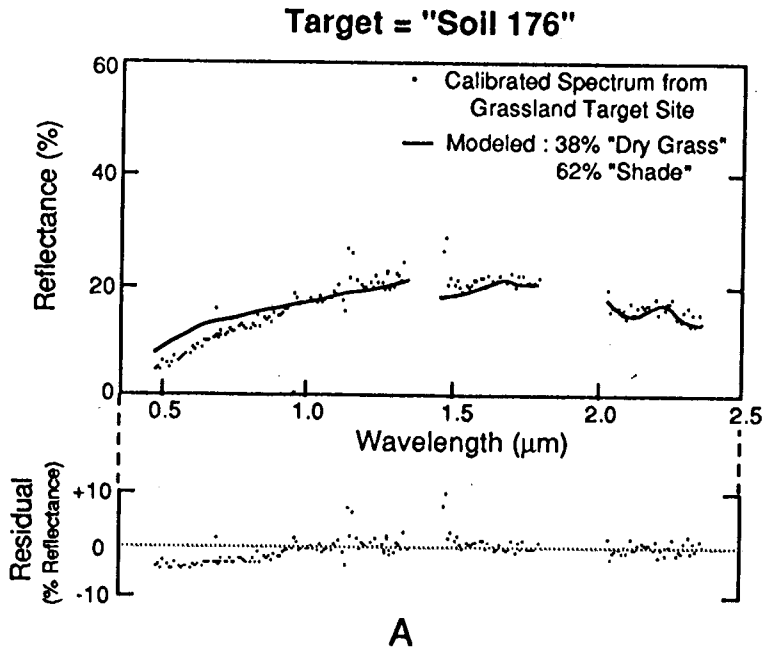

A

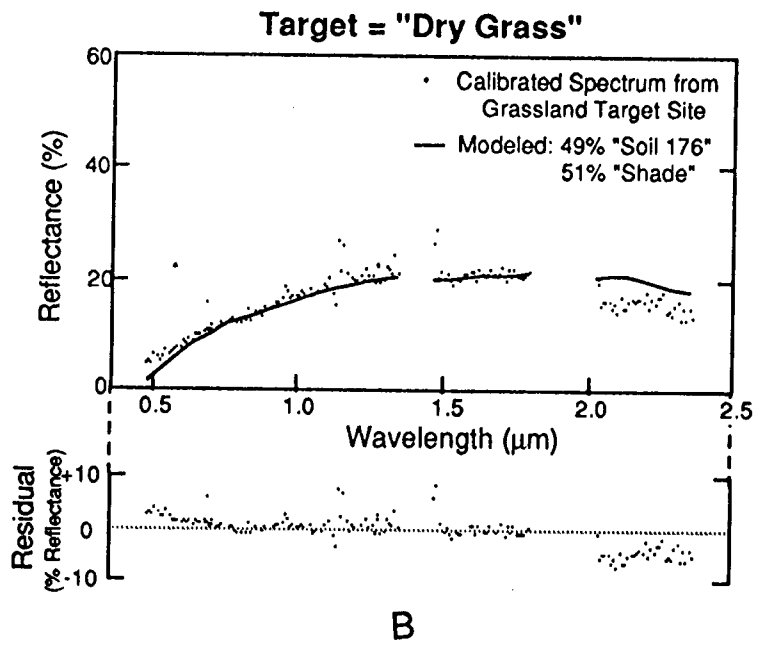

B

Figure 7. The bands in which the target is detectable using residual analysis depend upon which of the component spectra is the target. If the target is "soil 176", the largest band residuals occur at the lower wavelengths (A). However, if the target is "dry grass" the bands in which the target is most easily detected are the higher wavelengths (B).

Calibration of AVIRIS Digitized Data

Robert O. Green, Steven A. Larson, and H. Ian Novack
Jet Propulsion Laboratory
California Institute of Technology
Pasadena, California

Abstract. The Airborne Visible/Infrared Imaging Spectrometer (AVIRIS) is an Earth-observing imaging spectrometer that acquires data for scientific investigations of the surface and atmosphere. These data are distributed to investigators calibrated with respect to their spectral, radiometric, and geometric characteristics. The process of calibrating these data through application of the calibration data files and calibration algorithms is described in this paper.

1. Introduction

AVIRIS measures the total upwelling radiance from 400 to 2450 nm in the electromagnetic spectrum through 224 spectral channels. The spectral sampling interval and response function for each channel is nominally 10 nm. Spatial images of 11 by ≤100 km are acquired with approximately 20- by 20-m spatial resolution.

The calibration of AVIRIS requires four distinct processes which were originally described in part in 1987 (Vane et al., 1987). First, calibration measurements are acquired in the laboratory of the spectral, radiometric, and geometric characteristics of the sensor (Chrien et al., 1990). Second, these measurements are reduced to a set of calibration data files, which are compatible with AVIRIS data characteristics. Third, the laboratory calibration is validated through an in-flight calibration experiment. Fourth, science data are routinely calibrated with the calibration data files and distributed to requesting investigators. This paper describes and presents an example of this fourth process.

Data recorded on July 23, 1990 over the in-flight calibration site at Rogers Dry Lake, California, are used to demonstrate the process of the calibration of AVIRIS digitized data. An AVIRIS image of the calibration site is given in Figure 1 [see slide 9].

2. Radiometric Calibration

For every spatial resolution element, AVIRIS records the upwelling radiance as digitized numbers (DNs) ranging from 0 to 1024 for each of the 224 spectral channels. A digitized spectrum from the calibration site at Rogers Dry Lake is given in Figure 2. The shape of this spectrum is predominantly a consequence of the upwelling radiance, the instrument radiometric response, and the additive instrument dark current. Dark-current spectra are measured by AVIRIS at the end of each image scan-line. Individual dark-current spectra contain the full minimum to maximum noise properties of AVIRIS; therefore, the mean of 100 lines of dark-current spectra is formed to provide a low-noise spectrum. A spectrum of the mean dark current for the calibration site is given in Figure 3. This mean dark current for each channel and line, $DC_{c,l}$, is subtracted from the measured signal for each channel, line, and sample, $DN_{c,l,s}$, to generate a spectrum with values proportional to the upwelling radiance,

$DN'_{c,l,s}$, as shown in Equation 1. The Rogers Dry Lake calibration site spectrum from which the dark current has been subtracted is given in Figure 4.

$$DN'_{c,l,s} = DN_{c,l,s} - \overline{DC_{c,l}} \quad (1)$$

To transform this spectrum to units of radiance, the radiometric calibration coefficients determined during the laboratory calibration are multiplied through the data. Figure 5 shows these coefficients for the data acquired during the AVIRIS operational period beginning July 23, 1990. These coefficients are in units of radiance per DN. A radiometric calibration coefficient is required for each of the 224 AVIRIS spectral channels. As given in Equation 2, the nadir upwelling radiance, $L_{c,l,s}$, is calculated through multiplication of the dark-current subtracted DN, $DN'_{c,l,s}$ by the radiometric calibration coefficients, RCC_c. The radiometrically corrected spectrum for the calibration site is given in Figure 6.

$$L_{c,l,s} = RCC_c \cdot DN'_{c,l,s} \quad (2)$$

For AVIRIS spectra measured off-nadir, a small cross-track vignetting correction is required. These factors compensate for the greater optical path through the hatch and foreoptics windows at the edge of the ±15-deg field of view. Vignetting correction factors are generated as part of the laboratory calibration prior to each operational period. A correction factor exists for each of the 614 cross-track elements and each spectral channel. Equation 3 describes the vignetting correction, where the radiance for each channel, image line, and cross-track sample, $L_{c,l,s}$, is multiplied by the vignetting correction factor, $VCF_{c,s}$, to generate the vignetting corrected radiance, $L'_{c,l,s}$. The vignetting correction factors valid for the calibration experiment data for spectral channel 130 are shown in Figure 7.

$$L'_{c,l,s} = VCF_{c,s} \cdot L_{c,l,s} \quad (3)$$

In addition to radiometric calibration, an estimate of radiometric precision is provided as the noise-equivalent-delta-radiance (NEdL) with all distributed AVIRIS data. This estimate is derived from the dark current measured at the end of each image line. These dark-current data provide the sensor response to a homogeneous dark target and the variations in these data are used to estimate the instrument noise. In Figure 8, the root-mean-squared-deviation (RMSD) for the dark current measured in the laboratory is compared to the RMSD for the signal measured over the integrating sphere, a homogeneous bright target. In Figure 9, the in-flight RMSD of the dark current and the RMSD of a 2 by 10 element area over the Rogers Dry Lake calibration site are given. For both the laboratory and in-flight conditions, the end-of-line dark-current measurements are shown to accurately assess AVIRIS noise properties. For every AVIRIS data scene, the in-flight NEdL is determined as the dark-current derived noise multiplied by the radiometric calibration coefficients. The NEdL spectrum for the Rogers Dry Lake data is shown in Figure 10. This NEdL reports the precision of the calibrated radiance spectra for every spatial element in the AVIRIS data set.

3. Spectral Calibration

The spectral position and spectral response function for each of the 224 AVIRIS channels are determined in the laboratory prior to each period of data acquisition. A plot of the wavelength position versus the channel number for data acquisition

beginning on July 23, 1990 is given in Figure 11. The channel spectral response functions as the full width at half maximum (FWHM) of corresponding Gaussian functions are given in Figure 12. The four distinct regions in each of these figures correspond to the four spectrometers used by AVIRIS to cover the range from 400 to 2450 nm. The spectral calibration objective is to determine these spectral characteristics to better than ±2 nm. Spectral calibration data are essential for physically based analysis of the AVIRIS data and for comparison of AVIRIS spectra acquired in one period to those acquired in another as well as for comparison of AVIRIS data with spectra measured by other instruments. Spectral calibration data files are distributed with all AVIRIS data.

4. Geometric Calibration

AVIRIS is a scanning imaging spectrometer which acquires cross-track spatial elements through movement of a scan mirror and along-track elements through the forward motion of the aircraft platform. The number of cross-track elements in a scan is fixed at 614 and along-track elements vary from 500 to 5000 depending on the length of the flight line. In the laboratory prior to each operational period, the spatial sampling and spatial response functions of AVIRIS are measured. For the period beginning March 7, 1991, the sampling was determined as 17 m by 17 m at nadir with the aircraft moving at 734 km/h. The spatial response FWHM was determined as 20-m along track by 21-m cross track.

A geometric correction is applied to AVIRIS data to compensate for the readout-delay of the spectrometer detector arrays. The delay in time from reading the first detector to reading the sixty-fourth detector in the spectrometer arrays is slightly less than 17 m of cross-track displacement on the surface. A linear interpolation is used to resample the cross-track elements for each channel. Equation 4 gives the resulting radiance, $L''_{s,d}$, for the linear interpolation between the radiance in each cross-track sample, $L'_{s,d}$, and the adjacent sample, $L'_{s+1,d}$, as a function of detector array element. There are 32 detector elements in spectrometer A and 64 elements in spectrometers B, C, and D. This resampling brings the channels in the four spectrometer arrays into nominal spatial coregistration.

$$L''_{s,d} = [(d-1)/66] \cdot L'_{s+1,d} + [(67-d)/66] \cdot L'_{s,d} \qquad (4)$$

5. Additional Calibration Information

Data from the aircraft navigation system, engineering parameters from the AVIRIS sensor, and the signal from an AVIRIS reference light source are acquired in conjunction with all data. Table 1 gives the navigation parameters recorded with each scan-line of data. Engineering parameters are listed in Table 2. The reference source is viewed by AVIRIS through four filter positions before and after each flight line. These filter positions provide a high-intensity, low-intensity, spectrally distinct and dark signal. In each filter position, 614 spectra are acquired with the 224 AVIRIS channels. These navigation, engineering, and reference data are included with all distributed AVIRIS data.

6. Calibration Validation

The in-flight spectral and radiometric calibration of AVIRIS is validated through implementation of calibration science experiments (Green et al., 1988; Conel et al., 1988; and Green et al., 1990). These experiments predict the upwelling radiance expected at AVIRIS through in situ field measurements of the surface and atmosphere which are used to constrain a radiative transfer code. For the calibration experiments in 1990, the LOWTRAN 7 (Kneizys et al., 1989) radiative transfer code was used. In future, MODTRAN (Berk et al., 1989) is planned to be used. The AVIRIS laboratory calibrated radiance over the calibration site is evaluated with respect to the calibration experiment predicted radiance. This comparison provides a rigorous validation because the AVIRIS measured and the radiative transfer predicted radiance are derived from two completely independent pathways. The AVIRIS radiance is calibrated based upon a National Institute of Standard and Technology (NIST) irradiance lamp and the predicted radiance is based upon an exoatmospheric solar irradiance spectrum. Results from the in-flight calibration experiment completed on July 23, 1990 are given in Figure 12. Excluding the regions of strong atmospheric water absorption the absolute radiometric agreement between the measured and predicted spectrum is better than 8%. A continuing AVIRIS objective is to further improve and validate the absolute radiometric calibration.

7. Conclusion

An essential process in the calibration of AVIRIS is the routine calibration of the digitized data with respect to their radiometric, spectral, and geometric characteristics. Radiometric calibration results in a transformation of the measured signal to units of total upwelling radiance. Spectral calibration of the data is achieved by providing the laboratory-determined channel positions and response functions for the 224 AVIRIS channels. Geometric calibration is fulfilled through detector readout delay corrections and distribution of the laboratory-determined spatial sampling and response function. Navigation, engineering, and reference light source data are provided to allow further characterization of the AVIRIS data. Because the operational environment (ambient conditions at 20-km altitude) differs substantially from the laboratory calibration environment, the in-flight characteristics are validated periodically through in-flight calibration experiments. All data used for the calibration of AVIRIS data are included with the distributed data to facilitate quantitative analysis by the science investigator. This calibration process is required for quantitative analysis of AVIRIS data as well as for comparison of AVIRIS data acquired from different regions, from different times and with data measured by different instruments.

Acknowledgment

This research was carried out at the Jet Propulsion Laboratory, California Institute of Technology, under contract with the National Aeronautics and Space Administration.

References

- Berk, A., L. S. Bernstein, and D. C. Roberson, *MODTRAN: A Moderate Resolution Model for LOWTRAN 7*, U.S. Air Force Geophysical Laboratory, Hanscom Air Force Base, Massachusetts, 1989.

- Chrien, T. G., R. O. Green, and M. Eastwood, "Laboratory Spectral and Radiometric Calibration of the Airborne Visible/Infrared Imaging Spectrometer (AVIRIS)," *Imaging Spectroscopy of the Terrestrial Environment*, SPIE Vol. 1298, 1990.

- Conel, J. E., R. O. Green, R. E. Alley, C. J. Bruegge, V. Carrere, J. S. Margolis, G. Vane, T. G. Chrien, P. N. Slater, S. F. Biggar, P. M. Teillet, R. D. Jackson, and M. S. Moran, "In-Flight Radiometric Calibration of the Airborne Visible/Infrared Imaging Spectrometer (AVIRIS)," *Recent Advances in Sensors, Radiometry and Data Processing for Remote Sensing*, SPIE Vol. 924, 1988.

- Green, R. O., G. Vane, and J. E. Conel, "Determination of Aspects of the In-Flight Spectral, Radiometric, Spatial and Signal-to-Noise Performance of the Airborne Visible/Infrared Imaging Spectrometer Over Mountain Pass, Ca.,"*Proceedings of the Airborne Visible/Infrared Imaging Spectrometer (AVIRIS) Performance Evaluation Workshop*, JPL Publication 88-38, 162-184, 1988.

- Green, R. O., J. E. Conel, J. S. Margolis, V. Carrere, C. J. Bruegge, M. Rast, and G. Hoover, "In-Flight Validation and Calibration of the Spectral and Radiometric Characteristics of the Airborne Visible/Infrared Imaging Spectrometer (AVIRIS)," *Imaging Spectroscopy of the Terrestrial Environment*, SPIE Vol. 1298, 1990.

- Kneizys, F. X., E. P. Shettle, G. P. Anderson, L. W. Abrew, J. H. Chetwynd, J. E. A. Shelby, and W. O. Gallery, *Atmospheric Transmittance/Radiance: Computer Code LOWTRAN 7*, U.S. Air Force Geophysical Laboratory, Hanscom Air Force Base, Massachusetts, 1989.

- Vane, G., T. G. Chrien, E. A. Miller, and J. H. Reimer, "Spectral and Radiometric Calibration of the Airborne Visible/Infrared Imaging Spectrometer (AVIRIS) Flight and Ground Data Processing System," *Imaging Spectroscopy II: 20-21 August 1987, San Diego, California*, SPIE Vol. 834, 1987.

Tables and Figures

Table 1. AVIRIS aircraft navigation data

Record No.	Parameter	Record No.	Parameter
1	Flight number	11	North-South velocity
2	Flight line	12	East-West velocity
3	Year	13	True heading
4	Month	14	Ground speed
5	Day	15	Vertical velocity
6	Hour	16	Altitude
7	Minute	17	True air speed
8	Second	18	Pitch
9	Latitude	19	Roll
10	Longitude		

Table 2. AVIRIS sensor data

Record No.	Parameter	Record No.	Parameter
1	A detector array temperature	14	Analog voltage (+20)
2	B detector array temperature	15	Analog voltage (-20)
3	C detector array temperature	16	Digital voltage (+5)
4	D detector array temperature	17	Aircraft power (+28)
5	A spectrometer temperature	19	Analog voltage (+8)
6	B spectrometer temperature	20	Reference lamp current
7	C spectrometer temperature	21	Hardware status codes
8	D spectrometer temperature	22	Focus position
9	Foreoptics temperature	23-33	Scan mirror encoder marks
10	Scan drive temperature	34-44	Sensor roll gyro
11	Analog electronics temp.	45-53	Sensor pitch gyro
12	Digital electronics temperature	97-112	Firmware status
13	Power supplies temperature		

Figure 1. AVIRIS image over Rogers Dry Lake, California, acquired on July 23, 1990. The in-flight calibration site is shown as site A in the image [see slide 9].

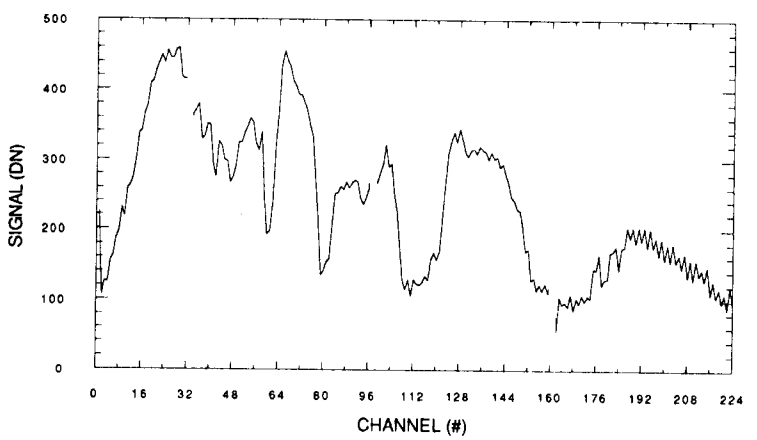

Figure 2. Spectrum of the signal measured by AVIRIS over the Rogers Dry Lake, California, calibration site on July 23, 1990.

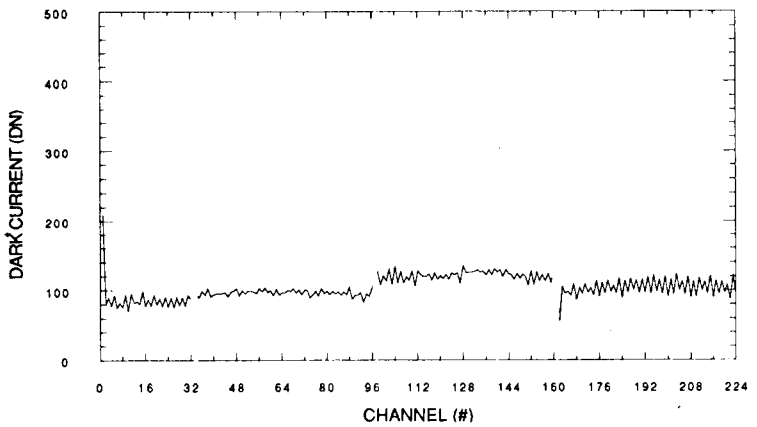

Figure 3. Mean dark-current spectrum for the calibration site. Dark-current data are measured at the end of each cross-track line of data acquired.

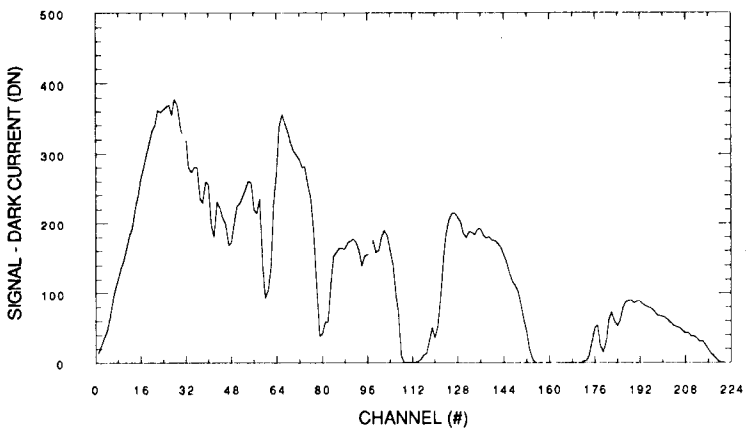

Figure 4. An AVIRIS spectrum with dark current subtracted of the Rogers Dry Lake, California, calibration site.

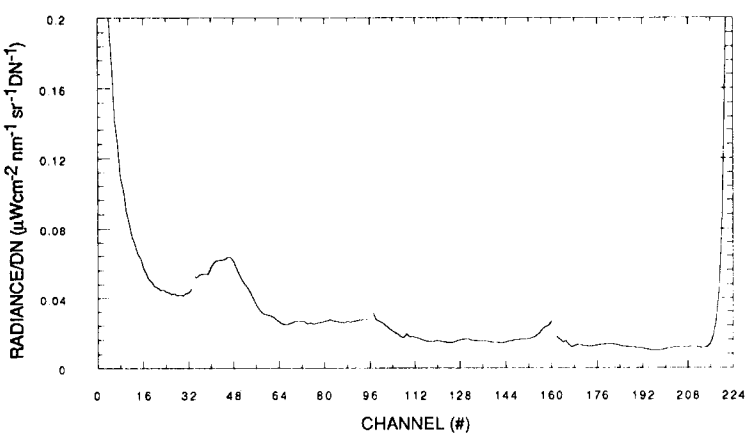

Figure 5. The radiometric calibration coefficients determined in the laboratory.

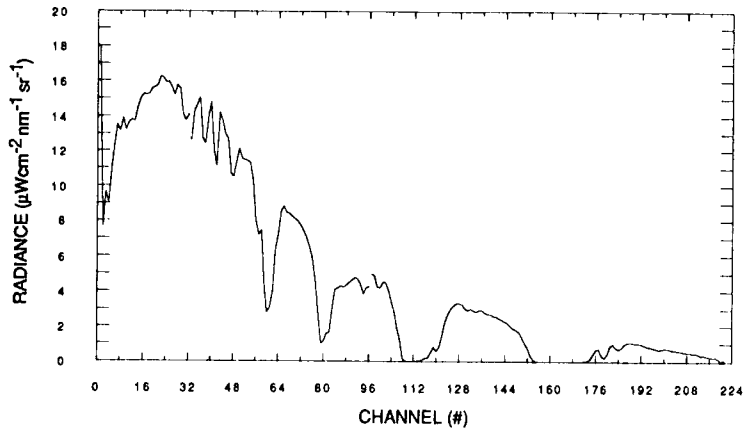

Figure 6. Radiometrically calibrated AVIRIS spectrum.

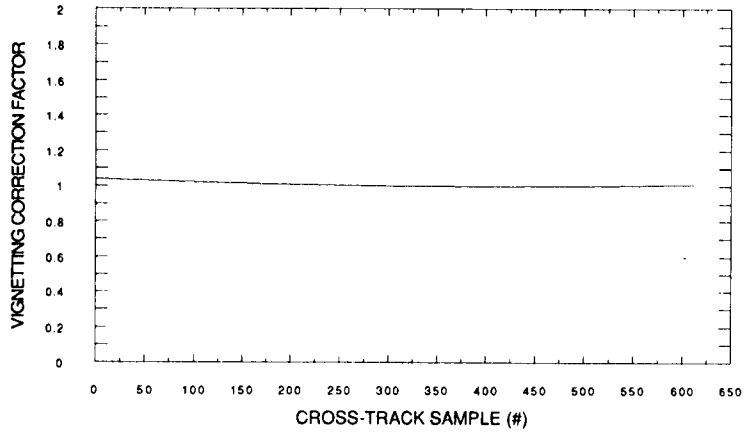

Figure 7. Cross-track vignetting correction factors for channel 130. Vignetting correction factors are determined in the laboratory for each spectral channel.

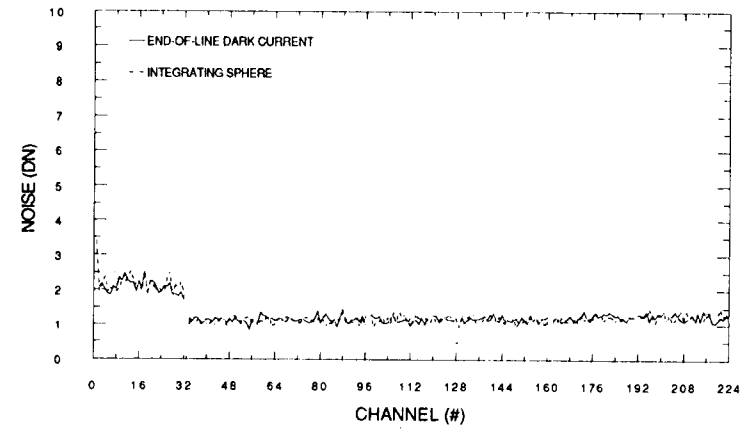

Figure 8. AVIRIS noise spectrum determined both from the laboratory integrating sphere signal and the end-of-line dark current.

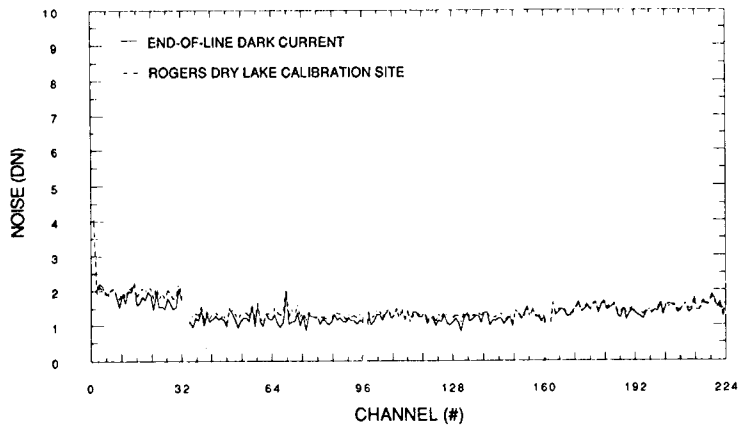

Figure 9. In-flight noise determined from the homogeneous Rogers Dry Lake, California, calibration surface and end-of-line dark current.

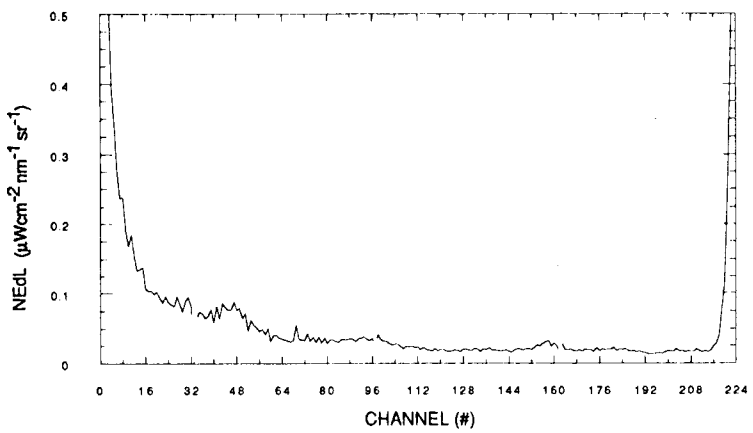

Figure 10. Radiometric precision is determined as the DN noise calibrated to units of radiance. This noise-equivalent-delta-radiance (NEdL) represents the precision at 1 root-mean-squared-deviation (RMSD) for AVIRIS radiance spectra.

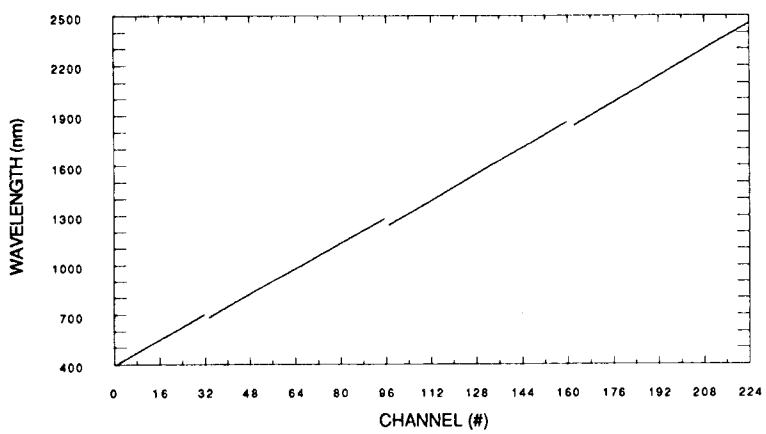

Figure 11. The spectral channel position of the 224 AVIRIS channels as measured in the laboratory.

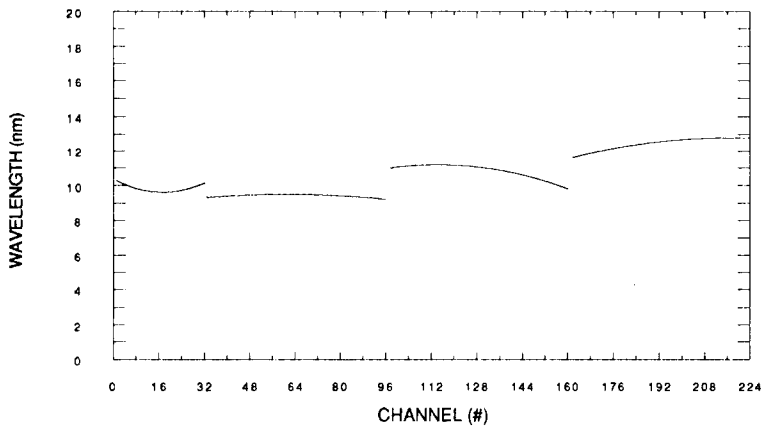

Figure 12. The spectral response function of the 224 AVIRIS channels. Spectral response is reported as the full width and half maximum of the corresponding Gaussian function.

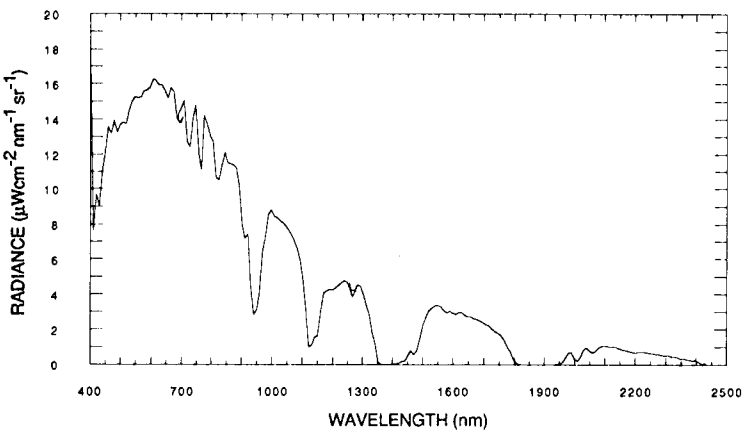

Figure 13. Spectrally and radiometrically calibrated AVIRIS spectrum of the calibration site at Rogers Dry Lake, California.

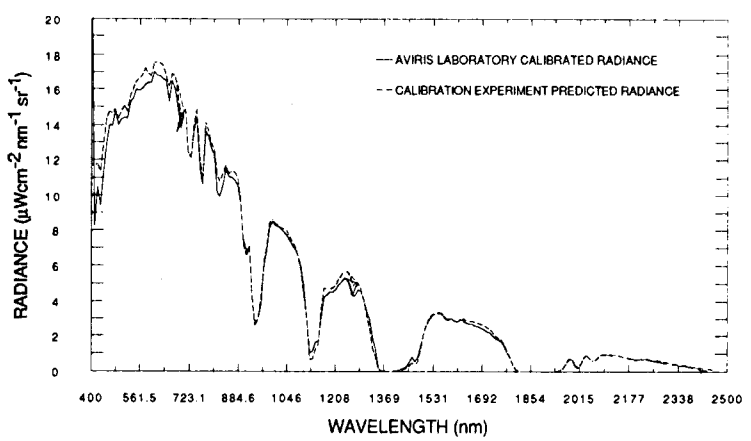

Figure 14. Comparison of the AVIRIS-measured spectrum from the calibration site and a radiative transfer-code predicted spectrum.

Browse Level Compression of AVIRIS Data Using Vector Quantization on a Massively Parallel Machine

M. Manohar
Universities Space Research Association
NASA Goddard Space Flight Center
Greenbelt, Maryland

James C. Tilton
NASA Goddard Space Flight Center
Greenbelt, Maryland

Abstract. This paper describes and evaluates two Vector Quantization (VQ) approaches for compressing high spectral resolution AVIRIS (Airborne Visible/Infrared Imaging Spectrometer) image data by a factor of over 22. This highly compressed data is useful for "browsing" through several data sets in order to select the best data sets for a particular application, or for preliminary analysis. The two VQ approaches differ in the codebook generation methods, which are Linde-Buzo-Gray (LBG) in one case and a Self Organizing Feature Map (SOFM) based on neural models in the other. Both spectral and spatial correlations have been exploited to improve on coding efficiency. The codebook generation and coding portions of these VQ algorithms have been implemented on a massively parallel SIMD machine, the MasPar MP-1. However, the reconstruction of the compressed data is a simple table lookup which is efficiently performed on a sequential machine. The results are evaluated for accuracy by comparing the results from detecting minerals with the SPAM (Spectral Analysis Manager) software package in the original and reconstructed data sets.

I. Introduction

Each scene from the Airborne Visible/Infrared Imaging Spectrometer (AVIRIS) consists of over 140 megabytes of data. This large amount of data leads to significant difficulties in data archival, access and dissemination of AVIRIS data. One area that data compression can be of immediate assistance is in the access and dissemination of browse quality versions of AVIRIS data for the selection and preliminary analysis of data from the AVIRIS data archive.

AVIRIS data contains a great deal of redundancy that data compression can exploit to reduce data values by as much as 20 to 50 times. When compressed with appropriate techniques, this highly compressed AVIRIS browse data appears visually very similar to the original data, and still retains much of its scientific information content, making possible a preliminary analysis of the data. Of course, the final analysis will require the original data, or data reconstructed from a lossless compression of the data.

In earlier experiments [1], browse data with a compression factor of 18 was produced from AVHRR (Advanced Very High Resolution Radiometer). This data was processed to obtain Sea Surface Temperature (SST) maps. (SST maps are a standard product generated from AVHRR data and ancillary data. These maps are regularly used by scientists who study the Earth's oceans and climate.) For the best compression method, the mean error in the SST maps was only 0.5°C.

Unlike AVHRR data with 5 spectral bands, the AVIRIS data has as many as 224 spectral bands. In performing VQ on this data, it must be judiciously grouped into vectors so both spatial and spectral correlations are utilized. A small data cube of 128 rows by 256 columns of 32 spectral bands was used in these experiments. Training and coding were made computationally efficient by (i) dividing the spectrum into four parts of eight bands each, and (ii) parallel implementation on MasPar MP-1 massively parallel computer.

This paper describes and evaluates two Vector Quantization (VQ) compression approaches for producing browse versions of AVIRIS data. In the first VQ approach the optimal codebook is generated by well known Linde-Buzo-Gray (LBG) algorithm that is based on k-means clustering algorithm. The second employs a more innovative technique called Self Organizing Feature Maps (SOFM) based on the neural models due to Kohonen. The compression

approaches are evaluated by compression ratio (or data rate), computational requirements, and the image and analysis errors introduced due to lossy compression. The SPAM (Spectral Analysis Manager) package was used to produce mineral maps from the original and reconstructed data sets. These mineral maps were then analyzed for error.

II. Compression Based on Vector Quantization

Vector Quantization (VQ) is motivated by rate-distortion theory [2] which states that better performance can be achieved by coding vectors rather than scalars. To effectively exploit spatial and spectral correlations among image pixels in VQ, the image is partitioned into two dimensional cells of fixed size in all spectral bands. The pixels in each $k = w_r x w_c$ of a rectangular cell of each spectral band are scanned in raster scan order and are taken to be a one-dimensional vector of size k in band sequential (BSQ) order. As the image is scanned, each vector is compared to standard vectors in a codebook. The address of the standard vector in the codebook that most closely matches the input vector is transmitted or stored as the code for that cell. Compression is obtained because the address bits are much fewer than the number of bits required for representing each vector, and because the number of elements transmitted or stored is less than the original number of pixels by a factor equal to the vector size. Thus, the smaller the codebook size (m), and the larger the vector size (k), the more efficient is the compression (fewer bits are required per pixel).

This relationship of codebook size and vector size to compression efficiency is illustrated by the expression for the number of bits required per pixel, or compression rate (r).

$$r = 1/k * \log_2 m \text{ bits/pixel} \tag{1}$$

A particular rate can be accomplished by several possible pairs of m and k. Selecting small values of the codebook size, m, is not very effective because r changes as logarithm of m. Increasing the vector size is more effective since the rate, r, increases linearly with 1/k. Thus, the change in rate, r, is more rapid with k than m, suggesting that large vector dimensions should be used.

In designing a VQ compressor, one must also consider the distortion introduced by the VQ process. The most commonly used distortion measure is the mean squared error between input image and reconstructed image. Although this measure does not directly show how close visually the reconstructed image is to the original image, it is used because it is mathematically tractable, and does give some sense of difference between the two images.

Here we use the average mean squared error as a distortion measure for quantifying the performance of the encoder. If Xi, and χ_i are the input vector and reproduced vector respectively, the average distortion, d, is given by

$$d = 1/n \sum (X_i - \chi_i)^2 \tag{2}$$

where n is the number of vectors from the input image. For given rate, r (bits/pixel), and given distortion measure, d, the vector dimension, k (pixels), and the codebook size, m, can be optimally determined [3].

Another common distortion measure frequently used is the signal to noise ratio (or signal to quantization noise ratio [4]), defined as:

$$SNR = 10 \log_{10} E(\|x\|^2) / d \tag{3}$$

where $E(\|x\|^2)$ is the average signal energy, and d is as given in Eq. 2.

As noted earlier, large vector dimensions should be used to achieve low compression rates. Large vector dimensions, however, are difficult to handle even in parallel machines. For a given

codebook size, the computational requirements are directly proportional to the vector dimension. Since larger vector dimensions are also recommended to exploit the image spatial correlations effectively, trade-offs must be made between computational requirements and compression performance (rate and distortion).

The greatest drawback of VQ is that it is computationally very demanding. The bulk of the time is consumed exhaustively searching the codebook to find the closest match to a given input vector from among the code words in the candidate set. Different methods have been developed to speed the search by structuring the codebook, at the cost of reducing the compression factor. Parallelization is an obvious solution to this search problem in both codebook generation as well as in data encoding.

The VQ can be conveniently described by assuming an array of cells configured in two-dimensional lattice. This array holds the representative samples to the input set, also called the codebook. The most important function of the VQ is to learn from the input samples the most optimal codebook containing fewer number of samples than the input set. Let the input event space be represented by

$$\xi = \{X_1, X_2, .., X_i, ..., X_n\} \text{ where } X_i = (x_{i1}, x_{i2}, ..., x_{ik})^t$$

and the output space or codebook by

$$\psi = \{Y_1, Y_2, ..., Y_j, ..., Y_m\} \text{ where } Y_j = (y_{j1}, y_{j2}, ..., y_{jk})^t$$

In all practical situations the codebook size, m << n (the number of vectors extracted from the input image). The compression ratio is given by $(n*b)/\log_2 m$, where b is number of bits per vector.

In the training process ψ is learned from ξ such that the many to one mapping of all the vectors $X_i \in \xi$ onto $Y_j \in \psi$ results in minimum error. The learning starts from some initial state, $Y_j(0)$. After X_i is compared with all samples in ψ, the most closely matching vector, Y_c, is called the *winner*. The *winner* Y_c is updated such that X_i and Y_c match even more closely in subsequent iterations. This is competitive learning. Using the Euclidean distance measure for matching, the identification of the winner can be mathematically represented as:

$$\| X_i - Y_c \| = \min_{\forall j \in m} \| X_i - Y_j \| \tag{4}$$

Y_c is the closest match to the input sample X_i from mean squared error point of view.

Next, Y_c is updated according to the following rule in order to make the match even closer between successive iterations, t and t+1:

$$\begin{aligned} Y_j(t+1) &= Y_j(t) + \alpha(t)(X_i - Y_j(t)) && \text{for } j = c \\ Y_j(t+1) &= Y_j(t) && \text{for } j \neq c \end{aligned} \tag{5}$$

where $\alpha(t)$ is a monotonically decreasing sequence of scalar values in t, making the error minimization converge locally. When the updating rule of Eq. 5 is applied, the error minimizes asymptotically. The input sample X_i is selected randomly from the event set ξ.

A. VQ using LBG algorithm

The first of the two approaches to VQ explored here uses the well known Linde-Buzo-Gray (LBG) algorithm, based on the k-means clustering algorithm, to train the codebook[4]. In this approach, the vectors extracted from the input multispectral images are clustered into a finite number of classes (equal to the size of the code book) in k-dimensional space, where k is the dimension of the vector.

In the LBG algorithm, the initial state, $Y_i \in \psi$ for all i $\in$ (1..m), is selected randomly from input sample set, ξ. Next, the competitive learning process is carried out by first accumulating the subsets of training samples from ξ that map onto each location of the codebook, ψ, based on Eq. 4. Then the updating operation is performed in a single step by using the mean of the samples that mapped onto each of the codebook locations. The accumulating and updating steps are then carried out iteratively until convergence [4].

The LBG algorithm maps input samples onto one of m different codebook vectors. The mapping is done regardless of the index value, i, of the codebook vector, so that the m cells act independently. Thus, the input vectors are mapped to the index i in haphazard order. The impact of this in pattern recognition accuracy is debatable, but it certainly slows the classification speed of incoming features, because of the exhaustive search required to determine the matching pattern in the index range. This haphazard mapping is also contrary to the way in which biological cells or neurons interact spatially to provide a topologically ordered map of input features. Kohonen's work on Self Organizing Feature Maps (SOFM) achieves this topological property of the neural systems by modifying the update rule in Eq. 5, as discussed in the following section.

B. VQ using SOFM algorithm

In the SOFM training process, the values $Y_i \in \psi$, are initialized with random values. The values $Y_i \in \psi$ are then treated as a two-dimensional neural lattice space ($m = m_r x m_c$), and updated not only at the location of the winner, Y_c, but also in a spatial neighborhood, N_c. The function, $\alpha(t)$ in Eq. 5 is replaced by $h_{cj}(t)\varepsilon(t)$, which not only decreases with time, but also becomes more peaked spatially with time. The function $h_{cj}(t)$ initially has a broad spatial spread, which becomes more localized at the winner location, Y_c, in each ensuing iteration. Thus, the cell values, which initially have random value, organize themselves to match the events of the input space, while retaining the distance relations of the higher dimensional input space in two-dimensional lattice locations of the cells [5-7].

III. Massively Parallel Implementation of VQ

VQ image compression consists of a training phase, coding phase, and decoding phase. In our case, the training phase consists of generating a codebook using either the LBG or SOFM algorithm. The coding phase consists primarily of searching through the codebook for the best match. The decoding phase consists of a straightforward table lookup from the codebook, producing a reconstructed image.

The training phase is very computationally very intensive. For every sample presented, the entire codebook must be searched to decide the winner. Then the codebook must be updated in the winner's location and in the neighborhood of winner. With a naive codebook structure, the algorithm makes an exhaustive search of the codebook as many times as the network is presented with training samples.

On sequential machines, search times may be improved by organizing the entries in efficient tree structures, such as pruned tree K-D tree structures. These tree structures reduce the search from O(m) to O(log m), provided the tree is nearly balanced, where m is codebook size. These speedups are obtained by effectively increasing codebook size, thus increasing storage requirements, and decreasing the compression factor. However, on parallel machines, it is straightforward to improve the search time without increasing the codebook size.

Being readily available in our facility, the MasPar model MP-1 was used as our implementation platform. The MasPar MP-1 is a fine grained SIMD machine with 8192 4-bit processors organized in a 128 row by 64 column array. The codebook size was set to be less than or equal to 128x64, so each entry of codebook maps on single processor, minimizing the data movement among the processors. VQ compression using LBG and SOFM was

implemented on the MasPar MP-1 using a C-like language called MPL (MasPar Language). In MPL, "plural" variables are arrays equal in size to the processor array, which have a value in each processor's local memory.

A. Training

1. Initializing the Codebook. The first steps in the training process are to select the codebook and vector sizes, and to initialize the codebook. The codebook size, m, and vector size, k, are normally selected based on the compression factor and distortion specifications for a particular application. However, as we noted earlier, the change in compression rate, r, is more rapid with k than m. Therefore, larger-sized codebooks provide improvement in signal to noise ratio without appreciably affecting compression ratio (doubling the codebook size reduces the compressor rate by only one bit/pixel). Further, in the MasPar implementation, the computational requirement, T, is unaffected by codebook size as long as it is less than the PE array size. However, when the codebook size is more than PE array size, the computational requirements go up as follows:

$$T = T_0 \lceil m/nproc \rceil \qquad \text{for } m > nproc$$

where nproc is number of PE's in the array (size of PE array), and m is the size of codebook. T_0 is computational requirement for m = nproc.

Considering the above, the best choice for codebook size in the MasPar implementation is an integer multiple of the number of processors in the MasPar, nproc. Further adjustments in compressor rate can be best achieved by varying the vector size, k.

For LBG, the codebook is initialized by randomly selected vectors from the input image. The SOFM training algorithm uses random number generator for codebook initialization. For this purpose, a plural floating point array of random numbers between 0 and 1.0 is generated on MasPar in few machine cycles using an MPL built-in function called p_random.

2. Computing the winner for each sample. After the codebook is initialized, the input image pixel values are normalized with respect to the maximum pixel value, and the image is decomposed into a set of vectors at randomly chosen locations in the image. Each of these vectors are broadcast in turn to all PE's in the array, and the Euclidean distance between the input vector and codebook is computed at all locations. The location where the value is minimum can be found by using the reduction operator which finds the minimum value of the array.

3. Updating. For the LBG algorithm, the winner locations accumulate all the vectors during the iteration. At the end of the iteration the contents of the winner is updated to be the centroid of all the vectors. For SOFM, however, the updating is performed for every incoming vector in the neighborhood, N_c, of the winner.

Each cycle of computing the winners and updating the codebook is called an epoch. the codebook is updated until there is no appreciable change in the codebook from one epoch to the next. For most practical problems, for error less than 1%, these algorithms converge in 10-15 epoches.

B. Coding

After the training phase, the codebook is frozen and used for coding images of the class whose subset was used for generating the codebook. The coding consists of exhaustive searching through the codebook for every sample to be coded. Since the codebook is loaded into

the PE array's local memory, the computational requirement for exhaustive search is proportional to the size of the vector. Further, it is independent of the size of the codebook as long as the codebook size is less than or equal to the size of the PE array. In sequential coding this search would be proportional to the product of codebook size and vector size. Thus, the parallel version could be faster than the sequential search by a factor as much as the size of the codebook. The coding procedure is as follows.

1. Extract a vector of size k from the input image (in raster scan order),
2. Broadcast this vector into the local memory of all PE's,
3. Compute a distance measure (such as Euclidean distance) between the vector and the codebook at each PE,
4. Find the minimum of the Euclidean distance, and
5. Store or transmit the address bits of the PE where minimum value of the Euclidean measure is obtained.
6. Repeat 1-5 for until the entire image is scanned.

The coding procedure is basically the same as computing the winner in one epoch of the training phase. The difference is in the order in which the vectors are extracted from the image. In the coding phase, the data can be extracted in any convenient order. However, in the training phase, the extraction order should be random to avoid introducing an order dependent bias into the codebook.

C. Decoding

Decoding is reconstructing the image from the address bits of each vector. This is a table lookup process in which the codebook vector for each address is substituted for the image data values. This process is sequential and can be carried out on sequential machines more efficiently than parallel machines.

IV. Evaluation Scheme

The data compression approaches are compared here in terms of distortion measures for a given compression ratio, and in terms of an analysis application. The distortion measures employed are Mean Square Error (Eq. 2) and SNR (Eq. 3). The compression ration (CR) is the ratio of number of input bits to the number of output bits.

AVIRIS data sets are high spectral resolution images which are used for many applications such as geological, vegetation, and atmospheric studies. The Spectral Analysis Manager (SPAM) software package has been developed at Jet Propulsion Laboratory to analyze this and other imaging spectrometry data. It enables the user to store the spectral characteristics of land features obtained by field experiments and detect the pixels having similar characteristics in the image.

A. Spectral signature matching

SPAM's high speed spectral matching algorithm, *find*, employs binary encoding of the spectral characteristics of pixels or minerals (in mineral analysis application) to matching them to stored patterns [8]. Given a prototype spectrum, SPAM binary encodes each pixel in an image and decides whether or not the pixel belongs to a stored prototype class by comparing their amplitude and slope Hamming distances to user specified thresholds.

B. Mixture Component Analysis

The spectrum of an image pixel represents the total energy reflected by the atmosphere and earth's surface within the gathering instruments field of view. Ignoring the atmospheric effects, the pixel energy can be considered to be a weighted combination of the energy reflected by several surface components and is expressed as follows:

$$S = \sum_{k} C_k D S_k + A \qquad (6)$$

where C_k is a nonnegative constant proportional to the fractional surface composition for k^{th} mineral, D is a diagonal matrix whose entries are the product of the solar illumination and atmospheric transmissivity for each of the k minerals, S_k is the spectrum of the k^{th} mineral, and A is a constant vector. Given the values of the S and S_k, C_k can be estimated by a constrained least squares technique.

V. EXPERIMENTAL RESULTS

The original data set used this study consists of a data cube of 128 rows by 256 columns by 32 spectral bands from the April 13, 1989 Rogers Dry Lake data set. The 32 spectral bands correspond to band 172 (wavelength = 1.9343) thru 203 (wavelength = 2.2416) in the AVIRIS data format. The first six bands of the image data set is shown in Fig. 1(a). The input data cube was divided into 4 full image size parts, but with only 8 contiguous spectral bands. Separate codebooks were generated for each of these four subdata cubes. To exploit both spatial and spectral correlations, a 32 element vector was used for Vector Quantization, made up of a 2 by 2 spatial component and an 8 band spectral component.

Codebooks were generated using both LBG and SOFM algorithms on the MasPar, and the original data set was coded and further compressed with lossless coding. The compression results are shown in the Table I.

The compressed and reconstructed results and the error images from these techniques are shown in Fig. 1 (a-e). LBG technique performed better than SOFM in terms of mean squared distortion. This is also evident in Fig.'s 1(c) and 1(e). The coding time was about 30 seconds for the data size of 128x256x32. This corresponds roughly to a 0.3 megabit/second rate. Efforts are under way to improve the coding speed to 1 megabit/second.

A. Spectral signature matching

The test samples taken from the image data have spectral characteristics similar to some minerals stored in the library of SPAM. These minerals are sphalerite, colemanite, and brucite. We are not claiming that these minerals are present in this data set. However, if these minerals are detected in the compressed data similarly to how they were detected in the original data, then we infer that the compressed data worked for this application as well as original data. The results of the spectral matching are given in the Table II.

The spatial locations where these minerals are detected roughly are same. Sphalarite locations in the three images are shown in Fig. 2 (a-c) with yellow spots. It is very interesting to see that in all three mineral detections SOFM performs better than LBG algorithm in this application implying that MSE is not the appropriate evaluation criterion for this application.

B. Mixture Component Analysis

In this experiment a spectral plot at location pixel, line (26,17) is broken up into fractions of above three mineral spectral characteristics. The results are given in the Table III. The results of this analysis from SPAM are shown in Fig. 3 (a-c). From this, one can see that both LBG and SOFM algorithms have same composition at the above pixel location and they each differ very little from the original data.

VI. Conclusions

We have shown that hyperspectral data from instruments like AVIRIS can be compressed for archival and distribution over the computer network. In this work we have used two algorithms of vector quantization and obtained compression ratio of over 20 with minimal effects on the analysis of the data. This has been shown by objective evaluation of data applying the compressed as well original data to mineral studies in geology.

References

1. Tilton, J. C., Han, D. and Manohar, M., "Compression Experiments with AVHRR data", Proc.of Data Compression Conference, April 8-11, 1991, pp. 411-420.
2. Shannon, C. E., "A Mathematical Theory of Communication," Bell Systems Technical Journal, Vol. 27, pp. 379-423, 1948.
3. Lookabaugh, T. M. and Gray, R. M., "High Resolution Quantization Theory and the Vector Quantizer Advantage," IEEE Transactions on Information Theory, Vol. 35, No. 5., 1989.
4. Gray, R. M., "Vector Quantization," IEEE ASSP Magazine, pp. 4-28, April 1984.
5. Kohonen, T., "Clustering Taxonomy, and Topological Maps of Patterns," Proceedings of the International Conference on Pattern Recognition, pp. 114-128, 1982.
6. Kohonen, T., "Self-Organized Formation of Topologically Correct Feature Maps," Biological Cybernetics, Vol. 43, pp. 59-69, 1982.
7. Kohonen, T., "The Self-Organizing Map," Proceedings of the IEEE, Vol. 78, No. 9, pp. 1464-1480, 1990.
8. Mazer, A. S. et al., "Image Processing Software for Imaging Spectrometry Data Analysis," Remote Sensing of Environment, Vol. 24, pp. 201-210, 1988.

Table I. Comparison of LBG and SOFM coding performance.

Method	CR	MSE	SNR (db)
LBG data	22.12	3.13	31.06
SOFM data	22.43	6.39	34.14

Table II. Comparison of reconstructed data from LBG and SOFM with original data in the detection of minerals.

Minerals	Error threshold	Original data	LBG data	SOFM data
Sphalerite.f	0	3636	3975	3666
Colemanite.m	1	3678	4013	3763
Brucite.c	1	106	70	112

Table III. The mineral composition of a spectral sample taken at column 26 and row 17.

Data	Sphalerite	Colemanite	Brucite
Original	0.1718	0.0000	0.9428
LBG	0.1788	0.0000	0.9450
SOFM	0.1714	0.0000	0.9443

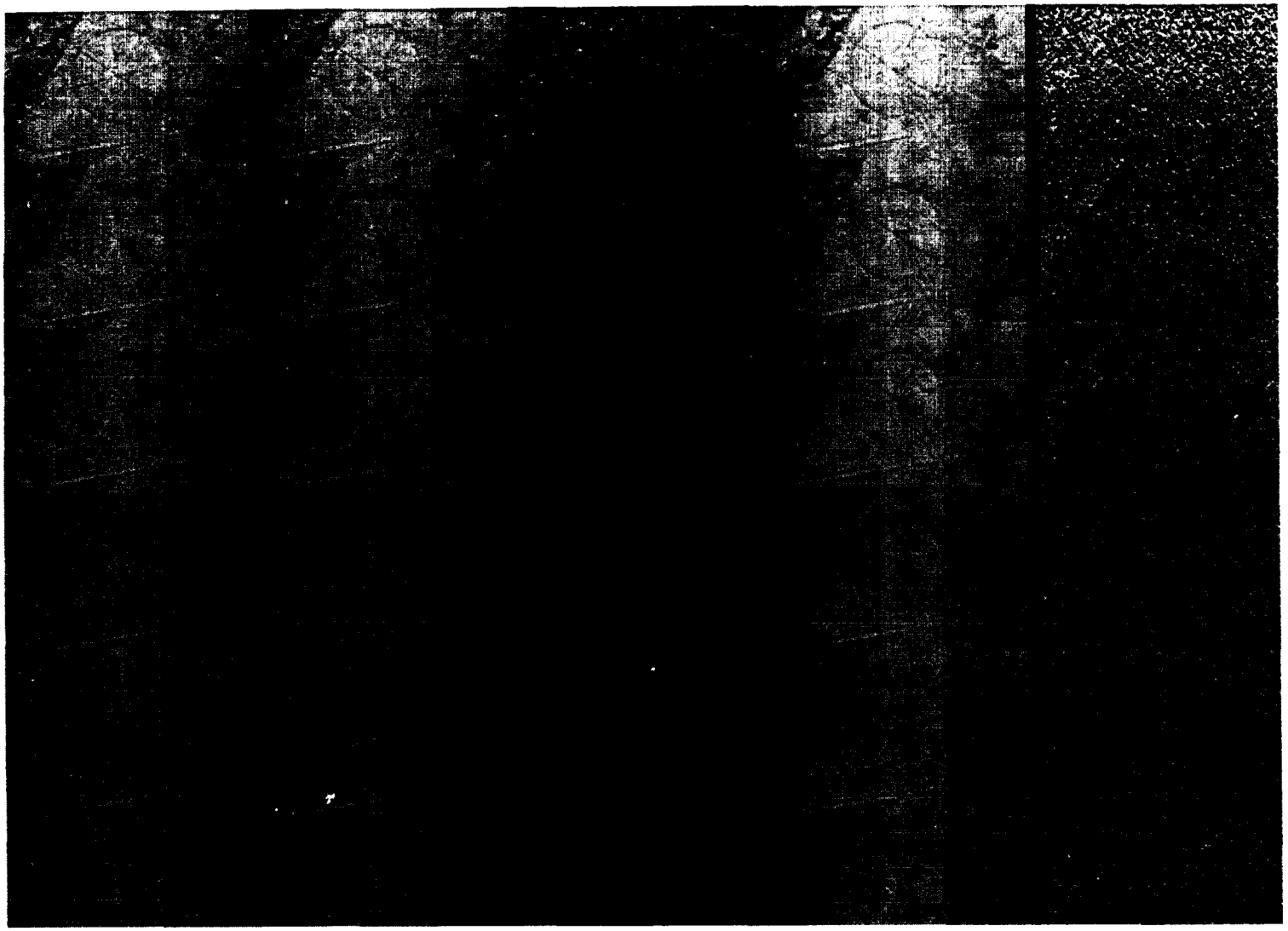

(a) (b) (c) (d) (e)

Figure 1. (a) Bands 172-177 of Rogers Dry Lake data, (b) reconstructed image from LBG coding, (c) error image between *a* and *b*, (d) reconstructed image from SOFM coding, and (e) error image between *a* and *d*.

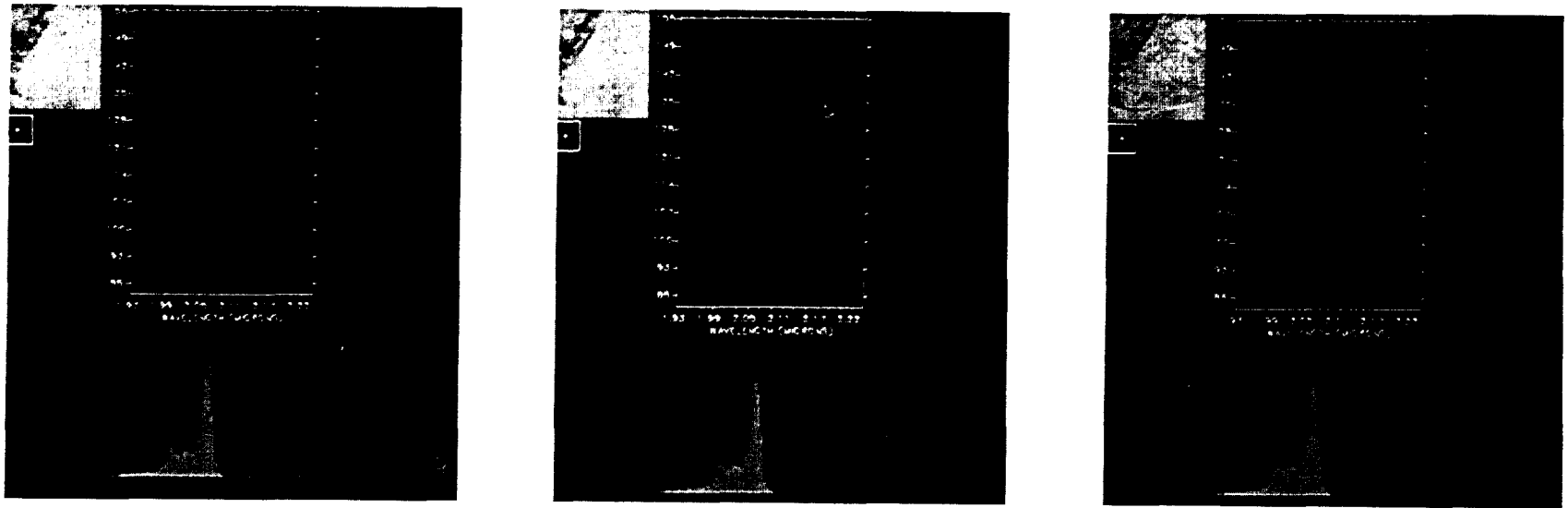

(a) (b) (c)

Figure 2. Location of samples (yellow) that matched sphalerite with 0 threshold. (a) Location of matched 3636 samples in original data, (b) location of 3976 matched samples in LBG reconstructed data, and (c) location of 3666 samples matched in SOFM reconstructed data.

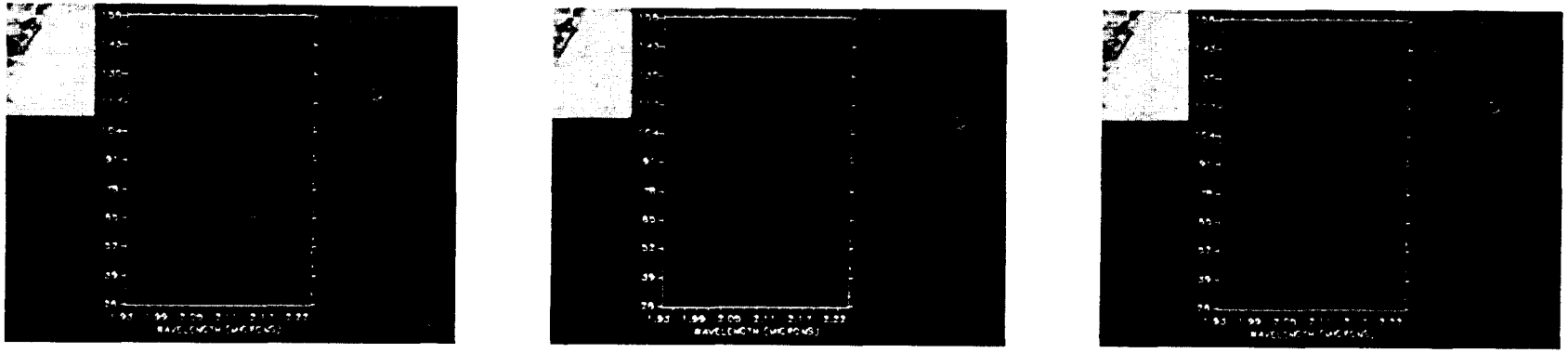

(a) (b) (c)

Figure 3. Mineral composition of sample at line 17 and column 26 using least square fitting. Mineral composition (a) for original data, (b) for LBG reconstructed data, and (c) for SOFM reconstructed data.

Display and Analysis of AVIRIS Data on Personal Computers

W.T. Jansen
WTJ Software Services
San Mateo, California

C. D. Elvidge and Zhikang Chen
Desert Research Institute
University of Nevada System
Reno, Nevada

ABSTRACT

A software system for the display and analysis of AVIRIS data has been developed for 386 and 486 computers equipped with super VGA graphics. The software has functions for simultaneous display of 1) three band color composite imagery, 2) 5X magnification of color imagery, 3) image cube cross section, and 4) full spectrum from any pixel or any group of pixels. Other functions permit the extraction of pixel digital number (DN) values, application of gains and offsets (e.g. conversion to ground reflectance), and spectral matching using spectral libraries. Additional functions are currently being implemented to meet the requirements of AVIRIS researchers.

I. INTRODUCTION

Images of the planet Earth acquired from space give both a regional and global perspective to scientists studying static features and dynamic processes on the surface of the globe. Since the early 1960s, various satellites have been transmitting images of the earth. The Landsat Thematic Mapper (TM), Multispectral Scanner (MSS), SPOT, and other satellites measure radiance values at several points on the electro-magnetic spectrum. Color images can be reconstructed from the data transmitted.

Though spatially limited, data from airborne imaging spectrometers show much more detail in measured spectra than current satellite data gathering instruments. There are more data channels (i.e., 64 for GERIS and 224 for AVIRIS), and each of the channels covers a narrower spectral range resulting in a more precise definition of absorption and emission features in the spectrum gathered. Patterns of absorption features assist the identification, rather than the mere discrimination, of earth surface materials.

In the past, when only a few channels of data were available, it was useful to display individual channels as individual colors (i.e., Red, Green, Blue) on a monitor allowing the observer to estimate the relationships between the data channels as defined by the hue, intensity, and saturation of the pixels in the resulting image. To use more of the measured data channels in the final display, each of the primary RGB colors could be a function of two or more channels (i.e., a ratio, product, difference, or some other function). Existing image processing methods emphasize the variation of colors in the resulting image to simplify the interpretation which by this time has become more of an art than a science. This method of data analysis is impractical for imaging spectrometry as the large number of channels overwhelms the ability of the RGB display to show visually discernible differences.

We experienced the need to go beyond the display of images generated by a few selected channels, and wanted to show and compare complete spectra from pixels in the same (or any other) image and the spectra from a large reference library. In our system, cross-comparisons between image and library spectra are made to identify pixel composition and mineral distribution. A variety of functions are available to allow detailed study of spatial and spectral relationships in the data in real time.

II. SYSTEM FUNCTIONALITY

The system can be broken down into six primary features (see Figure 1).

A. Data Import and Pre-processing

Data from the AVIRIS scanner and others is typically distributed on 9-track CCT magnetic tapes.We import this data by copying the files directly from the tape to a hard disk. A program merges the calibration information from the tape and data measured in the field, and then implements several coefficients to convert the scanned digital numbers to emissivity spectra.

B. Library Creation

The steps taken to develop the standard spectral library consisted of the following:

1. Collect and prepare mineral and vegetational standards
2. Measure standard spectral at high resolution
3. Create and manage high resolution spectral library
4. Resample library to scanner resolution.

Steps 1-3 have been executed by the staff at CSIRO, Sydney, Australia, resulting in a library containing over 200 mineral spectra. At present time, a vegetation library is being created. Other spectral libraries will be included as they become available.

A program has been developed to resample the high resolution library to the resolution of the most commonly used airborne and satellite scanners. The spectral positions of both incoming and outgoing channel windows can be tracked. Custom definition of a series of spectral windows allows the user to re-define the scanner characteristics as field instruments are re-calibrated.

C. Image Loading

Imagery prepared in section A above is loaded for display by this program.The user selects up to three bands from the spectral image file and a contrast stretch to create a composite RGB image for the display screen. Alternatively, by loading a co-registered, user created image and then linking it to the original spectral data file, the validity of user-defined pre-processing techniques can be examined. If images are larger than 512x512 pixels, either the entire image subsampled to that size, or a full resolution sub-image can be shown. Images are loaded into high resolution VGA.

D. Screen Display

Figure 2 shows the flow diagram for the core program in the software system. After an image has been loaded, the user interface screen layout appears as shown in Figure 3. (A sample screen is shown in Figure 4). The user interface screen has seven distinct components:

1. Image area

Displays the image to be interpreted and a freely roaming cursor under mouse control that quickly points to any pixel. Spectral classification maps are also displayed here. Toggles between maps and loaded RGB images.

2. Spectral graph

Typically shows up to three spectra: 1) the spectrum for the pixel identified by the image cursor, 2) the contents of a temporary spectral memory, and 3) an averaged spectrum from several user-defined pixels. Also shows up to three vertical RGB cursors. The RGB cursors initially indicate which channels were used to display the image. Subsequently, they can be moved to identify spectral features and to modify the contents of the zoom window, the scanline display, and the image area.

3. Zoom window

Magnifies a portion of the image centered on the image cursor so individual pixels can be identified easily. It can be switched to show an enlarged, more highly resolved version of the scanline display window or scatter diagrams for any channel pairs.

4. Scanline display window

Represents a spatial-spectral cross section of all the spectra along the image scanline on

which the image cursor is currently located. It can also be switched to show the relative intensity values along that same scanline for the channels currently identified by the RGB cursors and the computed relative spectral differences.

5. Information line

Displays information relating to: 1) image cursor position and size, 2) the RGB cursors' wavelength, intensity, and channel values, 3) the user selectable wavelength range of the spectral graph, and 4) relative spectral similarity values between the displayed spectra. When the library function is invoked, it also indicates the name of the mineral or other specimen whose spectrum is being shown.

6. Color ramp

The colors in the ramp are modified along with the rest of the screen as the various functions in the color modification menu are exercised (brightness, contrast, saturation, etc.).

7. Menu

Indicates the currently available functional choices from the multiple-level hierarchically structured menu system.

E. Analytical Tools

The tools listed below are those we felt were of most immediate need to the hyperspectral analyst. The open architecture of the software will accommodate expanded and new functionality.

1. Spectral comparisons

Spectra can be saved on screen for immediate comparisons with other spectra on the same image. Image spectra can also be compared with reference library or imported spectra.

2. Spectral averaging

Averaged spectra, from variably sized rectangles or randomly selected pixels, can be displayed and saved on the disk in ASCII format for subsequent processing or plotting. They can also be recalled so that direct, on-screen spectral comparisons can be made with data from other images.

3. Spectral channel profiles

Up to three channel profiles along a scanline can be displayed to show the relative channel values and hence the existence and location of spectral absorption features.

4. Spectral stacking

Stacking of a series of spectra from adjacent pixels allows tracking of spectral features as a function of position in the image. A spatial-spectral surface is shown emulating a 3-D terrain diagram. Through color coding and density slicing, spectral digital number (DN) contours are readily observed.

5. Image data cube cross section

Represents a spatial-spectral cross-section of all the spectra along the image scanline on which the image cursor is currently located. Density slicing brings out the spatial relationship of spectral features.

6. Color stretching

Performs visual display enhancement to bring out features in the data. This includes all standard color stretching techniques such as contrast and brightness control, histogram, and gaussian equalization, color inversion, and density slicing. These are all performed in real-time under mouse control, with the changes recorded both graphically and numerically. The effects of the changes are shown instantaneously throughout the screen, including the color ramp. Furthermore, the system is capable of real-time stretching in the IHS domain.

7. Pan and zoom

Rapid access to the spectral information at any pixel is provided by moving the image cursor. The zoom window is instantaneously updated as image or spectral cursors are moved. The spectral cursors are used to identify wavelength, digital number (DN), and channel number.

F. Import and Export of Spectral and Image Data

1. Spectral import and export

At almost all levels of the core program, it is possible by a single key stroke to import and export spectra. Spectra extracted from the image or library are saved in a "spectral register" that allows one to average and compare spectra. The resulting averaged spectrum may be saved to a disk file in ASCII format for plotting or further examination. The output file also contains the coordinates of the spectral source pixels. Similarly, data from such an ASCII file can be loaded into the spectral register for comparisons to spectra in the currently displayed image.

2. Image import and export

The user can make a hard copy of an image modified by color stretching or other image processing functions by saving it to a disk file. The entire screen or just the image portion can be saved. An example of a saved screen displaying an AVIRIS image is shown in Figure 4. Saved spectral classification images can be combined to create mineral distribution maps. The RGB cursors can be used to select the channels when importing an alternative image.

III. CONCLUSION

The emphasis of this system is to analyze spectra and to extend such analysis to the spatial domain. Displaying both images and complete spectra simultaneously, the system is optimized for use with remotely sensed data having large numbers of spectral bands. Some image processing functions have been omitted as they are readily available from other sources. By creating the ability to load the results of external image processing in conjunction with spectral image data cubes, we provide the best of both worlds. The user can experiment with various surface characterization techniques and check the results against the original spectral information.

We have created a set of PC-based tools that present and interpret spectral data from satellites and airborne imaging spectrometers. As a diagnostic tool for identifying the biological and mineralogical composition of the earth's surface, the system addresses the special needs of scientists using data from a variety of imaging spectrometers. The system helps relate variations in image pixel spectra to physically meaningful, spectral reflectance knowledge bases.

REFERENCES

Fred Kruse, et al., Photogrammetric Engineering & Remote Sensing, January, 1990, pp. 83-92.
Jon Huntington and A. A. Green, Bicentennial Gold, Melbourne, May, 1988, pp. 246-258.

ACKNOWLEDGEMENTS

We would like to thank the following individuals for their encouragement, support, and valued assistance with the development of the system: Russ Cowart, Jon Huntington, and Fred Kruse.

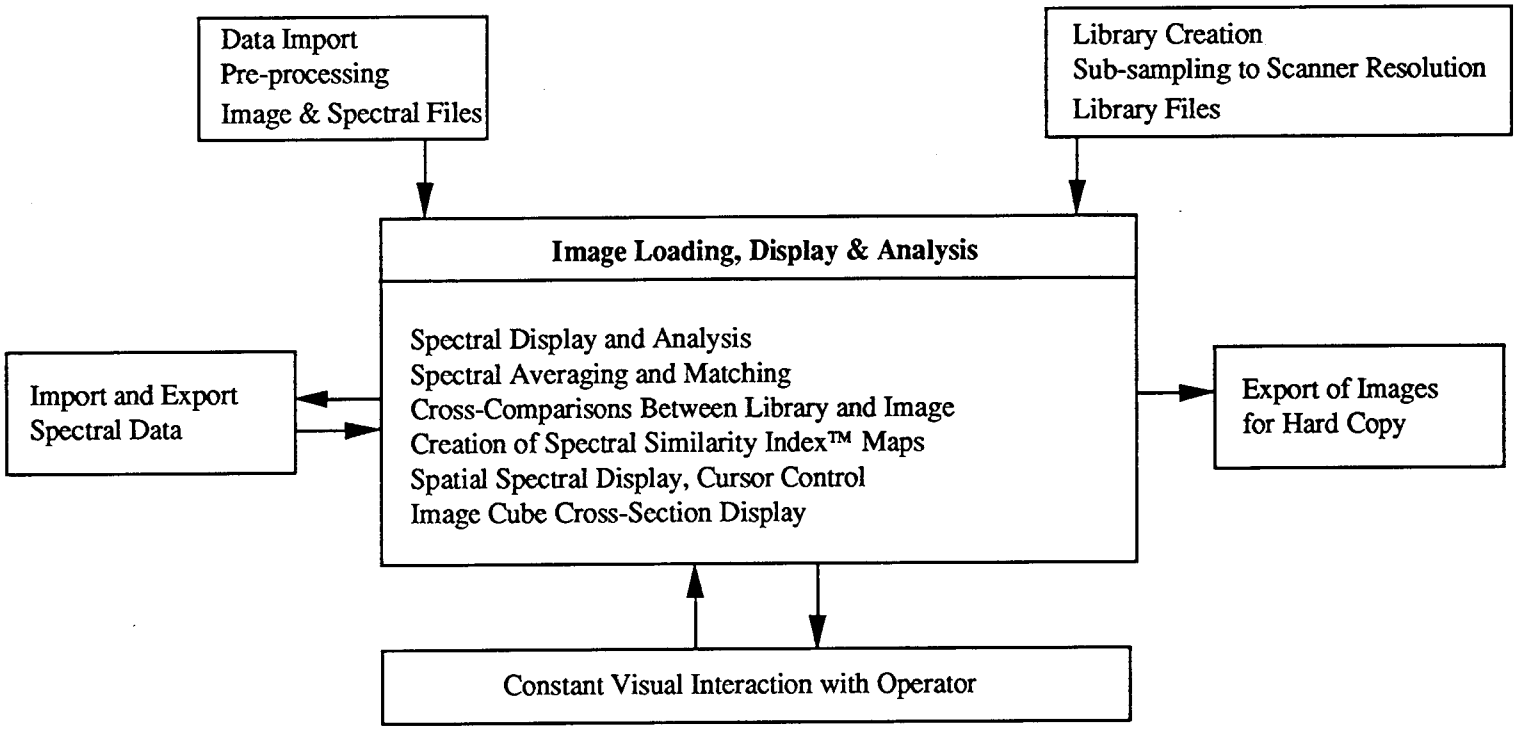

Figure 1: System Functionality

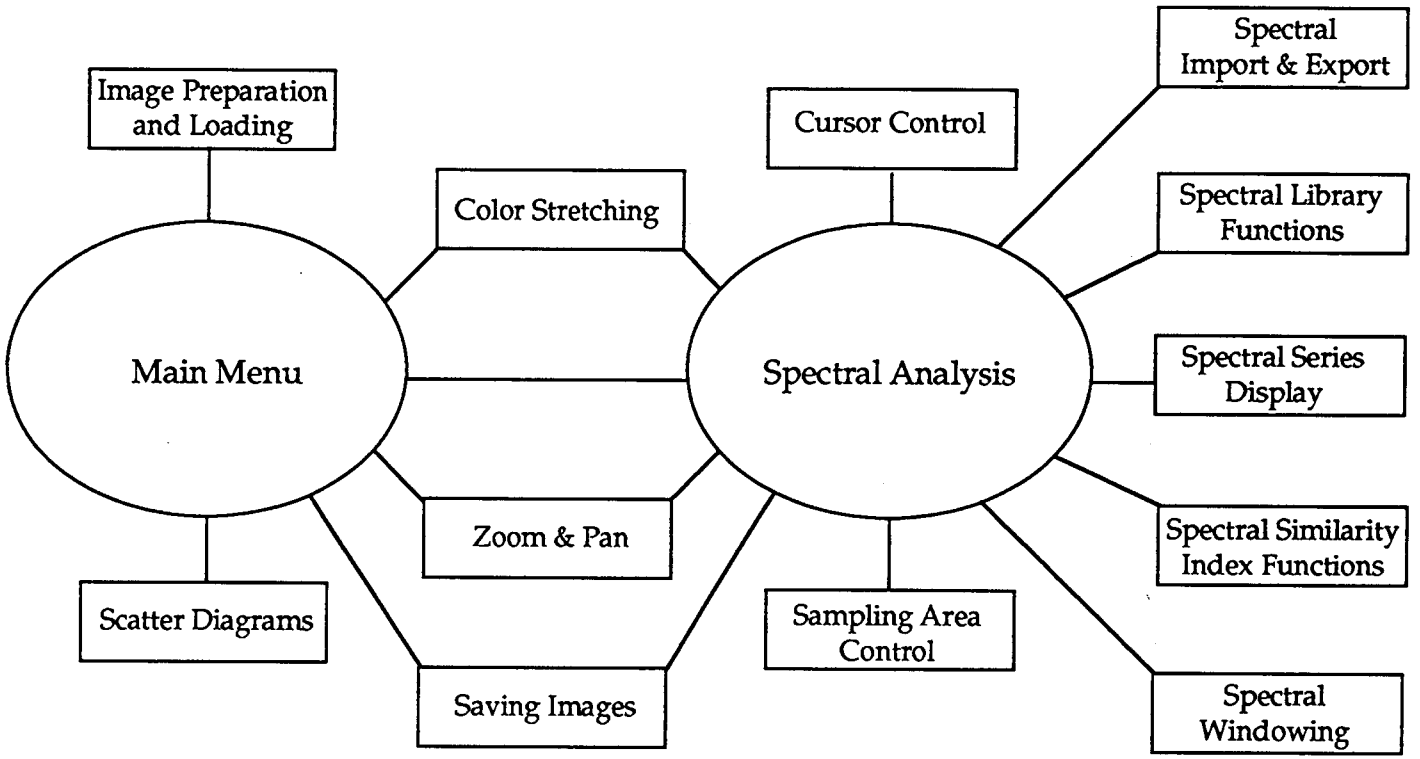

Figure 2: Core Program Flow Diagram

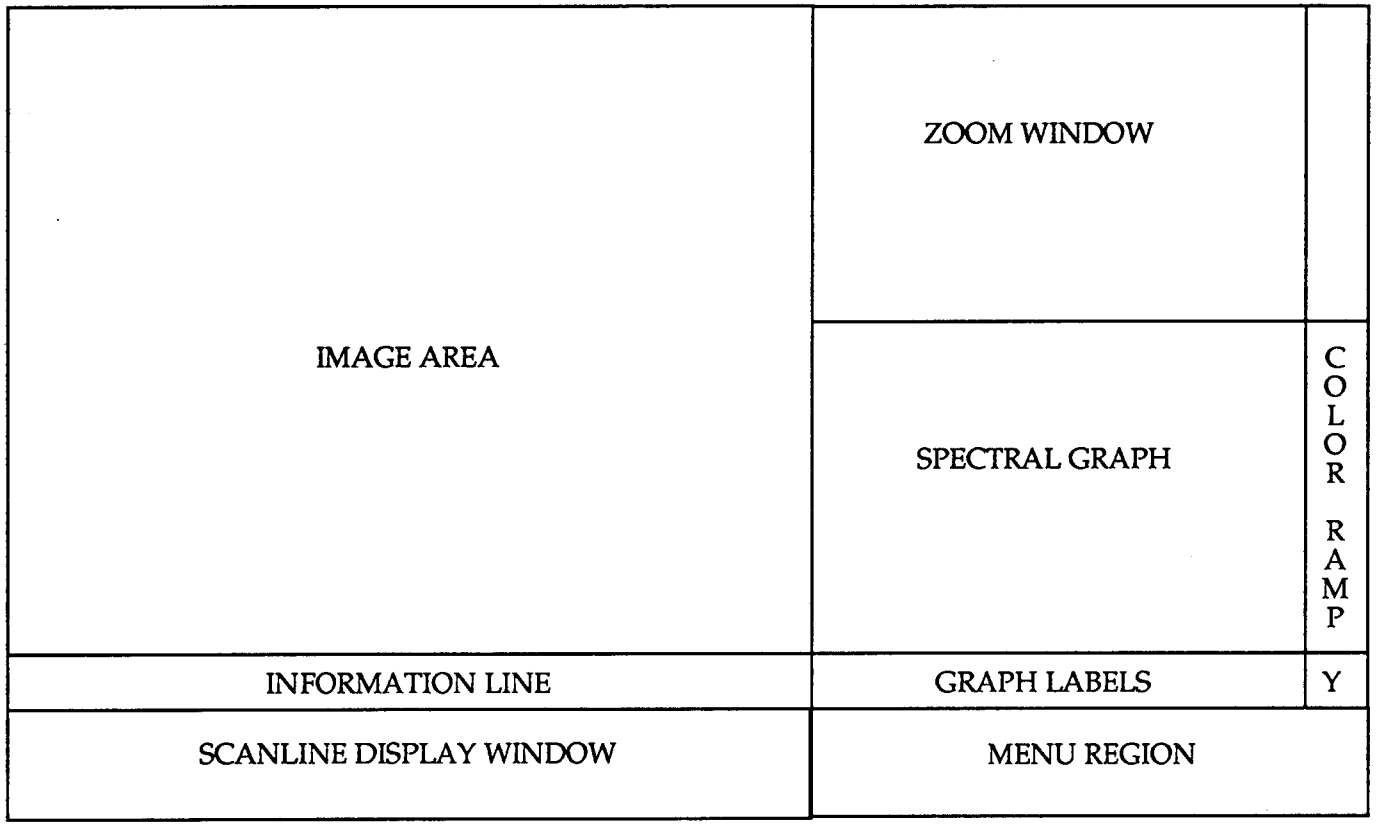

Figure 3: User Interface Screen

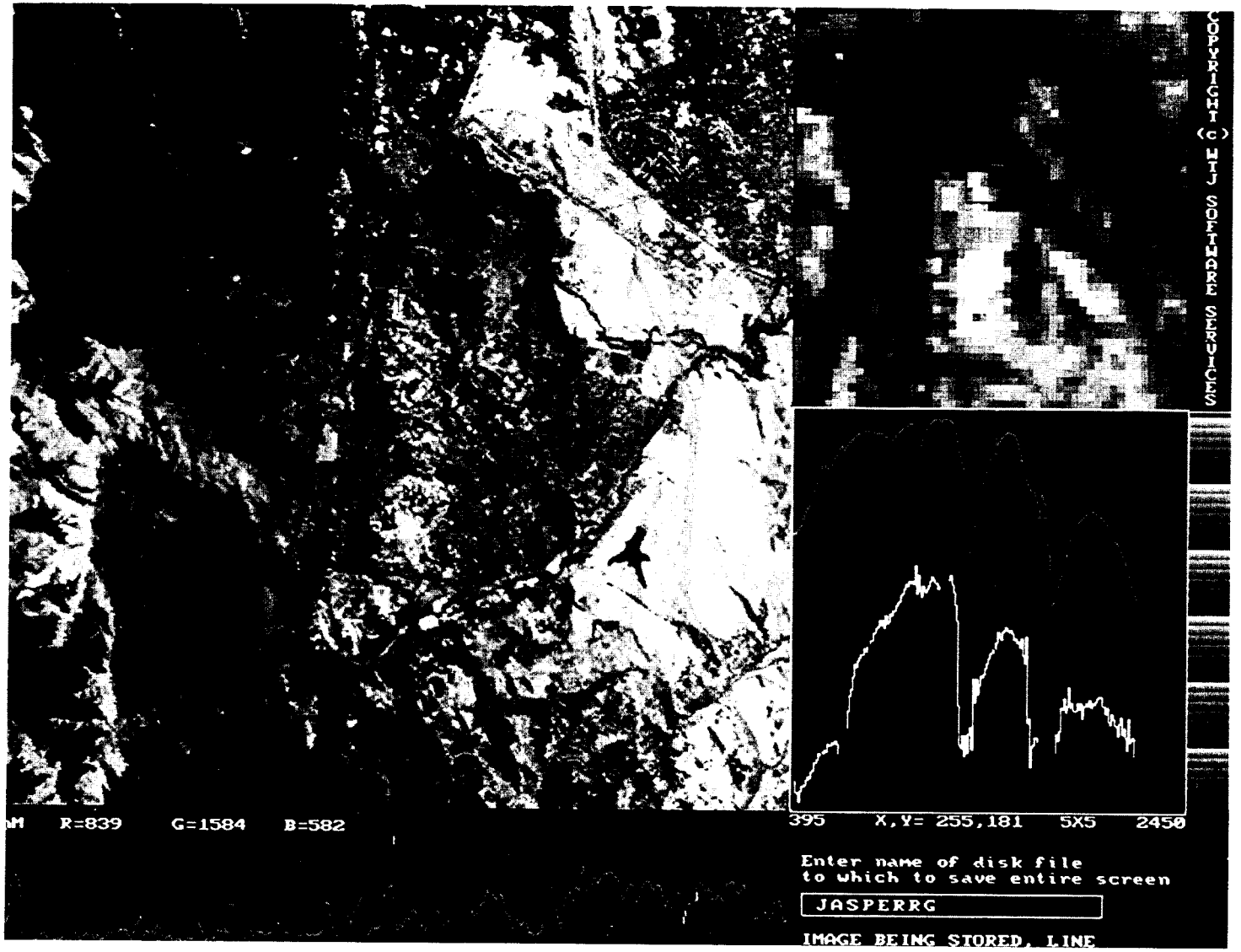

Figure 4: Saved Screen Displaying AVIRIS Image and Spectra [see slide 10]

Fast, Interactive Analysis of AVIRIS Data Using nPDF

Haluk Cetin, Timothy Warner and Donald Levandowski
Department of Earth and Atmospheric Sciences
Purdue University
West Lafayette, Indiana

Abstract

The n-dimensional Probability Density Functions (nPDF) technique is a new approach to data analysis that is both user-interactive and extremely fast, making it attractive for the analysis of high dimensional data, such as AVIRIS. Both scene and training data are mapped into nPDF space, producing a graphical display of the spectral data distribution. By overlaying this data, informational classes may be identified in the nPDF spectral data, and a classification look-up table is generated by the analyst. Unlike the maximum likelihood, Mahalanobis, and minimum distance classifiers, nPDF classification run-time does not increase with number of classes, and increases very slowly with increasing number of bands. A test scene of agricultural fields in the Maricopa area of southern Arizona was selected to demonstrate the application of the nPDF approach for the analysis of AVIRIS data on a personal computer. Classification accuracy measurements of the test scene, using 15 AVIRIS bands, indicate the nPDF approach has an overall accuracy rate of 71%, compared to 53% for minimum distance, 67% for maximum likelihood, and 68% for Mahalanobis distance. Using training fields from the test area, the entire scene, covered by 512 lines by 614 pixels and 180 bands, representing over 56 megabytes of data, was classified in under 13 minutes on a personal computer.

I. Introduction

The commonly used classification strategies of maximum likelihood, Mahalanobis, and minimum distance all have a number of inherent limitations. These include:

A. The memory requirements of the computer routines tend to be very large for high dimensional data, and the run-times are very long.

B. The algorithms thus tend to be implemented in computer routines that allow for only a limited number of input bands.

C. The algorithms are relative classifiers, and thus training fields from all spectral classes need to be identified prior to classification.

D. Classes are described statistically, and thus it is impossible to check that the previous requirement (point C.) has been satisfied.

E. Class overlap can be shown for only two bands at a time.

F. Mahalanobis and maximum likelihood classifications assume the data is normally distributed.

The nPDF analysis and classification technique, described by Cetin (1990) and also by Cetin

and Levandowski (1991b), addresses all the problems of the traditional classifiers discussed above. This new procedure has been shown to be an effective tool in the analysis of Thematic Mapper (TM) data for mineral exploration (Cetin and Levandowski, 1991a), as well as for vegetation classification (Warner *et al.*, 1991a). Furthermore, the nPDF classification may be used to analyze the spectral and informational classes in multi-spectral thermal data (TIMS) (Warner *et al.*, 1991b).

In this paper the advantages of an nPDF approach for analysis of AVIRIS data will be discussed, with emphasis on the rapid run-times and the potential for analyzing high dimensional data. A test area from within an AVIRIS scene over the Maricopa Research Farm, in southern Arizona, is used to demonstrate the ability to process high dimensional data on a personal computer.

II. Methodology

The nPDF approach overcomes the problems of the complex spectral distribution of high dimensional data by combining both statistical and graphical methods in the analysis technique.

In three-dimensional feature space, the feature vector is defined by

$$\mathbf{X} = \begin{bmatrix} x_1 \\ x_2 \\ x_3 \end{bmatrix}$$

Figure 1 shows a generalized distribution of highly correlated, remotely sensed data in three-dimensional feature space. Instead of using the original feature space, the nPDF technique relies on the calculation of the Euclidean distance from each data point to selected corners of the feature space.

With a large number of closely spaced spectral bands, AVIRIS data tends to be highly correlated. We therefore choose corners 1 and 5, at opposite ends of the feature space (see Figure 1), for calculation of the nPDF components. For three-dimensional data, the Euclidean distances to the corners 1 and 5 are:

$$D_1 = \left[x_1^2 + x_2^2 + x_3^2 \right]^{1/2}$$

$$D_5 = \left[(MR - x_1)^2 + (MR - x_2)^2 + (MR - x_3)^2 \right]^{1/2}$$

where

MR = maximum range of input data. For example, for 8 bit data, MR = 255.

The general formula for the calculation of the nPDF components for a hyper-dimensional cube is described by Cetin and Levandowski (1991). For corners 1 and 5, the hyper-dimensional Euclidian distances are:

$$D_1 = \left[\sum_{j=1}^{n} x_j^2 \right]^{1/2}$$

$$D_5 = \left[\sum_{j=1}^{n} \left[MR - x_j^2 \right] \right]^{1/2}$$

where

n = number of input bands.

For displaying the nPDF components, a scaling function is applied to the distances calculated by the formulae given above, in order to ensure that the nPDF components will fall within a preselected range.

$$nPDF_1 = S * D_1 / (2^{BIT} * n^{1/2})$$

$$nPDF_5 = S * D_5 / (2^{BIT} * n^{1/2})$$

where

S = desired scale factor for the nPDF axes

BIT = number of bits of input data (8 bit for TM, etc.).

The $nPDF_1$ and $nPDF_5$ components are calculated on a pixel by pixel basis and entered in a frequency array to map the nPDF data distribution. The procedure is then repeated for the training fields, and a second frequency array is calculated. For supervised nPDF classification, the nPDF data and the training distributions are then overlaid. In this way the nPDF spectral distribution of the informational classes is identified, and boundaries may be drawn between classes by digitizing polygons on the screen. This polygon class information is converted to raster form, and is used as a look-up table to classify the input data on a pixel by pixel basis [see slides 11 and 12].

III. Mapping and classification of Arizona AVIRIS data

Figure 2 is an image of a single band (0.64 μm) of the AVIRIS scene of the Maricopa area of southern Arizona. This data was collected on October 4 1990. Statistics of the original AVIRIS data showed that 44 of the 224 bands had at least some negative DN values. These bands were

excluded from further analysis, leaving 180 bands remaining. It was also found that the radiometric range was limited to the equivalent of 8 bits (i.e. 256 DN levels) in most bands, except for a number of channels in the visible wavelengths. Thus, to reduce data volumes for handling full scenes of AVIRIS data, all data was scaled to an 8 bit range.

A test area (see Figure 3) was selected to compare the classification strategies of the different approaches. This test area is the Maricopa Research Farm, owned by the University of Arizona, and is located approximately 40 kilometers south of Phoenix. This research farm has been the site of intensive, remote sensing investigations since the mid-eighties (Jackson, 1990). Cover types present on the farm include cotton, alfalfa, bare soil, grapes and wheat stubble.

For comparison between nPDF and traditional classifiers, we were limited to 15 input bands, as this is the maximum number allowed by the image processing software that we used for the Mahalanobis, minimum distance and maximum likelihood classifications (ERDAS, 1990). Therefore, a maximum 15 AVIRIS bands, selected arbitrarily throughout the spectrum, were used. At the end of this section we describe the results of when all 180 bands are used.

Table 1 shows the percentage accuracy of the various routines for classifying the selected 15 bands of AVIRIS data of the Maricopa test site. The nPDF technique had the highest overall accuracy rate, 71%, compared to 53% for minimum distance, 67% for maximum likelihood, and 68% for Mahalanobis distance.

The nPDF technique is also very fast. Figure 4 shows that the run-times of the traditional techniques are several times longer than nPDF, and that for the Mahalanobis distance and maximum likelihood classifiers, run-times increase approximately exponentially with the number of bands. Furthermore, nPDF classification is unaffected by the number of classes (Figure 5), whereas the minimum distance run-time increases linearly, and the remaining classifiers increase approximately exponentially with number of classes.

To demonstrate the power of the nPDF approach, the entire AVIRIS scene of 512 lines by 614 pixels, with a total of 180 bands, representing over 56 megabytes of data, was classified using the Maricopa training information. This entire classification took 12 minutes and 48 seconds using a Northgate 25 megahertz, 486 personal computer.

IV. Discussion and Conclusions

The nPDF procedure is a significant improvement over the traditional approaches of Mahalanobis, minimum distance and maximum likelihood classifications. It is extremely fast, and yet also produces improved accuracy. Run-time does not depend on the number of classes, and run-time increases only slightly with increased bands. Mahalanobis and maximum likelihood classifiers increase approximately exponentially with the number of classes and the number of bands. The nPDF routine has a low memory requirement, making it suitable for processing AVIRIS and other high dimensional data on a personal computer.

The commonly-used classifiers - maximum likelihood, Mahalanobis and minimum distance - require the selection of training fields that encompasses all the spectral classes in the data, yet this is very difficult to check. In contrast, nPDF classification does not have this limitation because it is an absolute classifier. Furthermore, with the commonly-used classifiers, the

training distributions are specified statistically; whereas in nPDF, the spectral distribution of data, as well as training distribution, is mapped in a visual representation. This results in better understanding of the class distributions present in the data. Inter-class separability is visually depicted, and spectrally overlapping classes may be identified. If a significant amount of overlapping does occur, the user can try alternative nPDF transformations to achieve a better separation for those particular classes. Alternatively, because the user creates the classification look-up table, the overlapping area can be apportioned in some user-defined way between the particular classes.

V. References

Cetin, H., 1990. nPDF-An algorithm for mapping n-Dimensional Probability Density Functions for remotely sensed data. *Proceedings of the 10th Annual International Geoscience and Remote Sensing Symposium, IGARSS'90* Vol. 1: 353-356.

Cetin, H. and D. W. Levandowski, 1991a. An integrated study of remotely sensed and geophysical data for mineral exploration in Lincoln County, Nevada: A new approach to mapping hydrothermal alteration using Thematic Mapper data. *Proceedings of the Eighth Thematic Conference: Geologic Remote Sensing, April 29 - May 2 1991, Denver Colorado,* Vol 2: 1271 - 1278.

Cetin, H. and D. W. Levandowski, 1991b. Interactive classification and mapping of multi-dimensional remotely sensed data using n-dimensional probability density functions (nPDF). *Photogrammetric Engineering and Remote Sensing* (In press.)

ERDAS, 1990. *ERDAS Version 7.4 Users' Manual: Image Processing Module.* Atlanta, Georgia. 218pp.

Jackson, R. D., 1990. Foreword: The MAC experiments. *Remote Sensing of Environment* Vol. 32: 77 - 79.

Warner, T. A., D. J. Campagna, C. S. Evans, D. W. Levandowski and H. Cetin, 1991a. Analyzing remote sensing geobotanical trends in Quetico Provincial Park, Ontario, Canada, using digital elevation data. *Proceedings of the Eighth Thematic Conference: Geologic Remote Sensing, April 29 - May 2 1991, Denver Colorado,* Vol. 1: 349 - 360.

Warner, T. A., H. Cetin and D. W. Levandowski, 1991b. Analysis of TIMS data using nPDF. *Proceedings of the 3rd Thermal Infrared Multispectral Scanner (TIMS) Workshop,* 20 - 24 May 1991, JPL Pub. 91-29 (in press.)

VI. Acknowledgements

We are very grateful to Phil Slater and Ray Jackson for kindly providing the AVIRIS and ground reference data used in this study, as well as to Howell Johnson for his patient assistance. This study was supported by the Indiana Mining and Mineral Resources Research Institute (U.S. Bureau of Mines grant number G1104118) as well as a Purdue University David Ross Fellowship.

VII. Table

Table 1. Classification accuracy percentages

Cover Class	Maximum Likelihood	Mahalanobis	Minimum Distance	nPDF
Cotton 1	99.17	98.66	92.34	95.75
Cotton 2	41.34	44.99	53.20	59.61
Cotton 3	59.72	61.98	50.27	59.56
Cotton 4	98.34	97.97	56.93	98.97
Alfalfa	80.95	83.40	33.39	83.49
Grapes	79.53	77.56	65.02	85.27
Bare Soil	79.65	77.56	70.79	85.27
Wheat Stubble	64.59	66.43	55.41	65.88
Overall	**67.34**	**67.77**	**52.74**	**70.99**

VIII. Figures

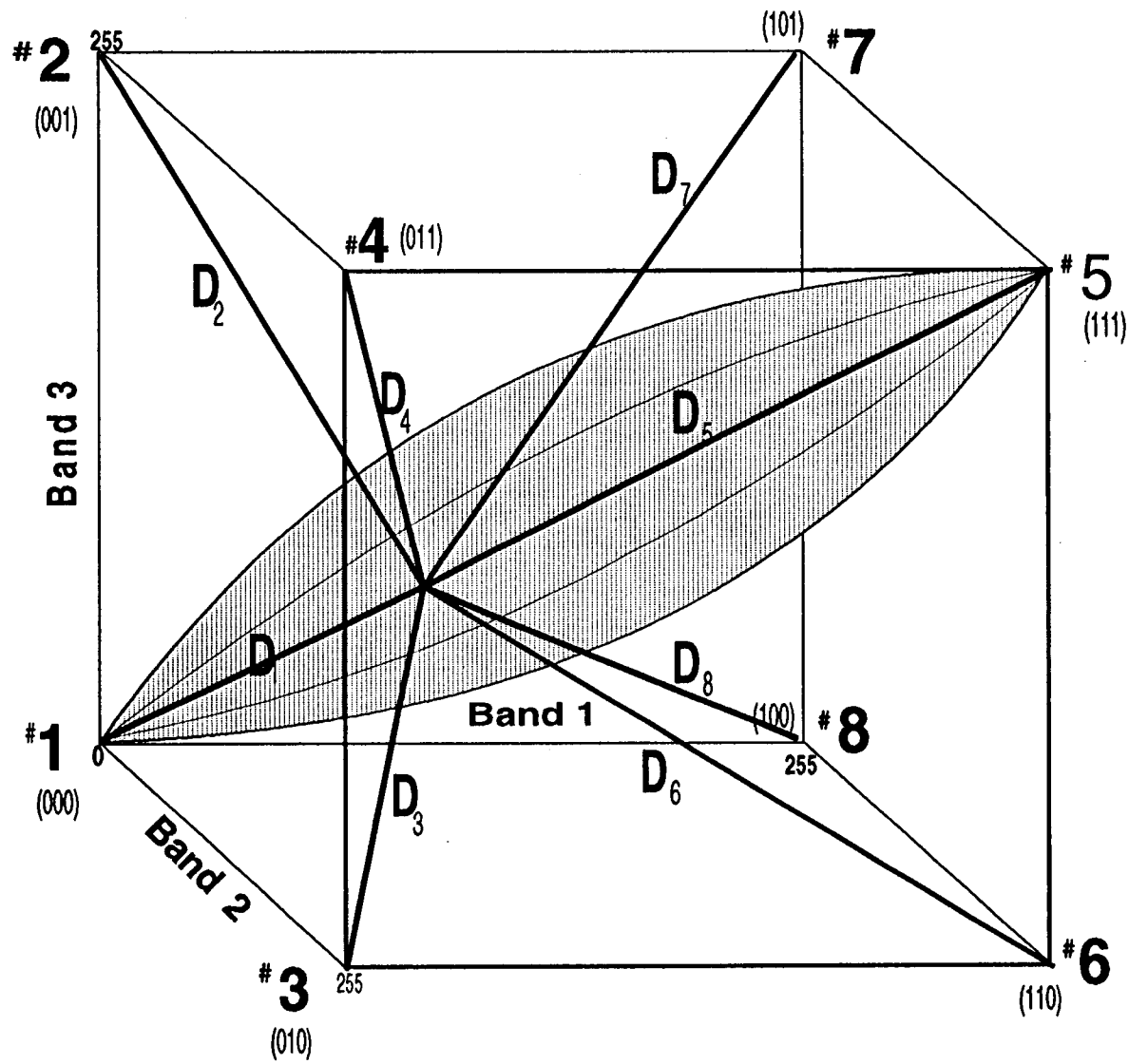

Figure 1. Three dimensional feature space showing schematic distribution of highly correlated data, and numbering convention for the corners of the data space.

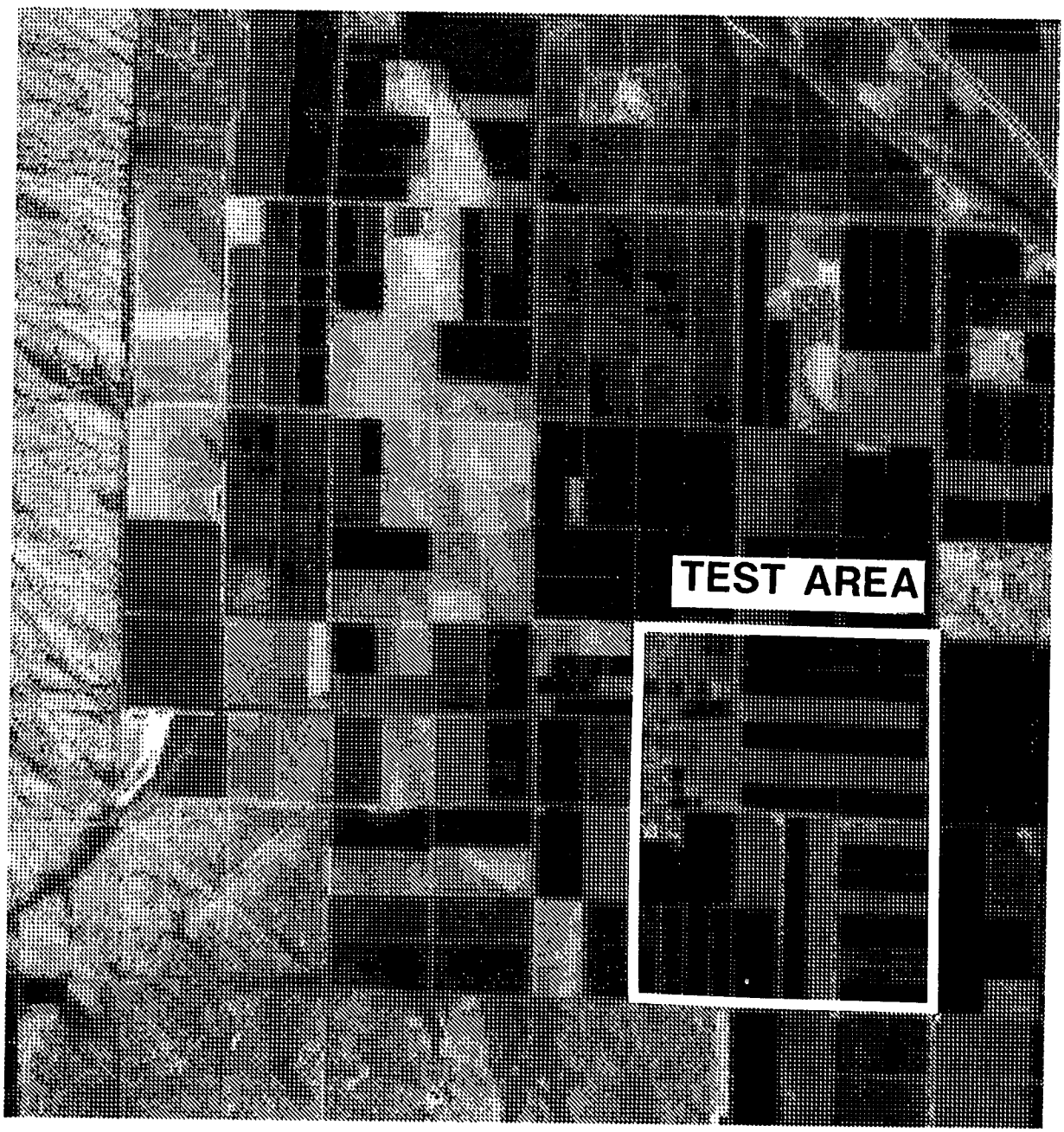

Figure 2. 0.64 μm image of Maricopa AVIRIS scene.

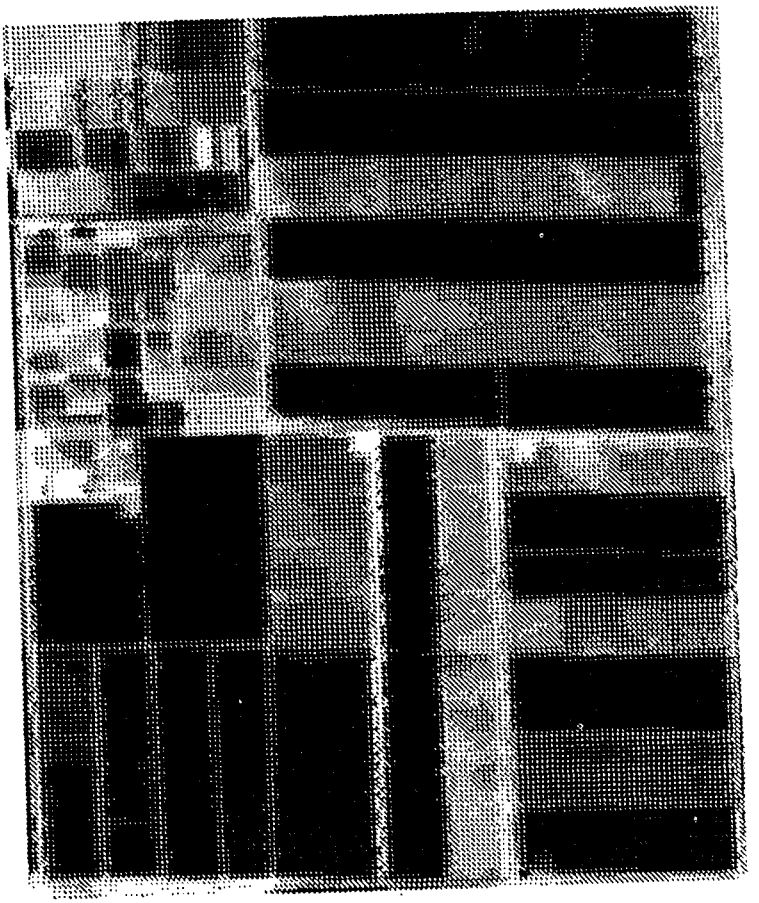

Figure 3. 0.64 μm image of Maricopa research farm.

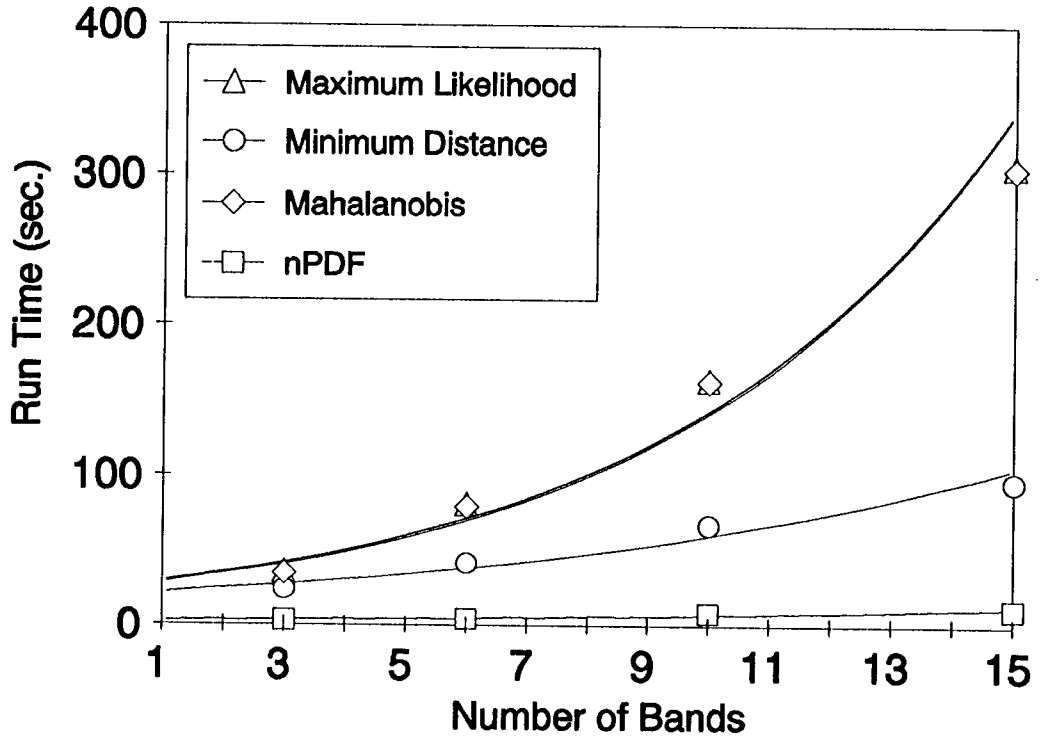

Figure 4. Graph of run-time versus number of bands.

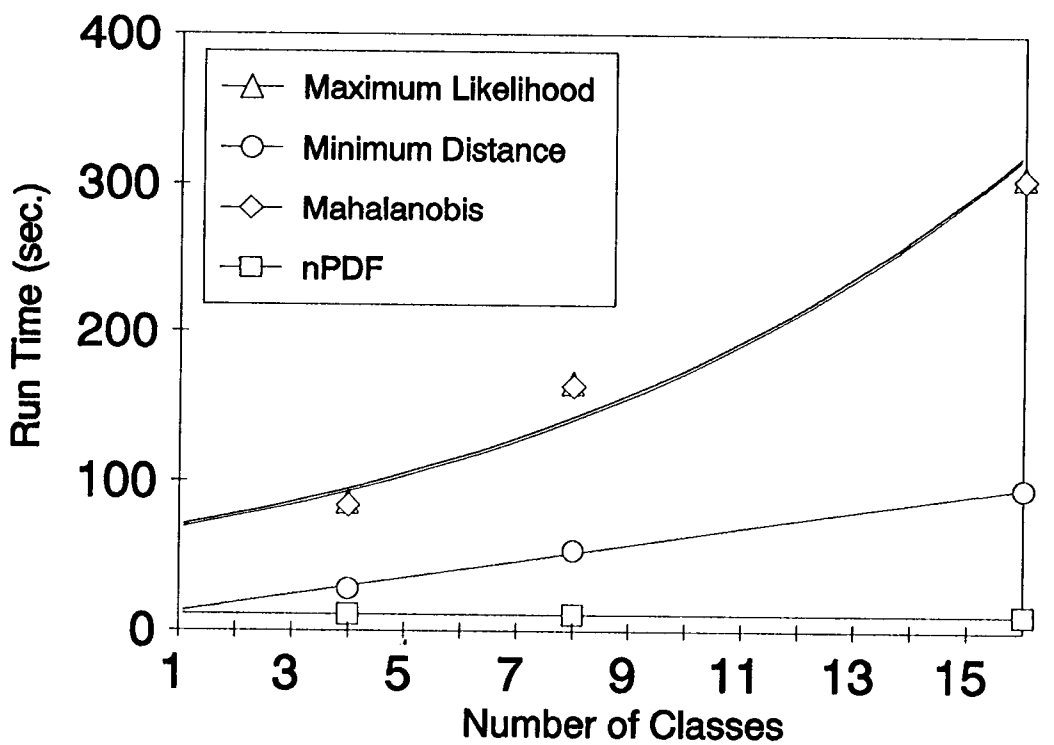

Figure 5. Graph of run-time versus number of classes.

Spectral Analysis Techniques for Classification of AVIRIS Data

Sylvia S. Shen, Bonnie Y. Trang and Mark T. Noga

Lockheed Palo Alto Research Labs
3251 Hanover St., Palo Alto, CA 94304

ABSTRACT

An advanced software system is described that allows scientists to perform effective and efficient analysis of high spectral resolution data. The principal focus is on new hyper-spectral information handling and extraction algorithms. Among these is an image classification technique which uses a set of diagnostic features derived from the absorption and emission bands of the spectra as discriminants. Another approach uses a new signature matching technique that employs geometric and structural information contained in the spectrum. The strategy here is to represent the spectrum by a tree, so that spectrum correlation can be performed by matching the nodes and branches of the signature and reference trees. The emphasis has been on producing fast spectral analysis techniques which allow all pixels in the scene having a signature similar to that of a specific class to be identified more effectively. Results of applying these techniques to AVIRIS data are also presented, along with a brief description of the current capabilities of our new hyper-spectral image analysis software system.

1. INTRODUCTION

The new generation of airborne and spaceborne sensor technologies offers the potential of producing broadly consistent image data with high spatial, spectral, and temporal resolutions. These types of remotely sensed image data are becoming the primary tool for studying many land and ocean processes. In fact, multispectral instruments such as the Landsat Multi-Spectral Scanner (MSS) and Thematic Mapper (TM), and NOAA's Advanced Very High Resolution Radiometer (AVHRR), have been used in land cover, land use, and meteorological studies for many years. These instruments typically provide data in 3 to 8 spectral bands. A new generation of imaging spectrometers such as JPL's Airborne Visible/Infrared Imaging Spectrometer (AVIRIS) has now been designed to disperse reflected solar electromagnetic energy from the earth's surface to form as many as 200 spectral images of the scene simultaneously. Unlike the traditional multispectral instruments, imaging spectrometers provide sufficient spectral resolution to allow unique spectral signatures to be extracted on a per-pixel basis, thus enabling direct surface material identification and more detailed analysis of the biophysical processes. However, the unprecedented volume and complexity of the new data presents a challenge to the traditional image analysis methods and requires that new approaches be developed to efficiently analyze the data.

This paper describes an advanced software system that we have developed to allow scientists to perform effective and efficient analysis of high spectral resolution data, e.g. AVIRIS, using moderate computing resources. The principal focus is on new hyper-spectral information handling and extraction techniques that we have developed. One of these is a hyper-spectral image classification technique which uses a set of diagnostic features derived from the absorption and emission bands of the spectra as discriminants. Since these bands are unique to the composition and structure of the material being analyzed, the derived features contain the key discriminating information for class identification. Another approach represents the spectrum as a tree, so that spectrum correlation can be performed by matching the nodes and branches of the trees, one representing the sample waveform signature and the other representing the signature of a known material (class). These fast spectral analysis techniques allow all pixels in the scene having a signature similar to that of a specific class to be identified more effectively. Results of applying these techniques to AVIRIS data are also presented, along with a brief description of the current capabilities of our hyper-spectral image analysis software system.

2. SPECTRAL ANALYSIS TECHNIQUES

Since the potential value of imaging spectrometers will not be realized without the development of new approaches to hyper-spectral information handling and extraction, the principal focus here is on special analysis techniques for data of high spectral dimensionality such as AVIRIS. AVIRIS is designed to acquire images with 20-m pixels simultaneously in 224 spectral bands covering the 0.4 - 2.5 μm wavelength region. Each pixel has associated with it 224 radiance values, or essentially a continuous radiance spectrum (see Figure 1). The high spectral sampling

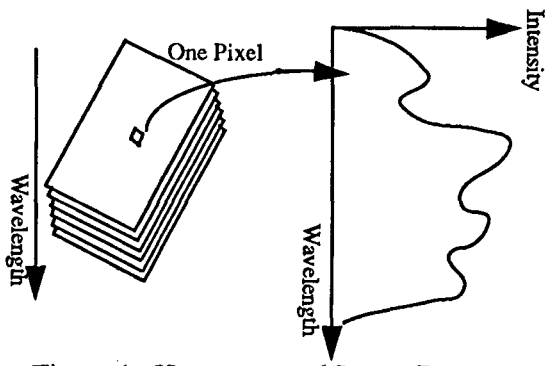

Figure 1. Hyper-spectral Image Data.

rate gives sufficient information to uniquely classify most terrestrial materials. To make effective use of this new class of data, the key step is to find a strategy to reduce dimensionality and at the same time retain sufficient information for class separation and identification. Described below are some of the spectral analysis techniques that we have developed for analyzing high spectral resolution image data.

2.1 Image Classification Based on Emission Band Characteristics

An analysis method that has been used and reported in the literature is based on the principal component transformation [1,2]. This transformation transforms the 224 spectral values into

224 uncorrelated coordinates. The first few coordinates, namely the principal components, are used as attributes for discriminating between classes. These principal components which are linear combinations of the original 224 spectral values, may be effective in separating certain classes. But they might not be optimal for separating certain other classes. Construction of this transformation, requiring on the order of 10^{13} arithmetic operations for a typical 11-km-square AVIRIS scene, can be computationally expensive [3]. Therefore, more efficient methods of extracting discriminant features are ultimately needed.

We have developed a scheme which uses attributes that are more characteristic of the radiance spectrum. Our method [4] uses a set of diagnostic features derived from the absorption and emission bands of the spectra. Because a material is specified by its composition and structure, which determine the specific energies at which the electronic excitations and molecular vibrations occur, each material has a characteristic set of excitation energies. When radiation at the appropriate energies penetrates into the material, it is absorbed by the excitation process, resulting in a loss of radiation at those specific excitation energies. These absorption bands are therefore diagnostic signatures of the material. Emission peaks are similarly diagnostic of the composition and structure of materials, although the signature phenomenology is somewhat different than that for the absorption bands. Emission peaks are typically the by-product of excitations. Excitation is followed by relaxation back to the ground state, this relaxation corresponds to a loss of energy by the excited species as it returns to its lower ground state configuration. This loss of energy takes the form of radiation emission at the specific energy of relaxation. Just as with the absorption bands, the emission peaks are also diagnostic signatures of the material.

Our method first extracts the positions, widths and strengths of the emission peaks from the spectra, and then uses them as attributes for class separation. Since these bands are unique to the composition and structure of the material being analyzed, the derived features contain the key discriminating information for class identification. A nonparametric classifier has also been developed based on these attributes for identifying the various classes in the scene. Training samples or prototype samples can be specified from the image data themselves or from a spectral reference library. Similar diagnostic features can be extracted from the absorption bands and used as discriminants for class separation and identification [4]. Furthermore, the combined set of features derived from both the emission and absorption bands can also be used as discriminants [4].

2.2. Spectrum Correlation Via Tree Matching

An alternative approach to pixel classification is to correlate the radiance spectrum of a given pixel with the library spectra of known classes. Matching by cross-correlation can often be very time-consuming. Therefore a fast spectral signature matching technique is needed. A binary spectral encoding algorithm was developed by Mazer et al [5] which uses a binary code vector constructed from the spectral amplitude and the local slope to represent the spectrum. It then uses Hamming distance as the similarity measure for signature matches. This type of signature matching techniques can be used to find all the pixels in the scene having a spectral signature similar to that of a specific class. Our strategy is to represent the spectrum by a more efficient data structure from a processing standpoint, namely a tree (see Figure 2), so that spectrum correlation can be performed by matching the nodes and branches of the trees. A tree, if properly de-

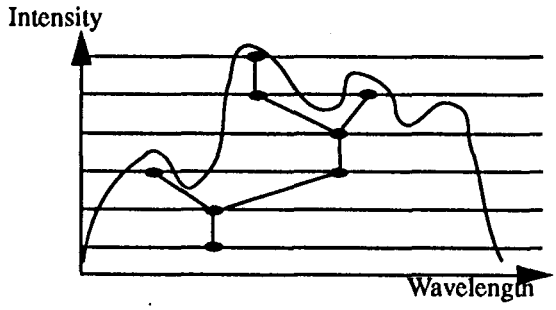

Figure 2. Tree Representation.

signed, can describe not only the succession of the peaks and the valleys of the spectrum, but also the relative height of these entities, and the self-embedded structure of the spectrum. We have developed a scheme to rapidly construct such trees from the pixel spectra. We have also developed an efficient recursive tree matching algorithm [6] based on a dissimilarity or distance measure as described below.

The tree matching approach can be best described as a recursive method that traverses two trees simultaneously looking for differences in the number and nodes and branches between the two trees. Signature and reference trees are first converted to general lists (lists of lists) because this data structure minimizes the number of pointers required to store any tree with an arbitrary number of branches per level (see Figure 3). The algorithm is complicated by the fact that, in

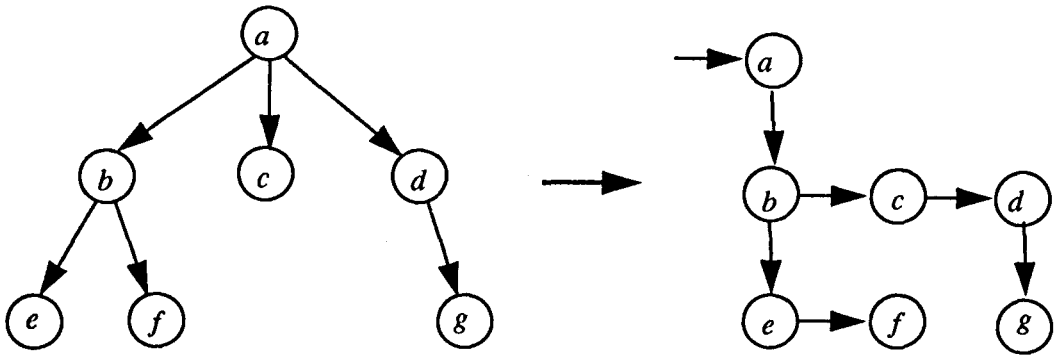

Figure 3. Tree to list mapping.

general, it is not possible to determine a priori how sublists should be paired (see Figure 4). Our approach, which is reasonable with respect to the intended application, is to compare all sublist combinations maintaining a left-to-right ordering. Fortunately, the recursion keeps track of all possible combinations of branch/node comparisons regardless of level. Before the traversal begins, the difference D is set to zero. When two trees differ at any level, a weighted value is added to D. At the end of the procedure, the minimal D is the value reported by the algorithm (see Figure 5). Definitions of the various functions used in the algorithm described in Figure 5 are

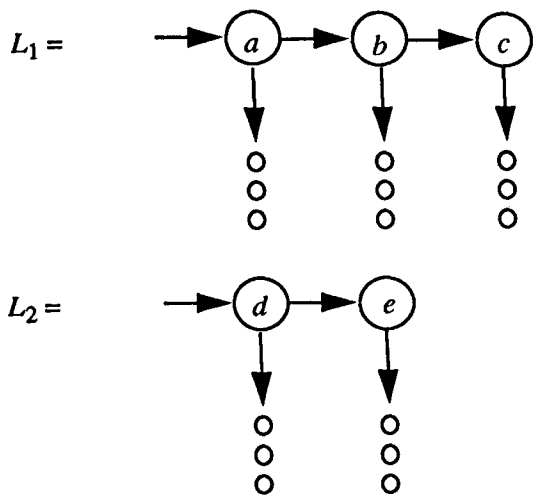

Figure 4. Should the sublists associated with the combinations (a,d) and (b,e) be paired, or should (b,d) and (c,e) be paired, etc.?

```
DIFF(L1,L2):
    if (IS_EMPTY(L1) and IS_EMPTY(L2)) return (0);
    else if (IS_EMPTY(L1)) return SIZE(L2);
    else if (IS_EMPTY(L2)) return SIZE(L1);
    else return (MIN3(DIFF(SUBS(L1),SUBS(L2)) + DIFF(TAIL(L1),TAIL(L2)),
                      1 + SIZE(SUBS(L1)) + DIFF(TAIL(L1),L2),
                      1 + SIZE(SUBS(L2)) + DIFF(L1,TAIL(L2)));
```

Figure 5. Tree difference algorithm, weighting factor is one per missing node.

as follows: The TAIL of a list is the list to the right of the head node, the SUBS of a list is the list below the head node, and the SIZE of a list is the total number of nodes in the list.

Again, the prototype spectra of the classes of interest can be specified from the image data themselves or from a spectral reference library. This technique is very efficient and can, much like the previous approaches, be used to search the entire scene for occurrences of similar spectra to those in the on-line spectral library of candidate materials.

3. RESULTS

We have applied both techniques to the 1987 AVIRIS data over Moffett Field area. Both algorithms have successfully identified 12 surface materials including asphalt, concrete, water, salt pond, grass, tree and shrubbery, soil, marsh, etc. The left image in Figure 6 shows the true RGB composite of the Moffett scene and the right image is the color coded classification results using the automated algorithm based on emission band characteristics as described in Section 2.1.

Highly comparable classification results have also been obtained using the tree matching technique. These algorithms can also be used for vegetation identification, mineral classification, and change detection. As an example, we have begun to scan the 1989 AVIRIS data over Jasper Ridge Biological Reserve for vegetation species using these techniques.

4. CURRENT SOFTWARE SYSTEM CAPABILITY

Effective use of new classes of data with high spectral dimensionality has motivated the development of a highly interactive software system that allows users to visually interact with the hyper-spectral data and their statistics. We have developed and implemented a variety of display and processing routines using low cost computer workstations. These routines perform functions such as image display, spectral curve plotting, histogramming, contrast adjustment, statistics calculation, zoom, thresholding, color coding, etc. Display and processing routines have been integrated with the special algorithms described in Section 2 to provide a wide range of capabilities to users for extracting information contained in the data.

The current system capabilities include rapid display of projection of hyper-spectral images in the spectral direction, cursor-designated spectral plots of single pixels or averages over a spatial window, the ability to generate, delete and update library (reference) radiance curves from specified regions in the scene, and display of spectra from a spectral library for visual comparison. There are also functions which perform linear, logarithmic and inverse logarithmic contrast enhancement, subwindow zoom, extraction of key discriminant features from radiance curves as described in Section 2.1, rapid unsupervised organization of pixels having similar spectral signatures (this enables a better understanding of the natural clustering and structure of the data), search of all the pixels in the scene having a spectral signature similar to a specified library spectrum for efficient scene classification using the signature matching techniques (e.g. tree matching, binary encoding, cross correlation, emission and absorption band characteristics, etc.) as described in Section 2 and portrayal of those pixels in a unique color. Color-map adjustment functions include designation of color codes for classes of interest, and display of color coded classification result, false color image and true color composite of the red, green and blue channels of the image data. Figure 7 shows a snapshot of a current version of our software system in operation.

5. CONCLUSIONS

Our advanced software system incorporates a wide variety of special algorithms and a large collection of display and processing tools to allow scientists to perform detailed analysis of data with high spectral dimensionality. The special hyper-spectral techniques can differentiate object substances that look identical to an analyst using conventional tools. More specifically, our techniques identify an object by detecting its absorption and emission band characteristics. Since every substance has a unique set of such bands, our techniques are more robust than the conventional methods. The display and processing tools allow the users to visually interact with the data and their statistics. This software system is highly interactive, maintainable, and extensible. All software is written in the C language under UNIX. The interactive portion of

the software is written for Silicon Graphics Iris 4D Workstations and their windowing environment. An X port is planned that would make the software usable from a number of different workstation platforms including those from Sun Microsystems. Implementation has been carried out in such a way as to make additions and modifications easy, while at the same time maintaining a user friendly application environment. So far, we have demonstrated that our software system is capable of extracting and identifying surface materials from AVIRIS-like data sets. The system has also been tested with synthetic high spectral resolution radiance data in a phenomenology study.

6. REFERENCES

[1] S. C. Feldman and J. V. Taranik, "Comparison of Techniques for Discriminating Hydrothermal Alteration Minerals with Airborne Imaging Spectrometers Data", Remote Sensing of Environment 24 (1988).

[2] A. Hutsinpiller, "Discrimination of Hydrothermal Alteration Mineral Assemblages at Virginia City, Nevada, Using the Airborne Imaging Spectrometer", Remote Sensing of Environment 24 (1988).

[3] G. Vane and A. F. H. Goetz, "Terrestrial Imaging Spectroscopy", Remote Sensing of Environment 24 (1988).

[4] S. S. Shen and B. Y. Trang, "A Feature Selection Technique for Classification of Hyper-Spectral AVIRIS Data", Proceedings of SPIE on Applications of Digital Image Processing, Vol. 1567 (1991).

[5] A. S. Mazer, M. Martin, M. Lee and J. E. Solomon, "Image Processing Software for Imaging Spectrometry Data Analysis", Remote Sensing of Environment 24 (1988).

[6] S. S. Shen, B. Y. Trang and M. T. Noga, "Hyper-Spectral Signature Correlation Via Tree Matching", in preparation.

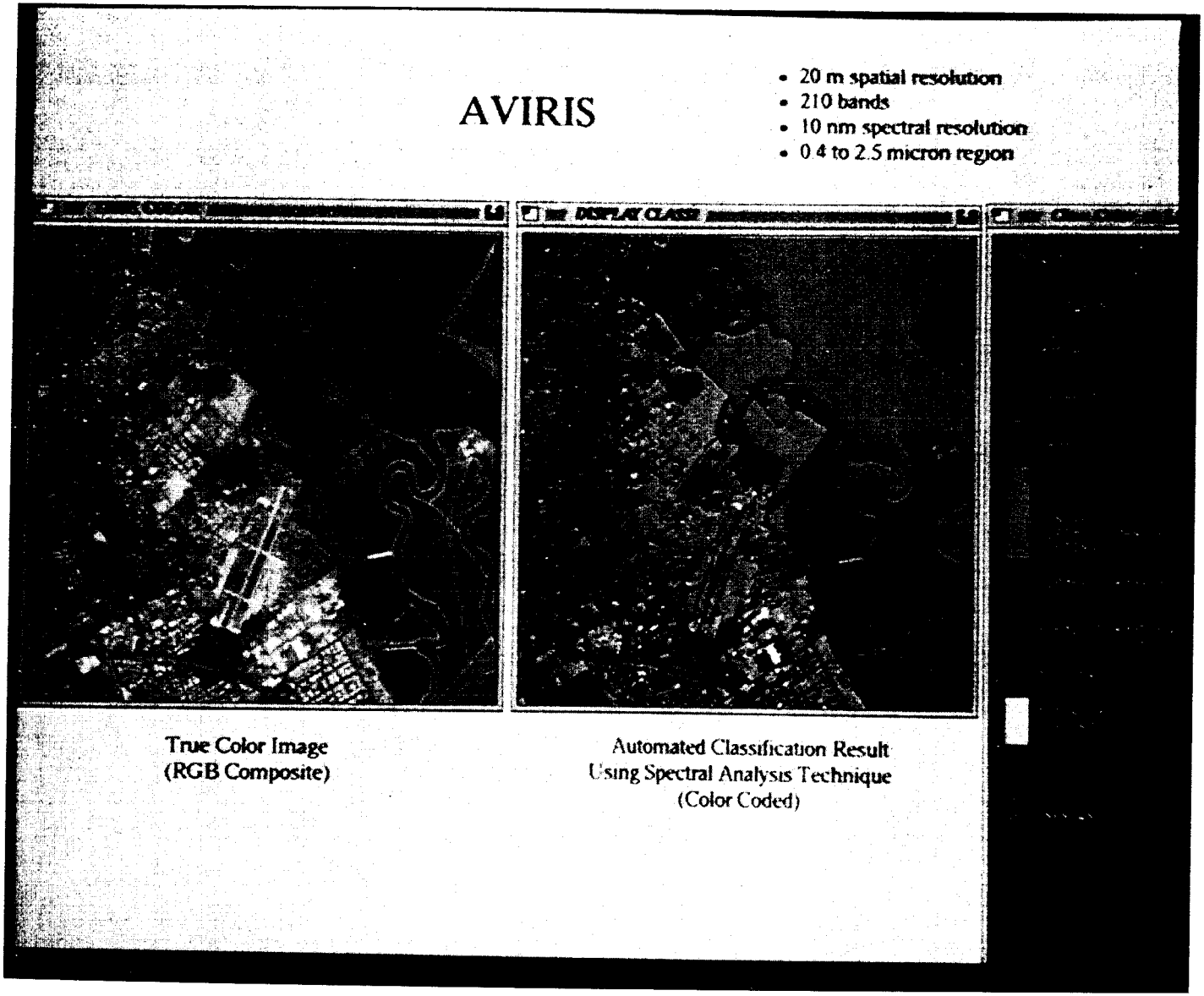

Figure 6: Automated Classification Results [see slide 13]

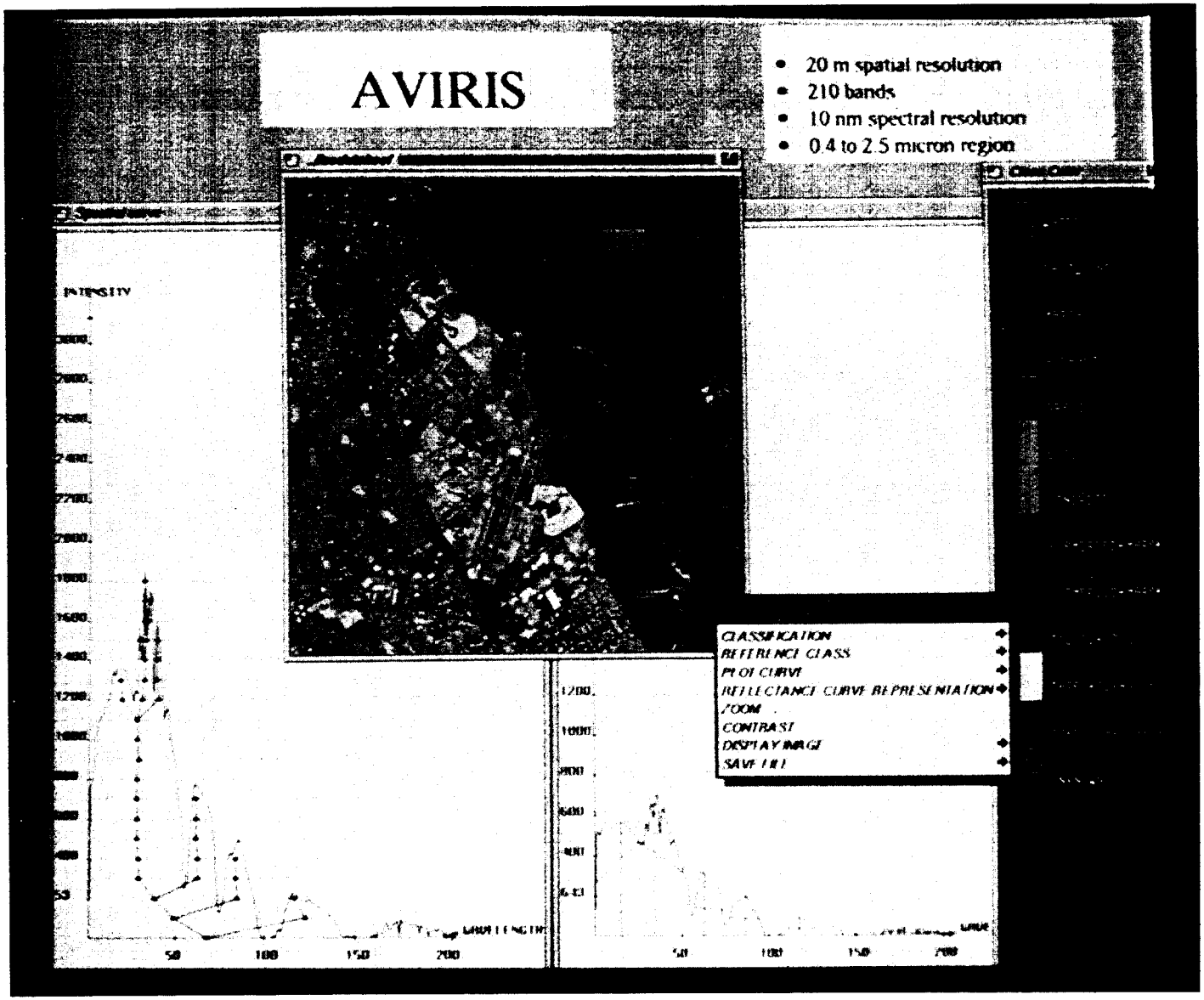

Figure 7: Advanced Hyper-Spectral Image Analysis Software System [see slide 14]

Curve Shape Matching, End-Member Selection and Mixture Modelling of AVIRIS and GER Data for Mapping Surface Mineralogy and Vegetation Communities

Steve Mackin
Adolf Ellissen Weg 16,
3400 Göttingen,
Germany.

Nick Drake
Dept. of Geography,
University of Reading,
United Kingdom.

Jeff Settle
NUTIS,
University of Reading,
United Kingdom.

Steve Briggs
BNSC/RSADU,
Monks Wood Station,
Abbots Ripton, Cambridgeshire,
United Kingdom.

Abstract. The availability of high spectral resolution data and laboratory collected spectra of surface materials allows the automatic identification of spectra collected by airborne instruments without the need of ground data. Using relatively simple matching techniques, the identity of the major components in each surface pixel can be obtained by comparison of the pixel spectra to each library spectra. A further step using an expert system can determine whether to accept or reject the basic shape match using several parameters such as flatness and spectral contrast (or separation) of materials. The output consists of a map of the identified materials with an indication of their purity. These end-members are input into a linear mixture model to determine the proportions of each identified material in each image pixel. An application of the method using both GER and AVIRIS data is given.

I. Introduction

Identification and mapping of surface mineralogy and vegetation community distribution are now possible by applying a shape analysis of high spectral resolution data using a minimum deviation algorithm. Using comparisons in shape of both overall curve and primary absorption features of each pixel to a library of reflectance spectra, the identity of each pixel can be determined.

Although an identity is established, the data is processed further using an expert system, to estimate the doubt associated with the matched identity and whether to accept or reject the identity based on the calculated doubt. Several parameters extracted from the data such as curve flatness and spectral contrast (or separation) are used at this stage. The output consists of relatively pure pixels of each identified component.

The purest pixels of each component identified by the expert system are input into a linear mixture model to estimate proportions of each component in each image pixel. Mixture modelling complements the expert system approach, as mixed pixels are not readily identified by matching to a library of pure materials.

II. Area of study

The methods were tested using both AVIRIS and GER data sets, collected over a site near Golconda in north central Nevada. The site covers the boundary between the Cambrian Preble Formation and the Ordovician Valmy Formation along the Getchell fault trend.

The geology of the Preble formation is primarily of interbedded folded quartzites and micaceous phyllites, with limited outcrops of blue grey, partly dolomitised limestone. Mineralisation is confined to N-S trending high angle vein systems, close to the Getchell fault. Some disseminated gold mineralisation is presently being mined in the area and seems to be related to silicification and the presence of abundant illite.

Vegetation cover is highly variable in this semi-arid terrain and consists primarily of scattered sage brush and grass, with limited development of annual shrubs in the stream beds.

The area is shown in Slide 15. The slide consists of four separate images. The image, top left, is a brightness image of the AVIRIS data covering the 2.0 mm to 2.5 mm wavelength region. The area of interest is shown outlined in red. There are two dark circular regions in the area of interest that correspond to a mineralised area currently being mined. North is to the right.

III. Processing and analysis of the data

The data processing and analysis consist of three stages. The first stage is shape matching of the reflectance spectrum of each data pixel to the library reflectance spectra. The data is converted to a set of percentage variations about the mean value, which allows matching of the data in a manner independent of the reflectance scale, which side steps the problems of shadowing and brightness variations due to grain size. This step is performed on both the overall curve shape and on smaller wavelength regions that define areas of characteristic absorption for each library material. This eliminates false matches, where the overall curve shape is well matched, but the error is concentrated on a small but characteristic absorption feature.

The second stage is a simple expert system, which evaluates parameters extracted from the data and spectral library to determine the doubt associated with the simple shape match. For example the accuracy of the match will be of the same order for the whole curve shape and for the characteristic absorptions; variations in accuracy between these two measures increase doubt. Another parameter is spectral contrast, or separation, for example, if a match score is moderate for the match of two materials in the library to the pixel spectrum and the separation of the two materials is quite low in the pure (library) state (e.g. Calcite and Siderite), the match may be accepted, with the proviso that the actual identity could be one or the other. While with the alternative, that given the moderate match score for the match of two materials in the library to the pixel spectrum and the separation of the two materials is quite high in the pure state (e.g. Calcite and Muscovite), the match may be rejected on the basis that it is most likely to be a mixture of dissimilar materials. The expert system basically ties together various parameters from the data and makes a decision to accept or reject the assigned pixel identity.

The third stage uses the output from the expert system stage to determine the end-members for the linear mixture model. The pixels with the highest match scores are the purest in the image; these are input as end-members into the mixture algorithm which estimates the proportion of each identified component in each image pixel. Estimation of the proportions **f** is based upon minimisation of the quadratic function:

$$(\mathbf{x} - \mathbf{Mf})^{T}\mathbf{N}^{-1}(\mathbf{x}-\mathbf{Mf})$$

where **x** = a pixel spectra
M = a matrix whose columns are end-member spectra
N = a variance-covariance matrix independent of **f**.

The above equation is subject to the following constraints,

$$0 < f_i < 1 \qquad i = 1,...c \quad \text{and}$$

$$f_1 + f_2 .... f_c = 1$$

Using this modified classical estimator error estimates can be calculated, for a two component mixture with the sum to one constraint imposed and with **N** given by **sI**, this quantity is given by :

$$\mathbf{E} = s/(\mathbf{m}_1-\mathbf{m}_2)^{T}(\mathbf{m}_1-\mathbf{m}_2)$$

and in this case the same for each component. This shows that the error on the estimate depends both on the level of noise in the scene and on the spectral separation of the components. When more than two components are present, **E** depends on the distance between the component and the closest mixture to it of the remaining end-member spectra.

IV. Geological application

Slide 15 contains four images. The top left image is the previously described AVIRIS brightness image. The image bottom left is a corresponding material identification map, again with north to the right. The map is based on shape analysis alone, prior to the expert system stage. The colour coding is as follows. Undifferentiated clays (muscovite, illite and kaolinite) are shown in red, dry vegetation in blue, chlorite in yellow and green vegetation in dark green. The clays are seen to dominate the area of interest (outlined in red in the brightness image) and are confined primarily to the phyllites of the Preble formation to the east of the Getchell fault (bottom quarter of the image). The only distinct feature to the west of the fault is an area rich in chlorite (yellow).

The image top right is another material identification map of the GER data over the outlined area of interest of the AVIRIS data. In this image, the clays are separated, red is illite, green is kaolinite and blue is muscovite. Note the rotation of the image relative to the AVIRIS data, here north is to the top. The bright red area (centre left of the top right image) is an area of illite, that corresponds to an

active mine area, with disseminated gold mineralisation. While the blue-green area consists of muscovite and kaolinite with no economic mineralisation. The image below (bottom right) is the corresponding map **after** the expert system stage, although the number of accepted pixels is reduced, the general distribution of clay materials remains unchanged, except for an area of illite (red) in the shape image (top right image, centre right), that is rejected in the expert system output (bottom right image). This essentially confines the illite distribution to the area of economic mineralisation currently being exploited (red, bottom right image).

The pixels with the highest matches from the material identification maps are the purest in the image and were used for input as end-members in the mixture algorithm. Seven end-members were identified by the expert system in the GER data. These were input into the mixture model and their **E** values are shown in column A, below.

End-members	A (%)	B(%)
Muscovite	16.5	9.0
Illite	8.4	
Dry vegetation	26.0	18.1
Calcite	14.2	11.9
Kaolinite	36.1	
Gypsum	32.2	
Green vegetation	11.9	8.4

The high errors using seven end-members provide proportion maps dominated by noise. To reduce this problem, those with the highest **E** values are dropped. Apart from the muscovite, these are the materials with 2.2 mm absorption features. As a result, muscovite acts as a composite "clay" end-member, but the errors are now reasonable (column B). The clay mixture map produces high estimates in the regions with clearly identified pixels from the shape match and expert system stages.

V. Vegetation application

Three vegetation communities are found in this region. In the dry periods the densities and the amount of dry and green material in their canopies differ. The graminaceous community consists of dense dry vegetation, while the chaemophytic community has an open canopy, with lower proportions of these materials and a lower density. As the amount of dry and green vegetation in each pixel is known it can be used to classify their distribution. If the geological mixture maps are added together a map is derived that depicts the amount of bare ground. These vegetation communities can now be thought of in terms of their distribution in the ternary mixture space of bare ground, green vegetation and dry vegetation. Where each community is dominant, it occupies a specific region of this mixture space.

A simple decision rule classifier can then be implemented to classify each community. If an area has >90% green vegetation for example, the annual shrub community will be dominant. A similar threshold on the dry vegetation will outline where the graminaceous community is dominant. A rather arbitrary threshold of >90% has been used to outline areas of dominantly bare ground. The

chaemophytic shrub community is highly variable in its density and also exhibits variations in the amount of dry and green vegetation in its canopy, it lies in the large region of this ternary mixture space not defined by the other decision rules.

Slide 16 shows the classified map resulting from this mixture space interpretation. The classes that are relatively pure such as the annual and graminaceous communities and the bare ground have solid colouring of green, yellow and red respectively. The region, where the chaemophytic shrub community dominates, exhibits large variations in density to show that a vegetation density map (derived by adding the dry and green vegetation maps together) is used as a backdrop. The community is displayed in various shades of cyan, where grey indicates a low density and bright cyan a high density.

VI. Conclusions

1. With current high spectral resolution data and a library of reflectance spectra, it is relatively easy to carry out a shape analysis of each pixel spectra and thus determine the identity of the spectrally dominant surface component.

2. An enhancement using an expert system stage that cross checks various data and library parameters enables a much clearer identification of materials present. With improvements it should allow the separation of components that would be misidentified using only the simple shape match.

3. Extraction of the purest material pixels provides an alternative method for determining end-members for a mixture model.

4. The mixture modelling extends the shape matching of pure materials to give a distribution of the identified components in each image pixel. However, very similar materials cannot be separated using mixture modelling due to their low contrast and high noise level of the imagery. They can be separated by the expert system as it uses a more robust matching technique, although the expert system cannot measure abundance or classify mixed pixels.

5. Linear mixture modelling, combined with field work to determine the vegetation phenology at the time of image acquisition and the various components in the plant canopy, is an effective method of deriving ecological parameters from imaging spectrometry data.

Preliminary Analysis of AVIRIS Data Acquired Over the Harvard Forest in Petersham, Massachusetts

M.E. Martin and J.D. Aber
Complex Systems Research Center
University of New Hampshire
Durham, New Hampshire

Abstract. The concentrations of nitrogen, lignin, and cellulose in canopy foliage are related to important ecosystem parameters such as litter decomposition rate, nutrient availability, and plant productivity. Previous work with both agricultural products and forest foliage has shown that relationships exist between reflectance at selected wavelengths in the near infrared (NIR) spectrum and nitrogen, lignin and cellulose concentrations. In this project, we extend this work to both the fresh leaf and canopy scale using data from an NIRS model 6250 spectrophotometer (leaf scale) and AVIRIS (canopy scale).

One-hundred seventy-five samples from eight deciduous and four conifer species were collected for the fresh leaf analysis. The laboratory spectra acquired for these samples ranged from 1100 to 2500 nm at 2-nm intervals with an effective bandwidth of 10 nm. Equations relating chemical concentration to NIR absorbance at 2170 nm (nitrogen), 2260 nm (lignin), and 1212 nm (cellulose) were developed with correlation coefficients of 0.89, 0.88, and 0.82, respectively.

AVIRIS data were acquired over the Harvard Forest in Petersham, Massachusetts, on 8 September 1990. Foliage samples collected from ten sites within several days of the overflight were analyzed for nitrogen, lignin, and cellulose content. A preliminary estimate of canopy lignin has been made using AVIRIS radiance data. Corrections for atmospheric effects will be made on this data using both LOWTRAN7 and field reflectance measurements. Retrieving canopy reflectance from AVIRIS data will be necessary for evaluating temporal changes occurring in canopy chemistry.

Increasing the signal-to-noise ratio of AVIRIS imagery through repeated sampling

Paul J. Curran
University College of Swansea
Singleton Park, Swansea, UK.

Jennifer L. Dungan
TGS Technology Inc., NASA/Ames
Moffett Field, California

Geoffrey M. Smith
University College of Swansea
Singleton Park, Swansea, UK.

Abstract. AVIRIS is currently one of the few imaging spectrometers available for investigations of the remote sensing of foliar chemistry. Unfortunately, the signal-to-noise ratio (SNR) of AVIRIS imagery is inadequate for discrimination of many of the spectral details associated with foliar chemicals. To increase the SNR of AVIRIS imagery the data can be averaged spatially but with a loss in spatial detail and an increase in the sample area needed in controlled field experiments. Here we investigated the potential of averaging temporally as a means of increasing the SNR of AVIRIS imagery. Three AVIRIS images were collected within a half hour period for a single study area in both March and September 1990. The SNR was estimated using 17-18, 2 x 2 matrices of spatially homogeneous pixels on both (i) the first image on each date and (ii) the temporal average of all three images on each date. Temporally averaging three AVIRIS images increased the SNR of the radiance spectra by an average of 66% and the derivative radiance spectra by an average of 50%. This technique offers the AVIRIS user increased SNR without the penalty of a decrease in spatial resolution. The adequacy of the resultant SNR for detecting signals caused by changes in foliar chemistry is still under investigation.

Introduction

The early flights of AVIRIS revealed a signal-to-noise ratio (SNR) that was less than that specified for the instrument (Vane *et al.*, 1988). Since then the SNR of AVIRIS imagery has increased but users, particularly those interested in vegetation, are looking for larger SNRs to enable the resolution of spectral details in radiance and derivative radiance spectra that have been associated with key foliar chemicals (Curran, 1990). Increasing the SNR by spatially averaging pixels is impractical for many of

these users because it would decrease the spatial detail and increase the sample area needed for controlled field experiments. At the first and second NASA workshops on the Remote Sensing of Plant Biochemical Content (Peterson and Dungan, 1990), it was suggested that the AVIRIS platform, NASA's ER-2 aircraft, could be used to permit temporal averaging of images as a means of increasing the SNR of AVIRIS data. This paper reports an experiment to determine if such temporal averaging improves this ratio.

Methods

AVIRIS data were acquired by NASA's ER-2 during 3 overpasses of a slash pine plantation near Gainesville, Florida on both 4 March 1990 and 6 September 1990. Between the first and last overpasses on each date there was an interval of approximately half an hour; from 19:02 GMT to 19:26 GMT in March and from 15:34 GMT to 16:00 GMT in September. Twenty plots were chosen for further analysis: on both fertilized and unfertilized forest and one each on pasture, bare ground, water and a road intersection. Radiance and derivative radiance spectra of these plots from the first overpass in September are illustrated in figure 1.

The study area was located on the images using a base map of the study site (Curran *et al.*, 1991) and an affine transform to relate map locations to image locations. The coefficients of the transform were generated using up to 12 ground control points distributed around the study area. The accuracy of the transform was estimated at ± 0.52 of a pixel. Some of the forested plots had been cropped off of the subscene during pre-processing, leaving a total of between 17 and 18 plots on which to estimate SNR.

Four methods have been used by investigators to estimate the SNR of AVIRIS data (Curran and Dungan, 1989). They differ primarily in the way that noise is measured. In the laboratory the noise is the standard deviation (s) of a mean ($\bar{x}$) signal, in the image data the noise can either be the s of the dark current, the s of a matrix of homogeneous pixels or the 'nugget' of a variogram calculated over a reasonably homogeneous transect or area. All of these measures are biased and so either inflate or deflate the SNR estimate in relation to that in the user's image. Here we used the ratio of the $\bar{x}$ to the s of a 2 x 2 matrix of pixels as our estimate of SNR. This gives an accurate estimate of the signal but an overestimate of the noise as it includes spatial variation among the 4 pixels.

A matrix of 2 x 2 pixels from an apparently homogeneous area was extracted from each plot for each image. The SNR of the radiance and derivative radiance spectra were calculated on data from one image from each date. To estimate the SNR of temporally averaged data, the SNR of the radiance and derivative radiance spectra were calculated on an average of data from three images for each date.

Results

Average SNR values for the 17-18 plots are summarized and presented in figure 2 and table 1. The SNR was larger in

(i) spectrometer B than in spectrometers A, C, or D.
(ii) September than in March imagery
(iii) radiance than in derivative radiance spectra and
(iv) temporally averaged data than in data from a single overpass.

Discussion

The reason for the larger SNR in spectrometer B than in A was not only because of the greater signal for most of the targets in the near infrared, but because of the periodic noise in spectrometer A, which has been a consistent problem with the instrument. The larger SNRs in September were caused by more signal than in March (figure 3) and because the levels of AVIRIS noise had been reduced during the summer of 1990 at the Jet Propulsion Laboratory. The SNR values were quite small in the derivative radiance spectra (figure 2b), reduced by about a factor of ten below the radiance SNRs.

The use of temporally averaged pixels has been shown in this study to increase the SNR of AVIRIS imagery, though this varied with spectrometer and date for both the radiance and derivative radiance spectra. For certain applications the resultant SNR may still be inadequate and so further research is required to determine the relationship between overpass number and SNR in each spectrometer and the number of overpasses needed to reach the asymptote in SNR for each spectrometer.

Conclusion

Temporally averaging three images of AVIRIS data increased the

SNR of radiance spectra by an average of 65% in March 1990 and 67% in September 1990 and increased the SNR of derivative radiance spectra by an average of 53% in March 1990 and 48% in September 1990.

References

Curran, P.J. (1990) Remote sensing of foliar chemistry. Remote Sensing of Environment, 29: 271-278.

Curran, P.J. and J.L. Dungan (1989) Estimation of signal-to-noise; a new procedure applied to AVIRIS data. IEEE Transactions on Geoscience and Remote Sensing, 27:620-628.

Curran, P.J., J.L. Dungan and H.L. Gholz (1991) Seasonal LAI in slash pine estimated with Landsat TM. Remote Sensing of Environment, in press.

Peterson, D.L. and J.L. Dungan (1990) Research directions in remote sensing of plant biochemical content. Applications and Developments in Imaging Spectrometry, British National Space Centre, London, U.K., pp. 48-53.

Vane, G., W.M. Porter, J.H. Reimer, T.G. Chrien and R.O. Green (1988) AVIRIS performance during the 1987 flight season: An AVIRIS project assessment and summary of the NASA-sponsored performance evaluation. In Vane, G. (ed) Proceedings of the Airborne Visible/Infrared Imaging Spectrometer (AVIRIS) Performance Evaluation Workshop, JPL Pub. 88-38, Jet Propulsion Laboratory, Pasadena, California, pp. 1-20.

Acknowledgements

The authors wish to thank Dr. Diane Wickland of NASA's Ecosystem Dynamics and Biogeochemical Processes Branch for sponsoring the AVIRIS data acquisition, the Natural Environment Research Council (UK) for funding GS, and Lee Johnson, Dr. Roy Armstrong and Dr. Giles Foody for their comments on the text.

Table 1. Percent increase in SNR between a single AVIRIS image and a temporal average of three AVIRIS images.

Date	Spectra	Spectrometer			
		A	B	C	D
March 4	Radiance	87	61	61	52
March 4	Derivative radiance	71	63	38	41
September 6	Radiance	114	52	33	68
September 6	Derivative radiance	38	70	48	35

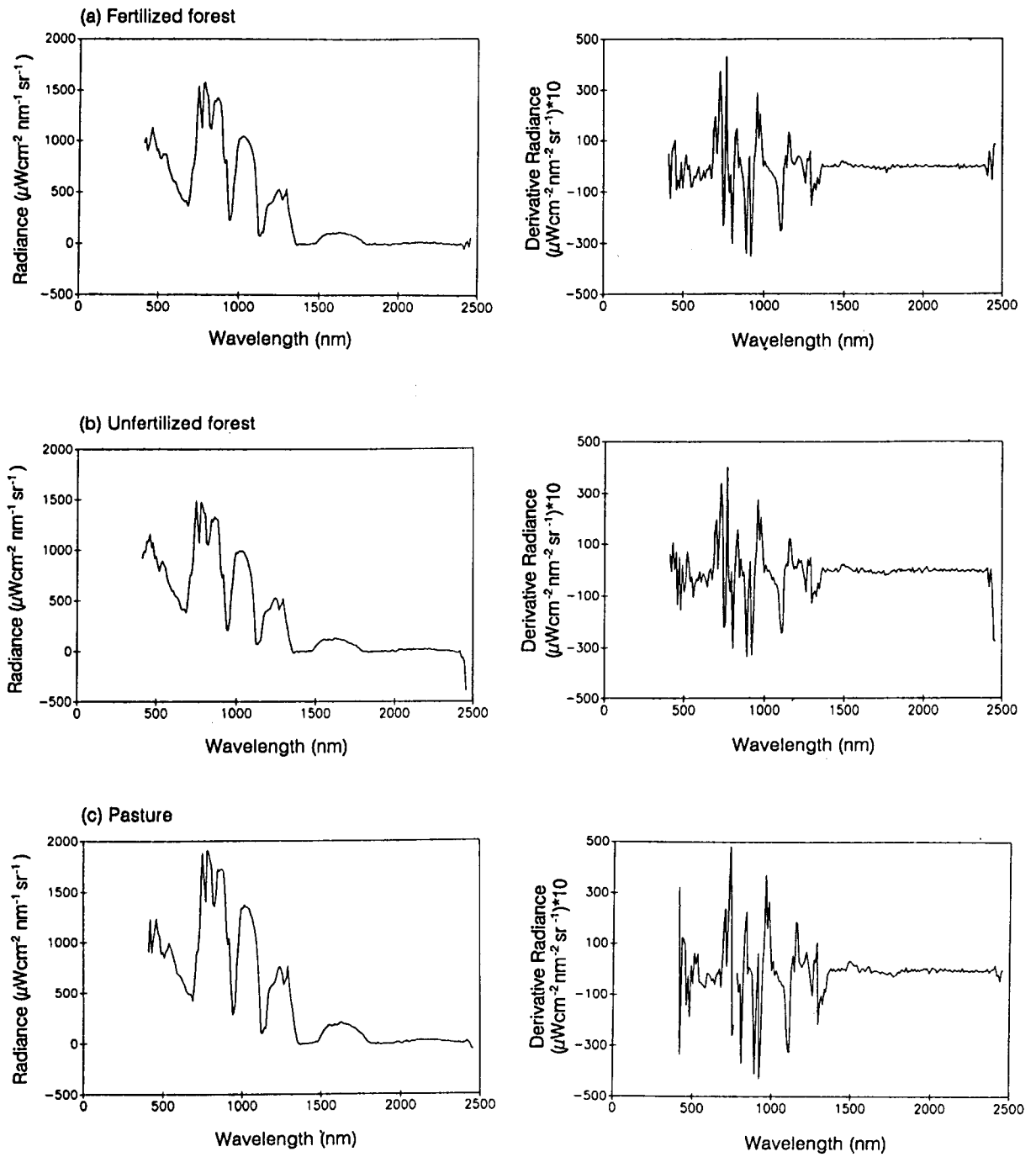

Figure 1. Radiance and derivative radiance spectra for the plots used for the estimation of SNR. These spectra are averages of the 2x2 matrices from the first overpass on September 6, 1990.

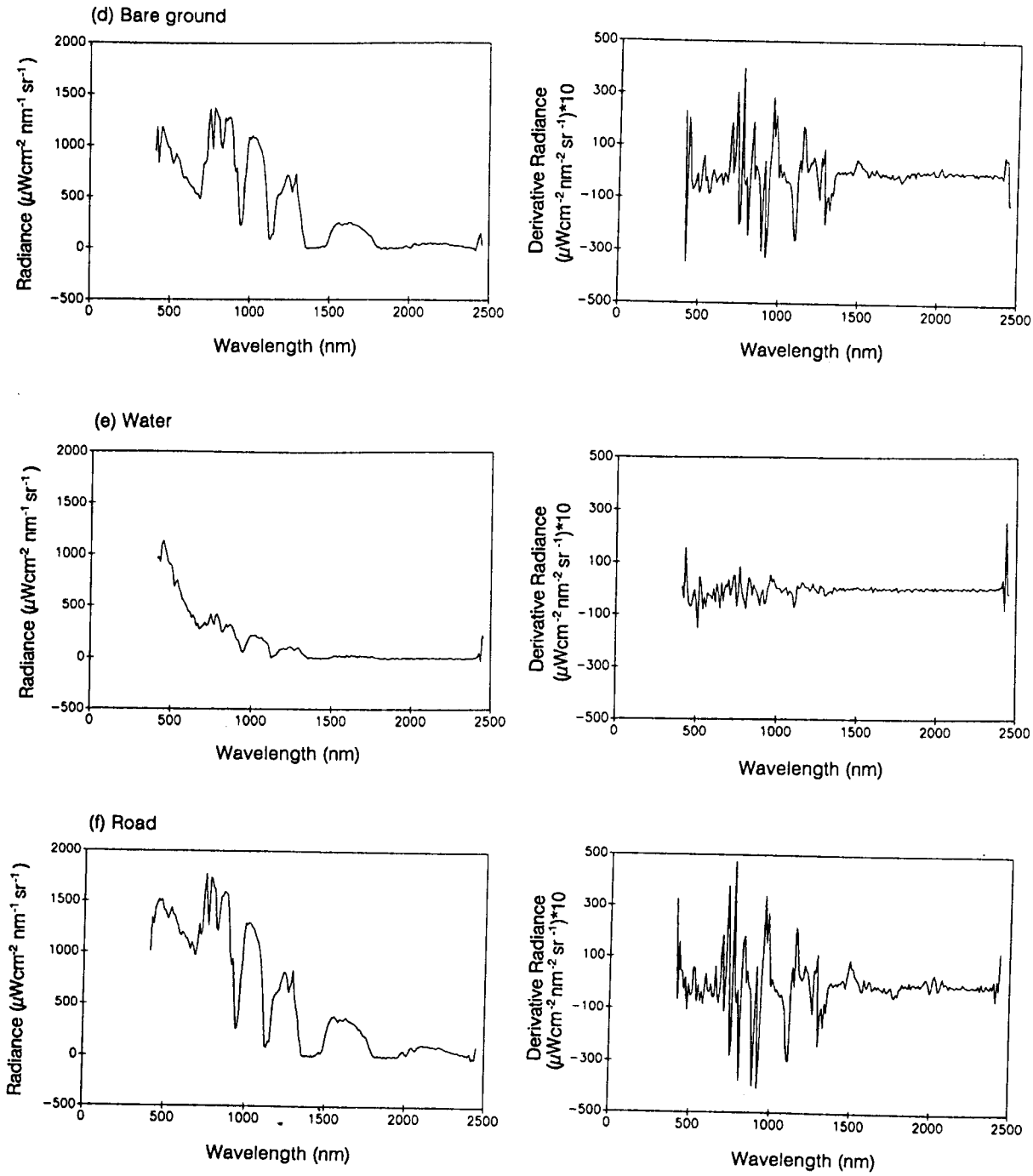

Figure 1. (continued)

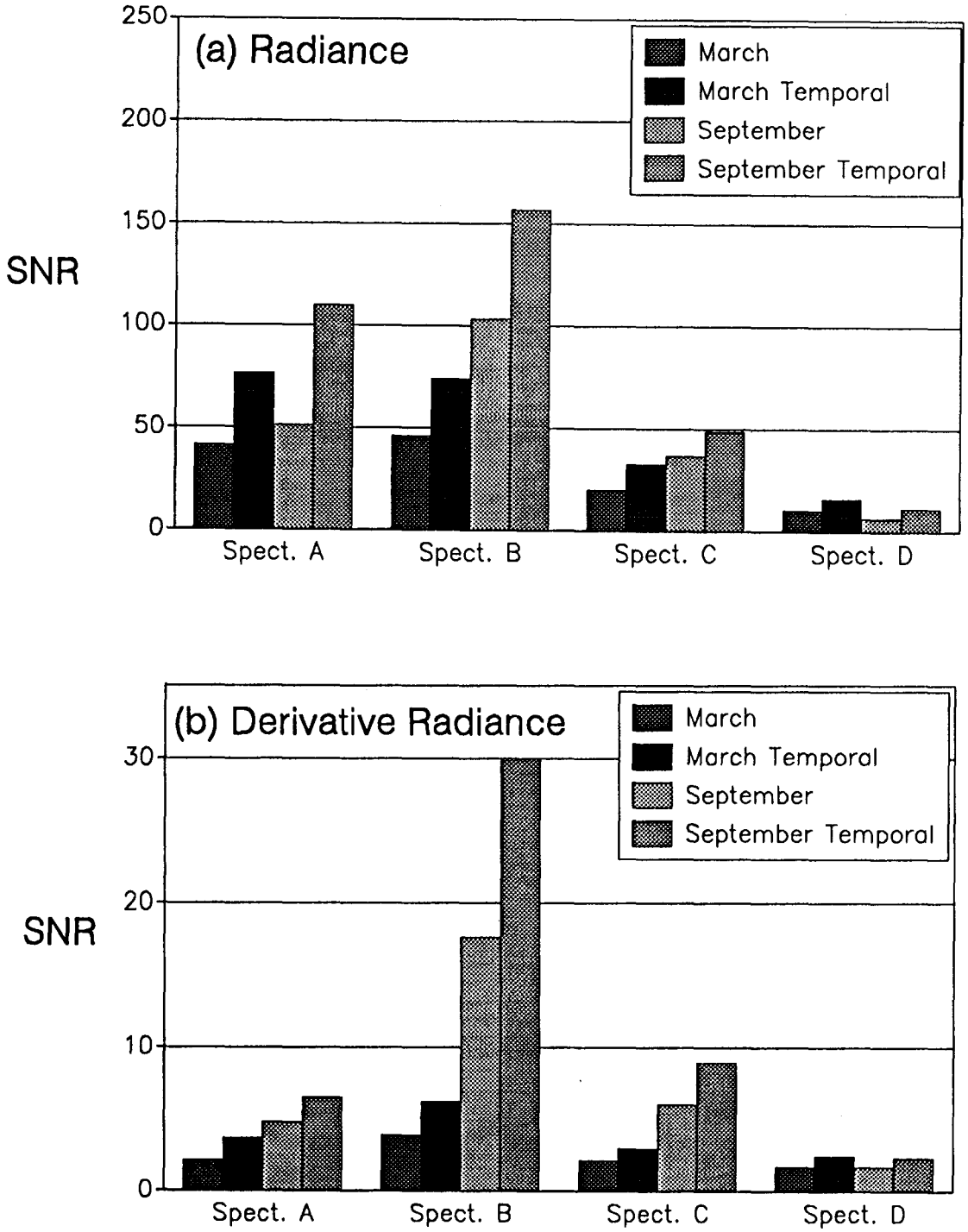

Figure 2. The SNR averaged by spectrometer for radiance spectra and derivative radiance spectra. Note the larger SNR for temporally averaged images and those recorded in September.

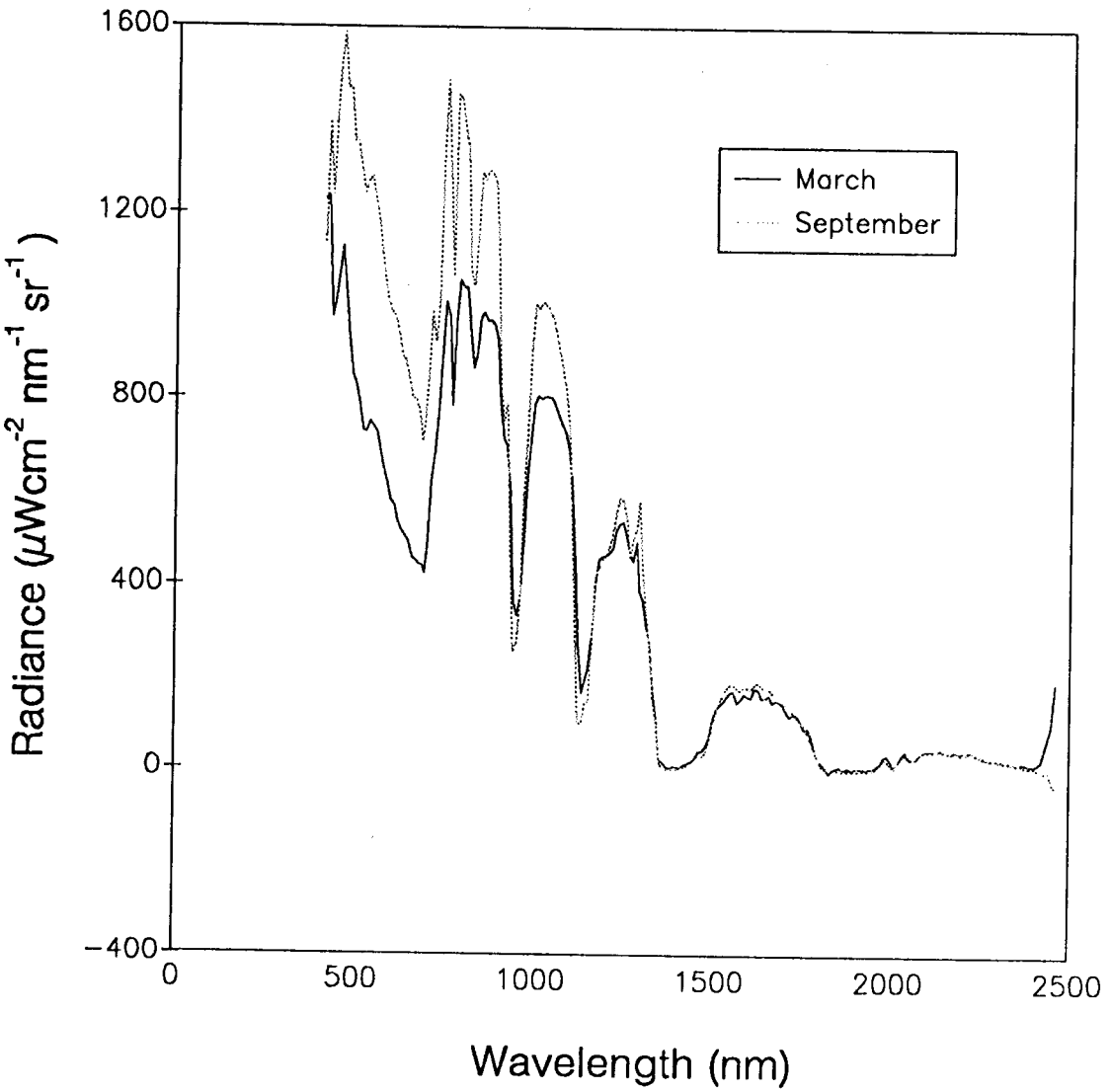

Figure 3. The average radiance for the last overpass on March 4 and September 6; note that the September image is brighter that the March image.

Classification of Forest Stands in British Columbia Using AVIRIS Data: A Preliminary Investigation

K. Staenz
Canada Centre for Remote Sensing
Ottawa, Ontario, Canada

D. Schanzer and C. Kushigbor
Intera Kenting
Ottawa, Ontario, Canada

Abstract

Data normalization for removal of atmospheric effects, data reduction (band-moment analysis, feature selection), and integration of Geographic Information System/Remote Sensing data were applied to an Airborne Visible/Infrared Imaging Spectrometer (AVIRIS) data set for an investigation of the potential for classification of forest stands within a mountain forest ecosystem. Preliminary classification accuracies of approximately 94%, achieved with the maximum likelihood classifier for the training data selected from homogeneous polygons, indicate that AVIRIS data have some potential for classification.

I. Introduction

Labelling of forest polygons with respect to species composition, tree height and age, crown closure, etc., is an important mandate within the British Columbia Ministry of Forests (BCMOF) for inventorying and inventory updates of the forest resources. The objectives of the inventory program are to develop and maintain a quantitative description of the forest resources in the province. Satellite and airborne imagery are viewed as a potential replacement of aerial photography which is used in the creation of the forest inventory polygons. The identification of homogeneous forest stands is a precursor to implementing a sampling strategy designed to assist in the interpretation of remotely sensed data. The main limitations to successful classification from remotely sensed data remains the non-homogeneity of many of the existing forest polygons.

In this paper, the separability of homogeneous forest polygons is investigated by maximum likelihood classification of band moments generated from the spectral signature of selected homogeneous forest polygons from an Airborne Visible/Infrared Imaging Spectrometer (AVIRIS) data set acquired over a forested area in British Columbia, Canada. The homogeneous polygons were identified by integration of the existing Geographic Information System (GIS) forest data base maintained by BCMOF. Moments are summary measures of the spectrum shape and were used to reduce the spectral dimensionality for classical discriminant analysis. Analysis procedures need to be developed to take advantage of the high spectral resolution of hyperspectral data sets such as AVIRIS at the least cost by minimizing the computation time. An additional challenge in the analysis of imaging spectrometer data includes the understanding of the interaction between the spectral signature and the atmosphere for data normalization purposes. The data processing was conducted using the Imaging Spectrometer Data Analyzer (ISDA) software package implemented

at the Canada Centre for Remote Sensing (Staenz and Goodenough, 1989).

II. Field Campaign

A. Data Acquisition

AVIRIS data were collected over three forested areas in the Kootenay Valley near Invermere in south-eastern British Columbia, Canada, on August 14, 1990 as part of a multi-aircraft campaign involving the CCRS C- and X-band SAR (Synthetic Aperture Radar) and 8-band pushbroom imager MEIS (Multi-detector Electro-optical Imaging Sensor). These instruments are described in detail by Till et al. (1986), Livingstone et al. (1987), and Porter and Sumark (1987). In addition, Landsat Thematic Mapper (TM) as well as SPOT High Resolution Visible (HRV) multi-spectral and panchromatic data were also acquired over the test sites together with aerial photography of 1:35,000 and 1:60,000 scales. Available GIS information of the test sites on a 1:20,000 scale include digital terrain models, forest inventory maps and forest attribute information. Ground reference information was collected on a point basis covering a circular area with a radius of 10 m. Such plots were then used to characterize the forest stands in terms of species composition, crown closure, age, nutrient regime, foliar chemistry, etc. Ground-based spectral measurements were carried out for data normalization purposes in an absolute sense over selected reference targets such as water, grass, and gravel.

B. Test Site

The test scene used for the investigation described in this paper is relatively flat with variations in elevation of less than 100 m and is situated between the Columbia and Kootenay Rivers, approximately 900 m above sea level. The climatic condition of the area is dry with a mean annual precipitation of 30 cm and the soil nutrient regime is poor to medium for the different forest stands. The combined influence of soil and climatic factors on vegetation result in the IDF (Interior Douglas Fir) biogeoclimatic zone (Krajina, 1969). Associated main tree species in the area are lodgepole pine (Pinus contorta Dougl.) and yellow pine (Pinus ponderosa Laws.) with some minor inclusion of englemann spruce (Picea englemanni Parry), larch (Larix Mill.), and aspen (Popolus tremuloides Michx.). The 30 to 200 year old forest stands were selectively logged several times over the years resulting in crown closures generally below 60 percent.

III. Data Analysis

A. Preprocessing

Radiometrically corrected (calibrated) AVIRIS data with a total of 224 bands covering a wavelength range from 400 to 2450 nm (Chrien et al., 1990; Green et al., 1990) were analyzed for this investigation. A distinct "herringbone" noise pattern predominated in the first 12 bands. In addition, these bands also indicated a periodic

noise pattern in the vertical and horizontal direction (Bailey, 1988). A removal of these fixed noise patterns was not carried out, hence these bands were not included for subsequent analysis. The last couple of bands containing erroneous data due to a low signal-to-noise ratio (SNR) were also eliminated. Overlapping bands between the spectrometers were then eliminated keeping the bands of the spectrometer with the higher SNR.

The data were then normalized using an altitude dependent version of the semi-analytical 5S code (Tanré et al., 1986; Teillet and Santer, 1991a; Teillet et al., 1991b) for a viewing angle dependent removal of the scattering effects and the flat-field approach (Roberts et al., 1986) for a first order correction of the gaseous transmittance. The spectrum from a paved road (main highway), used as a spectrally flat field, was divided into the spectrum of each pixel in the scene after correction for scattering effects. Input parameters for the 5S code run are listed in Table 1. The flat-field normalization technique is already quite effective as demonstrated in Figure 1 for different forest stands before and after normalization. However, the spectra in Figure 2 look more like typical vegetation curves after removing the scattering effects. These spectra have the distinct green peak at 545 nm, the chlorophyll well around 680 nm, and the infrared plateau beyond 750 nm. Most of the atmospheric absorption features were eliminated with the exception of the strong water vapour absorption regions around 1400 nm and 1900 nm. The amplitudes were therefore set to zero in these areas.

B. GIS Information

In order to access the GIS information, the forest cover map was registered to the AVIRIS scene with the nearest neighbour resampling technique resulting in a RMS error of ± 1.50 in the pixel direction and ± 0.95 in the line direction. GIS attribute information characterizing each forest stand (polygon) is then fully available for further processing of the data, i.e., for classification purposes and classification accuracy assessment. Map-to-image registration has the advantage of resampling only the map data (3 thematic channels) and leaving the pixel values in the scene (224 bands) unchanged. In this case, computation time is minimized and the radiometric accuracy is maintained.

C. Data Reduction

Moments were generated from the normalized AVIRIS data set in order to reduce the spectral dimensionality. This procedure was successfully used for the labelling of agricultural targets using imaging spectrometer data acquired with the Programmable Multispectral Imager (PMI) as reported by Staenz and Goodenough (1990). In this case, the band number was used for the band-moment calculations since the PMI bands are evenly spaced. For the AVIRIS data, however, the wavelength was included in the computation due to the different sampling intervals of the spectrometers and the wavelength gap between spectrometers which is on the order of half of the sampling interval. The formulae for the p^{th} moment, M_p, and the central

band moment, m_p, for the discrete case are (similar to Rundquist and Di, 1989):

$$M_p = \frac{1}{\Delta\lambda_T} \sum_{\lambda=\lambda_1}^{\lambda_n} [\lambda^P * f(\lambda) * \Delta\lambda] \tag{1}$$

and

$$m_P = \frac{1}{\Delta\lambda_T} \sum_{\lambda=\lambda_1}^{\lambda_n} [(\lambda-\bar{\lambda})^P * f(\lambda) * \Delta\lambda] \quad , \tag{2}$$

where

$$\Delta\lambda_T = \sum_{\lambda=\lambda_1}^{\lambda_n} \Delta\lambda \quad , \tag{3}$$

$$\bar{\lambda} = \frac{M_1}{M_0} \quad , \tag{4}$$

and $p = 0,1,2,...$ is the moment order, $\lambda = \lambda_1,...\lambda_n$, is the central wavelength in band 1,...n, $f(\lambda)$ is the pixel value for wavelength λ, $\Delta\lambda_T$ is the total wavelength range covered by the sensor, $\bar{\lambda}$ is the wavelength mean, and $\Delta\lambda$ is the average of the adjacent sampling intervals. In addition, the band-concentrated moment was calculated as follows:

$$m_{2c} = \frac{1}{\Delta\lambda_T} \sum_{\lambda=\lambda_1}^{\lambda_n} [(\lambda-|\lambda-\bar{\lambda}|)^2 * f(\lambda) * \Delta\lambda] \quad . \tag{5}$$

The normalized central band and normalized band-concentrated moment can be expressed as

$$\mu_P = \frac{m_p}{M_o} \text{ and } \mu_{2C} = \frac{m_{2c}}{M_o} \quad . \tag{6}$$

Further band-moment ratios were calculated as follows:

$$\gamma_1 = \frac{\mu_3}{\mu_2^{3/2}} \quad \text{and} \quad \gamma_2 = \frac{\mu_4}{\mu_2^2} - 3 \quad , \tag{7}$$

where γ_1 is the coefficient of skewness and γ_2 is the coefficient of excess (kurtosis).

The band-moment approach was applied in the spectral domain on each pixel resulting in the eight moments as follows: (1) ordinary moment (M_o), (2) mean (λ), (3) variance (μ_2), (4) 3rd moment (μ_3), (5) 4th moment (μ_4), (6) skewness (γ_1), (7) kurtosis (γ_2), and (8) band-concentrated moment (μ_{2c}). The computed real values of these moments were then transformed linearly into an 8-bit data set. The advantage of this technique is that it takes the entire spectrum into account and automatically reduces the dimensionality of the data set substantially without detailed knowledge of the spectrum itself.

D. Forest Stand Separability

Percent crown closure was selected as the separability criterion due to the importance of this parameter for growth and yield prediction modelling. Class generation as well as elimination of the non-productive forest and non-forest land was conducted according to the GIS information leaving the productive forest for subsequent analysis. Training samples, varying between 60 and 204 pixels for a specific class, were collected within homogeneous polygons in order to minimize the variation within a class. This selection criterion is important for classification purposes since a polygon can encompass a variety of crown closure classes. In this case, an integrated crown closure estimation of the major species is represented in the polygon label. This parameter derived from aerial photography is related to the timber volume which can cause additional problems for a discrimination of targets using remotely sensed data. The training data set consists of six classes as outlined in Table 2. Each of the classes covers a crown closure range of 10%, except for class six where categories were combined due to the limited number of polygons with a crown closure above 60%. The maximum likelihood classifier was then used to discriminate the training data based on selected band-moment combinations. The best subsets of the eight moments were derived on the basis of a feature selection using the branch and bound algorithm (Goodenough et al., 1978).

The weighted mean classification accuracy (± standard error of mean) varies from 51.67 ± 9.84% for the best single band (band-concentrated moment) to 93.81 ± 0.85% for the entire band set. An acceptable result of 89.56 ± 1.23% was already achieved with the best four-band combination (ordinary moment, variance, kurtosis, band-concentrated moment). Confusion between the crown closure classes could not be resolved entirely as shown in Table 2 for the eight-band combination. These preliminary results should be interpreted with caution because the training data for the crown closure classes were selected irrespective of species, age, height, and site quality. Combining a variety of forest stands into the training data was necessary to cover the full crown closure range for homogeneous polygons. In addition, the reliability of the polygon labels is not known. The results, however, show potential for the use of AVIRIS data in discriminating between homogeneous forest stands with different attributes.

IV Conclusion

Data normalization and data reduction procedures were applied to the AVIRIS data set prior to classification. Atmospheric correction using an altitude dependent version of 5S in order to remove the scattering effects and followed by a flat-field normalization to remove the gaseous absorption effects resulted in typical vegetation spectra for pixels from forested areas. In a next step, the normalized data set was reduced by a factor of 28 using the band-moment analysis approach.

Preliminary maximum likelihood classification of the band moments generated from the spectral signature of homogeneous forest stands resulted in 94% mean classification accuracy for the crown closure training data set. Caution should be used in the interpretation of the results, since the training data set was not controlled for species, age, height, and site quality. However, identification of homogeneous polygons appears possible, implying that potential exists for the use of AVIRIS data in improving or verifying the polygon homogeneity. The identification of homogeneous forest stands, combined with ground reference information, is a prerequisite for forest classification purposes using remotely sensed data.

Acknowledgement

The authors wish to thank the Inventory Branch of the British Columbia Ministry of Forests for their support of the entire project, and D.G. Goodenough and J.-F. Meunier for their assistance in data processing. Our thanks go to A. Kalil for word processing the manuscript.

References

Bailey, G.B., 1988, "AVIRIS Data Characteristics and Their Effects on Spectral Discrimination of Rocks Exposed in the Drum Mountains, Utah: Results of a Preliminary Study", Proceedings of the Airborne Visible/Infrared Imaging Spectrometer (AVIRIS) Performance Evaluation Workshop, JPL88-38, Pasadena, California, U.S.A., pp.109-121.

Chrien, T.G., R.O. Green, and M.L. Eastwood, 1990, "Accuracy of the Spectral and Radiometric Calibration of the Airborne Visible/Infrared Imaging Spectrometer (AVIRIS)", Proceedings of the Second Airborne Visible/Infrared Imaging Spectrometer (AVIRIS) Workshop, JPL90-54, Pasadena, California, U.S.A., pp.1-14.

Goodenough, D.G., P.M. Narendra, and K. O'Neill, 1978, "Feature Subset Selection in Remote Sensing", Canadian Journal of Remote Sensing, Vol.4, No.2, pp.143-148.

Green, R.O., J.E. Conel, V. Carrere, C.J. Bruegge, J.S. Margolis, M. Rast, and G. Hoover, 1990, "Determination of the In-Flight Spectral and Radiometric Characteristics of the Airborne Visible/Infrared Imaging Spectrometer (AVIRIS)", Proceedings of the Second Airborne Visible/Infrared Imaging Spectrometer (AVIRIS) Workshop, JPL90-54, Pasadena, California, U.S.A., pp.15-34.

Krajina, V.J., 1969, "Ecology of Forest Trees in British Columbia", Ecology of Western North America, Vol.1, No.2, pp.1-146.

Livingstone, C.L., A.L. Gray, R.K. Hawkins, J.G. Halbertsoma, R.A. Deane, and R.B. Olson, 1987, "CCRS C-band Airborne Radar-System Description and Test Results", Proceedings of the Eleventh Canadian Symposium on Remote Sensing, Waterloo, Ontario, Canada, pp.503-518.

Porter, W.M. and H.T. Sumark, 1987, "A System Overview of the Airborne Visible/-Infrared Imaging Spectrometer (AVIRIS)", Proceedings of the SPIE Conference on Imaging Spectrometry II, Vol.834, San Diego, California, U.S.A., pp.22-31.

Roberts, D.A., Y. Yamaguchi, and R.J.P. Lyon, 1986, "Comparison of Various Techniques for Calibration of AIS Data", Proceedings of the Second Airborne Imaging Spectrometer Analysis Workshop, JPL86-35, Pasadena, California, U.S.A., pp.21-30.

Rundquist, D.C. and L. Di, 1989, "Band-Moment Analysis of Imaging Spectrometer Data", Photogrammetric Engineering and Remote Sensing, Vol.55, No.2., pp.203-208.

Staenz, K. and D.G. Goodenough, 1990, "Airborne Imaging Spectrometer Data Analysis Applied to an Agricultural Data Set", Proceedings of ISPRS Mid-Term Symposium, Commission VII, Victoria, B.C., Canada, (in press).

Staenz, K. and D.G. Goodenough, 1989, "Imaging Spectrometer Data Analysis System", Proceedings of the Image Processing '89 ASPRS Conference, Sparks, Nevada, U.S.A., pp.12-22.

Tanré, D., C. Deroo, P. Duhaut, M. Herman, J.J. Morcrette, J. Perbos, and P.Y. Deschamps, 1986, Simulation of the Satellite Signal in the Solar Spectrum (5S) User's Guide, Laboratoire d'Optique Atmosphérique, Université des Sciences et Techniques de Lille, 58655 Villeneuve d'Ascq Cédex, France, 343 pages.

Teillet, P.M. and R. Santer, 1991a, "Terrain Elevation and Sensor Altitude Dependence in a Semi-Analytical Atmospheric Code", Canadian Journal of Remote Sensing, Vol.17, No.1, pp.36-44.

Teillet, P.M., K. Staenz, and G. Fedosejevs, 1991b, "A Prototype Atmospheric Correction Scheme for Airborne Imaging Spectrometer Data", Proceedings of the Fourteenth Canadian Symposium on Remote Sensing, Calgary, Alberta, Canada, pp.394-399.

Till, S.M., R.A. Neville, W.D. McColl, and R.P. Gauthier, 1986, "The MEIS II Push-broom Imager - Four Years of Operation", Proceedings of the ISPRS Symposium (ESA SP-151), Stuttgart, Germany, pp.247-253.

TABLE 1: 5S input parameters.

Atmospheric model	No gaseous absorption
Aerosol type	Continental model
Date of overflight	August 14, 1990
Solar zenith angle	35.69 degrees
Solar azimuth angle	182.73 degrees
Sensor zenith angle	Variable
Sensor azimuth angle	32.68 degrees
Ground elevation	0.900 km
Sensor altitude above sea level	19.844 km
Horizontal visibility	50 km

TABLE 2: Confusion matrix between six crown closure classes generated with the maximum likelihood classification procedure for the eight-band training data set. The crown closure classes are: (1) 6-15%, (2) 16-25%, (3) 26-35%, (4) 36-45%, (5) 46-55%, and (6) >56%.

CLASS	1	2	3	4	5	6
1	93.0	3.0	0.8	0.0	0.0	0.0
2	6.6	93.9	2.7	0.0	0.0	0.0
3	0.4	3.1	96.5	0.0	0.0	0.0
4	0.0	0.0	0.0	92.3	2.0	7.6
5	0.0	0.0	0.0	2.3	93.8	3.0
6	0.0	0.0	0.0	5.4	4.2	89.4
Unclassified	0.0	0.0	0.0	0.0	0.0	0.0

Figure 1a:

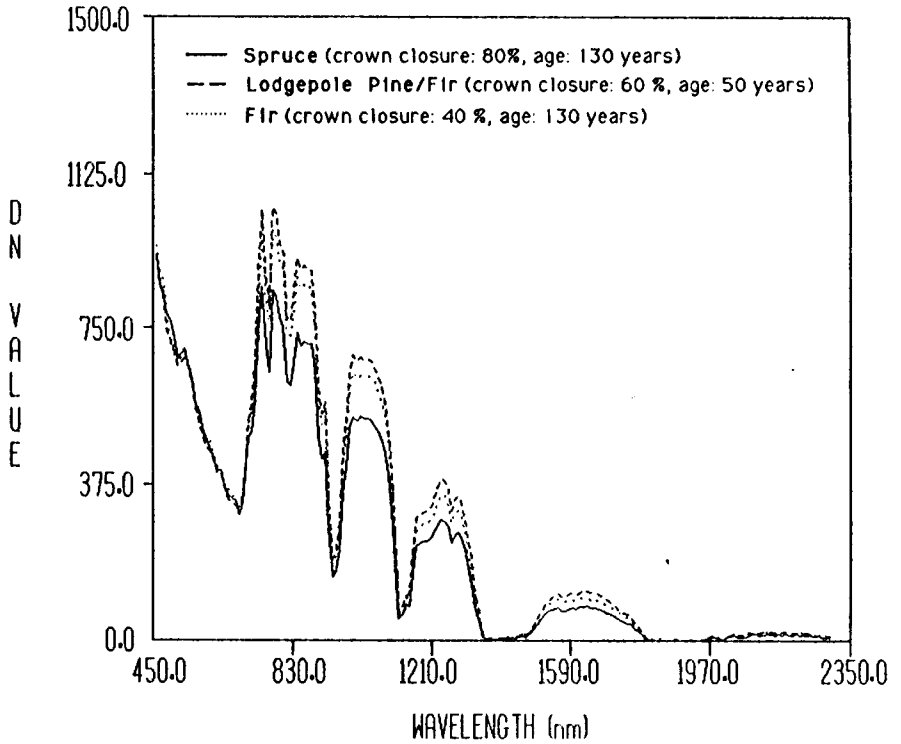

Figure 1b:

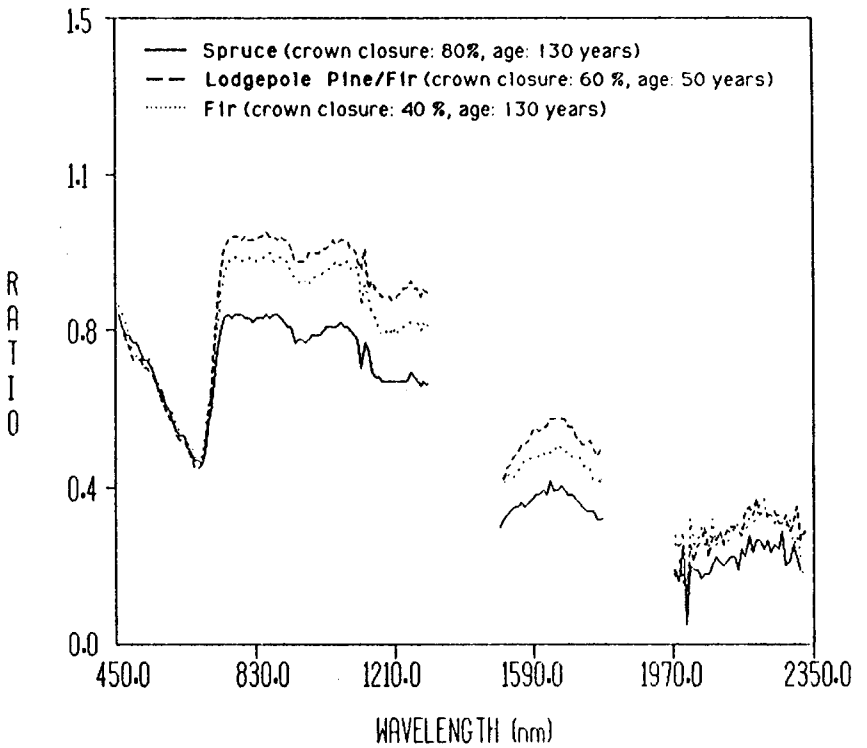

FIGURE 1: AVIRIS spectra of different forest targets (a) before and (b) after relative normalization using the flat-field approach.

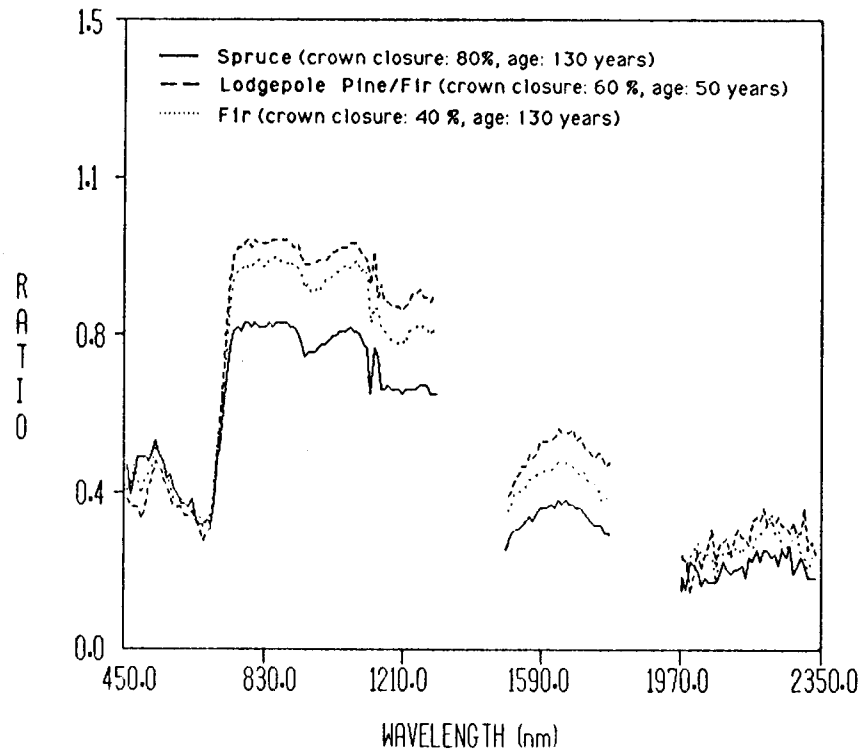

FIGURE 2: Data normalization applied to the spectra of Figure 1a using the 5S code followed by the flat-field approach.

DETECTION OF TRACE QUANTITIES OF GREEN VEGETATION IN AVIRIS DATA

Christopher D. Elvidge
Desert Research Institute
and Agricultural Experiment Station
University of Nevada System
Reno, Nevada

Zhikang Chen and
Fredrick P. Portigal
Desert Research Institute
University of Nevada System
Reno, Nevada

David P. Groeneveld
Inyo County Water Department
Bishop, California

ABSTRACT. The reflectance of an annual grassland area was tracked from spring through early summer and early fall using three dates of ground-reflectance calibrated AVIRIS data sets acquired in 1989. The grassland exhibited green vegetation spectral features in the spring. The dominant annual grasses were senesced in early summer and early fall imagery, though the site still had trace quantities of green herbaceous vegetation present. The chlorophyll red edge, from 700 to 730 um, is still present in the dry grassland spectra. This red edge, and the green vegetation it represents, would not have been detected with data from broadband sensors.

I. INTRODUCTION

The detection of trace quantities (less than 10% cover) of green vegetation using remotely sensed data continues to be problematic. A series of red versus near infrared (NIR) vegetation indices have been developed for use on data from multispectral instruments such as SPOT, Landsat Thematic Mapper, and NOAA AVHRR (Tucker, 1979). The red versus NIR vegetation indices operate by contrasting the magnitude of chlorophyll pigment absorptions in the red with the high reflectance of green leaves in the NIR. These broad band vegetation indices have not been effective under low green canopy cover conditions because background materials (rocks, soils, litter, and senesced plant materials) produce a range of vegetation index values (Elvidge and Lyon, 1985; Elvidge, 1990).

The advent of high spectral resolution remote sensing opens up the possibility of extending the detection limits for green

vegetation. The chlorophyll red edge (Collins, 1978) is the most prominent spectral feature of vegetation in the visible and near infrared region. The sharp definition of the chlorophyll red edge makes it an ideal feature to consider for use in detecting trace quantities of green vegetation. The detection and measurement of the chlorophyll red edge require high spectral resolution. Broad band sensors, such as SPOT or Thematic Mapper, are unable to directly measure this spectral feature.

Using 1988 and 1989 AVIRIS data converted to units of ground reflectance, the authors (Elvidge and Mouat, 1989; Elvidge et al., 1990) determined that the chlorophyll red edge persisted to levels of green vegetation covers of 3.0 to 5.0% for plantation grown pine trees. In this paper we report the results obtained from AVIRIS data extracted from an annual grassland on three dates in 1989, spanning spring, summer, and fall phenological conditions.

II. STUDY SITE

An AVIRIS flight line over Stanford University's 1200 acre Jasper Ridge Biological Preserve was established in 1987. In addition to Jasper Ridge, this flight line is designed to provide AVIRIS data of a series of calibration targets.

Jasper Ridge is located west of the main Stanford campus, in the foothills of the Santa Cruz Mountains. The preserve contains examples of the primary plant communities of the central California coast. Jasper Ridge has been the site of biological investigations for more than 90 years and has numerous ongoing ecological and physiological studies. The plant community used in this study is the annual grassland present on top of the ridge. A low altitude aerial photograph of the grassland is shown in Figure 1 (Slide 17). The species in this area are largely annuals, with introduced grasses making up the bulk of the biomass. The species present include: Wild Oat (Avena fatua), Slender Wild Oat (A. barbata), Soft Chess (Bromus mollis), Ripgut Grass (B. rigidus), and Tarweed (Madia sativa). In some portions of the grassland there is an encroachment of a perennial shrub known as Coyote bush (Baccharis pilarus).

The climate at Jasper Ridge is described as Mediterranean, with cool temperatures and the largest portion of the precipitation occurring as winter rains. Precipitation is variable but averages 60 to 75 cm per year. Summers are hot and dry. The plants at Jasper Ridge have developed a variety of strategies for adapting to summer drought conditions. Annual grassland species begin growth in the winter and complete their life cycle with seed production in the late spring. By early

summer the annual grasslands are largely senesced.

III. AVIRIS DATA ACQUISITION AND PREPROCESSING

The Jasper Ridge flight line was flown three times in 1989:

1. April 13, 1989 at 12:52 local time - Spring conditions.
2. June 2, 1989 at 13:07 local time - Early summer conditions.
3. September 20, 1989 at 13:48 local time - Early fall conditions.

The April and September data sets were radiometrically corrected at the Jet Propulsion Laboratory, using procedures described by Vane et al. (1987). The radiometric correction includes the following procedures:

1. Correction for vignetting effects (differences in the optical response, depending on the position in the field of view).

2. Subtraction of dark current values (recorded in-flight).

3. Conversion to units of radiance using preflight calibration. This procedure includes a normalization of the response for the individual detectors.

4. Cross track spatial resampling is performed to correct for the detector read out delay. This delay between the read out of successive bands results in a cross track shift of pixels amounting to one pixel between the first and last bands within a spectrometer.

The dark current file for the June data could not be recovered from the flight tape. As a result, the normal radiometric correction could not be applied to the data. The raw June data was simply corrected for the detector read out delay.

IV. CALIBRATION TO GROUND REFLECTANCE

The flight line contains five calibration targets that cover a wide range of reflectance values. The calibration targets are large homogeneous surfaces that are used to develop digital number (DN) to ground reflectance equations in each of the AVIRIS data sets. The brightest target is the flat-lying corrugated metal roof of San Francisco Water Department's Pulgas Balancing Reservoir. The roof is painted a buff tan color and is a reflectance of 35 to 45 %. There are two targets of intermediate brightness, an asphalt parking lot at Canada College and

Humpheries polo field, both having reflectance ranges of 10 to 30 %. Two dark targets are used, Searsville Lake and the black rubber running track at Canada College. The running track reflectance ranges from 1 to 3 %. The lake water is only used for calibration in the infrared, where its reflectance is in the 0.1 to 1.0 % range.

Laboratory reflectance spectra were acquired of samples of the calibration targets (except the lake). Lake water reflectance was measured in 1987 using a field spectrometer suspended over deep water. The digital number values for each calibration target pixel have been paired to the average ground reflectance value determined for the surface in each of the 224 bands. These DN - ground reflectance pairs were plotted and visually examined. Linear regression was used to develop equations to convert DN values into units of ground reflectance. This procedure was repeated for the three dates of imagery, producing three series of gains and offsets for converting AVIRIS DN values to units of ground reflectance. Figures showing the gains and offsets for the three dates of AVIRIS data are provided in Elvidge and Portigal (1990).

V. GRASSLAND SPECTRA

A block of 20 pixels (4 by 5) from the annual grassland was extracted from the three dates of AVIRIS data. The low altitude aerial photograph of Figure 1 was used to locate the same areas for extraction in the three data sets, and to avoid selection of pixels containing isolated trees present in the grassland. The DN values from each block of pixels were averaged and then converted into units of ground reflectance using the equation factors developed through the calibration procedure. The three dates of grassland spectra are plotted in Figure 2.
The three spectra are offset vertically to avoid overlap. The reflectance at 0.8 um is provided for each spectrum.

The April spectrum exhibits chlorophyll and leaf water absorption features, typical of lush green vegetation. Most of the annual plants which were green on April 13 are dry and brown by June 2. Major changes occur in the reflectance of the grassland with the onset of senescence. In the June spectrum there is a loss of chlorophyll absorption, a loss of water absorption at 1.15 um and at longer wavelengths. With the loss of absorption due to leaf water, lignin-cellulose absorptions emerge at 2.09 and 2.27 um. In addition, the slope of the 0.7 to 1.1 um region has increased in the June data. These spectral changes have been documented in laboratory reflectance spectra and are diagnostic for the transition from green to dry-senesced plant materials (Elvidge, 1987 and 1990). The staggered life

cycles of the annual plants present in the grassland means that there are still green plants present in June and September. The amount of green vegetation in June and September is less than 5 % cover and consists principally of tarweed and occasional Coyote bushes. The presence of trace quantities of green vegetation during June and September results in the minor chlorophyll red edge present in the spectra at 0.7 um.

VI. CONCLUSION

A series of spectral changes associated with phenological progression have been observed in annual grassland vegetation of the central California coast in three 1989 AVIRIS data sets spanning spring, early summer, and early fall conditions. The grassland spectrum derived from April data exhibits green vegetation spectral features (pronounced chlorophyll and leaf water absorptions, with high reflectance in the 0.8 to 1.2 um region). In the summer and fall data there is a loss of chlorophyll pigment and water absorption. The loss of chlorophyll pigment results in a major decline in the magnitude of the chlorophyll red edge. With the loss of leaf water absorption, there is an emergence of lignin-cellulose absorptions at 2.09 and 2.27 um.

The persistence of the chlorophyll red edge in the June and September data sets is attributed to the presence of trace quantities of green vegetation in the extracted pixels. There are several reasons why the chlorophyll red edge is useful for detecting trace quantities of green vegetation: 1) The chlorophyll red edge is the sharpest spectral feature of green leaves. That is to say, it is the region with the greatest change in reflectance over the smallest change in wavelength. 2) There are no other natural materials yielding an absorption edge of similar magnitude in the same spectral position. 3) There is good solar illumination from 0.7 to 0.8 um. While the wavelength position of the chlorophyll red edge may not be measurable at low green vegetation covers, the presence and magnitude of the chlorophyll red edge may prove to be of great value in detecting and quantifying trace quantities of green vegetation.

REFERENCES

Collins, W., 1978, Remote sensing of crop type and maturity. Photogrammetric Engineering and Remote Sensing, v. 44, p. 43-55.

Elvidge, C.D., 1987, Reflectance characteristics of dry plant materials. Proceedings of International Symposium on Remote

Sensing of Environment, pp. 721-733, ERIM, Ann Arbor, Michigan.

Elvidge, C.D., 1990, Visible and near infrared reflectance characteristics of dry plant materials. International Journal of Remote Sensing, v. 11, p. 1775-1795.

Elvidge, C.D. and Lyon, R.J.P., 1985, Influence of rock-soil spectral variation on the assessment of green biomass. Remote Sensing of Environment, v. 17, p. 265-279.

Elvidge, C.D. and Mouat, D.A., 1989, Analysis of green vegetation detection limits in 1988 AVIRIS data. Proceedings of International Symposium on Remote Sensing of Environment, Seventh Thematic Conference, Remote Sensing for Exploration Geology, 10 p., ERIM, Calgary, Canada.

Elvidge, C.D. and Portigal, F.P., 1990, Reflectance spectra of green and dry vegetation derived from 1989 AVIRIS data. Proceedings of the Fifth Australasian Remote Sensing Conference, Perth, Australia, p. 185-196.

Elvidge, C.D., Portigal, F.P., Mouat, D.A., 1990, Detection of trace quantities of green vegetation in 1989 AVIRIS data. Proceedings of the Second Airborne Visible/Infrared Imaging Spectrometer (AVIRIS) Workshop, JPL Publication 90-56.

Tucker, C.J., 1979, Red and photographic infrared linear combinations for monitoring vegetation. Remote Sensing of Environment, v. 10, p. 127-150.

Vane, G., 1987, First results from the Airborne Visible/Infrared Imaging Spectrometer (AVIRIS). In Airborne Visible/Infrared Imaging Spectrometer (AVIRIS): A Description of the Sensor, Ground Data Processing Facility, Laboratory Calibration, and First Results, JPL Publication 87-38, p. 89-97.

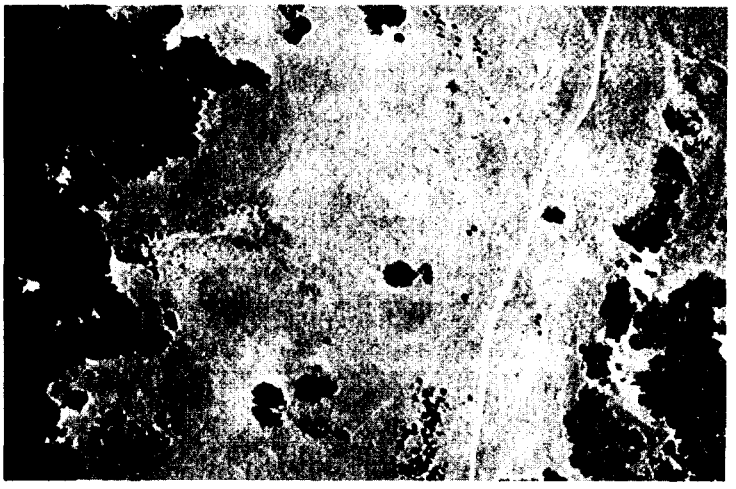

Figure 1. Low altitude aerial photograph of the annual grassland at Jasper Ridge. The grassland is located in the central portion of the slide, with chaparral and oak woodlands present at the edges of the photograph. AVIRIS pixels were extracted from the grassland for the three dates of imagery. The isolated trees in the grassland were avoided during pixel extraction [see slide 17]

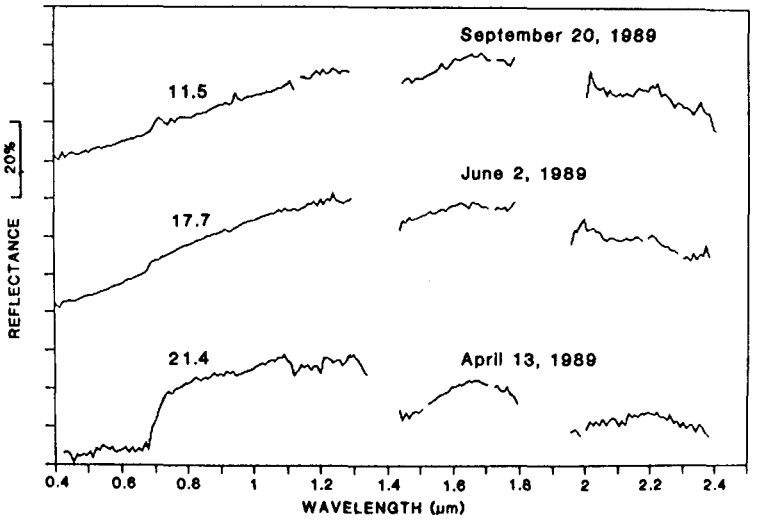

Figure 2. AVIRIS reflectance spectra for the ungrazed grassland from three 1989 AVIRIS data sets. The spectra are derived from the average DNs from a block of pixels from each date which were converted to units of ground reflectance using the calibations presented in Figures 1-3. The spectra have been offset vertically to avoid overlap. The reflectance at 0.8 um is provided for each spectrum

AVIRIS Observation of Forest Ecosystems Along the Oregon Transect

Lee F. Johnson
TGS Technology Inc., NASA/Ames
Moffett Field CA

David L. Peterson
NASA/Ames Research Center
Moffett Field CA

Abstract. AVIRIS data have been acquired over several diverse forest sites in support of the Oregon Transect Ecosystem Research project. Overflights have occurred at key times during the growing season to assess the temporal and spatial sensitivity of AVIRIS spectra to foliar biochemical concentration. Preliminary analysis includes an image-based estimation of signal-to-noise, comparison with other imaging spectrometers, and stepwise regression against laboratory-determined nitrogen concentration.

I. Introduction

The Oregon Transect Ecosystem Research (OTTER) project is studying biogeochemical cycling along a climatic and fertility gradient in western Oregon. The transect extends from the Pacific coast inland approximately 200 km. Six study sites (Figure 1) represent a broad range in ecosystem structure and function. Two sites are subdivided into control and fertilizer amended plots, while a third site contains coniferous and broadleaf plots.

A variety of remotely-sensed and in-situ measurements are being used to characterize forest physiological and structural parameters, nutrient cycling, and biochemistry. These measurements will be transformed into ecosystem process rates and fluxes by use of the FOREST-BGC model (Running and Coughlan, 1988). The overall OTTER goal is to test and validate FOREST-BGC, which will be driven with remotely-derived measurements to the extent possible.

Within the OTTER project, the sensitivity of AVIRIS to the quantity of plant biochemical constituents is being examined. Such sensitivity would provide insight into ecosystem carbon and nitrogen cycles. For instance, starch, sugars and carbohydrates are related to rates of carbon assimilation, above and below ground carbon allocation, carbon turnover, growth, maintenance, and respiration. Nitrogen and lignin affect the rate of litter decomposition, which in turn regulates the amount of nitrogen available for uptake, volatilization (of N_2O), and leaching (of NO_3^-).

The ability to reliably measure foliar biochemical components from first principles is hampered by incomplete knowledge concerning internal

leaf scattering and absorption properties arising from the presence of biochemical compounds. The various co-occurring constituents are composed of similar molecular bonds (eg: C-H, N-H, O-H) and thus have overlapping absorption features, forming functional groups which cluster at several locations in the near-infrared (NIR) region. Atmospheric water vapor, foliar water, and soil moisture pose another complicating factor. O-H bonds of free or bound water absorb strongly, and co-vary with biochemicals to differing degrees. Other factors which influence the remotely sensed spectra, yet are not directly related to biochemical optical properties, include plant morphology, leaf angle and leaf area distribution, and canopy architecture.

Over the past several decades, researchers in the agricultural sciences have met with considerable success in drawing statistical relationships between forage biochemical constituency and laboratory-derived NIR spectra (Marten *et al.*, 1989). Recent studies have built upon these methods to develop statistical relationships between forest biochemical concentration and canopy upwelling radiance as measured by imaging spectrometers (Peterson *et al.*, 1988; Wessman *et al.*, 1989; Swanberg and Matson, 1989). The availability of laboratory biochemical assay (nitrogen, lignin, starch, chlorophyll, cellulose, amino acids, sugar) in conjunction with the OTTER AVIRIS observations establishes a basis for a comparison of statistical results with these previous studies. In addition, lab spectra performed on samples collected at fertilized and control plots will be of use in identifying overt indications of biochemical content variation, particularly nitrogen, in the AVIRIS spectra.

II. Data Analysis

AVIRIS data were acquired across the transect in March, August, and October of 1990. These data, along with an acquisition in late May 1991, provide observations which coincide with distinct forest developmental stages: budbreak, full leaf-out, maximum water stress, and dormancy. Each mission was supported by two sunphotometers to provide atmospheric optical depth readings at or near the time of overflight for each site. Also during each mission, foliage samples were collected from five trees at each plot and assayed for several biochemical constituents. Spectral measurements were made at spectrally flat fields near each site with a field spectroradiometer (Spectron Engineering, Inc., 1990) during two overflights. A discussion of preliminary evaluation and analysis of these datasets follows.

A. Signal-to-Noise

The signal-to-noise ratio (SNR) was estimated in five channels as the ratio of the mean to the standard deviation of AVIRIS at-sensor radiance within a 3x3 pixel matrix over an apparently homogeneous sandspit approximately 5x5 pixels in size (Figure 2). Each SNR was calculated as the mean SNR of three neighboring channels. The sandspit reflectance was estimated as the quotient of the surface radiance (*π) divided by the incoming irradiance, modeled by an atmospheric correction algorithm (Fraser *et al.*, 1989). Estimated reflectance trended from ~20% at 635nm up to ~40% at 2119nm. Observation dates 8/90 and 10/90 were compared with pre-OTTER data flown in 6/89 and 9/89. The target was obscured by cloud cover in the 3/90 dataset.

The limited target size and uncertainty about atmospheric conditions during the 1989 flights reduce confidence in the absolute values presented. Nonetheless, an interesting trend is apparent. SNR in the 1989 data, particularly the June dataset, diminished markedly in the longer wavelengths with respect to the visible channel (635nm). The 1990 data, particularly the August dataset, were more constant across the spectral regions. Presumably this is due at least in part to noise-reduction modifications made to AVIRIS during 1990.

B. Inter-Sensor Comparison

During the August 1990 campaign, nearly simultaneous observations were made at several sites by AVIRIS, the Advanced Solid-State Array Spectroradiometer (ASAS) (Irons *et al.*, 1991), and the Compact Airborne Spectrographic Imager (CASI) (Borstad and Hill, 1989). ASAS was flown at 15000 feet above-ground-level (AGL) aboard the NASA C-130; CASI was flown at 5000 feet AGL aboard a light aircraft. ASAS is a pointable instrument which measures the 462-865 spectral region in 29 channels; the nadir view is used for the present comparison. CASI samples the 425-950nm spectral region in 288 channels.

Figure 3a shows a comparison of raw data for the alder (*Alnus rubra*) plot at site #1 from the three spectrometers. AVIRIS and CASI data were acquired about 90 minutes after solar noon on 14-August-1990, while ASAS were acquired about 60 minutes before solar noon. The spectra show the additive influence of atmospheric path radiance, most obvious in the visible channels, as a function of flight altitude. The green peak, chlorophyll trough, and major atmospheric absorption features appear well aligned.

An atmospheric correction procedure (Fraser *et al.*, 1989), using optical depth readings made at the site approximately 90 minutes after the AVIRIS flight, was used to convert at-sensor radiance into surface radiance (Figure 3b). The correction included all AVIRIS and ASAS channels in the 500-900nm region, along with a subset of the 288 CASI channels. The correction removed the path radiance from the visible channels. The ASAS measurement is greater than that of the other sensors in the NIR, primarily because these data were measured with a higher solar elevation (56.5° vs. 51°). The AVIRIS and CASI measurements agree to within 1 $\mu W/cm^2/sr/nm$ in the NIR region.

All datasets were converted into reflectance by dividing the estimated surface radiance ($*\pi$) by the downward irradiance estimated by the algorithm (Figure 3c). All datasets agree to within about 1-2% absolute reflectance except at the longer wavelengths, where AVIRIS and CASI differ by about 4%.

C. Statistical Analysis

The OTTER sites represent a gradient in major variables which affect plant chemical and physical characteristics: species, seasonal growth stage, stand maturity, availability of water, nutrients and light, and climatic conditions, among others. The sites are representative of a broad cross-section of mid-latitude forest ecosystems. Reflectance spectra from these sites may be regressed against laboratory chemical assay to develop predictive equations for biochemical concentration.

Nitrogen (N) concentration (mg/g) was estimated for each plot as the mean of laboratory assays performed on five foliage samples collected throughout the plot. Stepwise multilinear regression was used to calculate the correlation of the AVIRIS (3x3 pixel average) NIR spectra for two overflights with plot N concentration. AVIRIS data taken over all conifer sites during the 8/90 and 10/90 flights were converted to 1st-difference spectra representing the slope between each neighboring channel pair. Conversion to 1st-difference emphasizes structure due to the relatively weak biochemical absorptions which are superimposed upon dominating water absorption features.

Results presented herein are based on a small sample size and should be considered preliminary at this time. Regressions with small sample size, though insufficient for development of analytical equations, may

however indicate measurement potential for a given constituent (Barton and Cavanagh, 1988). If the selected wavelengths make physical sense, this would be a good indication as well.

A total of 58 channels per date were used as candidate independent variables, occupying the region 1122-1350nm and 1500-1787nm. These regions are known to contain biochemical absorption features (Williams and Norris, 1987), with relatively low interference from water absorption. Three-term stepwise results are shown in Tables 1a and 1b. Essentially the same wavelengths were chosen in the first and second positions for each date, albeit in different order. The stepwise procedure was re-run on 30 channels between 1500-1787nm for both dates (Tables 1c and 1d). The 1540/1550nm selections correspond with a selection at 1555nm found in an earlier N-concentration study using the JPL Airborne Imaging Spectrometer (AIS) data over Oregon conifers (Swanberg and Peterson, 1988). The 1658nm selection in both of the 8/90 datasets is close to a selection of 1655nm made in a previous AIS study of N-concentration in Douglas-fir in New Mexico (Swanberg and Matson, 1989).

For reference, Table 1 shows the center wavelength of the established protein absorption feature (after Williams and Norris, 1987) which is nearest to each wavelength selected in the stepwise procedure. Features centered at the reference locations are typically 10-20nm or more at full-width-half-maximum. As most organic nitrogen is held by proteins, it might be expected that waveband selections for N-concentration would occur in the vicinity of these absorption feature. An absorption peak, due to saturation, may be insensitive to biochemical concentration. Information regarding biochemical concentration is often found instead along the wings of the absorption feature, and is convolved with other absorption features occurring in the same functional group. Most of the wavelength selections appear to be associated with a reference protein feature. Some selections occur near the reference absorption peak, while others differ by up to ~30nm.

III. Future Work

The OTTER design presents an opportunity to explore the effect of biochemistry upon AVIRIS spectra with a statistical approach. Development of prediction equations for several biochemicals will proceed at such time as a full set of AVIRIS data has been collected, and the wet chemistry is completed. Appropriately corrected multi-season AVIRIS data will be pooled, and relationships with plot biochemical concentration

will be established by stepwise regression and partial least squares (Sjostrom *et al.*, 1983) techniques.

Fertilizer amendment at Scio provides the opportunity to examine laboratory and AVIRIS spectra for overt biochemical influence, while controlling for complicating differential factors such as species, topography, atmosphere, and canopy architecture. Initial assay results show that fertilizer amendment at the Scio site has created a (60m x 60m) plot with elevated N-concentration (~.5% absolute) above that found at a neighboring control plot. The 5/91 AVIRIS overflight will be supported by comprehensive harvest of fertilized and control foliage at Scio, to include acquisition of laboratory spectra and assay for N-concentration.

Acknowledgements

This research was supported by the Earth Science and Applications Division and the Life Sciences Division of the National Aeronautics and Space Administration. The foliage samples were collected by John Runyon and Richard McCreight (Oregon State University). The biochemical assay was performed by Dr. Pamela Matson and Christine Billow (NASA/Ames Research Center). The manuscript benefitted from review by Jennifer Dungan and Dr. Roy Armstrong (NASA/Ames Research Center).

References

Barton, F.E., and Cavanagh, G.C., "The Calibration of NIR Reflectance Spectrometer for the Determination of Diverse Compositional Parameters," *J. Am. Oil Chem Soc.*, 65:768-773, 1988.

Borstad, G.A. and Hill, D.A., "Using Visible Range Imaging Spectrometers to Map Ocean Phenomena," Proceedings SPIE Advanced Optical Instrumentation for Remote Sensing of the Earth's Surface from Space, 1129:130-136, 1989.

Franklin, J.F., and Dyrness, C.T., "Natural Vegetation of Oregon and Washington," General Technical Report PNW-8, Pacific Northwest Forest and Range Experiment Station, Portland ORE, 1973.

Fraser, R.S., Ferrare, R.A., Kaufman, Y.J., and Mattoo, S., "Algorithm for Atmospheric Corrections of Aircraft and Satellite Imagery," NASA Technical Memorandum #100751, 106 pp., 1989.

Irons, J.R., Ranson, K.J., Williams, D.L., Irish, R.R., and Huegel, F.G., "An Off-Nadir-Pointing Imaging Spectroradiometer for Terrestrial Ecosystem Studies," *IEEE Transactions on Geoscience and Remote Sensing*, 29:66-74, 1991.

Marten, G.C., Shenk, J.S., and Barton, F.E. (Eds.), "Near Infrared Reflectance Spectroscopy (NIRS): Analysis of Forage Quality," UDSA/ARS Agriculture Handbook No. 643, (revised with supplements), 110 pp., 1989.

Peterson, D.L, Aber, J.D., Matson, P.A., Card, D.H., Swanberg, N.A., Wessman, C.A., and Spanner, M.A., "Remote Sensing of Forest Canopy and Leaf Biochemical Contents," *Remote Sensing of Environment*, 24:85-108, 1988.

Running, S.W. and Coughlan, J.C., "A General Model of Forest Ecosystem Processes for Regional Applications I.: Hydrologic Balance, Canopy Gas Exchange and Primary Production Processes," *Ecological Modelling*, 42:125-154, 1988.

Sjostrom, M., Wold, S., Lindberg, W., Persson, J., Martens, H., "A Multivariate Calibration Problem Solved by Partial Least-Squares Models in Latent Variables," *Analytica Chimica Acta*, 150:61-70, 1983.

Spectron Engineering, Inc., "SE590 Field-Portable Data-Logging Spectroradiometer," Denver CO, 1990.

Swanberg, N.A. and Matson, P.A., "Determining Experimentally Induced Variation in Coniferous Canopy Chemistry with Airborne Imaging Spectrometer Data," Proceedings IEEE International Geoscience and Remote Sensing Symposium, 4:2090-2092, 1989.

Swanberg, N.A. and Peterson, D.L., "Using the Airborne Imaging Spectrometer to Determine Nitrogen and Lignin Concentrations in Coniferous Forest Canopies," Internal Report, NASA/Ames-Ecosystem Science and Technology Branch, 1988.

Wessman, C.A., Aber, J.D., Peterson, D.L., "An Evaluation of Imaging Spectrometry for Estimating Forest Canopy," *Int'l J. Remote Sensing*, 10:1293-1316, 1989.

Williams, P.C. and Norris, K.H., Eds., "Near-Infrared Technology in the Agricultural and Food Industries," monograph published by the American Association of Cereal Chemists, Inc., St. Paul MINN, 1987.

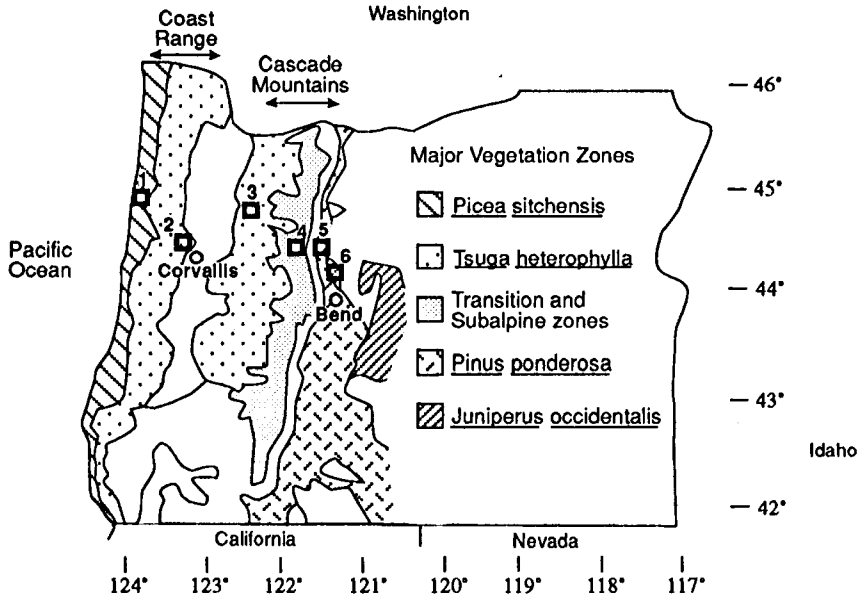

Figure 1. Study site map. 1 = CH-A (alder) and CH-H (hemlock); 2 = WW; 3 = SC-C (control) and SC-F (fertilized); 4 = SA; 5 = ME-C (control) and ME-F (fertilized); 6 = JU. (vegetation zones after Franklin and Dyrness, 1973)

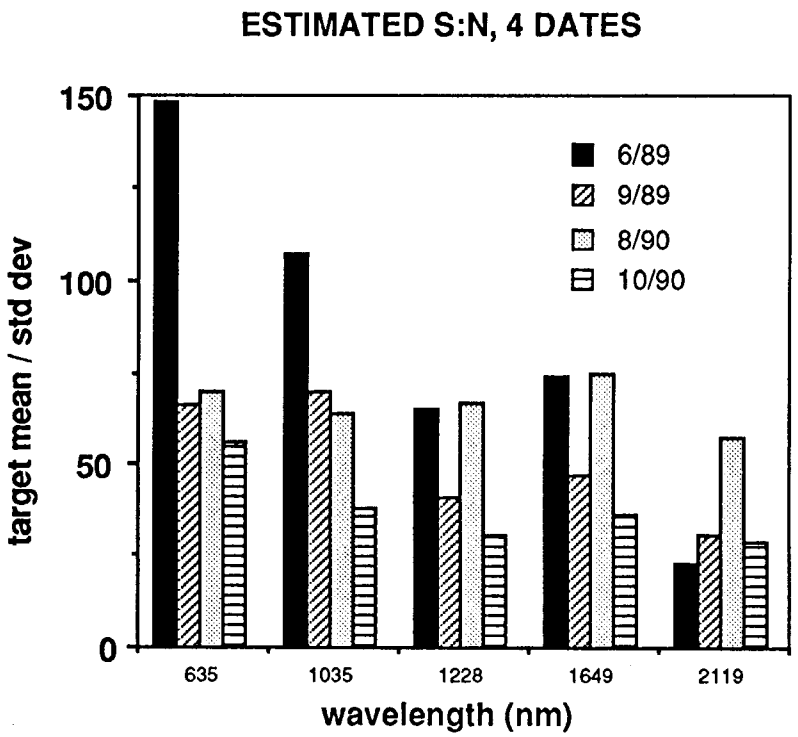

Figure 2. Estimated signal-to-noise in four datasets. S:N estimated as the mean / standard deviation of 3x3 pixels above a uniform target.

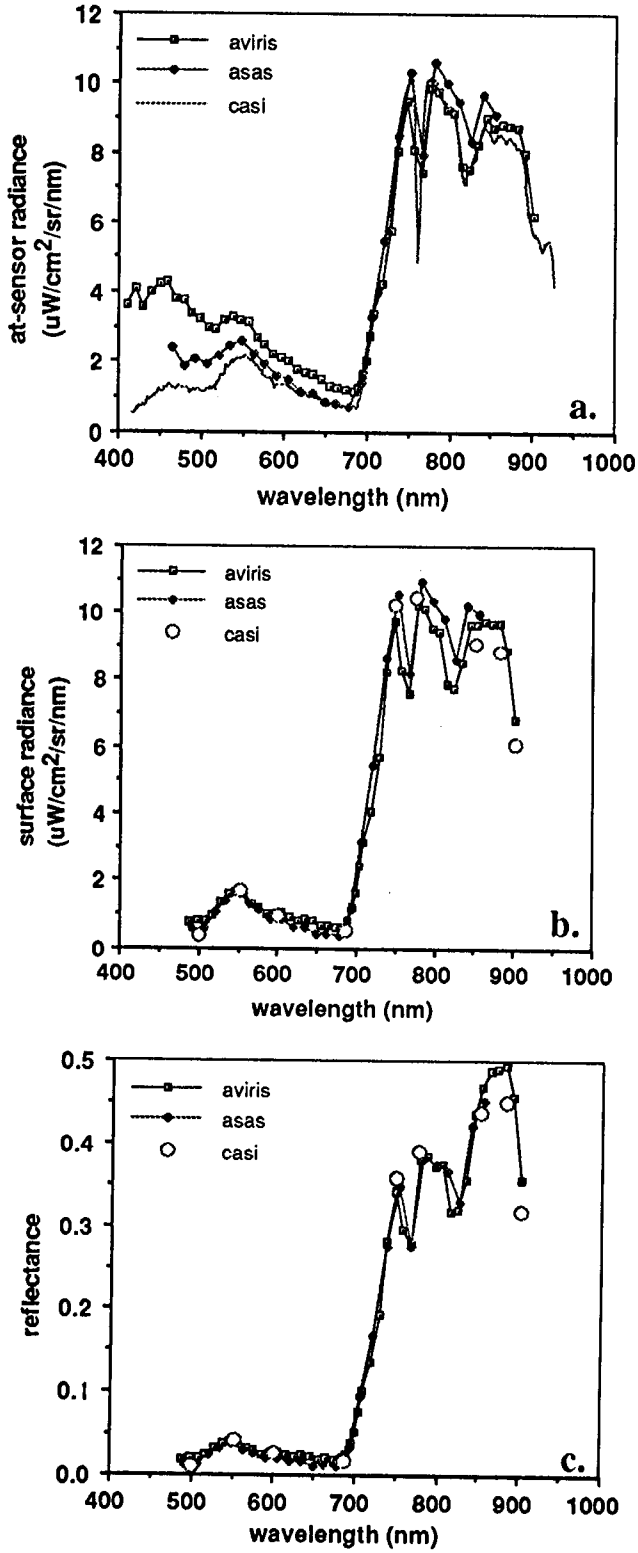

Figure 3. Inter-sensor comparison above alder plot (CH-A) on 8/14/90. a) at-sensor radiance b) surface radiance c) reflectance. Flight altitudes above ground were: AVIRIS, 65000'; ASAS, 15000'; CASI, 5000'. Optical depth at the time of overflight was ~0.5.

	Wavelength Selection (in order)	Nearest Protein Feature	R^2 (per step)	SEE (per step)	n	date
	1322	(1357^2)	0.76	0.95		
a.	1209	(1187^4)	0.91	0.65	8	8/90
	1658	(1690^4)	0.98	0.35		
	1199	(1187^4)	0.56	0.84		
b.	1332	(1357^2)	0.86	0.52	8	10/90
	1276	(1276^2)	0.94	0.38		
	1658	(1690^4)	0.30	1.61		
c.	1550	(1570^2)	0.42	1.61	8	8/90
	1757	(1757^1)	0.85	0.92		
	1718	(1735^2)	0.76	0.87		
d.	1738	(1735^2)	0.88	0.48	8	10/90
	1540	(1570^2)	0.99	0.10		

Table 1. Results of 3-term stepwise regression against nitrogen concentration, NIR region, for the 8/90 and 10/90 flights. Included for reference are the nearest established protien absorbtion features. Superscripts represent relative strength of feature, 4 being the strongest (Williams and Norris, 1987).

Retrieval of Reflectance From AVIRIS-Measured Radiance Using a Radiative Transfer Code

Robert O. Green

Jet Propulsion Laboratory
California Institute of Technology
Pasadena, California

Abstract. Calibrated radiance data measured by the Airborne Visible/Infrared Imaging Spectrometer (AVIRIS) are reduced to reflectance using a radiative transfer code. Reflectance is derived through compensation of the solar irradiance spectrum, solar-illumination geometry, atmospheric water vapor absorption, atmospheric scattering, absorption of the well-mixed gases, and an estimate of surface slope. Solar irradiance, illumination, and an atmospheric model are established from the location, season, and time of AVIRIS data acquisition. For each AVIRIS spatial resolution element, an estimate of total-column water vapor was derived directly from the AVIRIS radiance data. A retrieval of the surface-pressure elevation was generated from the 760-nm oxygen absorption band and the 2070-nm carbon-dioxide band measured within the AVIRIS spectrum. In situ measurements of atmospheric optical depths were used to constrain the atmospheric scattering properties at a point location. Scattering was extrapolated throughout the scene based upon the derived surface-pressure estimates. Absorption caused by well-mixed gases was constrained by the pressure elevation determinations. From the total-column water determination and an assumption of expected lateral homogeneity of water vapor over short distances, surface slopes were estimated for each spatial element. These parameters were used to constrain a radiative transfer code for retrieval of reflectance from AVIRIS measured radiance. The retrieval algorithm is evaluated with AVIRIS imagery acquired over a region where spectra of two surface targets have been independently acquired. The precision and accuracy of the retrieval algorithm are discussed.

1. Introduction

An algorithm to retrieve surface reflectance directly from AVIRIS-measured radiance using the LOWTRAN 7 (Kneizys et al., 1989) radiative transfer code is described.

AVIRIS measures the total upwelling radiance incident at the sensor with 224 spectral channels from 400 to 2450 nm in the electromagnetic spectrum. The spectral sampling interval and response function at full-width half-maximum (FWHM) throughput is nominally 10 nm. AVIRIS images are acquired with a width of 11 km and a length ranging from 10 to 100 km. The spatial resolution is nominally 20-by-20 m for all 224 spectral channels. The spectral as well as radiometric characteristics are determined for each channel during a laboratory calibration (Chrien et al., 1990a).

The AVIRIS data described here were acquired over the Clark Mountains, California, on July 23, 1990 at 20:20 universal coordinated time (UCT). These data were measured as part of an in-flight validation and calibration experiment undertaken to assess AVIRIS in-flight performance. Data were acquired over an occurrence of the

mineral bastnaesite, which possesses 12 strong absorption features (Adams, 1965) within the AVIRIS spectral range. These known absorptions allow confirmation of the in-flight spectral calibration of AVIRIS (Green et al., 1988). The region covered by this data set is approximately 11-by-40 km trending northwest along the eastern flank of the Clark Mountains. Figure 1 shows the coverage of these AVIRIS data, as well as the location of sites A, B, and C, where surface and atmospheric measurements were acquired.

Measurements from the onboard reference were used to modify the radiometric calibration of the in-flight measured radiance. Based on a preliminary analysis in the laboratory, the onboard calibrator is stable to 2% (Chrien, 1990b). To correct the in-flight data, a ratio for each channel was formed between the signal from the onboard reference at the time of the laboratory calibration to the signal at the time of the data acquisition. This ratio deviated from unity at the ±5% level. These correction factors were multiplied against the Clark Mountains radiance to place an improved radiometric calibration on the in-flight data.

Surface-reflectance spectra were acquired in conjunction with the AVIRIS data acquisition. A set of 16 reflectance spectra from a 50-by-50-m asphalt parking lot located at site A was measured. These spectra were acquired with a field spectrometer that has a spectral channel sampling interval and a response function FWHM of less than 5 nm. This high spectral resolution is required for valid convolution of the field-reflectance spectra to the 10-nm spectral characteristics of AVIRIS. In addition to the asphalt spectra, a spectrum of the mineral bastnaesite was acquired from a laboratory mineral sample. This spectrally distinct mineral occurs on the surface at site B in the Clark Mountains AVIRIS data set. Figure 2 shows the mean reflectance of the asphalt parking lot and the bastnaesite targets.

At site C, atmospheric optical depths were measured on July 23, 1990 in support of the AVIRIS spectral calibration and validation experiment. The solar radiometer used has 10 discrete spectral channels with 10-nm response function FWHM positioned at 370, 400, 440, 520, 610, 670, 780, 870, 940, and 1030 nm. These data were reduced to atmospherical optical depth with the Langley plot method (Kastner, 1985). The reduced optical depths were used to constrain the LOWTRAN 7 midlatitude summer atmospheric model for analysis of the AVIRIS radiance data. The resulting measured optical depths and corresponding modeled LOWTRAN 7 optical depths for site C are given in Figure 3.

2. Reflectance Retrieval Algorithm

An algorithm to retrieve reflectance directly from imaging-spectrometer-measured radiance using a radiative transfer code was originally developed for data acquired from the Airborne Imaging Spectrometer (AIS) (Conel et al., 1987). The method has since been augmented and used with AVIRIS data (Green et al., 1990a, and Green, 1990b). The algorithm presented here has been refined and expanded to maximize utilization of parameters derived directly from AVIRIS data for the retrieval of reflectance.

This algorithm treats the total upwelling radiance measured by AVIRIS for each spectral channel, L_t, as the combination of the two-way transmitted surface-reflected radiance, L_r, plus atmospheric path scattering radiance, L_p, as given in Equation 1.

$$L_t = L_r + L_p \quad (1)$$

The reflected radiance, L_r, is isolated in Equation 2 through subtraction of the path radiance component, L_p, from the total measured radiance, L_t. The path radiance is that radiance measured by AVIRIS derived solely from the atmosphere. The path radiance calculated with LOWTRAN 7 for an atmospheric model that is constrained by solar-illumination geometry, pressure elevation, water vapor absorption, atmospheric scattering, and well-mixed gas absorption is derived for each spatial resolution element.

$$L_r = L_t - L_p \quad (2)$$

The resulting AVIRIS-reflected radiance component is given in Equation 3, as the solar irradiance multiplied by the cosine of the solar zenith angle over pi steradians, $E_S\cos\theta/\pi$, which is multiplied by the downward atmospheric transmittance T_d, surface reflectance ρ, and upward atmospheric transmittance T_U.

$$L_r = [E_S\cos\theta/\pi]T_d\rho T_u \quad (3)$$

Using LOWTRAN 7, the reflected radiance for a 100% reflectance lambertian surface is calculated for the illumination and atmosphere determined for each AVIRIS spatial element, L_{r100}. The ratio of the AVIRIS-measured reflected radiance and the LOWTRAN 7 modeled 100% reflectance radiance is given in Equation 4.

$$L_r / L_{r100} = [E_S\cos\theta/\pi]T_d\rho T_u / [E_S\cos\theta/\pi]T_d\rho_{100}T_u \quad (4)$$

This ratio is solved for AVIRIS lambertian equivalent reflectance as in Equation 5.

$$\rho = (L_r/L_{r100})\rho_{100} \quad (5)$$

This approach of modeling the atmospheric path radiance and a known surface-reflected radiance for retrieval of reflectance is adopted because only limited modifications to existing radiative transfer codes such as LOWTRAN 7 are required for implementation.

3. Constraint of Radiative Transfer Code

Retrieval of reflectance from AVIRIS radiance with this algorithm requires the accurate constraint of the radiative transfer code of the atmosphere and illumination for each spatial resolution element.

The solar spectrum contained within the LOWTRAN 7 radiative transfer code is used as the exoatmospheric irradiance. Solar-illumination geometry is constrained by

the latitude, longitude, and time of the AVIRIS data acquisition over the Clark Mountains. A midlatitude, summer, and rural atmospheric model was used based on the location and season of data acquisition.

Total-column atmospheric water vapor is constrained based on a retrieval for each spatial element of the Clark Mountains AVIRIS data using the continuum interpolated band-ratio algorithm (Green et al., 1989). Accuracy of this algorithm has been established with respect to radiosonde and other spectroscopic water recoveries (Bruegge et al., 1990). Results from this retrieval are shown in Figure 4 [see slide 18] along with a composite image comprising three AVIRIS radiance channels. Retrieved water vapor amounts vary from 8 to 22 mm across the image. This extreme variability is driven largely by change in atmospheric path length as a function of surface elevation because water vapor absorbs strongly over much of the AVIRIS spectral range, an accurate estimate of water vapor is required for accurate reflectance retrieval. An error of 30% in estimation of atmospheric water vapor in the retrieval of reflectance may lead to errors of 10% in the retrieved reflectance (Green, 1989). In the future, a more robust inversion algorithm that applies a nonlinear least-squares approach with compensation for leaf water absorption (Green, 1991) will be used for the retrieval of atmospheric water vapor from AVIRIS radiance.

Optical depth measurements were acquired for constraint of atmospheric transmission and scattering characteristics at site C. These optical depths were extrapolated throughout the AVIRIS data set based on an estimate of the surface-pressure elevation. The pressure elevation was derived from the absorption of the 760-nm oxygen band measured within the AVIRIS spectrum. A continuum interpolated band ratio was calculated for this oxygen band for the Clark Mountains data set and was calibrated to surface-pressure elevation with LOWTRAN 7. For a single-resolution element, the precision of pressure element retrieval was determined as 12%. To improve the local precision with some loss of spatial resolution, a 9-by-9 spatial element filter was applied. An image of the retrieved pressure elevation is given in Figure 5 [see slide 19].

In addition to oxygen, the abundance of carbon dioxide was derived from the calibrated AVIRIS radiance using the 2070-nm absorption band. Again, a continuum interpolated band ratio calibrated through LOWTRAN 7 was used. An image of the retrieved carbon dioxide is given in Figure 6. This carbon dioxide retrieval also offers an estimate of surface-pressure elevation and is less influenced by atmospheric scattering.

Absorption of the well-mixed gases in the AVIRIS spectral range was varied based on the surface-pressure elevation. Ozone absorption was constrained based on the latitude and season of the AVIRIS acquisition.

An approach to estimating surface slope from the AVIRIS data set was investigated. This method requires precise retrievals of the water vapor from AVIRIS radiance and an assumption of expected lateral homogeneity of water vapor over short distances. From the Clark Mountains water vapor image, the equivalent surface elevations were calculated for each spatial element for the midlatitude summer atmospheric model with LOWTRAN 7. Estimates of the slope for each spatial element

were then calculated as the normal to a surface fit to the 3-by-3 encompassing spatial elements. A surface-slope correction image of the secant of the angle between the surface normal and the illumination direction is given in Figure 7. This slope correction image properly indicates a slope away from the illumination direction on the northern side of Clark Mountains. The validity of these slope estimates is a function of the dominance of topography in the modulation of water vapor abundance over the 3-by-3 spatial element regions. Further evaluation of this technique will require analysis with digital elevation data co-registered with the AVIRIS imagery.

4. Retrieval of Reflectance From AVIRIS Radiance

The reflectance retrieval algorithm constrained by the derived atmospheric characteristics was applied to the AVIRIS radiance imagery of the Clark Mountains. As an example of the radiance data, Figure 8 shows the measured radiance spectra for the asphalt and bastnaesite targets. Application of the retrieval algorithm resulted in the reflectance spectra given in Figure 9. For the asphalt target, the absolute agreement is good across the spectral range with an absence of evidence for uncompensated water vapor absorption or atmospheric scattering artifacts. The unique spectral features of the bastnaesite target in the 500 to 900 nm range are recovered accurately. Complete agreement between the laboratory and AVIRIS bastnaesite reflectance is not expected, based on the differing sampling scale of the laboratory and AVIRIS spectrometers. With the reduction of the AVIRIS radiance to reflectance analyses for the quantitative identification, assessment and monitoring of surface spectral reflectance characteristics become possible.

5. Error Discussion

The precision of the reflectance spectra retrieved through this algorithm relies on the precision of the AVIRIS-measured radiance and of the parameters used to constrain the radiative transfer code. Precision of the AVIRIS data and derived parameters is a function of the instrument performance, atmospheric characteristic, surface reflectance, and illumination geometry. Additional analyses are required to quantify the influence of these factors on the retrieved reflectance over the Clark Mountains.

Accuracy of the retrieval depends on the accuracy of AVIRIS spectral and radiometric calibration. For example, errors in the knowledge of the in-flight spectral characteristic of AVIRIS will cause significant errors in the retrieved reflectance. These errors result from the many strong absorptions present in terrestrial radiance spectra (Green et al., 1990a). Fortunately, uncertainty in the in-flight spectra characteristics of AVIRIS may be assessed and corrected based on the imaging spectrometer data themselves (Conel et al., 1987; Green et al., 1988; and Green et al., 1990a). Uncertainty in the absolute radiometric calibration of AVIRIS will introduce proportional uncertainty in retrieved reflectance. Efforts are ongoing to maintain, monitor, and improve the absolute calibration accuracy of AVIRIS (Chrien et al., 1990a, and Green et al., 1990a).

Accuracy of the radiative transfer code and model atmosphere directly influences the retrieved reflectance. Currently, the MODTRAN radiative transfer code

(Berk et al., 1989) is being evaluated as a potential improvement over LOWTRAN 7. MODTRAN operates at a higher spectral resolution and more accurately models water vapor absorption. Other radiative transfer codes that more fully treat atmospheric scattering and surface bidirectional reflectance are being examined as well.

The parameters used to constrain the radiative transfer code for reflectance retrieval directly affect the accuracy of the result. Ideally, all atmospheric and surface-slope parameters should be known for each AVIRIS spatial resolution element. In the absence of independent knowledge of these constraining parameters, algorithms for deriving estimates of these parameters from the AVIRIS radiance data have been developed. Validation of the accuracy of the retrievals of water vapor, oxygen, and carbon-dioxide abundance, as well as the parameters derived from these abundances, is essential to establishing the accuracy of the reflectance retrieval. Efforts are ongoing with in situ field validations and computational sensitivity analyses to determine these accuracies.

6. Conclusion

Reflectance spectra were successfully retrieved from calibrated AVIRIS radiance data using the LOWTRAN 7 radiative transfer code. This reflectance retrieval algorithm was constrained by parameters derived largely from the AVIRIS radiance data themselves. For the Clark Mountains AVIRIS data set, comparison of the AVIRIS retrieved reflectance and reflectance spectra from two surface sites showed consistent agreement. Work is required to further validate the accuracy of the derived constraining parameters and of the retrieved surface reflectance over a range of atmospheric and surface conditions. As presented, this algorithm provides an approach for the routine retrieval of reflectance from imaging-spectrometer-measured radiance. Retrieval of reflectance is essential for the quantitative investigation of surface composition, for the comparison of surfaces from one region to another, and for the study of surfaces and surface processes through time.

Acknowledgment

This research was carried out at the Jet Propulsion Laboratory, California Institute of Technology, under contract with the National Aeronautics and Space Administration.

References

Adams, J.W., "The visible region absorption spectra of rare-earth minerals," *The Amer. Min.*, 50, 356-367, 1965.

Berk, A., L.S. Bernstein, and D.C. Roberson, *MODTRAN: A Moderate Resolution Model for LOWTRAN 7*, U.S. Air Force Geophysical Laboratory (AFGL), Hanscom Air Force Base, Massachusetts, 1989.

Bruegge, C.J., J.E. Conel, J.S. Margolis, R.O. Green, G. Toon, V. Carrere, R.G. Holm, and G. Hoover, "In situ atmospheric water vapor retrieval in support of AVIRIS validation," *Imaging Spectroscopy of the Terrestrial Environment*, SPIE Vol. 1298, 1990 (in press).

Chrien, T.G., R.O. Green, and M. Eastwood, "Laboratory spectral and radiometric calibration of the Airborne Visible/Infrared Imaging Spectrometer (AVIRIS)," *Imaging Spectroscopy of the Terrestrial Environment*, SPIE Vol. 1298, 1990a (in press).

Chrien, T.G., personal communication, Jet Propulsion Laboratory, Pasadena, California, 1990b.

Conel, J.E., R.O. Green, G. Vane, C.J. Bruegge, R.E. Alley, and B.J. Curtiss, "AIS-2 Radiometry and A Comparison of Methods for the Recovery of Ground Reflectance," *Proceedings of the Third Airborne Imaging Spectrometer Data Analysis Workshop*, (G. Vane, ed.), JPL Publication 87-30, Jet Propulsion Laboratory, Pasadena, California, 1987.

Conel, J.E., R.O. Green, V. Carrere, J.S. Margolis, R.E. Alley, G. Vane, C.J. Bruegge, and B.L. Gary, "Atmospheric Water Mapping with the Airborne Visible/Infrared Imaging Spectrometer (AVIRIS), Mountain Pass, California," *Proceedings of the Airborne Visible/Infrared Imaging Spectrometer (AVIRIS) Performance Evaluation Workshop,* (G. Vane, ed.),.JPL Publication 88-38, Jet Propulsion Laboratory, Pasadena, California, pp. 21-26, 1988.

Green, R.O., G. Vane, and J.E. Conel, "Determination of Aspects of the In-Flight Spectral, Radiometric, Spatial and Signal-to-Noise Performance of the Airborne Visible/Infrared Imaging Spectrometer Over Mountain Pass, California," *Proceedings of the Airborne Visible/Infrared Imaging Spectrometer (AVIRIS) Performance Evaluation Workshop*, (G. Vane, ed.), JPL Publication 88-38, Jet Propulsion Laboratory, Pasadena, California, pp. 162-184, 1988.

Green, R.O., V. Carrere, and J.E. Conel, "Measurement of atmospheric water vapor using the Airborne Visible/Infrared Imaging Spectrometer," *Image Processing '89,* American Society for Photogrammetry and Remote Sensing (ASPRS), 1989.

Green, R.O., J.E. Conel, J.S. Margolis, V. Carrere, C.J. Bruegge, and G. Hoover, "Determination of the In-Flight Spectral and Radiometric Characteristics of the Airborne Visible/Infrared Imaging Spectrometer (AVIRIS)," *Proceedings of the Second Airborne Visible/Infrared Imaging Spectrometer (AVIRIS) Workshop*, JPL Publication 90-54, Jet Propulsion Laboratory, Pasadena, California, 1990a.

Green, R.O., "Retrieval of Reflectance from Calibrated AVIRIS Radiance for Lithological Mapping of the Clark Mountains, California," *Proceedings of the Second Airborne Visible/Infrared Imaging Spectrometer (AVIRIS) Workshop*, JPL Publication 90-54, Jet Propulsion Laboratory, Pasadena, California, 1990b.

Green, R.O., J. E. Conel, J. Margolis, C. Bruegge, and G. Hoover, "An Inversion Algorithm for Retrieval of Atmospheric and Leaf Water Absorption from AVIRIS Radiance with Compensation for Atmospheric Scattering," *Proceedings of the Third Airborne Visible/Infrared Imaging Spectrometer (AVIRIS) Workshop*, JPL Publication 91-28, Jet Propulsion Laboratory, Pasadena, California, 1991 (this publication).

Kastner, C.J. (now Bruegge, C.J.), "In-flight absolute radiometric calibration of the Landsat Thematic Mapper," a Ph.D. Dissertation, University of Arizona, 1985.

Kneizys, F.X., E.P. Shettle, G.P. Anderson, L.W. Abrew, J.H. Chetwynd, J.E.A. Shelby, and W.O. Gallery, *Atmospheric Transmittance/Radiance: Computer Code LOWTRAN 7*, U.S. Air Force Geophysical Laboratory (AFGL), Hanscom Air Force Base, Massachusetts, 1989.

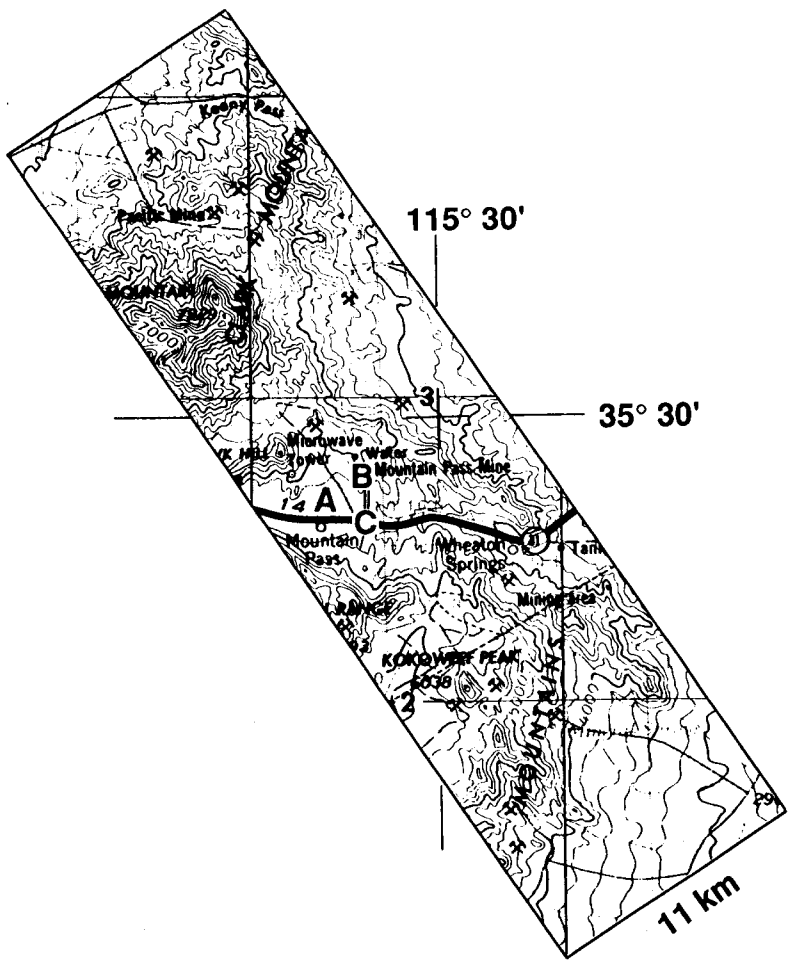

Figure 1. Location of the AVIRIS data set for the Clark Mountains, California. The targets A, B, and C, corresponding to an asphalt parking lot, bastnaesite mineral site, and atmospheric measurement site, are shown as well.

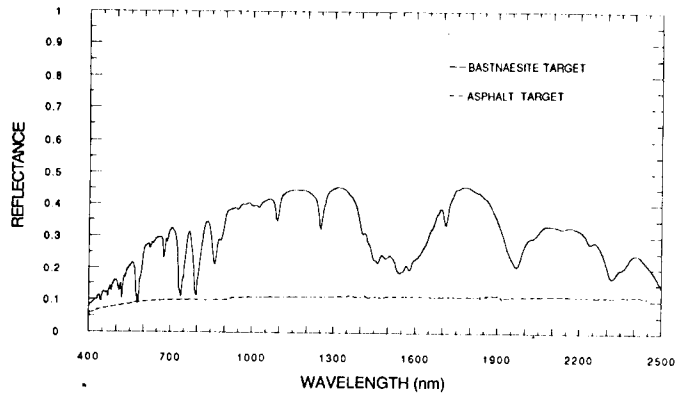

Figure 2. Reflectance of the asphalt target resulting from the mean of 16 in situ field spectra and the laboratory reflectance spectrum of the mineral bastnaesite.

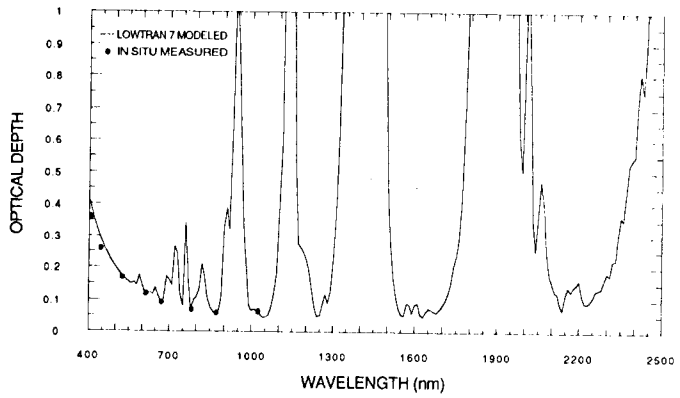

Figure 3. Discrete optical depths calculated from sun photometer measurements acquired adjacent to site A on the day of the AVIRIS overflight. The contiguous LOWTRAN 7 modeled optical depths determined to correspond to the measured discrete optical depths are also given.

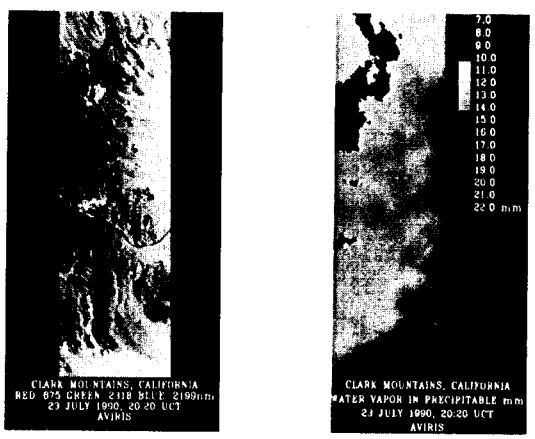

Figure 4. AVIRIS radiance image of the Clark Mountains scene on the left, and the total-column water vapor retrieved for that scene on the right. The water vapor varies from 8 to 22 mm of precipitable water within this 11- by-40-km region. [See slide 18].

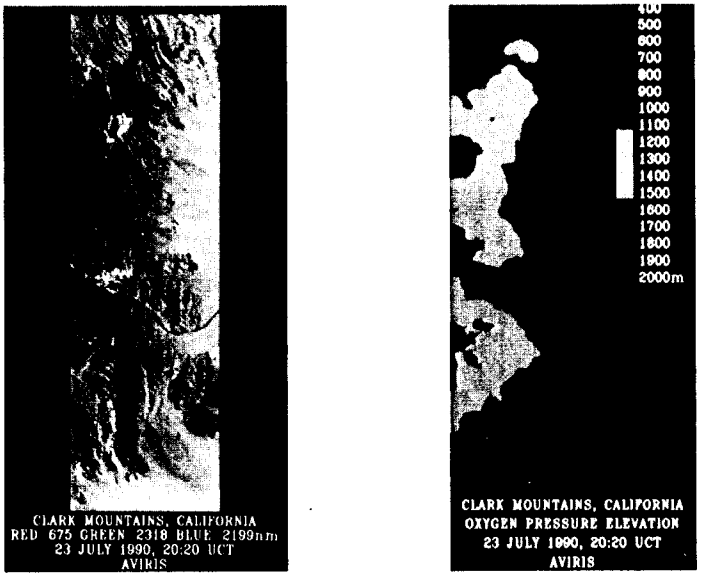

Figure 5. Surface-pressure elevation derived from the absorption of the 760-nm oxygen absorption band measured within the AVIRIS spectrum on the right. AVIRIS radiance image of the Clark Mountains scene on the left. [See slide 19.]

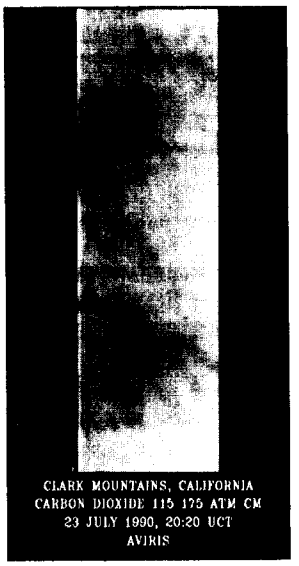

Figure 6. Retrieved carbon-dioxide abundance image from calibrated AVIRIS radiance data using the 2070-nm absorption band.

Figure 7. Estimation of surface slope through calculation of local relative elevations derived from water vapor retrieval.

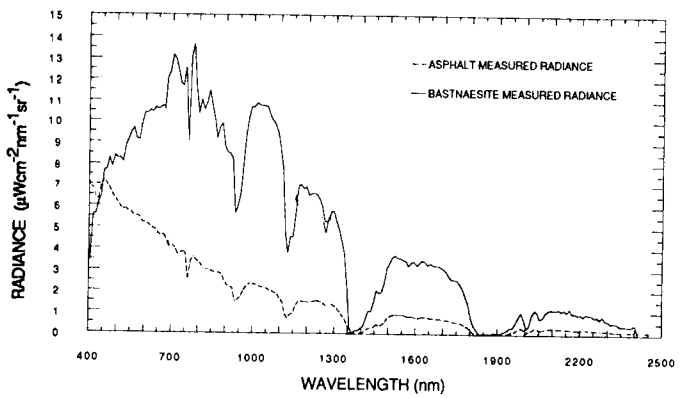

Figure 8. AVIRIS-calibrated radiance spectrum for the asphalt target and the bastnaesite target.

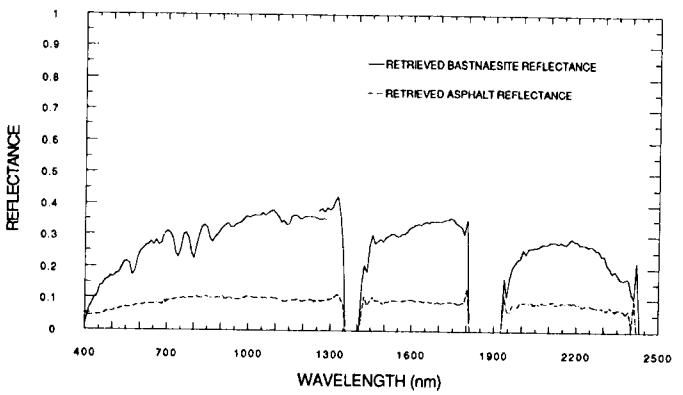

Figure 9. AVIRIS-retrieved reflectance for the asphalt target and the bastnaesite target.

APPLICATION OF AVIRIS WATER MAPPING CAPABILITIES TO THE PROBLEM OF REGIONAL SURFACE EVAPORATION

James E. Conel, Veronique Carrere, Robert O. Green, Jack S. Margolis, Carol Bruegge, Ronald E. Alley, Gordon Hoover, and Anne Nolin

Jet Propulsion Laboratory
California Institute of Technology
Pasadena, California

Introduction

Water vapor plays a major role in the energetics of the Earth's atmosphere. Despite its importance quantitative knowledge of global and even regional water and energy budgets is still lacking (WMO/TD No. 215). In hydrological work there is still no agreement on how regional evaporation at the river basin scale should be measured (Brutsaert, 1986). Well-established methods exist for point measurements using micrometeorological data (e.g., eddy correlation, energy budget and mean profile) (Brutsaert, 1982) and it would be straightforward to make large areal estimates from networks of such stations if such data sets were routinely available.

The focus of the present study is exploration of how the rapid, high-spatial-resolution, atmospheric water mapping capabilities of AVIRIS can be utilized, perhaps involving time sequences of observations, to provide a link between point measurements and larger areal or regional estimates of surface evaporation.

Atmospheric Water Vapor Measurements Provided by AVIRIS

AVIRIS makes measurements of the upward-directed spectral radiance between 400 and 2450 nm at an observational altitude of 20 km above the Earth's surface. The spectral resolution of about 10 nm allows resolution of the important near infrared atmospheric absorptions related to water vapor, among them are the bands at 940 and 1130 nm. We reported (Conel *et al.*, 1988; Conel *et al.*, 1989) the use of a simple two band ratio algorithm and the atmospheric model LOWTRAN 6 to derive estimates of the column abundance of atmospheric moisture. Subsequent modification of this algorithm using LOWTRAN 7 (*e.g.*, the so-called continuum interpolated band ratio (CIBR) of Green *et al.*, 1990) was introduced to account for multiple scattering and to help compensate for vulnerability of the initial simple ratio algorithm to surface reflectance variations because of surface vegetation or soil moisture. Frouin and Middleton (1990) presented another ratio algorithm based on the Tanre 5S code involving use of a narrow and a wide spectral channel centered on one another at the maximum of absorption of the 940 nm water band, and also designed to minimize surface reflectance interference. These ratio methods require assumptions about the atmospheric scattering model and the visibility or measurement of these critical parameters. These methods are subject to systematic errors in retrieved abundances with departures from the assumptions (Carrere *et al.*, 1990; Carrere and Conel, 1991). Gao and Goetz (1990) employed a nonlinear least square band fitting technique with the water absorption band model of Malkmus to provide estimates of atmospheric and surface moisture components. Their method does

not account for atmospheric scattering and is therefore best applied under conditions of high visibility (> 50 km). Green *et al.* (1991, these proceedings) developed a least square band fitting technique based on the MODTRAN atmospheric radiative transfer code that simultaneously estimates parameters of a surface reflectance model together with atmospheric moisture. The method specifically accounts for atmospheric water vapor absorption and aerosol multiple scattering through the MODTRAN model, once visibility is constrained in the code. The technique accounts for the presence of surface water resident in vegetation, as soil moisture, and as standing water, and appears capable of atmospheric moisture retrievals over water by using the path radiance term and the in-band combined absorption and scattering treatment contained in the model. The separation of surface and atmospheric moisture is possible because of differences in band shape and position (surface water shifted to "red") among these components.

We have compared the water abundances retrieved from AVIRIS via the LOWTRAN 7 code with column abundances measured simultaneously on the ground with a sun photometer (Bruegge *et al.*, 1990; Carrere and Conel, 1991) with agreement to within a few percent. Independent confirmation of these measurements was provided by comparison with column abundance retrievals from single-line atmospheric water vapor observations made with a high resolution Fourier Transform spectrometer (Bruegge, *et al.*, 1990). These latter estimates are derived from band parameters and a multiple-layer atmospheric line-by-line transmission model. The LOWTRAN 7-based and interferometer-based estimates agree to within 3%, whereas the scatter of the interferometer determinations using multiple lines was about 5%.

The precision of the described atmospheric water vapor retrievals has been estimated based on the noise characteristics of AVIRIS for the CIBR and Frouin algorithms using radiance measurements over water bodies where the surface reflectance is near zero. For example, for October 1990 observations at Salton Sea (Carrere and Conel, 1991), the uncertainties in water recoveries are less than about 10% for the CIBR, and less than about 2% for the Frouin algorithm, including both random and coherent noise components. The Frouin algorithm enjoys this advantage from use of multiple radiance measurements across the band in the algorithm.

The whisk-broom scanning mode of AVIRIS samples the ~11-km cross-track swath in increments of about 20 m, each in 1/12 of a second, or 100 km^2 in 42 sec. The total horizontal length of lines sampled per 100 km^2, considered as a profile, is nearly 5600 km. The time between possible successive AVIRIS observations over the same target may be constrained by operational considerations of the ER-2 aircraft platform at 11-12 minutes.

Application to the Problem of Regional Surface Evaporation

We investigated three well-known methods of estimating land (or water) surface evaporation: (1) a bulk transfer formulation (*e.g.*, Brutsaert, 1982; Liu, 1990), (2) the atmospheric water budget with surface evaporation evaluated as a residual (*e.g.*, Brutsaert, 1982), and (3) a water budget method employed regionally with long time averages (e.g., Peixoto, 1973; Peixoto and Oort, 1983). How can observations provided by AVIRIS, namely column moisture abundance and its changes with time from place to place, be used in applications of these methods?

(1) Bulk Transfer

A typical procedure for watershed-scale surface (Brutsaert, 1982, 1986) and ocean evaporative flux measurement (Liu, 1990) is based on application of the equation

$$E = C_E U_r \rho (q_s^*(T_s) - q_r) \quad (1)$$

where E is the surface evaporation in g/(cm^2 sec), C_E is the bulk transfer coefficient for water vapor, U_r the mean horizontal wind speed at reference height z_r above the surface, ρ the atmospheric density, $q_s^*(T_s)$ the saturation specific humidity at the surface temperature T_s, and q_r the mean specific humidity at the reference height. AVIRIS observations of water column abundance distribution in and of themselves cannot supply the surface temperature nor estimates of C_E, which must be obtained independently from in situ measurements or theoretical analysis (Deardorff, 1968; Liu *et al*, 1979; Brutsaert, 1979). The need to estimate C_E together with a surface resistance (in lieu of the term $q_s^*(T_s)$ in Equation 1 has led Brutsaert and Mawdsley (1976) to consider use of a uniform boundary layer model based on similarity principles for estimation of E. This model requires use of radiosonde data to obtain values of wind, temperature, and humidity at the upper and lower surfaces of the boundary layer.

Empirical relationships between the column abundance W supplied by AVIRIS and the specific humidity near the surface q_r may, however, be useful in estimating the latter quantity. Following Liu (1990) and others [see references in Liu (1990)] we compiled data from 2105 Rawinsonde flights (1986 to present) from Edwards Air Force Base, California (a desert environment), correlating total column water vapor abundance observed versus the ground-level absolute humidity. The resulting scatter plot, not edited for possible faulty observations, is shown in Figure 1. The trends illustrated are similar to those in radiosonde data compiled by Liu (1986) for oceanic sites, but with greater scatter in the present instance.

The preliminary compilation of Figure 1 is being extended to other Rawinsonde data sets including oceanic and coastal sites. The analysis of such might profitably be extended to seek additional (empirical) correlations of boundary layer thickness with absolute humidity at the upper boundary. Another area of interest is compilation of sun photometer measurements of water column abundance with measurements of ground-level absolute humidity that are independent of the Rawinsonde column measurement process. Such spectroscopic-based correlations will represent instantaneous line-of-sight to the sun measurements as opposed to ~1-hour-long averages characteristic of balloon ascents and will serve to characterize the time scale of surface humidity-column abundance correlations such as those depicted in Figure 1.

(2) Atmospheric Water Budget

Basis of the method – This method (see Peixoto, 1973; Brutsaert, 1982, p. 257ff.) evaluates the surface evaporation as a residual of the terms of the water budget equation for a control volume in the atmosphere. The general water balance equation for the atmosphere at a point is

$$\frac{\partial W}{\partial t} + \nabla \cdot \int_0^\infty U(z) q \rho dz = E - P \qquad (2)$$

where W is the column abundance, equal to $\int_0^\infty q\rho dz$, and U(z) is the horizontal wind velocity vector. The z-axis is vertical, positive upward, and t is the time. The right hand side of Equation 2 is the difference between evaporation and precipitation at the point considered. Multiplication by dA/A and integration over the horizontal extent of the volume secures the required areal average. Where areal averages are derived below from image data, they will be denoted by overbars. To simplify the discussion, we consider a situation of uniform unidirectional winds with height over the control volume so that rotation of the horizontal coordinate axes about the vertical reduces the divergence operator to a single derivative $\partial/\partial s$, say, where the s-axis is positive in the direction of the wind, whose velocity is $U_s(z)$. The integral in Equation 2 must be transformed to quantities observable by AVIRIS. This can be accomplished using the first theorem of mean value (Carslaw, 1950, p. 105ff.), in which case the integral becomes

$$\bar{U}_s \int_{z_0}^{z_t} q\rho dz = \bar{U}_s W \qquad (3)$$

In equation 3 z_0 is the surface height and z_t is the height of the top of the internal water vapor boundary layer. If $U_s(z)$ is continuous, U_s is given by

$$\bar{U}_s = \left(1/(z_t - z_0)\right) \int_{z_0}^{z_t} U_s(z) dz \qquad (4)$$

With these definitions, Equation 1 is transformed to

$$\frac{\partial W}{\partial t} + \bar{U}_s \frac{\partial W}{\partial s} = E - P \qquad (5)$$

All of the quantities on the left hand side of Equation 5 are, in principle, derivable from the AVIRIS images of W over a given area, the time derivative from sequences of images, and the spatial derivative point by point for each image from finite difference approximations. The spatial scale of recoverable fluctuations is $\geq$ 20 m for W and 40 m for $\partial W/\partial s$. The importance of variations below these lengths will need to be evaluated with field observations in particular cases.

Interpretation of the velocity $\bar{U}_s$ – The interpretation of $\bar{U}_s$ is more problematical. In this preliminary analysis we sought guidance from studies of the influence of wind shear on horizontal dispersion for instantaneous ground-level sources (Saffman, 1962; Smith, 1965; Csanady, 1969; Taylor, 1982). If the moisture is confined within a layer of constant thickness and there is neither loss nor gain of material at the upper and lower boundaries, then $\bar{U}_s$ can be thought of as the speed of horizontal translation of centroids of spatial fluctuations in W seen in successive images. If the atmosphere is unbounded, and the wind speed U(z) and eddy diffusivity K(z) increase upward according to az^m and bz^m respectively, then according to results of Saffman (1962) the centroid for a ground-level release at time t = 0 advances proportional to $at(bt)^{m/(2-n)}$. If the wind speed increases linearly with height (m = 1) and K is constant,

the centroid displacement is $\propto t^{3/2}$ (Saffman, 1962; Smith, 1965), and the speed $\propto t^{1/2}$. For power law variations in U and K with z, adopting values of m = 1/7 and n = 6/7 (*e.g.*, Brutsaert, 1982) gives a centroid translation $\propto t^{9/8}$ and speed $\propto t^{1/8}$. For all of these unbounded models, the apparent translation speed increases with time as material originally at the surface diffuses to regions of greater and greater wind speed at altitude.

In addition to wind shear in the surface layer, the trajectories of particles are influenced both by Coriolis forces and surface drag in the Ekman layer. Diffusion in the Ekman layer has been analyzed by Csanady (1969) and more recently by Taylor (1982). Figure 2 is taken from the latter paper. Initially symmetric instantaneous releases at the surface are quickly distorted into ellipsoidal-shaped distributions by wind shear. As time passes, the concentration distributions, here depicted by ellipses representing isopleths at a given height where the concentration is 60% of the centroid value, are displaced in the direction of ground-level wind shear. These distributions elongate, broaden, and twist in response to lateral diffusion and the change of wind direction aloft, with axes connecting centroids between levels eventually aligned with one another and at 45° to the geostrophic wind. Since a continuous surface source, say from evaporation of a small water body or wet field, might be visualized as a continuous distribution of such releases, an expanding rotated plume could be expected to emerge wherever atmospheric conditions permit Ekman spiral structures to form in the atmosphere.

AVIRIS water vapor image sequences and Rawinsonde data at Rogers Dry Lake-To investigate the question of recovering atmospheric motions from the water vapor maps, we used a sequence of four images obtained at Rogers Dry Lake, California as shown in Figure 3 (see paper by Green *et al.*, 1991 in these proceedings for color slides of these images). These data were acquired on July 23, 1990 as part of the in-flight radiometric calibration and stability analysis of AVIRIS. The water vapor column abundance maps were generated using the CIBR algorithm, and the data were filtered over 7 × 7 pixel subareas. The lower images depict the clear air conditions over the site as seen at a wavelength of 892 nm.

A rawinsonde was launched from Edwards Air Force Base at 1829 hr UCT and provided data on winds, temperature, and moisture aloft during a portion of the first AVIRIS overpass. The approximate trajectory of the balloon ascent from its point of origin is superposed on the first image panel (Fig. 3). The lower part of the ascent trajectory exhibits a clockwise rotation from ground level to approximately 6000 feet, possibly describing motion in the Ekman wind spiral. The winds aloft, absolute humidity and the total precipitable water distributions obtained are given in Figure 4.

Estimating $\bar{U}_s$ from image data – Two methods were used to derive estimates of $\bar{U}_s$ from the AVIRIS water map sequence at Rogers Dry Lake: (tracking of water cloud features between successive images, and (2) calculation of $\bar{U}_s$ from Equation (5).

Method 1 - Estimation of the average wind velocity from displacements of recognizable features in the column abundance distribution between successive images is straightforward to apply in principle, but difficult in practice because of large rapid changes in the distributions of W between

successive AVIRIS frames arising from shear, rotation, and diffusion. We studied the image sequence of Figure 3 for features and patterns that could be identified from image to image. While several candidate pairs could be identified, none were straightforward to match; furthermore it proved difficult to avoid a prejudice of wind direction (and to a lesser extent speed) induced by the rawinsonde results for that time period. Simple vectorial diagrams of the displacements for a few examples are shown in Figure 5. The evolution of such water vapor features would be aided by AVIRIS water images more closely spaced in time than the 11-12 minute intervals achieved in making the observations presented in Figure 3.

It is worth pointing out that the feature tracking method described here yields, according to Equation 5, a value for the average velocity $\bar{U}_s$ that will be independent of the presence of source or sink terms provided that these terms are constant in space but not necessarily in time. For example, the solution of Equation 5 for the initial value $W(x,0) = f(x)$ and a source term $\epsilon(x,t)$ is $W(x,t) = f(x - \bar{U}_s t) + \int_0^t \epsilon(\bar{U}_s \xi + x - \bar{U}_s t, \xi) d\xi$ (Zauderer, 1989). The initial pattern f(x), which can be introduced by advection, translates along the + x-axis with velocity $\bar{U}_s$, but is modified by the second term, if $\epsilon = \epsilon_0 g(t)$, $W(x,t) = f(x - \bar{U}_s t) + \epsilon_0 \int_0^t g(\xi) d\xi$, and the pattern translates along the + x-axis with velocity $\bar{U}_s$.

The tracking of features in the column abundance advancing under advection is feasible and can be seen from examination of Figure 6. These ground based data were acquired with water vapor channels of Reagan solar photometers at Ivanpah Playa in eastern California on March 7, 1991. The instruments were separated by approximately 1500 m along a line trending N30°W. The hourly average wind speed, wind direction, and standard deviation of the wind direction (σ_θ) were recorded at 10-m height above the playa surface at the southern station. The time interval between passage of the same feature over these stations depended on wind direction, and decreased as the wind shifted toward the northeast. Two stations are in general sufficient only to generate an apparent velocity of translation. The apparent velocity obtained is 2.85 m/sec at 7:30 AM PST versus ~ 8.0 m/sec at 10 m recorded by cup anemometer. These experiments will be repeated in the future as part of validation exercises for atmospheric water vapor retrieval, but instead using a network of surface water vapor measurement stations. Such areal arrays of observations should define more precisely the geometry of water vapor movements and permit a better comparison with wind speed measurements obtained with meteorological instruments.

Method 2 - In the absence of the source and sink terms E − P (a good approximation for Mojave Desert conditions in late July), Equation 5 gives

$$\bar{U}_s = - \frac{\partial W/\partial t}{\partial W/\partial s} \qquad (6)$$

To estimate $\bar{U}_s$ by this method, we generated averages of W and $\partial W/\partial s$ for the area common to the four water vapor maps of Figure 3. The derivative $\partial W/\partial s$ was formed from $\sqrt{[(\partial W/\partial x)^2 + (\partial W/\partial y)^2]}$. For this calculation the x- and y-axes were along the vertical and horizontal boundaries of each panel. Small adjustments for differences in panel orientation were also applied. Average values for the time and space derivatives of the common area, namely $\overline{\partial W/\partial t}$, $\overline{\partial W/\partial x}$, $\overline{\partial W/\partial y}$, and $\overline{\partial W/\partial s}$, are given in Figure 7. The values of $\bar{U}_s$ obtained

by application of Equation 6 have been plotted on the profile of rawinsonde-determined wind speed given previously in Figure 4. In Figure 4 the average value of the horizontal wind speed was calculated from the vertical profile to an altitude of 20,000 feet (altitude below which 99% of the water vapor resides) using Simpson's rule.

(3) Water Budget Method with Long-Time Averages

Peixoto (1973, p. 14) pointed out that a long time- (and areal-) averaged water vapor storage term $\langle \partial W/\partial t \rangle$ in Equation 1 is in general very small compared with the other terms, and thus for long enough averaging periods (*e.g.*, seasonal or yearly) the water vapor flux divergence can be used to estimate $\langle \overline{E-P} \rangle$. We looked at the precipitable water measurements obtained from the Edwards AFB, California, rawinsonde observations covering the period of 1986-present to understand the gross properties of the (twice daily sampled) precipitable water time series at this locality. Figure 8 illustrates both the long- (seasonal) and short-term variation of precipitable water W(t). Figure 9 is the average value $\langle W(t_N) \rangle$ of the departure of W(t) from its mean value $\langle W \rangle$ over the time interval as calculated from the formula

$$\langle W(t_N) \rangle = \frac{1}{N\Delta t} \sum_{i=1}^{N} [W(t_i) - \langle W \rangle] \qquad (7)$$

where Δt is the time interval between observations t_i. The average value of the time derivative $\langle \partial W(t_N)/\partial t \rangle = \partial \langle W(t_N) \rangle / \partial t \approx [\langle W(t_N) \rangle - \langle W(t_{N-1}) \rangle]/\Delta t$. The requirement of long time averages may be overly restrictive. Thus from the record of Figure 9, time intervals of slowly changing $\langle W(t_N) \rangle$ can be identified. For example, the period of days 240 - 360 in 1986 is an interval where the derivative is small, while for the period of days 1 - 240, the derivative is comparatively large. The actual condition is that $\langle \partial W/\partial t \rangle \ll \langle \nabla \cdot \int \rho q dz \rangle$, and so a complete discussion requires evaluation of the flux divergence. The spatial derivative requires observations at multiple stations. The question of estimating the magnitude of this term from the single-station rawinsonde records using its time variability is under study.

Acknowledgments

We want to thank Ms. Marian Durran, 6521 RANS/TSRCP, Edwards AFB for supplying the rawinsonde data. Mr. Tony Garcia of Molycorp (Division of Unocal) kindly made available the meteorological data from their tower at Ivanpah Playa. Steve Adams of JPL provided much appreciated computational support. This paper presents the results of one phase of research carried out at Jet Propulsion Laboratory, California Institute of Technology, under a contract with the National Aeronautics and Space Administration.

References

Bruegge, C.J., J.E. Conel, J.S. Margolis, R.O. Green, G. Toon, V. Carrere, R.G. Holm, and G. Hoover, 1990, *SPIE Vol. 1298*, 150-163.

Brutsaert, W., 1979, *Boundary-Layer Meteorol.*, 16, 365-388.

Brutsaert, W. 1982, *Evaporation into the atmosphere*, D. Reidel Publishing Company, Boston, 299 pp.

Brutsaert, W., 1986, *American Geophysical Union Paper No. 5W0661*, 39S-45S.

Brutsaert, W., and J.A. Mawdsley, 1976, *Water Resour. Res.*, 12(5), 852-858.

Carrere, V., J.E. Conel, R.O. Green, C. Bruegge, J. Margolis, and R. Alley, 1990, Proceedings of the Second Airborne Visible/Infrared Imaging Spectrometer (AVIRIS) Workshop (R.O. Green, ed.), *JPL Publication 90-54*, Jet Propulsion Laboratory, Pasadena, California, 107-128.

Carrere, V., and J.E. Conel, 1991, Comparison of two techniques for recovery of atmospheric water vapor total column abundance from imaging spectrometer data: sensitivity analysis and application to Airborne Visible/Infrared Imaging Spectrometer (AVIRIS) data, to be published.

Carslaw, H.S., 1950, *An introduction to the theory of Fourier's series and integrals (Third edition)*, Dover Publications, Inc., New York.

Conel, J.E., R.O. Green, V. Carrere, J.S. Margolis, G. Vane, C. Bruegge, and R.E. Alley, 1989, *IGARSS '89 Symposium Proceedings*, Vol. 4, 2658-2663.

Conel, J.E., R.O. Green, V. Carrere, J.S. Margolis, R.E. Alley, G. Vane, C.J. Bruegge, and B. Gary, 1988, in Proceedings of the Airborne Visible/ Infrared Imaging Spectrometer (AVIRIS) Performance Evaluation Workshop (G. Vane, ed.), *JPL Publication 88-38*, Jet Propulsion Laboratory, Pasadena, California, 21-29.

Csanady, G.T., 1969, *J. Atmos. Sci.*, 26, 414-426.

Deardorff, J.W., 1968, *J. Geophys. Res.*, 73, 2549-2557.

Frouin, R., and E. Middleton, 1990, *Proceedings of AMS Symposium on FIFE*, 70th AMS Annual Meeting, Anaheim, California, 135-139.

Gao, B.C., and A.F.H. Goetz, 1990, *J. Geophys. Res.*, 95, 3549-3564.

Green, R.O., V. Carrere, and J.E. Conel, 1990, *Proceedings of Image Processing '89, American Society for Photogrammetry and Remote Sensing, Sparks, Nevada*, 31-44.

Green, R.O., 1991, Proceedings of the Third Airborne Visible/Infrared Imaging Spectrometer (AVIRIS) Workshop (R.O. Green, ed.), this publication.

Liu, W.T., K.B. Katsaros, and J.A. Businger, 1979, *J. Atmos. Sci.*, 36, 1722-1735.

Liu, W.T., 1986, *Mon. Wea. Rev.*, 114, 1591-1602.

Liu, W.T., 1990, *Surface waves and fluxes, Vol. II* (G.L. Geernaert and W.J. Plant, eds.), Kluwer Academic Publishers, The Netherlands, 293-309.

Peixoto, J.P., 1973, *WMO/IHD Report No. 20*, World Meteorological Organization, Geneva, 83 pp.

Peixoto, J.P. and A.H. Oort, 1983, in *Variations in the global water budget* (A. Street-Perrott, *et al.*, eds.), D. Reidel Publishing Co., Boston, 5-65.

Saffman, P.G., 1962, *Quart. J. Roy. Meteor. Soc.*, 88, 382-393.

Smith, F.B., 1965, *Quart. J. Roy. Meteor. Soc.*, 91, 318-329.

Taylor, A.D., 1982, *J. Atmos. Sci.*, 39, 837-850.

World Meteorological Organization, 1988, Concept of the global energy and water cycle experiment, *WMO/TD-No. 215 (World Climate Research Program - 5)*.

Zauderer, E., 1989, *Partial differential equations of applied mathematics*, John Wiley and Sons, New York, 891 pp.

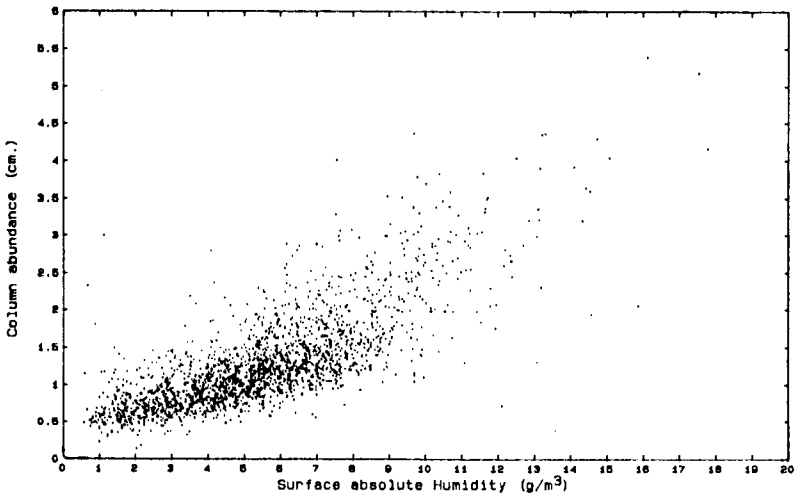

Fig. 1. Scatter plot of water vapor column abundance vs the surface value of absolute humidity for 2105 rawinsonde observations over the period 1986-present. Data courtesy of 6521 RANS/TSRCP, Edwards AFB.

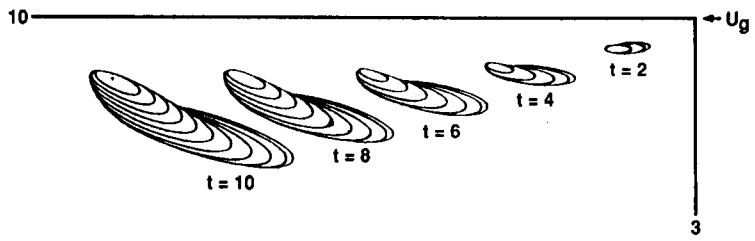

Fig. 2. Evolution in the Ekman layer of an instantaneous release at the surface. U_g is the geographic wind direction. The distance, height, and time coordinates are in non-dimensional units. From Taylor (1982).

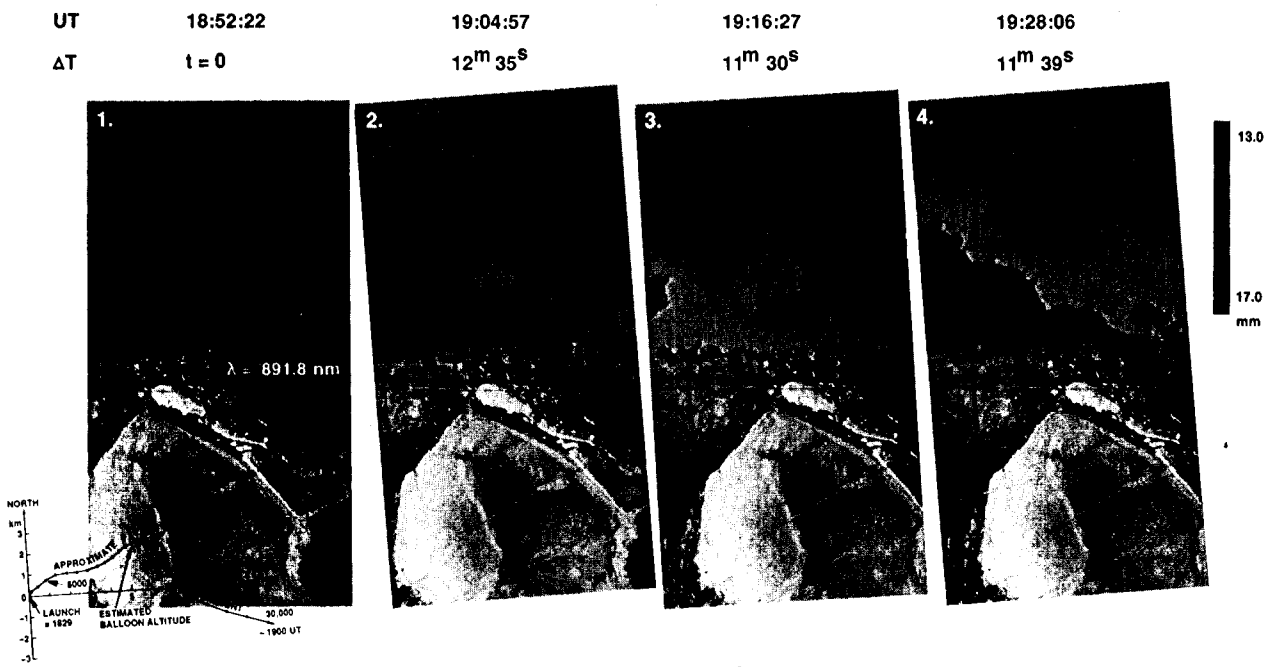

Fig. 3. Changes in water vapor column abundance with time at Rogers Dry Lake, July 23, 1990.

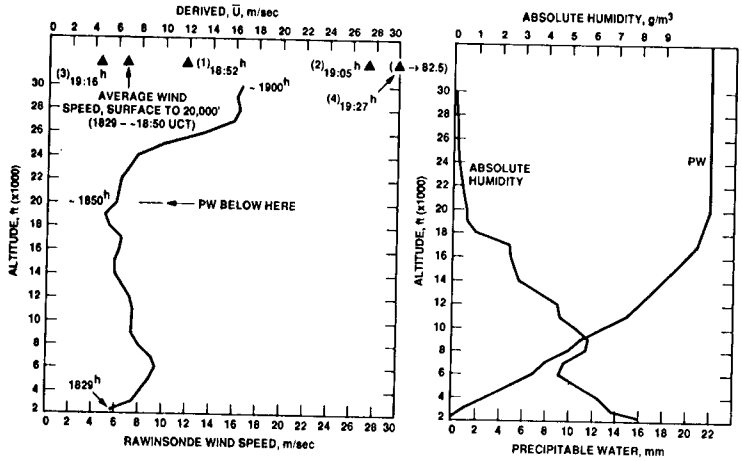

Fig. 4. Vertical profiles of wind speed, absolute humidity and precipitable water (PW) from the July 23, 1990 (18:29 hours UT) rawinsonde launch at Edwards AFB. The wind speeds Ū are derived from the image sequence of Figure 3 via Equation 6.

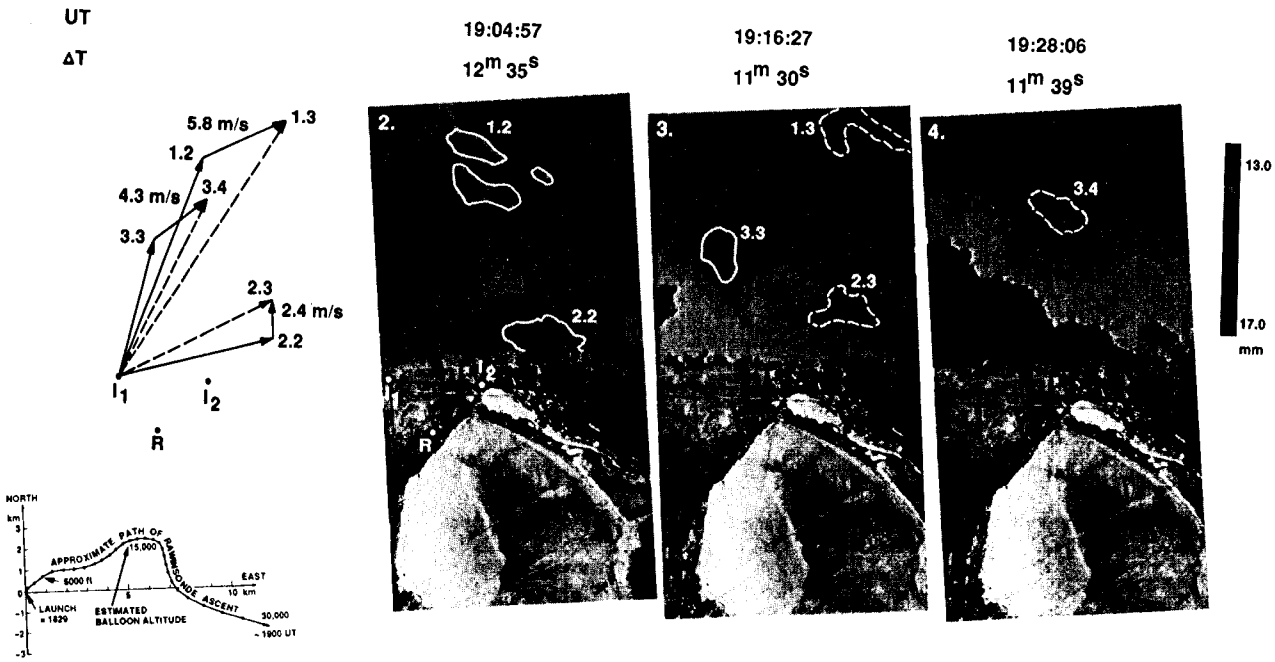

Fig. 5. Examples of possible displacements of water cloud features between water vapor scenes of Figure 3. The notation m.n = feature m.panel n.

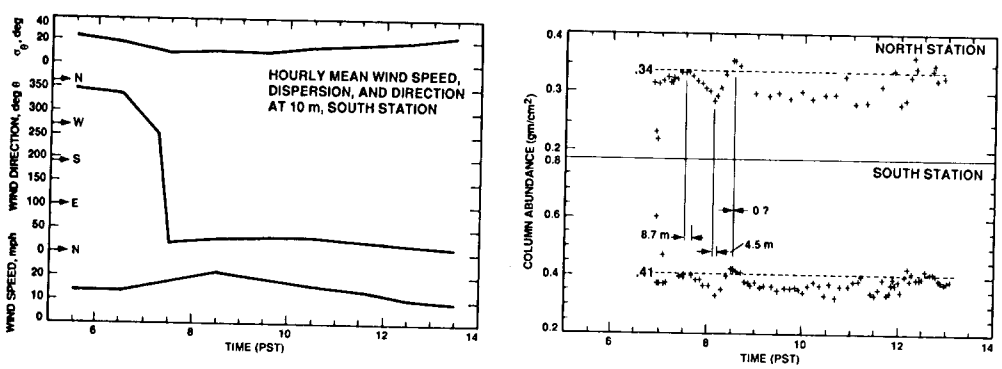

Fig. 6. Translation of water vapor features at Ivanpah Playa as measured with 940 nm water vapor channel of the Reagan sun photometers, March 7, 1991. Wind data courtesy of Molycorp, Division of Unocal.

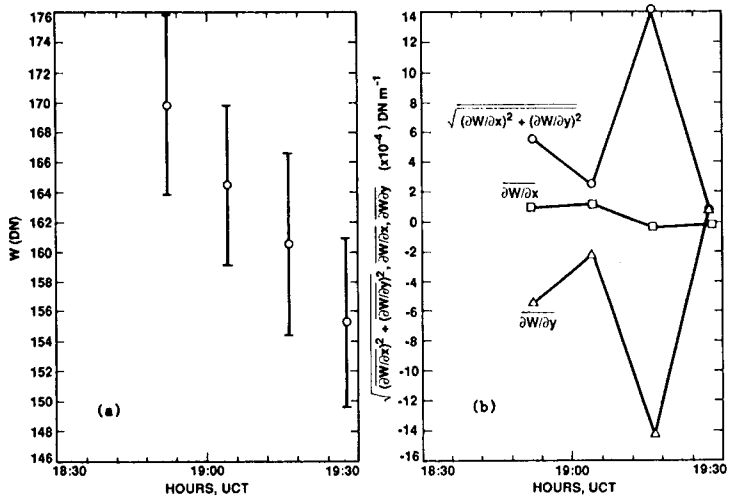

Fig. 7. (a) Time variability, and (b) Gradients of water vapor abundance averaged over the common area of successive water vapor maps in Figure 3.

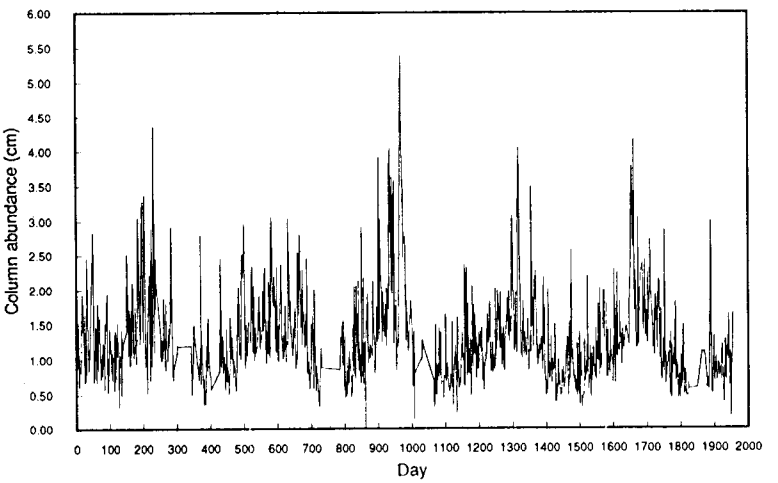

Fig. 8. Time series of water vapor column abundance as measured by rawinsonde for the period 1986-present, Edwards AFB, California. Data courtesy of 6521 RANS/TSRCP EAFB.

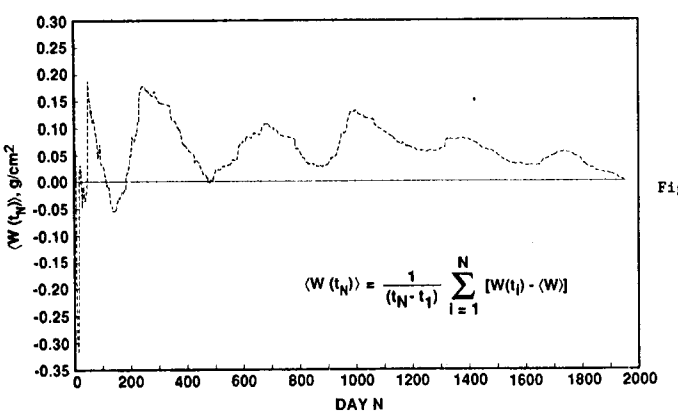

Fig. 9. Average value of the precipitable water abundance as function of time, derived from the time series of Figure 8.

CASE STUDIES OF WATER VAPOR AND SURFACE LIQUID WATER FROM AVIRIS DATA MEASURED OVER DENVER, CO AND DEATH VALLEY, CA

B.-C. Gao[1], K. S. Kierein-Young[1,2], A. F. H. Goetz[1,2],
E. R. Westwater[3], B. B. Stankov[3], and D. Birkenheuer[4]

[1]CSES/CIRES, Campus Box 449, University of Colorado, Boulder, CO
[2]Department of Geological Sciences, University of Colorado, Boulder, CO
[3]NOAA/ERL/ Wave Propagation Laboratory, Boulder, CO
[4]Cooperative Institute for Research in the Atmosphere (CIRA), Ft. Collins, CO

Abstract. High spatial resolution column atmospheric water vapor amounts and equivalent liquid water thicknesses of surface targets are retrieved from spectral data collected by the Airborne Visible/Infrared Imaging Spectrometer (AVIRIS). The retrievals are made using a nonlinear least squares curve fitting technique. Two case studies from AVIRIS data acquired over Denver-Platteville area, Colorado and over Death Valley, California are presented. The column water vapor values derived from AVIRIS data over the Denver-Platteville area are compared with those obtained from radiosondes, ground level upward-looking microwave radiometers, and geostationary satellite measurements. The column water vapor image shows spatial variation patterns related to the passage of a weather front system. The column water vapor amounts derived from AVIRIS data over Death Valley decrease with increasing surface elevation. The derived liquid water image clearly shows surface drainage patterns.

I. Introduction

Water vapor is one of the most important atmospheric gases. The integrated water vapor content from ground to space has important applications to meteorology, hydrology, climate, and radio interferometry. In this paper, the integrated water vapor content is referred to as column water vapor amount or as precipitable water vapor (PWV). The liquid water content of vegetation is related to the stress conditions of vegetation. Remote sensing of liquid water content of vegetation has important applications to forestry and agriculture. The soil moisture content is important to agriculture, forestry, hydrology, and engineering geology.

Satellite remote sensing of PWV with an accuracy of approximately 10% over the oceans using microwave emission measurements is a proven technique (Alishouse, 1983). However, the variability of land surface microwave emissivities poses difficulties in determining PWV over land from satellite microwave data. Column water vapor retrievals over land from satellite IR emission measurements using, for example, the split window technique (Chesters et al., 1983) are possible during clear conditions.

Recently, there have been several reported successes in remote sensing of column atmospheric water vapor amounts from aircraft measurements of solar radiation reflected by the land surface near 1 μm (Gao and Goetz, 1990; Conel et al., 1989; Frouin et al., 1990). These remote sensing techniques are referred to as optical techniques. Gao and Goetz (1990) have also reported the derivation of moisture content of vegetation using liquid water absorption features near 1 μm.

Column water vapor amounts can be obtained from the ground with upward-looking microwave radiometers (Hogg et al., 1983). The Wave Propagation Laboratory (WPL) of the National Oceanic and Atmospheric Administration (NOAA) operates a limited network of dual-channel microwave radiometers (Westwater and Snider, 1989). Radiometers are now routinely operated at Stapleton International Airport in Denver, Colorado and at Platteville, Colorado (approximately 60 km north of Denver). In order to verify the optical techniques, an experiment was designed. Specifically, the Airborne Visible/Infrared Imaging Spectrometer (AVIRIS) (Vane, 1987) was requested to make measurements over the Denver-Platteville area. Column water vapor amounts were to be retrieved from AVIRIS data and then compared with column water vapor amounts measured with the two microwave radiometers mentioned above. The AVIRIS made the measurements around 19:40 UTC 22 March 1990. At this time, the sky was clear. However, snow started later in the day. The AVIRIS measurements happened to be

conducted in the middle of another experimental project, the Winter Icing and Storm Project (WISP90) (Stankov et al., 1990) conducted by NOAA Forecast Systems Laboratory (FSL) for determining the utility of unattended microwave radiometers in detecting, and providing input to forecasts of aircraft icing. WISP90 collected data from microwave radiometers, infrared radiometers, lidar ceilometers, radio-acoustic sounding systems (RASS), and radiosondes at several locations in Colorado. Also, meteorological parameters were collected from approximately 20 surface stations in Colorado. Meanwhile, data from the Visible Infrared Spin Scan Radiometer (VISSR) Atmospheric Sounder (VAS) on the NOAA Geostational Operational Environmental Satellite (GOES) were collected and archived by NOAA FSL's Program for Regional Observing and Forescasting Services (PROFS). The WISP90 data provided information on the meteorological conditions around the AVIRIS measurements and allowed better interpretation of the AVIRIS and the microwave radiometers data. In this paper, the water vapor measurements with AVIRIS, microwave radiometers, and VAS are compared.

AVIRIS measurements over Death Valley, California were obtained on September 29, 1989 as part of the Geologic Remote Sensing Field Experiment (GRSFE). At the time of the overflight, some surface areas were wet, based on field observations. Measurements of reflectance spectra of samples collected from the field clearly showed liquid water absorption features near 0.98, 1.2, 1.6, and 2.2 μm. Because of the presence of wet surface areas when the AVIRIS measurements were made, we decided to further test the ability of the algorithm (Gao and Goetz, 1990) for simultaneous retrievals of the atmospheric water vapor amount and the surface liquid water content from the AVIRIS data. The results are described in this paper.

II. Imaging Spectrometers: the Optical Technique

Imaging spectrometers acquire images in hundreds of contiguous spectral bands such that for each picture element (pixel) a complete reflectance or emittance spectrum can be derived from the wavelength region covered (Goetz et al., 1985). AVIRIS is now an operational imaging spectrometer. This instrument images the Earth's surface in 224 spectral bands, each approximately 10 nm wide, covering the region 0.4-2.5 μm, from an ER-2 aircraft at an altitude of 20 km. The ground instantaneous field of view is 20 x 20 m^2.

A technique for simultaneous retrievals of atmospheric water vapor amount and surface liquid water content has been described by Gao and Goetz (1990). In this technique, the quantitative retrieval is made by curve fitting AVIRIS spectra with calculated spectra near 1 μm using atmospheric and liquid water transmission models, and a nonlinear least squares fitting technique. Figure 1 shows an example of spectral curve fitting for retrieving water vapor amount only. During the fitting process, the water vapor amount and the spectral background, a linear function of wavelength, are allowed to vary. The best estimates of the water vapor amount and the spectral background are obtained when the sum of the squared differences between the observed and the calculated spectra is minimized. Examples of fitting AVIRIS spectra over wet areas for simultaneous retrievals of atmospheric water vapor and surface liquid water content are presented later in this paper. Our technique is applicable for retrievals from AVIRIS data obtained on clear days with visibilities 20 km or greater. Because atmospheric scattering is not modeled directly, the technique is not applicable for retrievals from AVIRIS data measured on hazy days. Under these circumstances, the scattering effect must be modeled.

III. Results

Column water vapor amounts are retrieved from AVIRIS data measured over the Denver-Platteville area, and both column water vapor amounts and surface liquid water thicknesses are retrieved from AVIRIS data measured over Death Valley using the spectral curve fitting technique.

A. Denver-Platteville, Colorado

Figure 2a shows a 0.86 μm image of the Denver-Platteville area. The AVIRIS radiances were averaged spatially on a 2 x 2 pixel basis when the image was produced. The spatial averaging was necessary because of the limitation of our image processing hardware. The Denver Stapleton International Airport is at the lower left part of the image; Platteville is at the upper part. Highway 85, which connects Denver and Platteville, is seen as a curved line. The image covers a surface area of approximately 11 x 68 km^2.

Column water vapor amounts were retrieved by curve fitting the 0.94-μm water vapor band. The AVIRIS data were averaged spatially on a 4 x 4 pixel basis to decrease the computer time. The retrieval took approximately 25 hours on a Microvax III computer. Low vertical resolution temperature, pressure, and water vapor volume mixing

ratio profiles, measured near the airport by a six-channel microwave radiometer, were used in the spectral calculations during the curve fitting process. Figure 2b shows an image processed from the retrieved column water vapor values. To produce a water vapor image having the same size as the image in Fig. 2a, the retrieved water vapor values were zoomed spatially on a 2 x 2 pixel basis. The narrow vertical bar on the right side of Fig. 2b gives the scale of water vapor values from 0.53 cm (black) to 0.76 cm (white), a very small range. The column water vapor values in the entire scene had a mean of 0.640 cm and a standard deviation of 0.044 cm. Horizontal lines in Fig. 2b are due to small errors in the AVIRIS radiometric calibration. Larger scale features are also obvious in Fig. 2b. From the airport to Platteville, the image shows a dark-bright-dark-bright pattern.

A topographic map of the AVIRIS scene is shown in Fig. 2c. Generally, the surface elevation decreases from the airport area (~1630 m) to Platteville (~1450 m). Small variations of surface elevation in the east-west direction are also present. Column water vapor amount usually decreases as the surface elevation increases, because atmospheric water vapor concentration decreases rapidly with altitude. Therefore, the column water vapor amount from the airport to Platteville was expected to increase. The dark-bright-dark-bright pattern from bottom to top in Fig. 2b indicates that real spatial variation, not related to the topographic effects, of water vapor distributions existed when the AVIRIS data were acquired. The observed spatial variation of column water vapor amount on the order of 0.1 cm or less indicates the high precision with which column water vapor amounts can be determined from AVIRIS data.

Precipitable water vapor fields, at a grid spacing of approximately 10 km, over the Rocky Mountain foothills extending roughly 300 km in both the east-west and the north-south directions were obtained from VAS data using a regression technique described by Birkenheuer (1991). Bias existed between PWV values obtained from the VAS data alone and the "true" PWV values. In order to remove the bias, PWV values obtained from VAS data alone were raised or lowered by a constant based on PWV values measured with microwave radiometers at the airport and at Platteville. The resulting bias corrected PWV field at 18:45 UTC 22 March (approximately one hour before the AVIRIS measurements) revealed a gradient structure in the Denver-Platteville area, which is similar to the gradient structure in Fig. 2b.

Figure 3 shows time series of PWV at (a) Platteville, (b) Denver, and (c) Elbert on 22-23 March 1990. Elbert is located approximately 60 km southeast of Denver. The continuous curves show 2-min time series from microwave radiometers. The rectangles are from the Cross-chain Loran-C Atmospheric Sounding System (CLASS) radiosondes. The squares are from the National Weather Service (NWS) radiosondes. The dark circles are from the VAS adjusted images, and the open circles from the AVIRIS measurements. The PWV values from AVIRIS and from the microwave radiometer measurements agreed to within 0.1 cm, but the relative difference is greater than 10%.

Because the PWV values from the microwave radiometer at Elbert were not used in the bias corrections discussed above, comparing PWV values from the VAS data with bias corrections to those from the Elbert microwave radiometer measurements is a blind test of the VAS PWV analysis technique. Fig. 3c shows that the VAS PWV analysis reported a consistently higher level of PWV over Elbert. A possible explanation for the discrepancy is presented below. The ground instantaneous field of view of VAS data is approximately 10 km. This large field of view would tend to blend the lower moisture level at the higher elevation terrain, where the microwave radiometer was located, with the higher moisture levels at adjacent lower elevation terrains, effectively raising the analyzed amount of PWV in a region like that of Elbert.

Fig. 3b shows that a PWV difference of 3 mm existed between the radiometer and the radiosonde data at 2300 UTC. This difference was due to the NWS balloon moving into a region of dry air, and did not reflect the build-up of moisture that was observed during this time by all three microwave radiometers. That a build-up was occurring was also supported by the two special CLASS radiosondes released at Elbert at 0000 and 0300 UTC 23 March. This increase in moisture was followed by a well-documented event of supercooled liquid water that lasted for three days (Stankov et al., 1990). The conclusion of the NWS balloon moving into a dry air region was based on the analyses (Gao et al., 1991) of wind profiles measured at the airport and of meteorological data from approximately 20 surface stations located in different parts of Colorado.

B. Death Valley, California

Death Valley is located in the southeastern part of California, near the Nevada border. AVIRIS data over the area were collected on September 29, 1989 during the Geologic Remote Sensing Field Experiment (GRSFE). Figure 4a shows an AVIRIS image (0.68 μm) of the site. The valley floor is located between the Trail Canyon alluvial fan (upper left corner) and the hills of Artists Drive (right side). One road in the upper part of the image traverses the valley floor. Another road located on the right portion of the image is nearly parallel to the valley floor. There are a number of geologic units within the AVIRIS scene (Hunt and Mabey, 1966). The valley floor consists of playa and salt units mixed with clay. The bright white areas are mostly pure salts. Fig. 4b shows a topographic map of the scene. The upper left corner of the image has an elevation of approximately 60 m. The highest portion of the Artists Drive hills has an elevation of approximately 240 m. The valley floor is very flat and below sea level, with elevations between approximately -85 and -73 m. The central portion of the valley floor is slightly lower in elevation than the western and the eastern portions of the valley floor. Also, the southern portion of the valley floor is slightly lower than the northern portion of the valley floor.

At the time of the AVIRIS overflight, some surface areas were wet. Reflectance spectra of samples collected from the field were made with the Geophysical and Environmental Research (GER) portable spectrometer. Curve 1 of Figure 5 shows a reflectance spectrum of a field sample collected over a wet spot within the bright white area in the upper part of Fig. 4a. The liquid water features near 0.98, 1.2, 1.6, and 2.2 μm are clearly seen. Curve 2 of Fig. 5 shows a spectrum obtained by ratioing an AVIRIS spectrum (Spec1) over the wet bright white area in the upper part of Fig. 4a against an AVIRIS spectrum (Spec2) over a drier area just left of the wet white area. The same set of liquid water features are also obvious. Curve 3 shows a spectrum obtained by ratioing the Spec2 against an AVIRIS spectrum (Spec3) over a higher hill area. Atmospheric water vapor features near 0.94 and 1.14 μm are seen. This indicates that the lower elevation valley floor has more water vapor than the hill areas.

The spectral curve fitting technique described by Gao and Goetz (1990) was used to derive simultaneously the atmospheric column water vapor amount and the equivalent liquid water thickness of the surface from the AVIRIS data. In this technique, the atmospheric water vapor transmittances were calculated with a narrow-band model and the liquid water transmittances were calculated using the liquid water absorption coefficients compiled by Palmer and Williams (1974). Fig. 6a shows the curve fitting of Spec1 by including only atmospheric water vapor absorptions in the fitting process. The fitted spectrum has larger values of reflectance than the observed spectrum near 1.2 μm. The overall fitting between the two spectra is poor. Fig. 6b shows the curve fitting by including both the water vapor and the liquid water absorptions in the fitting process. Significant improvement in the overall fit is achieved.

Figures 7a and 7b show the column water vapor image and the liquid water image derived from the AVIRIS data. The water vapor amounts over the hills are smaller than those over the valley floor. This is due to the decreasing atmospheric water vapor concentration with altitude. The slightly smaller water vapor amounts near the upper left corner of Fig. 7a than those over the nearby valley floor can also be attributed to the topographic effect. The liquid water image in Fig. 7b shows clearly the drainage patterns. Based on the topographic map of Fig. 4b, liquid water will flow from the hills on the right side and from the area near the upper left corner into the valley floor after rain. Also, because the southern portion of the valley floor has slightly lower elevations than the northern portion of the valley floor, the liquid water will further flow from top to bottom. A road traversing the valley in the upper part of Fig. 4a is slightly elevated and has acted as a dam, blocking the natural flow of water from the upper valley to the lower valley and causing more white salt to be deposited in areas north of the road. The long narrow drainage pattern (Fig. 7b) below the road indicates that the pipe beneath the road allows the water to flow from the northern to the southern portions of the valley floor. The liquid water thicknesses within the drainage patterns vary between approximately 0.04 and 0.46 cm. Areas having large amounts of white salt deposits tend to have larger liquid water thicknesses. This may be a true indication of the wetness of the salts. Field observations showed that the white salt areas are wetter than nearby areas not covered by the white salts. On the other hand, the solar radiation near 1 μm can penetrate deeper into the white salt than other materials. This can also effectively increase the liquid water thicknesses over the white salt areas.

By comparing Figures 7a and 7b, it can be seen that over the valley floor the areas with more liquid water seem to have more atmospheric water vapor. This is most evident over the two large areas having white salt deposits (one in the upper part of the scene and one in the lower part of the scene). Therefore, the spatial variation in atmospheric water vapor may be related to the evaporation of surface liquid water. The spatial variation of column water vapor amounts over the valley can not be attributed to the topography because the valley floor is

relatively flat with elevation differences of 12 m or less. In the future, we plan to make further studies of the correlations among water vapor, surface liquid water, topography, and mineralogy.

IV. Summary and Conclusions

We compared PWV soundings from the three separate remote sensing systems: Optical, VAS, and microwave radiometers. The microwave measurements were also compared with soundings from both NWS and CLASS radiosondes. The microwave and optical measurements agreed to within 1 mm, and the comparisons with the radiosondes were also either good or explainable. Gradient structures of water vapor are observed in both PWV images derived from AVIRIS and VAS data. Because of its large field of view, VAS has difficulties in resolving small scale features near sharp discontinuities caused by terrain. Each of the techniques can provide complementary information of PWV. The optical technique provides column water vapor amounts during clear conditions at a precision better than 1 mm and at high spatial resolution. The microwave radiometer provides nearly continuous data during both clear and cloudy conditions, but only at a limited set of locations. The column water vapor amounts derived from microwave radiometer data can be used to quantitatively adjust satellite PWV images provided by the VAS sounder (Birkenheuer, 1991). Because of the good horizontal resolution provided by the optical technique, optical soundings could provide significant insight into horizontal transport of water vapor. Such soundings could also be useful for GOES VAS verification.

The column water vapor amounts derived from AVIRIS data over Death Valley decrease with increasing surface elevation. The liquid water image shows surface drainage patterns. The spatial variations in atmospheric water vapor over the valley may be related to the evaporation of surface liquid water. The distribution of mineral deposits over the valley may also be related to the surface drainage patterns.

Atmospheric water vapor is a very complex, highly mobile species and we have a long way to go to fully understand and analyze this variable.

Acknowledgments

The authors are grateful to R. O. Green of the Jet Propulsion Laboratory for providing the AVIRIS spectral data. This work was partially supported by the Jet Propulsion Laboratory, California Institute of Technology under contract 958039 and the FAA under the contract DTAF01-90-Z-02005.

References

Alishouse, J. C., Total precipitable water and rainfall determinations from the Seasat Scanning multichannel microwave radiometer, *J. Geophys. Res., 88*, 1929-1935, 1983.

Birkenheuer, D. L., An algorithm for operational water vapor analyses integrating GOES and dual-channel microwave radiometer data on the local scale, *J. Appl. Meteor.*, (in press).

Chesters, D. C., L. W. Uccellini, and W. D. Robinson, Low-level water vapor fields from the VISSR Atmospheric Sounder (VAS) "split-window" channels, *J. Clim. Appl. Meteor.*, 22, 725-743, 1983.

Conel, J. E., R. O. Green, V. Carrere, J. S. Margolis, G. Vane, C. Bruegge, and R. Alley, Spectroscopic measurement of atmospheric water vapor and schemes for determination of evaporation from land and water surface using the Airborne Visible/Infrared Imaging Spectrometer (AVIRIS), *Proceedings of the IEEE Geosciences and Remote Sensing Society/USRI 1989 International Symposium*, 2658-2663, 1989.

Frouin, R., P.-Y. Deschamps, and P. Lecomte, Determination from space of atmospheric total water vapor amounts by differential absorption near 940 nm: Theory and airborne verification, *J. Appl. Meteorol.*, 29, 448-460, 1990.

Gao., B.-C., Ed. R. Westwater, B. B. Stankov, D. Birkenheuer, and A. F. H. Goetz, Comparison of column water vapor measurements using downward-looking optical and infrared imaging systems and upward-looking microwave radiometers, Submitted to *J. Appl. Meteor.* in April, 1991.

Gao, B.-C., and A. F. H. Goetz, "Column Atmospheric Water Vapor and Vegetation Liquid Water Retrievals From Airborne Imaging Spectrometer Data", *J. Geophys. Res., 95*, 3549-3564, 1990.

Goetz, A. F. H., G. Vane, J. Solomon, and B. N. Rock, Imaging spectrometry for Earth remote sensing, *Science, 228*, 1147–1153, 1985.

Hogg, D. C., F. O. Guiraud, J. B. Snider, M. T. Decker, and E. R. Westwater, A steerable dual-channel microwave radiometer for measurement of water vapor and liquid in the troposphere, *J. Appl. Meteorol., 22*, 789–806, 1983.

Hunt, C. B., and D. R. Mabey, Stratigraphy and structure Death Valley, California, U. S. Geology Survey Professional Paper 494-A, 162 p., 1966.

Palmer, K. F., and D. Williams, Optical properties of water in the near infrared, *J. Opt. Soc. Am., 64*, 1107-1110, 1974.

Stankov, B. B., E. R. Westwater, J. B. Snider, and R. L. Weber, Remote sensor observations during WISP90: The use of microwave radiometers, RASS, and ceilometers for detection of aircraft icing conditions, NOAA Tech. Memo., ERL WPL-187, NOAA Wave Propagation Laboratory, Boulder, CO, 77pp., 1990.

Vane, G. (Ed.), Airborne visible/infrared imaging spectrometer (AVIRIS), *JPL Publ. 87-38*, Jet Propulsion Laboratory, Pasadena, Calif., 1987.

Westwater, Ed. R., and J. B. Snider, Applications of ground-based radiometric observations of millimeter wave radiation, *Alta Frequenza*. LVIII, 31-38, 1989.

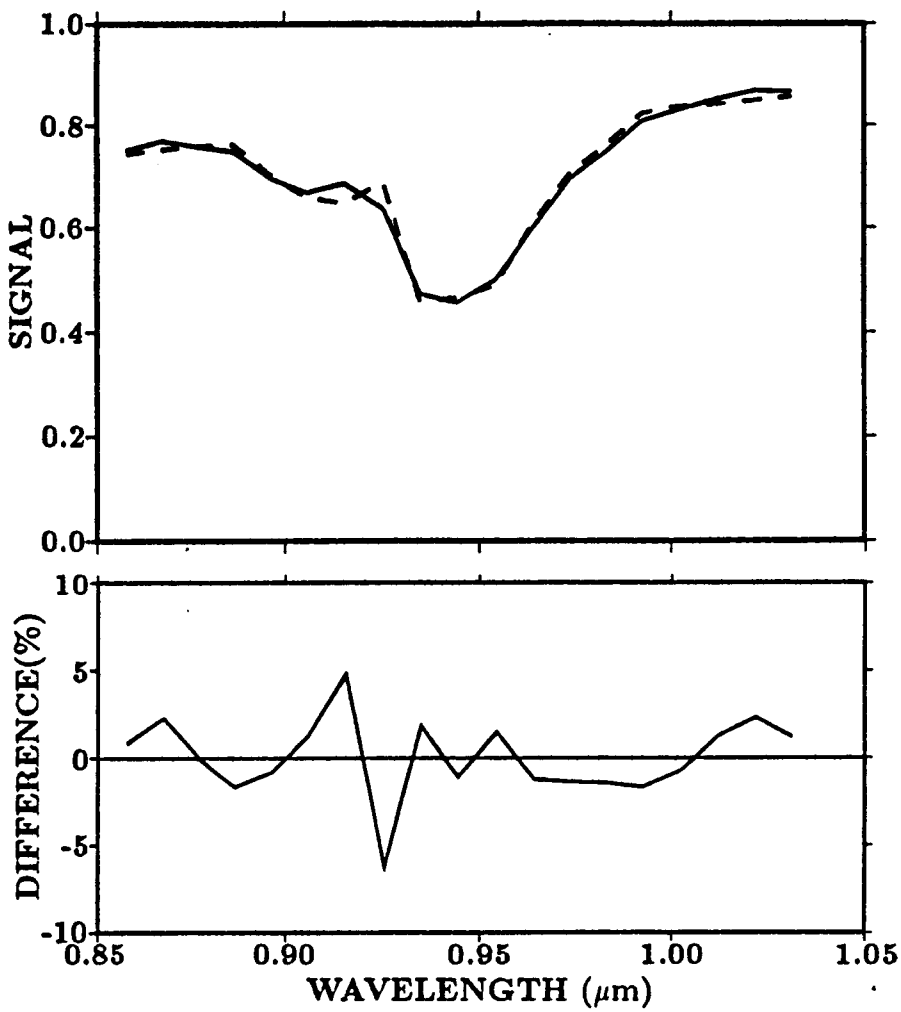

Fig. 1. An example of curve fitting of spectra. The top plot shows the observed spectrum (solid line) and the fitted spectrum (dashed line). The bottom plot shows the percentage differences between the observed and the fitted spectra.

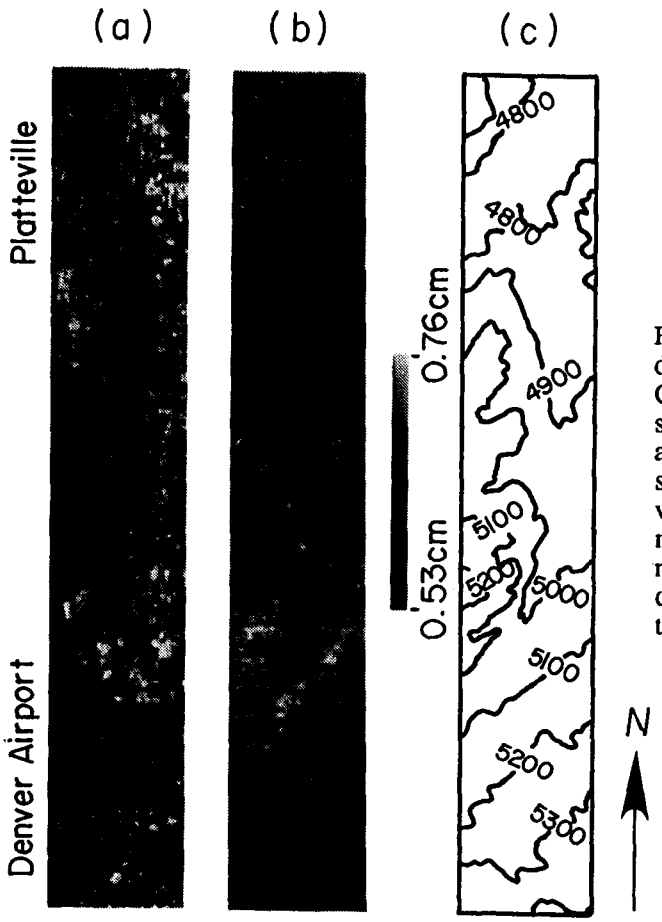

Fig. 2. Column water vapor retrievals from AVIRIS data measured over the Denver-Platteville area in Colorado on March 22, 1990. (a) An image of the scene processed from radiance of one channel centered at 0.86 μm, (b) a column water vapor image over the scene retrieved by curve fitting the 0.94-μm water vapor band absorption region, and (c) a topographic map of the scene. The elevations in the topographic map are in units of feet (1 foot = 30.48 cm). The distance from left to right side of the two images in this figure is approximately 11 km.

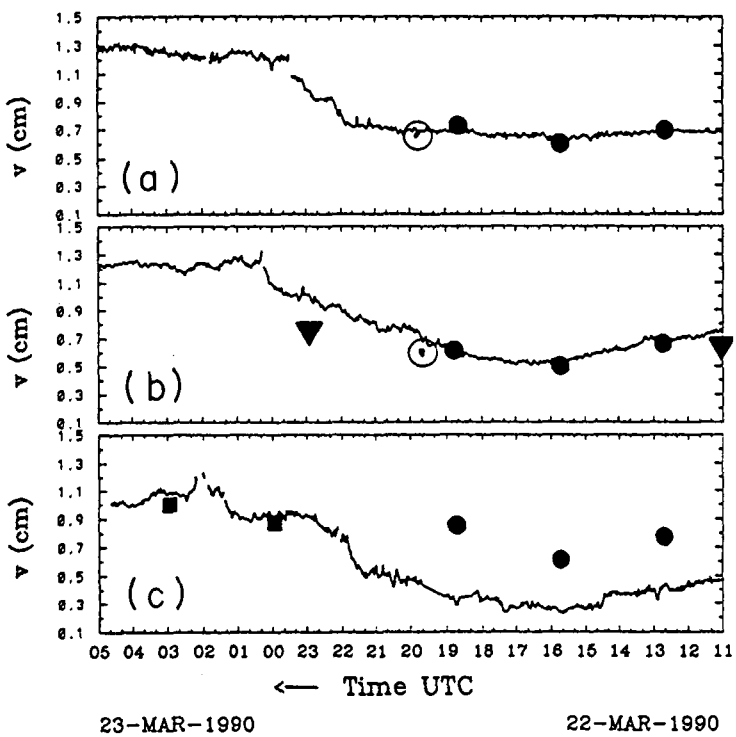

Fig. 3. Time series of precipitable water vapor at (a) Platteville, (b) Denver, and (c) Elbert on 22-23 March 1990. Continuous curves are from microwave radiometers, rectangles from CLASS radiosondes, squares from NWS radiosondes, dark circles from VAS-adjusted image, and open circles from AVIRIS.

(a)

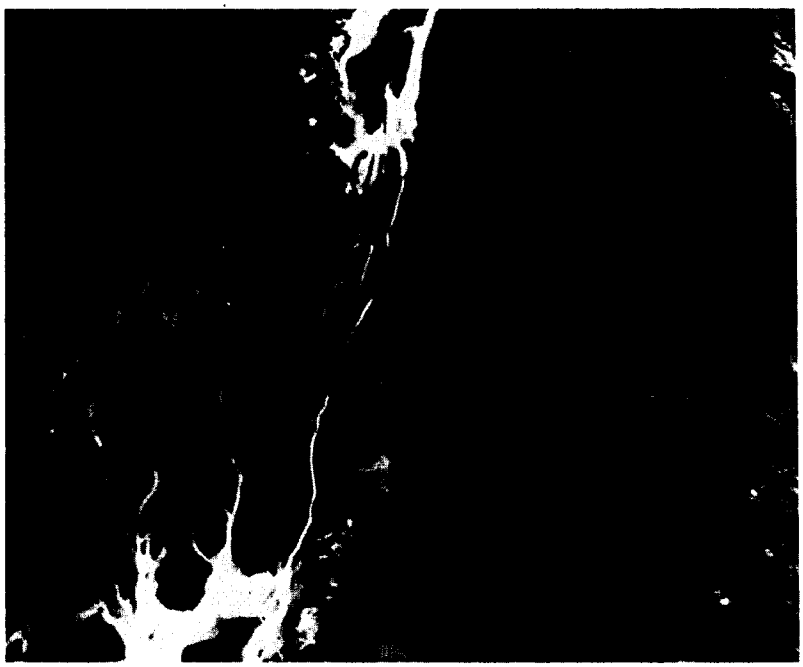

(b)

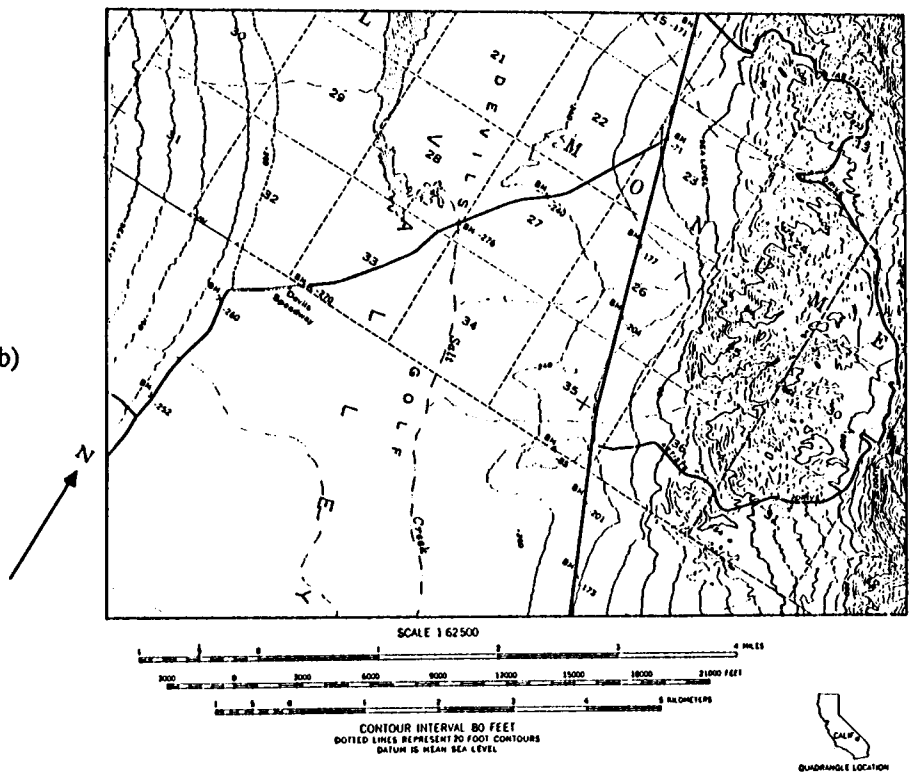

Fig. 4. (a) An image of Death Valley, California processed from radiance of one AVIRIS channel at 0.68 μm, and (b) a topographic map of the scene. The elevations in the topographic map are in units of feet (1 foot = 30.48 cm). The distance from left to right side of the image in this figure is approximately 12 km.

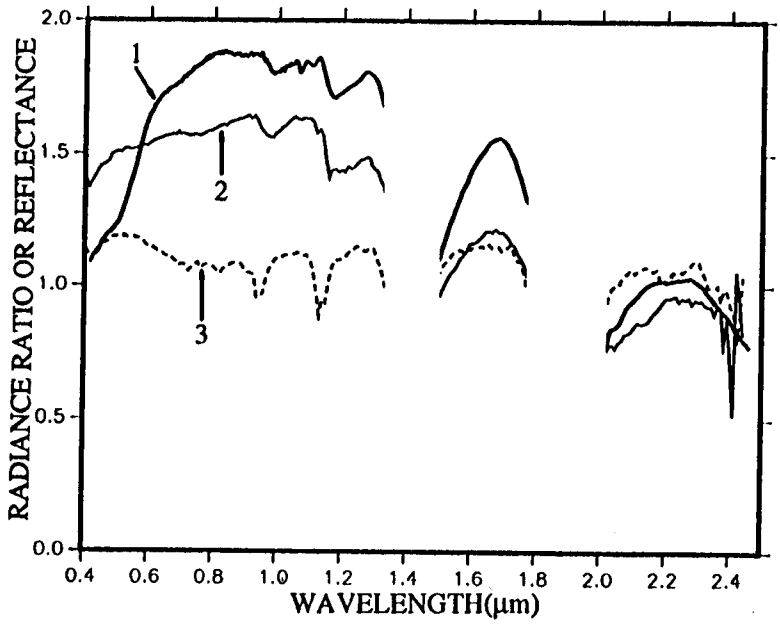

Fig. 5. A reflectance spectrum (multiplied by 5) of a wet sample collected from the field and two ratioed spectra from the AVIRIS data. See text for descriptions of the ratioed spectra.

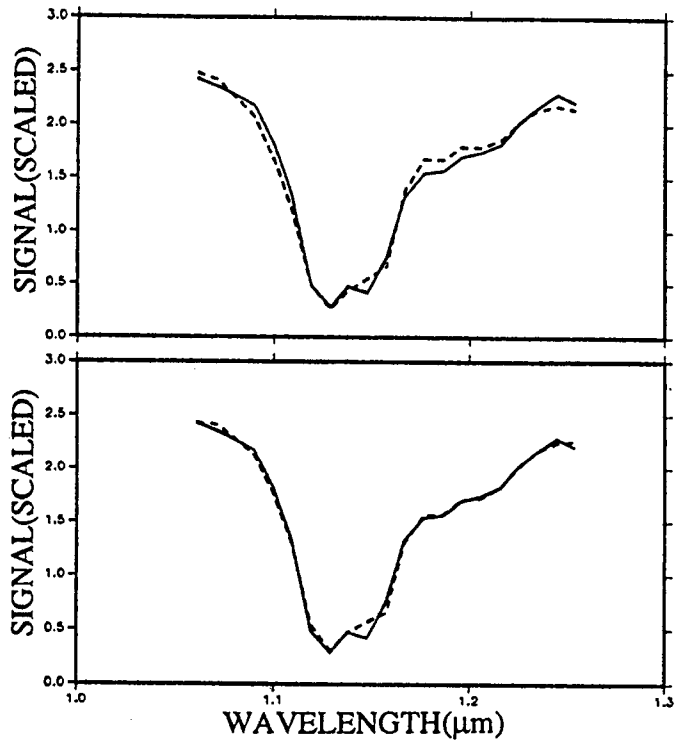

Fig. 6. Curve fitting of an AVIRIS spectrum over a bright, wet salt area. The top plot shows the observed spectrum (solid line) and the fitted spectrum (dashed line). Only the water vapor absorption is included in the fitting process. The bottom plot is similar to the top plot, except that both the water vapor and the liquid water absorptions are included in the fitting process.

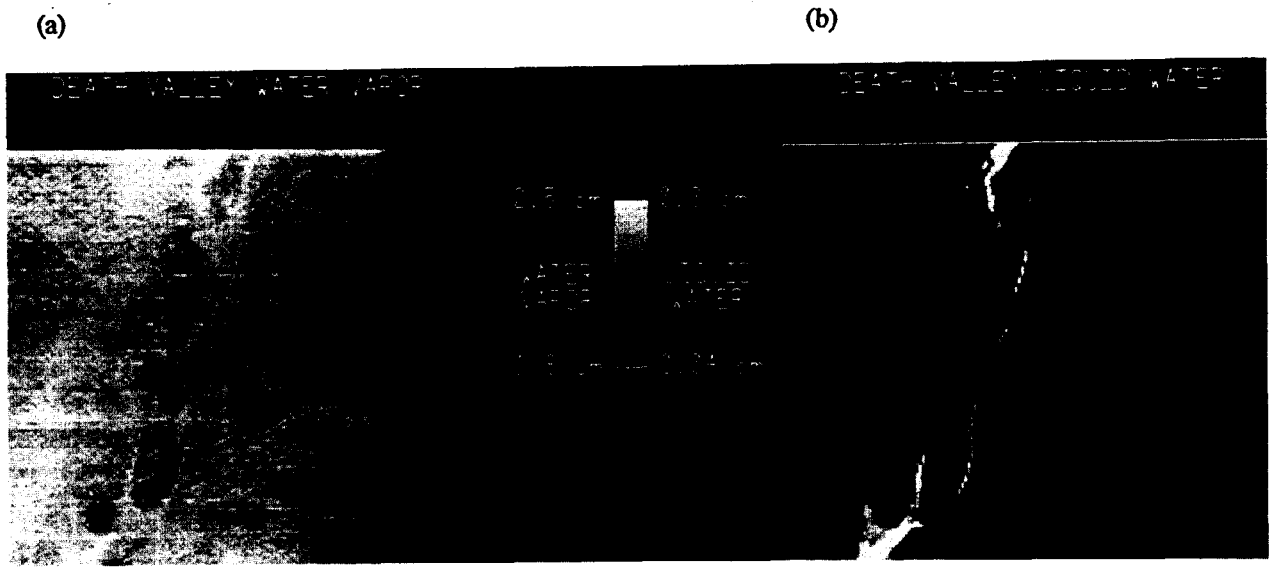

Fig. 7. Column water vapor image (a) and liquid water image (b) obtained from the AVIRIS over Death Valley.

CLOUD BASE HEIGHT AND OPTICAL THICKNESS RETRIEVALS USING AVIRIS DATA

T. A. Berendes, R. E. Feind, K.-S. Kuo and R. M. Welch

Institute of Atmospheric Sciences
South Dakota School of Mines and Technology
Rapid City, South Dakota

Abstract. In this preliminary study, a 3-band ratioing technique (Gao and Goetz, 1990a) is applied to high spectral and spatial resolution AVIRIS imagery as a front-end process for the estimation of cloud base height and optical thickness. Spatial averaging is also applied to the AVIRIS imagery to investigate the effect of low spatial resolution data in the estimation of the same cloud properties.

I. INTRODUCTION

Understanding the role of clouds in the Earth's radiation budget is one of the highest priority science objectives in the EOS (Earth Observing System) program. In order to fully understand the formation and feedback processes of clouds, an accurate measurement of their properties is necessary. Remotely sensed data by satellites is an important source of information for monitoring clouds globally. Therefore, development of algorithms for the retrieval of cloud properties from satellite based instruments is paramount.

The presence of clouds makes it difficult to accurately model the surface energy budget. An uncertainty in cloud base height of 100 mb (~ 1 km) at the 650 mb (~ 4 km) level leads to an error of 5 W/m^2 in surface flux (Gupta, 1989). The effect of clouds on surface fluxes decreases as cloud base height and relative humidity increase. An accurate method for estimating cloud base height will aid in the modeling of the earth's radiation budget.

The transmission, reflection, and absorption of radiation in a cloudy atmosphere is influenced, in part, by the cloud optical thickness. Therefore the variations of cloud optical thickness will pose a significant impact upon earth radiative energy budget. Accurate retrieval of optical thickness is needed to make a reasonable assessment of the earth's energy budget. This study investigates the effect of spatial resolution upon the retrieval of optical thickness.

Two scenes acquired by the AVIRIS instrument over the Belize, Central America area are used for analysis in this preliminary study. Figure 1 shows an example of one of the AVIRIS scenes. This scene is a 5-channel average for the wavelengths centered at 1.04 μm. The clouds present in this scene are fair weather cumulus. Spatially averaged versions of both scenes are also generated for the analysis so that the type of results expected from low spatial resolution instruments can be assessed.

This paper is divided into three primary sections. Section II discusses the application of a 3-band ratioing technique. In Section III, a recently developed technique for cloud base height estimation is described, and results at various simulated spatial resolution are obtained. Section IV discusses the methodology used for retrieving the cloud optical thickness by way of the Discrete Ordinate radiative transfer model. Results at various simulated spatial resolutions are presented.

II. 3-BAND RATIOING AND CLOUD IDENTIFICATION

A. Gao and Goetz Technique

The identification of clouds in remote sensing imagery is the first major step in determining cloud properties (e.g., optical thickness, particle size, etc.). Each image pixel must be classsified as either cloud or non-cloud. Cloud pixels are used to determine cloud properties, and non-cloud pixels are considered to be part of the background and are therefore ignored. Most existing cloud identification algorithms rely on the selection of a threshold. The choice of the threshold can be somewhat subjective. Therefore, the results of any type of cloud property analysis can be highly variable dependent on the type of cloud identification algorithm used.

When high spectral resolution data is available, like that available from AVIRIS, identification of clouds can be achieved with greater confidence. Gao and Goetz (1990a) developed a technique that takes advantage of this high spectral resolution imagery, and greatly facilitates the ability to distinguish between cloud and background pixels. First, a 5-channel averaged radiance is computed for each pixel over the water vapor absorption channels centered at 0.94 and 1.04 μm, and the water vapor window channel centered at 1.04 μm. The 5-channel averaging filters out some of the noise present in the single channel imagery while still retaining sufficient spectral resolution for the technique to work. Next, the ratio of the sum of the radiance from the two water vapor channels to twice the radiance of the window channel, is computed, i.e.,

$$BR = (rad(.94) + rad(1.14))/(2 * rad(1.04)).$$

(This process will be referred to as 3-band ratioing and the ratio obtained as 3-band ratio, hereinafter.) The 3-band ratio values typically range from 0 to 2 and, therefore, are scaled from 0 to 255 for display purposes.

In the 3-band ratioed imagery, the background (when it is land) is somewhat homogenized, while the clouds retain their features (see Gao and Goetz, 1990a, for examples). The effect can be explained by the fact that most soil ingredients have a linear spectral response over the 0.94 to 1.14 μm wavelength region (Gao and Goetz, 1990b), whereas clouds have a nonlinear response. However, over uneven terrain, a brightness gradient will appear in the background of the ratioed image, as higher terrain results in shorter water absorption paths, hence less water absorption and larger ratios. This effect makes cloud identification with this technique more difficult and can result in false classification of cloud pixels.

An example of the effect of 3-band ratioing can be seen in Fig. 2 and Fig. 3 in the lower right quadrant (annotated as BR). The background

appears to become somewhat homogeneous; however, salt and pepper type noise appears in the regions corresponding to cloud shadows. This is caused by the fact that, over areas containing cloud shadows, the denominator of the ratio becomes very small and results in relatively large ratio values. Past experience has revealed that the same effect is manifested over water areas. Therefore, it is necessary to apply thresholds to the 3-band ratioed image to separate cloud pixels from background pixels.

B. Thresholding

Identification of clouds in the 3-band ratioed image is based on two thresholds, both derived from the histograms of the three 5-channel averaged images centered at 0.94, 1.04, and 1.14 μm. The histograms for these three images for one of the scenes processed for this paper appears in Fig. 4. These histograms can be viewed as the composite of three classes of pixels -- shadows cast by clouds, background features, and clouds. In each of the three histograms, two distinctive local maxima can be observed. The first (from the left) corresponds to the distribution of cloud shadow pixels, and the second to the distribution of the background pixels. The tail that extends to the right corresponds to the distribution of the cloud pixels (which does not exhibit an obvious peak).

The local minimum for the 0.94 μm image, (that occurs between the local maxima for cloud shadow and background) is used as the first threshold. For example, in Fig. 4, a value of 275 is selected for the threshold and is annotated as .94 (shadows). All pixels in the 3-band ratioed image are set to the minimum ratio (effectively zero) for all corresponding pixels in the 0.94 μm image with gray levels below the aforementioned local minimum. This threshold effectively filters away the salt and pepper noise caused by the cloud shadows and/or water.

The second threshold is based on the location of the discernible knee in each of the three histograms that occurs to the right of the local maximum for the background. For example, the location of the knee points in Fig. 4 are 450, 1750, and 220, and are annotated as .94 (backgrd), 1.04 (backgrd), and 1.14 (backgrd), respectively. These three points are then applied in the 3-band ratio relation above and the resulting value is used as the second threshold. Any pixel value in the 3-band ratioed image less than the second threshold is also set to the minimum ratioed value. Any other pixel that is not set to the minimum ratioed value then corresponds to cloud pixels.

Results for the 3-band ratioed images, using the above described thresholding, appear in Figs. 5 and 6 in the lower right quadrant (annotated as BR). The process has the effect of converting the background to black while retaining the cloud features.

The resulting ratioed image can then be applied as a mask to other channels for cloud identification (as is done in a subsequent section for the determination of cloud edges in a cloud base height algorithm and of optical thickness).

The above described process for selecting the second threshold was arrived at empirically and is not technically satisfying. The "knee points" were selected intuitively as it seems to be a reasonable demarcation between

the distributions for background and cloud pixels. Investigation is currently being conducted to develop a more technically sound approach for selecting an optimum decision point between the background and cloud pixels in each of the three histograms. Then the process can be automated so that manual selection of those points is not required.

C. Alternative 3-Band Ratioing Techniques

Two other band ratio relationships are implemented and preliminary results are compared with those obtained above. (They are referred to as BR2 and BR3, to distinguish them from the ratio described above which will be referred to as BR1.) The alternative 3-band ratios are:

$$BR2 = (2 * rad(.94))/(rad(.84) + rad(1.04))$$

$$BR3 = (2 * rad(1.14))/(rad(1.04) + rad(1.24))$$

These ratios attempt to take advantage of the same response characteristics of soil constituents and clouds in various water vapor absorption and window bands.

In Figs. 7 through 10 appear the results for two scenes in which the three 3-band ratioing techniques are applied. As a reference, in the upper left quadrant is the image from the 5-channel averaged image centered at 1.04 μm. For both figures, the results from BR1, BR2, and BR3 appear in the upper right, lower left, and lower right quadrants, respectively. In Figs. 7 and 8 are the results before the two thresholds are applied, and in Fig. 9 and 10 are the results after the two thresholds are applied. The method for selecting the two thresholds in BR2 and BR3 is the same as in BR1 with the exception that, in BR3, the histogram for the image centered at 1.14 μm is used for selecting the cloud shadow threshold.

It appears that similar results are obtained using BR1 and BR2; however, BR3 appears to provide much poorer performance. It is not yet known whether another threshold selection for BR3 would provide improved performance, or if falsely classified cloud pixels in the background area have the same gray level values as correctly classified cloud pixels. Further investigation is required in this area.

On close inspection, some noise can be observed in the thresholded results for BR1 and BR2. Although not used here, application of a median filter is effective in removing the noise with minimal loss of cloud edge pixels.

III. CLOUD BASE HEIGHT ESTIMATION

A semi-automated technique has been developed to estimate cloud base height using AVIRIS data. The algorithm consists of the following major steps:

A. Preprocessing

B. Pattern Matching

C. Cloud Base Height Estimation

A. Preprocessing

The goal of preprocessing is to reduce the image to cloud and shadow edge elements. This step employs several image processing techniques. First, a median filter is applied to the image to eliminate noise. The median filter was chosen because it is a very effective noise removal technique which also preserves the edge transitions in the image.

The image is reduced to its edge elements by a Laplacian of Gaussian filter (Huertas and Medioni, 1986). The Gaussian function has the following form:

$$G(x,y) = \frac{1}{2\pi\sigma^2} \exp \frac{-(x^2 + y^2)}{2\sigma^2} \quad ,$$

where σ is the standard deviation; x and y are horizontal and vertical offsets from a pixel of interest.

The Laplacian of Gaussian operation is performed by taking the Laplacian of the Gaussian function and convolving the result with the median filtered image, f(x,y). This results in a binary image composed entirely of pixels which correspond to the locations of edge transitions in the median filtered image. This edgemap, $f_e(x,y)$ is obtained as follows:

$$fe(x,y) = \nabla^2 G(x,y) * f(x,y) \quad .$$

The Laplacian of Gaussian filter reduces the image to 1 pixel wide lines. Figure 11A shows the image from Fig. 1 after the Laplacian of Gaussian filter has been applied. At this point, the image contains a large number of edges which correspond to legitimate edge transitions, but are not of interest to this study. Only cloud and shadow edges are useful for cloud base height estimation. All other edges should be eliminated.

It is difficult to visually determine which edge pixels correspond to cloud or shadow edges in Fig. 11A. A technique which we call max/min thresholding (Berendes et al., 1991) is applied to eliminate extraneous edges and classify remaining ones as either cloud or shadow. Max/min thresholding constructs a localized histogram of gray level values surrounding each edge pixel in the median filtered image. The histograms typically have three peaks which correspond to cloud, background, and shadow pixels. If water is present, an additional peak will occur at a gray level below the shadow peak. The peaks of the histogram are found, and cloud and shadow thresholds are determined using a weighted averaging technique. The cloud and shadow thresholds are used to determine the type of transition which is occurring at an edge pixel. Since we are only interested in cloud and shadow edges, only the following transitions are of interest:

Cloud ⟷ Shadow

Cloud ⟷ Background

Background ⟷ Shadow

By applying the cloud and shadow thresholds, edge pixels which do not correspond to one of the above transitions are eliminated, and the remaining edge pixels are classified as either cloud or shadow.

The band ratioing technique described in the previous section has been used to eliminate the background and leave only the clouds in the image. This technique simplifies the basic algorithm since a simple threshold can be applied to the ratioed image to set clouds to one gray level. This creates a binary image from which edges can easily be determined by means of a Roberts operator. Therefore, the max/min thresholding is not used to determine cloud edges. Figure 11B shows the cloud edges of Fig. 1.

Since shadows are eliminated in the band ratioed image, max/min thresholding must still be used to find the shadow edges. The 1.04 μm band is used to find shadow edges because it provides good contrast between the shadows and the background. The max/min thresholding technique is used in this case to find only shadow edges and eliminate all others. Figure 11C shows the shadow edges extracted from Fig. 11A.

After cloud and shadow edges are found, they are combined together in one image. Figure 11D shows Fig. 11B combined with Fig. 11C. The brighter pixels are cloud edges, and the darker ones are shadow edges. Pattern matching can now be performed on this image.

B. Pattern Matching

The Generalized Hough Transform (Ballard, 1981) is a pattern matching technique which is capable of matching arbitrary patterns. In this case, cloud edges are matched with their corresponding shadow edges. The Generalized Hough Transform cloud base height algorithm can be described by the following steps:

1) Parameterize desired cloud edge with respect to an arbitrary fixed reference point near the cloud edge;
2) Within a search area, search for shadow edge which best matches the cloud edge.
3) Find the shadow edge which best matches the cloud edge and calculate the location of a new reference point with respect to the found shadow edge.

C. Cloud Base Height Estimation

Once the location of the new reference point has been determined, the separation distance between the two reference points can be used to determine the cloud base height using the following equation:

$$h = d/\tan \theta_0$$

where d is the separation distance, θ_0 is the solar zenith angle.

Currently, cloud edges are selected manually. Selection of cloud edges for pattern matching is a critical part of the algorithm. In order

to minimize possible effects of cloud vertical development, cloud edges which are roughly parallel to the solar azimutal plane, and lie at a maximum distance from the center of the cloud are chosen for pattern matching. Figure 12A shows the edges which are chosen for an idealized cloud. Edges near points P or R are chosen for pattern matching. If an edge near point C is chosen, the error x in Fig. 12A and 12B will represent an elongation of the shadow due to vertical development. If a hemispherical shape is assumed, the corresponding error in cloud base height is given by b in Fig. 12C.

The viewing angle of the aircraft can also cause errors in cloud base height calculations. In Fig. 12B, if the aircraft is viewing at an angle θ from nadir, it will "see" under the cloud. This causes the perceived distance d between the cloud and shadow to be greater than the actual distance. The opposite situation occurs if the viewing angle is from the other direction. In either case, a correction must be made to account for off nadir viewing. If a correction is not made, errors in cloud base height of several hundred meters can occur if the cloud is located toward the right or left edge of the image. This error has been corrected for in the results.

The previous techniques have been applied to two AVIRIS scenes. The results can be seen in Figs. 13 and 14. The numbers indicate base heights in meters of individual clouds. The original reference point is represented as a black cross and the new reference point is a white cross. The images are of the 1.04 μm band. Most of the clouds in both images have a base height between 1 and 1.5 km.

The cloud base height algorithm has been applied successfully to LANDSAT and AVIRIS data. Both of these data types have high spatial resolution; 20 m for AVIRIS, 28.5 m for LANDSAT TM, and 57 m for LANDSAT MSS. Since some of the EOS instruments will have much lower resolution, we would like to determine how the algorithm will work at lower spatial resolutions. The heights of three clouds are shown in Fig. 15. Their heights are calculated based on the full resolution of the data. The cloud base height algorithm is also applied to a spatially averaged version of the image in Fig. 15. Figure 16 shows the heights of the same clouds in a spatially averaged version of the same image. The image has been spatially averaged to an effective pixel resolution of 120 m and shown here at the original size of the image. Notice that the cloud base heights in the averaged image are all higher than their counterparts at the original resolution.

A detailed study of the effects of degraded spatial resolution will be performed in the near future. However, in a preliminary investigation it is clear that spatial resolution has a very strong effect on both the performance of the cloud base height algorithm and the results obtained by the method. The method fails when a spatial resolution of 240 m/pixel is used. In this case, the resulting image is too small to work with effectively. Small clouds and shadows are averaged into the background. These difficulties make it nearly impossible to study the effects of spatial resolutions coarser than 240 m/pixel. Even at 120 m/pixel spatial resolution, many clouds that are used successfully at 20 m/pixel resolution are unusable or not visible.

IV. OPTICAL THICKNESS RETRIEVAL

A. Procedure

For contouring optical thicknesses of clouds in an image, we first assume a reasonable cloud droplet size distribution for the type of clouds under study. In this case, we have chosen the well known C1 distribution (Diermendjian, 1969) which is considered reasonable for fair weather cumulus -- the type of clouds analyzed in this study. The C1 distribution is a modified gamma distribution with the following form:

$$n(r) = a\, r^{\alpha} \exp(-\, br^{\gamma}) \quad ,$$

where n(r) is the number concentration at radius r (in μm). The values of the parameters are a = 2.373, α = 6.0, b = 1.5, and γ = 1.0. This choice of parameters yields an effective radius of 6 μm.

We then run a Mie scattering calculation at 0.742 μm on this C1 cloud droplet size distribution to get the Legendre polynomial expansion for the scattering phase function. The 0.742 μm channel is chosen because, at this wavelength, reflectance becomes insensitive to cloud droplet size (effective radius) and is sufficiently long to avoid Rayleigh scattering (Nakajima and King, 1990). In turn, with other specification parameters, the Legendre polynomial expansion of the phase function is input to the Discrete Ordinate radiative transfer model which assumes plane-parallelism on the media. The other parameters include the solar zenith angle, background albedo, and optical thickness.

The solar zenith angle is calculated using local latitude, longitude, and time data from the navigation file associated with the image. The background albedo is assumed to be the value where the second local maximum occurs in the histogram for the 0.742 μm image (Wielicki and Welch, 1986). For example, for scene B, the background albedo is taken to be 22% (see Fig. 17). The set of optical thicknesses -- 0, 1, 2, 4, 8, 10, 12, 14, 16, 18, 20, 24, 28, 32, 40, 48 -- are chosen for calculation. For each optical thickness, the radiative transfer model returns the nadir reflectance that would be observed and is used for the optical thickness color-slicing of the 0.742 μm image.

B. Application of 3-Band Ratioing in the Determination of Cloud Optical Thickness

The 3-band ratioed images derived above are applied to the image corresponding to the 0.74 μm channel. All pixels in the 0.742 μm image are set to zero for any corresponding pixel in the band ratioed image with a minimum 3-band ratioed value. All other pixels (cloud pixels) retain their original value. In this way, all of the background is masked out, leaving only cloud pixels. Figure 18 shows a 0.742 μm image after being masked. Based on results from the Discrete Ordinate radiative transfer model, the cloud pixels are color sliced into 16 discrete optical thickness contours. Results for the two scenes studied appear in the upper left quadrants of Figs. 19 and 20 [see slides 20 and 21].

C. Reduced Spatial Resolution and Optical Thickness

In an attempt to better understand the relationship between optical thickness results obtained from high spatial resolution imagery (such as AVIRIS) and low spatial resolution imagery (such as MODIS), cloud optical thickness is recomputed for each of the two scenes for three additional cases. In the three cases, the high spatial resolution AVIRIS imagery is spatially averaged over 3 x 3, 6 x 6, and 12 x 12 pixel areas to simulate the imagery obtained from instruments with spatial resolutions of 60 m, 120 m, and 240 m (the highest spatial resolution available from MODIS), respectively. The results for optical thickness obtained from these spatially averaged images appear in Figs. 19 and 20, in the upper right, lower left, and lower right quadrants for 60 m, 120 m, and 240 m imagery, respectively.

A couple of observations can be made through inspection of these images. One is that the optical thickness appears to decrease as spatial resolution decreases. Optically thicker areas become thinner as they are averaged with neighboring thinner areas (such as background). Another is that the cellular structure of the clouds becomes obscured as spatial resolution is decreased.

The average optical thicknesses for each of the two scenes and for each of the spatially degraded images are calculated and are summarized below:

	Spatial Resolution	Average Optical Thickness
Scene A	20 m	6.12
	60 m	4.14
	120 m	4.13
	240 m	3.92
	480 m	3.35
	960 m	2.87
Scene B	20 m	6.32
	60 m	5.47
	120 m	5.45
	240 m	5.38
	480 m	5.05
	960 m	4.36

These results seem to support the above observation that, as spatial resolution is increased, so does optical thickness. However, these results are not sufficiently extensive to make that conclusion. Analysis of additional scenes is currently in progress to investigate this phenomena and will be reported on at a future date.

V. CONCLUSIONS

Three-band ratioing, followed by thresholding, appears to provide a reliable technique for identifying cloud pixels in high spectral resolution imagery. The ratioed image can be used as a mask to eliminate the effect of the background in cloud property retrievals.

The Hough Transform cloud base height algorithm has been successfully applied to AVIRIS data. The addition of the band ratioing technique simplifies the extraction of cloud edges from the scenes.

In this preliminary investigation, it has been observed that spatial resolution has a profound effect upon the performance and results of the cloud base height algorithm. At spatial resolutions less than 100 m/pixel, the cloud base height algorithm is more likely to fail to match cloud and shadow edges. The cloud base heights obtained at 120 m/pixel resolution are substantially higher than those obtained at 20 m/pixel resolution. It seems doubtful that the cloud base height algorithm could be applied successfully to data with a spatial resolution coarser than 150 m/pixel.

When simulating low spatial resolution, by spatially averaging high spatial resolution imagery, the overall optical thickness of clouds in a scene appears to decrease. This is evidenced by both the optical thickness contours and the values obtained for average optical thickness.

VI. Future Work

Only two scenes were analyzed in this study. The above described procedures need to be tested on many more. For example, they will be applied to a wider variety of scene types, including those that contain uneven terrain, water, snow, and other cloud types. The following will be investigated over this larger data set:

- Improved methods for selecting thresholds, that can be implemented in an autonomous environment.
- The effect of spatial resolution in cloud property retrievals, and, in particular, cloud base height, optical thickness, particle size, cloud size, and effective radius.
- The effect of various cloud droplet size distributions in the calculation of optical thickness.

References

Ballard, D. H., 1981: Generalizing the Hough Transform to detect arbitrary shapes. Pattern Recognition, 13, 111-122.

Berendes, T., S. K. Sengupta, R. M. Welch, B. A. Wielicki, and M. Navar, 1991: Cumulus cloud base height estimation from high spatial resolution Landsat data: A Hough transform approach. [Submitted to IEEE Trans. Geosci. Remote Sens.]

Diermendjian, D., 1969: Electromagnetic scattering on spherical polydispersions. American Elsevier Publishing Company, New York. 290 pp.

Gao, B-C., and A. F. H. Goetz, 1990a: Determination of cloud area from AVIRIS data. Proceedings 2nd AVIRIS Workshop. JPL Publication 90-54.

_____, and _____, 1990b: Column atmospheric water vapor and vegetation liquid water retrievals from airborne imaging spectrometer data. J. Geophys. Res., 90, D4, 3549-3564.

Gupta, S. K., 1989: A parameterization for longwave surface radiation from sun-synchronous satellite data. J. Climate, 2, 305-320.

Huertas, A., and G. Medioni, 1986: Detection of intensity changes with subpixel accuracy using Laplacian-Gaussian masks. IEEE Trans. Pattern Anal. Mach. Intell., 8, 651-664.

Nakajima, N., and M. D. King, 1990: Determination of the optical thickness and effective particle radius of clouds from reflected solar radiation measurements. Part 1: Theory. J. Atmos. Sci., 47, 1878-1893.

Wielicki, B. A., and R. M. Welch, 1986: Cumulus cloud properties derived using Landsat satellite data. J. Climate Appl. Meteor., 25, 261-276.

Acknowledgments

This work was conducted jointly under National Aeronautics and Space Administration (NASA) Contracts NAS5-30768 and NAS5-30958 and Jet Propulsion Laboratory Contract 000573907. Thanks are extended to Joie Robinson for typing this manuscript.

Fig. 1: 5-channel averaged radiance image for Scene A at 1.04 μm.

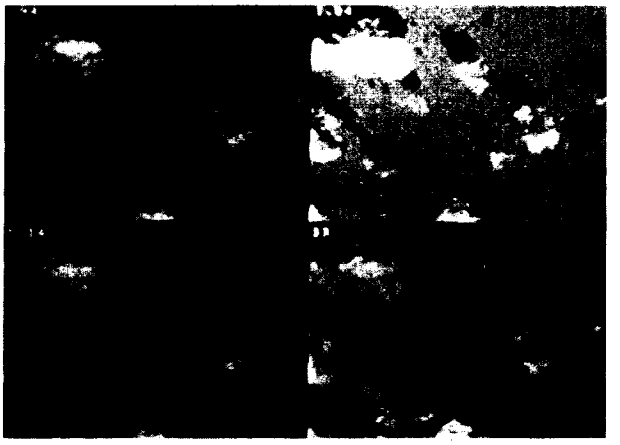

Fig. 2: 5-channel averaged radiance image for Scene A at 0.94 μm (upper left), 1.04 μm (upper right), 1.14 μm (lower left), and 3-band ratioed image (lower right).

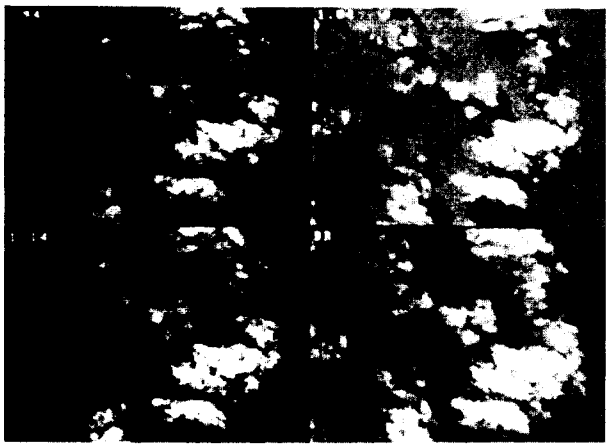

Fig. 3: Same as Fig. 2 for Scene B.

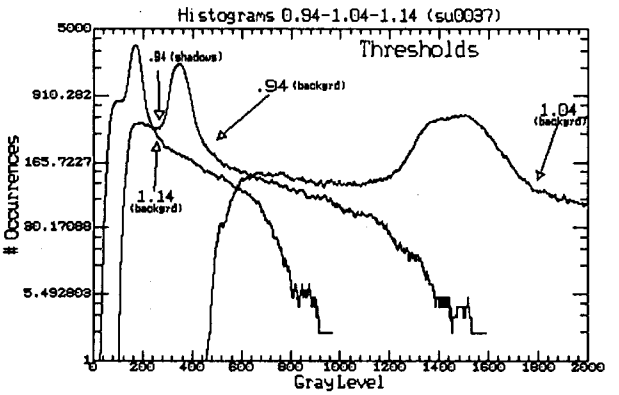

Fig. 4: Histograms for 5-channel averaged radiance images at 0.94, 1.04, and 1.14 μm for Scene B.

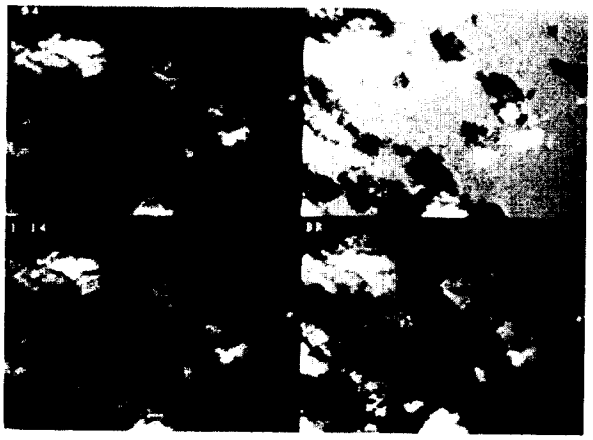

Fig. 5: 5-channel averaged radiance image for Scene A at 0.94 μm (upper left), 1.04 μm (upper right), 1.14 μm (lower left), and 3-band ratioed image with thresholding (lower right).

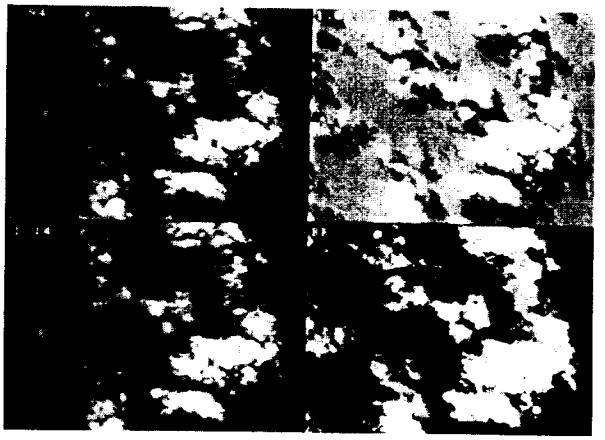

Fig. 6: Same as Fig. 5 for Scene B.

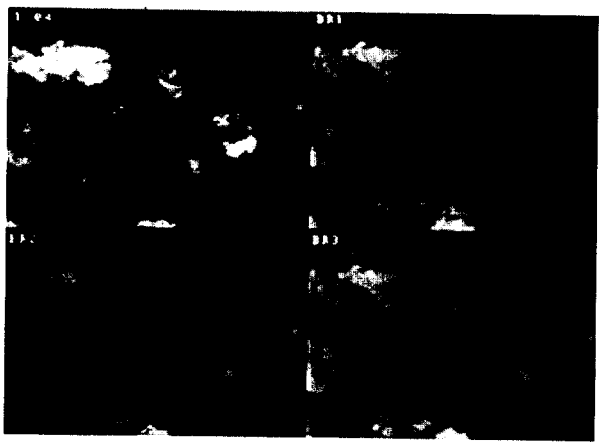

Fig. 7. 5-channel averaged radiance image for Scene A at 1.04 μm (upper left); 3-band ratioed image without thresholding using Gao and Goetz technique (upper right); alternative 3-band ratioed images without thresholding (lower left and lower right; see text for details).

Fig. 8: Same as Fig. 7 for Scene B.

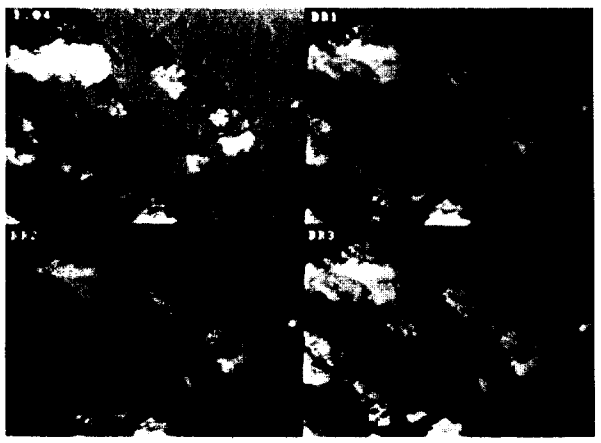

Fig. 9: 5-channel averaged radiance image for Scene A at 1.04 μm (upper left); 3-band ratioed image without thresholding using Gao and Goetz technique (upper right); alternative 3-band ratioed images with thresholding (lower left and lower right; see text for details).

Fig. 10: Same as Fig. 9 for Scene B.

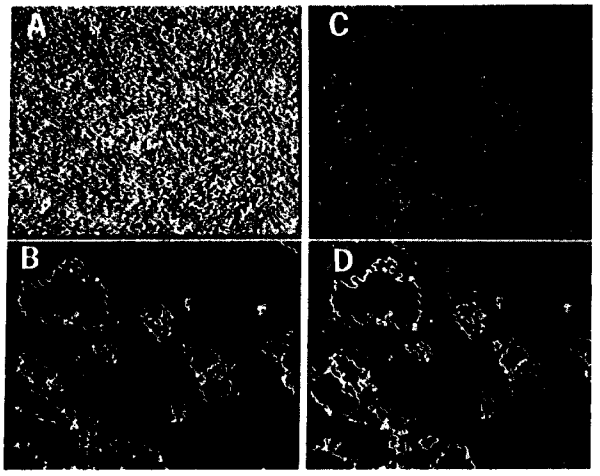

Fig. 11: A) Laplacian of Gaussian image of Fig. 1; B) cloud edges extracted from B-band ratioed image; C) shadow edges extracted from 1.04 μm band using max/min thresholding; and D) combination of Figs. B and C.

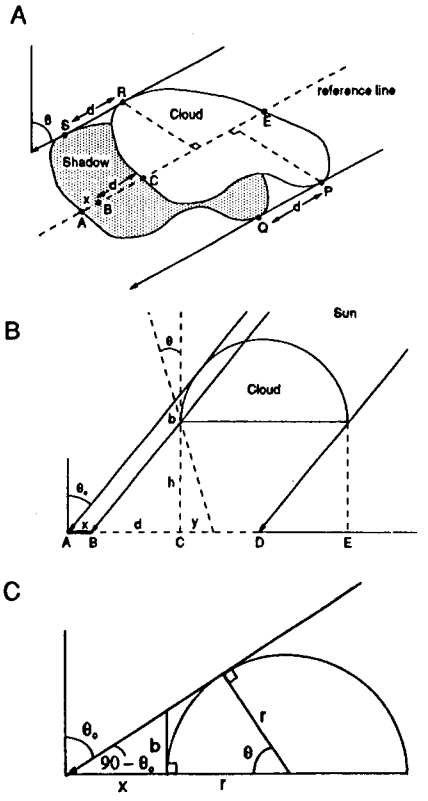

Fig. 12: A) An idealized cloud and its shadow; B) vertical cross section of Fig. A. Potential error in horizontal separation distance is given by x; and C) resulting error in cloud base height is b.

Fig. 13: Results of cloud base height estimation for Scene A. Black crosses are the original reference points. White crosses are the new reference points.

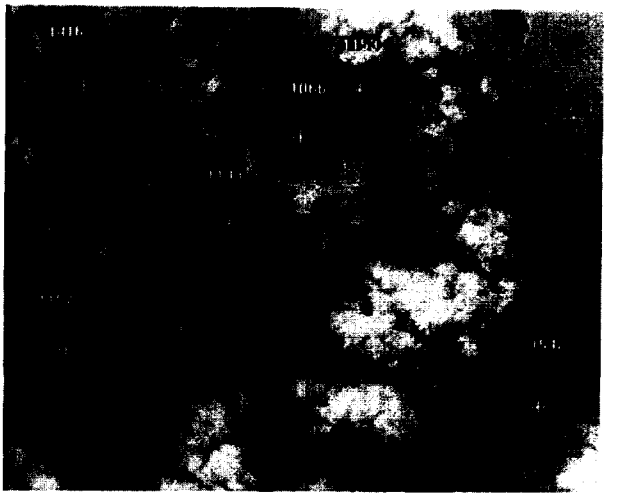

Fig. 14: Results of cloud base height estimation for Scene B. Black crosses are the original reference points. White crosses are the new reference points.

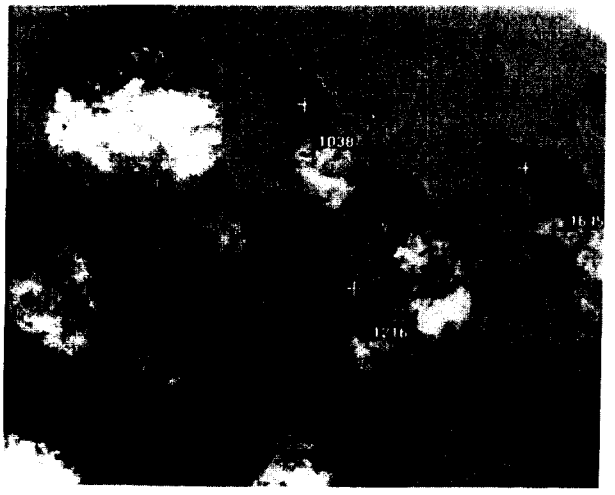

Fig. 15: Results of three selected clouds in Scene A at 20 m/pixel spatial resolution.

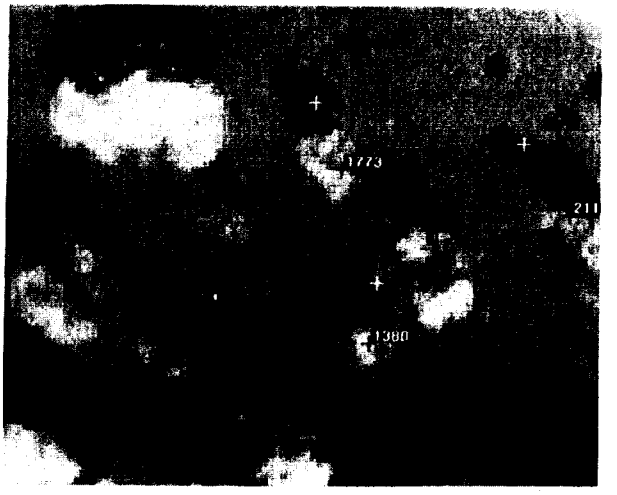

Fig. 16: Results of the same three clouds chosen in Fig. 15 at 120 m/pixel spatial resolution.

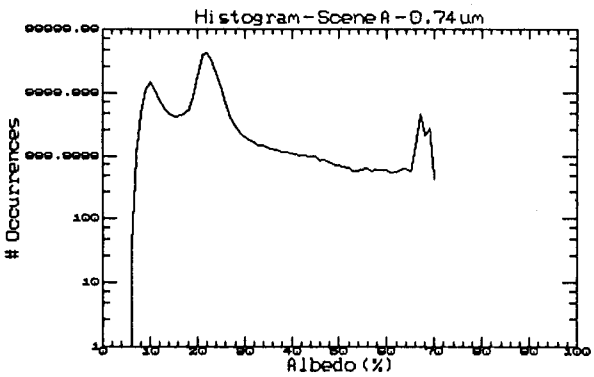

Fig. 17: Histogram of albedo for 0.742 μm image.

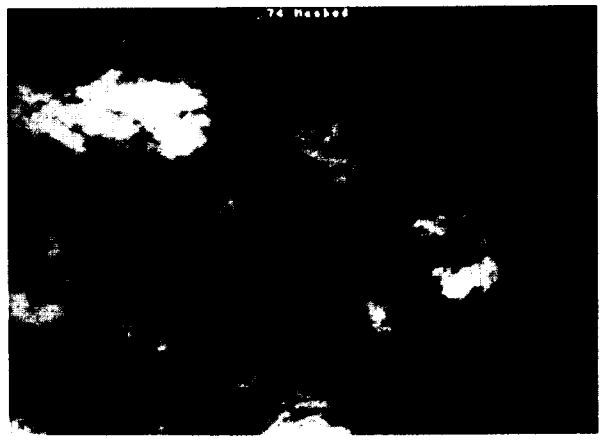

Fig. 18. A 0.742 μm image with background masked by 3-band ratioed image.

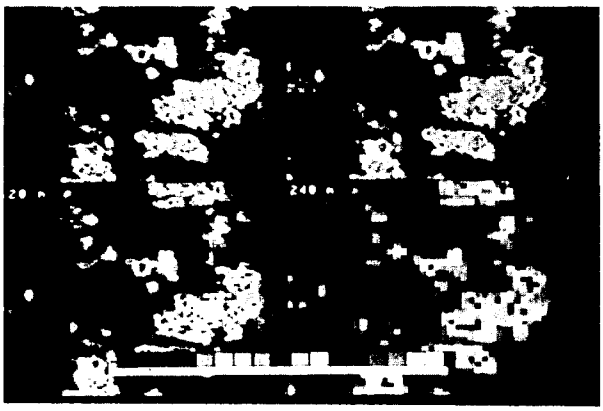

Fig. 19: Optical thickness contours for Scene A at 20 m, 60 m, 120 m, and 240 m spatial resolution: (see slide 20).

Fig. 20: Same as Fig. 19 for Scene B: (see slide 21).

ANALYSIS OF ALTERED VOLCANIC PYROCLASTS USING AVIRIS DATA

William H. Farrand and Robert B. Singer
Planetary Image Research Laboratory, LPL
University of Arizona
Tucson, Arizona

Abstract. Compositional changes that accompany the alteration of volcanic pyroclasts are discernible by visible and near infrared spectrometry. AVIRIS data from the Pavant Butte tuff cone in Millard County, Utah and the Lunar Crater Volcanic Field, Nevada were analyzed in order to map and study the pyroclastic deposits within those areas. Maps of the fractional abundance of select volcanic pyroclasts were produced via spectral mixture analysis. Pyroclastic materials used as spectral endmembers included palagonite tuff, oxidized basaltic cinders and rhyolite. Reference spectra of these and other endmembers were used to calibrate the data to reflectance. Band parameters, extracted from the AVIRIS data, of the 1-μm iron crystal-field absorption in Pavant Butte palagonite tuff indicated the action of spectral mixing between palagonitized and unpalagonitized tuffs. Further analysis of the Pavant Butte data indicated the presence of a previously undetected 2.2 μm Al-OH band in the palagonite tuff.

I. Introduction

Explosive volcanism has played a major role in the Cenozoic history of western North America and many other portions of the world that are adjacent to active plate margins. In many places, the pyroclastic debris from volcanic activity forms the majority of the stratigraphic record for Cenozoic times. Given the importance of such pyroclastic deposits, the ability to map and study them also takes on added significance. Remote sensing systems offer a synoptic view which can be used in an effective manner to analyze the diverse volcanic fields scattered across the globe.

Multispectral systems such as the Landsat Thematic Mapper (TM) have been effectively used in past studies to identify and map volcanic pyroclasts (e.g. Davis et al., 1987). With the advent of imaging spectrometers such as the Airborne Visible/Infrared Imaging Spectrometer (AVIRIS), new possibilities in volcanological research present themselves. While multispectral systems have proven quite effective in mapping volcanic pyroclasts, their limited spectral resolution prevents the unambiguous identification of composition. Imaging spectrometer systems can provide full spectral resolution across all or part of the visible and near infrared wavelength region. The ability to extract near-laboratory quality spectra from remotely sensed data offers the potential to study spatial variations in mineralogy over the extent of volcanic terrains as well to provide clues to the mode of emplacement and environment of alteration of the constituent pyroclastic deposits of such regions.

II. Field Areas

Imagery was acquired over two volcanic terrains within the Great Basin of western North America. The location of the two field areas is shown in Figure 1. The data sets from both regions were collected as part of multi-institution research projects. AVIRIS data were collected over the Pavant Butte tuff cone in Millard County, Utah as part of a Geosat

Committee sponsored research project focusing on the nearby Drum Mountains. AVIRIS and several other advanced airborne scanner data sets were acquired over the Lunar Crater Volcanic Field (LCVF) in northern Nye County, Nevada as part of the NASA-sponsored Geologic Remote Sensing Field Experiment (GRSFE) (Evans and Arvidson, 1991). The AVIRIS data for both Pavant Butte and the LCVF was collected in late September 1989.

Pavant Butte is the most prominent volcanic edifice in the basaltic volcanic fields of the Black Rock Desert of west-central Utah. It was first described by G.K. Gilbert (1890) and more recently by Oviatt and Nash (1989). Pavant Butte lies near the northwestern limb of the Pavant Volcanic Field (Hoover, 1974). The entire region lies in a graben valley within the eastern half of the Great Basin which during the late Wisconsin glaciation was covered by Lake Bonneville. Pavant Butte was erupted into the waters of Lake Bonneville between 16,000 and 15,300 yr B.P. (Oviatt and Nash, 1989).

Pavant Butte closely adheres to the model tuff cone stratigraphy described by Wohletz and Sheridan (1983). The tuff cone consists of a sequence of highly altered palagonite tuffs resting atop flat to shallowly dipping thinly bedded sideromelane (vitric basalt) tuffs. In places the sideromelane tuff is nearly unaltered. The palagonite tuff was originally blanketed by unpalagonitized "mantling tuffs" (Farrand, 1991; Farrand and Singer, in preparation) which have eroded away over broad expanses of the tuff cone to reveal the underlying palagonite tuff.

The second study area is the Lunar Crater Volcanic Field (LCVF) which lies halfway between the towns of Ely and Tonopah in northern Nye County, Nevada. The volcanic field receives its name from Lunar Crater, a spectacular maar crater over 1100 m in diameter and 130 m deep. In addition to Lunar Crater, there is the Easy Chair Crater tuff cone and maar which lies to the north. The LCVF proper consists of over 100 square miles of late Tertiary to Quaternary aged basalt flows, cinder cones and the two aforementioned maar craters (Scott and Trask, 1971).

The basaltic volcanics of the LCVF sit astride a sequence of Tertiary ignimbrites and silicic lava flows. The entire LCVF is, in fact, in the middle of the Lunar Lake caldera, the most recent caldera in the central Nevada caldron complex (Ekren, et al., 1974). The caldera receives its name from the dry lake bed in the middle of the LCVF. The Lunar Lake caldera was formed approximately 25 Ma B.P. About 375 km^3 of ash was ejected to form the tuff currently mapped as the tuff of Lunar Cuesta (Ekren, et al., 1973; Snyder, et al., 1972). The trace of the caldera is preserved today on the east by the arcuate ridge known as "the Wall". Subsequent to the ejection of the tuff of Lunar Cuesta and the accompanying caldera collapse, several more sequences of tuff were erupted interspersed with eruptions of rhyolitic, quartz latitic and andesitic lavas.

III. Volcanic Pyroclasts of Interest

Volcanic tephras can form by magmatic fragmentation, the disruption of magmas by internal volatiles, or by hydromagmatism, the explosive interaction of magma with external water. The nature of the resulting tephras provides clues as to which fragmentation was dominant and, if the latter process was responsible, about the amount of external water present at the time of eruption.

Basaltic hydrovolcanism produces a continuum of volcanic landforms (Wohletz and Sheridan, 1983). While the most prominent examples are the tuff rings and tuff cones produced by Surtseyan activity, even Strombolian edifices such as cinder cones can have phreatomagmatic episodes. Indeed, the oxidized cinders which are common at many cinder cones are probably the result of some small level of water/magma interaction.

Initially basaltic tephras are characterized by a very low overall reflectance. Figure 2a shows reflectance spectra of unoxidized basaltic cinders and nearly pristine sideromelane hydroclasts from Pavant Butte. As basaltic tephras alter, their visual and near infrared reflectance also changes. Figure 2b shows spectra of altered basaltic tephras.

The alteration of cinders takes the form of the development of well crystalline ferric oxide minerals, principally hematite, which have easily recognizable reflectance spectra. The process by which these cinders become oxidized has never been examined in any detail; however, it seems likely that the most oxidized cinders result from relatively high levels of interaction with water, either internal or external to the melt.

A combination of hydration and oxidation of the sideromelane in tuff cones produce the mineraloid palagonite. Palagonite tuffs, such as those from Easy Chair Crater and the cone portion of Pavant Butte, contain zeolites, poorly-crystalline smectite clays and ferric oxides. These components combine to produce reflectance spectra that are brighter and spectrally distinct from the tephras typically found in tuff rings.

With increasing oxidation there is a decrease in the center and depth of the "1-μm" band in laboratory spectra of tuff ring and tuff cone samples (Farrand and Singer, 1991). The laboratory spectra indicate that even as Fe^{3+} becomes more important, i.e. in the palagonite tuff samples, there is no development of a resolvable band at 0.86 or 0.9 μm which could be attributed to well-crystalline hematite or goethite. Instead absorption from ferrous and ferric phases seem to be contributing to one composite feature.

Near infrared spectrometry has also proven very effective in detecting poorly crystalline clay minerals in bulk samples of palagonite tuff. Absorptions at 2.2 μm in several tuff ring samples and at 2.3 μm in many tuff cone samples respectively indicate the presence of Al-OH and Mg-OH bearing clay structures.

In the reflectance spectra of silicic tephras, there is a trend which is in many respects opposite to that seen in the basaltic tephras. While basaltic tephras grow brighter with increasing alteration, silicic tephras grow darker with increasing devitrification (Levine, 1989). Compare the reflectance of the welded tuff in Figure 2a with that of the unwelded tuff in Figure 2b.

IV. Analysis Techniques

The method used to map pyroclastic deposits in this study was a procedure of spectral mixture modelling developed by J.B. Adams, M.O. Smith and co-workers at the University of Washington (e.g., Smith et al., 1990; Gillespie et al., 1990). The spectral mixture analysis used in this study assumes macroscopic mixing and hence is a linear model. The method is based on the assumption that virtually all of the spectral variation within a spectral image can be accounted for by a relatively small number of endmember spectra.

Materials that do not fit into the model reflectance dictated by those endmember spectra contribute to the residuals generated by the method.

There are two types of endmembers. An *image endmember* (*iem*) is the radiance spectrum of one or more pixels that is taken to be representative of a unique type of surface material. A *reference endmember* (*rem*) is a laboratory or field reflectance spectrum of that material. Image endmembers can consist of a mixture of reference endmembers.

The DN of a given band, b (DN_b), can be described in terms of the fractional contributions of its constituent endmembers by the following equation:

$$(1) \qquad DN_b = \Sigma F_i * DN_{i,b} + E_b \text{ with } \Sigma F_i = 1$$

where F_i is the fraction of endmember i; $DN_{i,b}$ is the radiance that endmember i is contributing in band b; E_b is the error for band b; and both summations are carried from i=1 to N where N is the number of endmembers. If there are M bands, the number of endmembers is constrained to be no greater than M + 1. Even for multispectral systems such as the Landsat TM this limit is seldom reached. For a system such as AVIRIS there is actually a surfeit of channels. Since this is the case, it is a good practice to delete the channels with the lowest signal/noise. These bands tend to be those covering the shortest and longest wavelength and those in the middle of atmospheric water absorption features. Consequently the analysis of the LCVF AVIRIS data was done with a 158 channel data set and the analysis of the AVIRIS data for Pavant Butte was done with 150 channels.

Spectral mixture analysis of multi-channel image data generates a fraction image for each endmember. Pixel DN within a fraction image is equivalent to the fractional abundance of that endmember within the area of the pixel. In addition to the fraction images, an RMS error image is generated wherein pixel DN represents the misfit between the image data and the model.

It was noted earlier that image endmembers do not consist of pure materials (although they can be nearly pure). By comparing the image endmember radiance spectra to reflectance spectra of the pure materials that the image endmembers are meant to represent, their actual makeup can be roughly determined. In the process, the image endmembers are "aligned" with their counterpart reference spectra and gain and offset spectra are generated relating image DN to ground reflectance. The equation that describes this process is as follows:

$$(2) \qquad G_b*DN_{i,b} + O_b = \Sigma F_r*R_{r,b} + E_b \text{ with } \Sigma F_r = 1$$

where $DN_{i,b}$ is the radiance or image DN in band b for image endmember i, G_b and O_b are respectively the gain and offset in band b, $R_{r,b}$ is the laboratory or field reflectance in band b for reference endmember r, F_r is the fraction of reference endmember r and E_b is the error in band b.

The values G_b accounts for multiplicative effects such as instrumental gain and atmospheric transmissivity. Likewise, the values O_b account for additive effects such as instrumental dark current and atmospheric path radiance.

V. Results

In the image endmember analysis of the Pavant Butte scene five *iems* were used: shade, playa, palagonite tuff, red soil and vegetation. The LCVF scene was modelled by four *iem*'s: shade, playa, oxidized cinders and rhyolite.

Figure 3 shows fraction images of four of the Pavant Butte *iems* plus the RMS error image. Slide 22 is a color composite of three of these fraction images with palagonite tuff displayed as red, vegetation as green and red soil as blue. The spectral mixture analysis did an excellent job of discriminating the palagonite tuffs. Moreover, the tuff is mapped equally well on both the northern and southern walls of the tuff cone indicating that the inclusion of shade as an endmember has accounted for variable lighting conditions caused by topography.

Slide 23 presents a color composite of the LCVF scene with the cinder fraction image as red, rhyolite as green and RMS error as blue. Vegetation was not included as an endmember thus vegetation-rich areas in the floors of washes appear as blue. Also the northern portion of the Lunar Lake playa appears as blue, indicating that its spectral signature was not modelled well by the playa image endmember (taken from the southern part of the playa). Subsections of the fraction images of cinders and rhyolite are also presented as Figures 4 and 5.

While the cinder fraction image does an excellent job of discriminating oxidized basaltic cinders, the rhyolite fraction image alarms for materials besides rhyolite. The rhyolite is the Rhyolite of Big Sand Spring Valley mapped by Ekren et al. (1974). Alluvial materials also appear bright in Figures 4b and 5b. This is not surprising in light of the fact that such materials are the erosional remnants of the silicic volcanics that surround the LCVF. A close inspection of Slide 22 or Figure 4b also shows some pixels rich in "rhyolite" in the walls of Easy Chair Crater. The reason for this confusion of rhyolite and basaltic tuff becomes apparent in Figure 6 which shows that AVIRIS reflectance spectra of the Rhyolite of Big Sand Springs Valley and Easy Chair Crater palagonite tuff are not dissimilar. Tuff is poorly exposed in the walls of Easy Chair Crater, thus the spectrum in Figure 6 represents a mixture of palagonite tuff and other materials which combine to produce a spectral signature similar to the rhyolite *iem*.

Corresponding laboratory and/or PIDAS spectra were available for all of these endmembers; thus the second stage of reference endmember modelling was conducted. The gains and offsets resulting from this analysis were used to calibrate the data to reflectance. Light and dark target PIDAS and RELAB spectra were also used to calibrate the data to reflectance. Results of the various calibration methods for a 3x3 pixel area of palagonite tuff on the slope of Pavant Butte are shown in Figure 7 with a RELAB sample spectrum (PB-2b) included for comparison. It can be seen in the figure that the empirical line calibration done with PIDAS data resulted in a lower overall reflectance than the empirical line calibration done with RELAB spectra or from the *rem* modelling. Moreover, the scatter in the data points of the two empirical line method calibrations is slightly higher than that which resulted from *rem* modelling. The gains and offsets resulting from the empirical line (RELAB) and *rem* modelling calibrations were each used to convert a portion of the Pavant Butte AVIRIS image cube to reflectance. A 9x9 pixel region on the playa

north of Pavant Butte had a higher standard deviation (over all 150 channels) for the empirical line calibration than for the *rem* modelling method.

This study was part of a larger investigation into the Vis/IR reflectance properties of hydrovolcanic basaltic tephras (Farrand, 1991). As part of the latter study it was discovered that as sideromelane is converted to palagonite, the band parameters of the iron crystal-field band near 1 μm are affected. The palagonitization process converts Fe^{2+} within the sideromelane to Fe^{3+} within poorly crystalline ferric oxides in the palagonite. The result in the 1 μm region is a shortening of that absorption feature's band center and a shallowing of the band depth (Farrand and Singer, 1991). Both of these effects are a consequence of the increasing influence of ferric over ferrous iron phases. The differences in band depth and center as measured at RELAB for samples of sideromelane and palagonite tuff are shown in Figure 8. Included in the sideromelane tuff field are points representing mantling tuff.

The 1-μm feature is clearly detectable on the AVIRIS derived palagonite tuff spectrum shown in Figure 6. 1-μm band parameters for several 3x3 pixel regions of tuff on the flanks of Pavant Butte are also plotted on Figure 8. The fact that the 1-μm band parameters measured by AVIRIS plot between the palagonite and sideromelane tuff fields indicates that there appears to be a mixture of reflected radiance from both palagonitized and unpalagonitized tuffs. This makes sense in view of the physical situation at Pavant Butte where there are broad expanses of palagonite tuff overlain in places by patches of mantling tuff.

Limited field sampling of the Pavant Butte palagonite tuffs missed a mineral phase which was detected by AVIRIS. Spectra of the palagonite tuffs collected (e.g. Figure 3) bore a 2.3 μm Mg-OH vibrational feature, but no 2.2 μm band. However, the 3x3 average pixel spectrum of Pavant Butte palagonite tuff that is shown in Figure 6 indicates that portions of the palagonitized tuff cone do have an absorption at 2.2 μm suggesting the presence of di- as well as trioctahedral clay minerals within the tuff.

VI. Conclusions

Altered volcanic pyroclasts can be readily mapped using a method of spectral mixture modelling. The most discriminable volcanic pyroclasts are those with the most unique spectral signatures. In the Lunar Crater Volcanic Field scene these were the oxidized basaltic cinders. In the Pavant Butte scene it was the palagonite tuff. In the LCVF scene rhyolite was used as an endmember; however, the resulting rhyolite fraction image also alarmed for alluvial materials and the palagonitic tuff of Easy Chair Crater. This non-uniqueness problem might be addressed by making better use of the residual images which can be generated for each band used in the analysis. While the reflectance spectra of Easy Chair Crater tuff and the Big Sand Springs Valley rhyolite resemble each other they are not the same and these differences should show up in the residuals.

Gains and offsets used to calibrate the data to reflectance were generated from both empirical line and reference endmember modelling methods. The latter method was found to be superior in a direct comparison.

Analysis of the Pavant Butte palagonite tuffs in reflectance demonstrated that even with good exposures of a material there can still be contributions to the detected radiance

from other materials within the field of view. In this case, small patches of mantling tuff atop the palagonite tuff skewed the parameters of the 1-μm iron crystal field band from those of pure palagonite tuff to a field between palagonitized and unpalagonitized tuffs. The detection of a previously undetected 2.2 μm absorption in the Pavant Butte palagonite tuffs is a good example of how imaging spectrometry can supplement field observations of altered volcanic tephras.

Acknowledgements

Laboratory sample spectra were obtained at Brown University's RELAB. AVIRIS data of Pavant Butte is courtesy of Bryan Bailey and Jon Dwyer of the U.S.G.S. Sioux Falls. Original code for the spectral mixture modelling work outlined in this paper was provided by John Adams and Milton Smith of the University of Washington. Thanks to Erzsebet Merenyi for help in adapting the spectral mixture code for use at the University of Arizona's Planetary Image Research Laboratory.

References

Davis, P.A., G.L. Berlin and P.S. Chavez, Jr. (1987) Discrimination of altered basaltic rocks in the southwestern United States by analysis of Landsat Thematic Mapper data. *Photogramm. Eng. and Rem. Sens.* **53**, 45-55.

Ekren, E.B., E.N. Hinrichs and G.L. Dixon (1973) Geologic map of The Wall quadrangle, Nye County, Nevada: U.S.G.S. Misc. Geol. Inv. Map I-719, scale 1:48,000.

Ekren, E.B., Quinlivan, W.D., Snyder, R.P., and Kleinhampl, F.J. (1974) Stratigraphy, structure, and geologic history of the Lunar Lake caldera of northern Nye County, Nevada. Jour. Res. U.S.G.S., 2, 599-608.

Evans, D.L. and R.E. Arvidson (1991) An overview of the Geologic Remote Sensing Field Experiment (GRSFE). *EOS (Trans. Am. Geophys. Union)* **72** (Spring meeting supplement), 176.

Farrand, W.H. (1991) Visible and near infrared reflectance of tuff rings and tuff cones. Ph.D. dissertation, University of Arizona, Tucson, 187 pp.

Farrand, W.H. and R.B. Singer (1991) Oxidation of basaltic tephras: Influence on reflectance in the 1 μm region. *Lunar and Planetary Science XXII*, Lunar and Planetary Institute, Houston, 365-366.

Farrand, W.H. and R.B. Singer, Alteration of hydrovolcanic basaltic ash: Observations with Vis/IR spectrometry. (paper in preparation for *J. of Geophys. Res.*)

Gilbert, G.K. (1890) Lake Bonneville: *U.S. Geological Survey Monograph 1*, 438 pp.

Gillespie, A.R., M.O. Smith, J.B. Adams, S.C. Willis, A.F. Fischer III and D.E. Sabol (1990) Interpretation of residual images: Spectral mixture analysis of AVIRIS images, Owens Valley, California. *Proceedings of the Second Airborne Visible/Infrared Imaging Spectrometer (AVIRIS) Workshop.* R.O. Green (ed.) JPL Publication 90-54, Jet Propulsion Laboratory, Pasadena, CA, 243-270.

Hoover, J.D. (1974) Periodic Quaternary volcanism in the Black Rock Desert, Utah. *Brigham Young University Geology Studies* **21**, 3-72.

Levine, A. (1989) Ash-flow zones of the Bishop Tuff: Detailed mapping with the Landsat Thematic Mapper. M.S. thesis, Arizona State University.

Oviatt, C.G. and W.P. Nash (1989) Late Pleistocene basaltic ash and volcanic eruptions in the Bonneville basin, Utah. *Geol. Soc. America Bull.* **101**, 292-303.

Scott, D.H. and Trask, N.J. (1971) Geology of the Lunar Crater volcanic field, Nye County, Nevada. USGS Prof. Paper 599-I.

Smith, M.O., S.L. Ustin, J.B. Adams and A.R. Gillespie (1990) Vegetation in deserts: 1. A regional measure of abundance from multispectral images. *Rem. Sens. Env.* **31**, 1-26.

Snyder, R.P., E.B. Ekren and G.L. Dixon (1972) Geologic map of the Lunar Crater quadrangle, Nye County, Nevada. U.S.G.S. Misc. Geol. Inv. Map I-700, scale 1:48,000.

Wohletz, K.H. and M.F. Sheridan (1983) Hydrovolcanic explosions II: Evolution of basaltic tuff rings and tuff cones. *Am. J. Sci.*, **283**, 385-413.

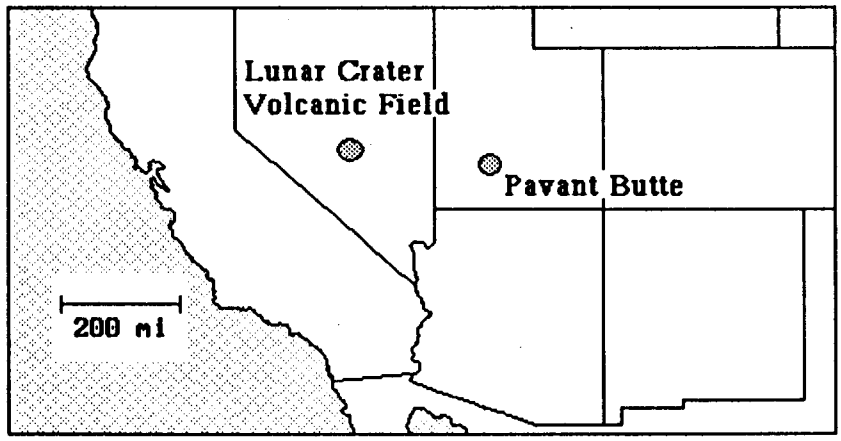

Figure 1: Locations of field sites.

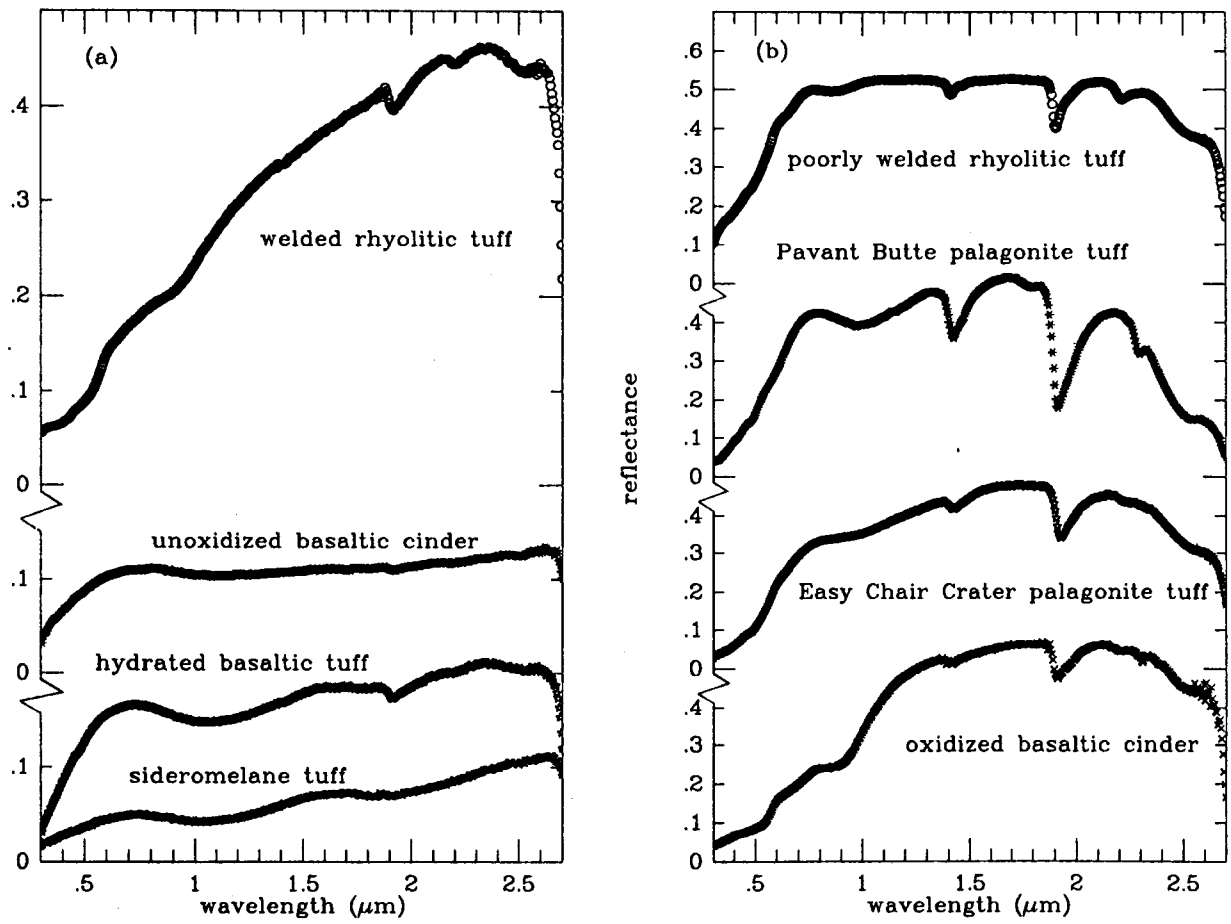

Figure 2: Reflectance spectra of volcanic pyroclasts measured at RELAB.

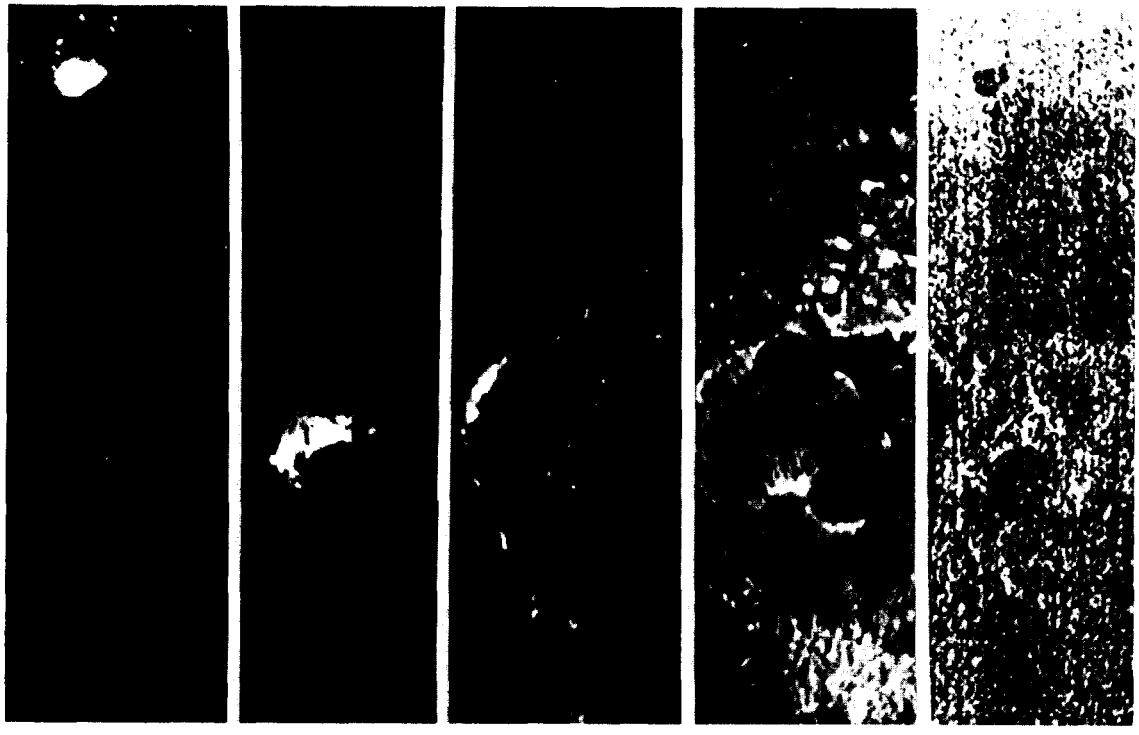

Figure 3: Fraction images of Pavant Butte *iems* plus RMS error. From left to right: playa, palagonite tuff, vegetation, red soil and RMS error. Shade is not shown.

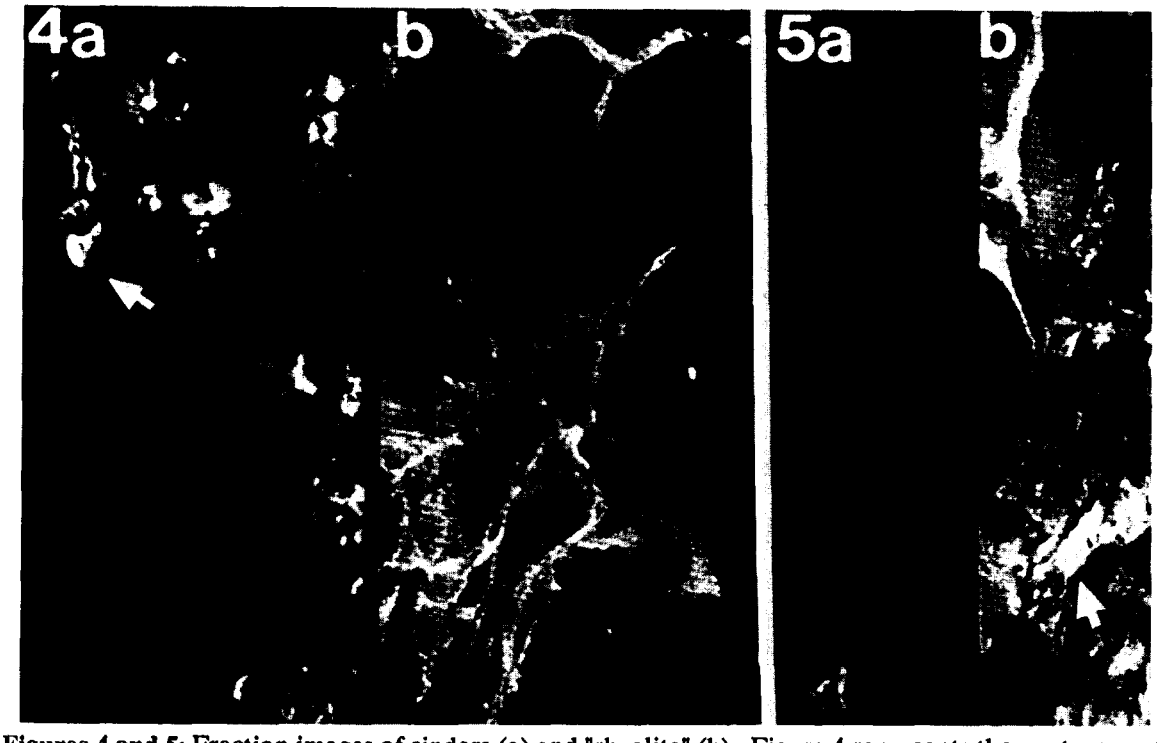

Figures 4 and 5: Fraction images of cinders (a) and "rhyolite" (b). Figure 4 represents the western portion of the LCVF scene. The cinder *iem* was extracted from the cinder cone north of Easy Chair Crater (indicated by the arrow). Figure 5 is the eastern portion of the LCVF scene. The arrow indicates where the rhyolite *iem* was extracted from.

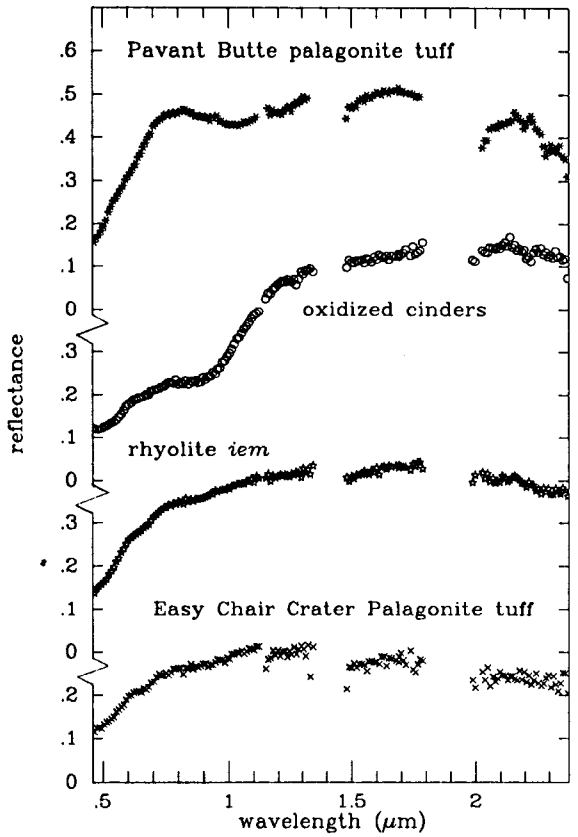

Figure 6: Reflectance spectra of volcanic pyroclasts extracted from AVIRIS image data. The resemblance of Easy Chair Crater tuff and the rhyolite *iem* accounts for basaltic tuff alarming as rhyolite in Figure 4a.

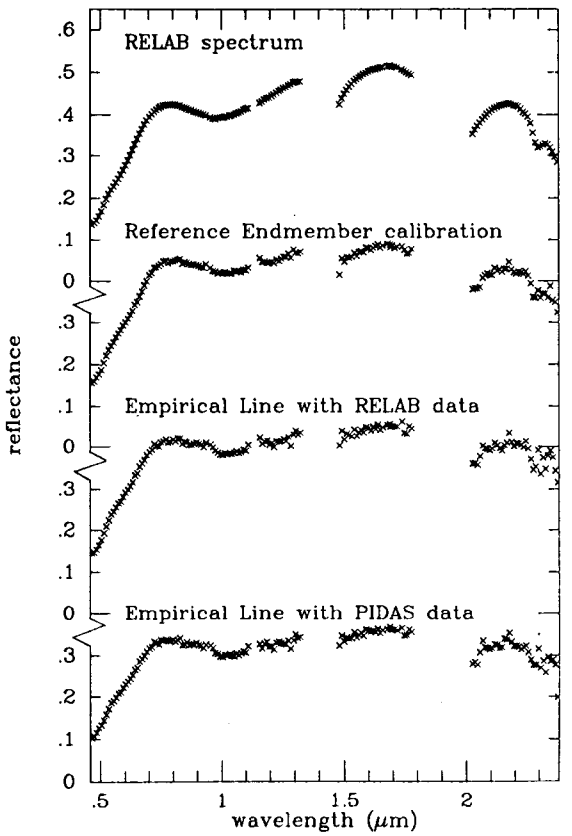

Figure 7: Comparison of methods for calibration to reflectance.

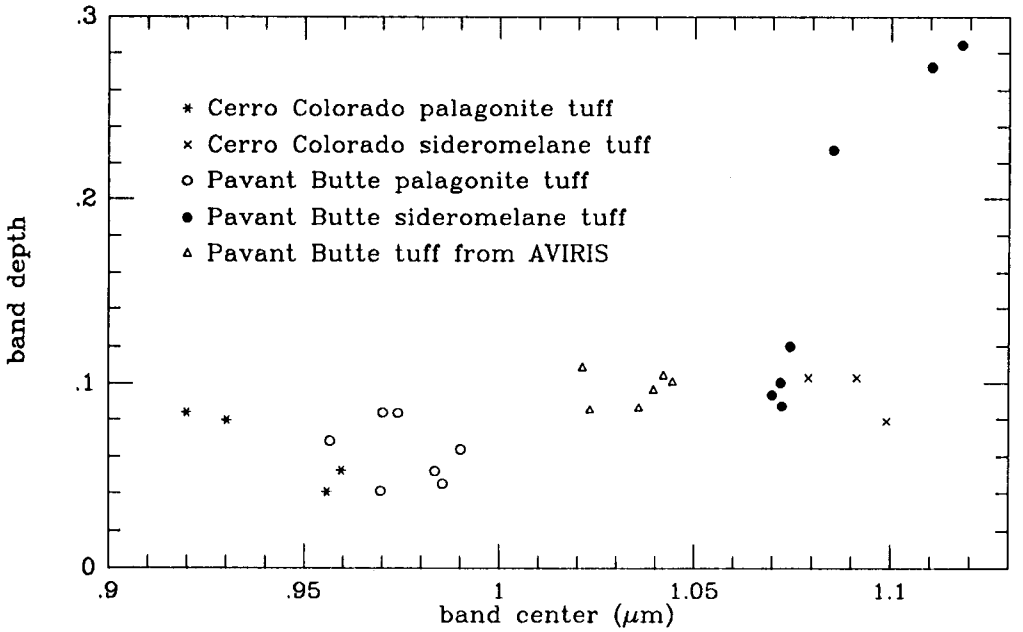

Figure 8: Band Depth vs. Band Center of 1 - μ feature

GEOLOGIC MAPPING IN DEATH VALLEY, CALIFORNIA/NEVADA USING NASA/JPL AIRBORNE SYSTEMS (AVIRIS, TIMS, AND AIRSAR)

Fred A. Kruse[1,2], John B. Dietz[1], and Kathryn S. Kierein-Young[1,2]

[1]Center for the Study of Earth from Space (CSES), CIRES
[2]Department of Geological Sciences
University of Colorado, Boulder, CO 80309

EXTENDED ABSTRACT

A multi-sensor aircraft campaign called the "Geologic Remote Sensing Field Experiment" (GRSFE) conducted during 1989 resulted in acquisition of high quality multispectral images in the visible, near infrared, shortwave infrared, thermal infrared, and microwave regions of the electromagnetic spectrum. The airborne data sets include the Airborne Visible/Infrared Imaging Spectrometer (AVIRIS) (0.4 - 2.5 μm, 224 bands), the Thermal Infrared Multispectral Scanner (TIMS) (8-12 μm, 6 bands) and the Airborne Synthetic Aperture Radar (AIRSAR) (P, L, and C band, quad polarization, multiple incidence angles). Ancillary data include Landsat Thematic Mapper (TM, 7 bands), laboratory and field spectral measurements, and traditional geologic mapping.

The GRSFE data for a site in the northern Death Valley (California and Nevada) region, USA were calibrated to physical units and geometrically registered to a map base. AVIRIS data were calibrated to reflectance using ground targets and the "empirical line" method. TIMS data were calibrated to radiance using the onboard blackbody measurements and converted to emissivity using the modelled emittance method (assuming an emissivity of 0.93 in band 6). AIRSAR phase, cross-talk, co-channel imbalance, and absolute radiometry were calibrated using data characteristics, theoretical models, and trihedral corner reflectors. The AVIRIS, TM, and TIMS were analyzed using both color images and digital spectral analysis. The AIRSAR data were analyzed using color images, and frequency and polarization signatures. The AVIRIS and TM visible and infrared multispectral remote sensing observations provided information about the surficial composition (mineralogy) of the rocks and soils. AVIRIS allowed identification and mapping of the minerals calcite, dolomite, sericite, hematite, and goethite based on their spectral signatures. Selected mineral mixtures were identified and mapped by utilizing discrete absorption bands in the visible portion of the spectrum for the iron oxides and bands in the shortwave infrared for the other minerals. TIMS spectral signatures in the thermal infrared region between 8 and 12 μm and emissivity ratio images provided compositional (lithological) information not contained in AVIRIS data (primarily silica

content information). Variation of the AIRSAR radar backscatter as a function of wavelength allowed mapping of varied surface morphology (relative surface roughness).

A variety of rock types, regional and localized lithological variation, and the effects of processes such as weathering, erosion, soil development, and faulting were detected and mapped using the optical remote sensing data. The Radar data were used to characterize both local and regional faulting and other geologic structures, particularly in unconsolidated alluvium. The integrated optical and microwave data sets provided complementary information that allowed identification and mapping of new structures, control of both lithology and alteration by structure, and associations of surface morphology and composition. This case study establishes that the use of combined optical and microwave image data for deriving physically based, quantitative measurements of the Earth's surface results in improved geologic mapping. The results to date are an improved understanding of the nature and distribution of structures, lithology, weathering, and alteration in the northern Death Valley Region. The research is presently being expanded to cover much of Death Valley from Artist's Drive northward. New geologic information derived from the quantitative remote sensing studies will be used to develop models that explain the interaction of complex depositional and erosional processes controlling the configuration of the modern land surface in this region.**

** This is a summary of results published during 1991 at two symposia. The complete references are listed below.

Kruse, F. A., and Dietz, J. B., 1991, Integration of optical and microwave images for geologic mapping and resource exploration: in Proceedings, International Symposium on Remote Sensing of Environment, Thematic Conference on Remote Sensing for Exploration Geology, 8th, 29 April - 2 May 1991, Denver, Colorado, Environmental Research Institute of Michigan, Ann Arbor, p. 535-548.

Kruse, F. A., and Dietz, J. B., 1991, Integration of diverse remote sensing data sets for geologic mapping and resource exploration: SPIE Symposium on Remote Sensing for Geology and Geophysics, 1-5 April 1991, Orlando, Florida, (in press).

Geologic Mapping of Keping Uplift, Northwestern Margin of the Tarim Basin Based on Absorption Features Using Hyper-multispectral Image Data

Kinya Okada
Japex Geoscience Institute, Inc.
Tokyo, Japan

Takumi Ohnuma
Japex Geoscience Institute, Inc.
Tokyo, Japan

Hiroshi Watanabe
Japex Geoscience Institute, Inc.
Tokyo, Japan

Abstract. A method for hyper-multispectral remote sensing data is developed, and some test results using Airborne Visible/Infrared Imaging Spectrometer (AVIRIS) and the Geophysical Environmental Research Co. 63-channel Airborne Imaging Spectrometer (GERAIS) data of the Cuprite mining districts are shown. The developed software is applied to GERAIS data acquired in October, 1990 over the eastern part of the Keping Uplift, located in the northwestern margin of the Tarim Basin, China. Several rocks and minerals are identified and mapped, including limestone and dolostone which are well discriminated.

I . Introduction

Laboratory spectra of rocks and minerals were shown to be useful in their discriminations. Most of the remote sensing data from satellites, however, have a limited number of band and it was not easy to identify surface materials in detail. On the other hand, airborne imaging spectrometers to acquire hyper-multispectral image data in the VNIR and SWIR have been developed. For geological mapping, particularly, absorption band imagery extracted from hyper-multispectral image data is shown to be useful because it has an ability to reveal the mineral compdsition of surface in detail.

Tarim Basin has been geologically investigated using remote sensing data with the cooperation of Chinese Academy of Sciences since 1987. This paper focused on the eastern part of the Keping Uplift, located in the northwestern margin of the Tarim Basin, where Palaeozoic sequences are well exposed. The data was collected by the Geophysical Environmental Research Co. (GER) 63-channel Airborne Imaging Spectrometer. The GER system has a single aperture with three separate spectrometers for three separate detector arrays and spectrally covers approximately from 400 nm to 2500 nm (Collins and Chang, 1988; Table 1). In this paper, we describe the methodology and its application to the Tarim Basin study for rock type discrimination using hyper-multispectral remote sensing data.

II . Methodology

AVIRIS and GERAIS data of the Cuprite mining districts were used as test data. The Cuprite area, located on the western edge of Nevada, is well known as a test site of a lot of airborne sensors. Ashley and Abrams (1980) describe geology, especially hydrothermal alteration of the Cuprite. The hydrothermal alteration areas are divided into three mappable zones: silicified rocks, opalized rocks, and argillized rocks. Opalized rocks contain alunite and kaolinite.

Our approach to spectral processing of hyper-multispectral image data consists of three steps: pre-processing, feature extraction, and

mapping (Okada and Iwashita, 1990). In the first two steps, a raw spectrum from each pixel is processed (Figure 1). The raw spectrum in radiance or digital number (DN) is influenced by several factors such as solar incident energy, atmospheric absorption and scattering, and topographic effects, in addition to the reflectance of surface materials.

Pre-processing converts a raw spectrum to a reflectance(-like) spectrum. For this conversion, a lot of techniques are proposed (Green and Craig, 1985, Kruse, 1988 etc.). In this study, we take a simple way in order to process rapidly a large volume of data. The conversion is accomplished by ratioing a raw spectrum data of each pixel to the average spectrum data over entire image. This process removes major solar radiation and atmospheric effects. However, if a major part of surface materials is homogeneous, this method is not effective, because the average spectrum includes reflectance feature. For the correction of topographic effects, the equal energy normalization is useful, however, this is likely to enhance noise components of very dark areas such as shadows which have low signal-to-noise ratio as well. Therefore, we did not apply the correction of topographic effects. Figure 2 shows a laboratory spectrum of a rock sample collected at Kaolinite Hill where kaolinite rich rocks are exposed and converted spectra of AVIRIS and GERAIS in the corresponding areas. The location and shape of absorption features in those spectra are similar one to the other. In particular, AVIRIS's spectrum shows the doublet feature around 2200 nm very well.

In the next step, we extract absorption features from reflectance(-like) spectrum using hull quotient (Green and Craig, 1985) or hull difference methods and derive six parameters for each absorption (Figure 3): the wavelength (λ), depth (D), width (W), symmetry (S), area (A) and slope of upper hull (θ). As shown in the Figure 3, width and symmetry parameters are defined based on the area of absorption parts. Usually, several absorption features are extracted in this processing. Then, a subindex is assigned to each absorption in decreasing order of depth. That is, wavelength parameter is represented such as $\lambda_1, \lambda_2, \cdots$. The hull difference method was applied in the actual processing for airborne data, since the hull quotient is likely to extract noise components as deep absorptions in very dark areas such as shadows. For the parameters except for depth and area, two methods provide mostly similar values.

Both AVIRIS and GERAIS data of the Cuprite were processed in the range of 2000 to 2400 nm as a test. A few absorption features were extracted and parameterized for each pixel. A simple way for mapping is to display six parameter-images based on the computed parameters. Figure 4 shows a set of color-coded parameter-images of AVIRIS for the deepest absorption: λ_1, D_1, W_1, S_1, A_1 and θ_1-image. The parameter-images of GERAIS show similar pattern to those of AVIRIS. The λ_1-image of AVIRIS, however, is distinguishable in absorption band due to its higher spectral resolution than GERAIS.

These six parameter-images are a set of basic image for analysis. The λ_1-image shows a zoning based on absorption band and enables an analyst to estimate some of surface materials. The D_1 and A_1-images indicate the distribution with a threshold values meaningfully deep absorption features. If other parameter-images are combined with D_1-image and/or A_1-image, parameter-images easy to interpret can be obtained. The W_1, S_1, and θ_1-images discriminate absorption features which have the same absorption band. The silicified zone (2250 nm absorption; orange

colored) and outer opalized and argillized zone (2160 to 2200 nm absorption; green to yellow colored) are clearly divided on the λ_1-image of AVIRIS. Furthermore, the difference of alunite (2160 nm; green colored) and kaolinite absorption band (2220 nm; yellow colored) is detectable. Mixed alunite and kaolinite area is expected to have yellow-green colored area. The W_1-image shows that alunite patterns of western area are wider than those of eastern area. This may relate to something like mixtures. In further analysis, the deepest absorption parameters should be combined with the second and/or third deepest ones and/or the parameters from other wavelength region such as visible region. An analyst can obtain mineralogical information of his study area using these parameter-images.

Ⅲ. Application to geological mapping in Yingan Shan area, the Tarim Basin, China

A. Purpose

We have been studying the geology of northern margin of the Tarim basin, China using satellite imagery such as LANDSAT and SPOT since 1987. One result of this investigation shows that satellite imagery is a quite useful tool for geological analysis, especially for the analysis of geological structure. However, generally speaking, lithological information obtained from satellite data are limited, because the bandwidths of the sensors loaded on satellite are too wide for detailed spectral discrimination.

In this paper, we use hyper-multispectral image data with high spectral resolution acquired from aircraft to remotely estimate the lithology of strata exposed at the surface.

The study area is Yingan Shan, the NW margin of the Tarim basin (Figure 5). The results illustrate an approach that is applicable to reconnaissance, especially to geological mapping.

B. Approach

We used following steps to map strata exposed in Yingan Shan area.

1. Field survey to get detailed stratigraphic information and rock samples.
   These samples are analyzed by chemical analysis, X-ray diffraction analysis, laboratory spectrum measurement, etc.
2. Acquisition of hyper-multispectral image data using GERAIS.
3. Data processing focused on the absorption wavelength and interpretation of absorption images.

In the following section, we will illustrate one of obtained several results about discrimination of limestones from dolostones distributed in this area.

C. Geological setting

The study area, Yingan Shan, is located in the Keping Uplift which defines the NW margin of the Tarim basin. The structure of Keping Uplift was analyzed using LANDSAT imagery by Nishidai and Berry (1990). Keping Uplift is characterized by thin-skinned imbricate thrusts. Yingan Shan is eastern part of the Uplift, therefore the structure style of the area

basically follows that of Keping Uplift. Thick Palaeozoic sequences are exposed throughout the Uplift (Hu et al., 1965). Uplift occurred during the Variscan orogenic movements. Mesozoic rock is absent (Tian et al., 1985). Palaeozoic sequences in Yingan Shan consist of Cambrian - lower Permian rocks excluding upper Ordovician and Carboniferous. From stratigraphic point of view, these sequences can be subdivided into three major sedimentation cycles (Hu et al.,1965) :

Cambrian - Ordovician cycle	: predominantly carbonates
Silurian - Devonian cycle	: predominantly terrigenic clastics
Permian cycle	: predominantly terrigenic clastics and carbonates

Approximately 4 km thick of marine and nonmarine strata are exposed in the area (Figure 6).

D. Spectral analysis of hyper-multispectral image data

It is well known that calcite has an absorption near 2330 nm while dolomite has one near 2300 nm (Hunt, 1982). We focused on these absorption features and tried to distinguish limestones from dolostones distributed in the area.

These deepest absorptions of calcite and dolomite in SWIR range must appear at the bands 55 and 53, respectively, in GERAIS hyper-multispectral image data used in this paper. However, because spectral smoothing is applied to data to reduce the influence of the noise, these absorptions will appear at the bands 54 - 56 and 52 - 54, for limestones and dolostones respectively.

Reflectance-like spectra processed from GERAIS data well demonstrate those features. Left image in Figure 7 is a false color image of a part of eastern Yingan Shan composed of the bands 6, 10 and 17. Center wavelength of these bands correspond to those of LANDSAT TM band 2, 3 and 4, respectively.In this figure, lower Cambrian dolostones are distributed around the area marked by "LINE 356" and middle Ordovician limestones are distributed around the area marked by "LINE 651". Figure 8(a) shows reflectance-like spectra along these image lines (pixel number increases from top to bottom). Figure 8(b) shows positions (bands) of absorptions calculated by the software developed in this study. From the comparison of absorption bands of both image lines, it is recognized that first absorption peaks (λ_1)of "LINE 356" appear near 2300 nm which may be due to dolomite and those of "LINE 651" appear near 2330 nm due to calcite. And in lower half of "LINE 651" of Figure 8(b), second absorption peaks (λ_2) appear around 2150 nm, which correspond to second absorption peak of calcite.

Right image in Figure 7 is λ_1-image superimposed on band 17. In this image, bluish color represent the area where limestones are distributed and greenish color represent that of dolostones. This result well corresponds to distribution of limestones and dolostones observed by the field survey.

The result of this study illustrates that λ_1-image produced from GERAIS data can be interpreted for the classification of limestones and dolostones. And also, clastic rocks may be able to be mapped as well as carbonate rocks using the software developed in the study. When combined with satellite imagery such as LANDSAT or SPOT, λ_1-image allows us to make accurate geological maps including mineralogical and lithological information.

IV. Conclusions

We proposed a technique for extracting six parameters to represent absorption features. This parameterization reduces a huge volume of image data with a lot of bands to a few parameter-images. In other words, it is a compression technique to display absorption features.

In the application of Tarim Basin, several minerals were identified and mapped using the parameter-images from GERAIS. Limestone and dolostone were clearly differentiated by detecting a slight shift of their absorption features. And the capability of hyper-multispectral data about rock type discrimination is well demonstrated.

References

Ashley, R. P. and Abrams, M. J. (1980)
Alteration Mapping Using Multispectral Images - Cuprite Mining District, Esmeralda County, Nevada, U. S. Geological Survey Open File Report, 80-367

Collins, W. E. and Chang S. (1988)
Application of Geophysical Environmental Research (GER) Airborne Scanner data for detection of hydrothermal alteration in NEVADA, Proceedings of the sixth Thematic conference of Remote Sensing for Exploration Geology, Houston, Texas, Environ.Res. Inst. Michigan, p. 123

Green, A. A. and Craig, M. D. (1985)
Analysis of aircraft spectrometer data with logarithmic residuals, Proceedings of the Airborne Imaging, Spectrometer Data Analysis Workshop, JPL PUBLICATION 85-41, p. 111-119

Hu, B., Wang, J. B., Gao, Z. J. and Fang, X. D. (1965)
Some geological problems of the Palaeozoic of the Tarim Basin, Acta Geol. Sinica, 45, (2), P. 131-142 (in Chinese)

Hunt, G. R., Ed. (1982)
Spectroscopic Properties of Rock and Minerals, In: Handbook of Physical Properties of Rocks, Vol. I, Chapter 3, CRC press, Florida, p. 295-385

Kruse, F. A. (1988)
Use of Airborne Imaging Spectrometer Data to Map Minerals Associated with Hydrothermally Altered Rocks in the Northern Grapevine Mountain, Nevada, and California, Remote Sensing Environment, 24, p. 31-51

Nishidai, T. and Berry, J. (1990)
Structure and Hydrocarbon potential of the Tarim Basin (NW China) from Satellite Imagery, Journal of Petroleum Geology, Vol. 13(1), p. 35-58

Okada, K. and Iwashita, A. (1990)
Hyper-Multispectral Image Analysis Based on Waveform Characteristics of spectral Curve, ADVANCED IN SPACE RESEARCH, Proceedings of the Twenty-Eighth Plenary Meeting held in The Hague, The Netherlands 1990, COSPAR, in press

Tian, Z., Chai, G. and Lin, L. (1985)
Tectonic evolution of the Tarim Basin and its hydrocarbon potential, Oil and Gas Geol., 6, (3), p. 250-258, (in Chinese)

Acknowledgement

The authors would like to thank Earth Resources Data Analysis Center (ERSDAC) for acceptance of publication and the Chinese Academy of Sciences for their cooperation about the data acquisition and the field survey.

Table 1 Band specification of the GER system.

Wavelength range (nm)	bandwidth (nm)	Number of band
430 - 970	23.4	24
1080 - 1800	120.0	7
1980 - 2500	16.3	32

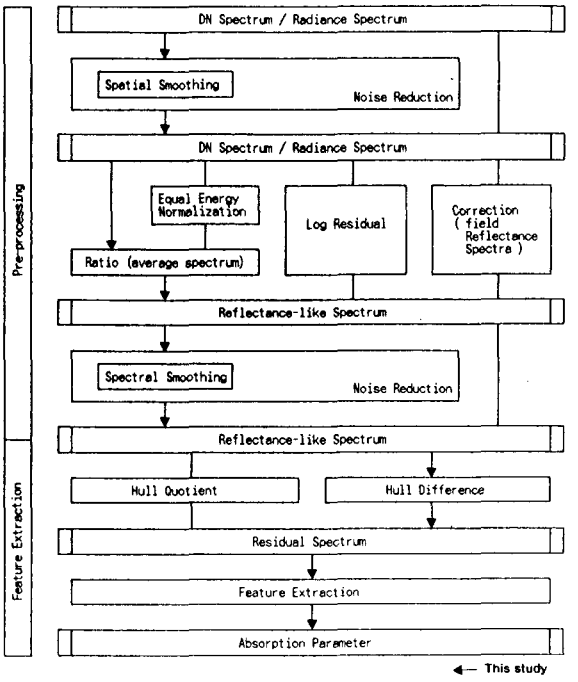

Figure 1 Flow chart of processing.

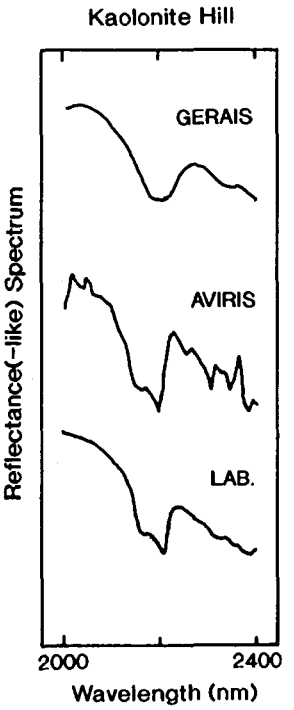

Figure 2

Comparison of a laboratory spectrum of a rock sample collected at Kaolinite Hill and converted spectra of AVIRIS and GERAIS in the corresponding areas.

wavelength : λ
depth : D
area : A
width : $W = A / D \times 2$
symmetry : $S = (A_{left} / A) \times 2 - 1$
slope of hull : $\theta = \tan^{-1} \left(\frac{R_e - R_s}{\lambda_e - \lambda_s} \right)$

Figure 3 Schematic diagram of definition of absorption parameters.

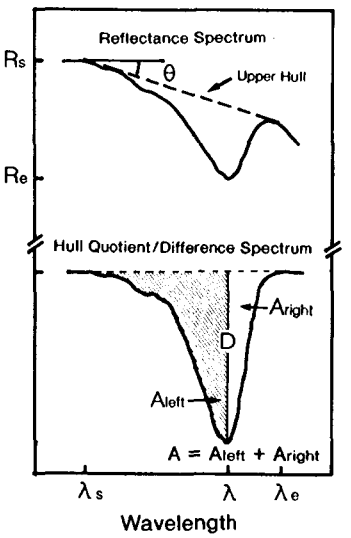

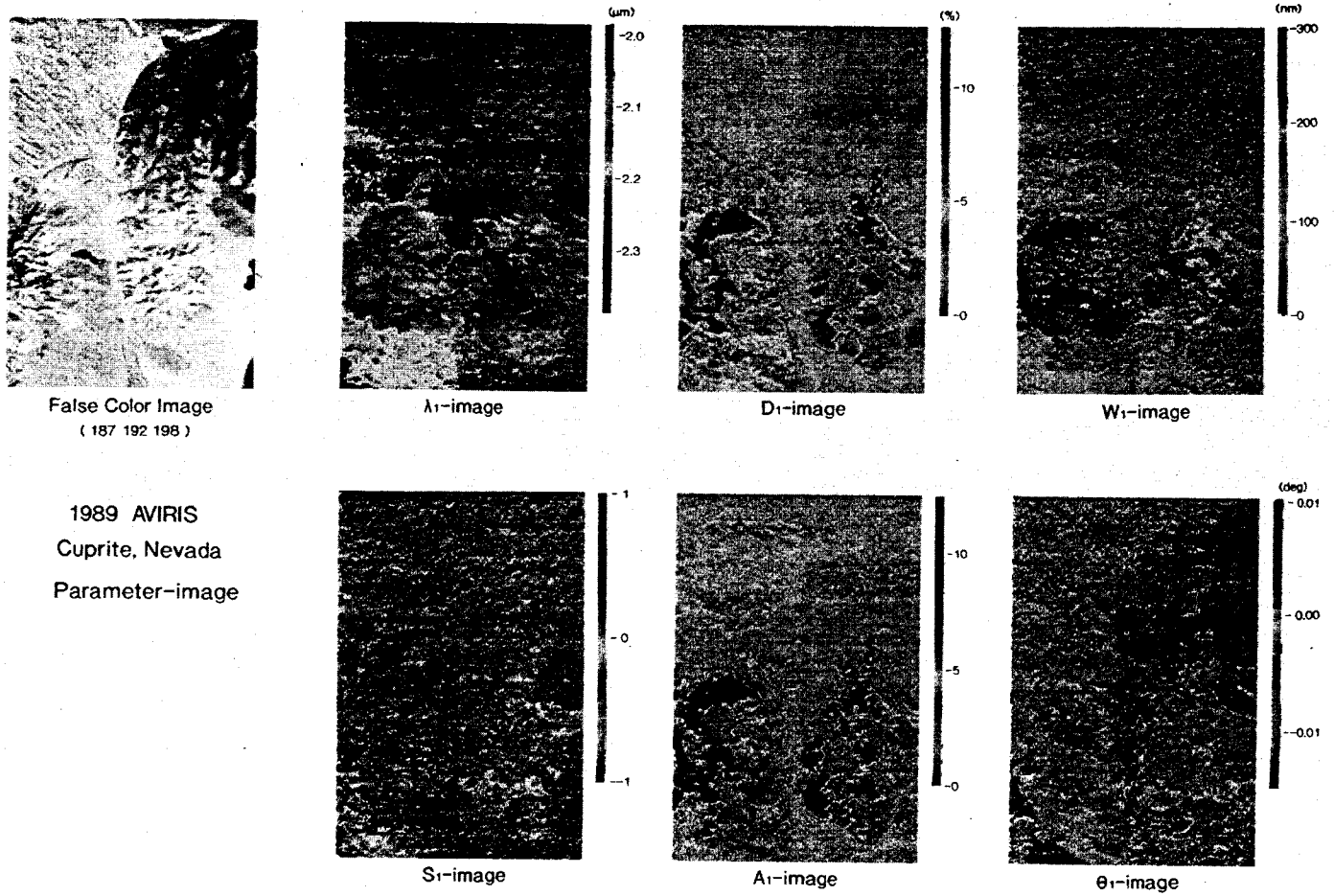

Figure 4 Color-coded parameter-images of AVIRIS for the deepest absorption (see slide 24).

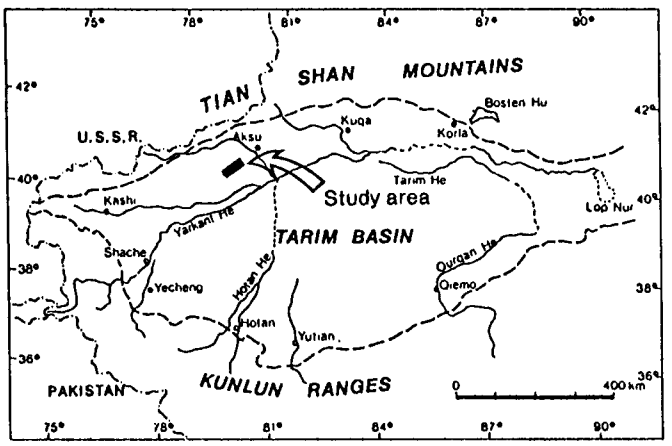

Figure 5 Locality map of the study area.

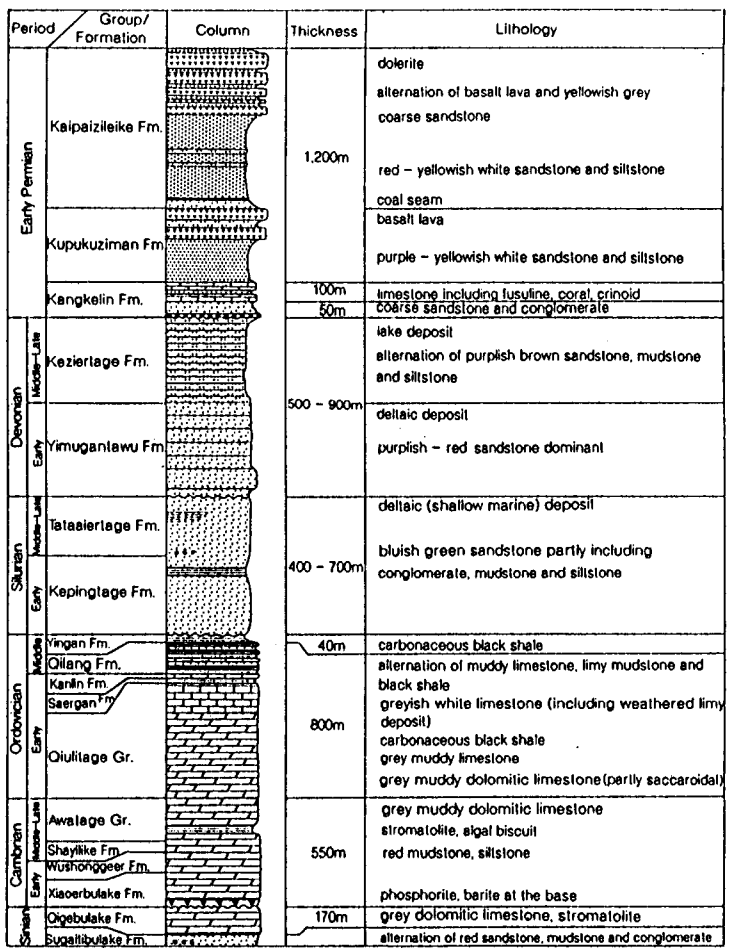

Figure 6 Generalized stratigraphic column of the study area.

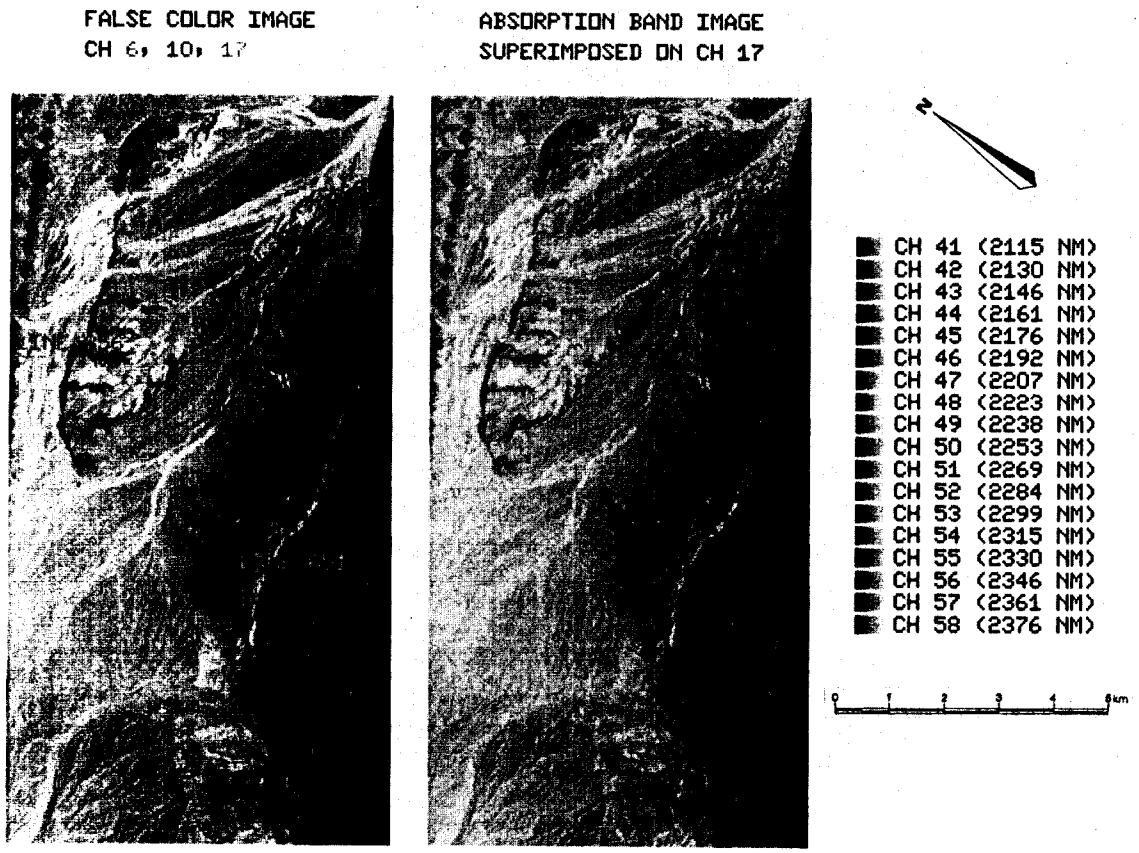

Figure 7 False color image and λ_1 image superimposed on band 17 for a part of eastern Yingan Shan (see slide 25).

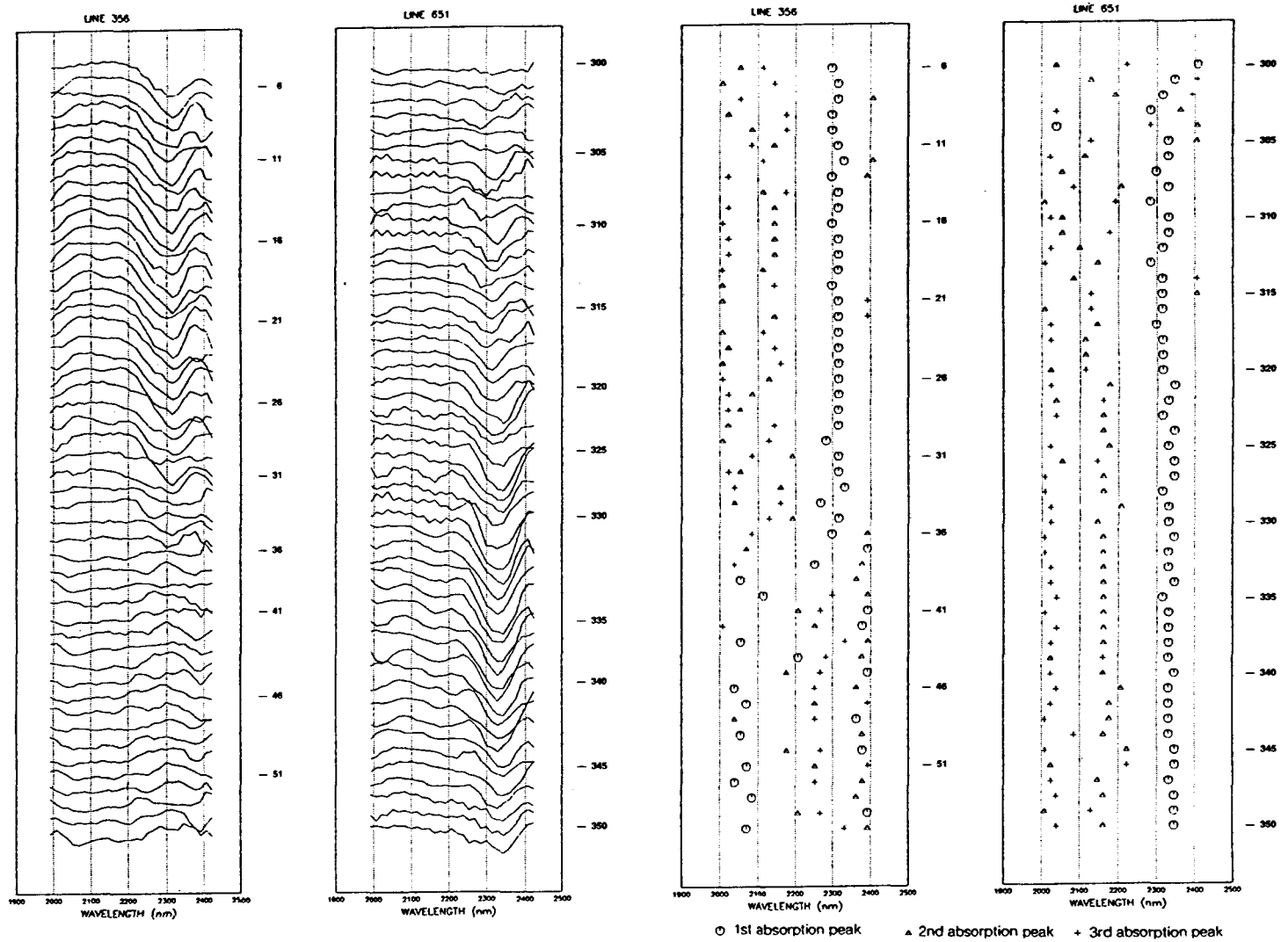

(a) (b)

Figure 8 Examples of reflectance-like spectra (a) and absorption peaks calculated by the software (b) for image lines in Figure 7.

The European Imaging Spectrometry Airborne Campaign - EISAC Selected Examples of Application Oriented Data Evaluation

J. Bodechtel & S. Sommer
AGF - Working Group Remote Sensing
University of Munich, Germany

H. Bach & W. Mauser
Inst. f. Phys. Geography
University of Freiburg, Germany

J. Hill & G. Maracci
Inst. f. Remote Sensing Appl.
EC Joint Research Centre, Italy

ABSTRACT

The paper summarizes the activities and the interim results of the European Imaging Spectroscopy Airborne Campaign (EISAC), that has been initiated jointly by the European Space Agency (ESA) and the Joint Research Centre (JRC) of the Commission of the European Communities. In the framework of the campaign, flights over 7 European test sites have been performed in May/June 1989.
The EISAC data evaluation programme comprises a wide range of applications in agriculture, forestry, geology/soil science and oceanography/marine biology. In a first phase, data evaluation was concentrated on quality assessment, radiometric and atmospheric correction of the airborne data. The second phase deals with spectral signature modelling and with the definition and evaluation of relevant surface parameters, aiming towards optimized approaches for the exploitation of the data of future spaceborne imaging spectrometers with medium (MERIS) and high spatial resolution (HRIS). Examples of spectral evaluation of GER data reveal the high potential of imaging spectrometry for the application of remote sensing in Europe.

I. INTRODUCTION

In the framework of the joint ESA/JRC EISAC campaign, between May 15th and the end of June 1989, imaging spectrometer flights over seven European test sites have been performed successfully as follows:

A. Test Sites (see Fig. 1)

1. Oceanographic test sites.

Test site	Applications
1. Skagerrak	- Monitoring of chlorophyll distribution and pollution of coastal waters (Norway).
2. North Sea, Waddensea, Helgoland	- Coastal Ecology, monitoring of sea water quality and algae blooms (W-Germany).
3. Northern Adria, Venice Lagoon, Sacca di Goro	- Monitoring of coastal ecology and sea water quality (Italy.)

2. Land applications test sites.

Test site	Applications

4. Upper Rhine Valley - Forestry, Agriculture (W-Germany).
5. Somerset Levels - Agriculture (United Kingdom).
6. Almaden - Soil Science, Vegetation (Spain).
7. Ardeche - Soil Science, Land Use (France, JRC experiment).

B. Airborne Data

Moniteq's Fluorescence Line Imager (FLI/PMI) and the 63 band multispectral scanner of Geophysical Environmental Research Corporation (GER) were the core sensors of the campaign. In addition the ITRES Compact Airborne Spectrographic Imager (CASI) was flown over two test sites.
The sensor deployment was technically supported by the German Air and Space Research Organization (DLR). The airborne operations were managed by GDTA (France).
The following airborne data has been acquired:

1. FLI/PMI data. The FLI instrument was flown, in spatial as well as in spectral mode, over all test sites, except the Ardeche.
Spectral range: 400 - 805 nm
Spectral sampling: spatial mode 8 selectable bands $\geq$ 2.6 nm bandwidth
spectral mode 288 bands each 2.6 nm wide
Number of acquired CCTs: 77 (1650 BPI)

2. GER data. Except the Helgoland and Somerset site, the GER instrument acquired data from all test sites.
Spectral range: 450 - 2500 nm
Spectral sampling: VIS/NIR: 450 - 843 nm, 31 bands each 12.3 nm (nominal)
SWIR I: 1440 - 1.80 nm, 4 bands each 120 nm
SWIR II: 2005 - 2500 nm, 28 bands each 16.2 nm
Number of acquired CCTs: 24 (6250 BPI)

3. Metric camera (RMK 15/23). 683 IR false colour photographs have been taken over all test sites, except the Ardeche.

4. CASI data. The two EISAC lines over the Skagerrak test site were covered also with CASI, which was deployed in the framework of the coincident Norwegian NORSMAP campaign. In 1990 the Freiburg test site was covered with CASI, in order to test its capabilities for land applications.
Spectral range: 400 - 900 nm
Spectral sampling: spatial mode 8 selectable bands $\geq$ 1.8 nm
spectral mode 288 bands each 1.8 nm wide

C. Radiometric Ground Truth

Parallel to the overflights on each test site an extensive ground measurement programme has been executed by local Coordinating Investigators (CI) supported by JRC. The following principal radiometric ground measurements have been performed:
- atmospheric measurements performed in coincidence with the overflights.

- continuous incoming irradiance measurements.
- measurements of spectral reflectance of selected sea surfaces, characteristic tidal (sandbars, algae and mud flats etc.) and land surfaces (bare soils, rocks, agricultural crops, natural vegetation etc.)
- continuous monitoring of selected reference targets during overflights and measurements for evaluation of view angle effects.

For the radiometric measurements a suite of instruments was available, including 2 GER D-IRIS, 1 GER S-IRIS, 3 Spectron Engineering SE 590 spectroradiometers. In addition bandpass radiometers and ratioing radiometers were deployed.
Principally atmospheric measurements were performed as in the follwing example of JRC measurements in Ardeche and the Upper Rhine Valley. At both test sites, measurements of the atmospheric beam transmittance were performed using a bandpass radiometer (EXOTECH) and a spectroradiometer (SE 590). The method used is that of Langley /5/. Some results of these measurements are shown in Fig.2 for the Upper Rhine Valley test site. A satisfactory agreement has been obtained between the two types of instruments although further measurements of this kind under stable atmospheric conditions are required in order to establish a fast and reliable procedure for the measurement of atmospheric beam transmittance in a continuous spectrum. In the case of the SE 590 measurements, a best fit of direct irradiance values and air mass has been established for the 252 channels of the spectroradiometer. This kind of data is directly applicable to the airborne data obtained during the overflights of the two test sites concerned and thus atmospheric corrections can be performed in order to have a better correlation between ground and airborne data.

II. EVALUATION PROGRAMME

The EISAC data sets comprising airborne and groundtruth data were distributed to more than 30 research institutes all over Europe.
The coordination of the EISAC data evaluation was entrusted to JRC Ispra.
The evaluation programme is scheduled to last until late 1991. In this context JRC lays its main emphasis on the following topics:
- Radiometric correction of data
- Atmospheric correction of data
- Spectral signature modelling
- Definition and evaluation of relevant surface parameters to be received by future spaceborne instruments regarding especially the modelling of a combined vegetation and ocean band set (i.e. midband frequency, bandwidth, number of bands?) of the Medium Resolution Imaging Spectrometer (MERIS) on the first ESA Polar Platform Mission.
- Data analysis in terms of applications in agriculture, forestry, soilscience and oceanography.

A campaign analysis workshop with 40 participants was held in April 1991 at JRC-Ispra to review the results of the campaign and to discuss the conclusions. 20 presentations gave an excellent impression of the results and also of the problems related to the use of imaging spectrometer data. The discussions revealed an excellent overview on the requirements of European users to future imaging spectrometers and airborne campaigns.

A. Assessment of Data Quality

The first phase of the evaluation programme was dedicated to the assessment of the data quality of the core sensors FLI/PMI and GER. The data has been investigated independently by JRC and the CIs, aiming mainly at the validation of noise level, effective spectral resolution and radiometric calibration /2,4/.

1. GER Data

The investigations of the different groups led to corresponding results for the GER instrument:

a) Signal/Noise ratio (SNR). Assuming that for a homogeneous target sample

SNR = Average Signal/Standard Deviation

the following SNRs have been estimated:

- VIS/NIR module:
  low reflectance targets (4-8% at 500 - 600 nm): SNR = 5-10
  high reflectance targets (20-50% at 750 - 850 nm): SNR =20-50
- SWIR II module:
  In the SWIR II spectrometer the SNR deteriorates with decreasing radiance levels due to atmospheric absorption. The best SNR (25-40) is found in GER bands 40-50, whereas SNRs decrease to about 5-10 in bands 36 - 38 and 55 - 63 /2/.

b) Effective spectral bandwidth. A comparison of Lowtran standard atmosphere absorption bands with GER spectra at band positions, potentially sensitive to gaseous absorptions, led to the conclusion that the nominal bandwidth of 12.3 nm in the VIS/NIR was not kept. An effective bandwidth of 50 nm has been estimated by modelling the appearance of the narrow oxygen absorption band at 760 nm for different band positions and bandwidths. First assuming that mechanical vibrations had caused the exceeded bandwidths, in the meantime investigations of DLR, Oberpfaffenhofen led to the conclusion that the VIS/NIR spectrometer was defocused (F. Lehmann, DLR, pers. communication 1990).
A slight overcompensation of atmospheric CO_2 absorption can be observed in band 39 (2054 nm), which might indicate that the given bandwidth of the SWIR II module (2000 - 2500 nm) is slightly exceeded /2/.

c) Radiometric calibration. The observation of considerable differences between GER spectra with applied preflight radiance factors and field spectra, measured during the overflights, required increased efforts to achieve reliable calibration factors on the basis of inflight data. DLR and JRC have been working independently on the development of above mentioned calibration files to be applied to the GER data of all EISAC test sites. In both cases the investigations led to new tables of radiance factors and offsets for all channels, which have been obtained by fitting the achieved GER radiances to radiances modeled on the basis of radiometric field measurements and radiative transfer calculations /2,4/.
Differences occurring between DLR and JRC calibrations may result from the

use of different atmospheric models (e.g. DLR, Lowtran 7 /4/; JRC, derivates of models developed by Tanrè et al. and Guzzi et al. /1,2,6,7/).

2. FLI/PMI data

SNRs over dark targets have been estimated in the range from 20 to 30 (GER 5-10). Generally the geometric characteristics of the roll corrected data are considered sufficient, whereas the radiometric quality suffers from the moderate SNR and the deficiencies listed below /3/:

a) Inter-camera calibration.
- strong differences between the four cameras, only gross errors removeable.
- no absolute, only cosmetic calibration possible.

b) Detector normalisation.
- dropped detector elements.
- great differences between the responses of the single detector elements.
- only cosmetic calibration working.
- residual noise apparent as a result of data processing.
- the absolute radiance level of the EISAC Somerset data is reduced by a factor of approx. 4 compared to 1988 data of the same site, possibly due to increasing, non-linear degradation of the detector elements (pers. communication S. Briggs & A. Jones, BNSC-NERC, 1989).

c) Geometric characteristics.
- the data appears compressed due to strong undersampling.
- residual high frequency jitter.

B. Atmospheric Correction of the Airborne Data

The comparison of airborne data with spectral field and laboratory measurements requires a conversion of the airborne data to reflectance factors. Different atmospheric models such as the LOWTRAN 7 code were used by the participating institutes.
The atmospheric correction model which was used by the JRC throughout the Ardeche study is based upon the formulation of radiative transfer as developed from Tanré et al. /6,7/ and it provides corrections for atmospheric absorption, scattering and pixel adjacency effects. Diffusion and absorption processes are assumed to be independent. Upward and downward transmission coefficients are therefore easily derived by introducing the auxiliary quantity of optical thickness τ which measures the total extinction of a light beam due to molecular and aerosol scattering passing through an airmass. The method was modified in order to account for atmospheric extinction processes as a function of altitude.

C. Recent Thematic Data Evaluation and Future Activities

Upon the basis of clarified data quality and of reliable in-flight calibration, the second phase of the EISAC programme, dedicated to thematic data evaluation, was started.
First attempts concentrated on the mapping of chlorophyll distribution and

pollution of coastal waters and on the spectral differentiation of various land surfaces and ground covers.

Encouraging results could be achieved in the discrimination of different soils and rocks by using their characteristic spectral features in the short wave infrared (SWIR) between 2.0 and 2.5 µm. The evaluation of GER data, obtained from bare rock and soil surfaces in the Ardeche test site (F), revealed identical absorption features in airborne as well as radiometric field and laboratory measurements, which correspond to the varying contents of Al-OH and CO_3 bearing minerals /2/. But also combined lignin and cellulose absorptions appear in spectra from the second GER SWIR spectrometer module, once the amount of green leaves in the observed vegetation is significantly reduced. This becomes clearly evident in spectral signatures derived from mature wheat and barley crops. Corresponding cellulose-lignin absorptions, though weaker, can also be identified in spectra from mediterranean shrublands (see Fig.3).

The Institute of Physical Geography at Freiburg concentrated on the modelling of the reflectance red edge and on the detection of irrigated fields in the Freiburg Upper Rhine Valley test site using the SWIR bands of GER. The combined set of image-truth and groundtruth data enabled the calculation of averaged spectra for selected soil and plant parameter combinations. This procedure considerably reduced system noise in the spectra.
Separate correlations between the parameters describing the Gauss function and the measured plant parameters were calculated for each soil type. The analysis showed highly significant correlations ($r > 0.93$) between both, the "minimum reflectance" and the "inflection wavelength of the red edge and the plant height of corn (Fig.4). The resulting regression functions for the correlation "minimum reflectance/plant height" vary strongly depending on the soil type of the considered field. In the opposite the "inflection wavelength" ($r = 0.997$) is not influenced by the signal of the underlaying soil. It is only determined by the plant parameters. Furthermore the suitability of the SWIR channels for the discrimination of dark clay soils from irrigated soils was shown. The water content of the top soil proofed to be well parameterized through a ratio between the reflectance at 2.16 and 2.04 micron ($r = 0.91$). A transfer of this relation to non-vegetated pixels in the GER data allowed a classification of the irrigated bare soils independent of the soil type.

With respect to the development of the Medium Resolution Imaging Spectrometer (MERIS), to be launched in the framework of the first ESA Polar Platform Mission, EISAC data furthermore will be used to investigate the:
- quantification of nature and physical status of vegetation communities.
- boundaries for the detection of plant spectral features in mixed soil-plant spectra.
- influence of different soil properties on the mixture of spectra.

Supplementary CASI data of the Freiburg test site, that has been flown on July 20th 1990, will be included into this part of the research programme. In the near future the European remote sensing community is looking forward to the deployment of JPL's AVIRIS in Europe in the period from June 13 to July 20, 1991.

III. CONCLUSIONS

The EISAC campaign provided high radiometric resolution airborne data and groundtruth of manifold European sea and land surfaces, covering a wide range of oceanographic and land applications. Upon this basis important experiences in the field of radiometric and atmospheric correction of imaging spectrometer data, obtained under European conditions, were gained. This new know how enables an improved application oriented evaluation of the EISAC data and a better definition of the requirements for future airborne imaging spectrometry campaigns in Europe.
The main problems of EISAC data evaluation are related to the following facts:

- the FLI/PMI as well as the GER sensor didn't provide the data quality that was expected according to the given pre-flight specifications.
- due to the latter fact and due to the lack of reliable informations about the pre-flight calibration, the data of both sensors had to be calibrated on the basis of in-flight radiometric and atmospheric measurements.
- the moderate SNR levels make it difficult to find reliable reference targets (i.e. large and homogeneous enough) for in-flight calibration. In addition pixel-by-pixel evaluations require the application of noise reduction algorithm, that may affect the information content of the data.

The above mentioned experiences demand a strict control of preflight specifications and calibration of the sensors in the preparation phase of future campaigns. At the given level of data quality increased emphasis has to be put on detailed atmospheric and meteorological measurements and on the careful selection of large and homogeneous in-flight calibration targets. For the future application of imaging spectrometry, an increased availability of imaging spectrometers covering the entire spectral region from 0.4 to 2.5 µm is needed, not only for remote sensing of soils and rocks but also in order to derive important plant biochemical/-physical parameters (e.g. Lignin, Protein features) in the the SWIR region for vegetation studies.

REFERENCES

1. GUZZI R., RIZZI R. & ZIBORDI G., 1987: Atmospheric correction of data measured by a flying platform over sea: elements of a model and its experimental validation. *Applied Optics*, 26, p. 3043-3051.

2. HILL J., 1990: Analysis of GER Imaging Spectrometer Data Acquired During the European Imaging Spectrometry Aircraft Campaign (EISAC)'89, Quality Assessments and First Results. Proceedings of the 10th EARSeL Symposium 1990, Toulouse, in press.

3. JONES A.R., WYATT B.K., WILSON A.K., PLUMMER S.E., BRIGGS S.A. & DRAKE N.A., 1990: Discrimination of nitrogen fertilizer levels on permanent graslands from ground- and aircraft-based imaging spectrometers. Proceedings of the 10th EARSeL Symposium 1990, Toulouse, in press.

4. LEHMANN F., MACKIN S., RICHTER R., ROTHFUSS H. & WALBRODT A., 1989: The European Imaging Spectroscopy Campaign 1989 (EISAC) - pre-processing, processing and data evaluation of the GER airborne imaging spectrometer data. Progress report to the JRC Ispra Establishment of the European

Communities. Institute for Opto-electronics, DLR - German Aerospace Research Establishment, Oberpfaffenhofen.

5. SHAW G., REAGAN A. & HERMAN B., 1973: Investigations of Atmospheric Extinction using direct solar radiation measurements made with a multiple wavelength radiometer. *Journal of Applied Meteorology* 12, 374-380.

6. TANRE D., HERMAN M. & DESCHAMPS P.Y., 1981: Influence of the background contribution upon space measurements of ground reflectance. *Applied Optics*, 20, 3676-3684.

7. TANRE D., DESCHAMPS P.Y., DUHAUT P. & HERMAN M.,1987: Adjacency effects produced by the atmospheric scattering in Thematic Mapper data. *Journal of Geophysical Research*, 92, D10, 12000-12006.

ACKNOWLEDGEMENTS

The authors want to thank the coordinating investigators L. Alberotanza (ISDGM-CNR, I, Northern Adria), S. Briggs, A. Jones (BNSC/NERC, UK, Somerset, Helgoland), R. Doerffer, D. Murphy (GKSS, D, Waddensea), B. Koch (Univ. Munich, D, Upper Rhine V.), F. Lehmann (DLR, D, Almaden), L. Pettersson (NRSC, N, Skagerrak) and M. Ruhland (Univ. Strasbourg, F, Upper Rhine V.) as well as the flight operation managers J.C. Morin (GDTA, F) and H. Finckenzeller (DLR, D).
Furthermore we acknowledge the excellent support of E. Attema, M. Rast (both ESA-ESTEC), J. Mègier, W. Mehl, and B. Sturm (all JRC-Ispra).

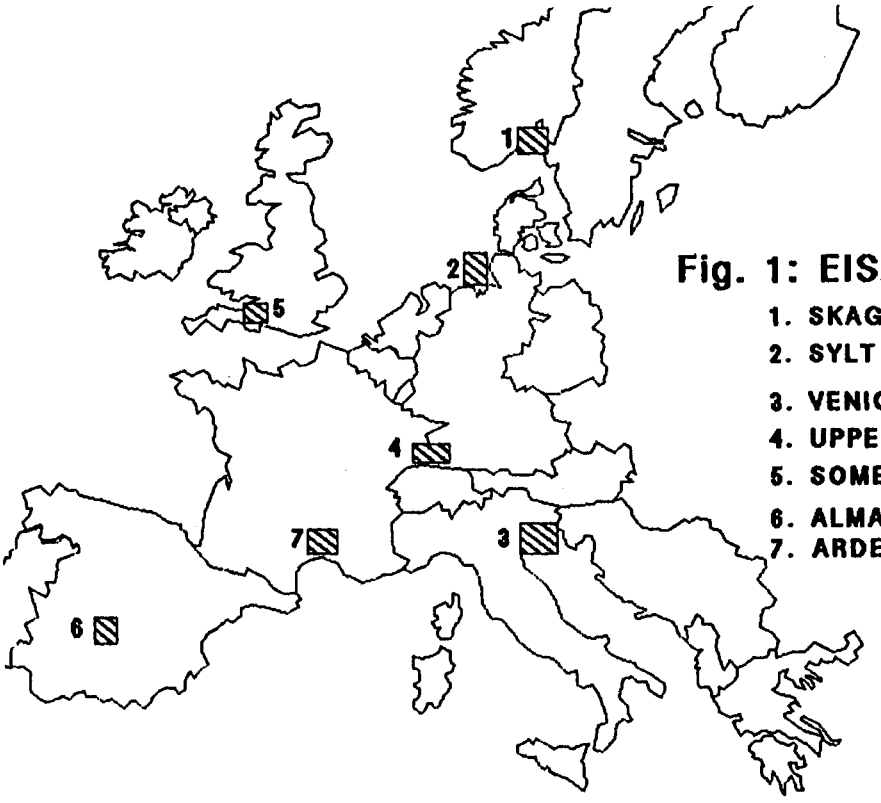

Fig. 1: EISAC TEST SITES

1. SKAGERRAK
2. SYLT AND HELGOLAND
3. VENICE AND SACCA DI GORO
4. UPPER RHINE VALLEY
5. SOMERSET LEVELS
6. ALMADEN
7. ARDECHE

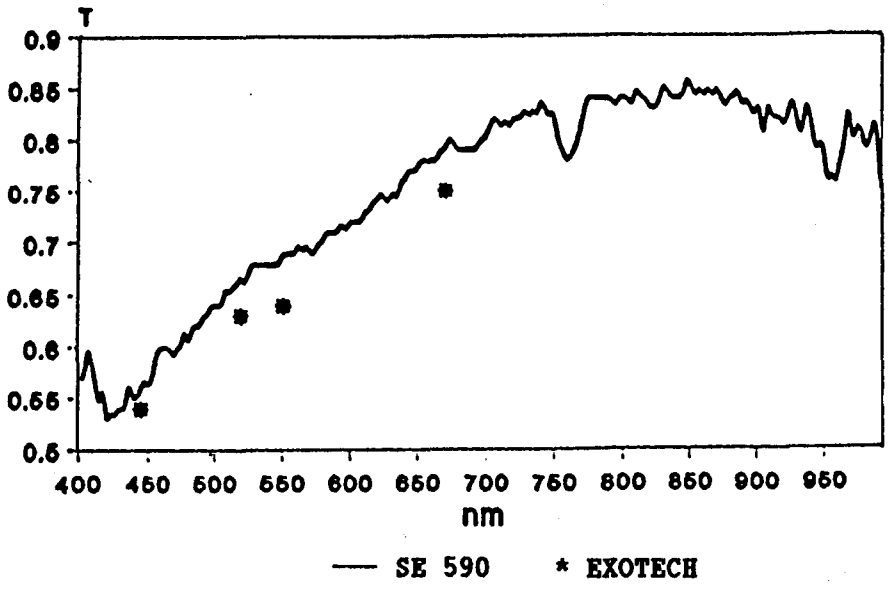

Fig.2: Atmospheric beam transmittance Upper Rhine Valley 13 June 1989

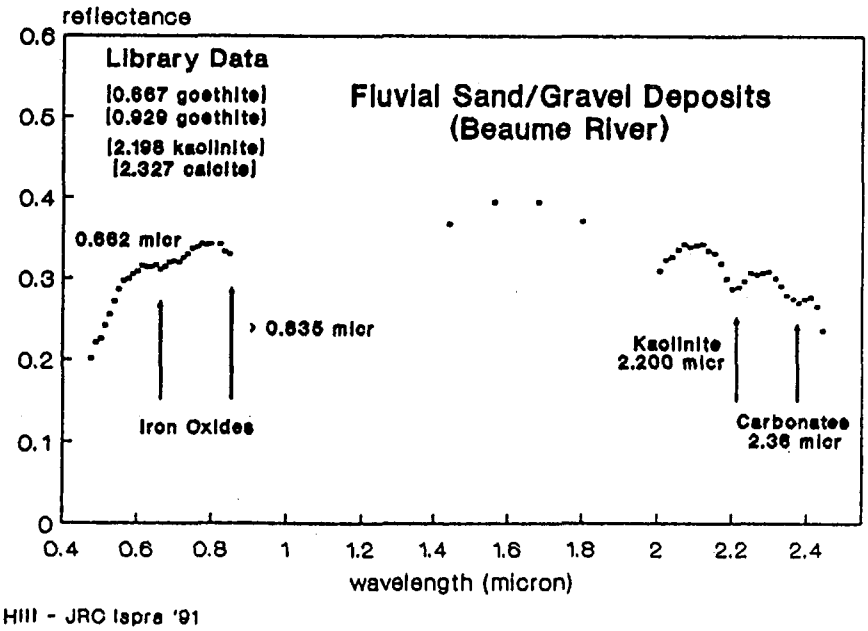

J. Hill - JRC Ispra '91

Fig.3a: GER reflectance spectrum of fluvial deposits from the Ardeche test site

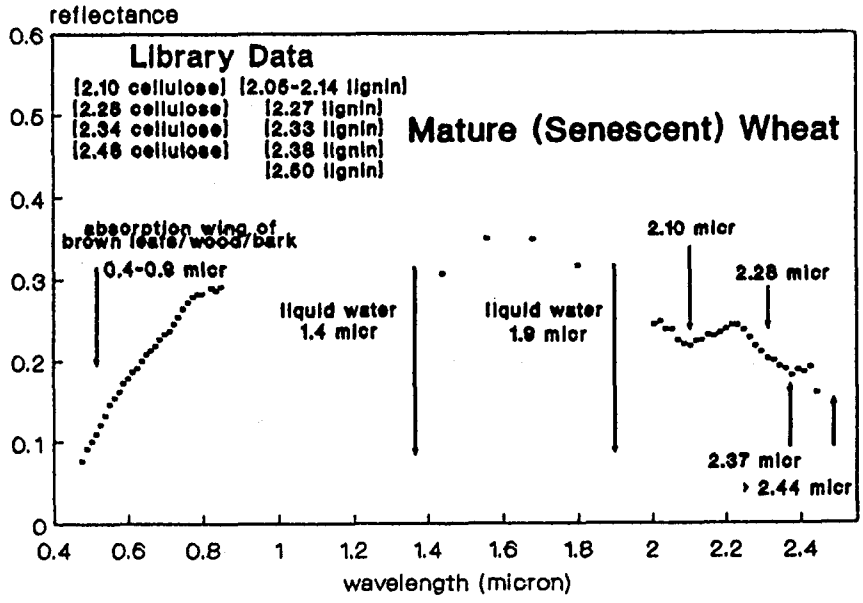

Fig.3b: GER reflectance spectrum of mature wheat in the Ardeche test site

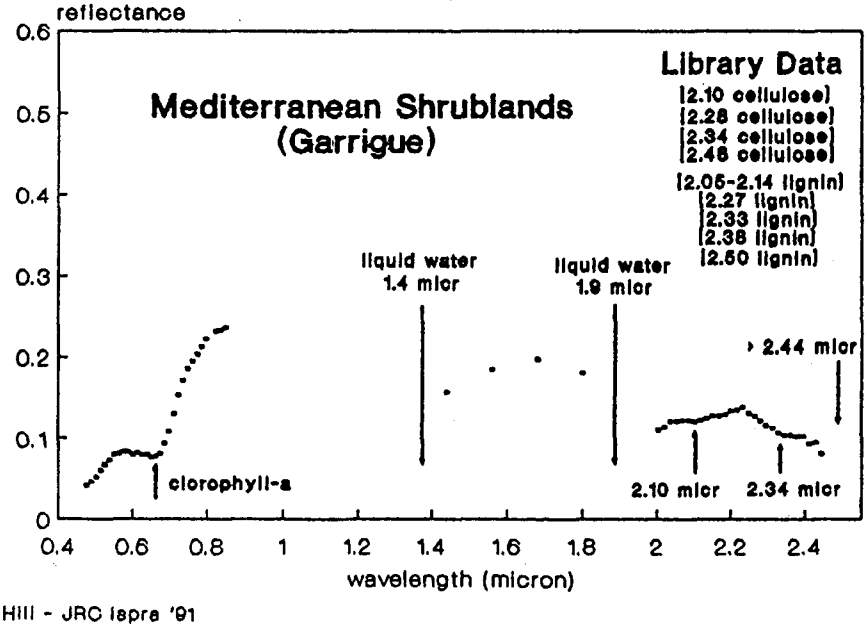

J. Hill - JRC Ispra '91

Fig.3c: GER reflectance spectrum of mediterranean shrublands in the Ardeche test site

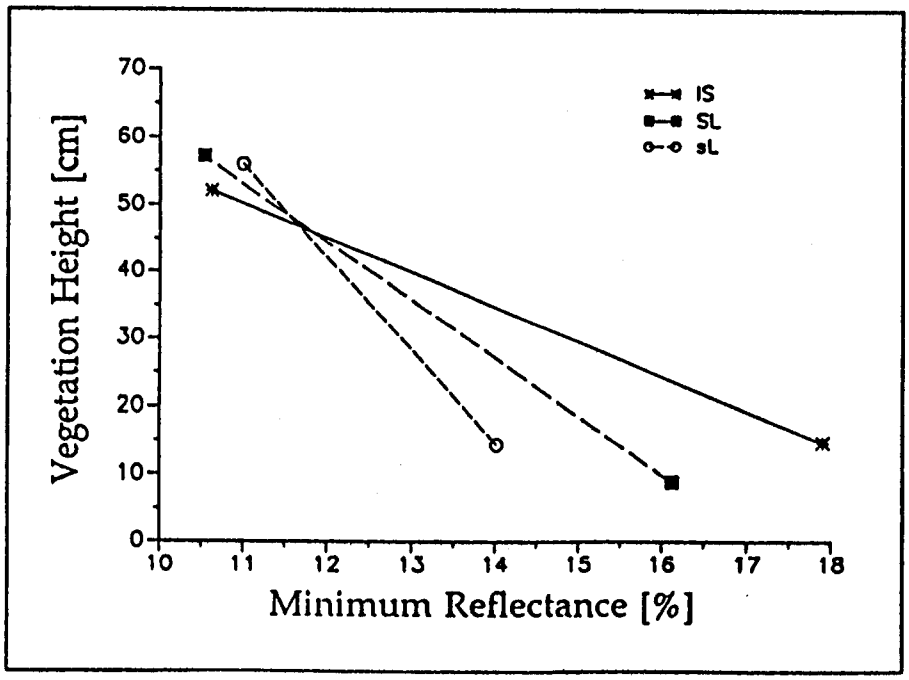

Fig.4a: Regression between "minimum reflectance" and vegetation height of corn on different soil types in the Upper Rhine Valley

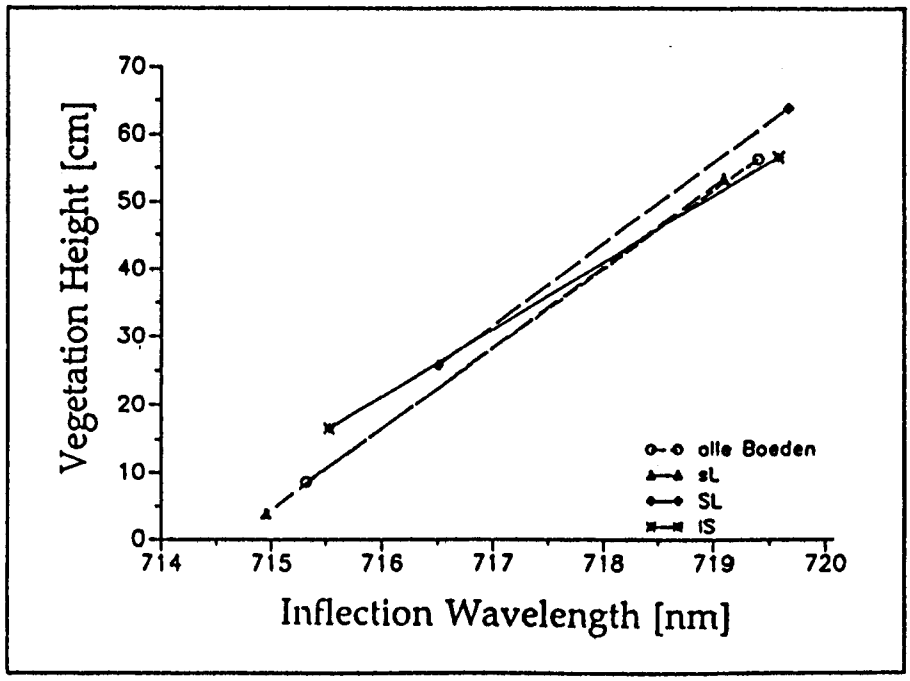

Fig.4b: Regression between "inflection wavelength" and vegetation height of corn on different soil types in the Upper Rhine Valley

Retrieval of Snow Properties from AVIRIS Data

Anne W. Nolin and Jeff Dozier

Center for Remote Sensing and Environmental Optics
The University of California
Santa Barbara, California

Abstract. A map of snow surface-layer grain size was produced and determination of thin snow areas was made using image data collected over the Sierra Nevada, California by the Airborne Visible/Infrared Imaging Spectrometer (AVIRIS). Quantitative estimates of snow grain size were formulated based on 1990 data collected over Mammoth Mountain. Because reflectance is sensitive to ice grain size in the near-infrared wavelengths, a single AVIRIS band, centered at 1.05 μm, was used. The AVIRIS data were atmospherically corrected to surface reflectance. A two-stream radiative transfer model was then used to formulate the relationship between grain size and snowpack reflectance for a wide range of ice sphere radii. A piecewise linear mapping provided a means for inverting the image data from reflectance to optically equivalent grain size. The color-coded grain size map illustrates the distribution of grain sizes over the Mammoth Mountain area. There is some correspondence between solar illumination angle and estimated grain size. Applying a spectral mixture model to a multi-band image of the area generated a "shade" component image which may aid in providing a correction factor for those snow-covered pixels which were not fully illuminated. Spectral mixture analysis was also used to map regions of thin snow using a 1989 Tioga Pass AVIRIS image. Using five spectral endmembers derived from the image, we were able to map thin snow, thick snow, water, rock/soil and vegetation.

I. Introduction

Recent research in the area of snow science has examined the hydrologic, climatologic and hydrochemical significance of seasonal snowpacks. While snow hydrologists have long been involved in determining the quantity of water held by the snowpack and the timing of melt, of newly found importance is the hydrochemical process of chemical elution from the snowpack and its effects on the aquatic ecology of alpine watersheds. Accurate assessment of the metamorphic state of the pack, as determined by changes in snow grain size, and of the timing and spatial distribution of snowmelt will help us understand the important hydrochemical processes in seasonal snowmelt.

Because snow is one of the brightest natural substances of great extent on this planet, it also plays a significant role in the global energy balance. Accurate parameterization of the temporal and spatial changes in surface albedo of seasonally snow-covered areas is essential for accuracy in climate models since these models require snow albedo values as as a lower boundary condition.

In this paper, we examine a technique for identifying areas of thin snow in an AVIRIS scene and we discuss the basis for, and show the preliminary results of, an inversion technique for mapping snow grain size using AVIRIS imagery.

II. Mapping Thin Snow Areas

One of the main problems in the remote sensing of snowpack properties has been the inability to distinguish between thin snow case and "dirty" snow since both have decreased albedo when compared to pure, thick snow. While the case of snow containing appreciable amounts of absorbing impurities (such as dust and soot) is an important area of investigation, in this paper we will will only be examining a technique for mapping of optically thin snow.

An optically thin snow is one whose reflectance is reduced by the effects of the underlying substrate such as rock or soil by at least 1% when compared to a very deep (optically semi-infinite) snowpack. Because the optical thickness of a snowpack varies with wavelength and with snow grain size, density, and physical depth, it is helpful to to express the minimum thickness of an optically semi-infinite snowpack in terms of snow water equivalence. For a solar zenith angle of 60°, Table 1 (from Dozier et al., 1989) shows the minimum values in millimeters of water equivalence.

TABLE 1. Snow-Water Equivalence (mm) of Semi-Infinite Snow Pack

λ	grain radius (μm)		
(μm)	50	300	1000
0.45	17	63	145
0.7	10	37	80
0.9	5	15	30
1.6	< 1	< 1	1

This table shows two things: first, that shorter wavelengths are transmitted farther and therefore more snow is needed for a snowpack to be semi-infinite, and, second, that when a snowpack comprises smaller ice grains, there are more scattering events so less snow is needed in order for it to behave as though it were semi-infinite. Therefore, estimates of grain size and snow water equivalence are needed to assess the effects of optically thin snow on albedo.

A 1989 AVIRIS image of the Tioga Pass region of the Sierra Nevada, California was used for this part of the work because it contained a fairly large 3 km by 3 km flat area with patchy thin snow adjacent to Tioga Lake. Concurrent ground truth measurements and snow stereologic measurements provided values for snow depth, grain size and density. Spectral mixture analysis was used to discriminate between areas of deep snow, thin snow, and bare ground in the image. This linear-mixing approach (Adams et al., 1989; Smith et al., 1990) can be used to generate fraction images and show relative abundances of spectral endmembers.

$$DN_c = \sum_{i=1}^{N} F_i \, DN_{i,c} + E_c \qquad (1)$$

where, DN_c is the radiometrically calibrated radiance in AVIRIS channel c.

F_i is the fraction of endmember i.

$DN_{i,c}$ is the radiance of endmember i in channel c.

N is the number of spectral endmembers.

E_c is the error for channel c of the fit of N spectral endmembers.

First, endmembers were selected using a 3-band color-composite AVIRIS image; these endmembers were water, thin snow, thick snow, rock/soil, and vegetation. The mixing algorithm was then applied to the AVIRIS data and endmember fractions were displayed. Slide 26 shows thick snow (dark blue), thin snow (light blue) and vegetation (green) and water (black) . Ground measurements indicate that thin snow depths ranged from .25 m to 1.25 m and thicker snowpack depths were as great as 2.5 m. Concurrent PIDAS (Portable Instantaneous and Display and Analysis Spectrometer) reflectance measurements showed that for the thinnest snowpack (SWE = .11 m) the soil substrate influenced the magnitude and shape of the snow spectral reflectance curve (Nolin et al., 1990). To provide a measure of the "fit" of the endmembers to the AVIRIS data, the root-mean-square (RMS) of the error for each channel was calculated. RMS values were displayed as DNs with higher DN corresponding to a greater RMS error. Although RMS DNs were as high as 12 in parts of the image, this was probably due to the fact that no shade endmember was used to in the spectral mixture analysis. There were no well-shaded pixels in the image and although water could have been used as a spectral proxy for shade, water was a separate endmember and so was not used to simulate shade. Also, non-linearities introduced from several sources reduced the accuracy of the outcome. These non-linearities are due to adjacency effects of bright pixels next to dark pixels adding some unaccounted-for path radiance, to the bidirectional reflectance effects of snow which are not considered here, and to the fact that snow in this region is also an intimate mixture of ice and absorbing impurities which cannot be modeled as a linear mixture. However, the fact remains that thin snow areas are easily discriminated from optically thick snowpacks in this AVIRIS image.

III. Grain size inversion model

The basis of the inversion approach used to obtain estimates of snow grain radii is fact that through the near-infrared portion of the spectrum, ice becomes is moderately absorbing. Figure 1 (from Dozier, 1989) shows that in the 0.9 μm to 1.3 μm region, snowpack reflectance is very sensitive to ice grain size. In contrast to the relatively deep transmission of visible wavelengths into the snowpack, this near-infrared absorption occurs over a vertical range in the snowpack on the order of millimeters. Warren and Wiscombe (1980) noted that increased grain size was primarily responsible for lower values of shortwave, spectrally integrated albedo.

To relate the optical properties of snowpacks to physical properties such as grain size, we rely on radiative transfer models. By making the assumption of spherically shaped ice crystals, the problem becomes far easier to calculate. The equivalent sphere is the one which has the same volume-to-surface ratio as the ice grain. For randomly oriented moderately non-spherical scatterers this is valid (Mugnai and Wiscombe, 1980) but this assumption may not hold for very new snow and oriented snow microstructure. The scattering properties for an ice sphere of appropriate radius r can be calculated by the Mie equations, the complex angular momentum approximation or, for larger grains, by geometric optics. Then the radiative transfer equation can be used to calculate the multiple scattering and absorption of the incident radiation. This is represented by:

$$\mu \frac{dL(\tau, \mu, \phi)}{d\tau} = -L(\tau, \mu, \phi) + J(\tau, \mu, \phi) \quad (2)$$

where, L is radiance at optical depth τ in direction θ, ϕ; ϕ is the azimuth; θ is the angle from zenith; and $\mu = \cos\theta$. J is the source function; it results from scattering of both direct and diffuse radiation or, at thermal wavelengths, emission. The spectral reflectance for direct and diffuse irradiance can thus be modeled from a knowledge of the snow's physical properties.

Given the Mie scattering parameters for spherical ice grains ranging in size from 40 μm to 2500 μm as input, a two-stream radiative transfer model calculated reflectances for each grain size at a wavelength of 1.05 μm. Figure 2 shows the relationship between grain size and reflectance as determined by the model. The wavelength, 1.05 μm, was chosen because it is in a spectral region where reflectance is particularly sensitive to grain radius size. There is also little atmospheric absorption in that region so that atmospheric correction of AVIRIS data is relatively low-error. A piecewise linear mapping was implemented to transform the modeled data to functions which could relate a reflectance value from the AVIRIS image to an optically equivalent grain radius.

Conversion of AVIRIS spectral radiance to surface reflectance was performed using LOWTRAN7 and a two-stream model. Running LOWTRAN7 with the parameters for a midlatitude winter atmosphere and with a visibility of 150 km, values of transmittance (T), single-scattering albedo ($\tilde{\omega}$), and asymmetry parameter (g) were generated. Atmospheric spectral transmittance was converted to optical thickness (τ = -log(T)), and these parameters, τ, ω, and g, were used to drive a radiative transfer model to obtain direct and diffuse irradiance at the surface and upwelling irradiance (Dubayah, 1990).

Next, application of a table look-up procedure using the reflectance-to-grain size relationships provided the conversion from a reflectance image to one which was a map of optically equivalent ice grain radii. Pixels whose values fell outside of the range of reflectances which could be mapped as ice grains were masked from the image (values set to zero). Note that these are optically equivalent (same volume-to-surface ratio) grain radii for ice grains comprising the surface layer of the snowpack and do not represent a depth-averaged grain size for the snowpack.

Slide 27 shows a single-band image of grain size which has been colored to show three distinct size categories of ice grains. North is to the lower left of the image, illumination by the sun is from the upper right of the image; the solar zenith angle for that date and time was 31°. Mammoth Mountain occupies the central portion of the image; the road leading to the ski area is visible on the lower left part, the ridge of the mountain runs from top to bottom of the image. The largest snow grains, those in the 1700 μm to 2500 μm size range, have been mapped as red. Those ranging in size from about 950 μm to 1690 μm are mapped as blue and the smallest grains in the image, 700 μm to 40 μm, are shown in yellow. As one might expect, there is a grain size gradient which roughly corresponds to elevation, with the largest grains at lower elevations and smaller grains higher up on the mountain. In addition, there seems to be correspondence between grain size and the amount of illumination by diffuse irradiance, with areas of greater illumination being mapped as smaller in size. To provide a better interpretation of the latter problem, the spectral mixing algorithm was applied to a multi-band AVIRIS image. Figure 3 is the fraction of "shade" as determined using endmembers identified in the image (rather than laboratory endmembers). Looking at the Mammoth Mountain part of the image, darker areas correspond to areas of more greater illumination while brighter pixels are those with lower illumination. This is not truly an image of the fraction of shade in each snow-covered pixel, rather it is more a measure of the effect of illumination by both direct and diffuse irradiance on the pixels. In complex topography, sources irradiance are not only the direct and diffuse irradiance from the sun and atmosphere, but direct and diffuse irradiance that has been reflected from topographic facets that face the area of interest. This is a complex modeling problem which has not yet been solved however, the "shade" image may allow us to better interpret and perhaps to calibrate grain size values obtained through this inversion technique.

IV. Conclusions

Our preliminary results show that we can successfully retrieve snowpack properties using high spectral resolution image data. The map of snow grain size which was produced from a single spectral band showed that grain sizes were within the expected physical range for that time of year. As expected, larger grain sizes were at the lower elevations. There also seemed to be a relationship between the amount of diffuse irradiance and the mapped grain size. The "shade" fraction image produced using spectral mixture analysis closely matches grain size patterns on the single band map leading us to believe that this image could provide an empirical means of correction. Clearly, more work needs to be done in this area but these early results are encouraging.

The spectral mixing technique was successful in discriminating between areas of optically thin and thick snow in the Tioga Pass area. Further acquisition of endmember spectra should continue so that we can map other snow types such as wet snow. The nonlinearities which are inherent in the snow mapping problems described in this paper require further investigation.

V. Acknowledgments

This work was supported by NASA grant NAGW-1265. The authors would also like to thank Dr. L.A.K. Mertes for providing access to and assistance with the Washington Image and Spectral Package (WISP) of the University of Washington, Geological Sciences Remote Sensing Laboratory (J. Adams, Director).

REFERENCES

Bohren, C. F., Multiple scattering of light and some of its observable consequences, *Amer. J. Phys.*, *55*, 524-533, 1987.

Chandrasekhar, S., *Radiative Transfer*, Dover Publications, New York, 1960.

Dozier, J., Spectral signature of alpine snow cover from the Landsat Thematic Mapper, *Remote Sens. Environ.*, *28*, 9-22, 1989.

Dozier, J., R. E. Davis, and A. W. Nolin, Reflectance and transmittance of snow at high spectral resolution, *Proceedings IGARSS '89*, 662-664, 1989.

Dubayah, R., The Topographic Variability of Clear-Sky Solar Radiation, Ph.D. Dissertation, 174 pp., Dept. Geogr., Santa Barbara, 1990.

Mugnai, A., and W.J. Wiscombe, Scattering of radiation by moderately nonspherical particles, *J. Atmos. Sci.*, *37*, 1291-1307, 1980.

Nolin, A. W., J. Dozier, and R. E. Davis, Bidirectional reflectance of optically thin snow, *Proceedings IGARSS '90*, 1159, 1990.

Nussenzveig, H. M.,and W. J. Wiscombe, Efficiency factors in Mie scattering, *Phys. Rev. Lett.*, *45*, 1490-1494, 1980.

Warren, S. G.,and W. J. Wiscombe, A model for the spectral albedo of snow, II, Snow containing atmospheric aerosols, *J. Atmos. Sci.*, *37*, 2734-2745, 1980.

Wiscombe, W. J., Improved Mie scattering algorithms, *Appl. Optics*, *19*, 1505-1509, 1980.

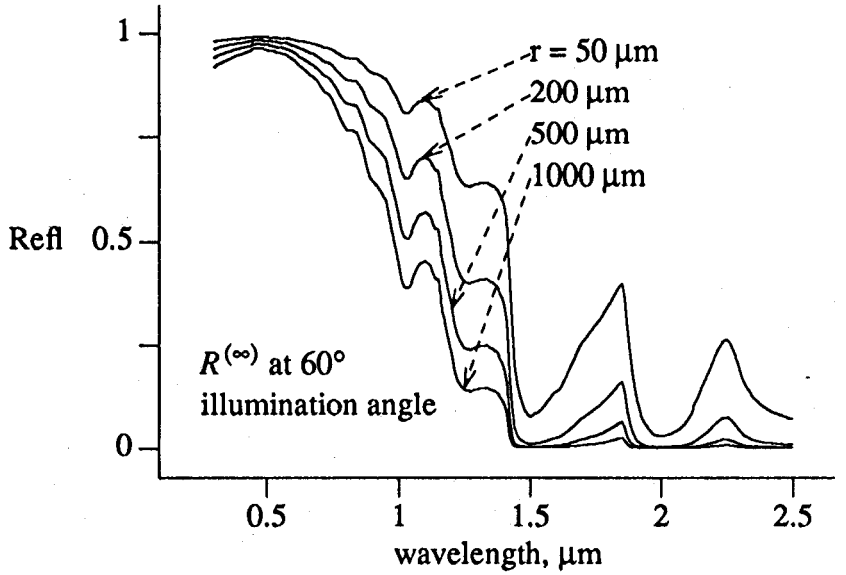

Figure 1. Modeled spectral reflectance of deep snow for different ice grain radii

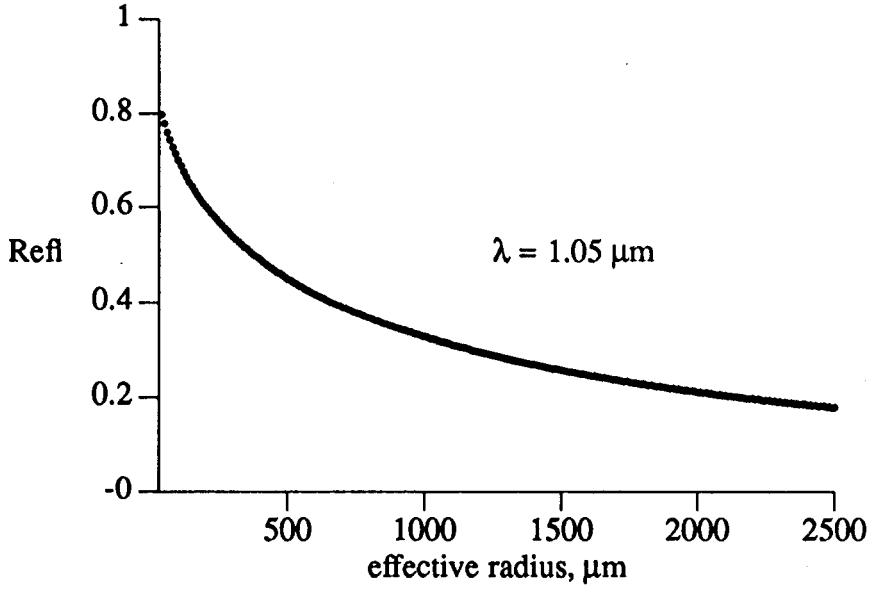

Figure 2. Two-stream model results showing relationship between optically equivalent grain size and snow reflectance

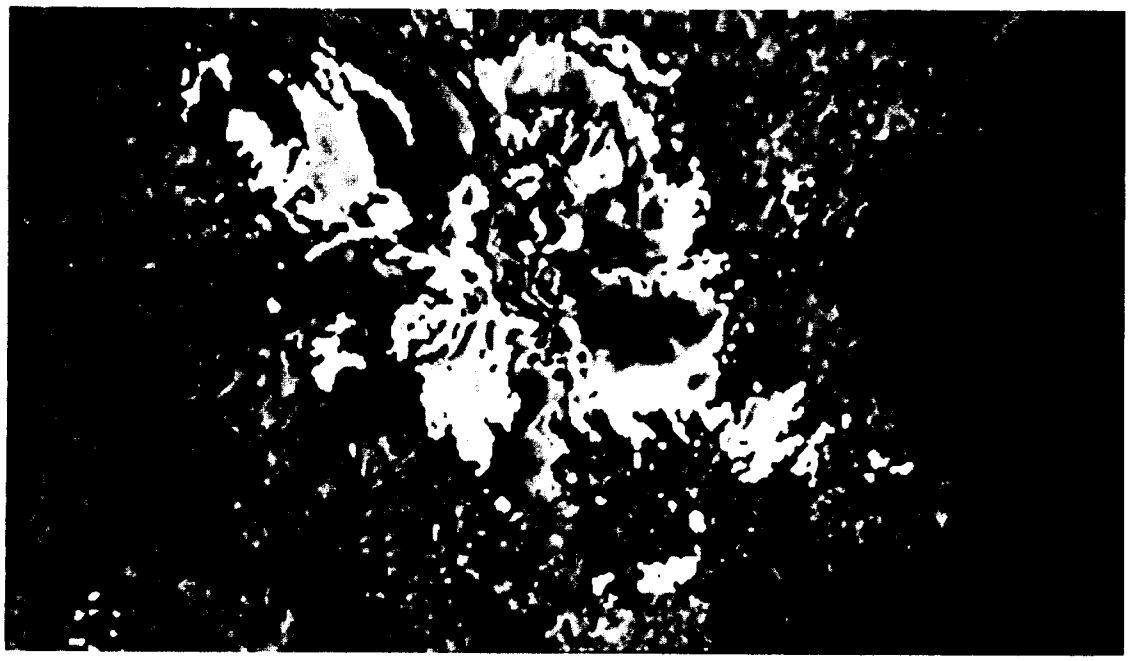

Figure 3. "Shade" fraction image of Mammoth Mountain. North is to the bottom left, solar illumination is from the upper right of the image. Mammoth Mountain is the relatively bright area in the central portion of the image which is bifurcated by a ridge, the dark band running roughly vertically through the middle of the image.

Examination of Chlorophyll Distribution in Lake Tahoe, Using the Airborne Visible/Infrared Imaging Spectrometer (AVIRIS)

Michael K. Hamilton, Curtiss O. Davis, Stuart H. Pilorz, and W. Joseph Rhea
Jet Propulsion Laboratory
California Institute of Technology
Pasadena, California

Kendall L. Carder
University of South Florida
Department of Marine Science
St. Petersburg, Florida

Abstract. An AVIRIS image was obtained for Lake Tahoe, California, on August 9, 1990, along with in situ data. Profiles of percent transmission of light, stimulated chlorophyll fluorescence, photosynthetically available radiation, and upwelling and downwelling irradiance and upwelling radiance in several spectral bands were measured in the water column, as well as the above-water spectral distribution of light. The image was atmospherically corrected using the LOWTRAN 7 atmospheric model, and the resulting image was examined for the presence of spurious periodicities. The low concentration of chlorophyll in the lake provided an increase in the upwelled radiance in the chlorophyll absorbing band, to the extent that pigment concentrations could be accurately modeled using a variant of the CZCS algorithm with the AVIRIS image. Although limnological sampling of the lake was insufficient for good statistical results, AVIRIS now appears to be useful in the mapping of surface chlorophyll in low concentrations, as are found in the oligotrophic ocean.

Introduction

Previous investigations using AVIRIS over water targets have demonstrated the presence of correlated noise in the data, and low signal to noise (S/N), which made it difficult to estimate the concentration of chlorophyll in the surface waters (Pilorz and Davis, 1990a; Melack and Pilorz, 1990). The Coastal Zone Color Scanner (CZCS) aboard the Nimbus-7 platform has been used to estimate the concentration of chlorophyll in surface waters, using ratios of reflected radiance for pairs of wavelengths that are pertinent to the absorption spectrum of the pigment (e.g., Gordon et al., 1983). Concentrations estimated in this way are obfuscated by the presence of multiple species with similar or overlapping spectra, and separation and identification of these require the finer spectral resolution of an instrument such as AVIRIS. However with limited S/N, applicability of the full spectral resolution of AVIRIS to dark targets such as bodies of water has yet to be realized. Pilorz and Davis (1990a) point out that, in order to discern a change in chlorophyll concentration of order 1 mg m^{-3}, it is necessary to resolve a signal of ~0.05 $\mu W\ cm^{-2}\ sr^{-1}\ nm^{-1}$.

AVIRIS was originally designed for land targets with 20%-50% reflectance; by comparison water targets have very low reflectances on the order of 2-5%. The first ocean data analyzed were collected from Monterey Bay in 1989, and problems such as patterned noise were discussed at length (Pilorz and Davis, 1990a,b). Subsequently, the design and engineering team has made great progress in improving the signal for ocean and freshwater studies, to the point that the signal in the visible and near IR is now over three times the original specifications.

In this study, the spectrum of upwelling radiance from Lake Tahoe, derived from the multispectral image, is compared to similar estimates made from in-water measurements, as well as theoretical values. The image is then used to estimate the concentration of chlorophyll at the surface, and the image-derived estimates are compared to bottle samples of chlorophyll and concentrations derived from in-water optical data that were collected in the lake. The average along-track and across-track power spectra are examined for the presence of significant peaks, indicating the presence of instrument-induced periodicities, and individual bands in the image are examined for the presence of large-scale banding not resolved using the spectral technique. These methods give an indication of whether the noise level of the image is still limiting the usefulness of AVIRIS for oceanographic and limnologic investigations.

Study Area

Lake Tahoe is the third largest alpine lake in the world with an average depth of 302 m and a maximum depth of 503 m. It is located at an elevation of 1906 m in the Sierra Nevada mountains on the California-Nevada border (Figure 1).

The water is extremely clear, with surface chlorophyll values <0.2 mg m^{-3}. The clarity of the water is maintained by the size of the lake itself, an effort by the local populace to divert sewage from surrounding areas, and the closed nature of the lake, in that there are no incoming tributaries.

Lake Tahoe was chosen as a study site because of its pure water and high altitude location. The low chlorophyll values are comparable to those found in the oligotrophic central gyres of the world ocean, and as such the lake represents the clear water end point in the range of oceanic and freshwater conditions. The area is easily accessible by boat and AVIRIS flyby. Its location at 1900 m in clear air (>100-km visibility) makes atmospheric correction easier and less sensitive to errors than scenes collected over marine targets. Further, the lack of a significant amount of absorption at wavelengths indicative of chlorophyll increases the signal at those wavelengths, making estimation of pigment using the wavelength-ratio method more accurate.

A dark, oligotrophic body of water such as Lake Tahoe should give a predictable multispectral image, in terms of its spatial consistency. The low level of surface chlorophyll, waste discharge from nearby communities, or significant tributary input makes the scene extremely homogeneous. Variations in this scene are unlikely to result from phytoplankton patchiness or point sources of effluent, and would most likely have been introduced by the instrument variability or noise.

Methods and Analytical Techniques

The overflight occurred at 10:30 PDT, and the plane had a heading of 110°. Solar zenith angle was 39.8°, and solar azimuth was 114.2°, so that the pilot was flying nearly directly into the sun to minimize sun glint and uneven illumination across the scene. The surface of the lake was flat and calm; wind speed was essentially zero at the time of the overflight.

In-water optical data were collected with an updated version of a Bio-Optical Profiling System (BOPS). The package is a Biospherical Instruments MER-1048 spectroradiometer which measures upwelling and downwelling spectral irradiance and upwelling spectral radiance, modified to include sensors for photosynthetically available radiation (PAR), depth, tilt, and roll. In addition, temperature, conductivity, chlorophyll fluorescence, and beam transmission were measured. The MER-1048 acquired data were averaged to four records a second. Other preprocessing included

filtering to remove obvious spikes and binning to one-meter averages. At each station, extracted chlorophyll and phaeopigments were measured on water samples immediately before or after the optical profile.

Specific absorption coefficients for particulates were obtained for surface waters and the total particulate absorption coefficient was determined, following the method of Mitchell and Kiefer (1988). Chlorophyll specific absorption coefficients were computed by dividing these measurements by the measured chlorophyll concentration. For filtered lake water absorption coefficients, the water was filtered a second time through a 0.2-μm Nucleopore filter and optical densities were measured with a Cary 2000 spectrophotometer using a 10-cm quartz cuvette. Non-pigmented particulate absorption was obtained by the hot methanol extraction method (Kishino et al., 1985), as modified by Roesler et al. (1989).

The image was corrected radiometrically, as well as for the effects of vignetting and dark current, using the calibration files provided with the data by the AVIRIS project. Atmospheric correction was performed with LOWTRAN-7 in radiance mode (e.g., van den Bosch and Alley, 1990), using a multiple-scattering midlatitude summer model with a visibility of 150 km and 1% surface albedo. The atmospheric radiance spectrum (Fig. 2a) was binned to the center wavelengths used by AVIRIS, and compared to the average radiance spectrum of the central 60x60 pixel subimage of the middle Lake Tahoe scene, which was completely over the water. The atmospheric spectrum was subtracted from the image on a band-by-band basis, yielding a corrected reflectance image to be used for the analysis. The mean uncorrected and corrected radiance spectra over the central subimage are shown in Figures 2a and 2b. Additionally, Figure 2b shows the upwelling radiance just above the surface, as calculated for each wavelength from the relationship (Gordon et al., 1988):

$$L_u^+ = \frac{E_d^+(1-\rho)(1-\bar{\rho})\ R}{Qn^2} \qquad (1)$$

where E_d^+ is the downwelling irradiance above the surface, ρ and $\bar{\rho}$ give the Fresnel reflectance for downwelling and upwelling radiation (both set equal to 0.02 for calm waters), R is the reflectance, and Q is 2π times the average cosine for upwelling radiance. Using the simplifying assumptions

$$R = \frac{E_u^-}{E_d^-}, \quad \text{and} \quad Q = \frac{E_u^-}{L_u^-} \qquad (2)$$

we arrive at the relation

$$L_u^+ = \left(\frac{0.96}{1.79}\right)\frac{E_d^+\ L_u^-}{E_d^-}. \qquad (3)$$

This agrees within a few percent of the simpler relation

$$L_u^+ = \left(\frac{0.98}{1.79}\right) L_u^- \qquad (4)$$

which was used to create the upwelling radiance depicted as the dashed line on Figure 2b. The discrete points on the figure represent, by way of another comparison, values for upwelling radiance in waters with a chlorophyll concentration of 0.15 mg m^{-3}, theoretically expected at 443, 520, and 550 nm (e.g., Gordon et al., 1988).

Selected bands of the central Lake Tahoe image, corresponding to center wavelengths 440 (band 5), 548 (band 16), and 557 (band 17) nm were examined in detail. These bands were selected because of the importance of the wavelengths to the absorption spectrum of chlorophyll, as well as to examine one band where the instrument has a higher noise level, and two adjacent bands (to look for features that persist between data channels).

For these bands, along-track and across-track power spectra were calculated as the product of the Fourier transform of each demeaned line of pixels (tapered with a Hanning windowing function) and the complex conjugate of the transform. This operation was carried out for every line of data at constant sample, or each sample on a line, resulting in the two unidirectional mean power spectra for the image.

Chlorophyll concentration was estimated for the surface waters of Lake Tahoe using the CZCS algorithm for low chlorophyll (Gordon et al., 1983), i.e.,

$$\log10[chla] = 0.053 + 1.71 \log10\left(\frac{Lw(550)}{Lw(443)}\right) \qquad (5)$$

where $L_W(550)$ and $L_W(443)$ are the values of upwelled radiance from the surface in 20 nm wide bands (full width half maximum) centered at 550 and 443 nm. The bands were approximated using the mean value of the bands bracketing each of the wavelengths, i.e., bands 5 and 6 for 440 nm, and 16 and 17 for 548 nm, which are 10 nm wide.

Results

The optical profiler data are presented in Figure 3. The temperature profile indicates a well-mixed upper 10 m, with a broad thermocline between 10 and 65 m. Chlorophyll fluorescence has a maximum at the base of the thermocline, which is indicative of a population of photosynthetically efficient phytoplankton, supported by a diffusive nutrient flux from below. Percent transmission of light is high (>90%) and is nearly uniform with depth, but with a small minimum at the base of the thermocline, caused by the phytoplankton living at that depth. PAR is attenuated with no significant deviations from the characteristic logarithmic profile that is to be expected from pure water (e.g., Smith and Baker, 1978).

Spectral absorption coefficients for pigments, particulates, and filtered water are shown in Figure 4. Near 450 nm, absorption due to gelbstoffe (dissolved organic substances) is nearly a factor of four greater than the corresponding absorption for chlorophyll and related pigments. Absorption by detritus is an order of magnitude less than absorption by pigmented particles. As expected for a clean alpine lake, these values are all very low when compared to the absorption coefficient of water.

The shape of the particulate absorption spectrum indicates the presence of chlorophyll; however the magnitude of the absorption feature near 440 nm (~0.01 m^{-1}), as well as the lack of a reduction in the upwelling radiance (L_U) at the same wavelength, implies a very low concentration. This has been verified with bottle samples. Concentration of chlorophyll in the surface waters was found to be

~0.15 mg m^{-3}, of the order expected in the oligotrophic ocean.

Figure 5 shows the standard deviation associated with the central subimage. The noise level in the blue end of the spectrum typically confounds attempts to estimate pigment concentrations. The mean signal from the image in the band closest to 440 nm is ~4 $\mu W\ cm^{-2}\ sr^{-1}\ nm^{-1}$, with a standard deviation of 0.27 giving an S/N of approximately 15:1. The mean atmospherically corrected signal has a magnitude of approximately 0.55 $\mu W\ cm^{-2}\ sr^{-1}\ nm^{-1}$, giving an S/N for the signal of ~2:1, after removing the effects of the atmosphere. To detect a change in surface chlorophyll in waters with high concentration on the order of 1 mg m^{-3}, it is necessary to resolve a signal of 0.05 $\mu W\ cm^{-2}\ sr^{-1}\ nm^{-1}$, necessitating a spatial averaging for quantitative determination of surface pigment.

The mean along-track and across-track power spectra are shown for three bands pertinent to absorption by pigments in Figure 6. Generally, band 5 shows the highest variance/cycle, as the instrument noise level is highest in the blue end of the spectrum. The along-track direction has generally featureless spectra, although some degree of spectral coherence can be seen. A high degree of power associated with the lowest frequency is probably due to the bowl shape of the vignetting effect. The lack of significant spectral peaks is to be expected from homogeneous surface concentrations of light-affecting constituents. In the across-track direction, however, there are several peaks which may be significant, and are seen to be reproducible between bands. Peaks at 0.05 and 0.065 cycles per pixel (corresponding to periodicities with spatial scales of 400 and 307 m, respectively) persist among bands 6, 16, and 17. This could be due to either low-frequency surface waves, or a vibration or electronic noise problem with the instrument. Another peak at 0.01 cpp (2000 m) is very significant and may represent a sampling problem. The fact that it gives a waveform every 100 pixels is suspicious.

Using the low-pigment variant of the CZCS algorithm (Gordon et al., 1983), an image representing surface chlorophyll concentration was constructed (Figure 7) using no spatial binning. As is to be expected, no significant pigment features are seen; the image is a low-value background, interspersed with random noise. The average estimated chlorophyll value for the center of the scene is 0.154 mg m^{-3}. This compares quite well with the value of 0.16 for the surface (5 m) sample from station 1, as well as the value of 0.15 mg m^{-3} calculated using the CZCS algorithm with the upwelling radiance values determined from the in-water measurements (Table 1).

A banding of the image is evident however, and an investigation of this phenomenon has shown it to be a ~1 DN jump, possibly due to the quantizer used to digitize the data. The mechanism for this deviation is enigmatic at this time; however the feature is not believed significant in the use of AVIRIS images for water targets.

Conclusions

Atmospherically corrected spectral radiance measured using AVIRIS agrees well with upwelling radiance derived from in-water spectral measurements and with theoretical estimates. Values of chlorophyll concentration, calculated using a variant of the CZCS algorithm with the AVIRIS image and checked with both bottle samples and in-water measurements of upwelling radiance, agree extremely well. This is in contrast to eutrophic bodies of water with high concentrations of pigment, where the signal received by the sensor is insufficient in the bands pertinent to absorption by chlorophyll to make good estimates (e.g., Melack and Pilorz, 1990). The signal-to-

noise level of AVIRIS has risen to the point where it is now useful in estimating low pigment concentrations in oligotrophic waters.

Spurious spectral peaks were found in the across-track direction of the Lake Tahoe central AVIRIS scene, and the source of these peaks warrants attention. In the image of estimated chlorophyll concentration, a banding is apparent that may be due to dark current subtraction, but is not necessarily significant in the applicability of AVIRIS images to water targets as it has a magnitude of ~1 DN.

Future modifications to the AVIRIS instrument to address the dark current and vignetting corrections over dark targets may be necessary, possibly a variable or interactive-type correction for the vignetting may be appropriate. Further, improvements in the level of signal to noise would make the data applicable without pixel binning to bodies of water with greater concentrations of absorbing pigments, such as coastal and eutrophic regions.

Acknowledgments

The authors thank the AVIRIS engineering team in general and Rob Green in particular for their continued effort to improve the performance of the instrument. We thank the AVIRIS operations team and the NASA Ames Research Center, High Altitude Branch for collecting the AVIRIS data. John Melack (U.C. Santa Barbara) organized the field work and Robert Richards (U.C. Davis) provided the ship support. Discussions with and editing by Jeannette van den Bosch were extremely helpful.

This work was carried out at the Jet Propulsion Laboratory, California Institute of Technology and at the University of South Florida, and was supported by contracts from the National Aeronautics and Space Administration to those Institutions. Reference herein to any specific commercial product, process, or service by trade name, trademark, manufacturer, or otherwise, does not constitute or imply its endorsement by the United States Government, the Jet Propulsion Laboratory, California Institute of Technology or the University of South Florida.

References

Gordon, H., D. Clark, J. Brown, O. Brown, R. Evans, and W. Broenkow, "Phytoplankton Pigment Concentrations in the Middle Atlantic Bight: Comparison of Ship Determinations and CZCS Estimates," *Applied Optics* 22 (1); 20-36, 1983.

Gordon, H., O. Brown, R. Evans, J. Brown, R. Smith, K. Baker, and D. Clark, "A Semianalytic Radiance Model of Ocean Color," *Journal of Geophysical Research* 93 (D9), 10,909-10,924, 1988.

Kishino, M., M. Takahashi, N. Okami, and S. Ichimura, "Estimation of Spectral Absorption Coefficients of Phytoplankton in the Sea," *Bull. of Mar. Sci.* 37 (2), 634-642, 1985.

Melack, J., and S. H. Pilorz, "Reflectance Spectra from Eutrophic Mono Lake, California, Measured With the Airborne Visible and Infrared Imaging Spectrometer (AVIRIS)," *Proceedings of the Second Airborne Visible / Infrared Imaging Spectrometer Workshop*, JPL Publication 90-54, Jet Propulsion Laboratory, Pasadena, California, 232-242, 1990.

Mitchell, B. G., and D. A. Kiefer, "Variability in Pigment-Specific Particulate Fluorescence and Absorption Spectra in the NE Pacific Ocean," *Deep Sea Research* 35 (5), 665-689, 1988.

Pilorz, S., and C. O. Davis, "Investigations of Ocean Reflectance With AVIRIS Data," *Proceedings of the Second Airborne Visible/Infrared Imaging Spectrometer Workshop*, JPL Publication 90-54, Jet Propulsion Laboratory, Pasadena, California, 224-231, 1990a.

Pilorz, S., and C. O. Davis, "Spectral Decomposition of Sea Surface Reflected Radiance," *Proceedings, IGARSS 1990* (1), 345-348, IEEE, 1990b.

Roesler, C. S., M. J. Perry, and K. L. Carder, "Modeling In Situ Phytoplankton Absorption From Total Absorption Spectra," *Limnol. Oceanogr.* 34 (8), 1510-1523, 1989.

Smith, R. C., C. R. Booth, and J. L. Star, "Oceanographic Bio-Optical Profiling System," *Applied Optics* 23, 2791-2797, 1984.

Smith, R. C, and K. Baker, "Optical Classification of Natural Waters," *Limnology and Oceanography* 23, 260-267, 1978.

Strickland, J. D. H., and T. R. Parsons, "A Practical Handbook of Seawater Analysis," *Fish. Res. Bd. Canada Bull.* 167, 311, 1972.

van den Bosch, J., and R. Alley, "Application of LOWTRAN 7 as an Atmospheric Correction to Airborne Visible/Infrared Imaging Spectrometer (AVIRIS) Data," *Proceedings of the Second Airborne Visible/Infrared Imaging Spectrometer Workshop*, JPL Publication 90-54, Jet Propulsion Laboratory, Pasadena, California, 78-81, 1990.

Table 1. Chlorophyll values measured at Station 1 and estimated from the optical data and the midlake AVIRIS image using the CZCS chlorophyll algorithm.

Method	depth m	Chlorophyll mg/m-3	Phaeopigments mg/m-3	Chl. + Phaeo. mg/m-3
Extracted chlorophyll	5	0.16	0.0	0.16
	50	0.37	0.0	0.37
	70	0.47	0.27	0.74
	100	0.19	0.12	0.31
Estimate from L_u data	surface	0.15		
Estimate from image	surface	0.154		

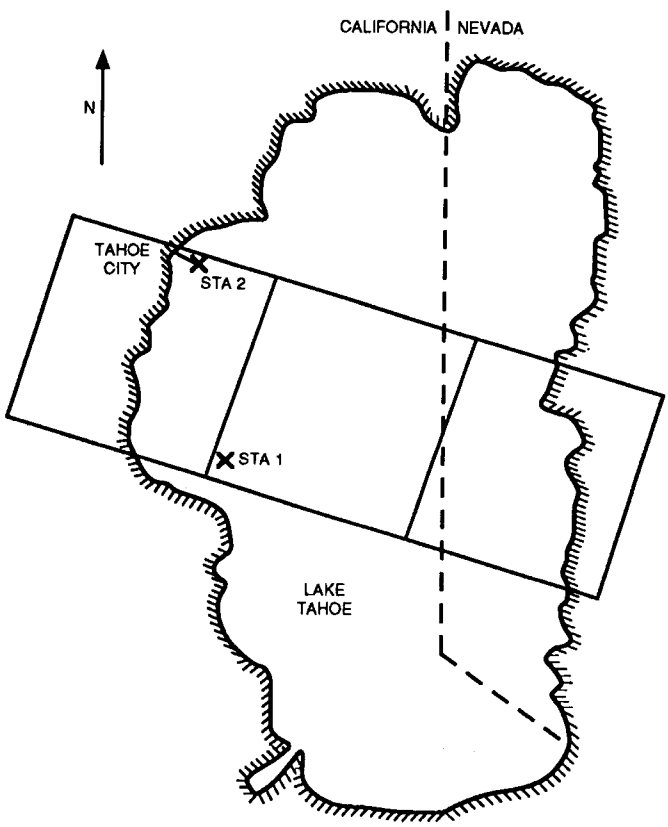

Figure 1. Map of the Lake Tahoe study site. The ER-2 flew from northwest to southeast taking three AVIRIS scenes as indicated by boxes in the figure. The in situ data presented in this paper were collected at station 1.

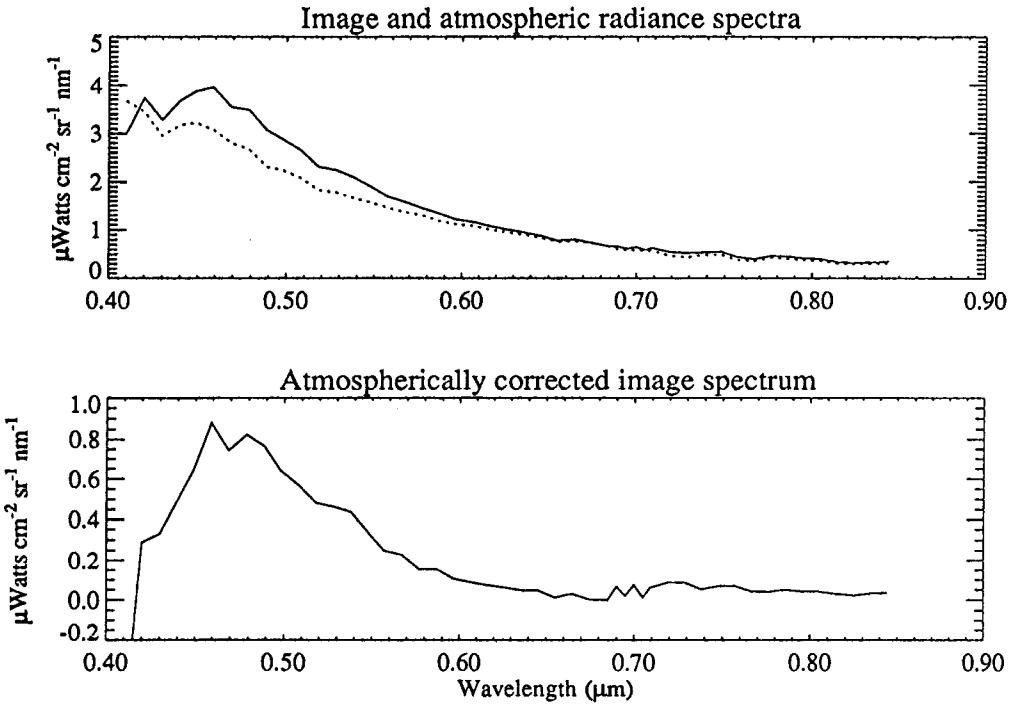

Figure 2a. Mean uncorrected image spectrum, with the modeled spectrum of atmospheric radiance, taken over the central 3600-pixel central subimage of the middle Lake Tahoe scene. Bottom panel shows difference between the two.

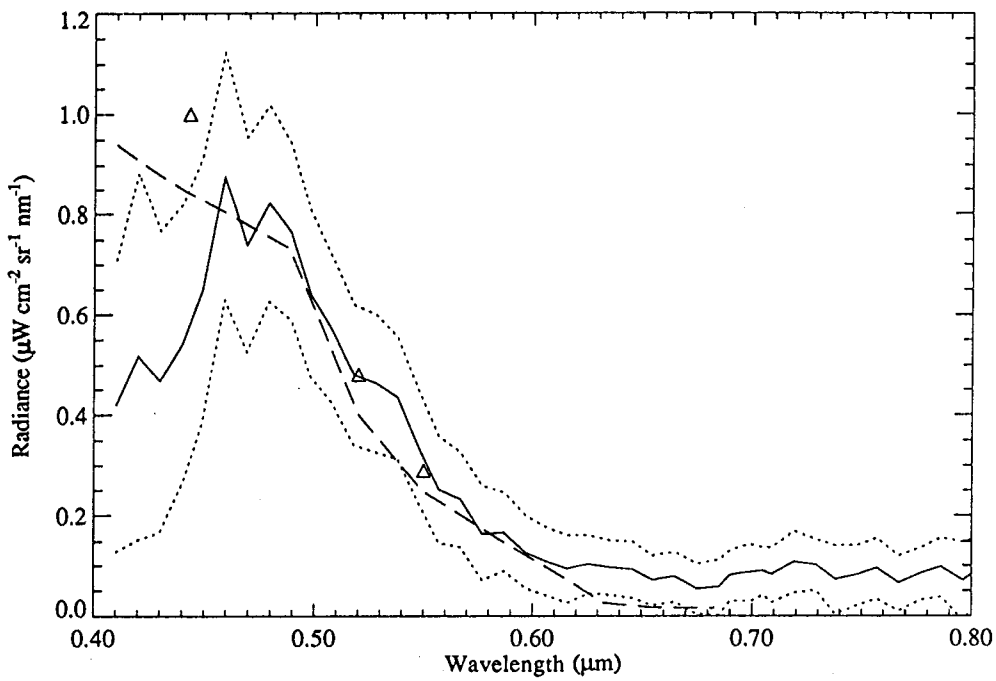

Figure 2b. Atmospherically corrected image spectrum, with a one standard deviation error envelope. The dashed line is the upwelling radiance derived from in-water measurements, and the points are the theoretical values of upwelling radiance for water with a chlorophyll concentration of 0.15 mg m^{-3}.

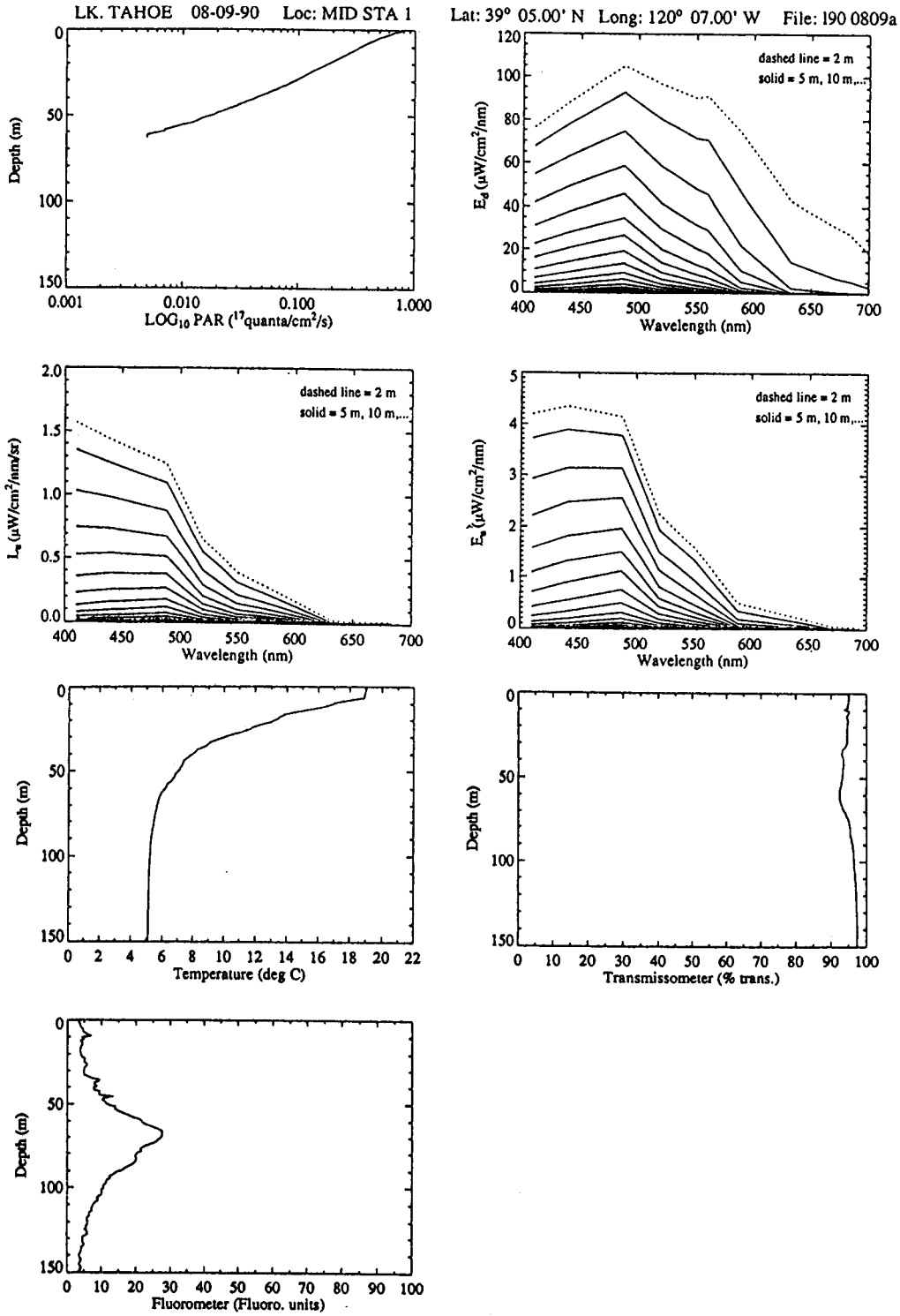

Figure 3. Data collected with the MER-1048 bio-optical profiling instrument package at station 1.

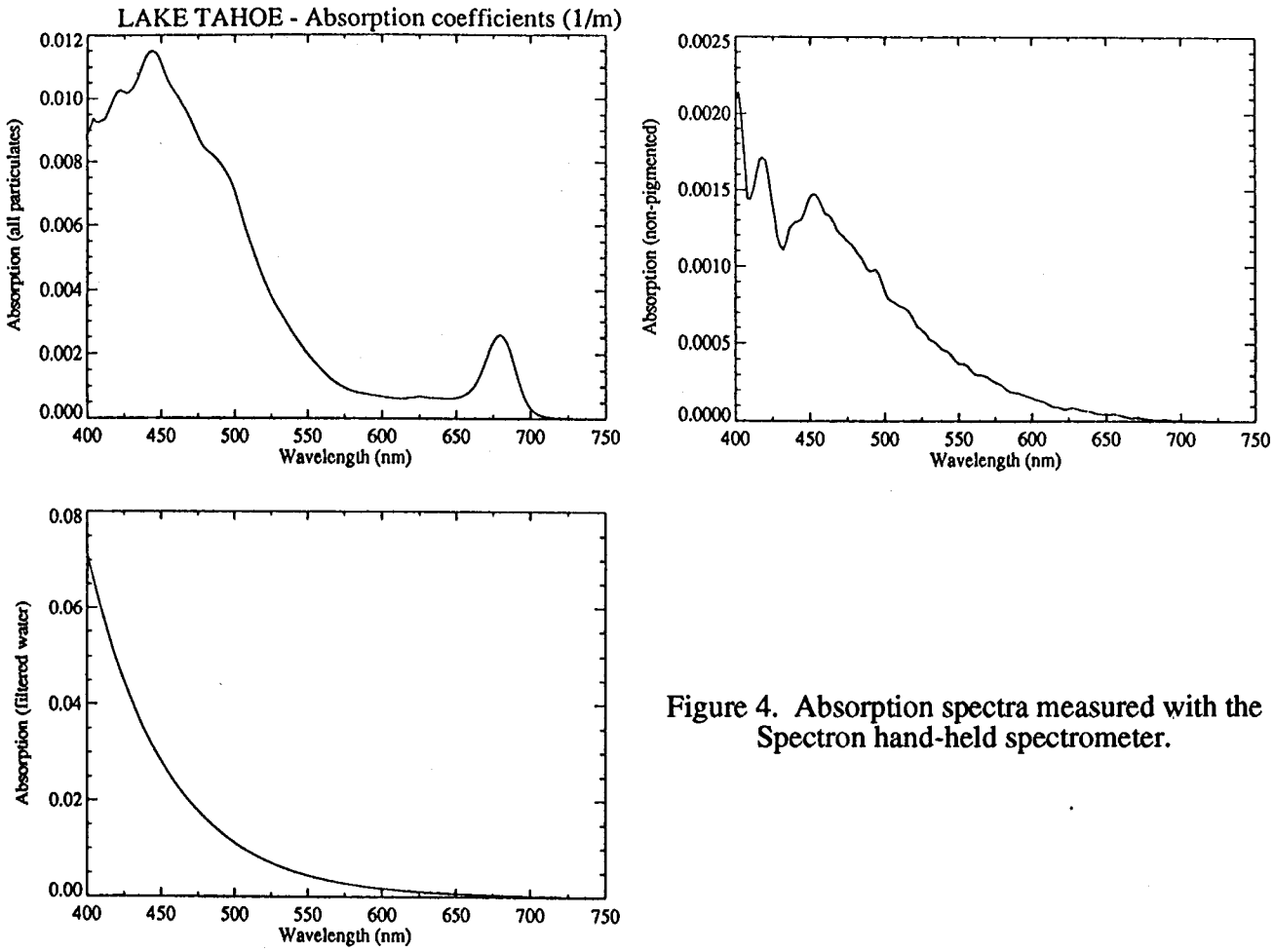

Figure 4. Absorption spectra measured with the Spectron hand-held spectrometer.

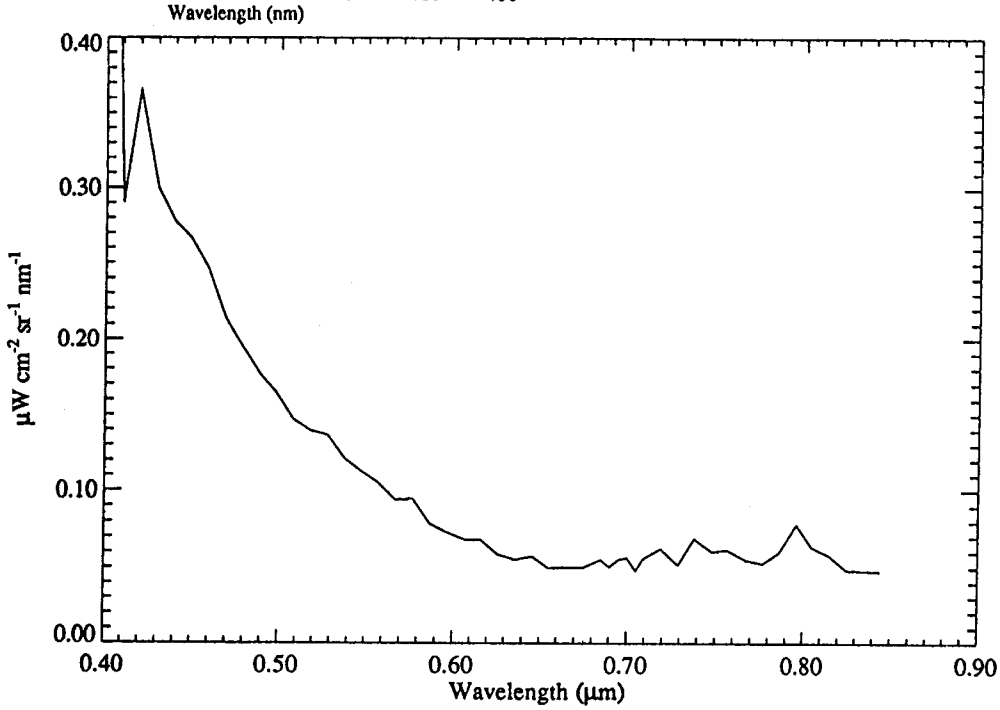

Figure 5. Spectrum of the standard deviation of the central portion of the atmospherically corrected image.

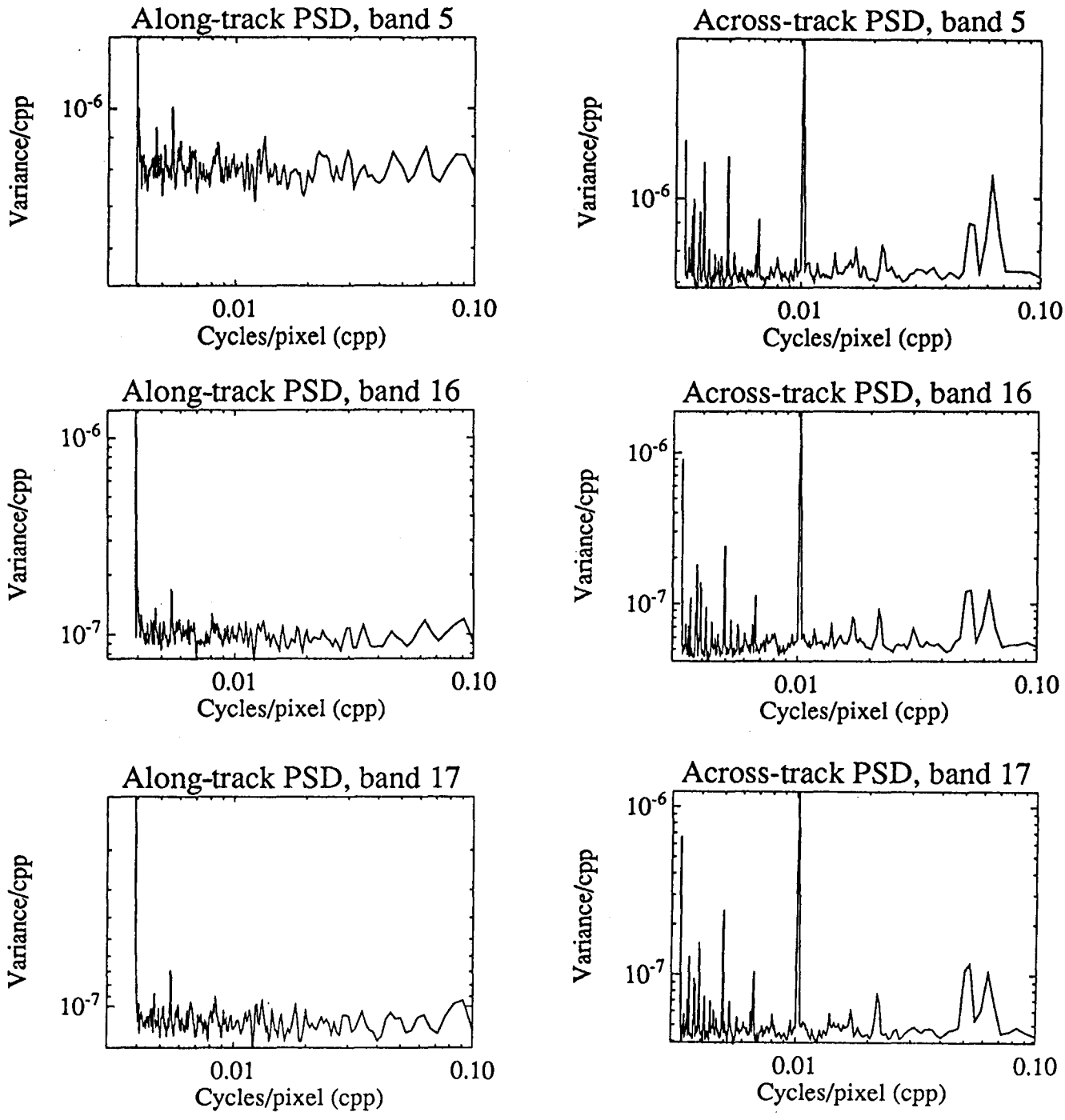

Figure 6. Along-track and across-track power spectra, for three bands from the image.

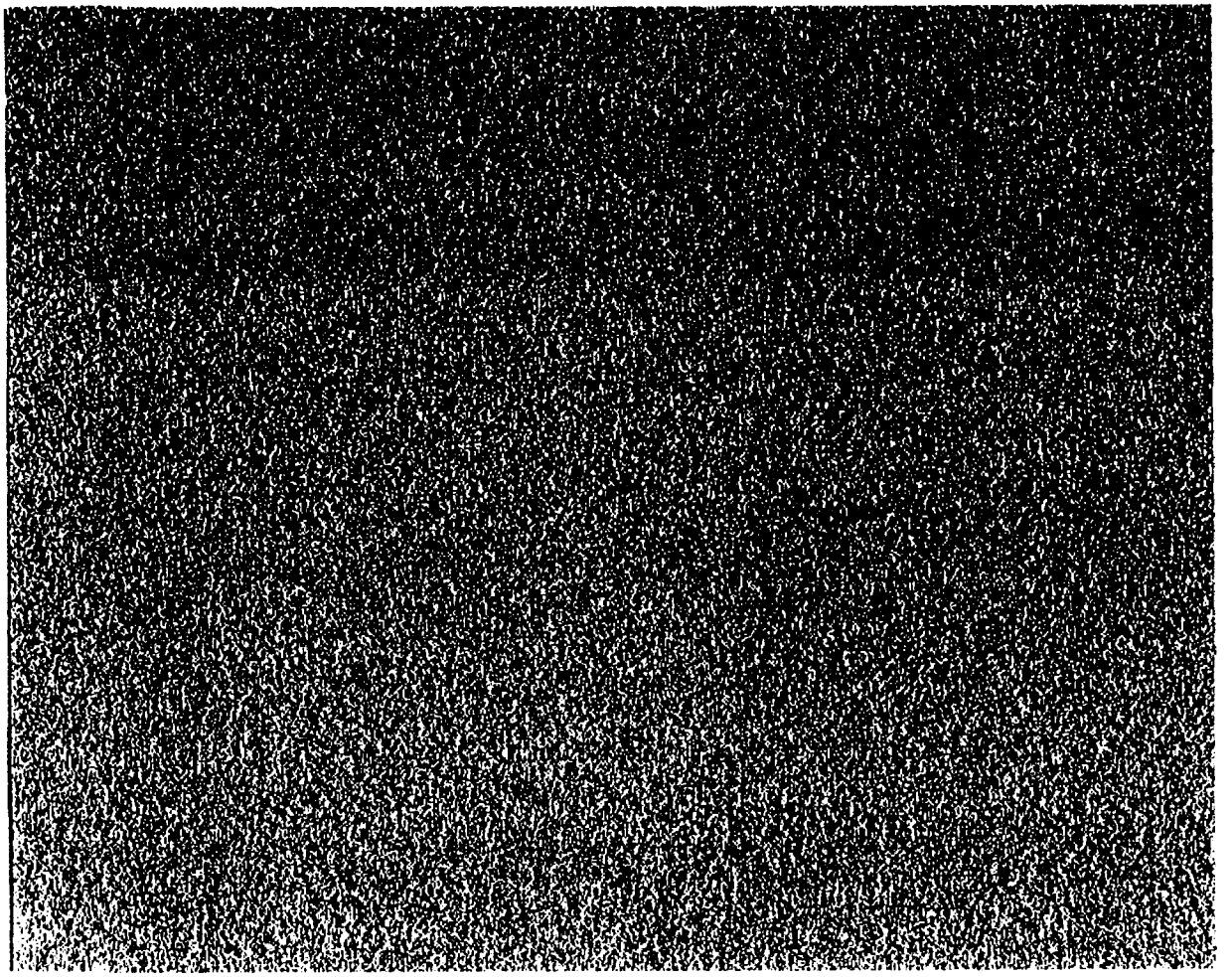

Figure 7. Image of estimated chlorophyll concentration in the surface waters. The direction of flight is toward the top of the page.

Current instrument status of the Airborne Visible/Infrared Imaging Spectrometer (AVIRIS)

Thomas G. Chrien, Michael L. Eastwood, Charles M. Sarture, Robert O. Green, and Wallace M. Porter

Infrared and Analytical Instruments Section
Jet Propulsion Laboratory, California Institute of Technology
Pasadena, California

ABSTRACT

The Airborne Visible/Infrared Imaging Spectrometer (AVIRIS) has been upgraded a number of times since its debut in 1987. This paper describes these improvements and is meant to serve as a reference for scientists working with AVIRIS data.

1. INTRODUCTION

AVIRIS is an airborne imaging spectrometer that utilizes a whiskbroom-type scanner coupled via optical fibers to four dispersive spectrometers.[1] These spectrometers provide complete spectral coverage over the visible and near-infrared wavelength regions from 0.4 to 2.45 micrometers. At any moment during flight, AVIRIS views a patch of the Earth's surface approximately 20 meters in diameter. At the same moment, the spectrometers and their line-array detectors capture the upwelling radiance spectrum of the materials in that patch of surface. This spectrum is digitized at 10-bit resolution and recorded on 1-inch high-density tape at a rate of 17 megabits/second. Each spectrum represents one pixel in an AVIRIS image, and the images are built up pixel by pixel, 614 pixels per scan line, 12 scan lines per second, as the ER-2 aircraft flies along at an altitude of 20 kilometers. Thus, AVIRIS acquires 7,368 spectra per second, a huge data volume by imaging instrument standards. Decommutation of the images from tape, calibration, distribution, and archiving of the imagery are performed at a dedicated data-processing facility at the Jet Propulsion Laboratory (JPL). AVIRIS has been operating since 1987, with continuous enhancements in data quality being made over the years, in the form of improved radiometric calibration and in-flight stability, a higher signal-to-noise ratio, improved scanner performance for geometric image fidelity, and enhanced instrument reliability (see Table 1).

Each flight season, AVIRIS has increased the annual number of square kilometers imaged: 7,400 in 1989, 90,000 in 1990, and 100,000 projected for 1991. AVIRIS has flown extensively over the United States, as well as sites in Canada and Central America, and most recently a wide variety of sites in Europe. AVIRIS data are finding wide utility in the areas of forest/vegetation ecosystem research, mineralogical surveying, oceanographic bioactivity, mountain snowpack analysis, and atmospheric water transport studies.[2] As the instrument's performance continues to improve, researchers in these fields will find additional value within the AVIRIS data, which we hope will lead to improved monitoring and understanding of geophysical and biological processes.

The following sections describe specific AVIRIS subsystems and changes made to them since 1987.

2. FOREOPTICS, FIBER OPTICS, AND IN-FLIGHT REFERENCE SOURCE

The AVIRIS scanner is a modified Kennedy scanner fitted with a custom scan mirror and aft optics. The aft optics image light onto the ends of four 200-micrometer-diameter fibers. From the 1987 to 1990 flight seasons, the optical components were exposed to the ambient atmosphere through the scan mirror aperture, thus allowing condensation to form on the surfaces once AVIRIS had landed after cold, high-altitude flights. Many of the front-surface mirrors had extensive degradation of their silver coatings by the end of four years of field operations. Before the 1991 flight season, all of the foreoptic mirrors were replaced, the scan mirror was resurfaced using replication technology* and a window with a special anti-reflection coating optimized for the short- and long-wavelength portions of the AVIRIS spectral range was placed over the entrance pupil. Also, the foreoptics housing was sealed and desiccant beds were placed inside the housing, as well as in the repressurization pathway for the air entering the housing upon aircraft descent. This ensures a benign environment for the front-surface silver-coated mirrors.

* From Ventura Optical Industries, Ventura, California.

Table 1. General Performance of AVIRIS

Parameter	Performance
Spectral coverage	0.40 to 2.45 micrometers
Spectral sampling interval	9.6 to 9.9 nanometers
Spectral channel width	9.8 to 12.5 nanometers FWHM
Number of spectral channels	224
Number of pixels per scan line	614
Number of scans per second	12
Instantaneous field-of-view (IFOV)	1.0 milliradians
Radiometric calibration accuracy	6%
In-flight stability	1%
Spectral calibration accuracy	±2 nanometers worst case

After this rework, the alignment and operation of the automatic focusing mechanism were tested and adjusted to the original design specifications. This mechanism keeps the fiber ends at the focal point of the system by responding to foreoptics housing temperature changes. The onboard computer monitors the temperature and alters the position of the mechanism's stepper motor based upon an empirically determined look-up table.

During 1990, the fiber optic harness was redesigned. This redesign accomplished two goals: first, it increased the ease of replacement in case of fiber damage, and second, it improved the utility of the In-Flight Reference Source (IFRS). The first feature resulted from the use of current fiber-optic connector technology. The original approach had used steel capillary tubes in a ball-joint mount[3], which allowed angular adjustment of the light cone coming out of the fiber onto the spherical mirror in the spectrometer, but which was very awkward to install and difficult to align. Angular adjustment of the fiber end was deemed to be an unnecessary requirement that had complicated the original design (measurement of actual fiber angles used ranged from 1° to 5°). The adoption of a modified biconic-type fiber connector** allowed easy removal and adjustment of a fiber in a spectrometer, thereby reducing the number of weeks required between instrument reassembly and completion of pre-season calibration.

The second feature of the redesigned fiber harness was a separate, anhydrous silica glass fiber bundle to channel light from the IFRS up to the foreoptics, as shown in Figure 1. These output fibers are arranged around the four input data fibers connected to the spectrometers. This arrangement allows the IFRS light to shine onto the backside of the shutter (sandblasted aluminum) and provide the spectrometers with a stable radiance source. In the previous implementation, the IFRS light was channeled to the spectrometers via separate fibers, thus bypassing the data fibers. This configuration allowed changes in the data fibers to go unnoticed and precluded any subsequent attempt to apply a correction to the radiometric calibration of the flight data based upon the IFRS signal acquired before each run.

Some care was required to produce IFRS light with spectral properties close enough to terrestrial radiance to provide useful signal levels in all four spectrometers. The 2,900-Kelvin color temperature of the quartz-halogen bulb was modified by a 2-millimeter-thick Schott KG-4 heat-absorbing glass filter. This spectral shaping, combined with the attenuation properties of the 1-meter length of anhydrous silica fiber† in the IFRS bundle, yields a useful (100 to 800 DN) signal over most of the 0.4- to 2.45-micrometer range. A current-controlled power supply for the quartz-halogen bulb was also added, which provides a radiant stability of ±3% for the IFRS output.

** From Fiberguide Industries, Highlight Division, Caldwell, Idaho.
† Anhydroguide G fiber, from Fiberguide Industries, Stirling, New Jersey.

ORIGINAL CONFIGURATION

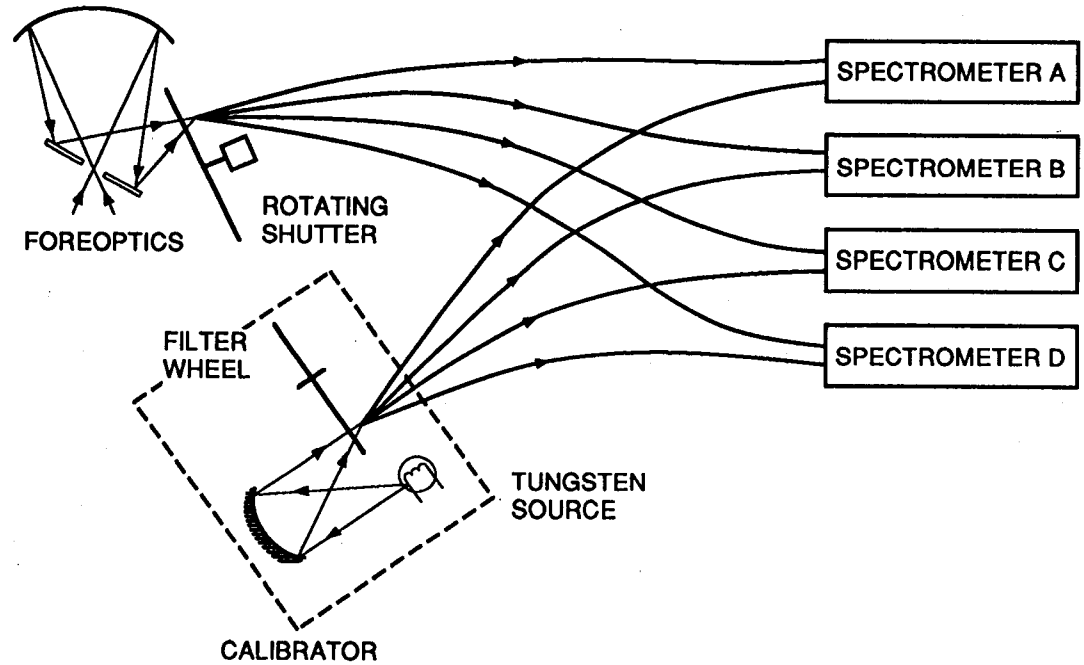

NEW CONFIGURATION

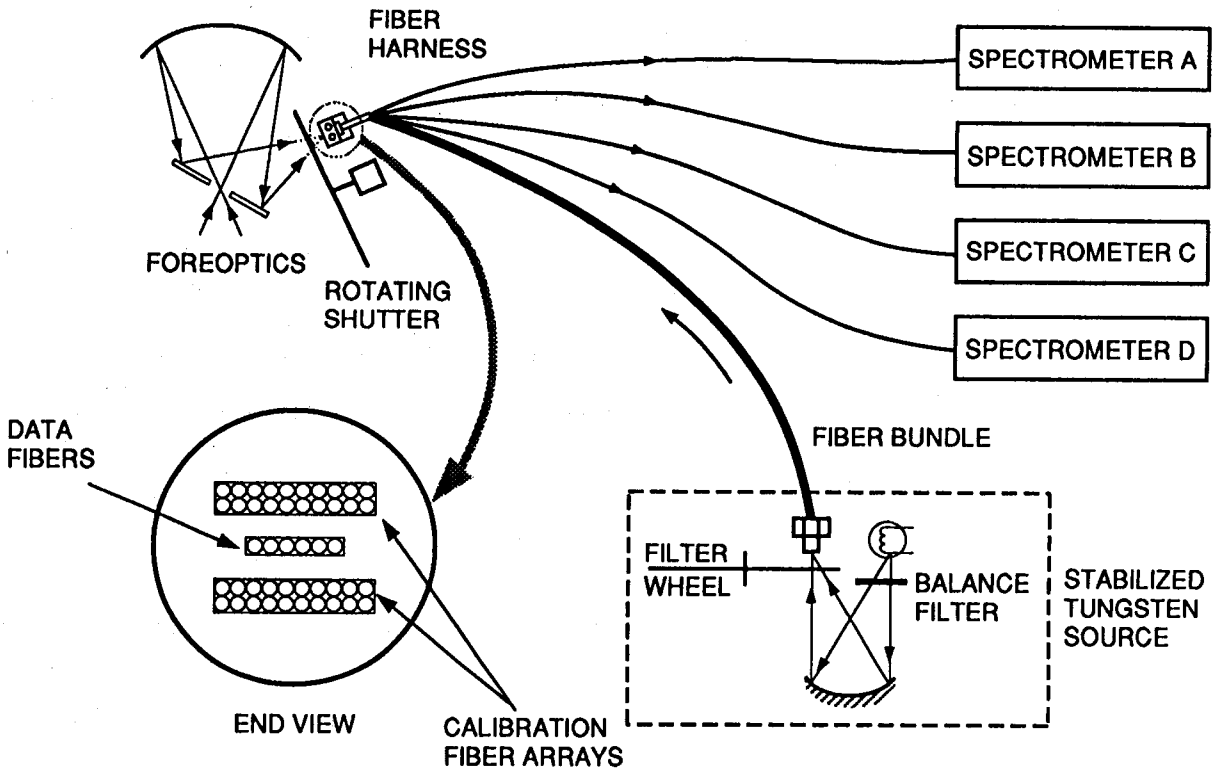

Figure 1.

3. SPECTROMETERS AND DETECTOR DEWARS

After the 1987 flight season, deficiencies in the stability of AVIRIS's radiometric and spectral response were discovered and steps were taken to rectify them.[4,5] Radiometric and spectral response stability is dependent upon many factors, but chiefly the mechanical stability of the spectrometer optical components relative to the detector arrays. Early in the development of the AVIRIS spectrometers, thermal control was identified as an important issue, since the Q-bay of the ER-2 aircraft can experience temperatures from +40° C immediately after launch down to -5° C during long high-altitude flights. The alignment-critical spectrometers were initially isolated from this frigid environment with a simple heating system and modest thermal blanketing. During 1988, several changes were made to improve the spectrometers' mechanical stability: First, the main support for the detector dewars on the spectrometer bodies was changed from Delrin (which was initially used for electrical isolation of the dewars) to aluminum, which improved the rigidity of that attachment. Second, the mounts fastening the spectrometers to the instrument frame were changed from rigid aluminum mounts to vibration-isolation mounts to prevent warpage of the frame from causing distortions in the spectrometer bodies. Third, a more sophisticated thermal control and blanketing approach was implemented.[6] These changes improved in-flight stability by an order of magnitude, from ±50% to ±5%.

Several failures of AVIRIS in the field can be attributed to water damage from condensation collected on the cold dewar surfaces during liquid nitrogen filling. This condensation dripped down into the spectrometers along a path that included the exposed ends of the hygroscopic zirconium-fluoride optical fibers. Before the 1990 flight season, AVIRIS was outfitted with new dewars that have improved cryogen fill and vent plumbing, and neoprene rubber skirts that encircle the dewars and prevent water or debris from getting into the spectrometers or near the fiber ends. However, humidity may still be able to slowly degrade the fluoride fibers along their lengths, even though they are in sealed sheaths. To prevent such damage from occurring and to improve overall system reliability, AVIRIS is now heated in the Q-bay with warm, desiccated air after flight. This warm air is provided by a special dry-air unit described in detail in Section 9.

4. SCAN DRIVE MECHANISM

During the 1989 and 1990 flight seasons, some imagery data showed evidence of scan drive jitter. Scenes over Los Angeles and over Stapleton Airport in Denver had scan line misregistrations from 1 to 3 pixels in magnitude that were visible in high-contrast features running parallel to the flight direction. Other images did not exhibit this artifact. Earlier, during initial testing in 1986, poor scan drive performance had been observed for some settings of the desmodromic cam clearances. The observation of scan drive jitter in the imagery prompted an effort to refurbish the scan drive, which, by the end of 1989, had exceeded its design lifetime of 600 hours by a factor of five.

The scan drive mechanism was first separated from the foreoptics, then disassembled. Next, the drive's components were closely inspected and new bearings installed. Finally, the drive was reassembled, with a redesigned coupling mechanism. This new coupling consisted of a flexible bellows structure secured to the drive and mirror shafts via cone-shaped locking rings. This design made reassembly and alignment easier and will make decoupling the scan drive from the foreoptics easier in the future. Though the coupling is expected to have adequate holding power, a preventive measure has been implemented to shut down the scan drive should the coupling ever slip. Such slippage could cause the drive mechanism to pound the scan mirror into the housing structure, causing potentially catastrophic damage. Hence, limit switches have been installed at the extremes of scan mirror travel to shut the drive down if contacted, and a software change in the data-processing facility allows monitoring of the scan drive linearity housekeeping data to detect any gradual coupling slippage.

The drive mechanism was tested at various operating temperatures and the overall drive linearity was found to be excellent, equal to or exceeding original performance levels. The pointing error was less than 0.5 milliradian (0.5 pixel) over the +30 to -30° C temperature range. Figure 2 shows a typical mirror pointing error for five consecutive scans at 25° C and 0° C. At room temperature, the residual oscillations in the pointing error profile appeared randomly variable and out of phase, but at lower temperatures, the oscillations grew increasingly consistent from scan to scan. The lower temperature performance may actually be better from an image fidelity standpoint: the change in pointing error from scan to scan for a given cross-track pixel would be less at a low temperature than it would be at room temperature. This would effectively bring the instrument's IFOV closer to the design goal and minimize the type of jitter seen in the Los Angeles and Stapleton Airport imagery. However, pointing misregistrations up to 0.4 pixel over a longer period of scans would still be possible; gyro roll correction can modify the mirror angle at which data acquisition actually begins.

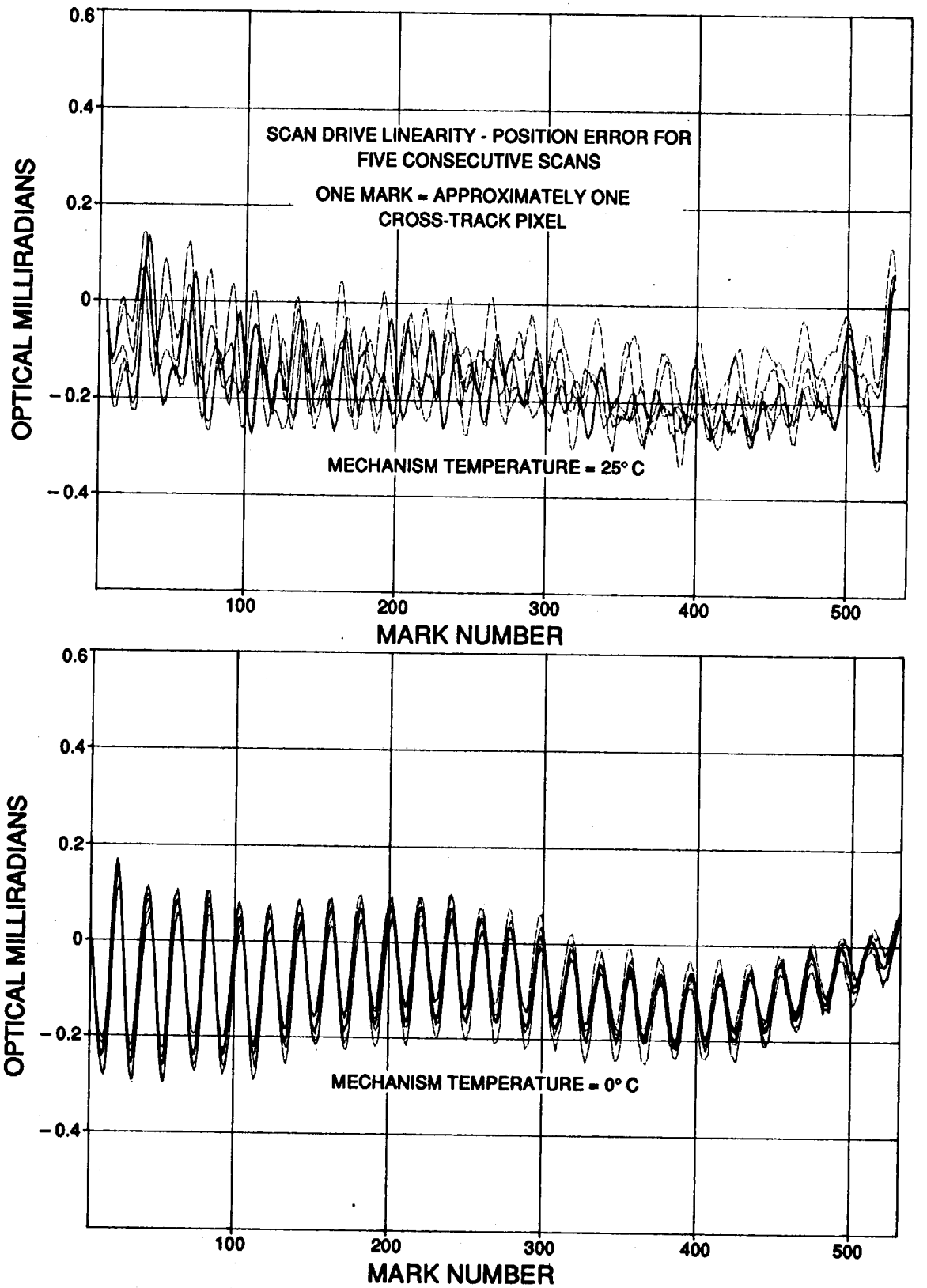
SCAN DRIVE LINEARITY - POSITION ERROR FOR
FIVE CONSECUTIVE SCANS
ONE MARK = APPROXIMATELY ONE
CROSS-TRACK PIXEL
MECHANISM TEMPERATURE = 25° C
OPTICAL MILLIRADIANS
MARK NUMBER
0.6
0.4
0.2
0
-0.2
-0.4
100
200
300
400
500
MECHANISM TEMPERATURE = 0° C
OPTICAL MILLIRADIANS
MARK NUMBER

Figure 2.

Table 2. Required and Achieved Performance of the AVIRIS Scan Drive

Parameter	Required	Achieved
Cumulative mirror pointing error over 1 scan line	0.5 pixel	< 0.45 pixel
Maximum scan-to-scan mirror pointing error for a given pixel:		
at 25° C	Not specified	0.3 pixel
at 10° C	Not specified	0.15 pixel
at 0° C	Not specified	0.08 pixel
Maximum pixel-to-pixel error within 1 scan line	0.1 pixel	0.08 pixel
Uncompensated motion of foreoptics housing due to vibration	0.1 pixel	0.05 pixel

Although the scan linearity appeared excellent (see Table 2), a residual scan-to-scan cross-track misregistration was detected after the scanner was integrated with the instrument. The IFOV of the foreoptics was measured at 1.0 milliradian with the scanner off and at 1.4 milliradians (RMS) with the scanner running. Figure 3 shows the IFOV response measured with the scan drive both on and off. Multiple peaks can be observed in the cross-track IFOV data taken with the scanner running. If the source of this IFOV broadening were the residual scan-to-scan pointing error discussed above, the profile would appear more Gaussian in shape.

Several potential sources of this broadening were investigated and absolved of blame: peak-to-peak vibration of the foreoptics housing was measured and found to be 0.048 milliradians in the cross-track direction (1/20th of a pixel); stability of the optical shaft encoder signals, which generate the start-of-scan signal, was confirmed; and cleanliness of the gyro roll correction signal was confirmed. A remaining candidate source of this image "jitter" is the position of the start-of-scan index pulse within the scan. Currently, the index pulse occurs very near the actual mirror turnaround; hence, any variation from scan to scan in the smoothness of the mirror turnaround can translate into a time variation for the beginning of a scan. This effect has been artificially demonstrated with data from the scan drive environmental testing. Unfortunately, simply moving the index pulse away from the scan turnaround position degrades the cross-track vignetting profile, although the jitter effect might be minimized with a very small adjustment. Greater adjustment may be possible by modifying a timing delay in the gyro roll correction loop.

5. SIGNAL CHAIN

Originally, AVIRIS was flown on a U-2 aircraft, and the weight limit this aircraft imposed on AVIRIS forced the design team to make a number of compromises in packaging the instrument electronics. When the U-2 was retired from the NASA fleet, AVIRIS was transferred to the ER-2 aircraft. The ER-2's heavier payload capability has allowed the sensitive detector timing generation electronics to be physically separated and opto-isolated from other digital electronics. This has resulted in a tremendous reduction in the noise, from between 4 to 6 DN over all four spectrometers in 1988 down to 1.5 to 2 DN in 1989 (see Table 3).

Before the 1990 summer flight season, detector preamp circuits were modified to accommodate new operational amplifiers with lower equivalent input noise and a higher slew rate. During noise-reduction efforts at the time of system integration, it was determined that timing jitter on the clock driver signal lines generated significant amounts of noise at the detector output.

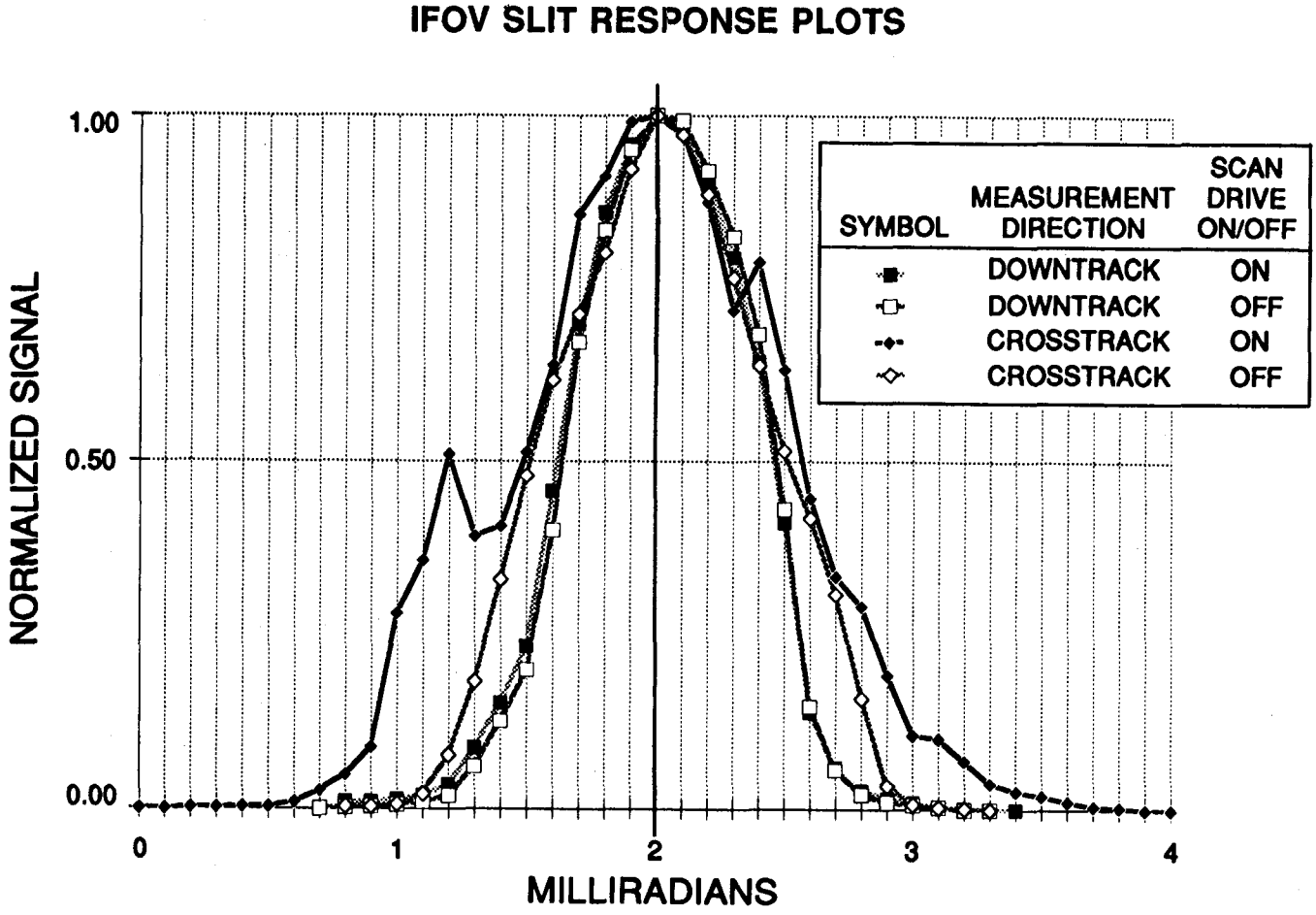

Figure 3.

One factor that aggravated this jitter was the opto-isolator used in the circuit. Device-to-device jitter performance variations were observed and a new opto-isolator type was selected. Also, the high-to-low transition at the opto-isolator output was observed to have markedly less jitter than the low-to-high transition. The high-to-low transition corresponds to the off-to-on transition of the LED, which has less uncertainty associated with its current vs. light output characteristic than the on-to-off transition does. The clock driver circuitry has been modified to use this cleaner signal edge.

Temperature sensor signal lines were also found to couple in noise from the instrument to the detector signals. These sensor lines were disconnected before the 1990 flight season. Self-induced noise was reduced further by improvements in cable shielding and component grounding. All these changes combined brought the overall noise level down to the 1.1- to 1.4-DN range in the lab, but the in-flight noise levels remain slightly higher. Future work will attempt to eliminate the noise coupling pathways that still remain in the system. In-flight noise levels should then approach those levels measured in the lab.

6. DIGITAL ELECTRONICS

At the beginning of the 1990 flight season, a problem developed in AVIRIS immediately after it arrived at the NASA/Ames Research Center in Mountain View, California. During the post-shipping checkout in the laboratory, the ground support equipment (GSE) computer would not display data from the instrument and indicated a "SYNC WORD NOT RECEIVED" error. The GSE processes instrument data major frame by major frame. It looks for the major frame sync word at the begin-

Table 3. Best In-Lab Noise Performance (RMS DN)[§]

Year	Spectrometer A	B	C	D
1987	4	3	7	10
1988	4.3	3.3	5.8	5.5
1989	1.6	1.9	1.9	1.5
1990	1.5	1.1	1.1	1.3
1991	1.35	1.05	1.1	1.2

[§] In-flight noise values are slightly higher.

ning of a major frame, and if that is incorrect, the GSE assumes that the entire major frame of data is bad. The GSE then issues only the error message.

The GSE instrument data simulator indicated that the GSE was operating properly. Troubleshooting then focused upon the embedded 8085-based multibus computer, which generates the sync word. The complexity of the instrument and the field environment mandated the assembly of a field tiger team. While troubleshooting progressed in the field, replacements for the three commercial boards in the computer were quickly procured. Science flights were suspended for a period of two weeks while operation of the instrument was restored and confidence reestablished. This episode clearly illustrated the need to stock field-replaceable parts for AVIRIS to minimize downtime during a busy flight season and maximize the chances to conclude a remote deployment successfully.

7. TAPE RECORDER

AVIRIS uses an Ampex AHBR-1700 high-density digital tape recorder with 5 gigabytes of storage. Up to 40 minutes of imaging data can be recorded onto a 14-by-1-inch reel of Ampex 799 certified tape. A brand-new, freshly degaussed reel is used for every flight. To satisfy tight weight and volume constraints, only half of the recording electronics are flown, leaving only the odd 14 tracks available for recording. For lower inter-track cross-talk and compatibility with the data facility playback unit (an Ampex HBR-3000), 28-track heads are used.

Over the more than three seasons that AVIRIS has been in service, the tape recorder has repeatedly been a source of difficulty in the field. The most critical problem has been the occasional inability of the data facility to read an AVIRIS tape. It has been recognized that the record-to-playback-speed ratio of 10.4 leaves no margin for misalignments between the instrument and the data facility machines. To prevent misalignments, preventive maintenance and alignment are performed on both tape units before the start of a season, then a test tape is run. This procedure has been in effect since the 1989 season and has resulted in good data transfer integrity; typical line dropout rates for the 1991 flight season are less than 1%.

In addition, tape path cleaning and tape threading—both labor-intensive activities—are performed during pre-flight preparation. To prevent tape misthreading, which would cause unreadable tapes, the buddy system is used: one person threads the tape and a different person checks the threading.

Two mechanical weak spots over the tape recorder's service life have been the tape tensioning brakes and the hub. These components have required unscheduled service several times and are expected to require attention again in the future. Improper tape tension compromises the quality of the recording and risks tape breakage in flight. The hub mechanism has been found to be intolerant to overtightening when a tape is being loaded, causing premature wear and greater difficulty in manual operation. A JPL-designed modification to the hub mechanism has made it more robust.

The AHBR-1700 model of tape recorder has been in existence for more than 15 years and is currently built to order only. The cost of stocking critical spare parts and procuring a backup tape recorder has become prohibitive. Experienced technical support has also become less available. Therefore, evaluation of a tape recorder update candidate is under way. The unit being evaluated is lighter, smaller in volume, and lower in cost, and it can record 80 minutes of AVIRIS data on a certified S-VHS cassette. Although not designed for a high-altitude airborne environment, this model is flown in low-altitude military airplanes and helicopters and endures other hostile environments. Acceptable operation will be demonstrated in simulated ER-2 mission environments before this unit is accepted as a replacement for the AHBR-1700.

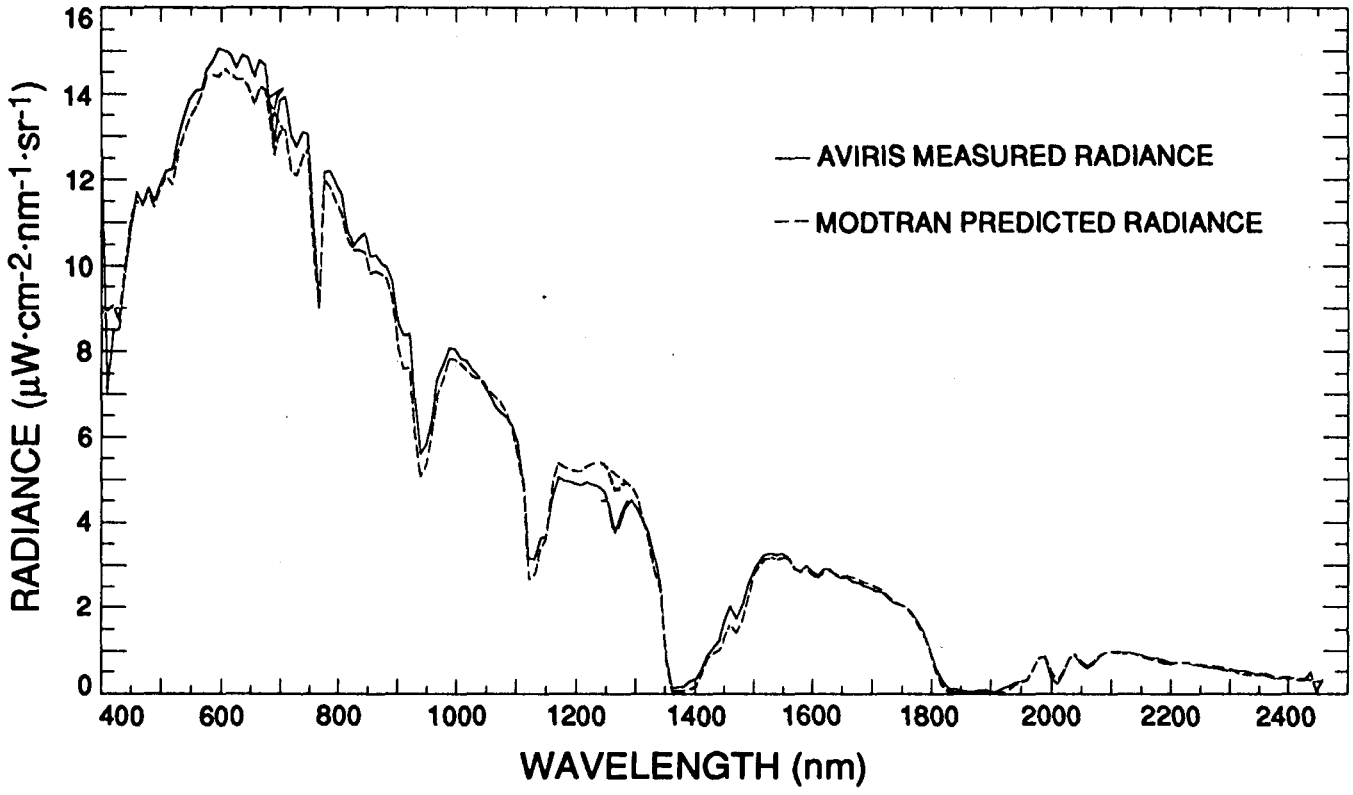

Figure 4.

8. CALIBRATION

Calibration allows quantitative analysis of AVIRIS-measured radiance as well as a comparison of data acquired from different regions and times. In addition, calibration is essential for analysis of AVIRIS data in conjunction with data measured by other surface, airborne, and spaceborne instruments. To provide confirmation of AVIRIS's in-flight characteristics, periodic validation/calibration experiments are performed.[7] During these experiments, measurements of the surface and atmosphere are acquired on the ground concurrently with AVIRIS's overflight. These *in situ* measurements are used to constrain the radiative transfer modeling algorithm and predict the upwelling radiance arriving at AVIRIS. Comparison of this predicted radiance with the AVIRIS reported radiance allows validation of the spectral and radiometric characteristics of AVIRIS in flight.

Figure 4 presents a comparison of the predicted and measured radiance for the AVIRIS in-flight validation/calibration experiment held at the Ivanpah Playa, California, on March 7, 1991. The agreement in spectral position of the atmospheric absorption features confirms AVIRIS's in-flight spectral characteristics. This agreement is assessed quantitatively through a non-linear least squares routine developed at JPL.[8] The absolute radiometric agreement between these data is better than 6%, excluding the strong atmospheric water bands at 1400 and 1900 nanometers. Figure 5 compares the signal-to-noise determined in flight for this experiment with the signal-to-noise requirement for AVIRIS. This requirement is based on a 50% reflectance surface illuminated at the 21.5° solar zenith angle (summer solstice, noon, 45° north latitude, sea level) through an atmosphere with 23 kilometers' visibility. In virtually all portions of the spectral range, AVIRIS is shown to exceed this requirement. AVIRIS's geometric characteristics are assessed through examination of linear features of high-reflectance contrast contained within the imagery.

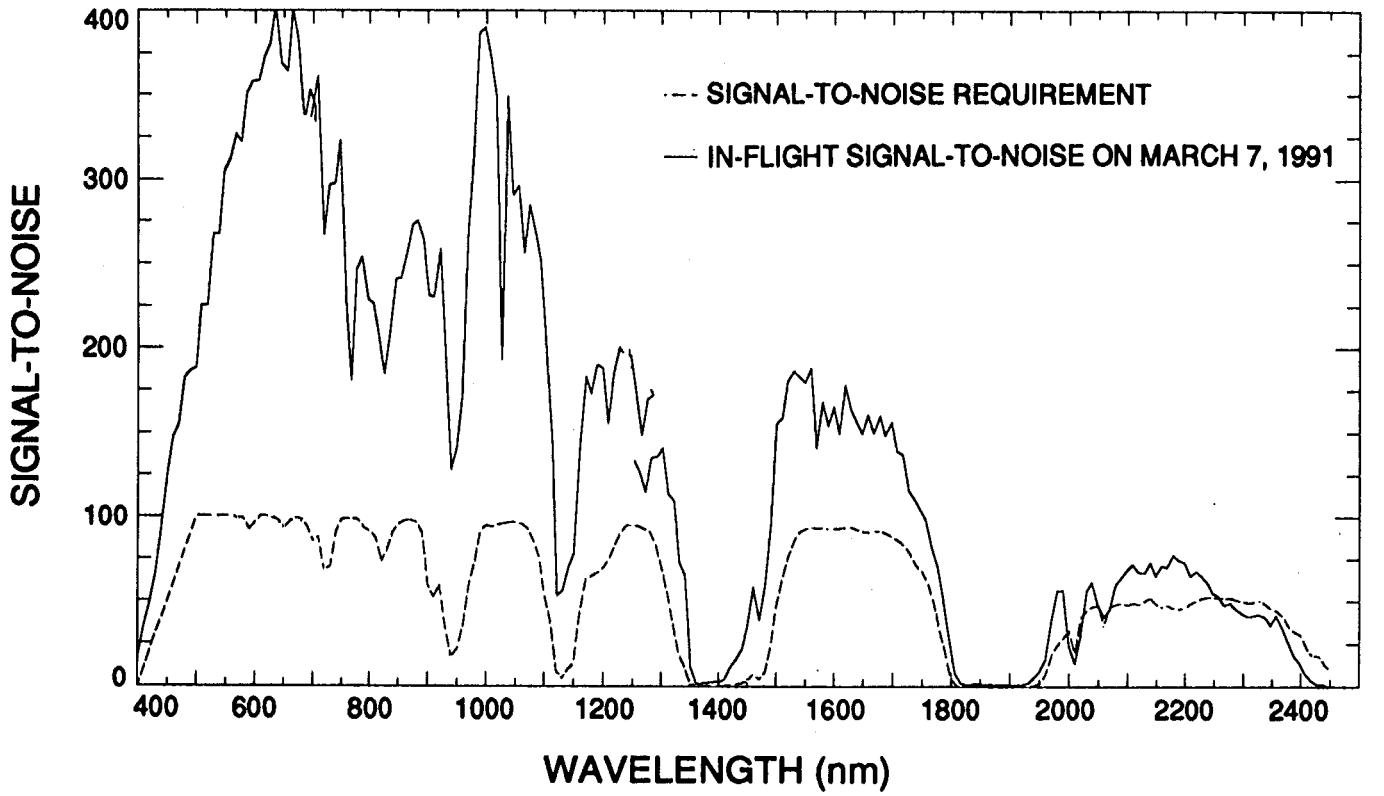

Figure 5.

During the 1990 flight season, the new foreoptics window generated a stray reflectance, which appeared as a 0.5% to 1% bump in the cross-track response near cross-track pixels 250 and 320 (the exact location depended upon the gyro roll correction at the time of data acquisition). This was found to be the result of reflected light off the fiber harness' polished end face traveling back through the foreoptics, reflecting off the window, and returning to the fibers. This minor artifact was removed before the 1991 flight season by applying an anti-reflection coating on the window and tilting the window so that any remaining return reflection missed the fiber ends.

9. GROUND SUPPORT EQUIPMENT

For the 1991 flight season, a second set of ground support equipment was assembled to ease logistical constraints and make more efficient use of the available prime flight season. When AVIRIS is deployed from the NASA/Ames Research Center (its normal base of operations) to a remote operations site, there is no longer instrument downtime while waiting for the GSE to arrive. With the GSE already in place, science flights can resume the day after the ferry flight arrives. This arrangement also makes overseas deployments feasible by eliminating the 6-week (or more) downtime required each way while the GSE is being shipped.

When AVIRIS began operating in the field in 1987, it was shipped on its transport cart inside a heavy two-piece wooden box whose lid was removable only by overhead hoisting (using a forklift or crane). A need to replace this huge shipping box with something easier to use and more suitable for long-term field operations quickly became apparent. Therefore, a lighter, yet more protective box has been built with a two-piece lid and an air-cushioned carrying frame inside. Three people can easily remove the cover. For strength and weatherability, the box has been constructed of fiberglass-covered plywood. The purpose

of the carrying frame is to provide a significant improvement in shock and vibration isolation during shipping. In addition, a climate-controlled air-ride van is always used for surface-shipping AVIRIS. The complex nature of the instrument, along with the desire to maintain stable calibration over a flight season, demands this level of care.

For a variety of scientific and logistic reasons, AVIRIS is frequently deployed to operational sites where the weather and humidity are potential causes of instrument performance degradation. This problem became apparent during AVIRIS's first deployment in 1987 to NASA's Goddard Space Flight Center/Wallops Flight Facility in eastern Virginia. In the normally high relative humidity there, the unprotected instrument began to deteriorate rapidly. After AVIRIS had been operated in an ambient environment of around 0° C during flights, heavy condensation was usually observed on the scan mirror.

AVIRIS degraded to the point where it was no longer yielding usable data and it was returned to JPL. Disassembly revealed that widespread damage, of varying severity, had occurred. The zirconium-fluoride IR fibers of the C and D spectrometers were beyond repair and had to be replaced. The lower spherical mirrors in all four spectrometers had condensation deposits, which were cleaned off, but which left behind minor corrosion damage to the coatings. The scan mirror had visible corrosion damage over its entire surface. However, the optical fiber and spectrometer repairs already performed had restored instrument performance to 90% of its previous level. Therefore, repair of the scan mirror was postponed until the time of the major foreoptics/scanner refurbishment discussed in Section 2.

In the winter of 1990, AVIRIS was deployed briefly to Kelly AFB in San Antonio, Texas. There, high humidity caused the loss of the D spectrometer signal once again. Although Kelly AFB normally has a benign environment at that time of year, a weather fluke brought in greater than 85% humidity. This impacted the instrument in less than a day. After this episode, the various safeguards against humidity described in Section 3 were implemented.

This marginal track record and a planned deployment to Wallops later in 1990 made the pressing need for environmental control painfully obvious. Therefore, a dry air unit (DAU)†† was procured that supplies 50 to 100 cubic feet per minute (cfm) of warm (32° to 38° C), dry (< 20% R.H.) air, and is used to purge the ER-2 equipment bay (the Q-bay) immediately following flights. The DAU is left on long enough to purge humid air out, as well as to warm the instrument to ambient levels. If the ambient humidity is high, the DAU purges the Q-bay between flights. When AVIRIS is out of the airplane, it is enclosed in the top portion of its shipping box, which is purged by the DAU. As an enhancement before the 1991 flight season, removable jack wheels have been installed on the top part of the box, to facilitate the opening and closing of the shipping box when AVIRIS is stored in the hanger. Two Wallops deployments that have occurred since the DAU's procurement have resulted in no instrument degradation attributable to humidity.

During AVIRIS's development and first flight season, the GSE used a desktop 8086/DOS computer for instrument checkout. This served the GSE's purpose, but the realities of pre-flight and the environment in the field, as well as the demands of laboratory calibration, required more timely performance and more thorough checkouts. An upgrade to a ruggedized industrial 286 with an EGA monitor made the GSE more user-friendly and durable.

During a shipping leg in the 1989 season, the laboratory rack containing the GSE computer was damaged, along with both the ground power supplies and the printer shipping box, due to improper securing inside the truck. To prevent such accidents from occurring in the future, the GSE computer, printer, and ground power supplies have been mounted in double-walled, foam-insulated, weatherproof, airline-rated transportable racks. No further equipment damage has resulted from shipping incidents.

When an anomaly occurs during instrument checkout, an instrument data simulator is used to effectively localize the problem between the instrument and the GSE. This has made troubleshooting expeditious in field operations as well as in the lab. Also, to facilitate troubleshooting and repair of the instrument in the field, a spare parts program is under way. Based on past experience and coordination of maintenance and upgrades, an inventory of field-replaceable components is accumulating.

†† From Later Engineering in Los Angeles, California.

10. CONCLUSIONS

Since 1987, AVIRIS has come a long way in fulfilling its original design goals and exceeding performance expectations. AVIRIS data have become increasingly useful for a widening range of remote sensing applications, and future efforts to improve the instrument will focus upon areas where the research community perceives the greatest need. The AVIRIS team will pursue these improvements as funding allows. Hopefully, AVIRIS will remain on the cutting edge of imaging spectroscopy and will contribute to the development of spaceborne sensors to be deployed in the next century.

11. ACKNOWLEDGMENTS

The AVIRIS team thanks Stan Jones, Charles Kurzweil, and Ron Steinkraus for their years of skilled work with the instrument hardware and sound advice on many issues, which together helped AVIRIS reach its current level of performance. The work described in this paper was carried out at the Jet Propulsion Laboratory, California Institute of Technology, under a contract with the National Aeronautics and Space Administration. Reference herein to any specific commercial product, process, or service by trade name, trademark, manufacturer, or otherwise, does not constitute or imply its endorsement by the United States Government or the Jet Propulsion Laboratory, California Institute of Technology.

12. REFERENCES

1. Wallace M. Porter and Harry T. Enmark, "A system overview of the Airborne Visible/Infrared Imaging Spectrometer (AVIRIS)," Proc. SPIE, 834, pp. 22–31, 1987.

2. Robert O. Green (editor), *Proceedings of the Second Airborne Visible/Infrared Imaging Spectrometer (AVIRIS) Workshop: June 4 and 5, 1990*, JPL Publication 90-54, Jet Propulsion Laboratory, Pasadena, California, 1990, and Robert O. Green (editor), *Proceedings of the Third Airborne Visible/Infrared Imaging Spectrometer (AVIRIS) Workshop: May 20 and 21, 1991*, JPL Publication 91-28, Jet Propulsion Laboratory, Pasadena, California, 1991 (this publication).

3. S.A. Macenka and M.P. Chrisp, "Airborne Visible/Infrared Imaging Spectrometer (AVIRIS): Spectrometer design and performance," Proc. SPIE, 834, pp. 32–43, 1987.

4. G. Vane, W.M. Porter, J.H. Reimer, T.G. Chrien, and R.O. Green, "AVIRIS performance during the 1987 flight season: An AVIRIS project assessment and summary of the NASA-sponsored performance evaluation," *Proceedings of the AVIRIS Performance Evaluation Workshop*, Gregg Vane (editor), JPL Publication 88-38, pp. 1–20, Jet Propulsion Laboratory, Pasadena, California, 1988.

5. G. Vane, T.G. Chrien, J.H. Reimer, R.O. Green, and J.E. Conel, "Comparison of laboratory calibrations of the Airborne Visible/Infrared Imaging Spectrometer (AVIRIS) at the beginning and end of the first flight season," Proc. SPIE, 924, pp. 168–178, 1988.

6. W.M. Porter, T.G. Chrien, E.G. Hansen, and C.M. Sarture, "Evolution of the Airborne Visible/Infrared Imaging Spectrometer (AVIRIS) flight and ground data processing system," Proc. SPIE, 1298, pp. 11–17, 1990.

7. R.O. Green, J.E. Conel, V. Carrere, C.J. Bruegge, J.S. Margolis, M. Rast, and G. Hoover, "Determination of the in-flight spectral and radiometric characteristics of the Airborne Visible/Infrared Imaging Spectrometer (AVIRIS)," *Proceedings of the Second Airborne Visible/Infrared Imaging Spectrometer (AVIRIS): June 4 and 5, 1990*, Robert O. Green (editor), JPL Publication 90-54, pp. 15–34, Jet Propulsion Laboratory, Pasadena, California, 1990.

8. R.O. Green, G. Vane, and J.E. Conel, "Determination of aspects of the in-flight spectral, radiometric, spatial, and signal-to-noise performance of the Airborne Visible/Infrared Imaging Spectrometer over Mountain Pass, Ca.," *Proceedings of the AVIRIS Performance Evaluation Workshop*, Gregg Vane (editor), JPL Publication 88-38, pp. 162–184, Jet Propulsion Laboratory, Pasadena, California, 1988.

THE I.R.O.E. ACTIVITY FOR THE AVIRIS CAMPAIGN IN EUROPE

Alessandro Barducci
Regione Toscana - Environment Dept.
Florence, ITALY

Ivan Pippi
C.N.R. - I.R.O.E.
Florence, ITALY

Abstract. This paper presents the activity of the I.R.O.E. in preparation to the next AVIRIS campaign in Europe. On the basis of the experience acquired during various remote sensing campaigns utilizing different aerospace sensors, we have developed a dedicate software to perform remote sensing image display and processing. This software program, named XIMATEL and written in C and FORTRAN-77 languages, uses the X-Window System graphics environment and allows the user to perform multitasking operations as well as to share graphics resources of different workstations connected through the Ethernet network link. XIMATEL provides the following relevant operations: multispectral and multitemporal analysis, geometrical and atmospheric corrections, spatial filtering, Fourier analysis, and thematic classification. In addition some preliminary results are presented and discussed.

I. INTRODUCTION

The remote sensing of the environment performed by aerospace sensors operating at visible and infrared wavelengths is an important tool for studying the Earth surface. Unfortunately the satellite sensors now available have poor spectral resolution for many applications.

For this reason a new generation of high spectral and spatial resolution sensors are planned to be placed in the near future on board the polar orbiting platforms. In order to test the performance of such instrumentation, some airborne imaging spectrometers have been built up [1]. Among them the AVIRIS (Airborne Visible/Infrared Imaging Spectrometer) represents the prototype for the spaceborne HIRIS (High-Resolution Imaging Spectrometer).

The AVIRIS operates in the whisk-broom imaging mode and has a spectral coverage from 0.40 to 2.44 um divided into 210 useful channels. The instantaneous field of view is 1 mrad and the number of cross-track pixels is 614. Since summer 1987 the AVIRIS, built by the JPL, has been operated on board the NASA ER-2 aircraft at an altitude of about 20 Km over many different sites in the United States. During next June and July the AVIRIS will fly for the first time in Europe.

II. I.R.O.E. ACTIVITY

The I.R.O.E. is interested in the development of new remote sensing sensors and has already been involved in various remote sensing campaigns utilizing different active and passive aerospace sensors. Moreover in the past it has received some AVIRIS images from the JPL in order to evaluate the sensor performance. Particular attention has been paid to the

development of new software packages which can perform the image processing and visualization starting from a great amount of data.

In order to evaluate the quality of the AVIRIS data collected over Italy during the next campaign in Europe, we will utilize the program named XIMATEL, developed in our institute.

A. SOFTWARE DEVELOPMENT

To satisfy the portability and compatibility requested by different potential users, this procedure has been developed in standard programming environments. The main program, which manages any graphics task, has been developed using the C programming language and the X-Window System graphics environment, and is connected to a wide data base containing spectral signatures of different constituents of the Earth surface, and to a library of subroutines, written in FORTRAN-77 language, for the image processing.

The X-Window System provides a user-server model in which the server carries out display and input services as demanded by the user application code. Communications between server and application are realized by means of a subroutine set, called X-lib, that provides building and decoding of message packets. The physical separation of the windowing system and of the server from the user application, based on a communication link, lends itself to implementations using high speed local area networks as the medium for message exchange. By allowing this separation user application can be executed on nodes different from the own workstation, eventually taking advantage of special or more powerful hardware.

As shown in Fig.1, XIMATEL as well as X-lib are device independent and adding or changing peripherals they only require X-server extension. This feature provides high portability for XIMATEL, getting the X-Window System more diffused.

The Fig.2 shows the manager panel of XIMATEL as displayed by a VAXstation 3500 running under the VMS operating system. It is made up of a menu bar, a window for input and output operations, and two windows for histogram and spectral features display. The six pull down menus enable various commands for image visualization and processing (such as load and save images trough disk files, false colours display, image corrections, image classifications, etc.). The main operations are discussed in the following sections.

1. IMAGE CORRECTIONS

Aerospace remote sensing images are affected by geometrical distortions as well as radiometric troubling. The geometrical distortions, due to perspective effects and optical aberrations, change the pixel positions and therefore mainly affect such applications as cartography. This effect is proportional to the field of view of the imaging system and is hence important for airborne observations but negligible in spaceborne ones. On the other hand optical degradation of the images, that happens during the radiation transfer within the atmosphere and sensor optics, changes the pixel radiance and its spectral features and therefore gives rise to errors when thematic classification or multispectral or multitemporal analysis are carried out. It is therefore necessary to eliminate these effects on the remotely sensed images before the image processing goes on.

(a) GEOMETRIC DISTORTION. A FORTRAN-77 subroutine of XIMATEL performs the geometric correction. This subroutine re-samples the image, positioning the new pixels at a priori computed locations so as to preserve the original metrics of the scene. The new pixel value of the corrected image by interpolation is calculated, allowing the user to choose between three different functions: the nearest pixel value, the straight line and the cubic splines. However this procedure does not correct for such factors as aircraft roll, pitch and true heading, ground holography and optical aberrations of imaging system, which generally create unpredictable distortions.

(b) ATMOSPHERIC EFFECTS. The aim of image remote sensing generally should be to evaluate the scene reflectance for visible and near infrared observations, or the scene emitted radiance for thermal infrared ones. It is nevertheless well known that the measured radiance is affected by the atmosphere as stated by the following relationship:

$$L_o(\lambda,\theta) = \frac{1}{\pi}[E(\lambda,\theta)\rho(\lambda) + \epsilon(\lambda)B(\lambda,T)]\exp[-\tau(\lambda)\sec(\theta)] + L_u(\lambda,\theta) \qquad (1)$$

where θ is the zenithal distances of the line of sight, Lo the observed radiance, E the irradiance at the ground, ρ the reflectance, ϵ the emissivity, B the Planck function and τ the atmosphere optical thickness. Lu is the up-welling radiance due to atmospheric scattering and thermal emission [2]. In the previous equation the cross-talk between different pixels, for example produced by atmospheric aerosol and telescope optics, is neglected.

If a physical model of atmosphere and solar irradiance is known, then it is possible to invert Eq.(1). XIMATEL uses the LOWTRAN 7 computer code [3] to calculate E, τ and Lu, and then retrieves the reflectance ρ for visible images or the blackbody radiance $\epsilon \cdot B$ for thermal infrared ones.

2. IMAGE PREPROCESSING

XIMATEL implements a set of FORTRAN-77 subroutines that carries out a series of mathematical elaboration on the images. These applications are regarded by XIMATEL as preprocessing and comprise the following relevant tasks: image enhancement by histogram equalization or hyperbolization, and smoothing.

To reduce the image noise by smoothing techniques, two different methods have been used: the selective local average, as edge preserving, iterative enhancement and local pixel selective smoothing, and special processing to eliminate fine amplitude components as symmetric hysteresis smoothing and median filter.

Furthermore XIMATEL allows us to perform the Fourier analysis of the images. A FORTRAN-77 subroutine of the XIMATEL achieves the two dimensional fast Fourier transform (FFT) of the image, and its power spectrum is displayed on the screen. It is also possible to multiply the FFT by an user supplied weighting function (filter), or by the FFT of another image (correlation) and then to compute the inverse transformation. The Fourier analysis also is a powerful tool to evaluate the imaging system performances, because it allows to recognize and to suppress such imaging noise as spikes or periodic patterns.

3. IMAGE PROCESSING

The processing is regarded by XIMATEL as the final step of image working out. To achieve the thematic classification, those applications that involve the recognition and the identification of structures and features in the images held are here executed. For this purpose XIMATEL utilizes various FORTRAN-77 subroutines, all based on two different approaches: histogram and spectral analysis.

The histogram approach is based on the maximum likelihood, or Bayes optimal classification. It treats the histogram as a multi-modal probability distribution given by a weighted sum of various probability density (Gaussian) functions, each one corresponding to different classes. The main problem, which is to compute the probability density functions and the respective weights, is solved by least squares fit, so that the maximum number of recognizable classes is only limited by the amount of grey levels of the raw image. XIMATEL performs maximum likelihood classification on single image and then display the image map together with synthetic and true histogram.

XIMATEL realizes the spectral analysis by looking for maximum correlation between the spectrum of each pixel of the image and the available laboratory reflectance spectra of different compounds stored into a data base. The output consists of the spectral response display of both image and laboratory spectra.

Furthermore XIMATEL provides a set of binary operators which may be applied to image couples. The operators set comprises the four arithmetical operations and the following bitwise operators: and, or, exclusive or.

B. PRELIMINARY RESULTS

To evaluate the AVIRIS performances, we have applied the XIMATEL procedure to data acquired over Cuprite and Moffett Field in 1989. Applying the histogram and the Fourier transform, the images at the central wavelength of each spectrometer have been analysed. The relevant result is the recognition of some periodic noise patterns present in all the considered images, as reported in Fig.3 for the channels 16 and 192. Their power spectra exhibit two spikes and some other vertical straight lines with a widespread frequency range, probably due to electromagnetic interferences or mechanical vibrations.

In addition the image classification using the maximum likelihood method and the spectral features analysis have been performed. We remark that the high spectral resolution and the extended photometric dynamics, typical of the AVIRIS data, allow to obtain detailed thematic maps.

III. CONCLUSIONS

The next European AVIRIS campaign will provide the remote sensing of the environment in several test areas. The extremely high data amount requires the use of powerful hardware and software processing systems. The I.R.O.E. is mainly interested in AVIRIS performances evaluation, also in comparison with the other sensors flying at the same time like the TIMS and the TMS.

Therefore we have realized the XIMATEL computer code, running under

the X-Window System, which performs multitasking operation as well as shares graphics resources of different workstations. It is also equipped with a subroutine set that enables us to perform the full image working out: from correcting for atmospheric effects and geometrical distortions up to the thematic classification. This software has been tested utilizing the AVIRIS data acquired over Cuprite and Moffett Field in 1989 and received by the JPL.

This work is partially supported by a cooperation agreement between C.N.R. and Regione Toscana.

REFERENCES

[1] Proceedings of "Imaging Spectroscopy of the Terrestrial Environment", G. Vane editor, SPIE vol.1298, 1990.

[2] P.N.Slater, "Remote Sensing - Optics and Optical System", Reading, Mass., Addison-Wesley, 1980.

[3] F.X.Kneizys, G.P.Anderson, E.P.Shettle, W.O.Gallery, L.W.Abreu, J.E.A.Selby, J.H.Chetwynd, S.A.Clough, "Users Guide to LOWTRAN 7", AFGL-TR-88-0177, 1988.

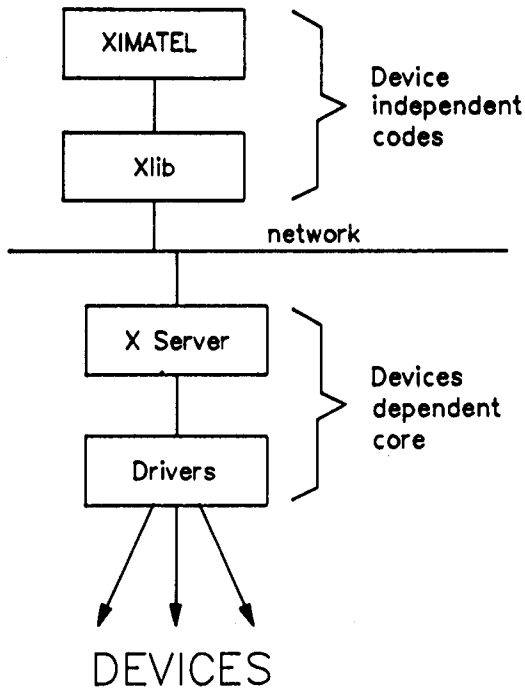

Fig. 1. The workstation configuration under X-Window System.

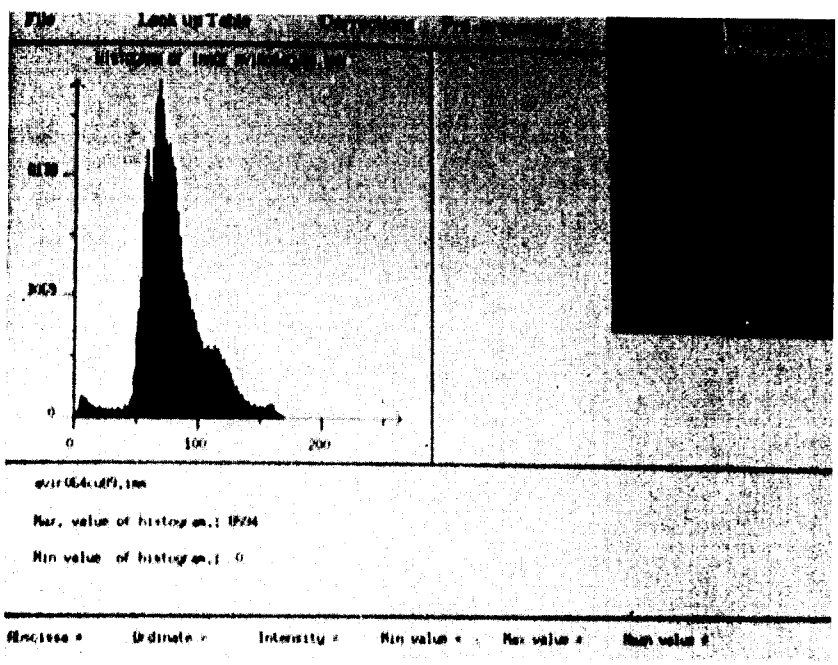

Fig. 2. XIMATEL panel manager.

(A)

(B)

Fig. 3. AVIRIS spectral images and their power spectrum (FFT). (A) Cuprite channel n.16 (0.5425 um); (B) Cuprite channel n.192 (2.1333 um);

(C)

(D)

(cont'd)

Fig. 3. AVIRIS spectral images and their power spectrum (FFT). (C) Moffett Field channel n.16 (0.5425 um); (D) Moffett Field channel n.192 (2.1333 um).

SLIDE CAPTIONS

Slide No.	Caption	Senior Author
1	An AVIRIS image cube for data acquired over Mount Shasta, California.	Green
2	The 224 images corresponding to each AVIRIS channel from 400 to 2450 nm for the Mount Shasta, California scene.	Green
3	A Spectral Mixture Analysis, Pine Creek, California: Red: Developed Soil. Blue: Underdeveloped Soil. Green: Vegetative.	Fischer
4	A false color composite showing visible, NIR, and SWIR green-leaf fractions estimated from the spectral subsets as red, green, and blue, respectively.	Roberts
5	Water vapor retrieved from four consecutive overflights of the AVIRIS calibration site at Rogers Dry Lake, California. Both lateral heterogeneity and variation in water vapor through time are shown.	Green
6	Retrieval of atmospheric and leaf water for pivot alfalfa fields from AVIRIS-measured radiance in Mesquite Valley, California. The images from top left to lower right are reflectance offset, reflectance slope, leaf water, atmospheric water vapor, residual radiance, and a number of iterations for solution.	Green
7	Scene classification of vegetation anomalies on the recultivated waste deposit area: Blue: No anomaly class. Light blue: Weak anomaly class. Dark green: Moderate anomaly class. Red: Strong anomaly class. An aerial photograph of the open site in October 1941 and 1943. The infill structures show a correlation with the distribution of the "strong" anomaly class. (British Crown Copyright, RAF photograph.)	Lehmann
8	Classification of GER Airborne Scanner Data (Reventon): (a) Black and white: GER band 7 (551 nm). Red, green, blue: Bare soil targets with different spectral signatures [see (c)].	Lehmann

(b) Red-green-blue natural color display, GER band combination:

Band 18: 687 nm (red).
Band 7: 551 nm (green).
Band 2: 489 nm (blue).

All bare soil targets are characterized by high intensities in channels 2, 7, and 18.

(c) SWIR wavelength range of soil spectra, selected as a basis for the classification [see (a)]. Spectral differences (albedo, absorption depth) are caused by variable mineral content.

Solid lines: Reflectance spectra retrieved from GER airborne scanner data.

Dotted lines: Field spectra of the corresponding target, acquired with the IRIS Mark IV spectroradiometer during the simultaneous ground truth.

9	An AVIRIS image over Rogers Dry Lake, California, acquired on July 23, 1990. The in-flight calibration site is shown as site A in the image.	Green
10	A Saved Screen Displaying AVIRIS Image and Spectra.	Jansen
11	nPDF Distribution of Test Area.	Cetin
12	nPDF Distribution of Training Fields.	Cetin
13	Automated Classification Results.	Shen
14	Advanced Hyper-Spectral Image Analysis Software System.	Shen
15	Four separate images:	Mackin

Top left is a brightness image of the AVIRIS data covering the 2.0 mm to 2.5 mm wavelength region. The area of interest is shown outlined in red. There are two dark circular regions in the area of interest that correspond to a mineralized area currently being mined. North is to the right.

Bottom left is an image of a corresponding material identification map, with north to the right. The map is based on shape analysis alone, prior to the expert system stage.

Red: Undifferentiated clays. (muscovite, illite, and kaolinite).
Blue: Dry vegetation.
Yellow: Chlorite.
Dark green: Green vegetation.

The clays are seen to dominate the area of interest (outlined in red in the brightness image) and are confined primarily to the phyllites of the Preble formation to the east of the Getchell fault (bottom quarter of the image). The only distinct feature to the west of the fault is an area rich in chlorite (yellow).

Top right is an image of another material identification map of the GER data over the outlined area of interest of the AVIRIS data. In this image, the clays are separated: red is illite, green is kaolinite, and blue is muscovite. Note the rotation of the image relative to the AVIRIS data; here north is to the top. The bright red area (center left of the top right image) is an area of illite, that corresponds to an active mine area, with disseminated gold mineralization. The blue-green area consists of muscovite and kaolinite with no economic mineralization.

Bottom right is an image of a corresponding map after the expert system stage. Although the number of accepted pixels is reduced, the general distribution of clay materials remains unchanged, except for an area of illite (red) in the shape image (top right image, center right), that is rejected in the expert system output (bottom right image). This essentially confines the illite distribution to the area of economic mineralization currently being exploited (red, bottom right image).

16 A classified map resulting from mixture space interpretation. The classes that are relatively pure such as the annual and graminaceous communities and the bare ground have solid coloring of green, yellow, and red respectively. The region, where the chaemophytic shrub community dominates, exhibits large variations in density to show this vegetation density map (derived by adding the dry and green vegetation maps together) is used as a backdrop. The community is displayed in various shades of cyan,where grey indicates a low density and bright cyan indicates a high density. Mackin

17 A low-altitude aerial photograph of the annual grassland at Jasper Ridge. The grassland is located in the central portion of the slide, with chaparral and oak woodlands present at the edges of the photograph. AVIRIS pixels were extracted from the grassland for the three dates of imagery. The isolated trees in the grassland were avoided during pixel extraction. Elvidge

18 An AVIRIS radiance image of the Clark Mountains scene on the left, and total-column water vapor retrieved from AVIRIS on the right. The water vapor varies from 8 to 22 mm of precipitable water within this 11-by-40-km region. Green

19	An AVIRIS radiance image of the Clark Mountains scene on the left. Surface-pressure elevation derived from the absorption of the 760-mm oxygen absorption band measured within the AVIRIS spectrum on the right.	Green
20	Optical thickness contours for Scene A at 20 m, 60 m, 120 m, and 240 m spatial resolution.	Berendes
21	Optical thickness contours for Scene B at 20 m, 60 m, 120 m, and 240 m spatial resolution.	Berendes
22	Identification of pixels rich in "rhyolit" in the walls of Easy Chair Crater.	Farrand
23	A color composite of the LCVF scene with the cinder fraction image as red, rhyolite as green, and RMS error as blue.	Farrand
24	Color-coded parameter images of AVIRIS for the deepest absorption.	Okeda
25	A false color image and a λ_1 image superimposed on band 17 for a part of eastern Yingan Shan.	Okeda
26	A 5-km x 5-km area of patchy, thin snow in Tioga Pass region, Sierra Nevada, California. Tioga Lake is partially ice/snow covered and is located in the center-right portion of the slide. North is to the upper right.	Nolin
27	An 8.5-km x 5-km image of snow grain size with Mammoth Mountain, California, in the central portion of the slide. Largest grains are red, large-medium grains are blue, and smallest grains are yellow.	Nolin